

AD A 045950

AFFDL-TR-77-40

12
S
K

**NOISE AND SONIC FATIGUE OF HIGH LIFT DEVICES
AEROACOUSTIC LOADS**

*DOUGLAS AIRCRAFT COMPANY
MCDONNELL DOUGLAS CORPORATION
3855 LAKEWOOD BLVD.
LONG BEACH, CALIFORNIA 90846*

JULY 1977

DDC
RECEIVED
OCT 25 1977
C

TECHNICAL REPORT AFFDL-TR-77-40
FINAL REPORT FOR PERIOD MARCH 1975-MAY 1977

AD NO. _____
DDC FILE COPY

Approved for public release; distribution unlimited


AIR FORCE FLIGHT DYNAMICS LABORATORY
AIR FORCE WRIGHT AERONAUTICAL LABORATORIES
AIR FORCE SYSTEMS COMMAND
WRIGHT-PATTERSON AIR FORCE BASE, OHIO 45433


NOTICES

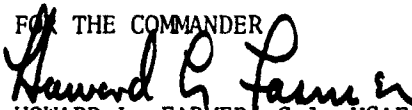
When Government drawings, specifications, or other data are used for any purpose other than in connection with a definitely related Government procurement operation, the United States Government thereby incurs no responsibility nor any obligation whatsoever; and the fact that the Government may have formulated, furnished, or in any way supplied the said drawings, specifications, or other data, is not to be regarded by implication or otherwise as in any manner licensing the holder or any other person or corporation, or conveying any rights or permission to manufacture, use, or sell any patented invention that may in any way be related thereto.


This report has been reviewed by the Information Office (OI) and is releasable to the National Technical Information Service (NTIS). At NTIS it will be available to the general public, including foreign nations.

This technical report has been reviewed and is approved for publication.


RALPH M. SHIMOVETZ
Project Engineer


ROBERT M. BADER, Chief
Structural Integrity Group
Structural Mechanics Division

FOR THE COMMANDER

HOWARD L. FARMER, Col, USAF
Chief, Structural Mechanics Division

ACCESSION for	White Section <input type="checkbox"/>
NTIS	Buff Section <input type="checkbox"/>
DDC	
UNANNOUNCED	
JUSTIFICATION	
BY	DISTRIBUTION/AVAILABILITY CODES
Dis:	3/77 SPECIAL
	

Copies of this report should not be returned unless return is required by security considerations, contractual obligations, or notice on a specific document.

Unclassified

SECURITY CLASSIFICATION OF THIS PAGE (When Data Entered)

REPORT DOCUMENTATION PAGE		READ INSTRUCTIONS BEFORE COMPLETING FORM	
18 (1) REPORT NUMBER AFFDL TR-77-40 ✓	2. GOVT ACCESSION NO.	3 RECIPIENT'S CATALOG NUMBER 9	
4 TITLE (and Subtitle) NOISE AND SONIC FATIGUE OF HIGH LIFT DEVICES. Aeroacoustic Loads.		5 TIME OF REPORT PERIOD COVERED Final Report. Mar 75 - May 77.	6 PERFORMING ORG. REPORT NUMBER
7 AUTHOR(S) H. L. / Leve, M. A. / Yeneriz, (USC) C. M. / Hooper, D. A. / Plocher		8 CONTRACT OR GRANT NUMBER(s) 15 F33615-75-C-3057 New	
9 PERFORMING ORGANIZATION NAME AND ADDRESS Douglas Aircraft Company ✓ 3855 Lakewood Blvd. Long Beach, California 90846		10 PROGRAM ELEMENT, PROJECT, TASK AREA & WORK UNIT NUMBERS 62201F / 1367 / 04/14 16 17 04	
11 CONTROLLING OFFICE NAME AND ADDRESS Air Force Flight Dynamics Laboratory Air Force Systems Command Wright-Patterson Air Force Base, Ohio 45433		12 REPORT NUMBER 11 July 77	13 NUMBER OF PAGES 368 (12) 393 p.
14 MONITORING AGENCY NAME & ADDRESS (if different from Controlling Office)		15 SECURITY CLASS (of this report) Unclassified 15a DECLASSIFICATION/DOWNGRADING SCHEDULE	
16 DISTRIBUTION STATEMENT (of this Report) Approved for public release; distribution unlimited			
17 DISTRIBUTION STATEMENT (of the abstract entered in Block 20, if different from Report)			
18 SUPPLEMENTARY NOTES (DAC) - Douglas Aircraft Company (USC) - University of Southern California (Subcontractor to DAC)			
19 KEY WORDS (Continue on reverse side if necessary and identify by block number) Externally Blown Flap Fluctuating Pressures Test Program Under-the-Wing Blowing Single-point Statistics Parameter Variations Over-the-Wing Blowing Two-point Statistics Non-Dimensional Parameters Jet Impingement Static Pressures Data Trends Aeroacoustic Loads Heat Transfer Prediction Methodology			
20 ABSTRACT (Continue on reverse side if necessary and identify by block number) An extensive experimental program, applicable to externally blown flaps (EBF) of STOL vehicles, was conducted providing detailed information on the surface loads produced during jet impingement. Test specimens used in the program were varied from a simple flat plate to a complicated wing-flaps configuration. An underlying premise concerning the test specimen selection was that simple plate specimens can provide useful			

DD FORM 1 JAN 73 1473

EDITION OF 1 NOV 65 IS OBSOLETE
S/N 0102-014-6601

Unclassified

SECURITY CLASSIFICATION OF THIS PAGE (When Data Entered)

116400

Jrac

Unclassified

SECURITY CLASSIFICATION OF THIS PAGE(When Data Entered)

20. ABSTRACT (cont.)

data for wing-flaps configurations. For several categories of parameters, a wide range of magnitudes were tested to cover possible EBF STOL design configurations. A prediction methodology was developed for the fluctuating pressure characteristics on surfaces exposed to the jet.

The test specimens included flat and curved plates and a wing-flaps model. The curved plates were continuous surfaces simulating under-the-wing blown flaps (UBF) and over-the-wing blown flaps (OBF) configurations. The wing-flaps model represented a UBF configuration. Besides the different specimens, the test program considered five categories of parameters; namely (1) jet Mach number, (2) temperature of the jet, (3) nozzle configuration, (4) relative position between nozzle and specimen, and (5) deflection angle at downstream edge of specimen. From the test results, a method is developed for predicting the fluctuating pressures produced during jet impingement on a flat plate. The flat plate data are then linked through the prediction method to the flap data for the RMS levels.

Data collected from the test cases for each specimen included static pressures and 'single and two-point' statistics of the fluctuating pressures. In addition, temperature data were obtained in flat plate cases for heat transfer studies. The purposes in measuring static pressures were to (a) locate stagnation points on the surface of the flat plate and (b) provide background information for understanding fluctuating pressure trends. The fluctuating pressure characteristics considered in the program were (1) overall RMS level, (2) frequency at the peak of the power spectrum, (3) half-power frequency of the power spectrum, (4) peak amplification or peakedness of the power spectrum, (5) high frequency rolloff rate of the power spectrum, (6) maximum magnitude of the narrow band correlation spectrum for separated locations, (7) frequency at the maximum of the narrow band correlation spectrum and (8) narrow band convection speed. These results for each test case are tabulated on layouts of the specimen surfaces showing them in their proper spatial relation to each other. The results are also plotted for ease in recognizing trends produced from parametric variations. The more pronounced trends are discussed along with possible reasons for them. *

Unclassified

SECURITY CLASSIFICATION OF THIS PAGE(When Data Entered)

FOREWORD

The work in this report was conducted by the Douglas Aircraft Company (DAC) under USAF Contract F33615-75-C-3057, Project 1367, "Structural Integrity for Military Aerospace Vehicles", Task No. 136704, "Aeroacoustic Problems in Flight Vehicles". The experimental portion of the project was subcontracted to the University of Southern California (USC). The work was accomplished under the direction of the Structural Integrity Branch, Structural Mechanics Division, Air Force Flight Dynamics Laboratory, Air Force Wright Aeronautical Laboratories, Wright-Patterson Air Force Base. Mr. R. M. Shimovetz, AFFDL/FBED, was Project Engineer.

The project was performed in the period from March 1975 to May 1977. Submittal of the report in May 1977 completed the technical effort. Dr. H. L. Leve (DAC) was Principal Investigator and was assisted by Mr. M. A. Yeneriz (DAC), Dr. C. M. Ho (USC) and Mr. D. A. Plocher (USC). In addition, acknowledgment for their efforts on the project is given to the following persons: Mr. G. E. Hinote (DAC), Mr. D. Irvin (USC) and Mr. R. D. Talmadge (AFFDL). Appreciation is also extended to Mr. H. F. Doering (DAC), Mr. R. M. Heimbaugh (DAC), Mr. D. E. Hines (DAC), Ms. B. B. Ingram (DAC) and Mr. N. S. M. Nosseir (USC).

TABLE OF CONTENTS

SECTION	PAGE
I INTRODUCTION	i
II TEST PROGRAM DESCRIPTION	6
1. Jet and Geometric Parameters	6
a. UBF Design	6
b. OBF Design	7
2. Parameter Ranges	8
a. UBF System	8
b. OBF System	9
3. Test Configurations	11
4. Test Cases	12
5. Test Data	15
a. Temperature Data	15
b. Fluctuating Pressure Data	16
III EXPERIMENTAL DETAILS	20
1. Test Items	21
a. Nozzles	21
(1) Round	22
(2) Lobed (Daisy)	22
(3) OBF	24
b. Plates	25
(1) Flat Plates	25
(2) UBF Curved Plates	26
(3) OBF Curved Plates	26
c. Wing-Flaps Model	28
2. Specimen Set-up	29
3. Instrumentation	35
a. Fluctuating Pressure Measurements	35
b. Static Pressure Measurements	38
c. Temperature Measurements	39
4. Data Processing	41
a. On-Site	41
b. Digital System	41

TABLE OF CONTENTS (cont'd.)

SECTION	PAGE
IV TEST RESULTS	45
1. Flat Plate	45
a. Static Pressure	45
b. RMS Level of Pressure Fluctuations	46
c. Spectra	47
d. Convection Velocity	49
e. Coherence	50
2. UBF Curved Plate	51
a. Static Pressure	51
b. RMS Level of Surface Pressure Fluctuation	51
c. Spectra	52
d. Coherence	53
e. Narrow Band Convection Speed	53
3. Wing-Flaps Model	54
a. RMS Level of Pressure Fluctuations	54
b. Spectra	54
c. Coherence	55
d. Narrow Band Convection Speed	55
4. OBF Curved Plate	55
a. Static Pressure Distribution	56
b. RMS Level of Pressure Fluctuations	56
c. Spectra	56
V DATA NORMALIZATION AND PREDICTION METHOD	99
1. Normalization Concept	107
a. Fluctuating Pressures	107
b. Heat Transfer from a Round Nozzle	106
2. Computational Procedure	108
a. Stagnation Point Location	108
b. Fluctuating Pressures-RMS Levels	109
(1) Circular Nozzle Geometry	109
(2) Daisy Nozzle Geometry	110

TABLE OF CONTENTS (cont'd.)

SECTION	PAGE
V DATA NORMALIZATION AND PREDICTION METHOD (cont'd.)	
c. Fluctuating Pressures-Power Spectrum Characteristics	114
d. Heat Transfer to a Flat Plate	117
VI CONCLUSIONS	135
APPENDIX A DETAIL TEST CASES	143
APPENDIX B LABORATORY DESCRIPTION	148
1. Air Supply System	149
2. Valve and Controller	149
3. Heater	149
4. Settling Chamber	150
5. Anechoic Chamber	151
APPENDIX C NOZZLE DETAILS	153
1. Lobed Nozzle Details	153
2. OBF Nozzle and Contraction Section Details	154
APPENDIX D INSTRUMENTATION LOCATIONS IN TEST SPECIMENS	155
1. Static and Fluctuating Pressure Measuring Plate	155
2. Thermocouple Plate	157
3. UBF Curved Plates	158
4. OBF Curved Plates	159
5. Wing-Flaps Model	160
APPENDIX E GEOMETRIC CENTER OF IMPINGEMENT	161
1. UBF Curved Plates	161
2. Wing-Flaps Model	162
APPENDIX F ACOUSTIC REASONANCE STUDY	164
APPENDIX G TEMPERATURE MEASUREMENTS	167
APPENDIX H STATIC PRESSURE MEASUREMENTS	176
APPENDIX I FLUCTUATING PRESSURE TRENDS	189
APPENDIX J TABULATIONS OF FLUCTUATING PRESSURE MEASUREMENTS	221
APPENDIX K FREE JET PROPERTIES	350
REFERENCES	368

LIST OF ILLUSTRATIONS

FIGURE		PAGE
1	Geometry of UBF Configuration	7
2	Geometry of OBF Configuration	7
3	Geometry of OBF Configuration with and without Lip Extension	10
4	Geometry of UBF Curved Plate Configuration	11
5	Geometry of Flat Plate Test Configuration	12
6	Typical Temperature Time History from Heat Transfer Test Procedure	16
7	Typical Power Spectrum for Surface Fluctuating Pressures	17
8	Illustration of Narrowband Correlation Spectrum	18
9	Convergent Round Nozzles and Contraction Section	22
10	Exit Cross Section of Lobed Nozzle	23
11	Components of Lobed Nozzle	23
12	Inside Contours of OBF Nozzle	24
13	Upper Lip Extension for OBF Nozzle	25
14	Cross Section Details of UBF Curved Plates	26
15	Cross Sections of Tested OBF Curved Plates	27
16	Wing-Flaps Model Cross Section Geometry	28
17	Wing Flaps Model Components	29
18	Reference Coordinate System at Nozzle Exit	30
19	Schematic of Specimen Support Fixture	32
20	UBF Curved Plate with Attached Supports	33
21	OBF Curved Plate with Attached Supports	33

LIST OF ILLUSTRATIONS (cont'd.)

FIGURE		PAGE
22	Set-up for Obtaining Transient Temperature Measurements	34
23	Geometric Center of Impingement on Flat Plate	35
24	Test Program Instrumentation	36
25	Fluctuating Pressure Pickup Installation on Plates	37
26	Fluctuating Pressure Pickup Installation on Wing-Flaps Model	37
27	Signal-Conditioning System for Fluctuating Pressure Measurements	38
28	Static Pressure Port	39
29	Calorimeter and Thermocouple Installation	40
30	Signal-Conditioning System for Temperature Measurements	40
31	Data Processing Flow Diagram	43
32	Static Pressure Distributions on a Flat Plate at $\beta = 90^\circ$ and Different X/D	57
33	Streamwise and Spanwise Static Pressure Distributions	58
34	Spreading Rates of Free and Impinging Jets	59
35	RMS Pressure Fluctuations in Spanwise Direction for $\beta = 90^\circ$ and at Different X/D	60
36	RMS Pressure Fluctuations in Chordwise Direction for $\beta = 90^\circ$ and at Different X/D	61
37	RMS Pressure Fluctuations in Spanwise Direction for $\beta = 50^\circ$ and at Different X/D	62
38	Mach Number Dependence of RMS Pressure Fluctuations	63
39	Comparison of RMS Pressure Fluctuations for Hot and Cold Jet	64
40	Comparison of RMS Pressure Fluctuations for an Infinite Plate and a Plate with Edge Effects	65

LIST OF ILLUSTRATIONS (cont'd.)

FIGURE		PAGE
41	Comparison of RMS Pressure Fluctuations for a Round Nozzle and a Lobed Nozzle	66
42	Characteristic Spectral Shapes on Flat Plate	67
43	Variation of Peak Amplification of Spectra in y-Direction	68
44	Variation in y-Direction of Peak Strouhal Number for Different X/D_j	69
45	Variation in y-Direction of Peak Strouhal Numbers Based on L_s and V_{∞} for Different X/D_j	69
46	Variation in y-Direction of Peak Strouhal Numbers for Different Mach Numbers	70
47	Variation of Rolloff Exponent in the y-Direction for Different X/D_j	70
48	Broad-Band Convection Speed as a Function of X/D_j	71
49	Narrow-Band Convection Speeds for Different X/D_j	72
50	Square Root of Coherence Spectrum	73
51	Maximum Square Root of Coherence Values (ρ_m) for Different Mach Numbers	74
52	Maximum Square Root of Coherence Values (ρ_m) for Different X/D_j	75
53	Maximum Square Root of Coherence Values (ρ_m) for Different Temperatures	76
54	Static Pressure Distributions for Different β_{T_0} and Different Mach Numbers on the UBF Curved Plates	77
55	Static Pressure Distributions for Different UBF Curved Plate Positions	78
56	RMS Pressure Fluctuations as a Function of M_j	79
57	Spatial Distribution of RMS Pressure Fluctuations on the UBF Curved Plates	80

LIST OF ILLUSTRATIONS (cont'd.)

FIGURE		PAGE
58	Ratio of RMS Fluctuating Pressures to Static Pressures Along Centerline Chord of UBF Curved Plate	81
59	Spatial Distribution of RMS Pressure Fluctuations for Different Plate Positions	82
60	Spatial Distribution of Peak Strouhal Numbers for Different M_j on $\beta_{TE} = 50^\circ$ Plate	83
61	Spatial Distribution of Peak Strouhal Numbers for Different Plate Positions	83
62	Spatial Distribution of Strouhal Numbers for Different M_j on $\beta_{TE} = 25^\circ$ Plate	84
63	Spatial Distribution of Roll-off Exponent on $\beta_{TE} = 25^\circ$ Plate for Different Mach Numbers	85
64	Spatial Distribution of Roll-off Exponent on $\beta_{TE} = 50^\circ$ Plate for Different Mach Numbers	85
65	Spatial Distribution of Roll-off Exponent for Different Plate Positions	86
66	Correlation Spectrum at a Location Along Centerline Chord of UBF Curved Plate	86
67	ρ_m for Adjacent Transducers and Different Mach Numbers	87
68	ρ_m for Adjacent Transducers and Different Plate Positions	88
69	Narrow Band Convection Speeds	89
70	Spanwise Distribution of RMS Pressure Fluctuations on Wing-Flaps Model and Curved Plate for $Z/D_j = 0.7$	90
71	Spanwise Distribution of RMS Pressure Fluctuations on Wing-Flaps Model and Curved Plate for $Z/D_j = 1.0$	91
72	Spanwise Distribution of RMS Pressure Fluctuations on the Flat and Curved Plates and the Wing-Flaps Model with a Lobed Nozzle	92

LIST OF ILLUSTRATIONS (cont'd.)

FIGURE		PAGE
73	Peak Strouhal Number Distribution in the y-Direction for Wing-Flaps Model	93
74	Variation of Roll-off Exponent in the y-Direction on the Wing-Flaps Model	93
75	Maximum Square Root of Coherence (ρ_m) for the Wing-Flaps Model	94
76	Normalized Convection Speed Between Flaps on the Wing-Flaps Model	95
77	Streamwise Static Pressure Distribution for OBF Configuration	96
78	Normalized Streamwise RMS Fluctuating Pressure Distribution for OBF Plate	97
79	Peak Strouhal Number Distribution in Streamwise Direction for OBF Plate	97
80	Roll-off Exponent in OBF Test Cases	98
81	Peak Velocity Decay Curve for Mixer-Nozzle	105
82	Multitube Coplanar Mixer Nozzle	111
83	Submerged Subsonic Jet	119
84	Impingement Test Schematic	120
85	Stagnation Point RMS Pressure Correlation on the Surface of a Flat Plate Submerged in a Subsonic Jet	121
86	Coefficients for Chordwise Distribution of RMS Level Versus Plate Inclination Angle for Flat Plate	122
87	Spanwise Distribution of RMS Level on Inclined Flat Plate at a Specified Chordwise Location	123
88	Correction Relationship for Spanwise Distributed RMS Levels Between Flat Plate and Aft Flap Lower Surface at $\beta = 50^\circ$	124
89	Corrected Spectrum Strouhal Number Versus Impingement Distance for Normally Impinged Flat Plate at Stagnation Point	125

LIST OF ILLUSTRATIONS (cont'd.)

FIGURE		PAGE
90	Spectrum Rolloff Exponent Versus Strouhal Number for Normally Impinged Flat Plate at Stagnation Point	126
91	Chordwise Maximum Half-Power Frequency Versus Impingement Distance for Normally Impinged Flat Plate	127
92	Chordwise Distribution of Spectrum Half-Power Frequency on Normally Impinged Flat Plate	128
93	Chordwise Distribution of Spectrum Rolloff Exponent on Normally Impinged Flat Plate	129
94	Chordwise Distribution for Spectrum Rolloff Exponent on Inclined Flat Plate	130
95	Chordwise Maximum Half-Power Frequency Versus Impingement Distance for Inclined Flat Plate	131
96	Chordwise Distribution of Spectrum Half-Power Frequency on an Inclined Flat Plate	132
97	Ratio of Turbulent Heat Transfer to that Predicted by Laminar Theory at the Stagnation Point of the Impinging Jet	133
98	Distribution of Turbulent Heat Transfer Coefficient for all Reynolds Numbers	134
B-1	Jet Noise Facilities at USC	148
B-2	Setting Chamber	150
B-3	Interior of Anechoic Chamber	151
B-4	Elevation through Anechoic Chamber	152
G-1	Transient Temperature Measurements	175
H-1	Static Pressure Measurements - Flat Plate-Round Nozzle	177
H-2	Static Pressure Measurements-Flat Plate-Daisy Nozzle	180
H-3	Static Pressure Measurements-UBF Curved Plates	183
H-4	Static Pressure Measurements-OBF Curved Plates	186
H-5	Static Pressure Measurements-Wing-Flaps Model	188

LIST OF ILLUSTRATIONS (cont'd.)

FIGURE		PAGE
I-1	Trend Data for RMS Level Along Centerline Chord-Flat Plate Configuration	191
I-2	Trend Data for Spectrum Half Power Frequency along Centerline Chord-Flat Plate Configuration	192
I-3	Trend Data for Spectrum Roll-off Exponent along Centerline Chord-Flat Plate Configuration	193
I-4	Trend Data for Spectrum Peak Amplification along Centerline Chord-Flat Plate Configuration	194
I-5	Trend Data for Correlation Lengths and Convection Speeds along Centerline Chord-Flat Plate Configuration	195
I-6	Trend Data for RMS Level along Spanlines - Flat Plate Configuration	196
I-7	Trend Data for Spectrum Half Power Frequency along Spanlines - Flat Plate Configuration	197
I-8	Trend Data for Spectrum Roll-off Exponent along Spanlines-Flat Plate Configuration	198
I-9	Trend Data for Spectrum Peak Amplification along Spanlines-Flat Plate Configuration	199
I-10	Trend Data for Correlation Lengths and Convection Speeds along Spanlines-Flat Plate Configuration	200
I-11	Trend Data for RMS Level-Flat Plate Configuration - Daisy Nozzle	201
I-12	Trend Data for Spectrum Half Power Frequency-Flat Plate Configuration - Daisy Nozzle	202
I-13	Trend Data for Spectrum Roll-off Exponent-Flat Plate Configuration - Daisy Nozzle	203
I-14	Trend Data for Spectrum Peak Amplification-Flat Plate Configuration - Daisy Nozzle	204
I-15	Trend Data for Correlation Lengths and Convection Speeds-Flat Plate Configuration - Daisy Nozzle	205

LIST OF ILLUSTRATIONS (cont'd.)

FIGURE		PAGE
I-16	Trend Data for RMS Level-UBF Curved Plate Configuration	206
I-17	Trend Data for Spectrum Half Power Frequency-UBF Curved Plate Configuration	207
I-18	Trend Data for Spectrum Roll-off Exponent-UBF Curved Plate Configuration	208
I-19	Trend Data for Spectrum Peak Amplification-UBF Curved Plate Configuration	209
I-20	Trend Data for Correlation Lengths and Convection Speeds-UBF Curved Plate Configuration	210
I-21	Trend Data for RMS Level-Wing-Flaps Configuration	211
I-22	Trend Data for Spectrum Half Power Frequency-Wing-Flaps Configuration	212
I-23	Trend Data for Spectrum Roll-off Exponent-Wing-Flaps Configuration	213
I-24	Trend Data for Spectrum Peak Amplification-Wing-Flaps Configuration	214
I-25	Trend Data for Correlation Lengths and Convection Speeds-Wing-Flaps Configuration	215
I-26	Trend Data for RMS Level-OBF Curved Plate Configuration	216
I-27	Trend Data for Spectrum Half Power Frequency-OBF Curved Plate Configuration	217
I-28	Trend Data for Spectrum Roll-off Exponent-OBF Curved Plate Configuration	218
I-29	Trend Data for Spectrum Peak Amplification-OBF Curved Plate Configuration	219
I-30	Trend Data for Correlation Lengths and Convection Speeds-OBF Curved Plate Configuration	220
K-1	Free Jet Properties-Centerline Total Temperature versus Centerline Distance	351

LIST OF ILLUSTRATIONS (cont'd.)

FIGURE		PAGE
K-2	Free Jet Properties-Centerline Velocity versus Centerline Distance	353
K-3	Free Jet Properties - $r_{1/2}$ versus Centerline Distance	358
K-4	Free Jet Properties - $q_{1/2}$ versus Centerline Distance	363

LIST OF TABLES

TABLE		PAGE
1	Selected Parameter Ranges for UBF Configuration	8
2	Selected Parameter Ranges for OBF Configuration	10
3	Specific Values used for Parameters in Test Program	14
4	Geometrical Data for Wing-Flaps Model	28
E-1	Impingement Centers - UBF Curved Plates	161
E-2	Impingement Centers - Wing-Flaps Model	163
F-1	Acoustic Resonance Results	165
G-1	Temperature Measurement Results-Case 13A	168
	(In consecutive order of Category 13 Cases in Appendix A)	1
G-7	Temperature Measurement Results - Case 13G	174
J-1	Pressure Measurement Results - Case 1A	223
	(In consecutive order of Categories 1 to 12 Cases in Appendix A)	1
J-63	Pressure Measurement Results - Case 12A	347
J-64	Maximum Correlations Across Thickness of Flaps for Wing-Flaps Model	349

LIST OF SYMBOLS

A	Area of calorimeter
C_0, C_1	Functions of β in formula for chordwise distribution of RMS levels on flat plate.
C_n	Nozzle coefficient
c	Specific heat of the calorimeter material
c_a	Aft flap chord length
c_f	Forward flap chord length
c_p	Specific heat at constant pressure of air
c_u	Chord length for UBF curved plate
c_w	Wing chord length
D, D_j	Circular nozzle diameter
D_e	Diameter of a circular nozzle whose area equals the area of the lobe of a lobed nozzle.
D_{ea}	Diameter of a circular nozzle whose area equals the exit area of a non-circular nozzle.
D^*	Corrected diameter in calculating Strouhal number for daisy nozzle.
f_m	Frequency at peak of narrowband correlation spectrum
f_p	Frequency at peak of power spectrum
$f_{1/2}$	Half-power frequency of power spectrum
f_R	Frequency associated with acoustic resonance
h	Turbulent heat transfer coefficient
h_{lam}	Laminar heat transfer coefficient
k	Thermal conductivity of air
$L, L(f)$	Narrowband correlation length (function of frequency)
L_{ff}	Maximum value of L over frequency

LIST OF SYMBOLS (cont'd.)

L_s	Length scale associated with static pressures
M	Mach number
m	Weight of calorimeter
Nu	Nusselt number
n	High frequency rolloff exponent of power spectrum
P	Peak amplification ratio of power spectrum
P_a	Ambient pressure
Pr	Prandtl number of air
P_{Tj}	Total pressure of jet at nozzle exit
P_{Tc}	Total pressure on centerline of free jet
p_s	Static pressure in psia
q	Dynamic pressure or heat flux
q'	Value of q at X'
R_j	$1/2 D_j$
R_{eq}	$1/2 D_{eq}$
Re	Reynold's number
r	Distance on flat plate in downstream direction from stagnation point
r_I	Distance on flat plate in downstream direction from center of jet impingement
Δr	Distance on flat plate between center of jet impingement and stagnation point
S_m	Strouhal number associated with f_m
S_p	Strouhal number associated with f_p
$S_{1/2}$	Strouhal number associated with $f_{1/2}$

LIST OF SYMBOLS (cont'd.)

$S_{1/2}^*$	Strouhal number associated with $f_{1/2}$ for daisy nozzle based on diameter D^*
$S'_{1/2}$	Strouhal number associated with $f_{1/2}$ for daisy nozzle based on diameter D_e .
S_R	Strouhal number associated with f_R
s	Distance along surface of UDF and ODF curved plates in downstream direction from leading edge
s_I	Value of s at geometric center of impingement on UDF curved plate
s_I^*	Distance complementary to s_I measured upstream from trailing edge
s_{aI}	Distance to the geometric center of impingement on the aft flap measured downstream from an origin at the 38.6% chord of the aft flap
s_{fI}	Distance to the geometric center of impingement on the forward flap measured downstream from an origin at the 38.8% chord of the forward flap
T_a	Ambient temperature
T_e	Equilibrium temperature
T_T, T_{Tj}	Total temperature of jet at nozzle exit
$T_{T\epsilon}$	Total temperature on centerline of free jet
T_w	Wall temperature
t_R	Temperature rise time
$V_c, V_c(f)$	Narrowband convection speed (function of frequency)
V_{cm}	Value of V_c at frequency f_m
\bar{V}_c	Broadband convection speed
V_e	Velocity at the edge of the boundary layer in the deflected flow
V_j	Velocity of jet at nozzle exit

LIST OF SYMBOLS (cont'd.)

V_q	Downstream velocity on centerline of free jet
V_{peak}	Maximum downstream velocity at downstream location in free jet
w	Distance on flat plate in upstream direction from center of plate
w_I	Distance from center of flat plate to geometric center of impingement
w/h	Aspect ratio of OBF nozzle exit
X, Y, Z	Coordinates from center of nozzle exit plane
X, X_I	Distance from nozzle exit to geometric center of impingement on flat plate
X_F	Distance from nozzle exit to geometric center of impingement on flap
X_{LE}	Distance of leading edge of UBF wing or UBF curved plate in downstream direction from nozzle exit
X_S	Distance from nozzle exit to geometric center of impingement on UBF curved plate
X'	Transformed value of X
x, y, z	Coordinate system attached to wing and curved plates at leading edge
x_I, z_I	Coordinates of geometric center of impingement on flap or UBF curved plate with respect to an origin at leading edge of specimen
y	Spanwise distance on specimen surface from centerline chord
z_{LE}	Vertical distance between jet centerline and leading edge of UBF curved plate
z_w	Vertical clearance between jet centerline and lower surface of UBF wing
β	Slope of flat plate measured from horizontal
β_a	Trailing edge slope of aft flap of UBF wing-flaps specimen
β_f	Trailing edge slope of forward flap of UBF wing-flaps specimen

LIST OF SYMBOLS (cont'd.)

β_{lip}	Upper lip slope at exit of OBF nozzle
β_{EX}	Slope of upper lip extension at exit of OBF nozzle
β_{TE}	Trailing edge slope of UBF or OBF curved plate
γ	Specific heat ratio for air
Δ	Separation distance between two points on surface of a specimen or the ratio $(c)_{flap} / (\sigma)_{plate}$
λ	A composite variable applied to formula for chordwise distribution of rolloff exponents on normally impinged flat plate
μ	Viscosity of air
ξ	A composite variable applied to formula for spanwise distribution of RMS levels on inclined flat plate
$\rho_p(f)$	Narrowband peak correlation of fluctuating pressures between two separated locations (function of frequency)
ρ_m	Maximum value of ρ over frequency
σ, RMS	Root-mean square value of fluctuating pressures
τ	Time from start of heat transfer test
Ω	Ratio of perimeter of mixer nozzle to perimeter of a circular nozzle with the same exit area

SUBSCRIPTS

j	Jet exit
max	Maximum value
Stag.Pt.	Stagnation point
CL	Centerline chord of specimen or centerline of free jet
1/2	Half-velocity point of free jet
∞	Free stream condition

SECTION I

INTRODUCTION

High lift components are utilized on STOL vehicles to permit their operation from short runways. The externally blown flap (EBF) concept of STOL design uses large flaps to turn the flow, inducing additional lift. Two approaches to turning the flow are under-the-wing blown flap (UBF) and over-the-wing blown flap (OBF). In both of these systems, the flaps are exposed to aeroacoustic and thermal environments determined by the jet flow over their surfaces. This exposure can produce significant levels of static pressure, fluctuating pressure and temperature on the flap surfaces.

The purpose of the test program discussed in this report was to increase the understanding of loads caused by jet impingement on STOL high lift surfaces and to provide a data base for defining a prediction methodology. The intent of the test program was met with a set of tests in which systematic changes were made in the jet and configuration variables. An important part of the test program was the use of different test specimens. Flat plates, curved plates and a wing-flaps model were tested. Some of the curved plates simulated UBF configurations, the others applied to OBF configurations. The UBF curved plate removed the complication of gaps occurring in the wing-flaps configurations while the flat plate further simplified the geometry of the solid boundaries affecting the flow. An underlying premise concerning this selection of test specimens was that the simple plate specimens can provide useful data for wing-flaps configurations.

A number of past studies provide useful data on the surface loadings produced during impingement. A basic study of a jet impinging on a flat plate is given in Reference 1. Information is provided relevant to the static pressure, fluctuating pressure and heat transfer conditions at the plate's surface. The test conditions of Reference 1 for fluctuating

pressure are low exit velocity (200 ft./sec.), large separation distances between plate and jet exit (greater than 10 diameters), and normal impingement. Attention in Reference 1 is given to obtaining statistical data (RMS values and power spectra) at the stagnation point on the plate.

The studies in Reference 2 are also performed on a flat plate at low exit velocity (136 ft./sec.), but do consider oblique impingement, smaller separation between the plate and jet exit (typically 7 diameters, but as low as 2 diameters for normal impingement), and locations removed from the stagnation point in the chordwise (streamwise) direction. The inclusion of a number of chordwise locations permits Reference 2 to give statistics at individual locations and at pairs of locations (e.g., correlation and convection speed data).

The amount of information on RMS levels and power spectra is considerably expanded for flat plates in Reference 3. This reference covers high jet exit velocities (above approximately 650 ft./sec.), oblique impingement, and separation distances from 3 to 12 diameters between the plate and jet exit. A large portion of the data in Reference 3, however, pertains to spatial locations beyond practical limits of STOL surface dimensions.

Reference 5 contains both 'single point' and 'two point' statistics for normal impingement. For a separation distance of 5 diameters between plate and nozzle exit, a detailed power spectra coverage is presented for the impingement region (and continued into the wall jet region). Also, correlation and phase information is supplied for this region. In Reference 5, the flow ran through a length of pipe before exiting. The enhanced mixing caused by this set-up introduced different results from those previously mentioned.

Although the tests in Reference 4 were performed on a curved plate simulating a UBF configuration, the results are closely akin to those

of a flat plate. Only slight turning of the flow occurred prior to impingement because of the large clearance distance (2 diameters) between the jet centerline and the leading edge of the plate. Also, a long trailing section was used thereby placing the trailing edge considerably downstream of the center of impingement. The results of Reference 4 show a close agreement with comparable flat plate measurements.

A comparison of the range of RMS values measured on flat plates with the range found on the flaps in UBF wing-flaps configurations is shown in Reference 6. Test data for a UBF wing-flaps design containing 3 flaps are given in Reference 7. This full scale configuration is subjected to the jet exhaust from a 6:1 by-pass ratio engine with internal mixing in a short duct prior to the round exit. A small scale model of the 3-flaps configuration was tested using a round nozzle and the results are reported in Reference 8. Reasonably close comparisons of RMS values on the aft flap of the model and full scale configuration were obtained for both takeoff and landing flap settings. Also, close results for the approach setting were found for the middle flap, but significant discrepancies occurred for the landing setting.

Test data for a curved plate simulating an OBF configuration are also reported in Reference 7. This full size configuration is subjected to the flow from an actual engine. Overall RMS levels and temperatures on the surface are reported. Static pressure distributions for the same configuration are found in Reference 22.

The above discussion provides a brief review of the published data relevant to the program discussed in this report. Without the availability of the flat plate data, a larger test program involving the flat plate would have been necessary. Existing data for the other types of test specimens were typically too meager to affect the scope of the testing. In reviewing the available flat plate data, further testing of this specimen was needed due to certain deficiencies. These included: (1) no testing other than with round nozzles, (2) no statistical information in the spanwise direction for oblique impingement, except for RMS

levels, (3) no data taken at elevated temperatures, (4) no information about edge effects, except for that derived from the curved plate test of Reference 4, and (5) no two-point statistical data as a function of frequency in the case of oblique impingement, except for the few results in Reference 6.

The test program described in Sections II and III involves an extensive number of cases of different combinations of parameter levels. The fluctuating pressure data derived from this program are intended to serve the needs of STOL vehicle design including, in particular, those of structural integrity under vibratory conditions.

The extent to which a structure responds to an external stimulus depends upon two things: (1) the intensity of the stimulus, and (2) how well the stimulus relates to the structure's natural modes of vibration. The intensity of the fluctuating pressure as a stimulus is described by the overall RMS level. Since structural responses can be magnified by excitations at natural frequencies, concern must be given to the character of the stimulus in the frequency domain. Because the fluctuating pressures vary randomly in time, power spectra and cross spectra are appropriate for defining their character. The task of describing these frequency dependent functions is considerably reduced by only viewing certain discrete features of the spectra. For characterizing the shape of the power spectra, four quantities were given attention. These are: (1) frequency at the peak, (2) the half-power frequency (where the spectrum is 3 dB down from the peak), (3) the rolloff rate of the spectrum at the half-power frequency, and (4) a measure defining the 'peakedness' of the spectrum. With knowledge of these quantities, a reasonable construction of the full power spectrum shape can be made.

From the cross spectra, correlation length spectra (or associated coherence spectra) and convection speed spectra were derived. Only the maximum value of a correlation length spectrum, the frequency at which

it occurs, and the convection speed at this frequency were considered within the scope of this study. This of course is not sufficient to describe the frequency dependent functions comprising a cross spectrum. This limited description of the cross spectral characteristics would typically cause some over-estimation when applied in vibration analyses.

The indicated characteristics of the power and cross spectra have been extracted from a large portion of the measured fluctuating pressures and are tabulated in Appendix J. Plots showing the trends of these characteristics for different parametric variations are given in Appendix I. A discussion of the more pronounced trends and some possible reasons for them are given in Section IV.

The trends for the fluctuating pressures are plotted in Appendix I. Non-dimensionalization for these plots was done using the properties of the flow at the jet exit. From these trends predictions concerning the fluctuating pressure characteristics can be made for cases in which the parameters have levels within or slightly beyond the limits considered in the test program. To make predictions for situations considerably beyond the range covered in the test program, more fundamental quantities are required for performing non-dimensionalizations. Some progress in this direction is made in Section V, even though the study was conducted within the limits prescribed by the test program. Conclusions drawn from the results of the program are given in Section VI.

SECTION II

TEST PROGRAM DESCRIPTION

The tests conducted for this study involve a group of test cases covering UBF and OBF configurations. Each test case is defined by a particular set of values for the jet and geometric parameters. In separate cases, a parameter may assume different levels. The levels used were selected from prescribed ranges. From each test case, measurements of the local surface pressures on the test specimens are obtained and analyzed for specific features. The various parts of the test program indicated above are discussed in the succeeding subsections.

1. JET AND GEOMETRIC PARAMETERS

There are many parameters influencing the loadings on the flap surfaces of EBF STOL systems. A discussion of these parameters follows for both the UBF and OBF concepts.

a. UBF Design

The major parameters for the UBF system include (a) flow properties at the nozzle exit (e.g., Mach No., total temperature, velocity), (b) nozzle geometry (e.g., round, lobed), (c) nozzle size, (d) nozzle exit plane position, (e) wing and flap chord dimensions, (f) flap deflection position and (e) geometry of slots. Some of the geometric features of the UBF configuration are illustrated in Figure 1.

The size of a round nozzle is designated by its diameter, D_j . The size of a lobed nozzle containing a centerbody around which the flow passes, however, is designated by the equivalent diameter, the diameter of a round nozzle having the same open area as the lobed nozzle. The position of the jet exit upstream from the leading edge of the wing is given by X_{LE} . The quantity X_F denotes the distance from the jet exit to the impingement point on the flaps. The minimum clearance distance between the jet centerline and the wing is designated by Z_W . The flap deflection is given by β_f and β_a , both angles relative to the wing reference plane (WRP in Figure 1.). The flap chord lengths, c_f and c_a , are indicated in the sketch,

but not shown is the wing chord length c_w . The wing chord length is measured from the wing leading edge to the aft flap trailing edge for the 0° , or fully retracted, flap setting.

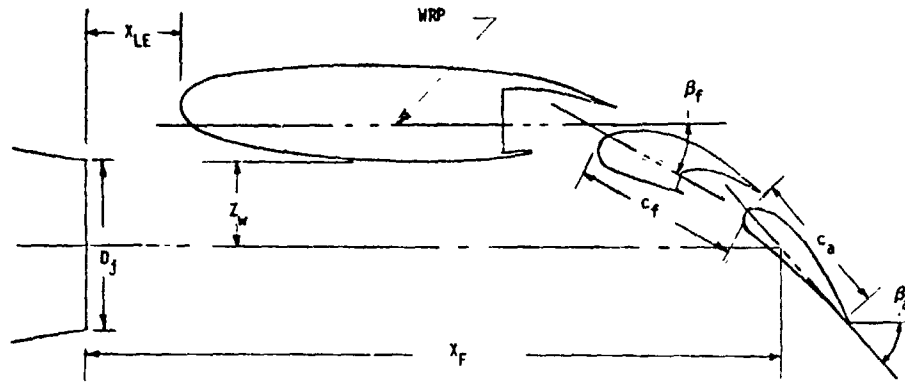


Figure 1. Geometry of UBF Configuration

b. OBF Design

The parameters for the OBF system include (a) properties of the flow at the nozzle exit, (b) nozzle geometry, (c) nozzle size, (d) position of the nozzle exit, (e) curvature of the wing and flap surfaces and (f) trailing edge deflection angle. The following sketch illustrates some of the geometric features of the OBF configuration:

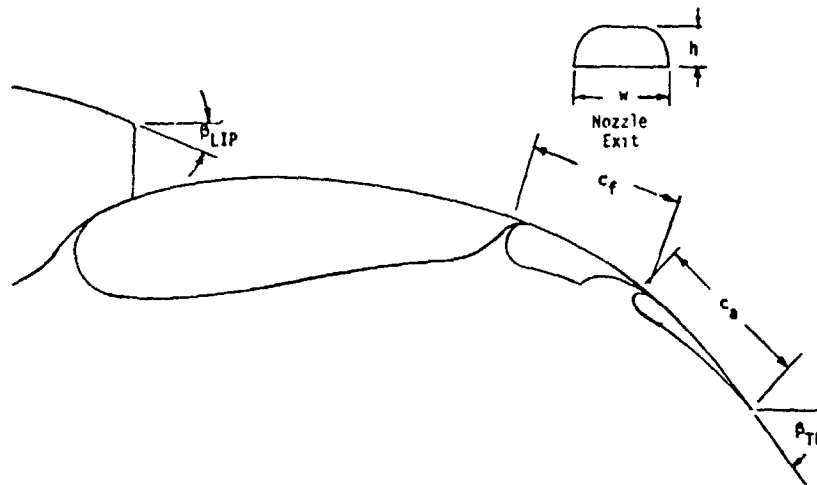


Figure 2. Geometry of OBF Configuration

The nozzle exit may be rectangular or D-shaped as shown in Figure 2. The width, w , and height, h , provide the nozzle exit aspect ratio, w/h . The flap chord lengths, c_f and c_a , are indicated in Figure 2. The flaps have continuously varying curvature.

2. PARAMETER RANGES

The data upon which parameter ranges are based come from full-scale designs, either actual or only conceived. This information was then applied to model scale configurations. Some of the ranges required modification as a result of certain limitations which will be subsequently discussed. For scaling purposes, it is appropriate to express the parameters as ratios or nondimensional quantities.

a. UBF System

The ranges selected for UBF system parameters are summarized in the following table:

TABLE 1.
SELECTED PARAMETER RANGES FOR UBF CONFIGURATION

NONDIMENSIONAL PARAMETER	RANGE
Z_w/D_j	0.5 - 1.0
X_{LE}/D_j	0 - 1.5
X_F/D_j	5 - 10
β_a	25° - 50°
c_f/c_w	0.42
c_a/c_w	0.26
D_j/c_w	0.2
M_j	.35 - .74
T_j/T_a	1.0 - 1.7

A consideration in the range selection for X_F is the avoidance of acoustic resonance when using the round nozzle (see Appendix F). This condition will not occur or at least will not be of significance for configurations having $X_F/D_j > 6.5$ or jet Mach Nos. $M_j \leq 0.5$ (Reference 9). This resonance is therefore only possible at the low end of the X_F/D_j range in combination with the high end of the M_j range. This combination was avoided for the round nozzle, but not for the lobed nozzle. No resonance was found for the lobed nozzle within the specified ranges.

The upper limit for M_j is associated with a landing approach power setting. Higher Mach Nos. would be applicable to takeoff conditions. Outside the resonance range, extensive study for M_j near its upper limit is unnecessary because of the available knowledge of Mach No. scaling effects (e.g., References 3, 7.)

The upper limit for the ratio of jet total temperature to ambient temperature, $T_j (^{\circ}R)/T_a (^{\circ}R)$, is dictated by the 450°F limitation on the fluctuating pressure transducers (see Section III-3). Even though there are only a few test cases in which the temperature of any pickup approaches the stagnation temperature of the hot jet, the limited temperature range imposed on the jet is a safeguard in preventing loss or degradation of pickups.

The chord ratios, c_f/c_w and c_a/c_w , are fixed by the dimensions of the wing-flaps model in the test program. Only one round nozzle, the two-inch diameter, and the lobed nozzle (same equivalent diameter) were used in tests involving the wing-flap configuration. The range of the aft flap deflection angle, β_a , reflects the variation from takeoff to landing approach settings. The angle between the forward and aft flaps was set permanently to 20° so the forward flap deflection β_f was always $(\beta_a - 20^{\circ})$.

b. OBF System

The geometry of the OBF system for these experiments is a simplification of an actual system in that a polished curved plate was used instead of a special wing and flaps. Use of the curved plate does, however, preserve the essential characteristic of an OBF system: There

are no spaces between the flaps. In addition the D-shaped nozzle used for this study was fitted with a removable upper lip extension. The lip extension tends to spread the flow laterally, wetting more of the wing surface so the flow is turned more effectively.

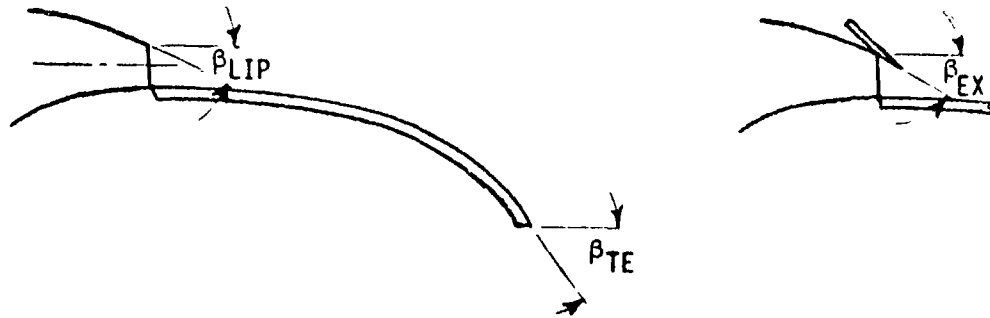


Figure 3. Geometry of OBF Configuration with and without Lip Extension

The value for each parameter shown in Figure 3 is constrained by the test configuration to one level except for the trailing edge angle, β_{TE} . A range is used for the parameter reflecting the variation between takeoff and landing approach. The ranges for jet Mach No. and temperature are the same as imposed on the UBF tests.

TABLE 2
SELECTED PARAMETER RANGES FOR OBF CONFIGURATION

NONDIMENSIONAL PARAMETER	RANGE
w/h	2.4
X_B/h	5.0
R_s/h	2.2
β_{LIP}	25°
β_{EX}	30°
β_{TE}	40° - 70°
M_j	.35 - .74
T_j/T_a	1.0 - 1.7

3. TEST CONFIGURATIONS

The most realistic UBF geometry is the wing-flaps configuration shown in Figure 1. The model used in the test is of the same design and is approximately 6% of full-scale. Some details of the model are described in the previous section. Considerably more detail is given in Section III-1c.

In order to remove the complication of the gaps in the wing-flaps configuration, a model without gaps was included in the test program. This model is a continuous curved plate as shown in Figure 4.

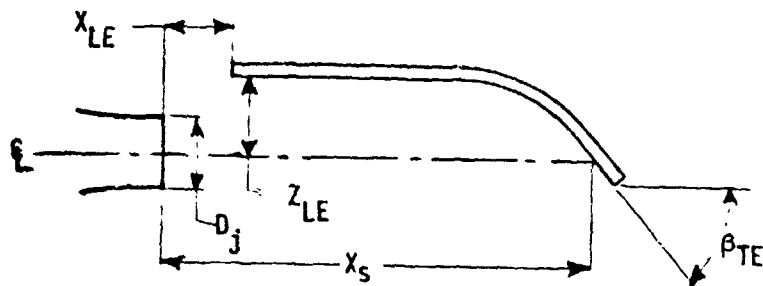


Figure 4. Geometry of UBF Curved Plate Configuration

The details of the UBF curved plates used in the program are given in Section III-1b. Some of the key parameters for this configuration are shown in Figure 4. The chord lengths of the two UBF curved plates used in the test program are nearly the same and for the subsequent discussion will be denoted by c_u .

The simplest model in the test program is a flat plate as sketched in Figure 5. The flat plate test eliminates complexities arising from the turning of the jet flow. Indicative of its simplicity is the relatively few parameters required to define a wide range of conditions. The flat plate details are described in Section III-1b.

Both round and lobed nozzles are used with the above test configurations. The details of the nozzles are given in Section III-1a.

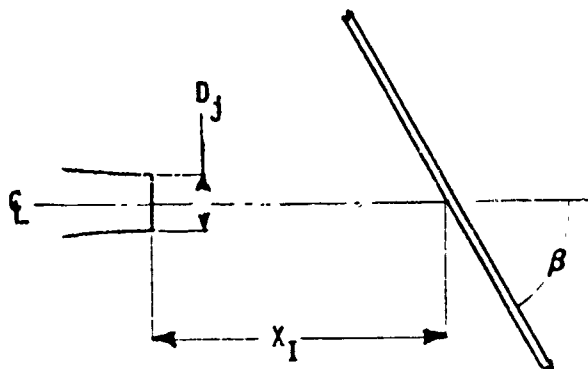


Figure 5. Geometry of Flat Plate Test Configuration

The OBF test configuration is shown in Figure 3 and some of its properties have been described in Section II-2. Considerably more detail is provided in Section III-1b. The details of the nozzle used with the OBF configuration are given in Section III-1a.

4. TEST CASES

The parameters involved in the UBF and OBF configurations are defined in Section II-1. The ranges used in the test program for these parameters are given in Section II-2. The parameters can be subdivided into those for which one, two or three levels are used in the testing. Exceptions to this are the parameter X_F/D_j for the wing-flaps and X_S/D_j for the UBF curved plates. These parameters as can be seen from Figures 1 and 4 are affected by the parameter X_{LE}/D_j and are very dependent upon the detailed geometry of the configuration. The specific values of these parameters used in the test program are provided in Appendix E.

Those parameters for which only one level was used are apparent from Tables 1 and 2. The temperature ratio (T_j/T_a) was applied at one level for the wing-flaps configuration (see Table 3). Included in the two level parameters were the temperature ratio for the flat and curved plate tests (T_j/T_a), the trailing edge deflection of the wing flaps (β_a), the trailing edge deflections of both the UBF and OBF curved plates (β_{TE}), the distance of the jet centerline from the leading edge surface for the UBF curved

plates (Z_{LE}/D_j) and the distance of the jet exit upstream of the leading edge for the UBF curved plates and wing-flaps configurations (X_{LE}/D_j). The levels used for these parameters are those given at the extremes of the ranges in Tables 1 and 2. The levels applied to the parameter Z_{LE}/D_j were 0.7 and 1.0.

The parameters for which three levels have been prescribed include the Mach No. (M_j), inclination angle for the flat plate (β), distance from nozzle exit to jet centerline intercept on flat plate (X_I/D_j) and clearance distance of jet centerline from wing surface (Z_W/D_j). The values used for M_j are 0.35, 0.5 and 0.74 with most testing done at 0.5. A few tests had a slight deviation from 0.5, some flat plate hot tests actually being 0.46. The three angles for β were 25° , 50° and 90° , first two of these conforming to the trailing edge deflections in the UBF configurations. For X_I/D_j , the levels of 5, 7 and 10 were used. It is to be noted that these levels are in the range shown in Table 1 for X_F/D_j . For the wing-flaps model, the levels for Z_W/D_j were 0.5, 0.7 and 1.0.

Table 3. summarizes the specific values applied to the parameters in the test program for the four test configurations.

A test case for a specific configuration is formed from a combination of the values given in Table 3. In the test program, 63 cases were conducted for static and fluctuating pressure data and 7 cases for temperature data. The pressure cases are grouped into 12 categories with a distinction being made in some categories concerning the nozzle type. These categories are as follows:

1. Flat Plate--Round Nozzle ($D_j = 1''$)--Cold Jet
2. Flat Plate--Round Nozzle ($D_j = 1''$)--Hot Jet
3. Flat Plate Edge--Round Nozzle ($D_j = 2''$)
4. Flat Plate--Daisy Nozzle ($D_{eq} = 2''$)
5. a. UBF Curved Plate-- $\beta_{TE} = 50^\circ$ --Daisy Nozzle ($D_{eq} = 2''$)
b. UBF Curved Plate-- $\beta_{TE} = 50^\circ$ --Round Nozzle ($D_j = 2''$)
6. UBF Curved Plate-- $\beta_{TE} = 25^\circ$ --Round Nozzle ($D_j = 2''$)

TABLE 3
SPECIFIC VALUES USED FOR PARAMETERS IN TEST PROGRAM

NONDIMENSIONAL PARAMETER	CONFIGURATION	VALUES
M_j	All	0.35, 0.5, 0.74
T_j/T_a	All, Except Wing-Flaps	1.0, 1.7
T_j/T_a	Wing-Flaps	1.0
X_I/D_j	Flat Plate	5, 7, 10
β	Flat Plate	25°, 50°, 90°
β_{TE}	UPF Curved Plates	25°, 50°
Z_{LE}/D_j	UBF Curved Plates	0.7, 1.0
X_{LE}/D_j	UBF Curved Plates	0, 1.5
D_j/c_u	UBF Curved Plates	.17
β_a	Wing-Flaps	25°, 50°
β_f	Wing-Flaps	5°, 30°
Z_w/D_j	Wing-Flaps	0.5, 0.7, 1.0
X_{LE}/D_j	Wing-Flaps	0, 1.5
D_j/c_w	Wing-Flaps	0.2
c_f/c_w	Wing-Flaps	0.42
c_a/c_w	Wing-Flaps	0.26
β_{TE}	OBF Curved Plates	40°, 70°
β_{LIP}	OBF Curved Plates	25°
β_{EX}	OBF Curved Plates	30°
w/h	OBF Curved Plates	2.4

7. Wing-Flaps Model-- $\beta_f/\beta_a = 5^\circ/25^\circ$ --Round Nozzle ($D_j = 2''$)
8. a. Wing-Flaps Model-- $\beta_f/\beta_a = 30^\circ/50^\circ$ --Round Nozzle ($D_j = 2''$)
b. Wing-Flaps Model-- $\beta_f/\beta_a = 30^\circ/50^\circ$ --Daisy Nozzle ($D_{eq} = 2''$)
9. OBF Curved Plate-- $\beta_{TE} = 70^\circ$ --With Lip Extension
10. OBF Curved Plate-- $\beta_{TE} = 70^\circ$ --No Lip Extension
11. OBF Curved Plate-- $\beta_{TE} = 40^\circ$ --With Lip Extension
12. OBF Curved Plate-- $\beta_{TE} = 40^\circ$ --No Lip Extension

A flat plate test was typically conducted with the jet centerline intercepting the plate at or near its center. Category 3 refers to cases in which the jet centerline intercepts the flat plate near its downstream edge. (See further description in Section III-2.)

The collection of temperature data was only taken with a flat plate configuration. The group of cases serving this purpose is placed in the following category:

13. a. Flat Plate--Daisy Nozzle ($D_{eq} = 2''$)--Hot Jet
b. Flat Plate--Round Nozzle ($D_j = 2''$)--Hot Jet

The category number and the associated number of cases in the category are as follows: 1. (15), 2. (3), 3. (4), 4. (9), 5. (10), 6. (4), 7. (2), 8. (7), 9. (3), 10. (1), 11. (4), 12. (1), 13. (7). The specific values used for the parameters in the cases included in the 13 categories of the test program are given in Appendix A.

5. TEST DATA

The test data produced by the test program consists of fluctuating pressures, static pressures and temperatures, all measured on the flap or plate surfaces in the previously defined configurations. Appendices G, H, I and J show the locations at which data are obtained. The fluctuating pressure at any location is a randomly varying quantity in time having stationary statistics (i.e., statistics which are not dependent upon the time origin selection within the duration of the recording). Each static

pressure is a single value acquired under equilibrium conditions. Temperature data was taken only with the flat plate and is obtained in a transient manner (see Section III-2). A temperature result at any location is an increasing curve with time approaching eventually toward an equilibrium level.

a. Temperature Data

A typical temperature result for a surface location is illustrated by Figure 6.

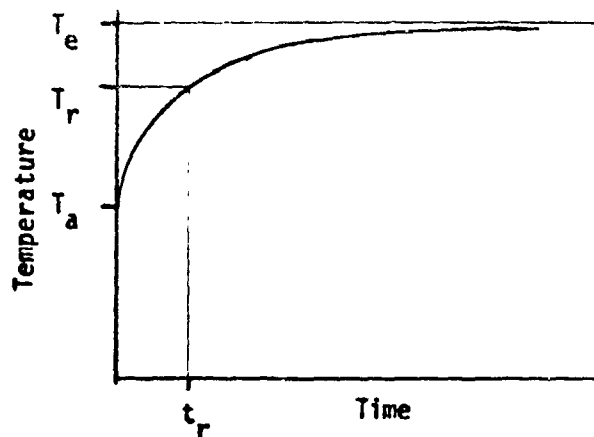


Figure 6. Typical Temperature Time History from Heat Transfer Test Procedure

The curve in the figure occurs from a sudden exposure of the pickup to the hot jet flow. The initial ambient temperature prior to this exposure is T_a and the eventual equilibrium temperature is T_e . This temperature result serves to define a heat transfer coefficient for the location where the temperature was measured. Useful for this purpose is the time t_r at which the temperature rises to a level $T_r = T_a + .63 \times (T_e - T_a)$. The time t_r will be referred to as the "rise" time.

b. Fluctuating Pressure Data

The random fluctuating pressure at a specific surface location is described by an overall RMS (root-mean-square) level and a power spectrum shape. The latter is a frequency dependent function whose ordinates give the MS (mean-square) contribution of each 1 Hz band. A typical power spectrum is depicted in Figure 7.

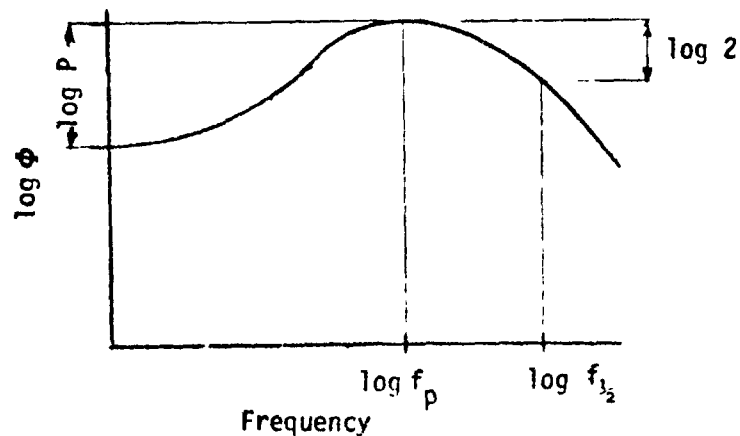


Figure 7. Typical Power Spectrum for Surface Fluctuating Pressures

There are many ways of presenting a power spectrum and the log-log form is chosen in Figure 7 to show some important features. The frequency at which the spectrum peaks is f_p . The origin in the figure can be considered as being very near zero such that its ordinate is well represented by $\log \phi(0)$. The "beakedness" or a "peak amplification" of the spectrum is denoted in Figure 7 by P . Specifically, $P = \phi(f_p)/\phi(0)$. At the half power frequency $f_{1/2}$, the ordinate of the power spectrum is one-half of its value at the peak; i.e., $\phi(f_{1/2})/\phi(f_p) = 1/2$. On a log-log scale, a linear rolloff of the power spectrum beyond the half-power frequency indicates that in this part of the spectrum ϕ is proportional to f^{-n} . The quantity "n" will be called the "rolloff exponent".

The overall RMS level and the quantities $f_{1/2}$, f_p , P and n give definition to the fluctuating pressure statistics at individual points on the exposed surfaces. Characterization of the fluctuating pressures suitable for flap loads applications also requires information on the statistics between any two surface points. For this purpose, correlations and phase spectra are useful.

Two random functions of time may be shifted in time with respect to each other and the similarity of the two shifted functions evaluated. How well these functions match for an arbitrary shift in time can be expressed by a number, the correlation coefficient, whose absolute value falls between 0 and 1. This range indicates a gradation from no correla-

tion (coefficient equal zero) to complete correlation (coefficient equal unity). The two random quantities can be shifted in time with respect to each other to produce a "best matching" of their magnitudes. For this situation, the largest value of the correlation coefficient, not necessarily unity, will be attained.

The random pressures occurring at two surface locations may be compared without performing any filtering of their frequency content. The correlations found under this circumstance are termed "broadband". However, "narrowband" correlations are generally desired for applications concerned with flap loads. For this purpose, corresponding narrowbands throughout the full frequency range are filtered or extracted from the two random signals. A correlation coefficient associated with the "best matching" can be attributed to each pair of random quantities produced from common bands. A plot depicting these peak correlation coefficients as a function of frequency is given in Figure 8.

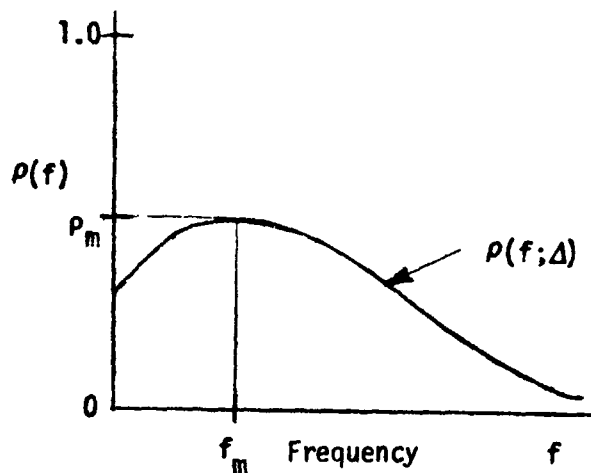


Figure 8. Illustration of Narrowband Correlation Spectrum

The narrowband correlation spectrum in Figure 8 depicts a form which quite often is obtained for a pair of locations separated by a distance Δ . The peak magnitude of this spectrum is designated by ρ_m and occurs at the frequency f_m .

Another way of exhibiting narrowband correlation data is by means of "correlation lengths". A coarse relationship between the correlation levels, ρ , and correlation lengths, L , is $\rho = \exp(-\Delta/L)$. Therefore, $L = \Delta / \ln(1/\rho)$ and in particular $L_m = \Delta / \ln(1/\rho_m)$. The length L_m is

SECTION III

EXPERIMENTAL DETAILS

The program testing was all performed in the Jet Noise Laboratory at the University of Southern California. The laboratory is built around a compressed air jet fed from five large storage vessels. The jet's stagnation pressure is regulated by a valve to within 3% gauge pressure. A heater downstream of the valve and prior to the settling chamber may be used to raise the air temperature. The settling or stagnation chamber has materials and screens to provide low turbulence conditions in the flow upstream of the nozzle exit. A smooth contraction leads from the settling chamber to the nozzle exit.

The jet exhausts into a 3800 cu. ft. anechoic chamber. Reference 12 gives the properties of the free jet in this chamber.

The test specimens described in the previous section were mounted in the path of the jet. A fixture on which the specimens are attached had the capability to move in any of six degrees-of-freedom and therefore to place a specimen in proper orientation relative to the jet.

The specimens had a specific number and arrangement of holes for inserting transducers to measure surface fluctuating pressures. Only a small number of holes were used at any time because of a limited number of pickups. Performing a sequence of tests in which the specimen was successively shifted laterally relative to the jet permitted adequate surface coverage with the use of a few pickups.

A number of static taps were also built into the specimens to obtain the surface static pressures. The shifting accomplished for the fluctuating pressures simultaneously provided the surface coverage necessary for the static pressures.

Surface temperature measurements for heat transfer purposes were taken over a flat plate by using small copper disks inserted in holes with

one face flush with the surface and insulated from the plate. A thermocouple junction was formed on the unexposed face of the disk. The number of disks placed in the plate was sufficient to obtain the necessary surface coverage without shifting.

The data from the static pressure and temperature measurements were FM recorded on magnetic tapes and subsequently read onto strip charts. The fluctuating pressure data was similarly recorded and then played-back through an A/D converter for processing. The processing was done through a digital system with the capability of obtaining the functions described in Section II-5.

A detailed description of the laboratory in which the tests were conducted is given in Appendix B. Further details relevant to the other items mentioned above are found in the following subsections.

1. TEST ITEMS

The two distinct parts defining a test configuration are the nozzle and the test specimen. These parts are set-up inside the anechoic chamber described in Appendix B-5. The nozzle was interfaced with the settling chamber (Figure B-2) through a contraction section. The fixture upon which the specimens are mounted was supported from the floor of the chamber. This fixture was specially designed for the test program to position the specimen about the fixed nozzle.

Descriptions of the test specimens and nozzles, in more detail than presented in Section II are given in the subsequent discussions. A description of the specimen support fixture is found in Section III-2.

a. Nozzles

The three nozzle configurations used in the test program are (1) round, (2) lobed (daisy) and (3) D-shaped or OBF. Tests involving the flat plates, OBF curved plates and wing-flap model were performed with both the round and lobed nozzles. The D-shaped nozzle was part of the OBF system.

(1) Round

Surface pressure measurements on the flat plate were in most cases made with the 1" diameter round nozzle. A 2" diameter was used for all other tests involving the round nozzle (see Section II-4 or Appendix A). These two round nozzles interchangeably fit the contraction section which couples them to the downstream end of the settling chamber.

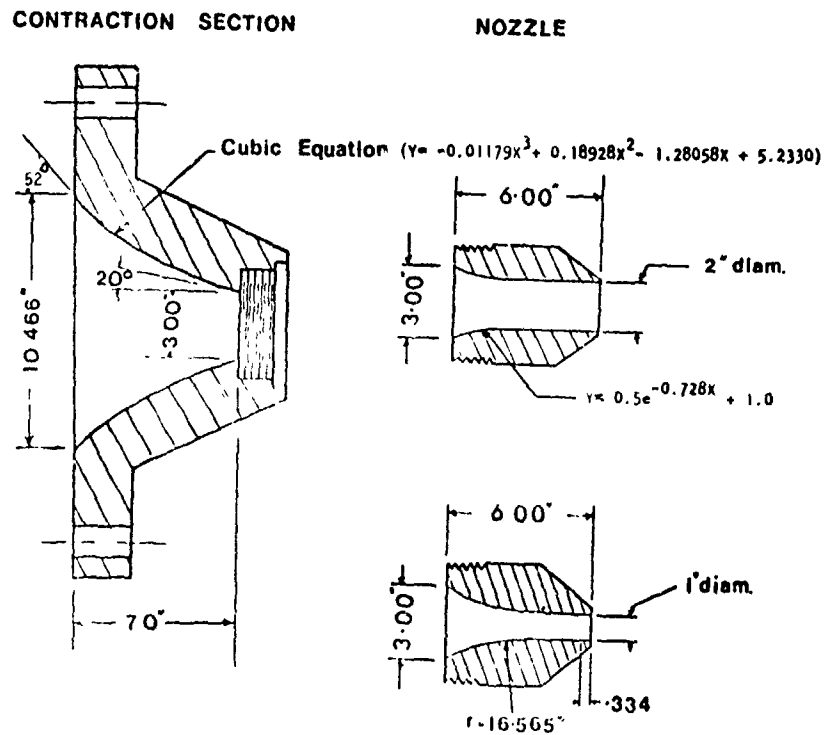


Figure 9. Convergent Round Nozzles and Contraction Section

Both nozzles and the contraction section, shown in Figure 9, are made of stainless steel. The upstream diameters of the nozzles are matched to the 3" diameter of the contraction section to within .001". The slopes of the internal contours are also matched at this junction.

(2) Lobed (Daisy)

The lobed nozzle used in the test program is configured at its exit as shown in Figure 10.

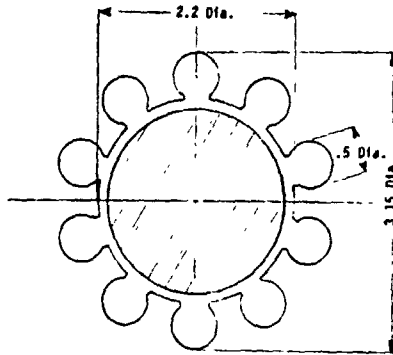


Figure 10. Exit Cross Section of Lobed Nozzle

The lobed nozzle consists of a lobed section threaded into an initial section, a center-body, and three struts mounting the

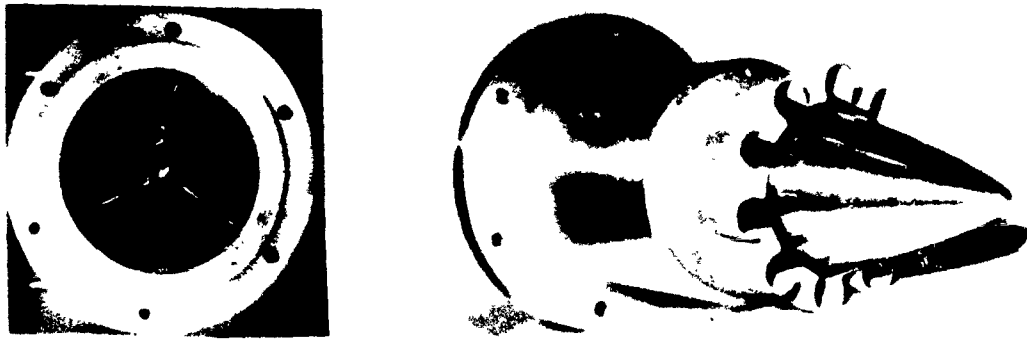


Figure 11. Components of Lobed Nozzle

centerbody (see photographs in Figure 11). The lobed exit section was cast in stainless steel. The initial piece was made of stainless steel and has a constant outer diameter with a flange on the upstream end. The centerbody is supported near its upstream end inside the initial section with three streamlined struts. The area of the lobed nozzle at its exit approximately equals that of a 2" diameter round nozzle.

The details of the lobed nozzle construction are given in Appendix C-1. Coupling this nozzle with the settling chamber requires a different contraction section from that shown in Figure 9. A common contraction section was fabricated for the lobed and OBF nozzles and its description is provided in the subsequent discussions. The method of attachment to the contraction section is the same for both nozzles.

(3) OBF

Inside contours of the OBF nozzle used in the test program are given in Figure 12.

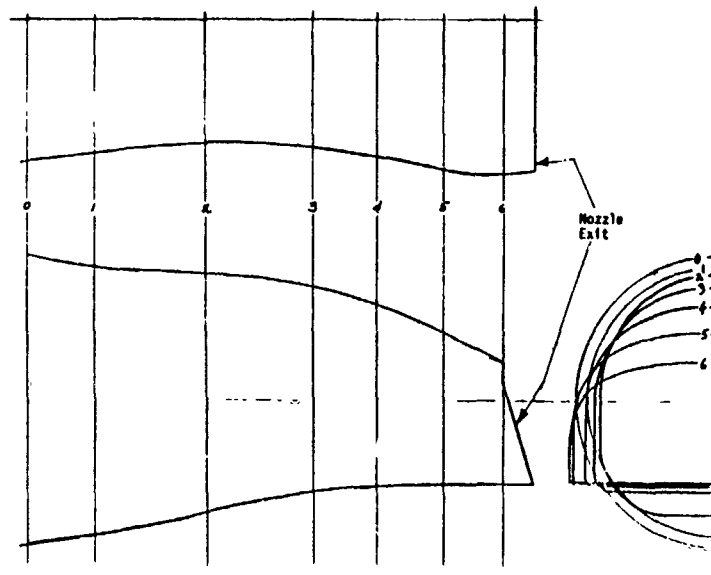


Figure 12. Inside Contours of OBF Nozzle

The upper inside surface of the OBF nozzle slopes downward at a 25° angle near the exit. The D-shaped exit has an aspect ratio of 2.4 and is approximately the area of a 2 inch round nozzle. For a majority of the tests, the upper lip extension shown in the photograph in Figure 13 was attached to the nozzle.

The nozzle was machined from a block of aluminum and a flange was welded to the upstream end providing a coupling to the contract-

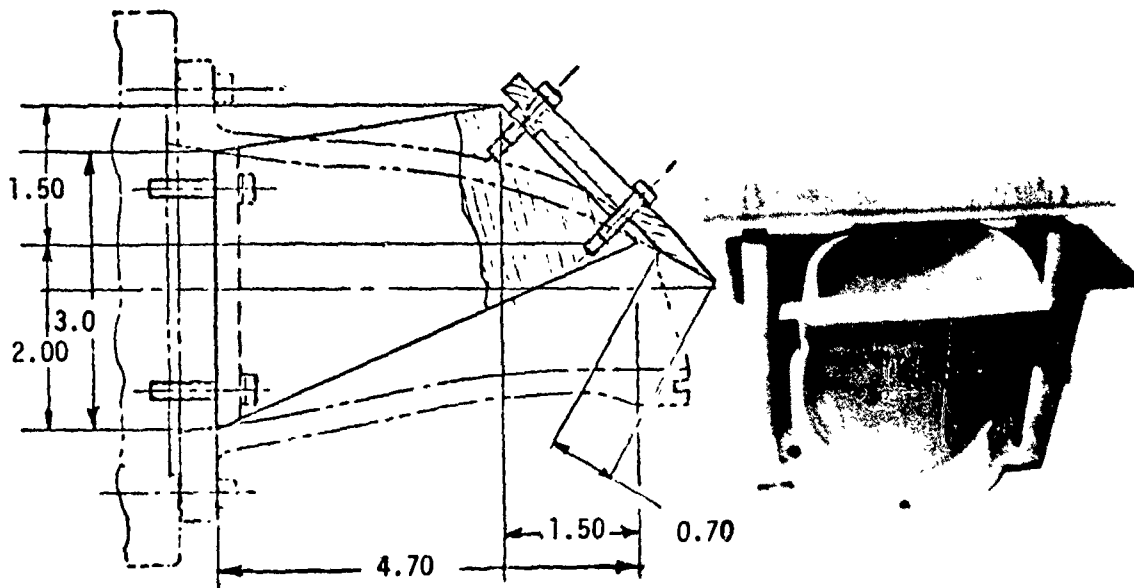


Figure 13. Upper Lip Extension for OBF Nozzle

ion section. A groove was cut into the wall of the nozzle at the lower edge of the exit to receive the tongue at the leading edge of the OBF plate. More details of the nozzle are provided in Appendix C-2. The contraction section to which the OBF nozzle attaches is also detailed in this appendix. The contraction section is made from low carbon steel, and is coated with Sermetal W, an inorganically bonded alumina coating.

b. Plates

The three forms or shapes of plates used in the test program (see Section II) are (1) flat, (2) curved simulating an UBF configuration and (3) curved simulating an OBF configuration. These last two shapes are referred to, respectively, as the UBF curved plate and OBF curved plate.

(1) Flat Plates

There were two flat plates used in the test program; one for pressure measurements and the other for temperature measurements. Both plates are low carbon steel with dimensions 30" x 30" x 1/4" thick. The surfaces of the plates are finished to 60 microinches.

Holes are placed in the two plates for insertion of instrumentation. The positions of these holes are given in Appendix D.

(2) UBF Curved Plates

A UBF curved plate was previously illustrated in Figure 4. The leading portion of the plate is flat, followed by a circular arc and ending with a short flat trailing section. Two curved plates were built for the test program; one with a trailing edge deflection angle $\beta_{TE} = 50^\circ$ and the other with $\beta_{TE} = 25^\circ$. The dimensions defining the streamwise profiles of the two plates are given in Figure 14. These profiles are the same for all spanwise locations.

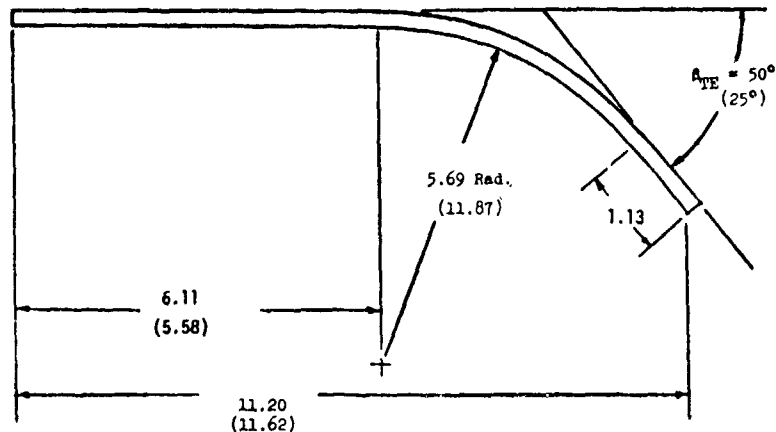


Figure 14. Cross Section Details of UBF Curved Plates

The span of each curved plate is 30 inches. Both plates have a thickness of 1/4 inch and their surfaces which are exposed to the jet flow are finished to 60 microinches. The hole patterns incorporated in the plates for instrumentation are displayed with dimensions in Appendix D-3. The plates' material is low carbon steel.

(3) OBF Curved Plates

A schematic of an OBF curved plate was given in Figure 3. As constructed for the test program, the plate is curved everywhere along its streamwise profile with the greatest curvature occurring in the trailing half. The basic plate used in the program has a trailing edge deflection $\beta_{TE} = 40^\circ$. A larger trailing edge deflection of $\beta_{TE} = 70^\circ$ is obtained by attaching an extension to the trailing edge of the basic plate. The following figure shows the streamwise profile of the plate and the attachment of the trailing edge. The tongue at the leading edge of the plate fits into a groove below the nozzle exit. Sufficient clearance is allowed to permit lateral shifting of the plate relative to the nozzle.

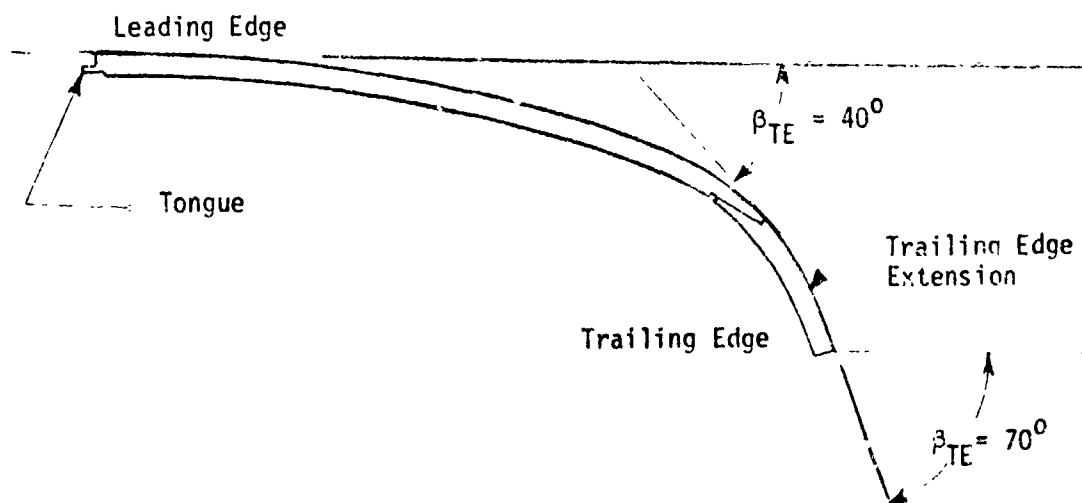


Figure 15. Cross Sections of Tested OBF Curved Plates

The continuously changing curvature for the profiles makes it unsuitable to give dimensions in Figure 15. The dimensioning of the hole locations incorporated for instrumentation given in Appendix D-4 provides sufficient numerical detail for the profile depicted in Figure 15.

The OBF curved plates have spans of 30 inches and are 1/4 inch thick. The surfaces exposed to the jet flow are finished to 60 microinches. The plates' material is low carbon steel.

c. Wing-Flaps Model

A cross section view of the geometry of the wing-flaps model set to a deflection $\beta_f/\beta_a = 30^\circ/50^\circ$ is shown in Figure 16. As indicated in the figure, the wing chord, $c_w = 9.64$ in.

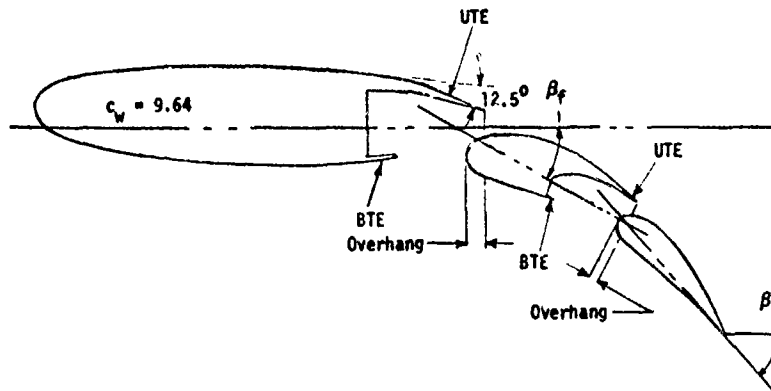


Figure 16. Wing-Flaps Model Cross Section Geometry

The following table gives numerical data concerning the geometry shown in Figure 16.

TABLE 4
GEOMETRICAL DATA FOR
WING-FLAPS MODEL

COMPONENT	CHORD RATIO	DEFL. ANGLE	UTE % c_w	BTE % c_w	L.E. % c_w	GAP % c_w	OVER-HANG % c_w
WING - SPOILER			76	59.5	0		
	c_f/c_w	β_f					
FORWARD FLAP	.42	0° 30°	86	75	58 73.84	5.34	1.36
	c_a/c_w	β_a					
AFT FLAP	.26	0° 50°	100	100	74 85	3.0	1.0

The span of the wing-flaps model is approximately 60 in. The wing of the model has large end plates at both ends of its span. The forward flap has plates at both ends of its span which fit inside of the wing end plates. Finally, the aft flap end plates fit inside of the forward flap end plates. The photograph in Figure 17 shows this end plate arrangement. Holes in the end plates permit setting specific flap deflections. Intermediate deflections can be set with the use of clamps.

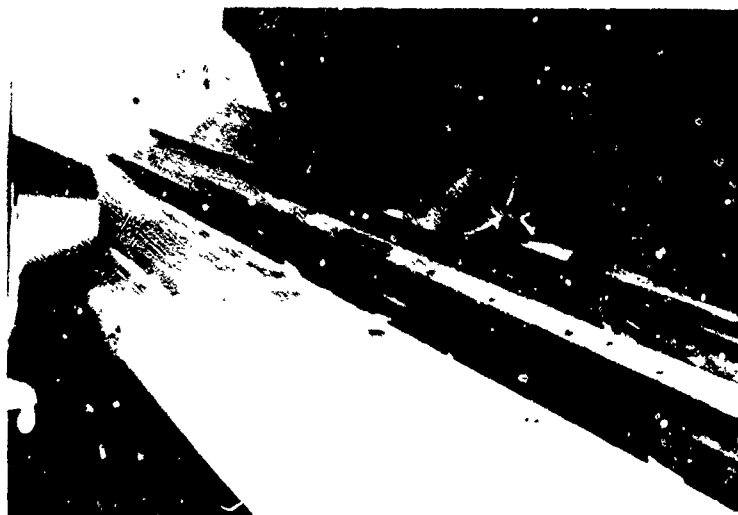


Figure 17. Wing Flaps Model Components

The wing of the model is aluminum and the flaps are stainless steel. Four plugs, each containing three fluctuating pressure transducers, are embedded in the flaps. Static taps are also incorporated in the model. The locations of the instrumentation are described in Appendix D-5.

2. SPECIMEN SET-UP

A test specimen's positioning is referenced to a coordinate system fixed at the center of the nozzle exit. In the actual tests, all test specimens were inverted so the jet flow along a specimen's surface was directed toward the ceiling of the anechoic chamber after leaving the

downstream edge. The subsequent discussion will consider all test specimens turned over so that the resultant lift is upward. Viewing the set-ups this way, the right-hand XYZ system in Figure 18 will be taken as the basic reference.

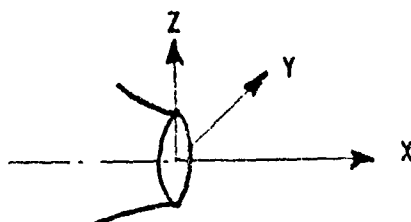


Figure 18. Reference Coordinate System at Nozzle Exit

The extent of freedom in positioning differs for the various test specimens. All specimens can be moved in the Y direction (plus or minus) relative to the nozzle. A number of distinct lateral (i.e., Y) positions were used for each test case listed in Appendix A. Typically, four positions were applied to flat plate cases and three for the other cases. The flat plate lateral positions ranged from $Y = -1/2$ to $Y = 2 1/2$ with the most common set being $Y = -1/2, 0, 1$ and $1 1/2$. In most of the curved plate cases, the set of lateral positions are $Y = 0, 1$ and 2 . For the wing-flaps, $Y = 0, -1$ and -2 are used.

At the position $Y = 0$, the specimens had their chord at the span center in line with the center of the nozzle. A limited number of pickups for a test case were placed along this chord, as well as at locations away from it. These instruments remained fixed on the specimen while it was shifted laterally to obtain the necessary spatial coverage. The long spans provided for each specimen allow the extent of lateral shifting indicated above without introducing edge effects.

It should be noted at this point that each case definition

given in Appendix A incorporates all of the lateral positions for the case. The test results found from each of the lateral positions are combined when displaying the results for a case later in this report.

No additional freedom of movement was made available for the OBF curved plates. For the UBF curved plates and wing-flaps cases, movements of the specimens in the X and Z directions were also required. To cover the flat plate cases, X, Z and pitch (β) movements were necessary. (β is a rotation about the Y axis and is positive when the downstream edge of the plate is furthest from the jet exit).

To accomplish the positioning prescribed in the test cases and discussed above, a support fixture for the specimens was needed to produce movements in the X, Y, Z and β directions. The fixture fabricated for the test program provided all six possible motions as illustrated in Figure 19.

The flat plate specimens were bolted at their edges to the top frame (i.e., pitch frame) of the support fixture. The curved plate specimens carried thick plates at the ends of their spans. These end plates are shown in the photographs in Figures 20 and 21 for the UBF and OBF curved plates. The end plates of a curved plate specimen are placed on members of the support fixture's upper frame and attached by screws.

The common span length (30 inches) prescribed for the flat and curved plate specimens simplified their attachment to the support fixture. The large plates at the ends of the wing-flaps (see Figure 17), however, are separated by approximately 60 inches, so a special rectangular framework was constructed to fasten the model to the pitching frame.

The flat plate set-up for temperature testing involved some special features. In order to perform a transient temperature test for heat transfer studies, a means was needed for preventing exposure of the thermocouples to the jet until the temperature of the jet flow essentially attained equilibrium. This was accomplished with a panel and rails for the panel to slide over. (See photograph in Figure 22). The rails were

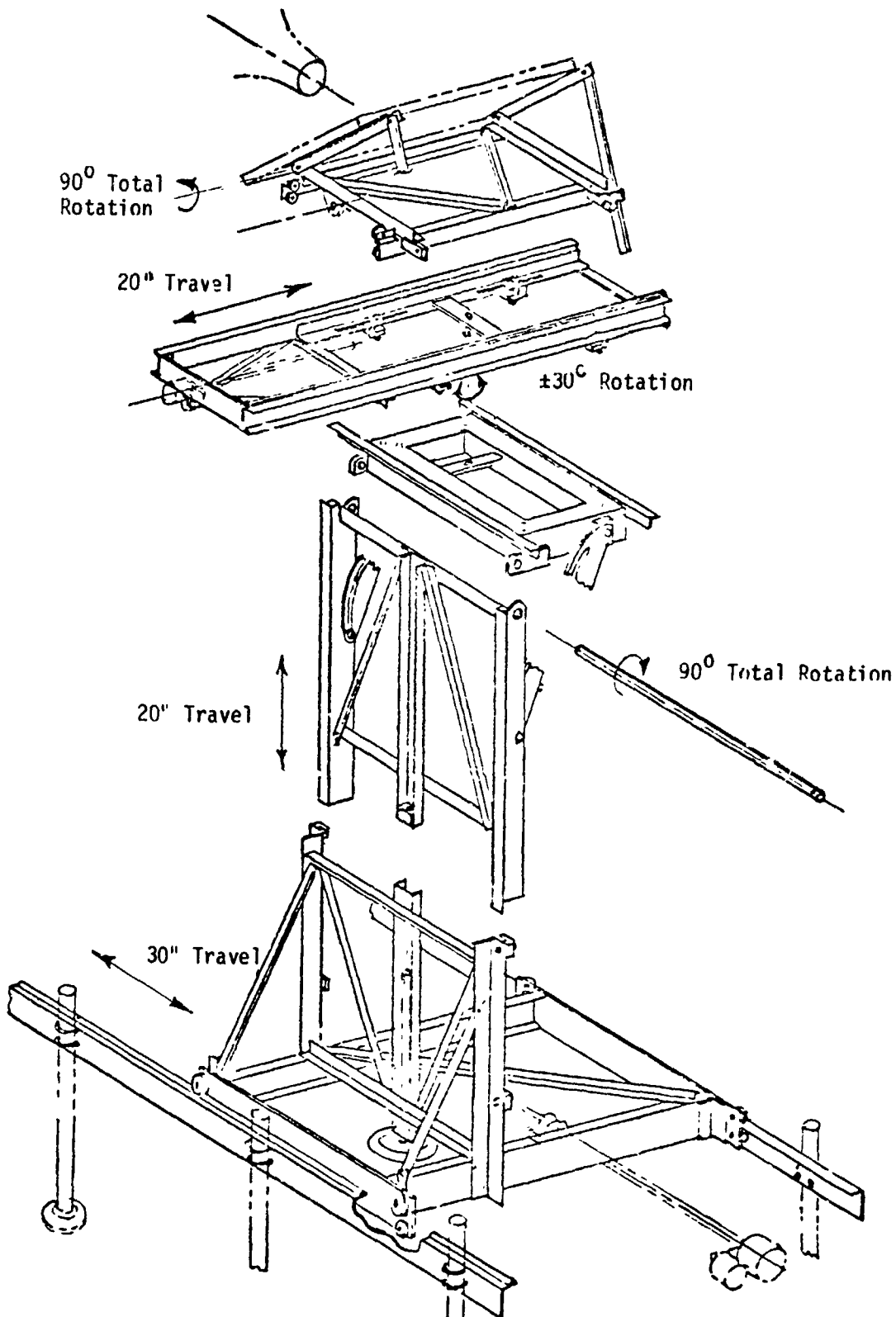


Figure 19. Schematic of Specimen Support Fixture



Figure 20. UBF Curved Plate with Attached Supports



Figure 21. OBF Curved Plate with Attached Supports

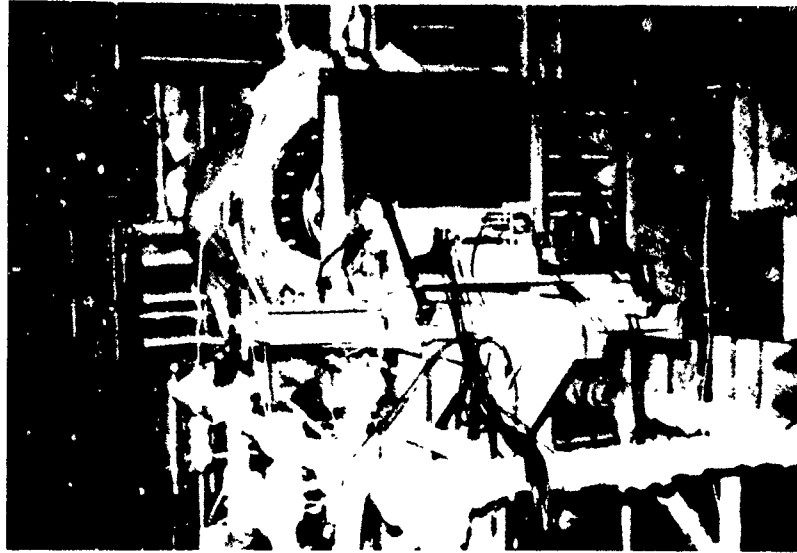


Figure 22: Set-up for Obtaining Transient Temperature Measurements

attached to the upstream and downstream edges of the plate. Initially, the panel was placed in front of the thermocouples until the jet reached the desired temperature. Using a pulley arrangement at this point, the panel is quickly pulled to the side providing a sudden exposure of the thermocouples.

The positioning of the curved plates and wing-flaps model are sufficiently defined by the case descriptions in Appendix A. The flat plates require a further detail. It is necessary in their cases to specify the location at which the jet centerline intercepts the surface.

Figure 23 shows a side view of the flat plate and nozzle. The dimension w_I gives the needed information. For the flat plate test cases in categories 1, 2, 4 and 13 (see Section II-4), the intercept of the jet centerline on the plate is either at the plate center or upstream from center. In all category 3 cases, the intercept point was at a location

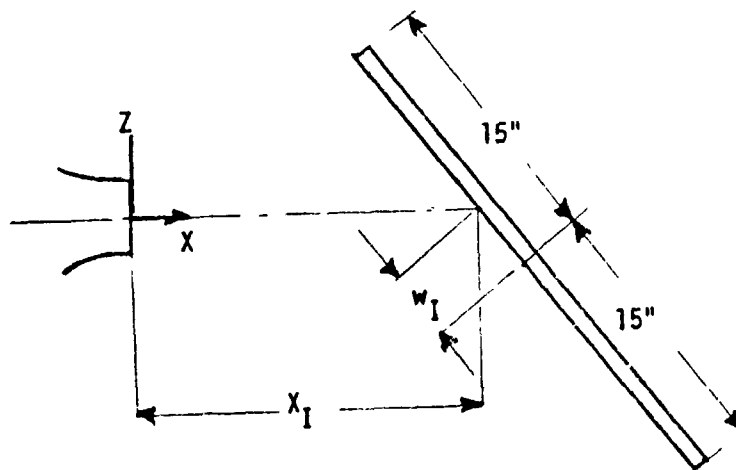


Figure 23. Geometric Center of Impingement on Flat Plate 1 1/2 inches from the downstream edge ($w_I = -13 \frac{1}{2}$ inches). The location of the intercept in the category 13 cases was always at $w_I = 0$. For categories 1 and 2, the intercept point depends on the angle β as follows: $w_I = 0$ for $\beta = 90^\circ$; $w_I = + \frac{1}{2}$ inch for $\beta = 50^\circ$ and $w_I = +1$ inch for $\beta = 25^\circ$. For category 4, the lobed nozzle cases, these dimensions for w_I were doubled.

The above detail defines the geometric centers of impingement for all flat plate set-ups. For the UBF curved plates and wing-flaps model set-ups, the geometric centers of impingement are described in Appendix E.

3. INSTRUMENTATION

The various instrumentation used in this program is shown in Figure 24. The following sections give further details for the instrumentation.

a. Fluctuating Pressure Measurements

Pressure fluctuations on the surfaces of the flat plate, the OBF plate, and the UBF plate were measured with high temperature Kulite XTEL-1-190-25G one-eighth inch pressure transducers with Type B screens. These transducers are piezoresistive bridges bonded to the back side of metallic diaphragms. Since temperature is a problem in any semiconductor circuitry, there is a temperature compensating network, effective from 80°F to 450°F,

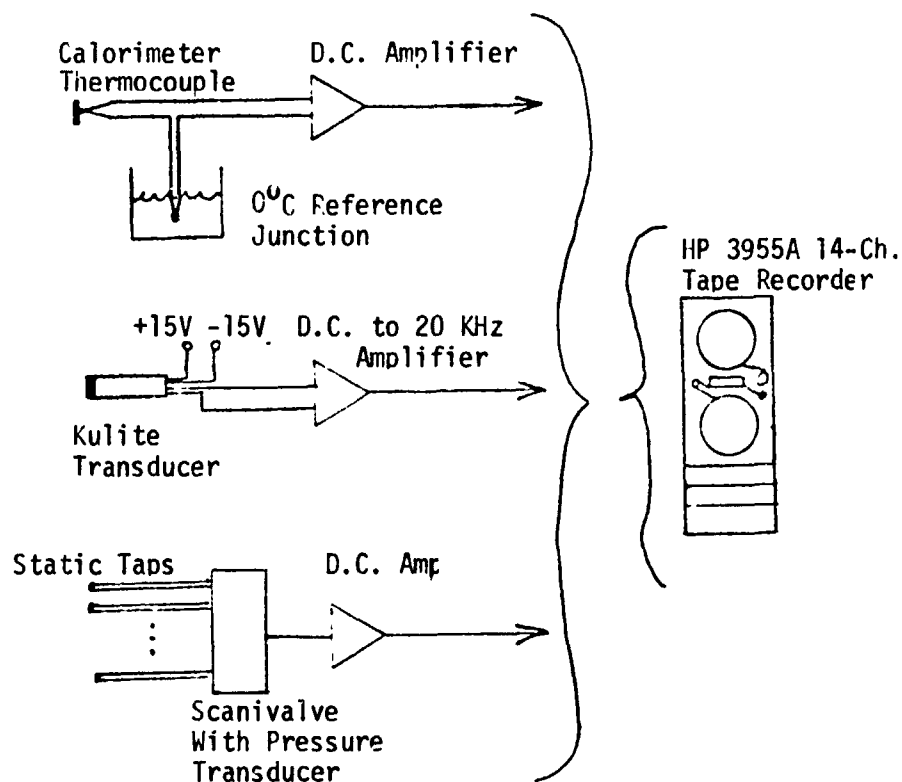


Figure 24. Test Program Instrumentation

built into the rear of each transducer housing. During mounting the transducers were screwed into threaded holes until the screens were flush with the surface to be exposed to flow (see Figure 25). This mounting arrangement was less than ideal since insertion and removal would often break off screens and sometimes cause the transducer to fail entirely. Threaded plugs were installed in the holes not occupied by a transducer.

The wing-flaps model was also instrumented with pressure transducers. These were Kulite Model XCQH-17-093-5D and were permanently installed in the brass adaptor shown in Figure 26. A total of four adaptors were used, each containing three transducers. One adaptor was installed on the upper surface and one on the lower surface of each flap. Since these Kulite transducers are rated at only 5 psi, the static pressure is carried to the back side of the diaphragm cancelling the effects of the extremely low frequency (i.e., constant) pressures fluctuations.

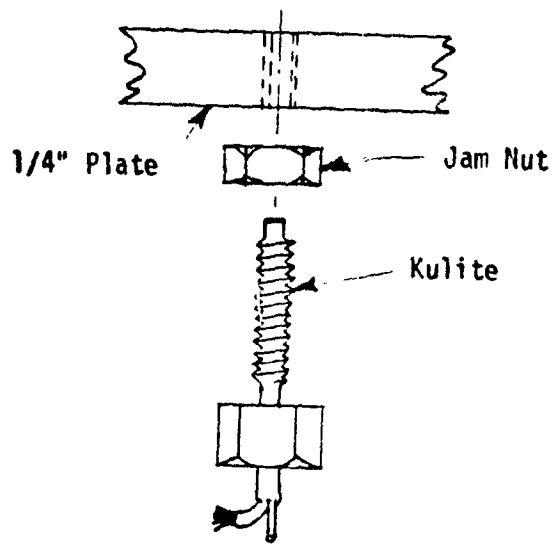


Figure 25. Fluctuating Pressure Pickup Installation on Plates

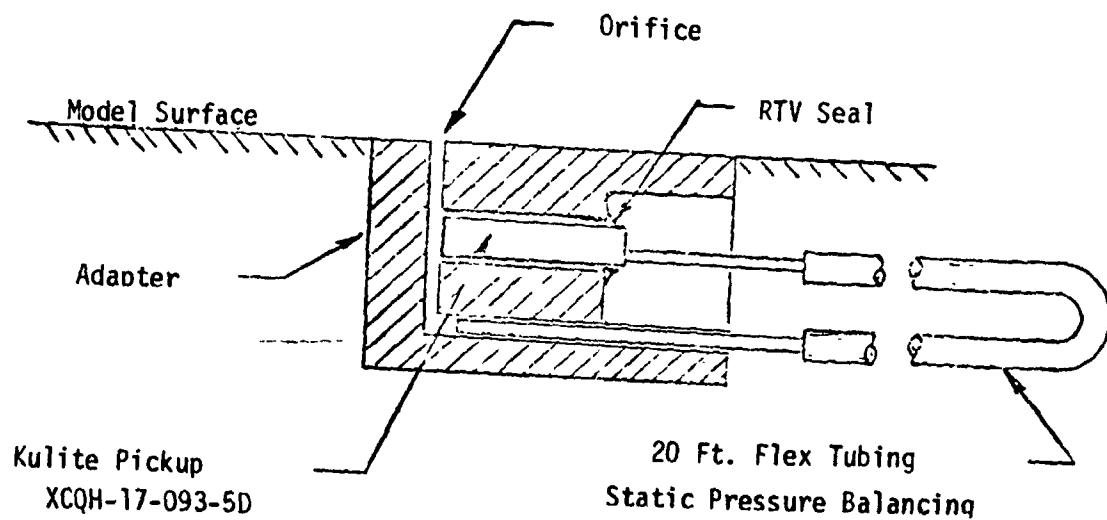


Figure 26. Fluctuating Pressure Pickup Installation on Wing-Flaps Model

For both the plate specimens and the wing-flaps model the Kulites were excited with a constant DC voltage carried from the instrumentation area to the transducers inside the anechoic room by a shielded cable. The signals were carried out: de again in a large cable of individually shielded twisted pairs to the double ended input of the amplifiers shown in Figure 27. These two stage amplifiers each have a frequency response

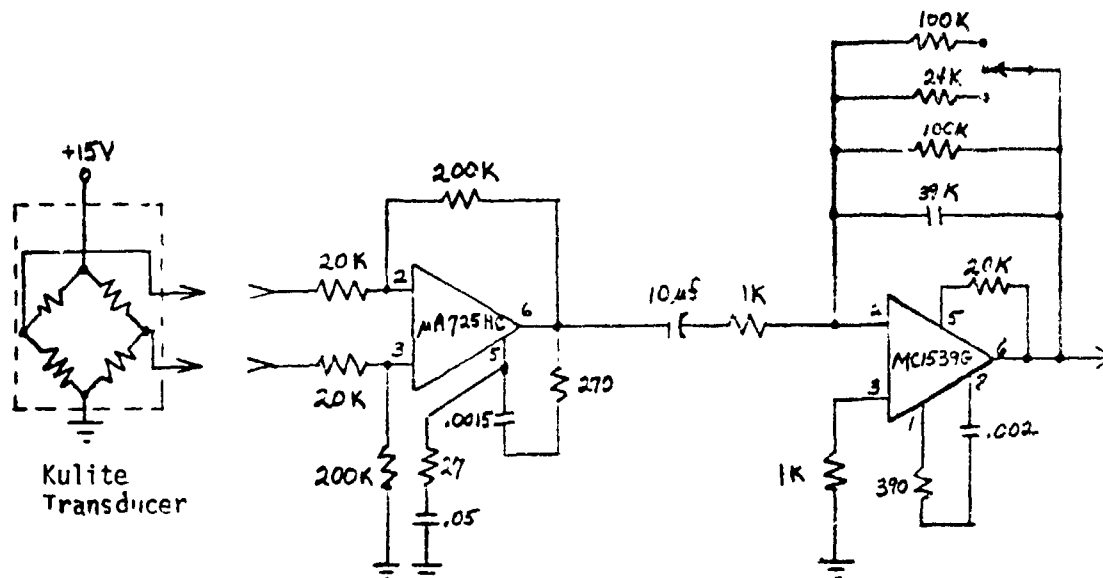


Figure 27. Signal-Conditioning System for Fluctuating Pressure Measurements

of 10 Hz to above 20 kHz. The amplified signal was then FM recorded on a Hewlett-Packard 3955A tape recording system running at 60 ips. The high frequency cutoff from the transducer through the tape recorder is 20 kHz due to limitations of the tape recorder.

b. Static Pressure Measurements

The static pressure port used on the flat and curved plates is shown in Figure 28. The ports are designed to be inserted into threaded holes in the specimen and adjusted until flush in the same way as the Kulite transducers. The port is made of .042 inch O.D. by .022 inch I.D. stainless steel tubing inserted into a threaded sleeve and brazed. At the back side (away from the flow) the static pressure port was connected to a Scanivalve with plastic tubing. There were forty-six ports in the

flat plate, twenty-two in each UBF curved plate, and twenty in the OBF plate (sixteen in the plate and four in the trailing edge extension).

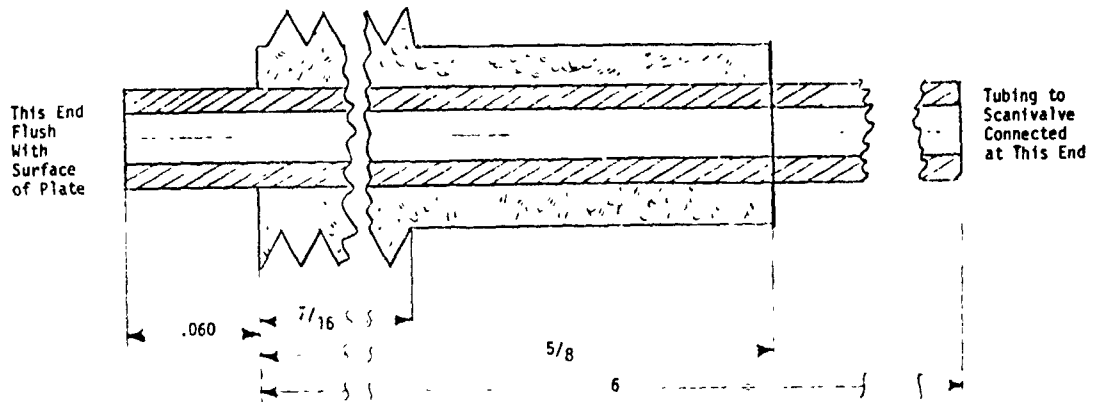


Figure 28. Static Pressure Port

The wing-flaps model contained sixty static pressure ports built into the airfoils of the model. All sixty orifices lie on the same chord, twenty-seven on the wing, eighteen on the forward flap and fifteen on the aft flap. The ports on this model are connected with plastic tubing to a double Scanivalve in the same way that the ports on the plate models were connected.

Static pressure measurement was done with a fifteen psi Statham strain gauge pressure transducer fitted to the Scanivalve. In addition to the ports connected with the static pressure ports, two other Scanivalve ports served to provide a calibration - one vented to atmospheric pressure and another connected to a known pressure. The pressure transducer output was amplified with a differential DC amplifier and then recorded on magnetic tape.

c. Temperature Measurements

Transient and steady-state temperature measurements on the flat plate were made with the thermocouples shown in Figure 29. The copper-constantan thermocouple welded to the thin copper disk provides the temperature measurement while the glass-silicon laminate insulates the disk from everything except the airflow. The thermocouple signal is

carried to the amplifier and ice bath (Figure 30) outside the anechoic room with shielded thermocouple extension cable. The amplified signal is then recorded FM. A calibration is provided by recording the signal when the calorimeter is at room temperature and (1) the reference junction is at 212°F and when (2) the reference junction is at 32°F.

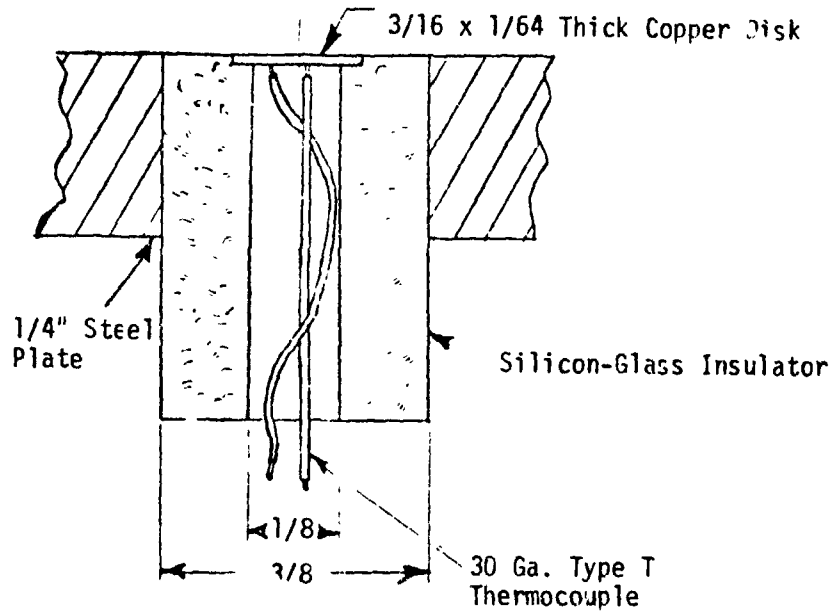


Figure 29. Calorimeter and Thermocouple Installation

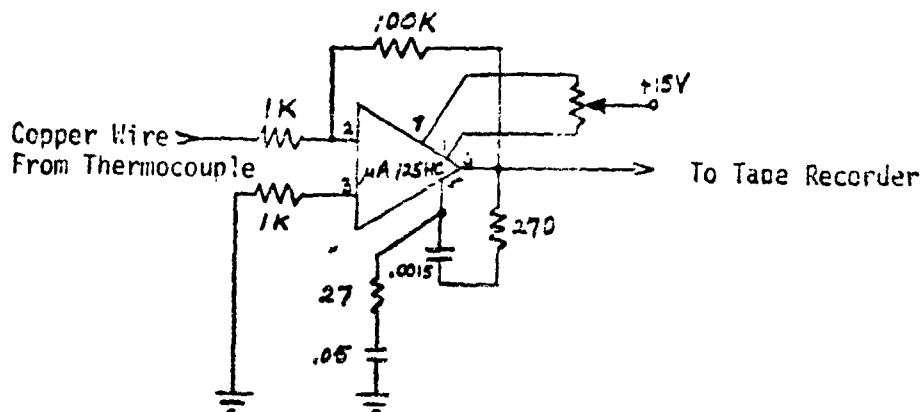


Figure 30. Signal-Conditioning System for Temperature Measurements

4. DATA PROCESSING

The data processing to be discussed refers to that conducted on the fluctuating pressure data. No special processing was performed on the acquired static pressure and temperature data.

There were two phases to the fluctuating pressure data processing. The first was performed on-site and used for discerning the quality of the data soon after acquisition. The second phase involved a comprehensive processing that gave the frequency dependent functions described in Section II-5.

a. On-Site

All acquired channels of fluctuating pressure data were analyzed for overall RMS values using a B & K Model 2409 true RMS meter. In addition, power spectra were obtained for selected channels. This was accomplished using Spectral Dynamics SD301C analyzer and SD309 averager along with an x-y plotter. The spectral analyzer covered the full 20 kHz range in 500 increments ($\Delta f = 40$ Hz) using a bandwidth of 60 Hz ($1.5 \times \Delta f$).

b. Digital System

The major data processing in the program was performed digitally at AFFDL using the Hewlett-Packard HP5451B system which is built around a 2100 series computer. The data processing flow diagram is shown in Figure 31.

The processing was conducted to 10 kHz. A sampling rate of 20,000 samples/second was applied to each analyzed channel using the HP5466 A/D converter. From each channel, 1024 sampled values were included in a record operated on by a fast Fourier transform routine. This provided a frequency increment $\Delta f = 20,000/1024 \approx 20$ Hz. A total of 50 of these records of 1024 sampled values constituted the complete ensemble processed for each channel. That is, a record length of approximately 2.5 seconds was used. The power spectrum of each channel and the cross

spectrum (co and quad) of the two channels were obtained for each pair of records of 1024 values and averaged over the 50 sets. The result of this was raw estimates for the two power spectra and for the co and quad spectra. These four functions, each containing 512 magnitudes, were saved on disk. In a subsequent operation the raw power spectra were smoothed and placed on plots using Versatec Model 1600.

In conjunction with the smoothed power spectra, the cross spectrum is defined by a correlation spectrum ($\rho(f)$ in Section II-5) and a phase spectrum ($\theta^\circ(f)$ in Section II-5). To obtain these spectra, the raw forms of the power spectra and co and quad spectra were transformed to auto and cross correlation functions, respectively. These time dependent functions were multiplied by a window and then transformed back into the frequency domain. Essentially smoothed power spectra and co and quad spectra were produced and these in turn were manipulated to obtain the coherence spectrum, $\rho^2(f)$, and a phase spectrum constrained between $+180^\circ$ and -180° . Subsequently, these spectra were operated upon to arrive at $\rho(f)$ and $\theta^\circ(f)$; the latter being a 'straightening-out' or 'unwinding' of the previously constrained spectrum. These spectra were then plotted using the Versatec plotter.

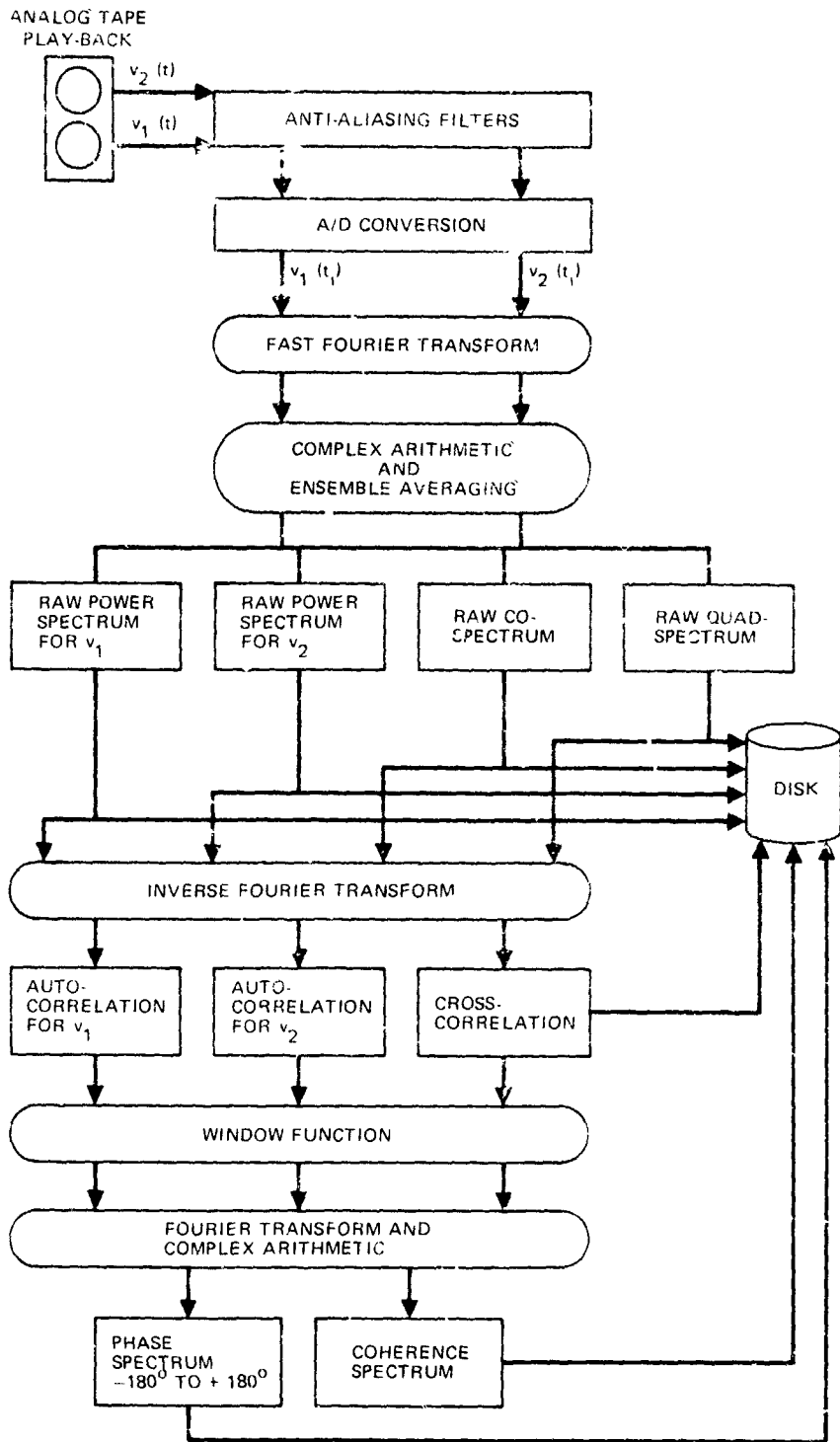


FIGURE 31. DATA PROCESSING FLOW DIAGRAM

THE FOLLOWING OPERATIONS ARE PERFORMED
 USING THE DISK OPERATING SYSTEM WHICH
 INCLUDES FORTRAN

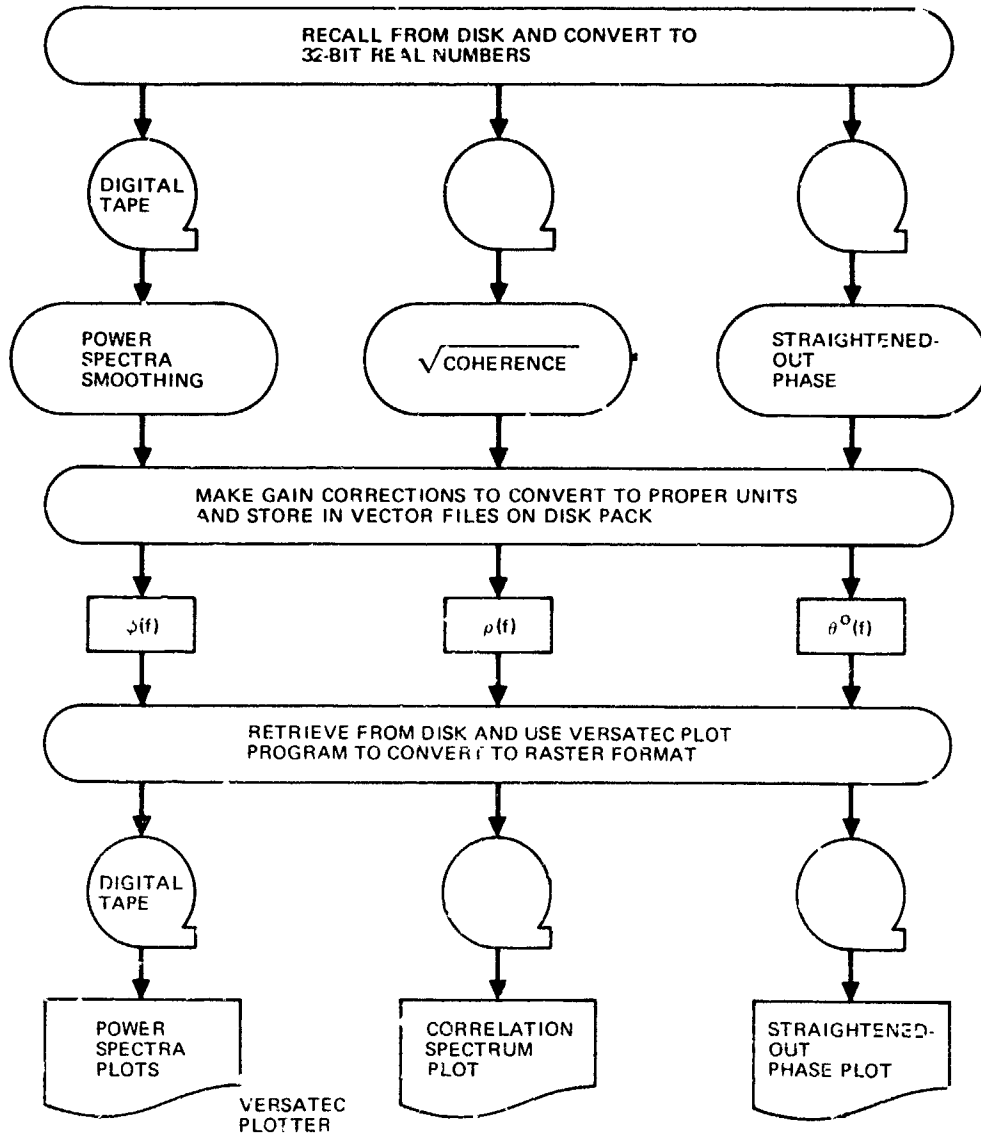


FIGURE 31. DATA PROCESSING FLOW DIAGRAM (CONT'D)

SECTION IV

TEST RESULTS

The data collected from the experimental program are presented in Appendices G through J. This section is primarily concerned with the analyses of the fluctuating pressure trends in Appendix I. Serving this analysis are the static pressure data given in Appendix H. (The temperature data in Appendix G is not applied in this section but considered in Section V-1b). The four test specimens are treated separately in this section. It is the intention of the following discussion to present the most significant trends found in the data for each of the specimens.

1. FLAT PLATE

The flat plate can be used as a model for a STOL airplane surface exposed to a turbulent jet. The advantages of using a flat plate are evident - the simple configuration offers basic information about the properties of an impinging jet and is unaffected by the complicated geometry of the wing and flaps.

a. Static Pressure

The static pressure profile for normal impingement is shown in Figure 32. The spreading of the impinging jet is evident by comparing the profiles measured at $X/D_j = 7$ and at $X/D_j = 10$. For oblique impingement, the mean flow is not symmetric in the chordwise (streamwise) direction. This fact is reflected in the static pressure measurements (Figure 33). A length scale, L_s , was chosen for indicating the spreading of the impinging jet. L_s is defined as the distance between two points where the static pressure is half the maximum static pressure. Therefore, the length scale also indicates the size of a region of highest loading, $[p_s/(p_s \text{ at stag. pt.})] > 0.5$. The values of L_s are plotted against the distance between the plate and the nozzle (Figure 34). For oblique impingement, the streamwise spreading is greater than the spanwise spreading. The streamwise spreading at oblique impingement is also greater than at normal impingement. The spreading of a free jet based

upon velocity profile is given in Appendix K-3, as well as in Reference 1 (Part 1). This result is shown for comparison.

b. RMS Level of Pressure Fluctuations

For the jet impinging perpendicular to the plate ($\beta = 90^\circ$), the levels of pressure fluctuations are as shown in Figure 35. When $x/D_j = 5$, the profile indicates that the potential core still exists. When the plate is moved downstream to $X/D_j = 7$ and 10, the profiles are still not in asymptotic state. In the spanwise direction for $y/D_j > 4.5$, the levels of fluctuating pressure are almost equal for all X/D_j values. This is apparently due to the development of the wall jet.

The pressure fluctuations have a "two-peak" profile when the jet impinges on the plate with an oblique angle. The fluctuations tend to peak near the stagnation point. Downstream of the stagnation point the level first falls off but then rises to a secondary peak before falling further. The data presented in Figures 36 and 37 are limited to a region close to the stagnation point, $y/D_j \leq 2$ and $r/D_j \leq 2$, so the double peak profile does not appear. The data in Figure 36 confirm results in Reference 3; that is, the RMS pressure fluctuation has a steeper gradient for lower X/D_j near the stagnation point in the case $\beta = 50^\circ$. In Figure 37, the data in spanwise direction also show significant gradients, but less sensitivity to X/D_j .

Figure 38 presents the effect of Mach number on fluctuating pressure at different angles of inclination. The result that the pressure fluctuations are scaled to the second power of Mach number ($0.35 \leq M_j \leq 0.74$) offers simple design information.

The jet was heated to more than 900°R to examine the temperature's effect on the pressure fluctuations. For a free jet, it is well known that the high temperature will enhance the entrainment, hence the spreading of the hot jet will be faster than the cold jet. The measurement of the fluctuating pressure on the plate (Figure 39) reflects that the same phenomenon appears in an impinging jet. The levels of fluctuating

pressure at the stagnation point are essentially unaffected by the temperature of the jet. At other locations, the levels are typically higher for the hot jet.

For studying the edge effects, the flat plate is moved so that the intersection point of the axis of the jet with the plate is $1\frac{1}{2}$ inches (or $\frac{3}{4} D_j$) away from the downstream edge. A comparison of results from the center of the plate and the edge effect data is made in Figure 40. Apparently the presence of an edge generates high pressure fluctuations. A similar result was found in Reference 4 for a jet impinging on a curved plate. By extending the trailing edge further downstream from the center of jet impingement, it was found in Reference 4 that the edge effect will diminish.

A daisy nozzle with an equivalent diameter of two inches was used. The levels of fluctuating pressures were compared (Figure 41) for a round nozzle at $X/D_j = 5$ and a daisy nozzle at $X/D_{eq} = 5$. The pressure fluctuations from a daisy nozzle are substantially lower than that of a round nozzle.

c. Spectra

The spectra of pressure fluctuations were measured at several locations on the plate's surface in each test case. There are two contrasting spectral shapes (Figure 42). The spectral shape of the first type is essentially constant in the initial portion, then rolls-off rapidly at the high frequency end. This type of spectrum is found near the stagnation point. For the second type of spectrum, there is a well-defined peak in the spectral distribution. At locations far removed from the stagnation point, the spectra are of the second type. A transition between the two shapes occurs as the location moves away from the stagnation point.

This result can be seen clearly from the spatial distribution of the peak amplification of the spectra, P , (Figure 43). (See Section II-5 for definition of P .) For $y/D_j < 1$, P is near unity. It then increases until $y/D_j = 2$. Beyond $y/D_j = 2$, it decreases with distance for

the shown X/D_j range. From Figure 42, it is clear that the low frequency pressure fluctuations decrease with the distance from the stagnation point. High frequency pressure fluctuations tend to increase due to development of turbulence.

The Strouhal numbers based upon the peak power frequency, $S_p = f_p D_j / V_j$, are shown in Figure 44. For a free jet, the potential core ends at about $X/D_j = 6$. For a jet impinging on a plate, there is no experimental information on the length of the potential core, but from some indirect experimental evidence it is speculated that the potential core will intercept a plate placed less than six diameters away from the nozzle. The large shedding vortices found in the free jet then still appear in the flow field over the plate's surface. Since the Strouhal numbers, S_p , are found to be in the vicinity of 0.3 for $X/D_j = 5$, the peak spectral component might be a contribution from the large shedding vortices impinging on the plate. At $X/D_j = 5$, the distribution of the Strouhal numbers S_p exhibits a peak between $y/D_j = 1.0$ and 2.0.

Beyond the potential core, approximately $X/D_j > 6$, the maximum velocity will be less than the jet exit velocity. In this region the Strouhal number, $S_p = f_p D_j / V_j$, substantially decreases with increasing X/D_j . This tendency may be diminished by reconsidering the definition of the Strouhal number.

The turbulent flow has multiple length scales, such as the integral scale, indicating roughly the size of large turbulent structures, and the Kolmogoroff scale, indicating the size of small turbulent eddies. The integral scale usually is about the length of $2r_{1/2}$ (see Figure K-3) of the jet. The length scale L_s is a measure of the spreading of the jet, so it is close to the integral scale for the turbulence. Another Strouhal number can be defined using the frequency at the spectral peak, f_p , the length scale, L_s , and V_{q_2} , the maximum velocity of a free jet measured at the X/D_j of the plate. The new Strouhal numbers, $S_p^* = f_p L_s / V_{q_2}$, are presented in Figure 45 for different X/D_j and bring the data closer together than shown in Figure 44. This implies that the pressure fluctuations at peak power are produced by the large scale turbulent structures.

If length scale, L_s , is a measure of the integral scale, then L_s/V_e is a characteristic time for the passage of the large scale turbulent structures. For small X/D_j , $L_s = D_j$ and $V_e = V_j$ so V_j/D_j is the passage frequency in this case. Varying the exit velocity changes the passage frequency of the large scale structures. The effect of the exit velocity can be viewed from the previously defined Strouhal number S_p . Figure 46 shows the Strouhal number S_p does not vary with Mach number. This is additional evidence of the relationship between the peak power frequency and the large scale structures.

As can be observed in Figure 42, the power spectra at locations downstream of the stagnation point contain a higher fraction of the total energy in the higher frequencies than do spectra taken near the stagnation point. The reason is that since the turbulence is more developed downstream, more energy has been transferred from the low frequency, large scale turbulence into the higher frequency, small scale turbulence. This can also be seen by plotting the roll-off exponent, n , against the distance from stagnation point, (Figure 47). (See Section II-5 for definition of n .) The values of roll-off exponent decrease rapidly for $y/D_j < 1$, then reach an asymptotic value, $n = 2$, as the flow becomes a wall jet. The value of n also decreases with X/D_j for the same measuring location. This can also be explained by the fact that when the plate is further downstream, the small scale turbulence is more fully developed.

The tested daisy nozzle has an equivalent diameter, D_{eq} , of 2". At $X/D_{eq} \geq 8$, the spectra obtained over the spatial region of coverage were essentially flat. The high frequency roll-off of the spectra was steep for all tested plate positions with typical values for n between 3 and 5.

d. Convection Velocity

The broadband convection velocity, \bar{V}_c , is taken from the space-time correlation between two measuring stations. The distance between the two stations, Δ , divided by the time delay at maximum correlation of the unfiltered data is the convection velocity. The normalized convection velocity for different plate locations is displayed in Figure 48. The

broadband convection velocity is about 60% of the jet exit velocity. The ratio, \bar{V}_c/V_j , does not change with Mach number.

The broadband convection velocity is a weighted average of the convection velocities of turbulent eddies at all wavelengths. Eddies of different sizes or different wavelength may not be convected at the same speed (References 13 and 14). The narrowband convection velocity, $V_c(f) = 360 f \Delta / \theta^\circ(f)$, indicates the speed of eddies of different wavelength. " $\theta^\circ(f)$ " is the phase angle at frequency f of the cross spectrum between the two measuring points. The narrowband convection velocity is about 12% of the jet exit velocity at $f = 100$ Hz (Figure 49) and increases to $.75 V_j$ at $f = 5000$ Hz. Interestingly enough, the broadband convection velocity has the same value as the narrowband convection velocity at a frequency f_c associated with a Strouhal number $S_c = 0.3$, where $S_c = f_c D_j / V_j$.

e. Coherence

The square root of the coherence is the narrowband correlation coefficient $\rho(f)$ previously defined in Section II-5. In Figure 50, the maximum value of the square root of the coherence occurs at $S_m = f_m D_j / V_j = 0.3$, where f_m is the frequency at the maximum. This indicates that the shedding vortices may play an important role in the maximum coherence. The maxima are compared for different test conditions in Figure 51 to Figure 53. A feature in all test situations is that the maximum, ρ_m , increases from the stagnation point in the streamwise direction and also increases with the distance from the centerline in the spanwise direction.

The variation of Mach number has no significant influence on the maximum values, ρ_m , (Figure 51), because these values are related to the development of shedding vortices, while Mach number only affects the passing frequency. Changing the position of the plate does change ρ_m . In the streamwise direction, ρ_m increases with X/D_j . In the spanwise direction, it decreases with X/D_j . However, no explanation is available. The temperature of the jet was raised to $910^\circ R$ to examine the influence of temperature on ρ_m . The value of ρ_m decreases at high jet temperature but only to a small extent.

2. UBF CURVED PLATE

In the present experiment, the curved plates are used in order to eliminate the complicated geometric boundary of the wing and flap model while retaining the curvature effect lost with the flat plate. The two curved plates used in the experiment have different trailing edge deflection angles so the effect of curvature on fluctuating pressure can be examined. The Mach number is varied from 0.35 to 0.74. The distance between the jet and the plate is changed. Though the change is very much limited by geometry, some significant effects are found. Mean surface pressure, level of fluctuating pressure, spectra, convection velocity, and coherence characteristics of the surface pressures are discussed in the following subsections.

a. Static Pressure

In general, the static pressure distribution starts with an adverse pressure gradient near the leading edge, as the pressure increases to a maximum, and then becomes favorable toward the trailing edge. Both the favorable and adverse pressure gradients are sensitive to the geometry of the plates. As expected, the pressure gradient and the peak pressure on the plate with a 50° deflection angle are both higher than on the plate with a 25° deflection angle (Figure 54). For the same curved plate, the pressure distribution can be collapsed to a single curve if the pressure is normalized to the jet's dynamic pressure (Figure 54). The profile also changes with the relative position between the nozzle and the plate (Figure 55). The variation caused by moving the plate in the streamwise, X, direction is less than that caused by movement in the Z direction. This is because the flow properties have a much larger gradient in the Z direction.

b. RMS Level of Surface Pressure Fluctuation

As with the static pressure, the RMS values of the fluctuating pressures can be scaled to the jet's dynamic pressure (Figure 56). An interesting phenomenon is observed in the spatial distribution of the

RMS values. For the same Mach number, the maximum fluctuation levels are of the same order for two different plates (Figure 57). It is speculated that the reason for this is as follows: The pressure fluctuation is related to the fluctuating velocity, and the velocity fluctuation has developed to the same state for similar downstream locations on the two plates.

The spatial distribution of RMS values can be seen (Figure 57) to have different patterns for the two plates. This is a result of the difference in curvature. Evidence for this conclusion is that the spatial distributions of the RMS values normalized by the local mean pressure have the same shape (Figure 58). The difference in magnitude of the normalized profile is due to the large difference in values of mean pressures on the two plates. The results of varying the relative position between nozzle and plate are similar to the mean pressure; i.e., the effect of changing streamwise distance is not as pronounced as changing Z_{LE} (Figure 59).

c. Spectra

For dynamic loading studies, the magnitude of the fluctuating pressures is not the only important information; spectra are also needed. The Strouhal numbers, $f_p D_j / V_j$, based upon the peak power frequency, range from 0.2 to 0.4 (Figures 60, 61 and 62) with a representative value near 0.3. It is to be noted that the Strouhal number, 0.3, is very close to the most unstable mode of a free jet (Reference 10). This is an indication that the peak spectral component may be associated with large shedding vortices.

The roll-off exponent n (see Section II-5) is seen in Figure 63 to be a decreasing function of the streamwise distance approaching a value of 2 at the downstream end. This implies that the flow is still in a developing range. Relatively more high frequency components are generated at downstream stations. The roll-off exponents do not vary appreciably with Mach number, deflection angle (Figures 63 and 64), or the relative positions of the jet and plate (Figure 65). This is because the changes in geometry or deflection angle mostly affect the

3. WING-FLAPS MODEL

The experimental results of the flat plate and the curved plate provided basic information about the fluctuating pressures from the flow surface interaction. The wing-flaps configuration is considerably more complicated in geometry. The presence of gaps between surfaces will affect the surface pressure fluctuations. The purpose of testing the wing-flaps model is to find the surface load properties for a realistic UBF geometry and to link these properties to those measured in the more basic configurations.

a. RMS Level of Pressure Fluctuations

The spanwise distributions of pressure fluctuations on the two flaps for one of the test configurations are displayed in Figure 70. The fluctuating pressure level is usually higher on the aft flap than on the forward flap. The pressure distribution on a curved plate is included in Figure 70 for comparison. For $y/D_j > 0.5$, the RMS pressure fluctuation on a curved plate is close to that on the lower surfaces of the two flaps. For $y/D_j < 0.5$, the pressure fluctuations on the curved plate exceed those on the two flaps. However, for a slight change in Z_w (Figure 71), a significant difference was found. This strong sensitivity of the RMS levels to changes in Z_w was also found for the curved plates from corresponding changes of Z_{LE} .

For a daisy nozzle test, the pressure fluctuations were considerably lower than for a round nozzle. The same result was found for the basic configurations. The largest pressure fluctuations on the flat plate and on the curved plates for a daisy nozzle test are of the same order as on the wing-flaps model (Figure 72).

b. Spectra

The spanwise distribution of the Strouhal numbers based on the peak power frequency, $S_p = f_p D_j / V_j$, are shown in Figure 73. The values of the Strouhal numbers start near 0.3, close to the centerline, and decrease

to 0.2. Apparently, the large shedding vortices still play an important role in generating the pressure fluctuations on the wing-flaps system. The spanwise distribution of the roll-off exponent, n , (Figure 74) is very nearly constant at a value of 2.

c. Coherence

The maximum values of the square root of coherence, ρ_m , on the two flaps are presented in Figure 75. The increasing values of ρ_m with distance from centerline was found for both the curved plate and wing-flaps model.

d. Narrowband Convection Speed

The narrowband convection speed, $V_c(f)$, on the wing-flaps model is a function of wave number. The convection speed $V_c(f)$ normalized to the jet velocity is about 0.25 at low frequency (Figure 76) and increases with frequency to a value of 0.75. A similar relation between $V_c(f)$ and f is found for the curved plates (Figure 69).

4. OBF CURVED PLATE

The alternative to the UBF approach of STOL design is to mount the jet engine above the wing. According to the Coanda effect, the exhaust gases from the jet engine will follow the contour of the upper surface of the wing and flaps and be deflected downward generating additional lift. In this test program, the OBF system is tested in a limited number of test cases. A preliminary test indicated that the original design of the nozzle did not produce a desirable flow condition on the surface of the plate. (Evidence of this can be seen from the static pressure distribution in Figure H-4.) To correct this, an extension was added to the upper surface at the nozzle exit. From the surface static pressure measurements, it can be inferred that some deficiency in the flow condition still remains, but the condition is much improved by using the extension. Due to limited scope of the experiment, no further improvement was made. However, some interesting features of this flow configuration were found that are believed relevant to OBF systems.

a. Static Pressure Distribution

The static pressure distributions are shown in Figure 77. The profiles of different deflection angles ($\beta_{TE} = 40^\circ$ and 70°) and of different Mach numbers can be collapsed into a single curve by normalizing the static pressure to q_j . The positive pressure near the exit of the nozzle is caused by the nozzle extension directing the flow down onto the plate. The first negative pressure peak from the leading edge might be indicative of a tendency toward local separation.

b. RMS Level of Pressure Fluctuations

For $\beta_{TE} = 40^\circ$, the pressure fluctuations increase with distance from the leading edge (Figure 78). Similar to the other test models, the level of fluctuating pressure can be scaled to the dynamic pressure, q_j , or in other words to the second power of Mach number, M_j^2 . By adding an extension plate at the trailing edge, the deflection angle changes from 40° to 70° . The pressure fluctuations differ only moderately at common locations on the two models. The influence of the downstream boundary condition is therefore relatively weak beyond a small distance upstream from the trailing edge.

c. Spectra

The Strouhal number based upon peak power frequency, $S_p = f_p D_{eq} / V_j$, is a decreasing function of the distance from the leading edge (Figure 79).

For the roll-off exponent, n , the values of n decrease in the downstream direction (Figure 80). The asymptotic value of n at downstream locations is 2.

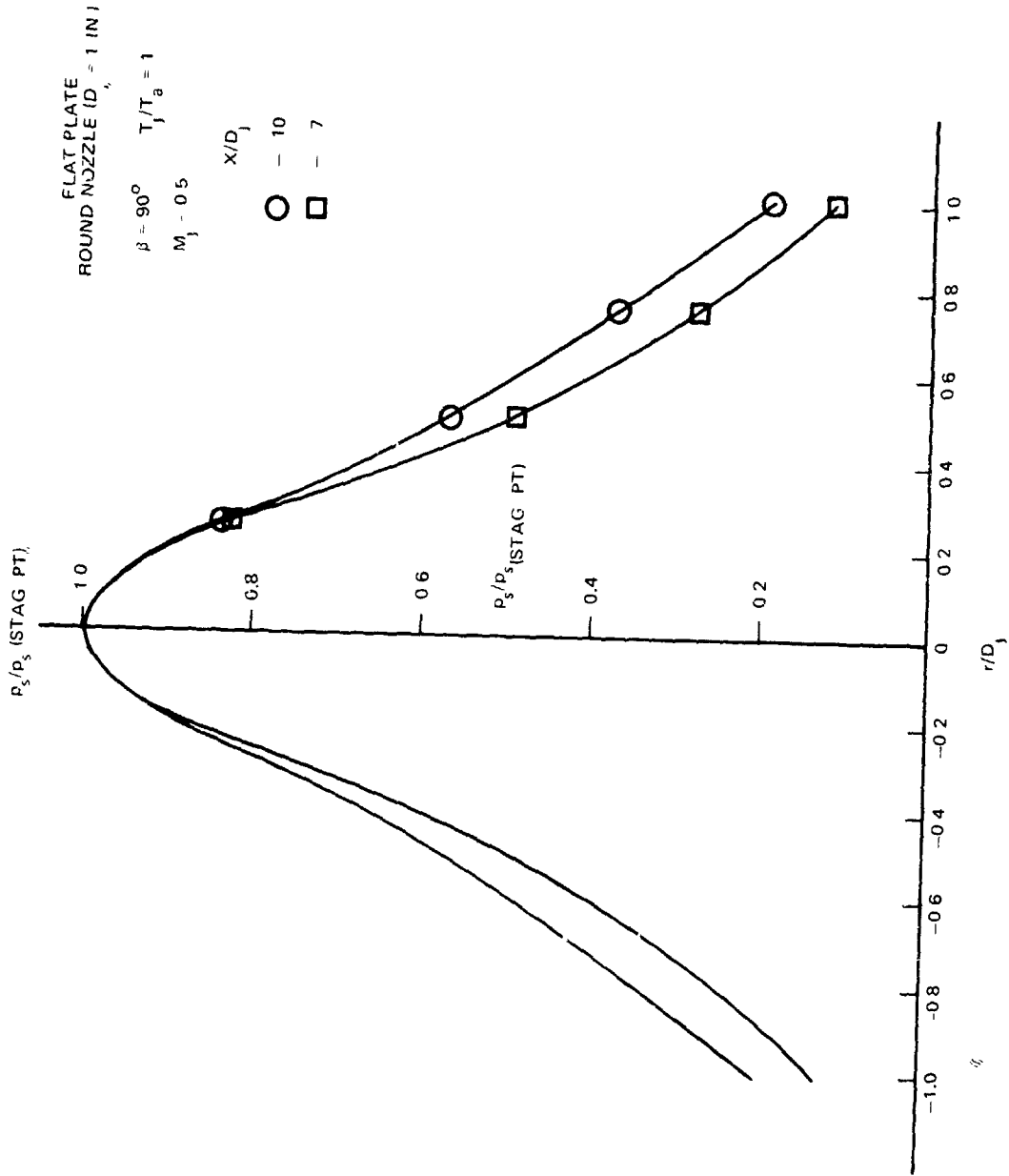


FIGURE 32. STATIC PRESSURE DISTRIBUTIONS ON A FLAT PLATE AT $\beta = 90$ DEG AND DIFFERENT x/D_1

FLAT PLATE
ROUND NOZZLE ($D_j = 1$ IN)

$\beta = 50^\circ, T_j/T_a = 1$

$X/D_j = 7$

$M_j = 0.5$

○ SPANWISE ($r/D_j = 0$)
 △ STREAMWISE ($y/D_j = 0$)

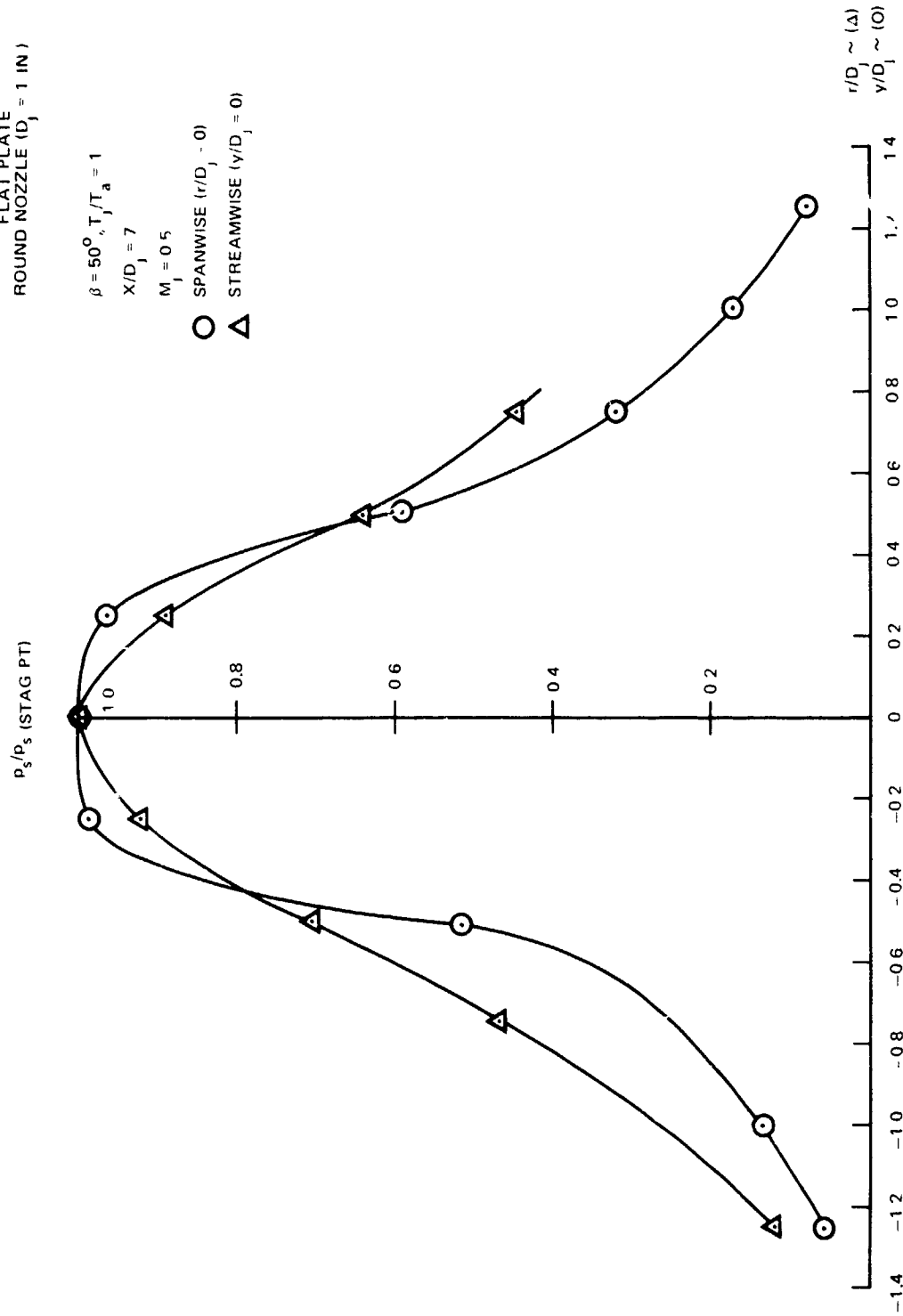


FIGURE 33. STREAMWISE AND SPANWISE STATIC PRESSURE DISTRIBUTIONS

FLAT PLATE
 ROUND NOZZLE ($D_j = 1$ IN) $M_j = 0.5$
 $T_j/T_a = 10$

IMPINGING JET $\left\{ \begin{array}{l} \beta = 50^\circ \\ \beta = 90^\circ \end{array} \right. \left\{ \begin{array}{l} \Delta \sim \text{STREAMWISE, } v/D_j = 0 \\ \circ \sim \text{SPANWISE, } v/D_j = 0 \end{array} \right.$

$\diamond \sim$ FREE JET (FIGURE K-3)

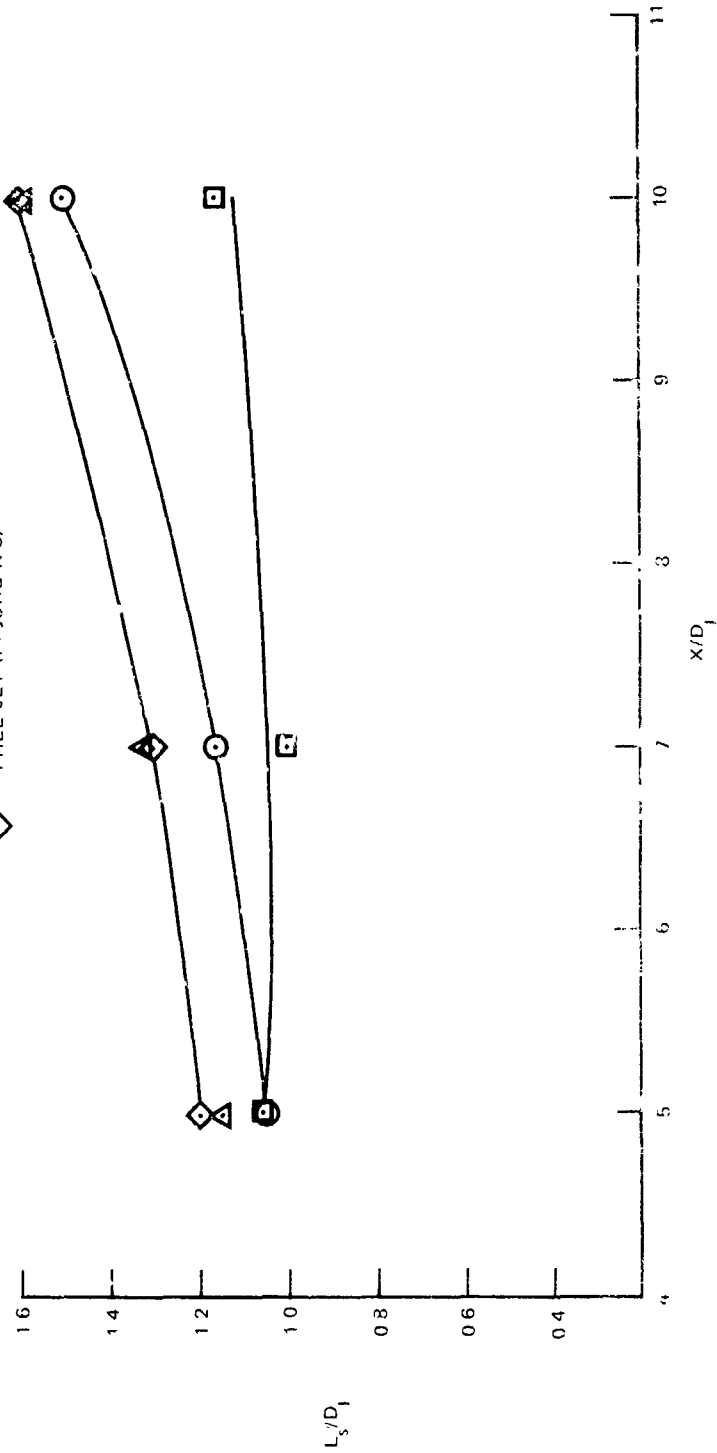


FIGURE 34. SPREADING RATES OF FREE AND IMPINGING JETS

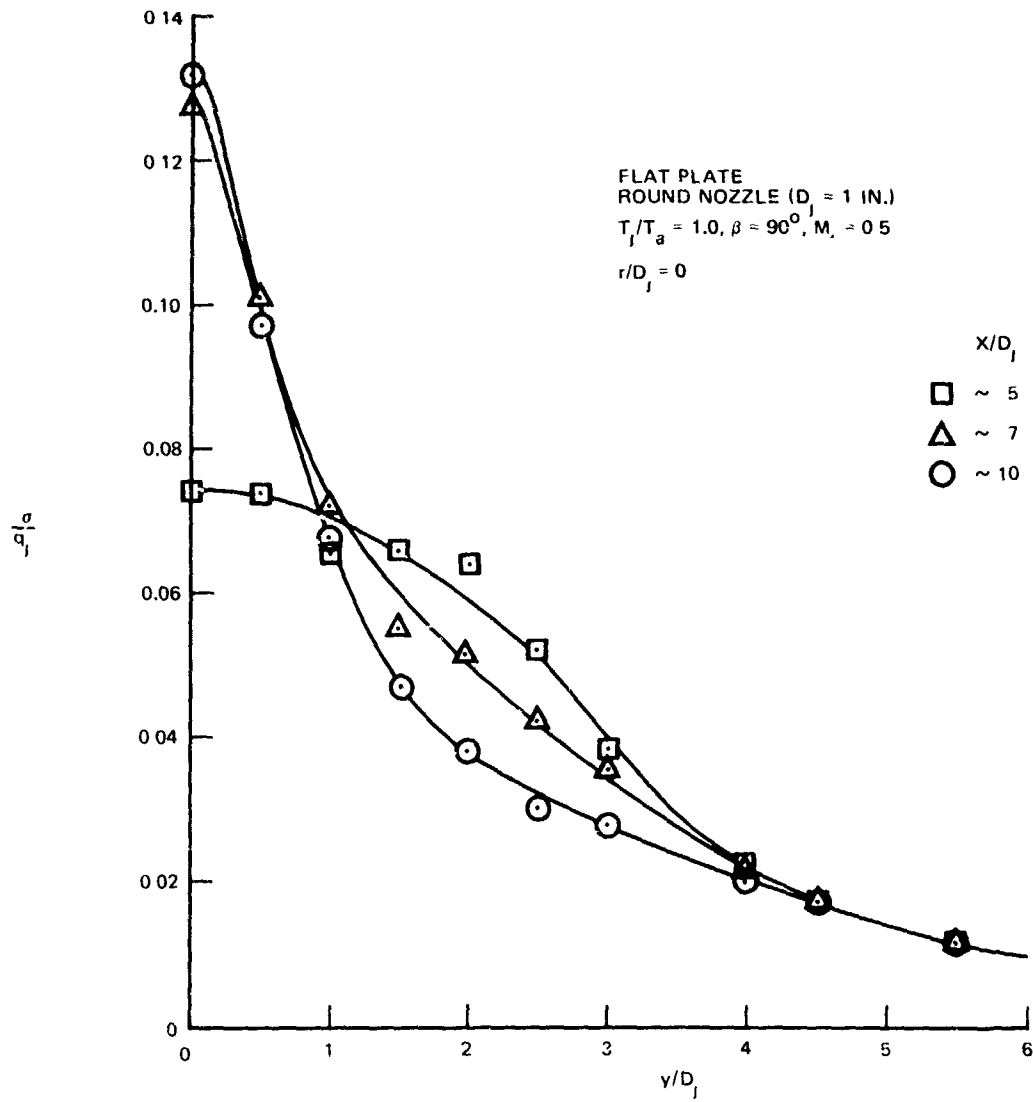


FIGURE 35. RMS PRESSURE FLUCTUATIONS IN SPANWISE DIRECTION FOR $\beta = 90$ DEG AND AT DIFFERENT X/D_1

FLAT PLATE
 ROUND NOZZLE ($D_1 = 1$ IN.)
 $T_j/T_a = 1.0, M_1 = 0.5$
 $\beta = 50^\circ, y/D_1 = 0$

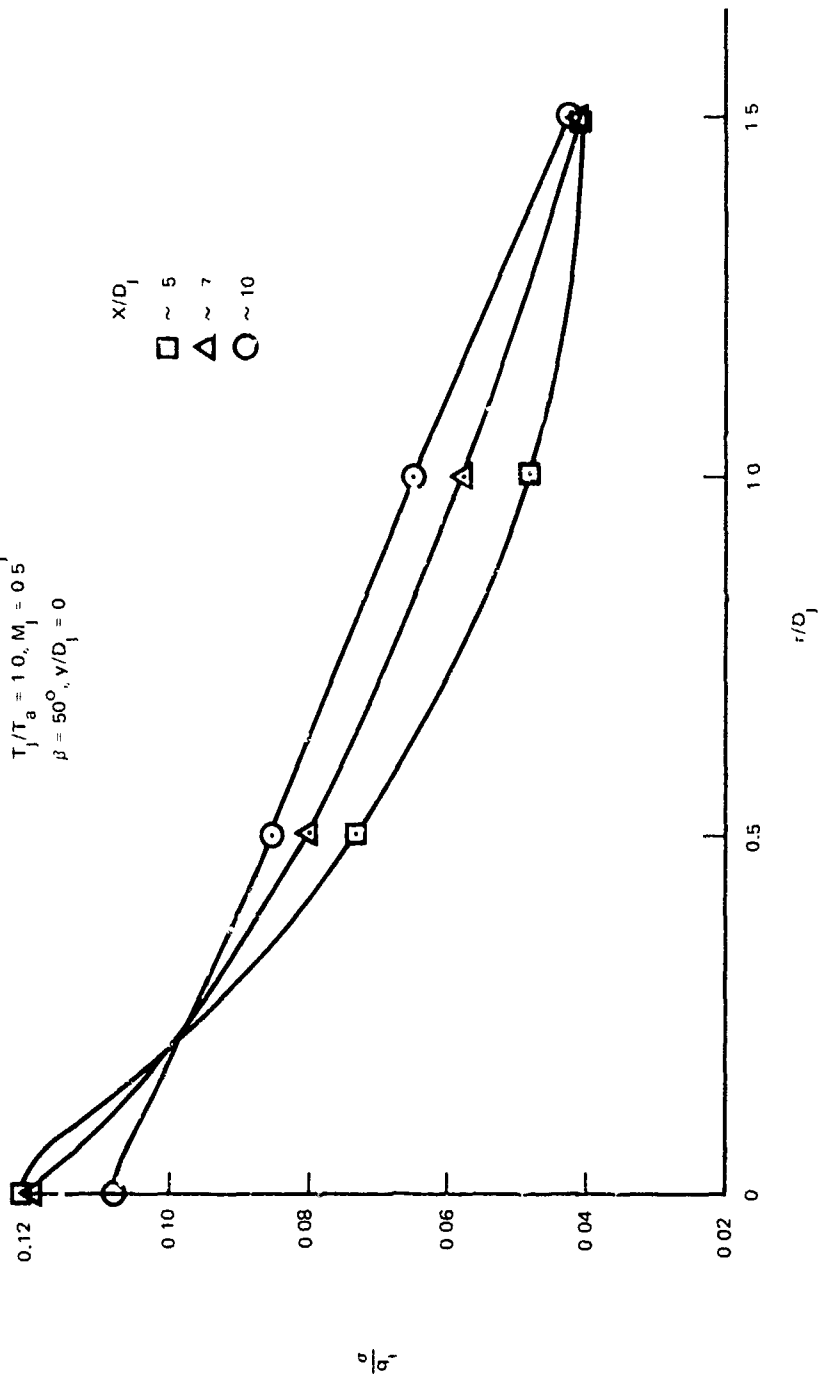


FIGURE 36. RMS PRESSURE FLUCTUATIONS IN CHORDWISE DIRECTION FOR $\beta = 90$ DEG AND AT DIFFERENT X/D_1

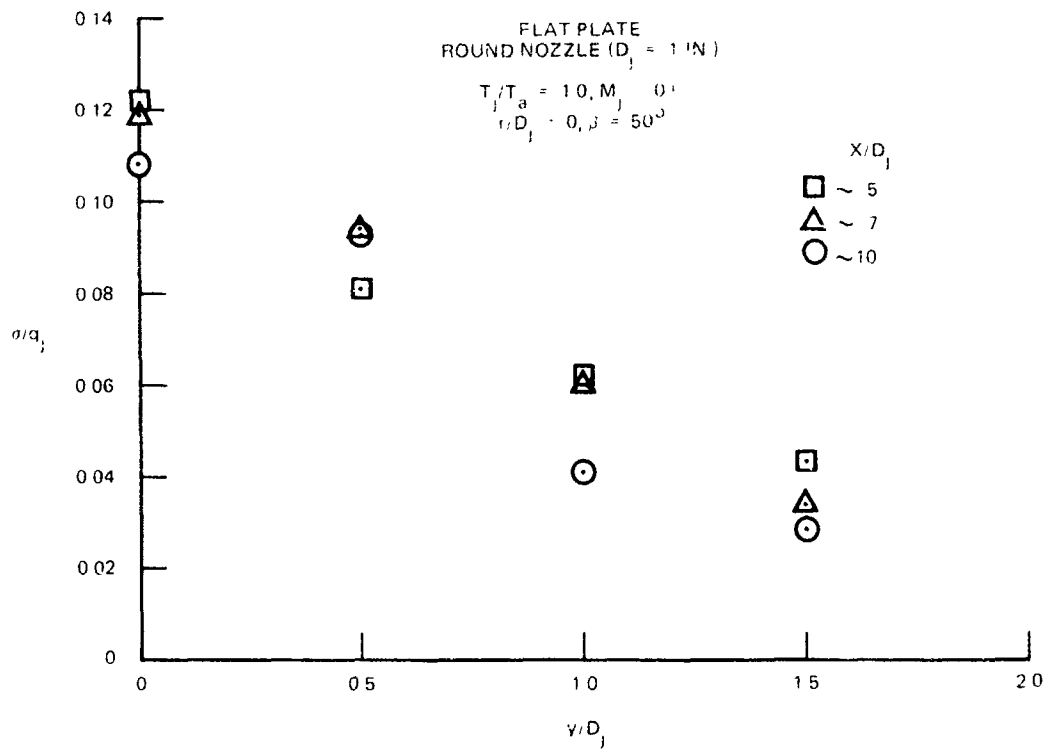


FIGURE 37. RMS PRESSURE FLUCTUATIONS IN SPANWISE DIRECTION FOR $\beta = 50$ DEGREES AND AT DIFFERENT X/D_1

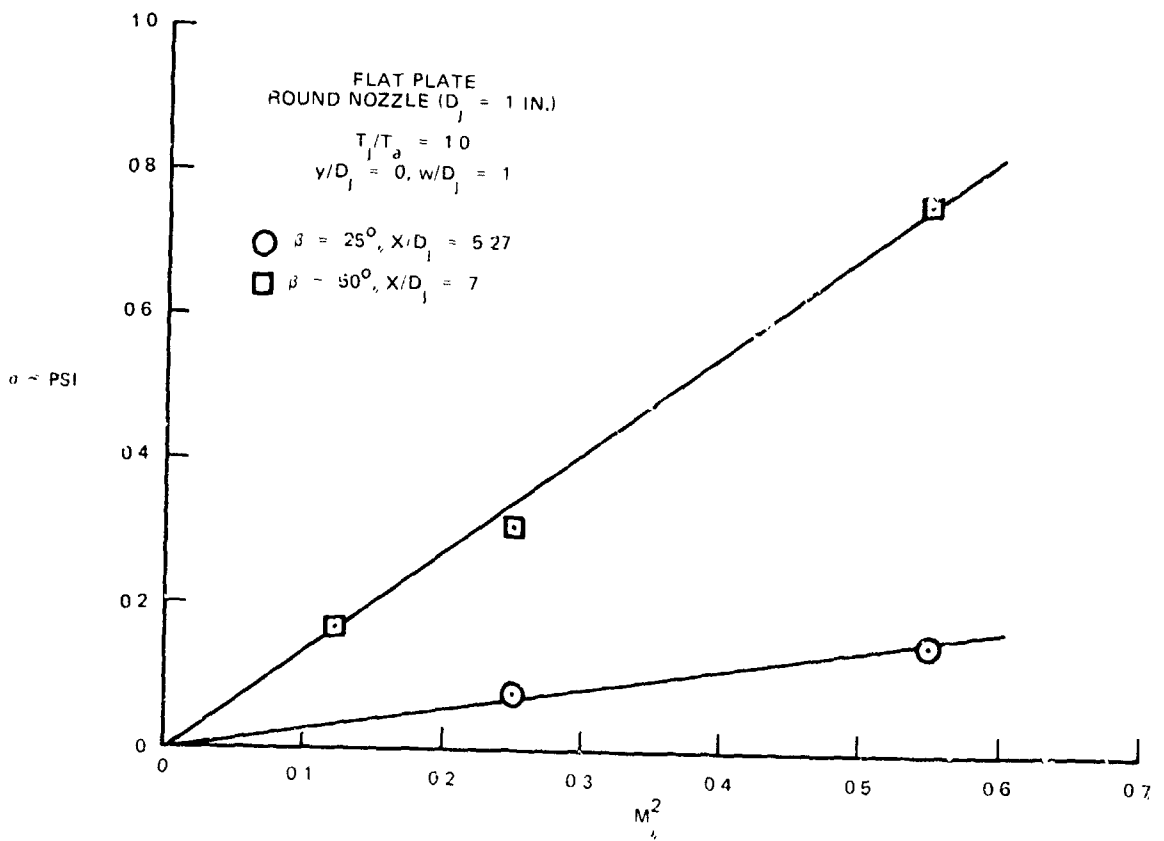


FIGURE 38. MACH NUMBER DEPENDENCE OF RMS PRESSURE FLUCTUATIONS

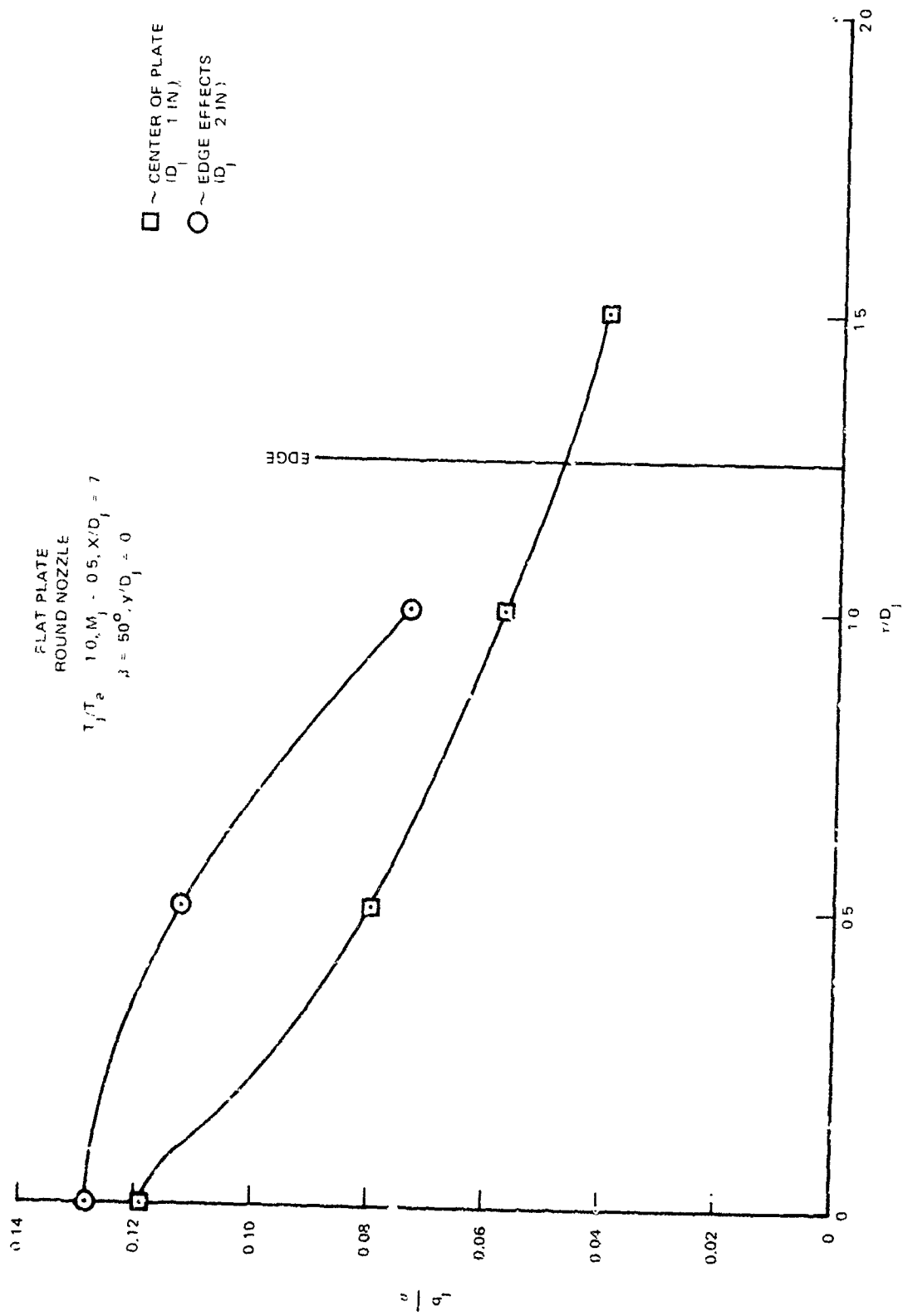


FIGURE 40. COMPARISON OF RMS PRESSURE FLUCTUATIONS FOR AN INFINITE PLATE AND A PLATE WITH EDGE EFFECTS

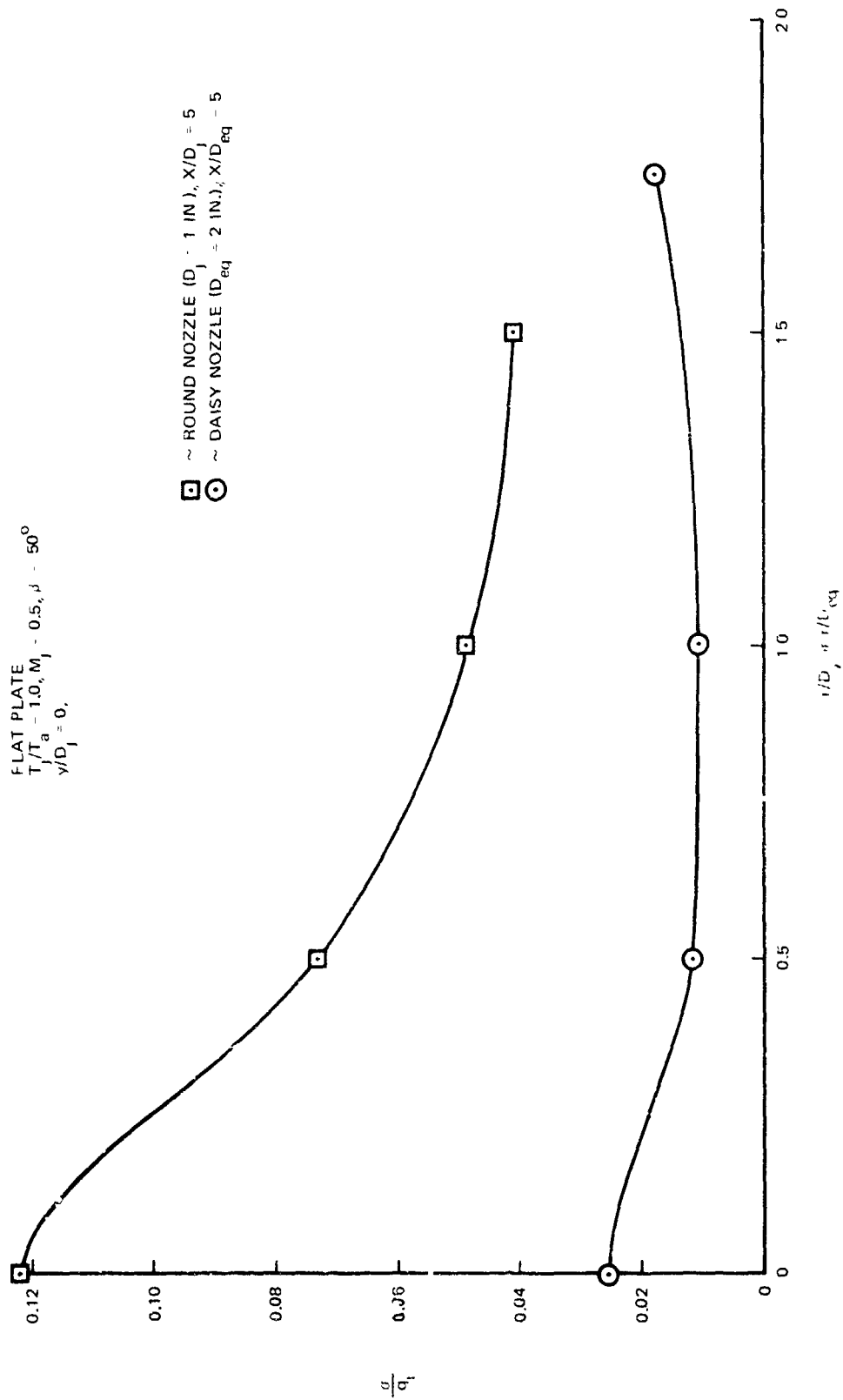


FIGURE 41. COMPARISON OF RMS PRESSURE FLUCTUATIONS FOR A ROUND NOZZLE AND A LOBED NOZZLE

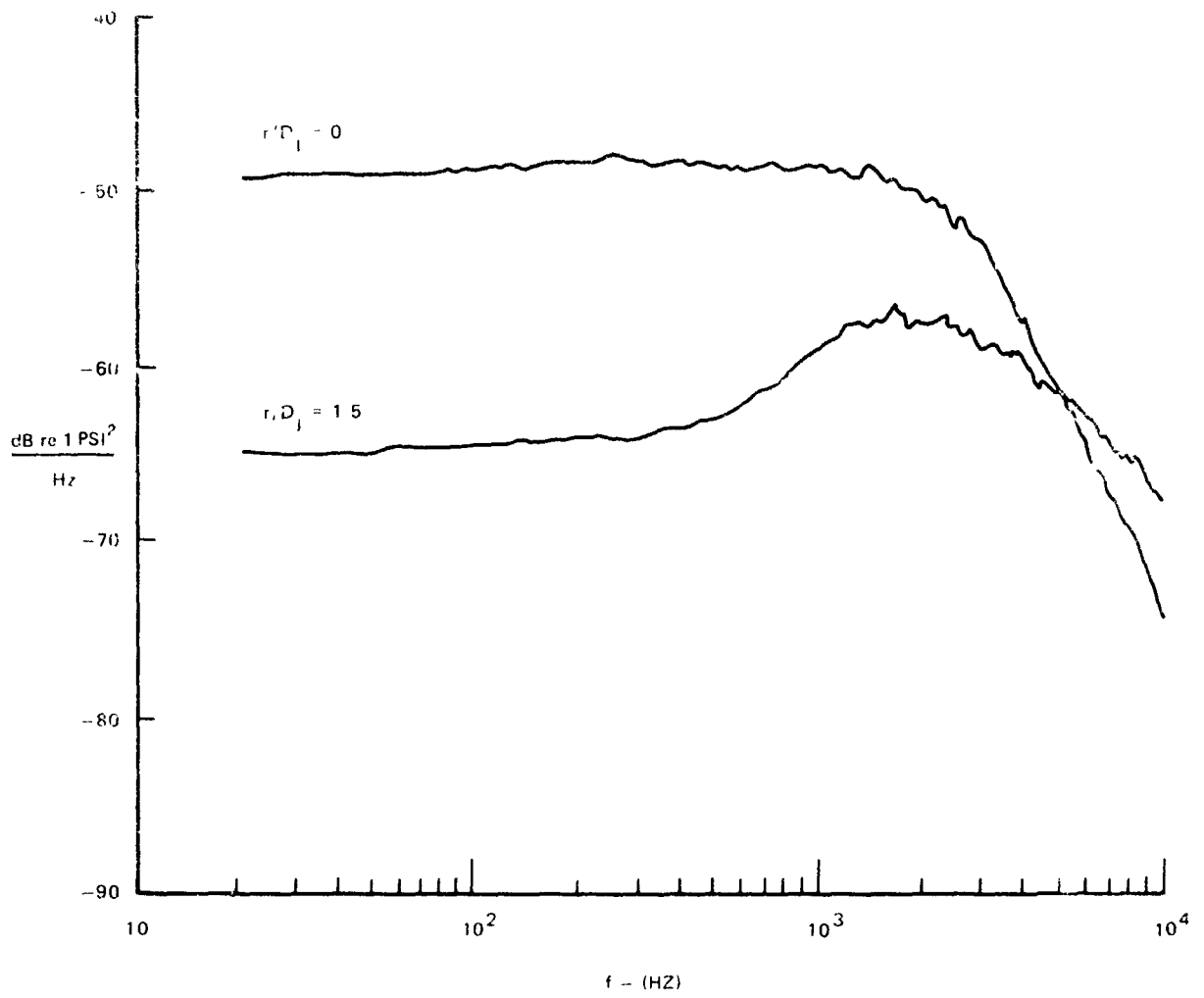


FIGURE 42. CHARACTERISTIC SPECTRAL SHAPES ON FLAT PLATE

FLAT PLATE
 ROUND NOZZLE ($D_j = 1$ IN.)
 $T_1/T_a = 1.0$, $M_1 = 0.5$, $\beta = 90^\circ$, $r/D_j = 0$

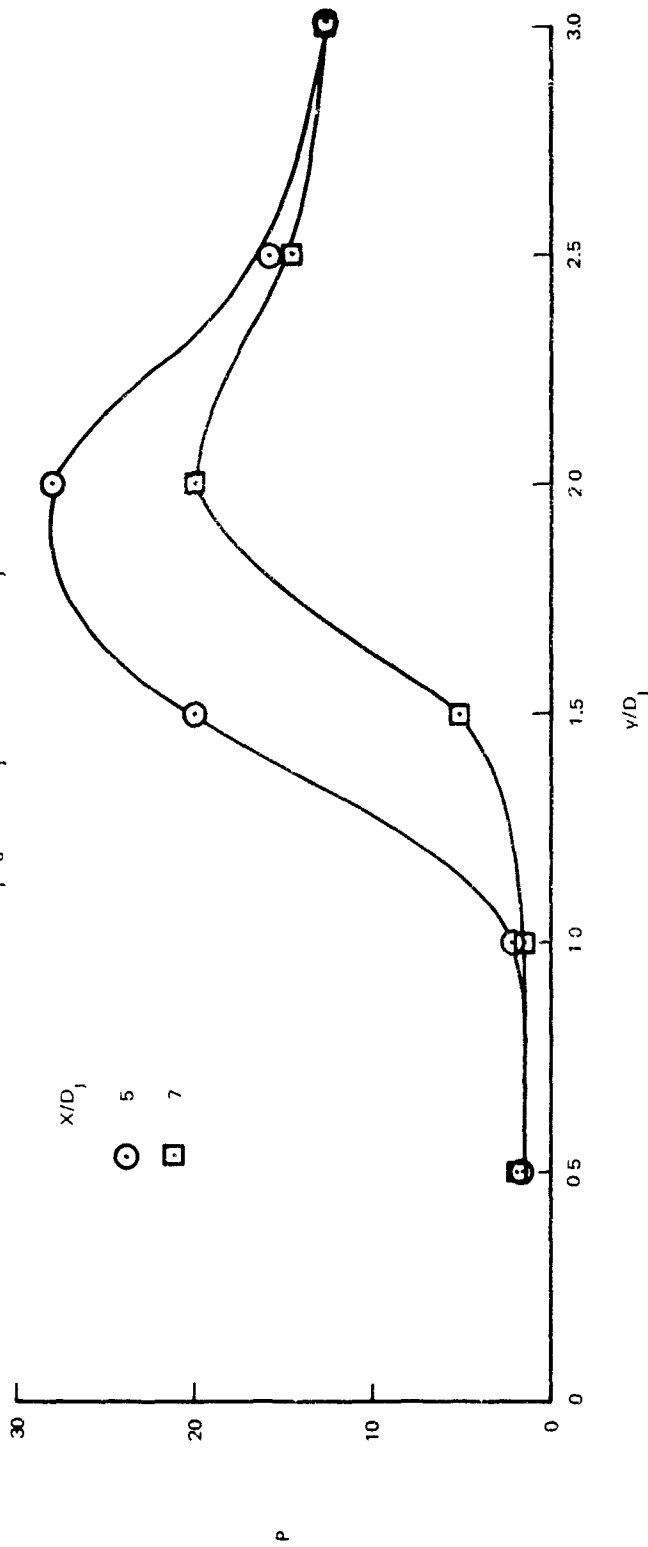


FIGURE 43. VARIATION OF PEAK AMPLIFICATION OF SPECTRA IN y-DIRECTION

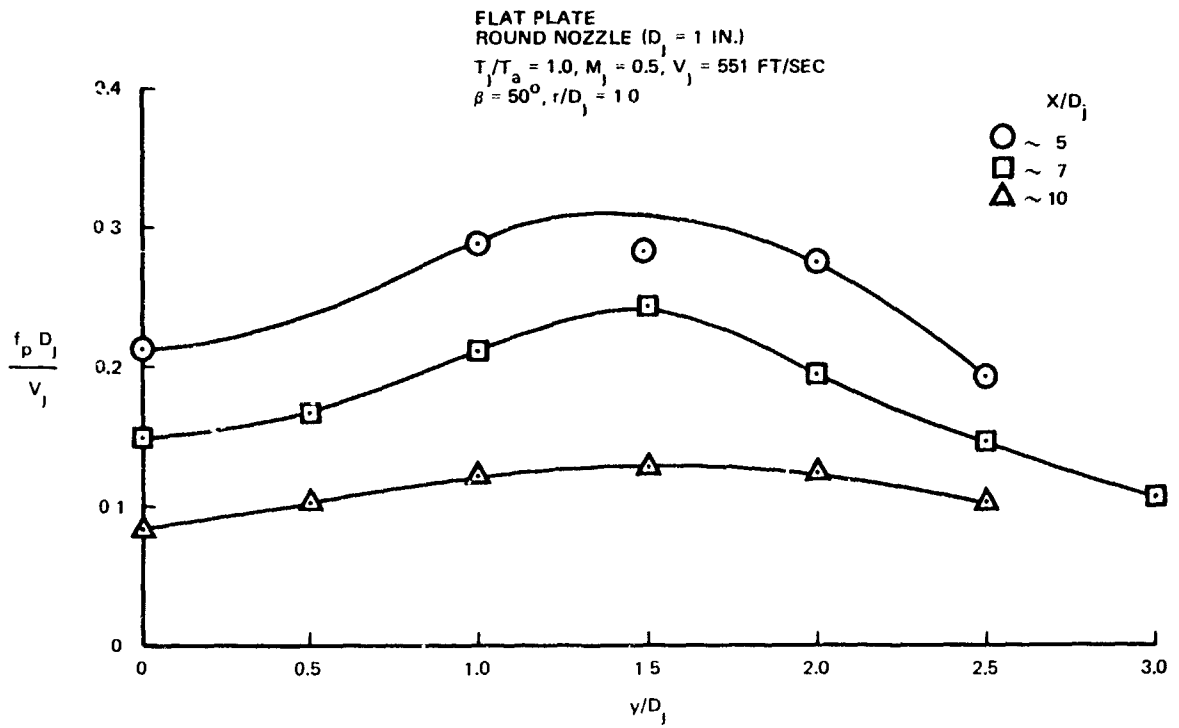


FIGURE 44. VARIATION IN y -DIRECTION OF PEAK STROUHAL NUMBER FOR DIFFERENT X/D_j

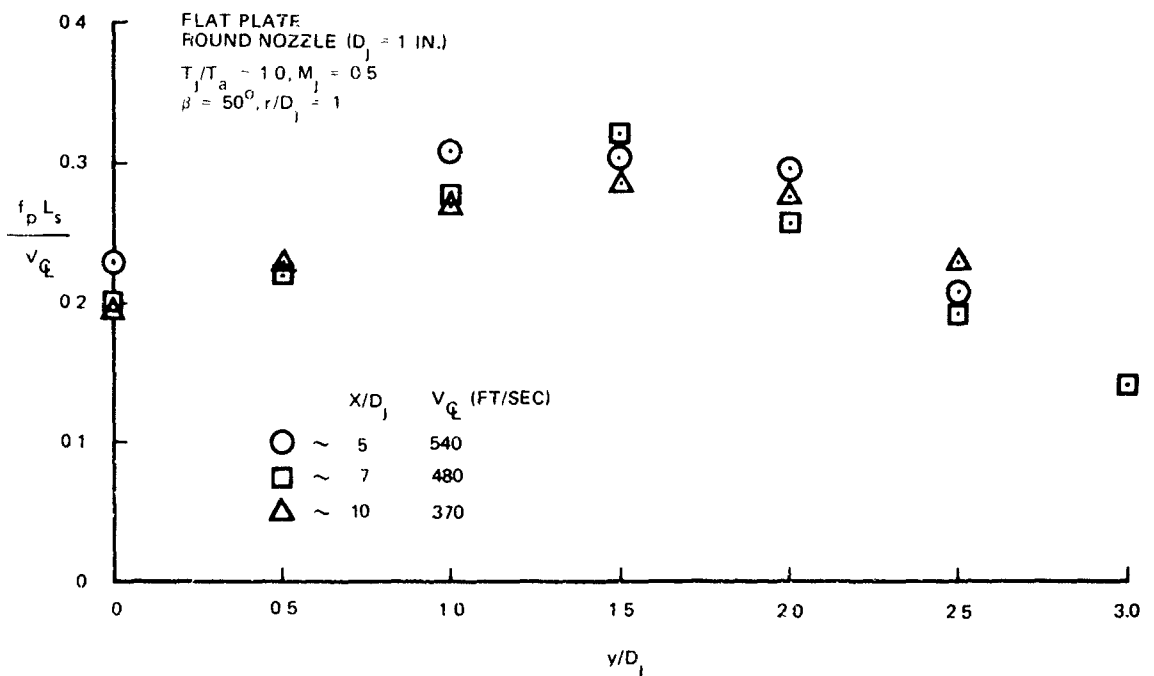


FIGURE 45. VARIATION IN y -DIRECTION OF PEAK STROUHAL NUMBERS BASED ON L_s AND V_q FOR DIFFERENT X/D_j

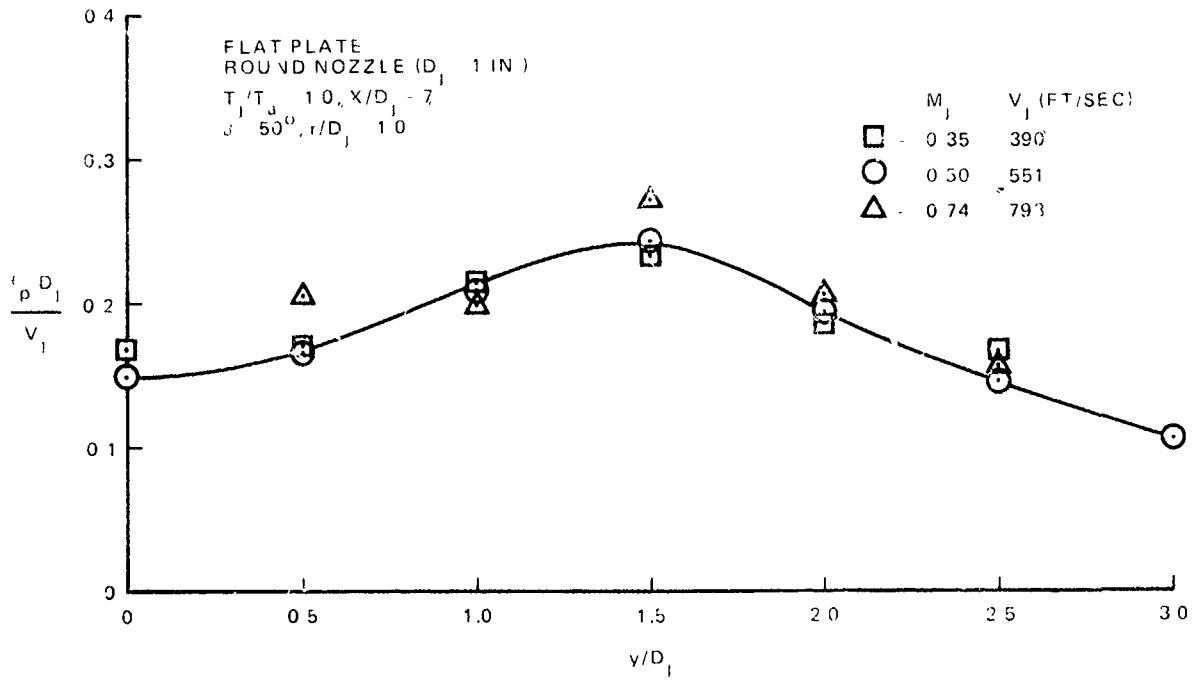


FIGURE 46. VARIATION IN y DIRECTION OF PEAK STROUHAL NUMBERS FOR DIFFERENT MACH NUMBERS

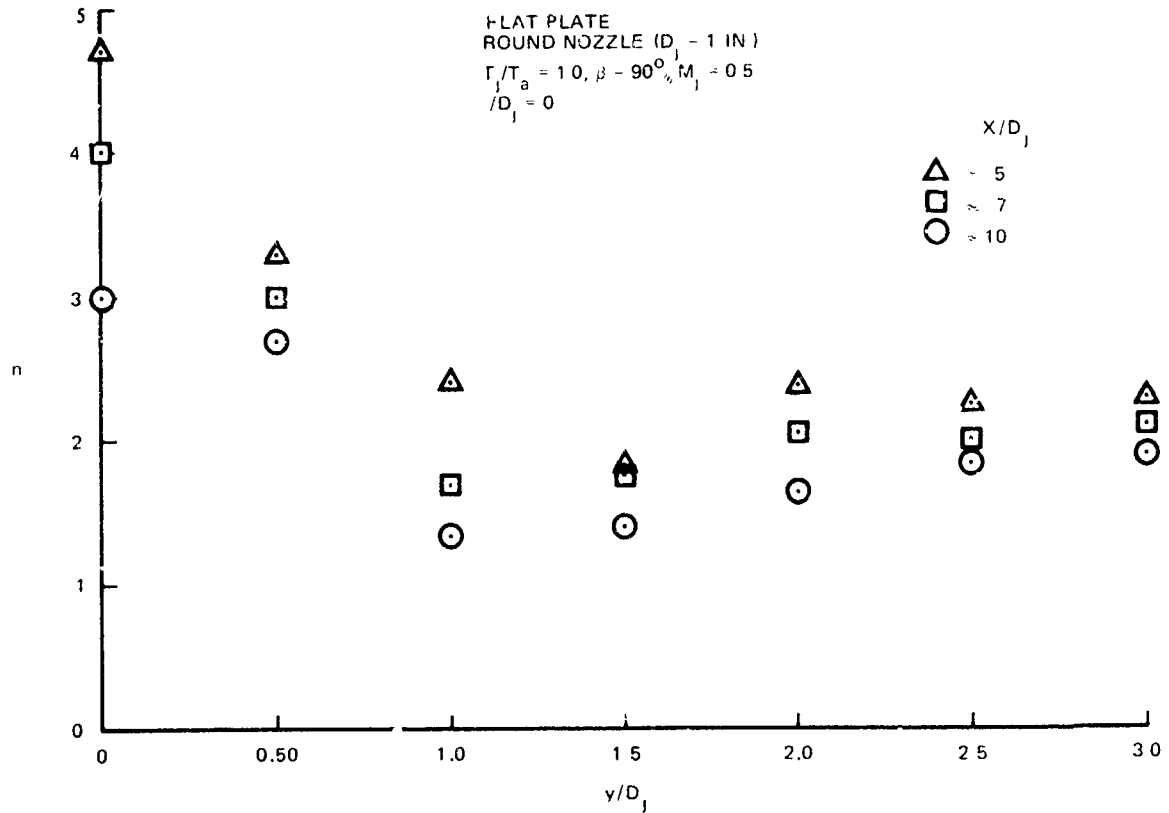


FIGURE 47. VARIATION OF ROLLOFF EXPONENT IN THE y -DIRECTION FOR DIFFERENT X/D_1

FLAT PLATE
 ROUND NOZZLE ($D_1 = 1$ IN.)
 $T_J/T_a = 1.0, \beta = 25^\circ, v/D_1 = 0$

	M_1	V_1 (FT/SEC)
\square	50	551
\triangle	74	793

CHORDWISE CONVECTION SPEED AT $r/D_1 = 1.5$
 BASED ON DOWNSTREAM SEPARATION DISTANCE $\Delta/D_1 = 1$

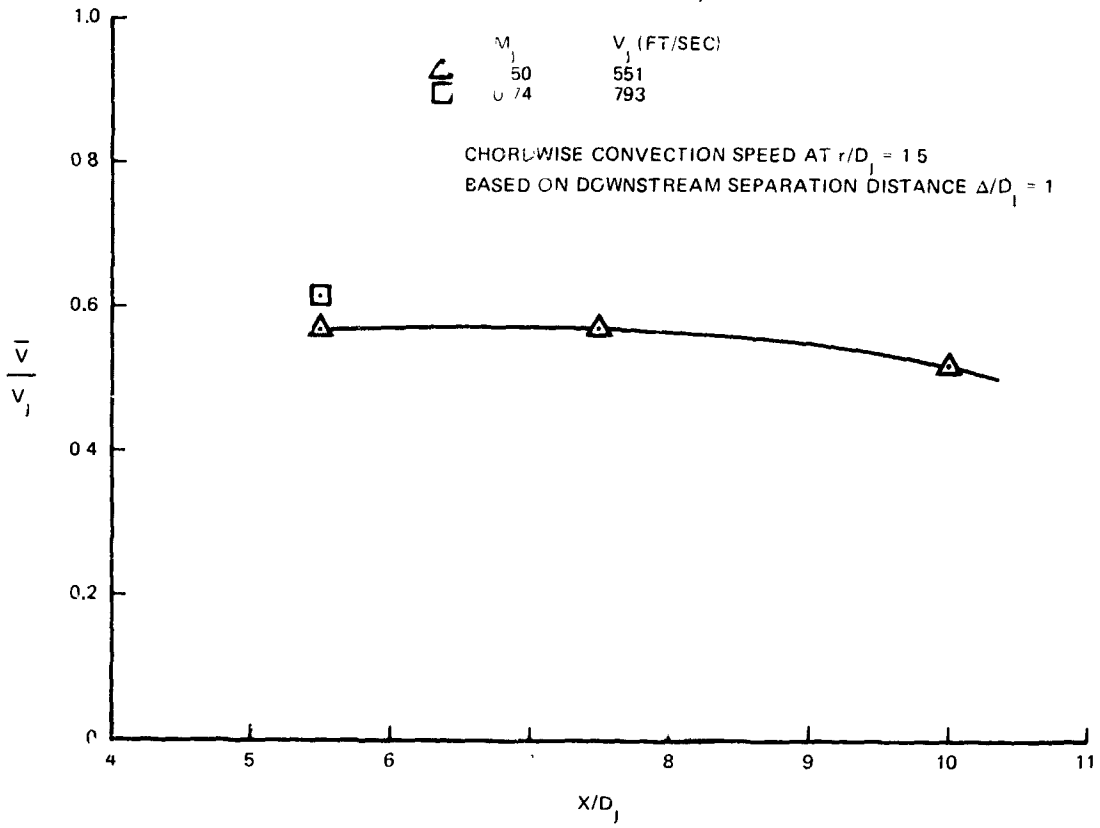


FIGURE 48. BROAD-BAND CONVECTION SPEED AS A FUNCTION OF X/D_1

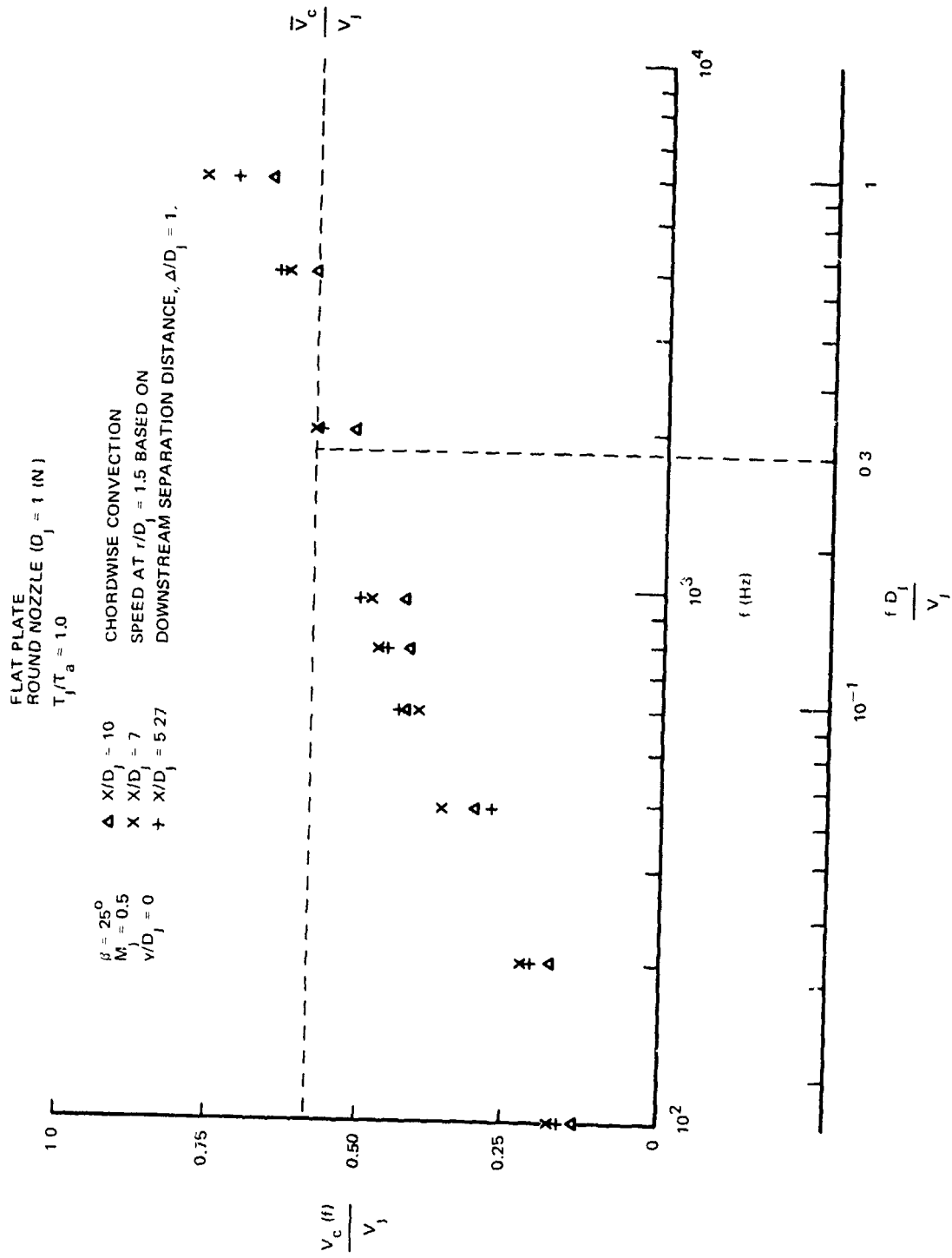


FIGURE 49. NARROW-BAND CONVECTION SPEEDS FOR DIFFERENT X/D_j

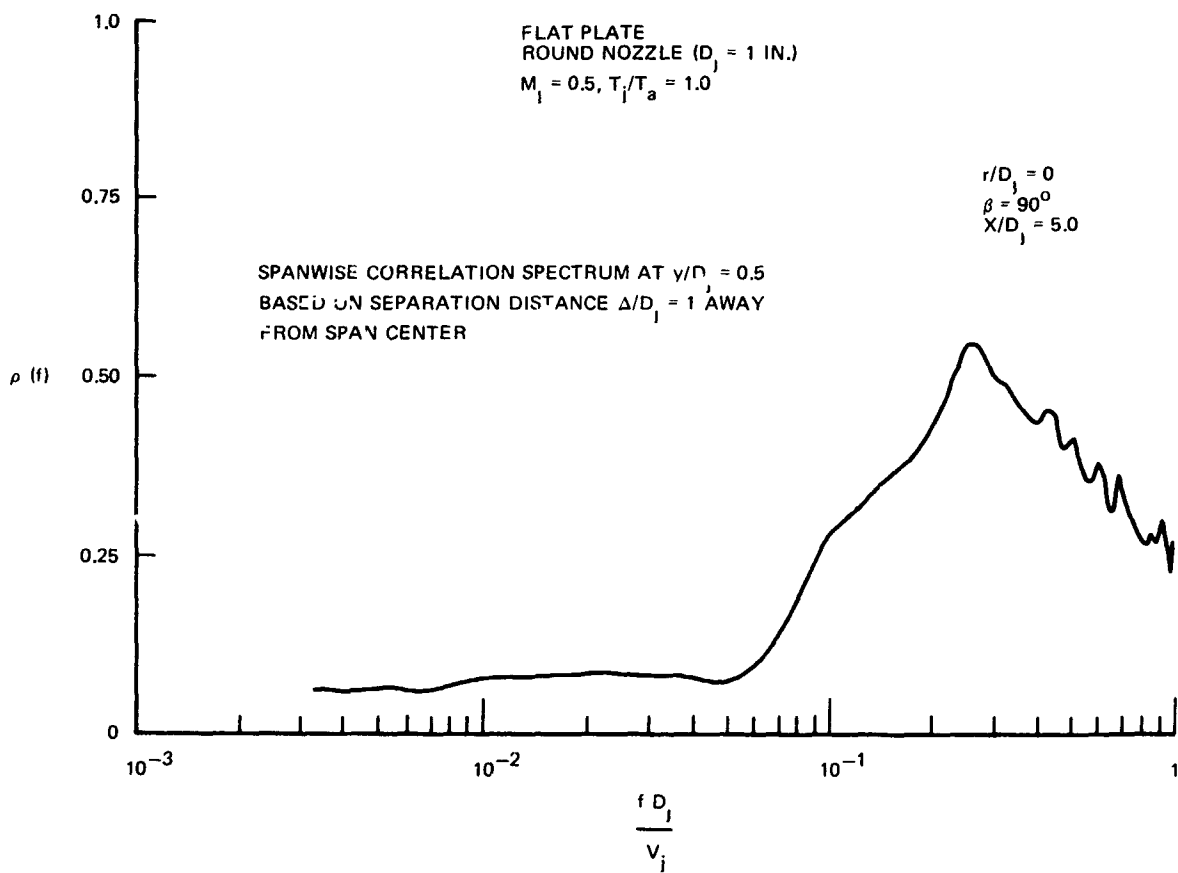


FIGURE 50. SQUARE ROOT OF COHERENCE SPECTRUM

FLAT PLATE
 ROUND NOZZLE ($D_j = 1$ IN)
 $T_j/T_a = 1.0$, $X/D_j = 5$
 $\beta = 50^\circ$

	M_j
()	~ 0.50
< >	~ 0.35

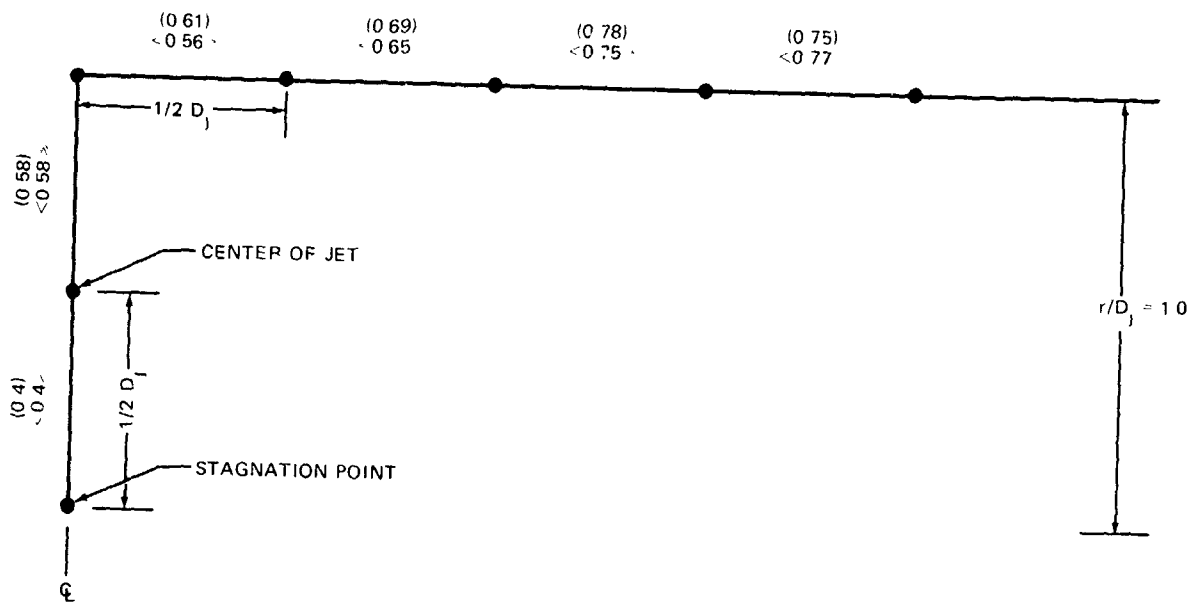


FIGURE 51. MAXIMUM SQUARE ROOT OF COHERENCE VALUES (ρ_m) FOR DIFFERENT MACH NUMBERS

FLAT PLATE
 ROUND NOZZLE ($D_j = 1$ IN)
 $T_j/T_a = 1.0, M_j = 0.5$
 $\beta = 50^\circ$

	X/D_j
[]	~ 5
()	~ 7
< >	~ 10

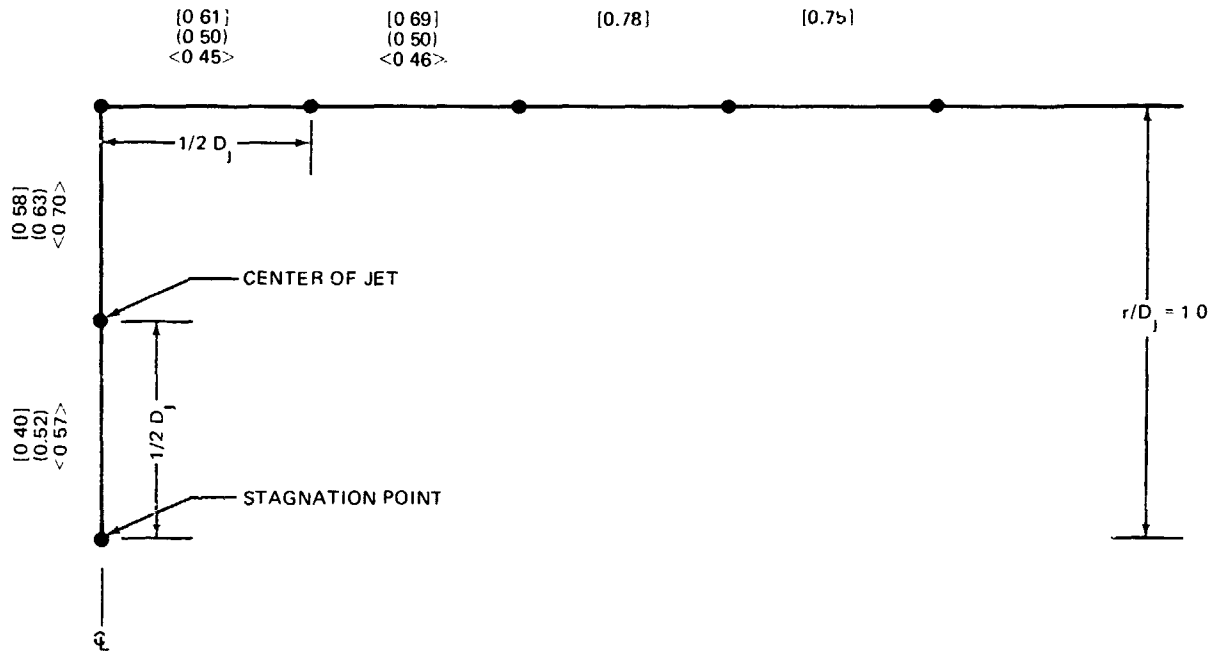


FIGURE 52. MAXIMUM SQUARE ROOT OF COHERENCE VALUES (ρ_m) FOR DIFFERENT X/D_j

FLAT PLATE
 ROUND NOZZLE ($D_j = 1$ IN)

$\beta = 50^\circ$ $X/D_j = 7$

$\langle \rangle \sim M_j = 0.50, T_j/T_a = 1.0$

$() \sim M_j = 0.46, T_j/T_a = 1.7$

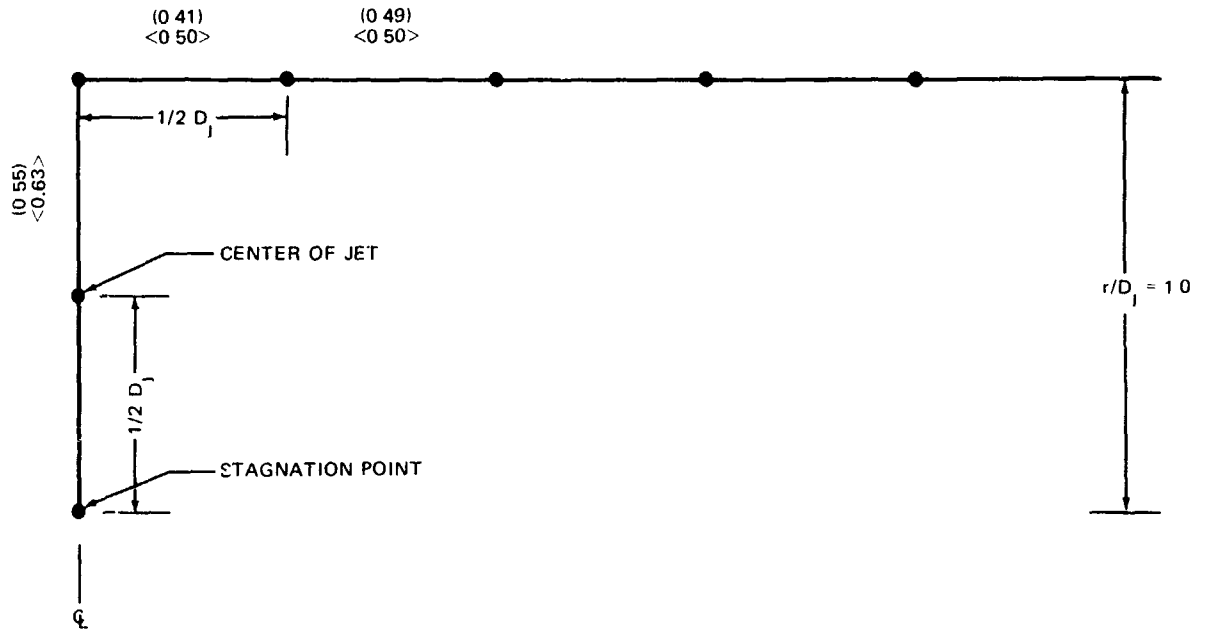


FIGURE 53. MAXIMUM SQUARE ROOT OF COHERENCE VALUES (ρ_m) FOR DIFFERENT TEMPERATURES

UBF CURVED PLATES
 ROUND NOZZLE ($D_1 = 2$ IN.)
 $T_j/T_a = 1.0$

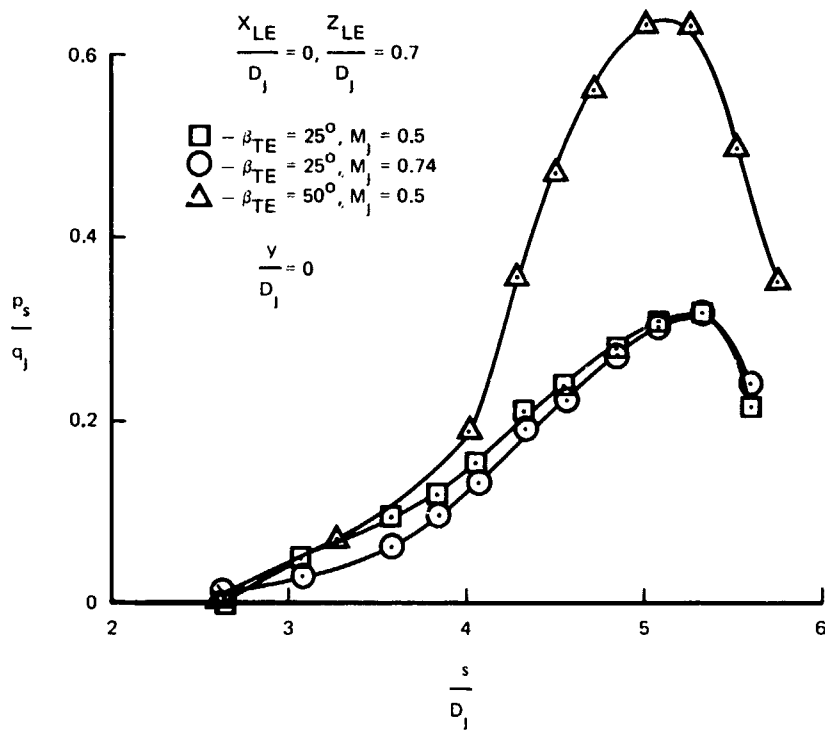


FIGURE 54. STATIC PRESSURE DISTRIBUTIONS FOR DIFFERENT β_{TE} AND DIFFERENT MACH NUMBERS ON THE UBF CURVED PLATES

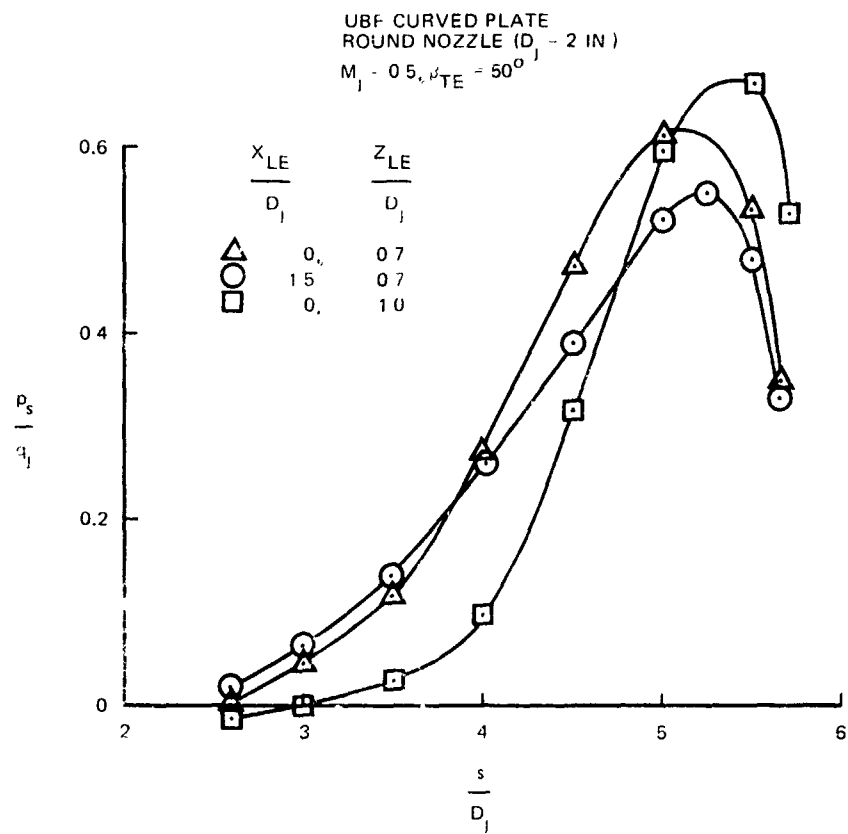


FIGURE 55. STATIC PRESSURE DISTRIBUTIONS FOR DIFFERENT UBF CURVED PLATE POSITIONS

UBF CURVED PLATES
 ROUND NOZZLE (D_j IN.)
 T_j/T_a = 1.0

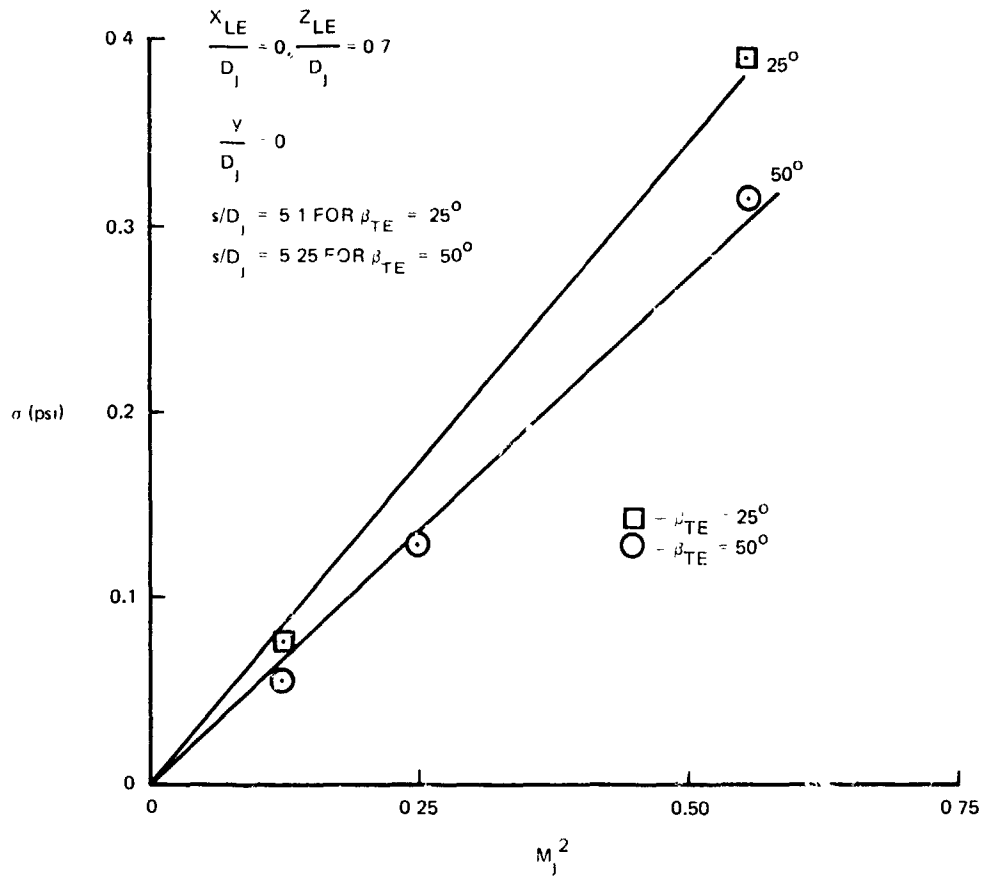


FIGURE 56. RMS PRESSURE FLUCTUATIONS AS A FUNCTION OF M_j

UBF CURVED PLATES
 ROUND NOZZLE ($D_1 = 2$ IN.)
 $T_1/T_a = 1.0$

$$\frac{x_{LE}}{D_1} = 0, \frac{z_{LE}}{D_1} = 0.7, M_1 = 0.5$$

○ - $\beta_{TE} = 50^\circ$
 □ - $\beta_{TE} = 25^\circ$

$$\frac{y}{D_1} = 0$$

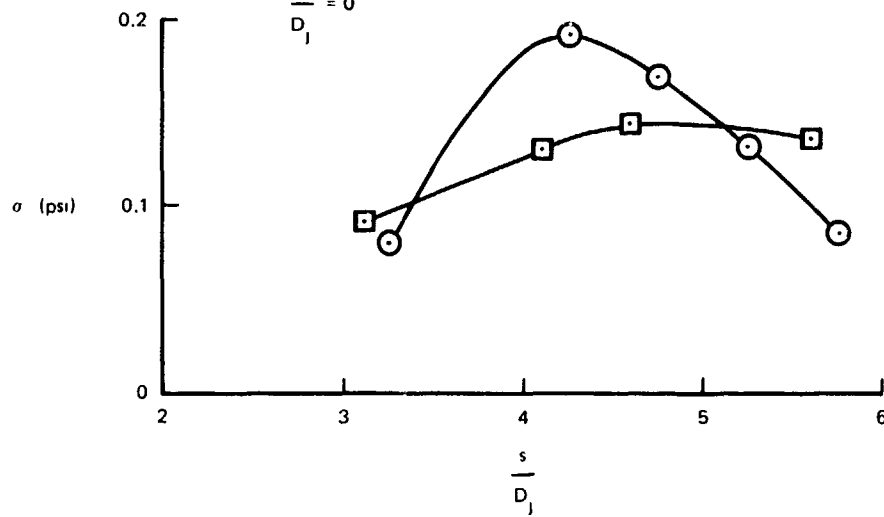


FIGURE 57. SPATIAL DISTRIBUTION OF RMS PRESSURE FLUCTUATIONS ON THE UBF CURVED PLATES

UBF CURVED PLATES
 ROUND NOZZLE ($D_1 = 2$ IN.)
 $T_1/T_a = 1.0, M_1 = 0.5$
 $X_{LE}/D_1 = 0, Z_{LE}/D_1 = 0.7$
 $v/d_1 = 0$

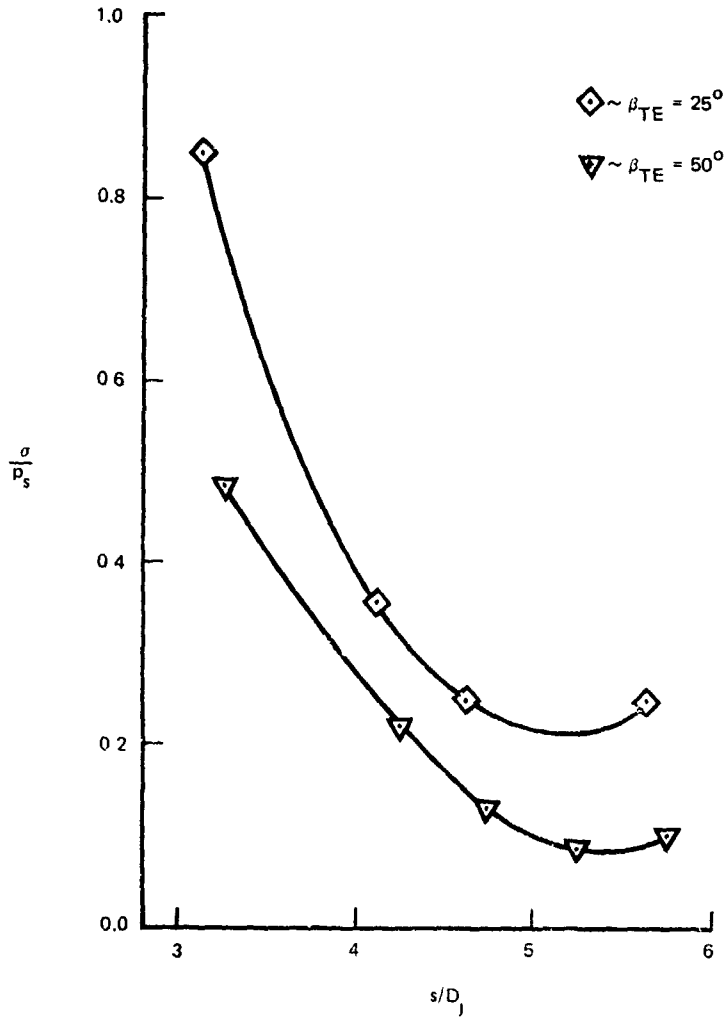


FIGURE 58. RATIO OF RMS FLUCTUATING PRESSURES TO STATIC PRESSURES ALONG CENTERLINE CHORD OF UBF CURVED PLATE

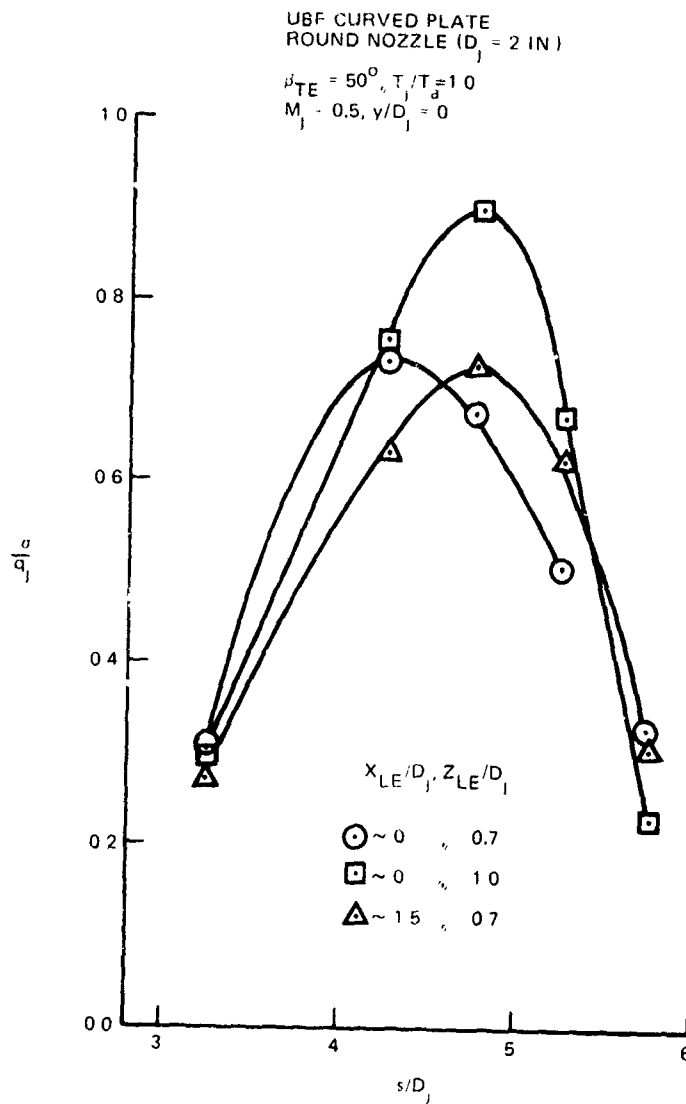


FIGURE 59. SPATIAL DISTRIBUTION OF RMS PRESSURE FLUCTUATIONS FOR DIFFERENT PLATE POSITIONS

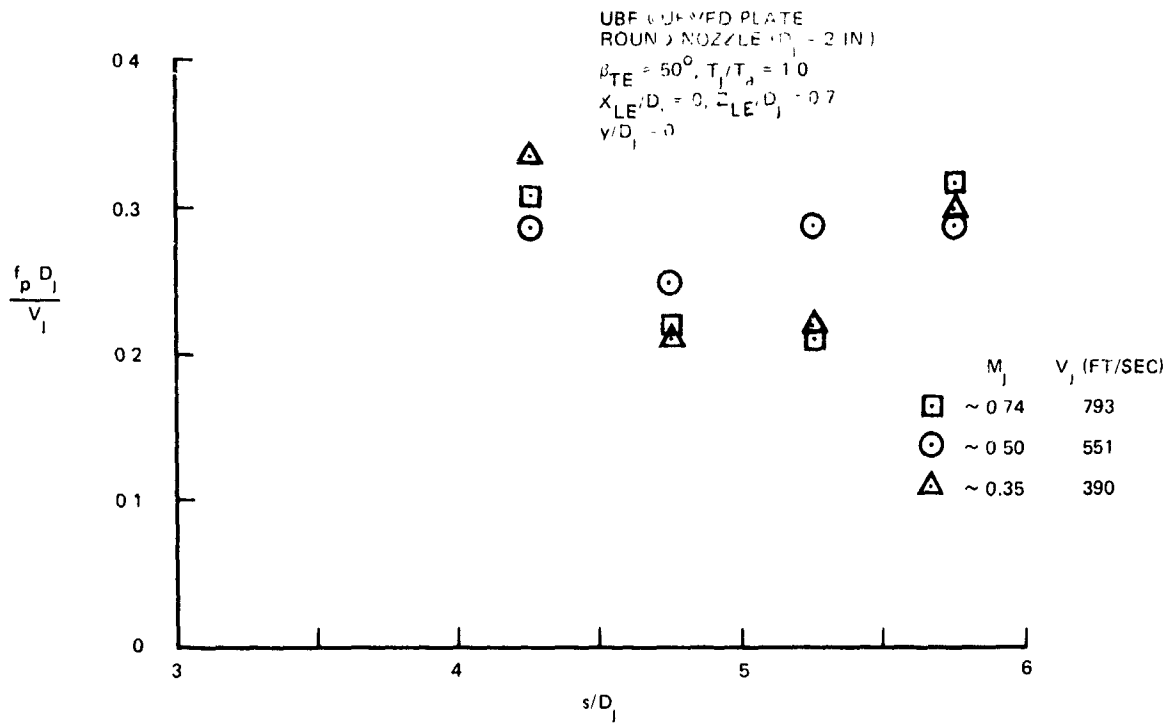


FIGURE 60. SPATIAL DISTRIBUTION OF PEAK STROUHAL NUMBERS FOR DIFFERENT M_1 ON $\beta_{TE} = 50$ -DEG PLATE

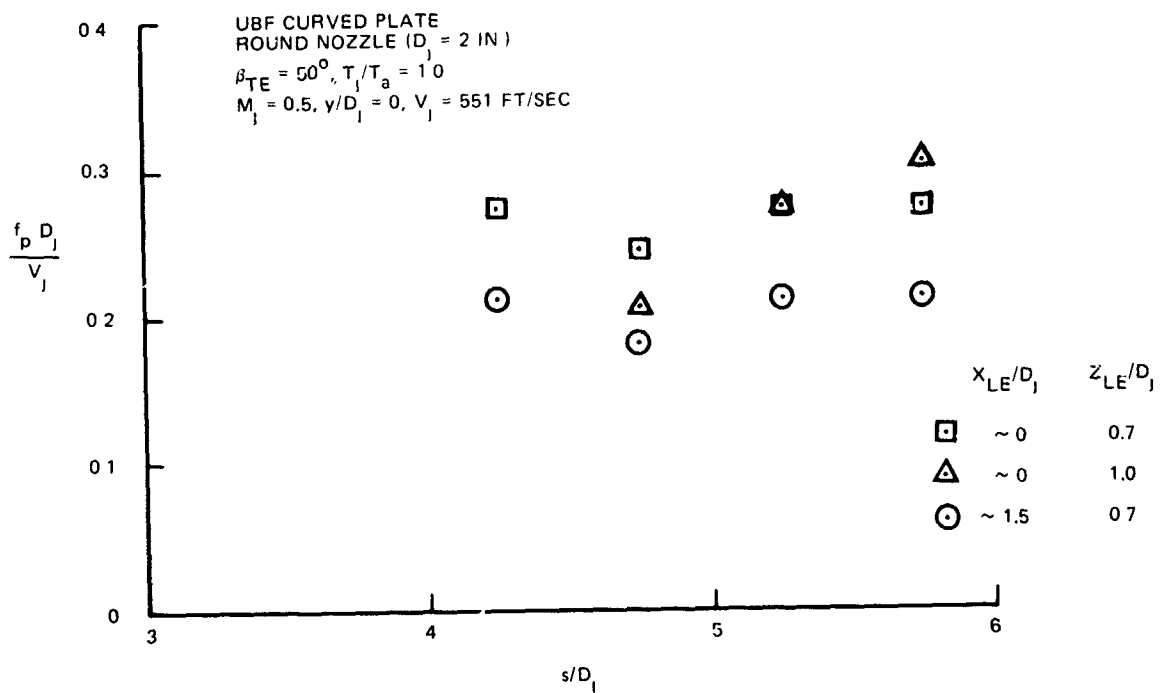


FIGURE 61. SPATIAL DISTRIBUTION OF PEAK STROUHAL NUMBERS FOR DIFFERENT PLATE POSITIONS

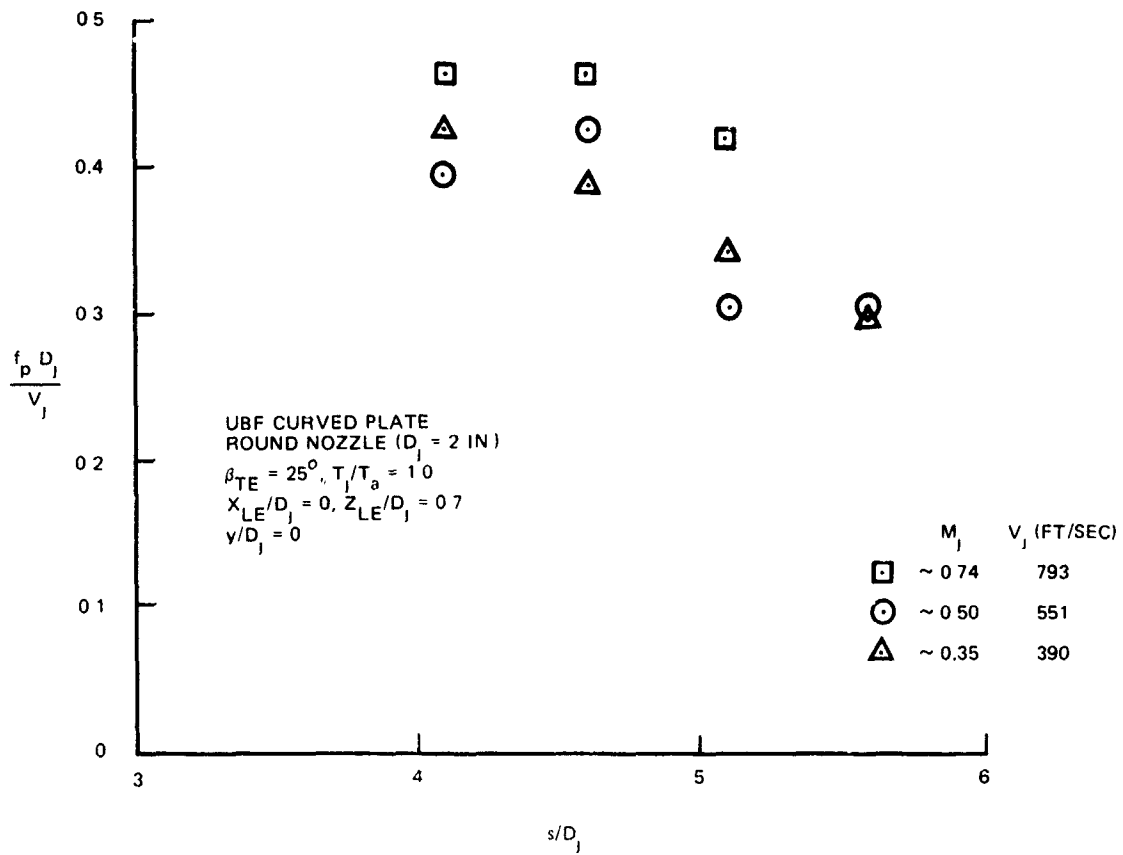


FIGURE 62. SPATIAL DISTRIBUTION OF STROUHAL NUMBERS FOR DIFFERENT M_j ON $\beta_{TE} = 25$ -DEG PLATE

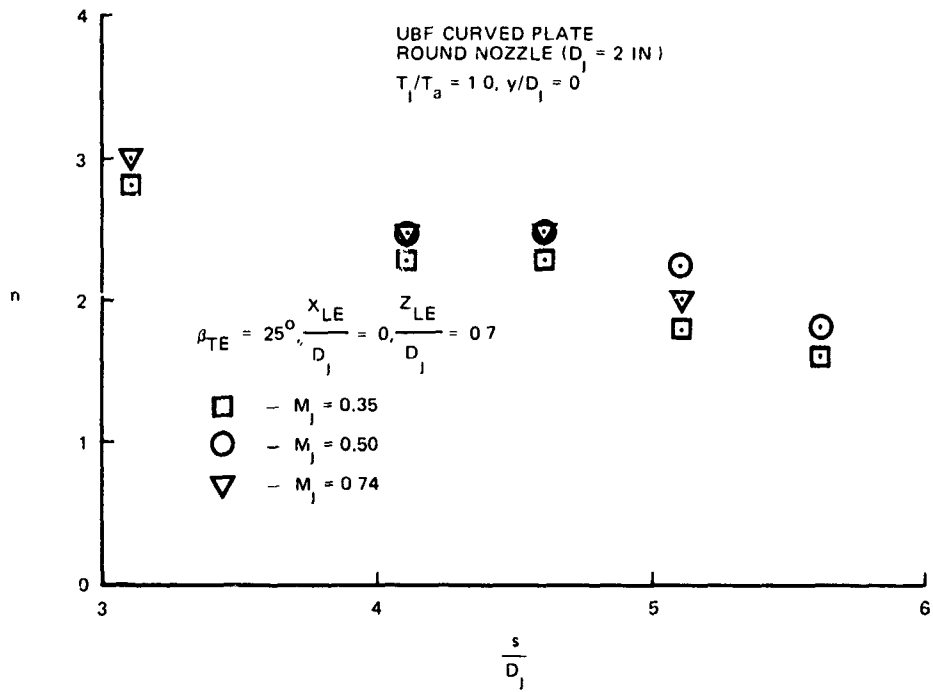


FIGURE 63. SPATIAL DISTRIBUTION OF ROLL-OFF EXPONENT ON $\beta_{TE} = 25$ -DEG PLATE FOR DIFFERENT MACH NUMBERS

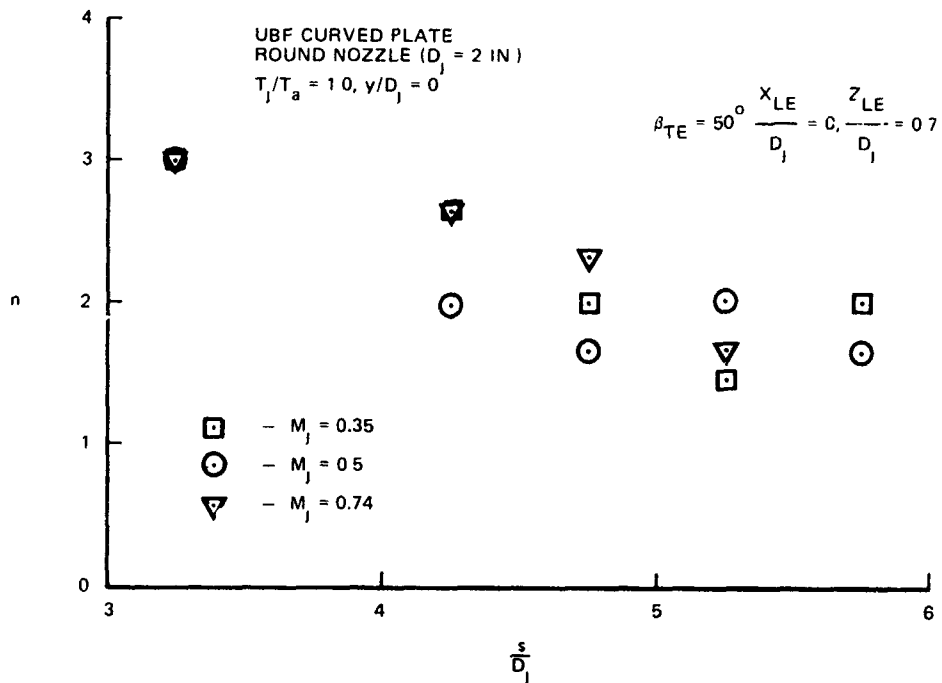


FIGURE 64. SPATIAL DISTRIBUTION OF ROLL-OFF EXPONENT ON $\beta_{TE} = 50$ -DEG PLATE FOR DIFFERENT MACH NUMBERS

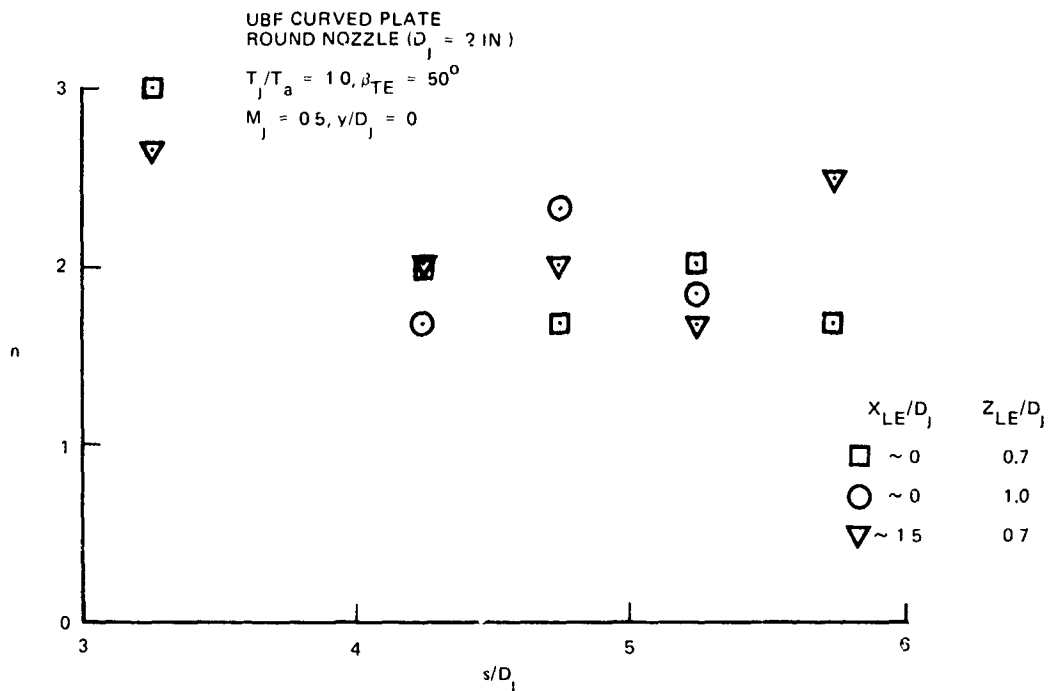


FIGURE 65. SPATIAL DISTRIBUTION OF ROLL-OFF EXPONENT FOR DIFFERENT PLATE POSITIONS

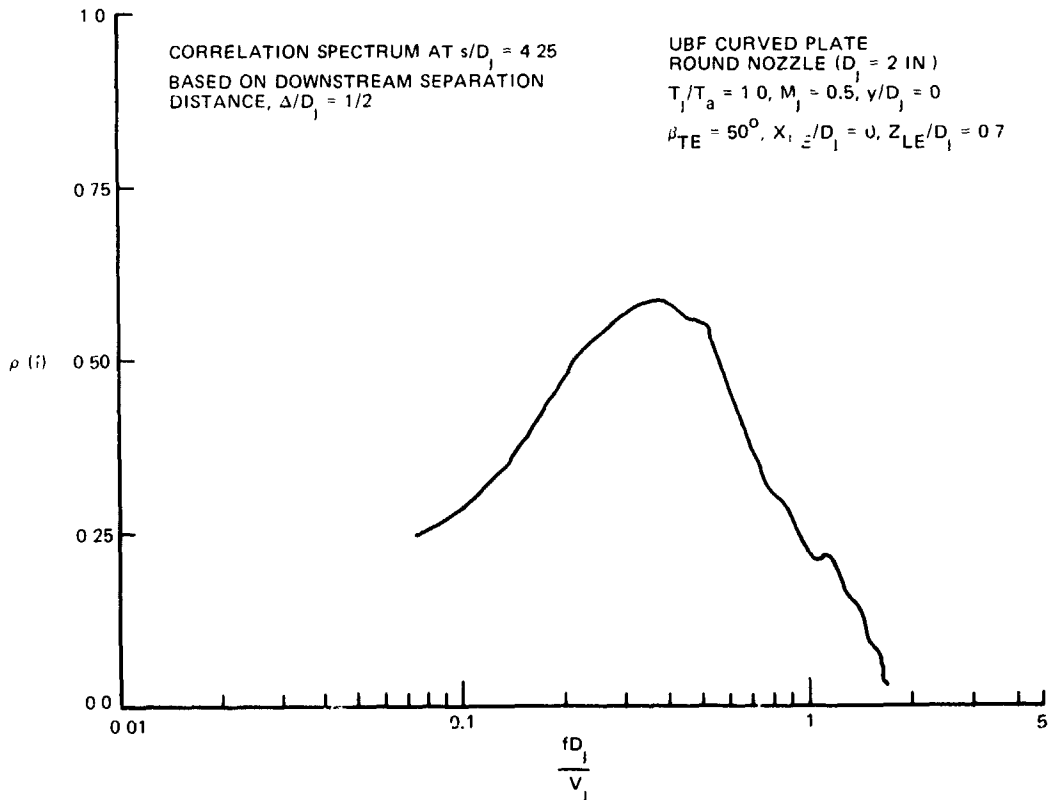


FIGURE 66. CORRELATION SPECTRUM AT A LOCATION ALONG CENTERLINE CHORD OF UBF CURVED PLATE

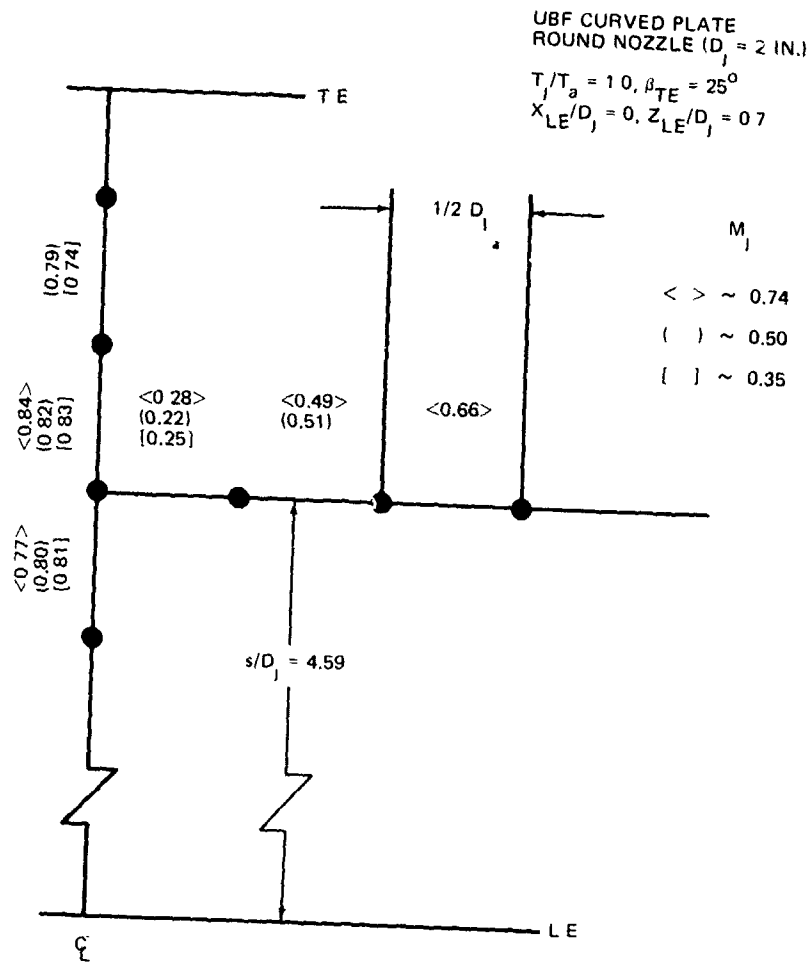


FIGURE 67. ρ_m FOR ADJACENT TRANSDUCERS AND DIFFERENT MACH NUMBERS

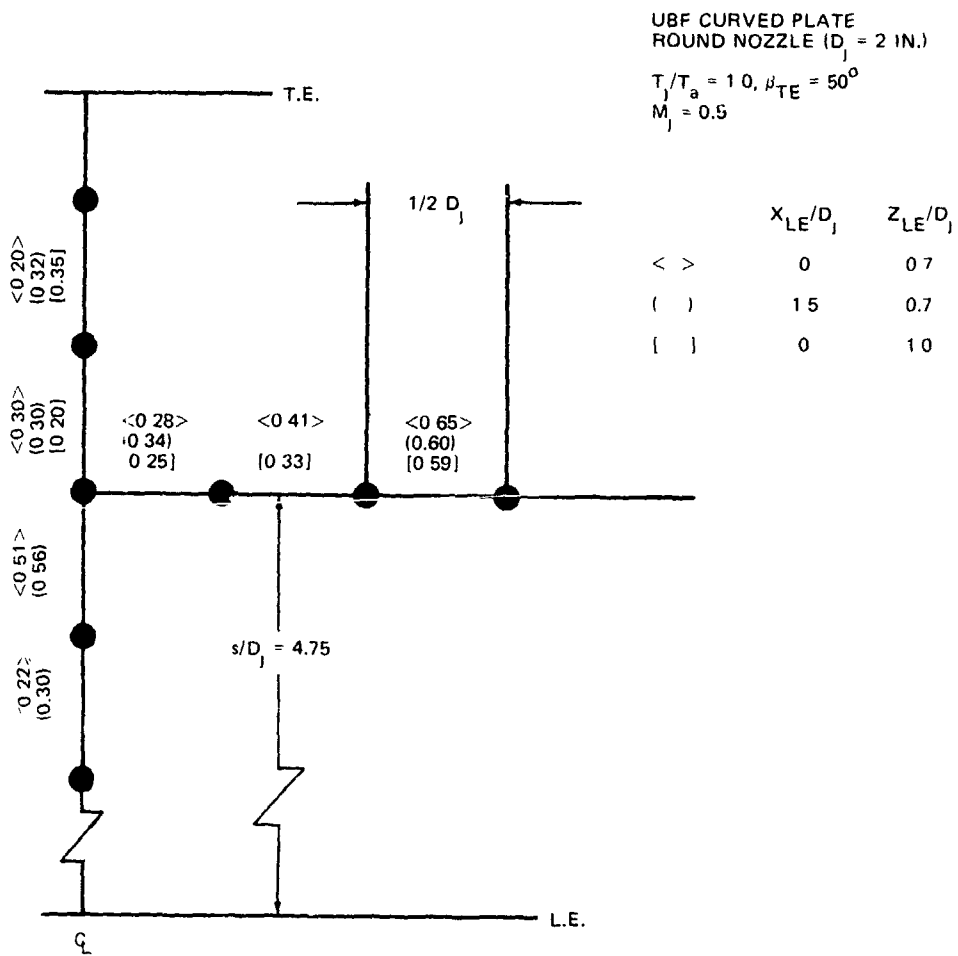


FIGURE 68. ρ_m FOR ADJACENT TRANSDUCERS AND DIFFERENT PLATE POSITIONS

UBF CURVED PLATES
 ROUND NOZZLE ($D_j = 2$ IN)

$T_j/T_a = 1.0$

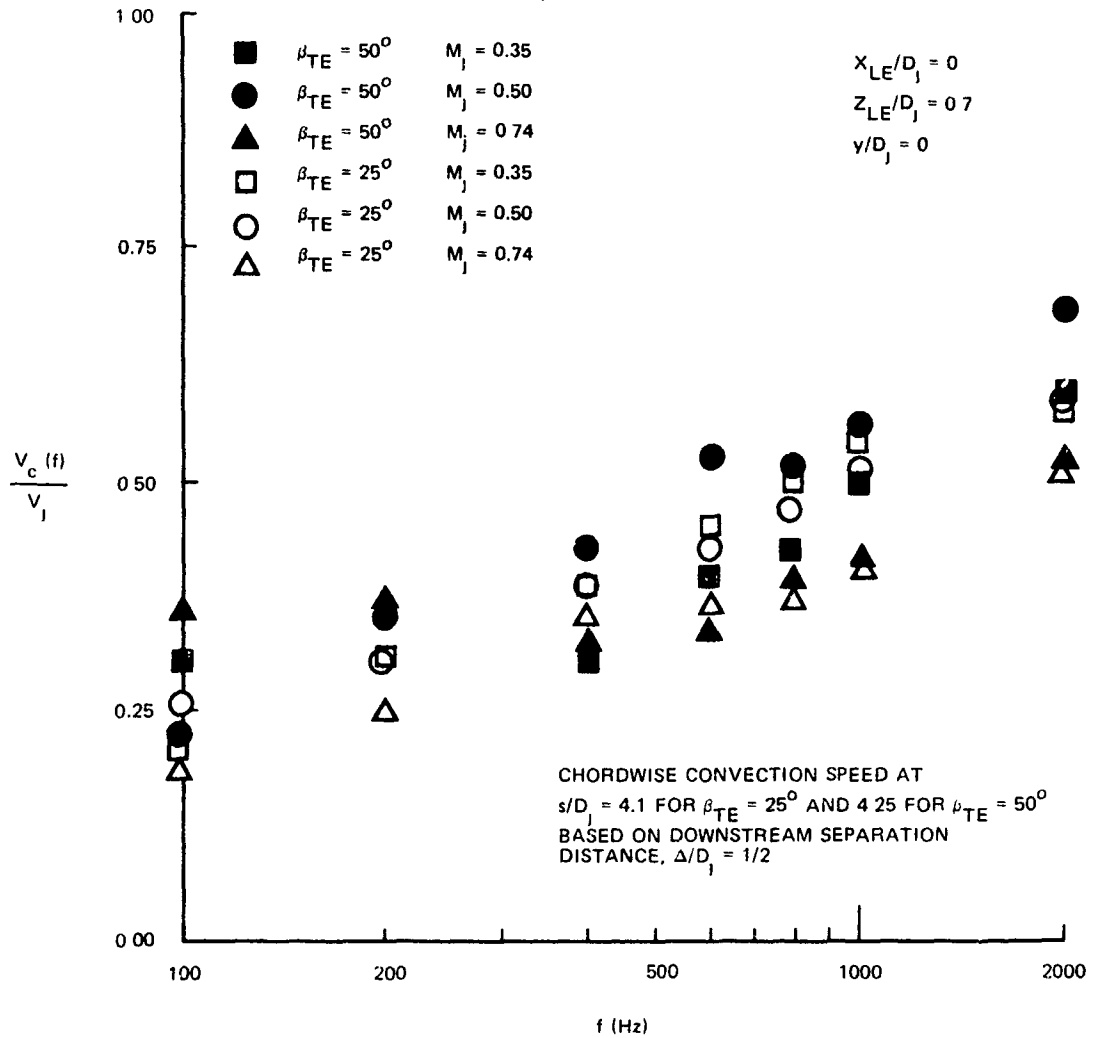


FIGURE 69. NARROW-BAND CONVECTION SPEEDS

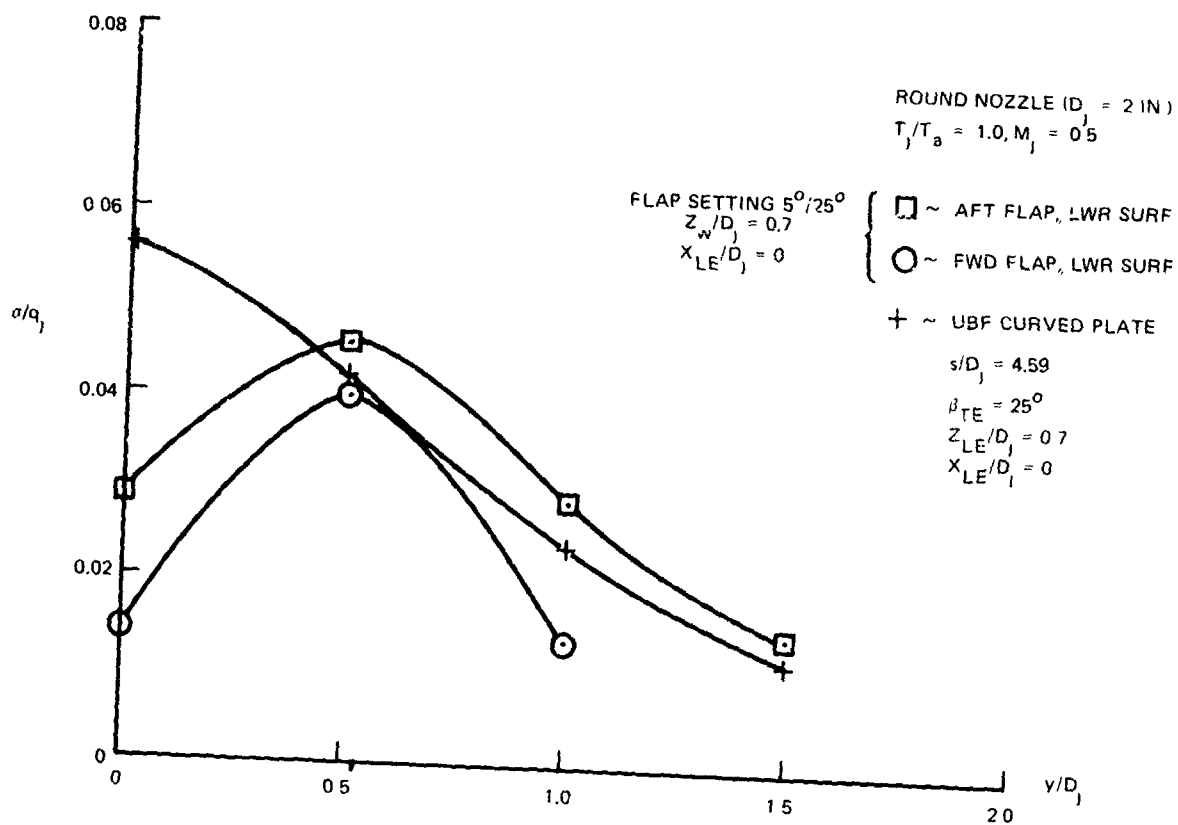


FIGURE 70. SPANWISE DISTRIBUTION OF RMS PRESSURE FLUCTUATIONS ON WING-FLAPS MODEL AND CURVED PLATE FOR $Z/D_j = 0.7$

ROUND NOZZLE ($D_j = 2$ IN.)

$T_j/T_a = 1.0, M_j = 0.5$

FLAP SETTING $5^\circ/25^\circ$
 $Z_w/D_j = 1.0$
 $X_{LE}/D_j = 0$

\square ~ AFT FLAP, LWR SURF
 \circ ~ FWD FLAP, LWR SURF

+ ~ UBF CURVED PLATE
 $s/D_j = 4.59$
 $\beta_{TE} = 25^\circ$
 $Z_{LE}/D_j = 1.0$
 $X_{LE}/D_j = 0$

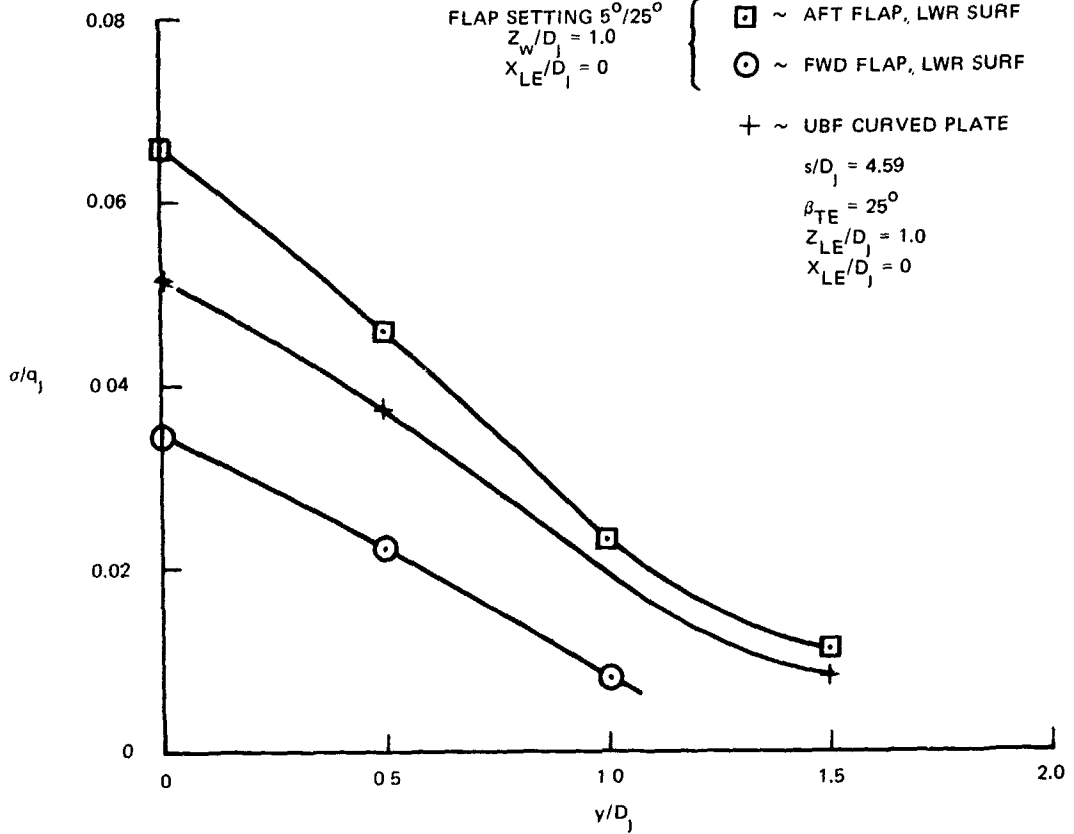


FIGURE 71. SPANWISE DISTRIBUTION OF RMS PRESSURE FLUCTUATIONS ON WING-FLAPS MODEL AND CURVED PLATE FOR $Z/D_j = 1.0$

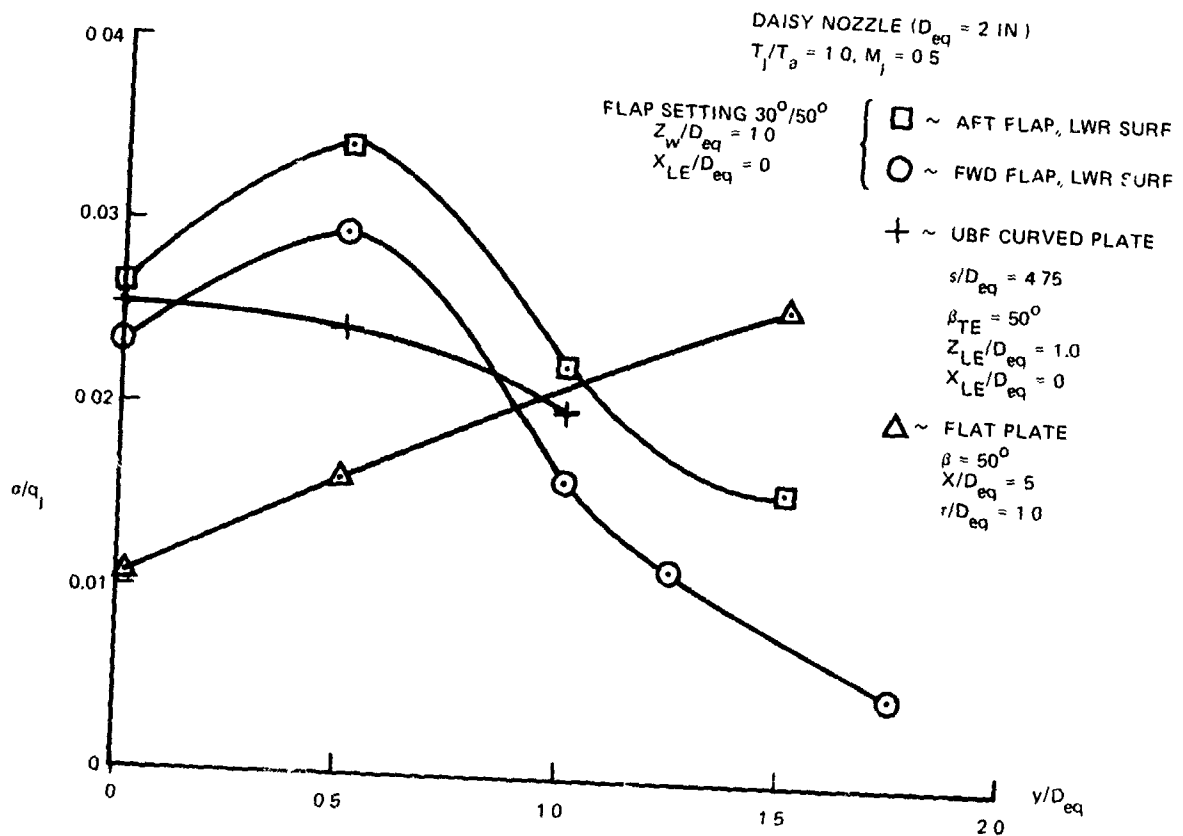


FIGURE 72. SPANWISE DISTRIBUTION OF RMS PRESSURE FLUCTUATIONS ON THE FLAT AND CURVED PLATES AND THE WING-FLAPS MODEL WITH A LOBED NOZZLE

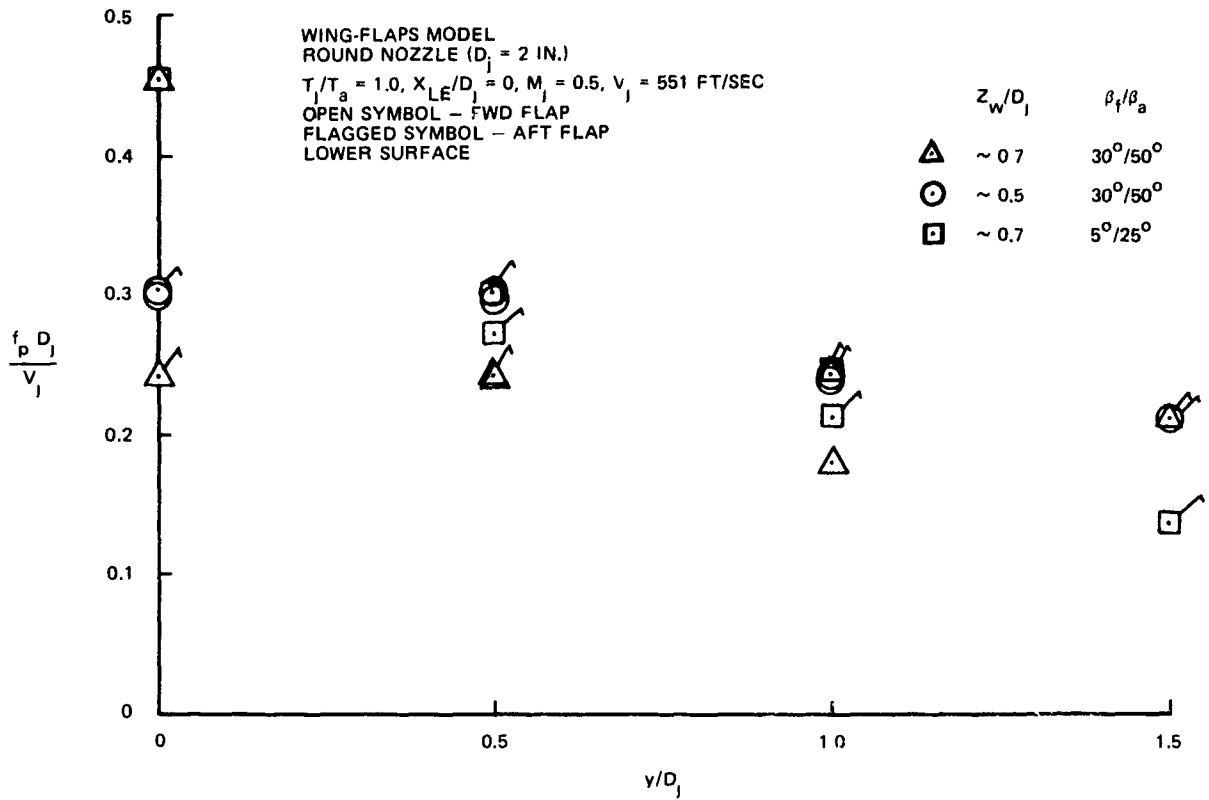


FIGURE 73. PEAK STROUHAL NUMBER DISTRIBUTION IN THE y -DIRECTION FOR WING-FLAPS MODEL

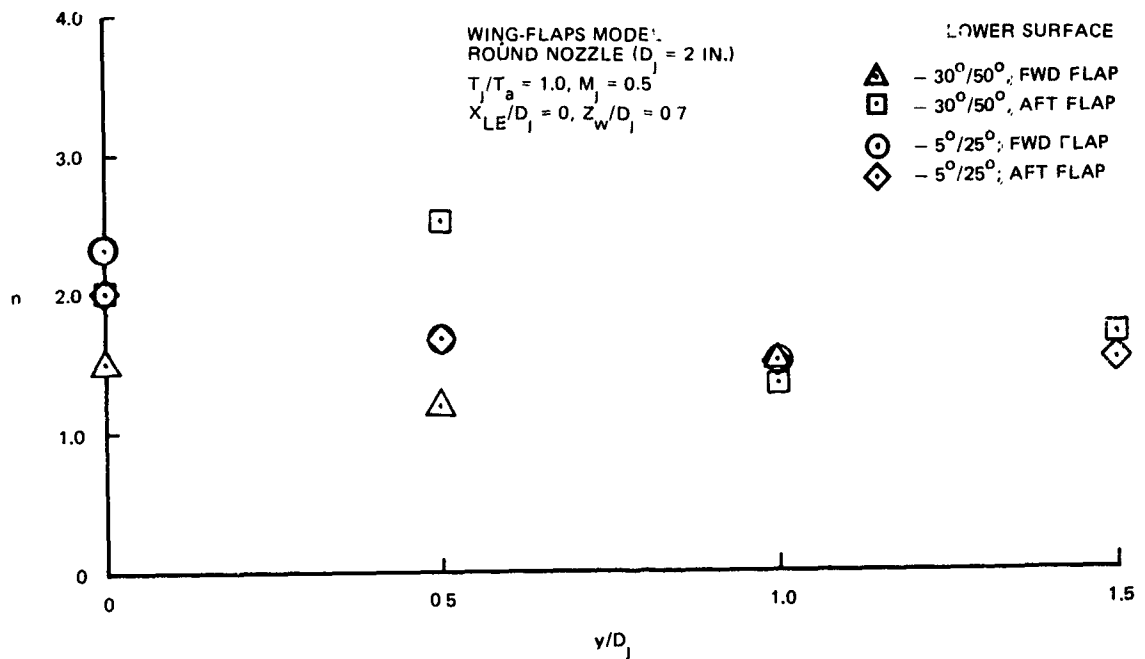


FIGURE 74. VARIATION OF ROLL-OFF EXPONENT IN THE y -DIRECTION ON THE WING-FLAPS MODEL

WING-FLAPS MODEL
 ROUND NOZZLE ($D_j = 2$ IN)

$T_j/T_a = 1.0, M_j = 0.5, \beta_f/\beta_a = 30^\circ/50^\circ$
 $X_{LE}/D_j = 0, Z_w/D_j = 1.0$

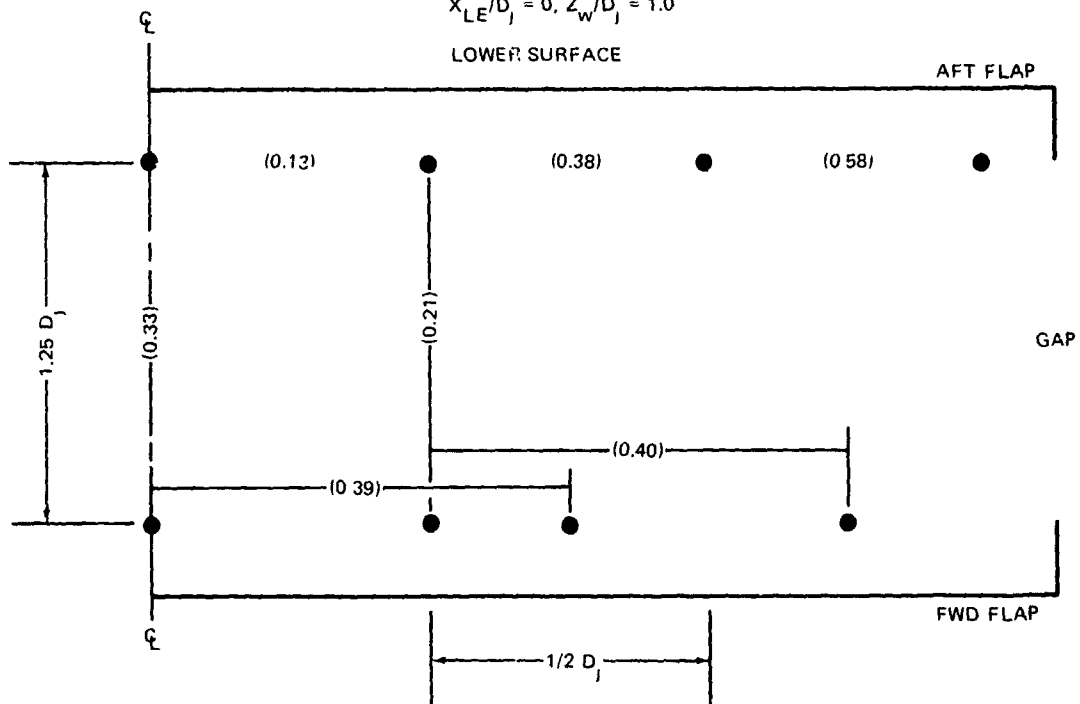


FIGURE 75. MAXIMUM SQUARE ROOT OF COHERENCE (ρ_m) FOR THE WING-FLAPS MODEL

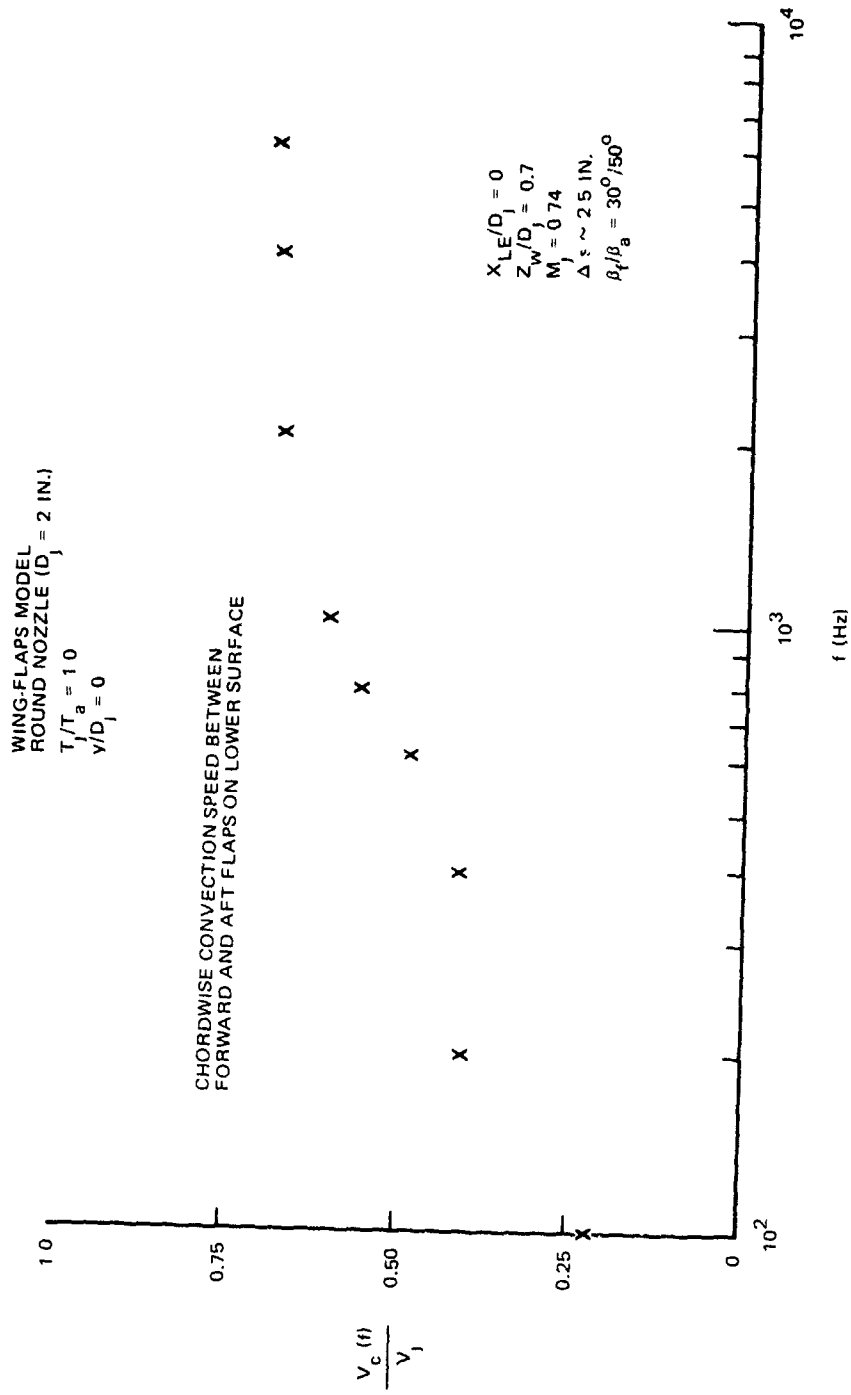


FIGURE 76. NORMALIZED CONVECTION SPEED BETWEEN FLAPS ON THE WING-FLAPS MODEL

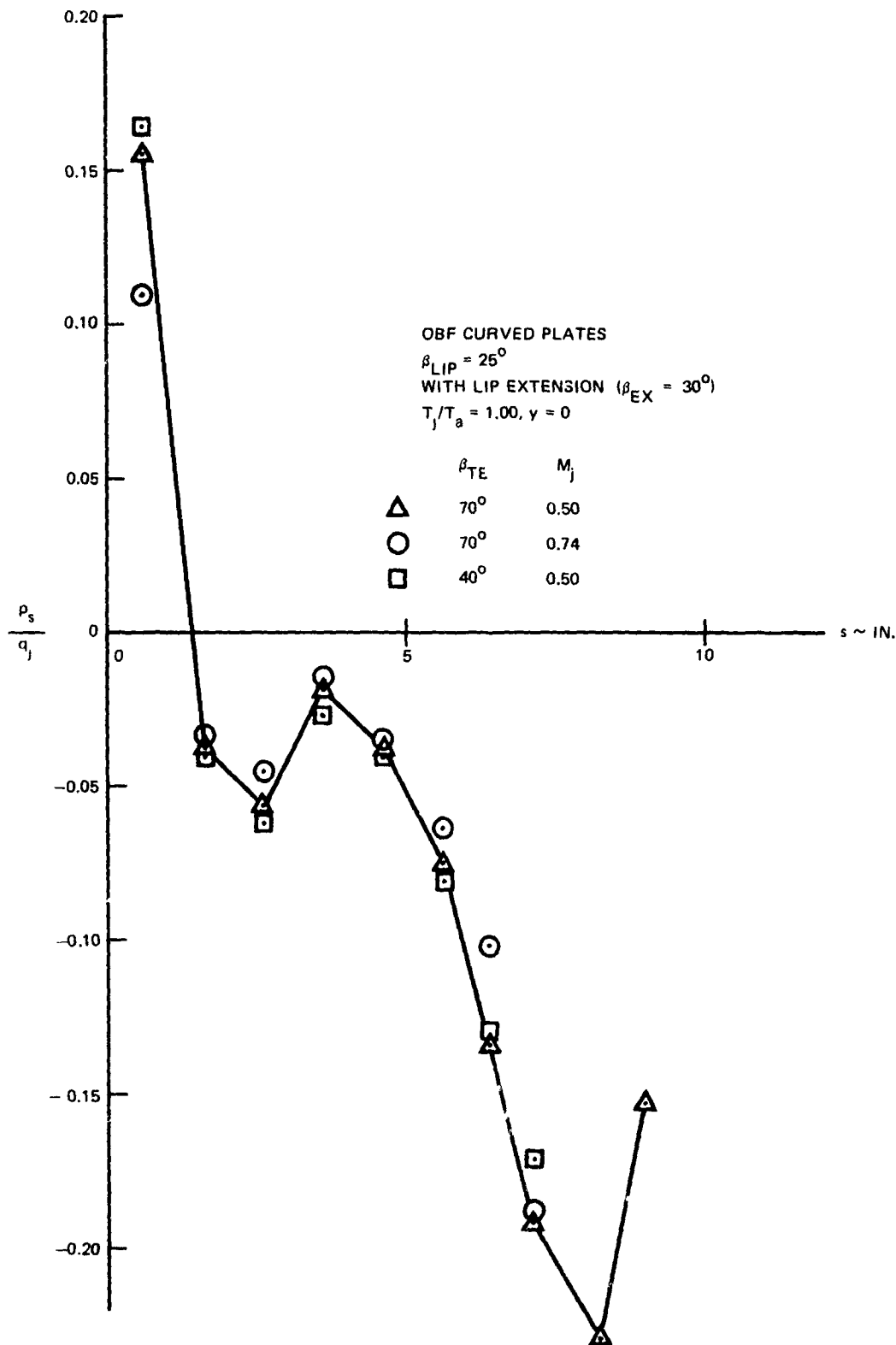


FIGURE 77. STREAMWISE STATIC PRESSURE DISTRIBUTION FOR OBF CONFIGURATION

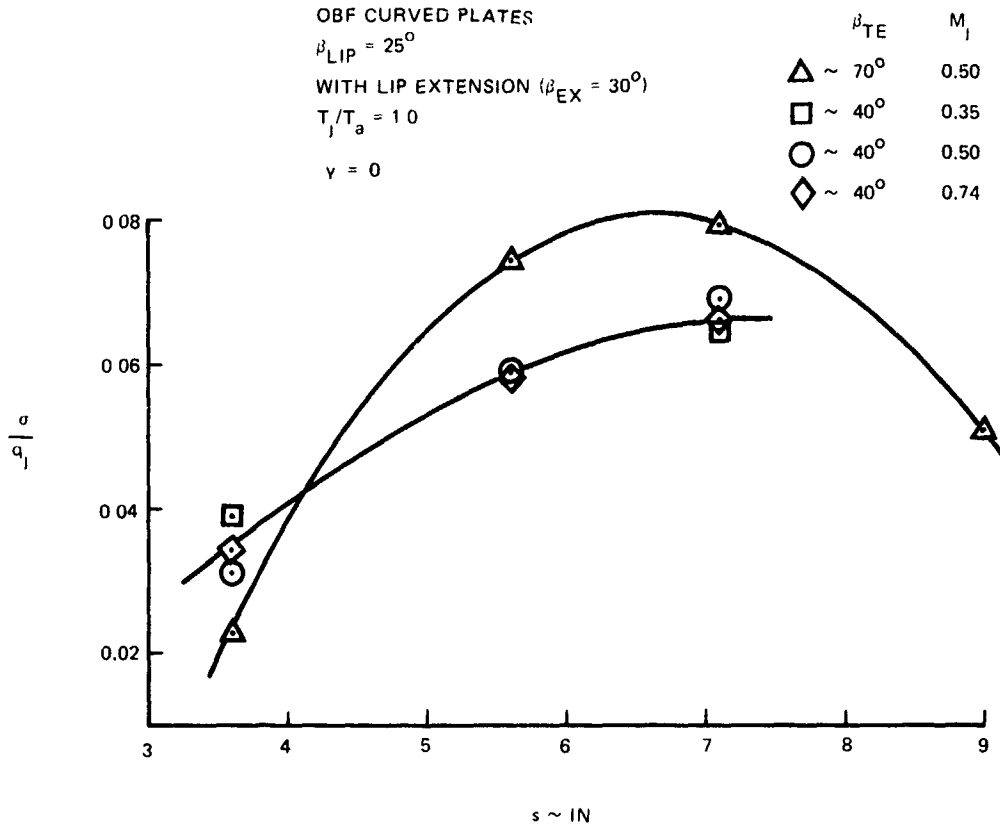


FIGURE 78. NORMALIZED STREAMWISE RMS FLUCTUATING PRESSURE DISTRIBUTION FOR OBF PLATE

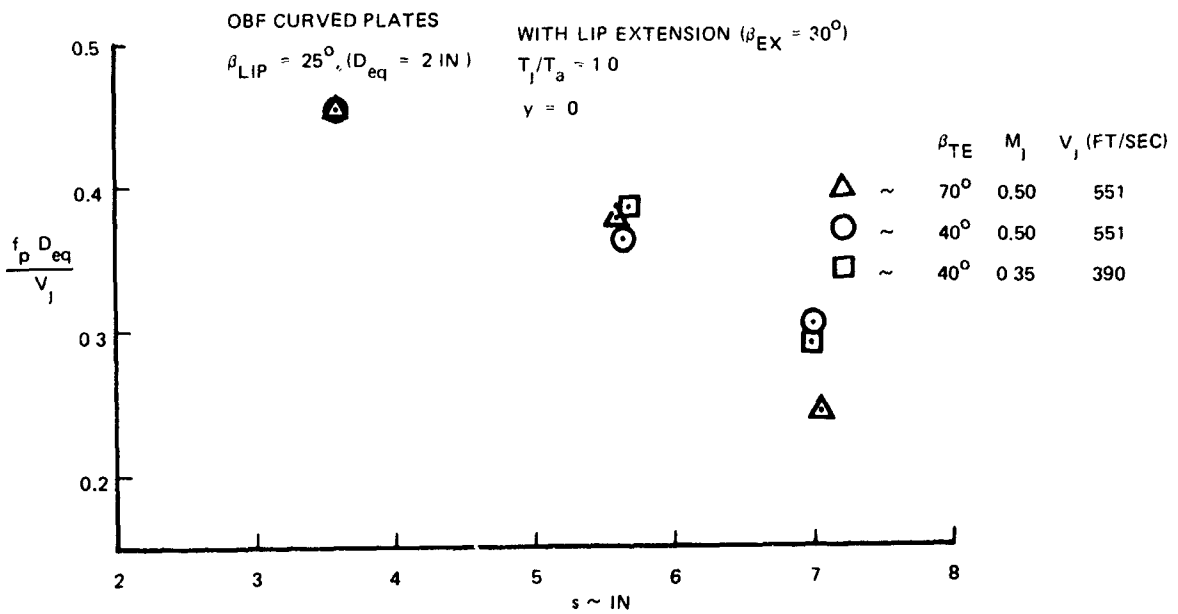


FIGURE 79. PEAK STROUHAL NUMBER DISTRIBUTION IN STREAMWISE DIRECTION FOR OBF PLATE

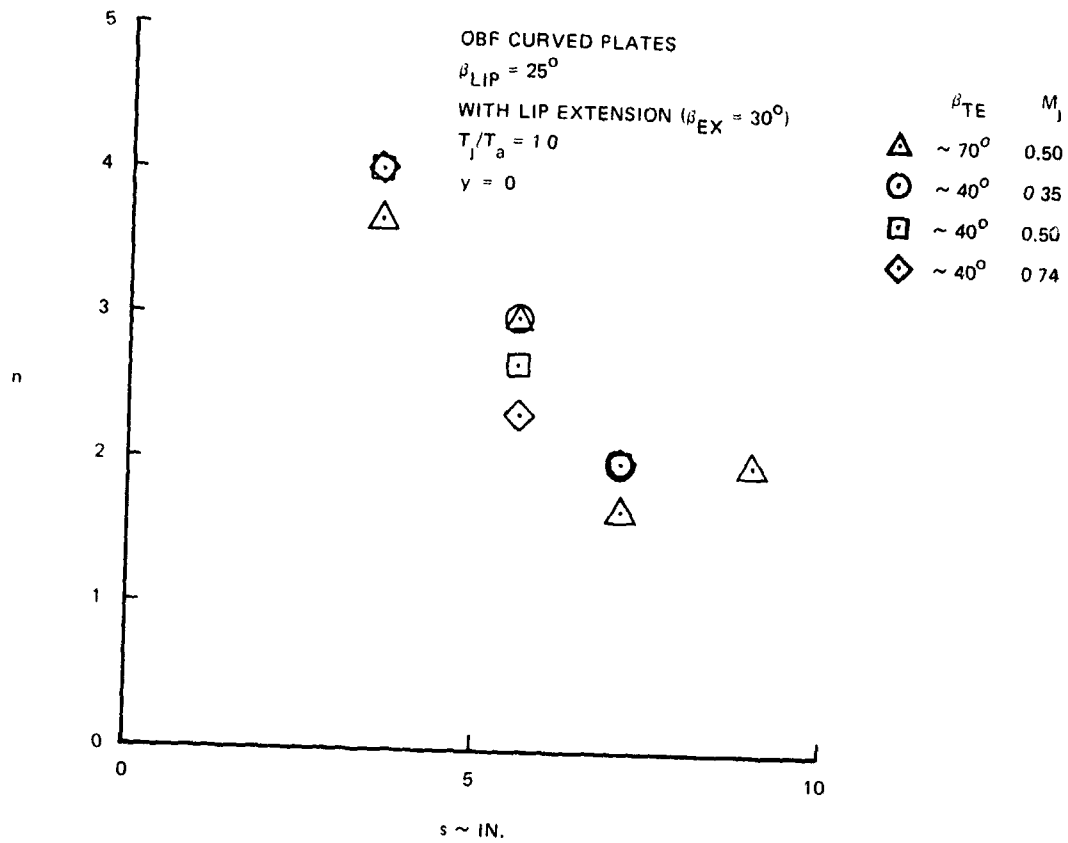


FIGURE 80. ROLL-OFF EXPONENT IN OBF TEST CASES

Test results indicate that the existence of a stagnation point plays an important role in the surface distribution of fluctuating pressure and in the steady-state heat transfer coefficient. A stagnation point on an object impinged upon by a jet permits the flow to split and establish a strong pressure gradient in the vicinity of the stagnation point in contrast to a case in which the flow simply follows a curved surface without a stagnation region. From the analysis of data from the test program and other sources, it appears that the levels of RMS pressure and heat transfer are strongly affected by the local mean pressure gradient. Unfortunately within the time devoted to this project, it was not possible to establish an explicit relationship among these quantities.

Since an inclined flat plate and an under-the-wing blown flap configuration both have well established stagnation regions, early in the development of this methodology it was thought that a method to predict pressure fluctuations and heat transfer on an inclined flat plate could successfully be extended to the flap. But it was also recognized that there was no known reliable theoretical solution to the problem, even with as simple a configuration as a flat plate. This is primarily due to the change of turbulent characteristics from that of the free jet in the region 2-3 velocity half radii upstream from the plate.

Therefore, it was decided to establish a fully or semi-empirical method to estimate the distribution of a desired property. The steps in doing this were as follows for a UBF configuration:

1. Select the proper normalizing parameters for different quantities of interest (e.g. RMS pressure, half power frequency, roll-off exponent, heat transfer coefficient, etc., hereinafter called dependent variables) from the mean properties of the undisturbed free jet. This is for ease of future use of the method since analysis of the turbulent mixing of a free jet for its mean properties is well established.

2. Select the proper grouping of these parameters with experimentally obtained dependent variables so that data can be presented and formulated in a non-dimensional form.

3. Establish a method to locate the stagnation point and refer all of the dependent variables elsewhere on the specimen to those at the stagnation point.

4. Relate the values of dependent variables at the stagnation point of an inclined plate to those of a normal plate.

5. Formulate chordwise downstream distribution of dependent variables along the intersection of the jet vertical plane with the inclined plate. The downstream direction from the stagnation point was only considered because the stagnation point on a flap lower surface is near the leading edge.

6. Formulate spanwise distribution of the dependent variables at any chordwise location.

7. Relate the distribution of the desired dependent variable on the inclined plate to that on the flap configuration at the same angle setting. This is done by establishing a correction factor which is a function of the geometric parameters of the flap and plate configuration as well as the jet exit Mach number and the streamwise location of the test specimen.

1. NORMALIZATION CONCEPT

a. Fluctuating Pressures

Turbulence extracts energy from the mean flow at large scales and in turn the large scale structure supplies energy to small scale eddies by vortex stretching. This energy is then dissipated into heat energy at a rate which may be shown to be proportional to the mean square vorticity fluctuations if the Reynolds number is sufficiently large. Stresses in a fluid element working against the mean strain rate produce deformation work, part of which is the contribution of viscous stresses which are always negative. Therefore, it represents a loss of mean kinetic energy. The remaining part of the deformation work is the contribution of Reynolds stresses which is also dissipative for the mean kinetic energy in most flow situations (negative values of Reynolds stresses tend to occur with positive strain rates). However, the deformation work due to the Reynolds stresses which is lost by the

mean flow is gained by the turbulence. In other words, this work serves to exchange kinetic energy between the mean flow and the turbulence, and thus it represents turbulence production. In the case of the free turbulent jet, therefore, turbulence kinetic energy production is at a maximum in the heavily sheared region where the product of Reynolds stresses and mean rate of strain is at its peak value. Within the first 7-8 nozzle diameters this region is very distinct and occurs in the vicinity of velocity half points. Thereafter it gradually moves outward and flattens out.

The fluctuating pressure is considered to be mainly made up of two components. One component is due to the turbulent-turbulent interaction (P'_{TT}) which involves spatial gradients of higher order fluctuating velocity correlations. If local homogeneity of turbulence is assumed to simplify the analysis, this component can be shown to be a function of velocity intensity alone (References 16 and 17). The other component is from the turbulence-mean shear interaction (P'_{TM}) which involves only gradients of Reynolds stresses and is shown to be a function of transverse turbulent velocity intensity, velocity space scale and the mean velocity gradient. This means that P'_{TM} will be at its maximum value where turbulence kinetic energy is maximum. Because of the flat characteristics of turbulence intensity beyond 8-10 nozzle diameters, it can safely be stated that a maximum of turbulence kinetic energy also occurs at the velocity half region of the jet. Consequently, it appears reasonable to assume that the major contribution to the fluctuating pressure spectra in the stagnation region (within two half-jet radii of the plate) of the specimen comes from this area of the undisturbed jet. Likewise, in the wall jet region, the velocity half point farthest from the surface of the specimen may be thought of as playing the same role as the free jet velocity half point plays in the stagnation region.

It follows from the above discussion that the preferred normalizing parameters in the development of the method of prediction of many of the dependent variables are those computed at the half radius of the undisturbed jet at an axial location where the test specimen would have been positioned. From the test results obtained in this program the

pertinent information needed for the dynamic analysis of a structure includes RMS level, half power frequency, roll-off exponent, peak amplification factor, and maximum correlation length of the fluctuating pressure on the surface of the test specimen exposed to the jet. As indicated earlier, this information cannot be theoretically derived. Therefore another approach to a prediction method probably would be to relate empirically the measurements of the above fluctuating pressure characteristics at the velocity half point of the undisturbed jet to the corresponding measurements at the surface of the test specimen.

The scope of this program unfortunately did not permit an investigation of fluctuating properties in a free jet. Therefore, it was decided to use some of the mean flow properties of the free jet to normalize and collapse experimentally measured and statistically processed data.

The most significant normalization parameter for the RMS pressure at the stagnation point of a normally impinged plate was found to be the mean dynamic pressure ($q_{1/2}$) at the velocity half point of the free jet. In the case of an oblique impingement, the stagnation pressure on an inclined plate is related in Reference 1 to that of a normal plate by the function $\sin^2 \beta$. The reasoning for this relationship is that only the component of axial flow velocity normal to the inclined plate stagnates and therefore contributes to the stagnation pressure. Assuming that the significant part of $q_{1/2}$ also comes from the normal component of velocity, $q'_{1/2}$ is put in the form:

$$q'_{1/2} = q_{1/2} \sin^2 \beta$$

where $q_{1/2}$ is evaluated at a given X/R_j . Then a new fictitious distance X'/R_j is defined such that $q_{1/2}$ there is equal to $q'_{1/2}$. (See Figure 83). This is the distance used in the ordinate of Figure 85 to evaluate the RMS pressure at the stagnation point of an inclined plate. Of course if the plate is normal to the flow, both the X'/R_j and $q'_{1/2}$ degenerate into X/R_j and $q_{1/2}$ respectively.

Mean flow properties of a submerged turbulent free jet which are pertinent to the calculation of RMS pressure can be obtained from a computer program like the one given in Reference 11. For convenience, however, properties of the cold and hot jets at several jet Mach numbers have been calculated by a Douglas Aircraft Company computer program and are presented in Appendix K.

Chordwise and spanwise distributions of RMS pressure on a flat plate are scaled to the stagnation point values. These results are then extended to predict spanwise distributions of RMS pressure on a flap configuration at an angle setting of 50° . This is accomplished by means of a set of correction curves as shown in Figure 88.

Half power frequency ($f_{1/2}$) at the stagnation point of a normally impinged plate is best expressed in the form of a Strouhal number based on nozzle diameter and initial jet velocity. Roll-off exponent (n), also at the stagnation point, is shown to be a function of Strouhal number. Stagnation point values of ($f_{1/2}$) and (n) for an inclined plate ($\beta = 50^\circ$) are related to those of a normal plate by multiplying the latter by $\sqrt{\sin\beta}$. Chordwise distributions of ($f_{1/2}$) and (n) are then related to the stagnation point values.

Although the foregoing discussion applies to both round and mixer nozzles, the latter introduces more complication as presented below:

Mixer-type nozzles are multi-element nozzles designed to promote turbulent mixing between the nozzle flow and its surrounding medium. Daisy nozzles such as the one which was tested in this program are mixer nozzles with individual elements uniformly distributed around a common centerline. The flow field of these nozzles depends not only on the initial nozzle conditions, but also on numerous other factors such as:

1. geometry of elements
2. element spacing (e.g., number of elements)
3. existence of a centerbody (bullet)
4. radial gap between the inner surface of elements and the bullet.

Since the flow field of these nozzles is three dimensional and turbulent, there is no known working analytical tool at present for predicting its mean properties. Therefore, it has to be analyzed by either semi-or fully-empirical methods.

The exhaust plume of a mixer-nozzle is usually divided into three regions as shown in the following sketch.

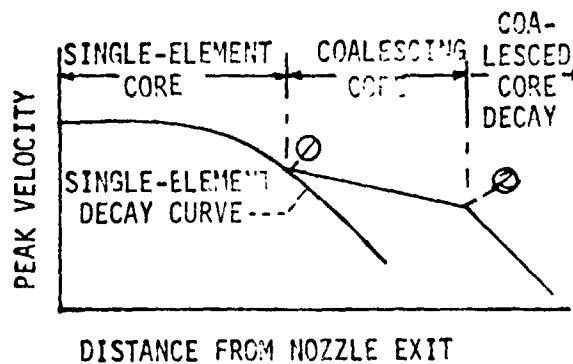


Figure 81. Peak Velocity Decay Curve For Mixer-Nozzle

The single element decay region is characterized by independent behavior of the elements of the mixer nozzle. Somewhat downstream from the nozzle exit, however, the mixing zone between two consecutive elements starts coalescing (hence the name "coalescing core:), and this process continues on until the plume becomes a fully developed circular jet. The region beyond this point is called the coalesced core region.

If experimental flow field data for a particular type of mixer nozzle is not available, methods can be devised to calculate it approximately. One such method is to use empirical equations which are developed using the data available from tests of a large class of mixer nozzles. If the nozzle to be analyzed roughly falls into one of these categories, and if the information desired is in the vicinity of or downstream from the coalesced core region, the results predicted by this method are fairly satisfactory.

The flow field of the mixer nozzle tested in this program was not surveyed. Since properties of the flow field were needed in the normalization of some of the surface fluctuating pressure characteristics

presented in this report, the empirical method indicated above was adopted. For this purpose, the data in Reference 15 were used.

The nozzle tested in this program is a 10-lobe nozzle with nearly circular lobes as shown in Figure 10. The area of the annular gap between the plug and the inner surface of the lobes constitutes nearly 33% of the total open area of the nozzle. Such a large gap does not allow the peak velocity to decay rapidly. The nozzle selected from those tested in Reference 15 as most representative of the used nozzle is the coplanar-multi-tube configuration with one tube at the center of the cluster (see Figure 82). The center tube gives a reduction of the rate of decay of peak velocity with distance similar to that produced by the annular gap of the daisy nozzle.

The computational procedure to predict $(f_{1/2})$, (n) and RMS pressure on a flat plate for both types of tested nozzles and extension of the method of prediction of RMS pressure to the flap configuration are presented subsequently in this section. The derived curves and equations contained in the procedure are given primarily for convenience. Since data points are also shown in the figures, it is left to one's discretion whether to use the displayed data or the derived expressions.

Also it should be noted that the relations for the daisy nozzle are at best approximate. However, the parameters selected for normalization in this case appear to be important in order to bring daisy and round nozzle data together. Whenever flow field data from a particular daisy nozzle is available, the presented relations should be upgraded.

b. Heat Transfer From a Round Nozzle

In this program, heat transfer measurements to a flat plate from a hot impinging jet were obtained by recording the temperature-time history of thin circular copper elements of small radius (calorimeters) distributed on and insulated from the test plate as shown in Figure 29. This is commonly known as a transient technique and relies on the heat transfer coefficient to be nearly time independent.

Assuming that almost all of the local heat energy from the hot jet goes to raise the temperature of the calorimeters (minimum loss to

the environment), a simple heat balance equation can be set up;

$$-mc \frac{d}{d\tau} (T_{T_{\infty}} - T_w) = hA (T_{T_{\infty}} - T_w)$$

where

- m = Weight of the calorimeter
- c = Specific heat of the calorimeter material
- $T_{T_{\infty}}$ = Local stagnation temperature at the centerline of the undisturbed jet (reference temperature)
- T_w = Temperature of the calorimeter
- h = Heat transfer coefficient
- τ = Time (from initial exposure)

Integrating this equation, the following result is found:

$$\frac{T_{T_{\infty}} - T_w}{T_{T_{\infty}} - T_{\infty}} = e^{-\frac{\tau}{\tau_c}}$$

where $\tau_c = \frac{mc}{hA}$ is the time constant

From this development it is seen that constant h implies constant τ_c . But in the series of tests performed in this program, τ_c was found to be increasing substantially with time. The reason for this behavior is not yet fully understood and needs investigation.

When it was realized that τ_c was a function of time, no rational method of data reduction to obtain heat transfer coefficients could be established. Therefore, the method of prediction of heat transfer to a normally impinged plate as presented in Reference 1 was adopted and slightly modified to extend it to an inclined plate. Details of the computational procedure are presented later in this section.

Since laminar heating at the stagnation point has been extensively studied in the past, the basic approach to stagnation point heat transfer by a turbulent jet is to relate it to that of the laminar jet by means of a correction factor. This factor is, in general, a function of the free stream turbulence level, an appropriate Reynolds number, and the ratio of integral scale of turbulence to the length used in defining

Reynolds numbers. Local heat transfer rates were correlated with the properties of the free jet in the plane of impingement, a local temperature difference, and the distance from the point of impingement normalized with the half radius of the jet in the plane of impingement.

The tests in Reference 1 covered a range of initial jet velocities from 200 fps to 700 fps; Reynolds numbers, based on the half radius and local centerline conditions of the free jet, from 3.08×10^4 to 1.12×10^5 and impingement distances, measured from the nozzle exit, from 7 to 30 nozzle diameters. For ease of reference some of the findings from these extensive series of tests are summarized below:

1. Stagnation point heat transfer is relatively high compared to that of the wall jet region at low Reynolds number, and this ratio becomes smaller as the Reynolds number is increased.

2. Heat transfer near the stagnation point behaves in a manner similar to that of a laminar boundary layer on a surface having the same pressure distribution.

3. Heat transfer rates from turbulent jets are 1.5 to 2 times larger than the calculated laminar values.

4. Away from the stagnation point on the plate, heat transfer behaves in a manner similar to a normal turbulent boundary layer which develops in an external flow having a free-stream velocity equal to the local maximum velocity in the wall jet.

5. The correction factor, while being a strong function of impingement distance, has a weak dependence on the Reynolds number.

6. There is a general increase in the value of the correction factor with local jet turbulence intensity.

2. COMPUTATIONAL PROCEDURE

a. Stagnation Point Location

The stagnation point location on a flat plate relative to the center of impingement for a circular nozzle is determined as follows:

1. Obtain $r_{1/2}$ from a plot of $r_{1/2}$ vs X/R_j given in Appendix K for the prescribed jet condition.

2. Calculate Δr (Figure 84) from:

$$\Delta r = 0.7 (r_{1/2}) (\cot \beta)^{1.2}$$
 measured upstream from the point of intersection of the jet centerline with the plate.

b. Fluctuating Pressures - RMS Levels

Calculation of RMS pressures on a flat plate under hot or cold flow conditions is performed in the following manner:

(1) Circular Nozzle Geometry

The information below needs to be given to begin the calculation.

1. Position in the (r,y) coordinate system where the RMS pressures are to be estimated.

2. Nozzle and jet characteristics ($R_j, M_j, P_{T_j}, T_{T_j}$, Nozzle Exit Geometry, Ω).

3. Centerline distance between jet exit and plane of impingement, (X) .

4. Plate inclination, (β) .

Proceed as follows:

1. For the specified nozzle exit geometry and flow conditions, obtain $(q_{1/2}/q_j)$ at the given (X/R_j) from supplied plots in Appendix K.

2. Compute $q_j = 1/2 \gamma P_\infty M_j^2$,

3. Calculate $(q'_{1/2}/q_j)$ from $q'_{1/2}/q_j = (q_{1/2}/q_j) \sin^2 \beta$ for $22.5^\circ \leq \beta \leq 90^\circ$.

4. Reenter the curve of $(q_{1/2}/q_j)$ vs X/R_j at the value of $(q'_{1/2}/q_j)$ and obtain the value of (X/R_j) which is identified as (X'/R_j)

5. Calculate $(q'_{1/2})$ from steps 2 and 3.

6. Calculate $(\sigma_{\text{stag.pt.}})$ within the range

$9 < (X'/R_j) (\sin \beta / \Omega)^{1/3} < 45$ and $22.5^\circ \leq \beta \leq 90^\circ$ from:

$$\sigma_{\text{stag.pt.}} = (q'_{1/2}) (1.3242 \times 10^{-2}) [(X'/R_j)(\sin \beta/\Omega)^{1/3}]^{1.43703}$$

(See Figure 85)

7. Read (C_0) and (C_1) at desired (β) from Figure 86.
 $22.5^\circ \leq \beta \leq 50^\circ$, & $\beta = 90^\circ$

8. Calculate (σ) at the given (r) from:

$$a = C_0 (X/R_j) + C_1, \quad 10 \leq X/R_j \leq 20$$

$$\sigma/\sigma_{\text{stag.pt.}} = a^{-(r/R_j)}, \quad 0 \leq r/R_j < 6$$

NOTE: The above equations apply only in the downstream direction from the stagnation point.

9. Calculate (σ) for the given (y) from:

$$\sigma/\sigma = \text{sech } \xi$$

where

$$\xi = [0.753 - 3.92 (X/R_j)^{-1}] (y/R_j)$$

$$\text{and } 0 \leq y/R_j \leq 3; \quad 10 \leq X/R_j \leq 20; \quad \beta = 50^\circ$$

(See Figure 87)

Following is the procedure to extend the foregoing flat plate computations to the flap configuration:

1. Read (Δ) at given (y) and (Z_w) from Figure 88 where $0 \leq y/R_j \leq 3$.

2. Compute $(\sigma)_{\text{flap}}$ from:

$$(\sigma)_{\text{flap}} = (\Delta) (\sigma)_{\text{plate}} \text{ for } \beta = 50^\circ \text{ only.}$$

NOTE: The only (Δ) curves shown are for the case $\beta = 50^\circ$ and $r/R_j = 1$. It is suggested that these (Δ) curves be used in all other chordwise locations until further flap data are available.

(2) Daisy Nozzle Geometry

Nozzle tested in this program has the following geometric properties:

Number of lobes = 10 Exit area = 3.1416 in²

Plug diameter at exit = 2 in.

Gap between plug and inner surface of lobes \cong 0.16 in.

Gap area \cong 1.0856 in²

Diameter of circular nozzle whose area is equal to the gap area = 1.1757 in. (it is identified as D_o)

Total lobe area \cong 2.056 in²

Outside diameter at exit = 3.1 in.

Length of bullet from exit = 3.3 in.

Wetted perimeter at exit \cong 24.16 in.

Area per circular element \cong 0.2056 in²

Diameter of a circular nozzle whose area is equal to that of a single element (in this case, it is the diameter of the element itself and identified as D_e) = 0.5116 in.

Diameter of a circular nozzle whose area is equal to that of mixer nozzle (it is identified as D_{eq}) = 2 in.

Equivalent mixer nozzle selected from Reference 15 and sketched below is a multitube coplanar nozzle with one ring of circular elements located around one central circular tube.

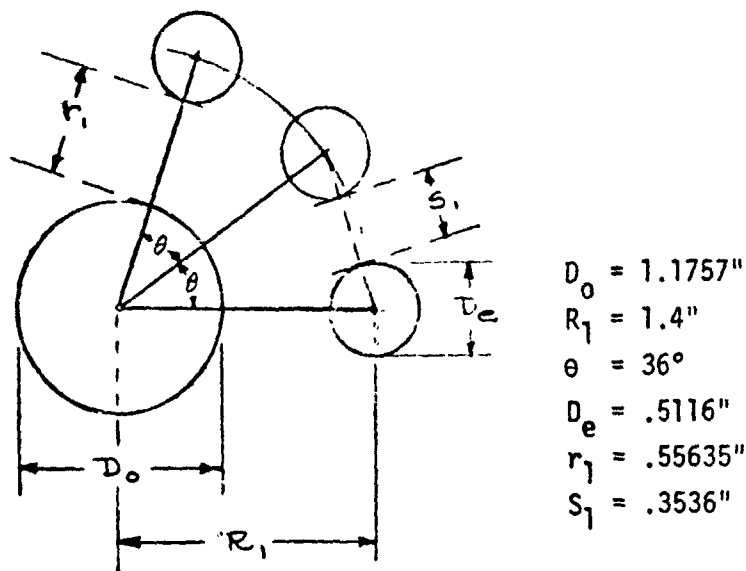


Figure 82. Multitube Coplanar Mixer Nozzle

Area of an outer element and radius of the ring to the center of an element are made equal to those of the actual daisy nozzle. Furthermore, area of the center tube is the same as the gap area of the daisy.

Following is the procedure to calculate $(q_{1/2})$ which is used to normalize RMS pressure at the stagnation point of a flat plate when it is impinged by the jet of the daisy nozzle tested:

1. Calculate $f(D_e/D_h)$ from:

$$f\left(\frac{D_e}{D_h}\right) = \left[1 + 2.67\left(\frac{D_e}{D_h} - 1\right)\right]^{-1} \quad \text{Equation 4 of Reference 15}$$

where D_h is the hydraulic diameter of an element. In this case $D_e/D_h = 1$ since the elements are circular. Therefore,

$$f\left(\frac{D_e}{D_h}\right) = 1$$

2. Calculate $f(r/S)$ from:

$$f(r/S) = \left[1 + 0.33\left(\frac{r_1}{S_1}\right)\left(\frac{D_e}{D_o}\right)^3\left(\frac{V_s}{V_j}\right)^2\right]^{-1} \quad \text{Equation 5 of Reference 15}$$

where $\frac{V_s}{V_j}$ is the ratio of bypass jet velocity to core velocity, and in this case, it is unity.

$$f(r/S) = \left[1 + (0.33)(1.5734)(.4351)^3\right]^{-1} \doteq 0.959$$

3. Calculate $Z_{\textcircled{1}}$ from:

$$Z_{\textcircled{1}} = \left(\frac{X}{C_n D_e \sqrt{1 + M_j}}\right)_{\textcircled{1}} = 12 \left[1 + (1/4)\left(\frac{S_1}{D_e}\right)^{2/3}\right] \left(\frac{S_1}{D_e}\right)^{1/3} f\left(\frac{D_e}{D_h}\right) f\left(\frac{r}{S}\right)$$

Equation 3 of Reference 15.

where nozzle coefficient $C_n = 0.828$.

$$Z_{\textcircled{1}} = 12 \left[1 + (1/4)(0.6913)^{2/3} \right] (0.6913)^{1/3} (1)(0.959) = 12.164$$

Therefore, for the test Mach number, $M_j = 0.5$, we have:

$$\left(\frac{X}{D_e} \right)_{\textcircled{1}} = (12.164)(0.828) \sqrt{1 + 0.5} = 12.335$$

4. Enter to $\frac{V_c}{V_j}$ vs. $\frac{X}{R_j}$ plot for $M_j = 0.5$ in Appendix K with $\frac{X}{R_j} = 2 (12.335) = 24.67$, and read off $\left(\frac{V_c}{V_j} \right)_{\textcircled{1}} = 0.585$.

5. Calculate $\left(\frac{V_{\text{peak}}}{V_j} \right)_{\textcircled{1} \rightarrow \textcircled{2}}$ from:

$$\left(\frac{V_{\text{peak}}}{V_j} \right)_{\textcircled{1} \rightarrow \textcircled{2}} = \left(\frac{V_c}{V_j} \right)_{\textcircled{1}} \left(\frac{Z_{\textcircled{1}}}{c_n D_e \sqrt{1 + M_j}} \right)^{1/5} \quad \text{Equation 7 of Reference 15}$$

$$\left(\frac{V_{\text{peak}}}{V_j} \right)_{\textcircled{1} \rightarrow \textcircled{2}} = (0.585) \left[\frac{12.164}{(0.828)(0.5116)\sqrt{1 + 0.5}} \right]^{1/5} = 0.5335$$

6. Reenter to $\frac{V_c}{V_j}$ vs. $\frac{X}{R_j}$ plot with $\left(\frac{V_{\text{peak}}}{V_j} \right)_{\textcircled{1} \rightarrow \textcircled{2}} = 0.5335$

$$\text{and read off } \left(\frac{X}{R_e} \right)_{\textcircled{1} \rightarrow \textcircled{2}} = \left(\frac{X}{R_j} \right)_{\textcircled{1} \rightarrow \textcircled{2}} = 26.8 \quad (P_e = 1/2 P_e)$$

7. Enter $\frac{q_{1/2}}{q_j}$ vs. $\frac{X}{R_j}$ plot again for $M_j = 0.5$ in the Appendix K

$$\text{with } \left(\frac{X}{R_j} \right)_{\textcircled{1} \rightarrow \textcircled{2}} = 26.8 \text{ and read off } \left(\frac{q_{1/2}}{q_j} \right)_{\textcircled{1} \rightarrow \textcircled{2}} = 0.07.$$

8. Compute q_j from:

$$q_j = 1/2 \gamma P_\infty M_j^2 = (0.7) (14.7) (0.5)^2 = 2.5715 \text{ psi.}$$

Therefore, from Steps 7 and 8, obtain $(q_{1/2})_{1-2}$:

$$(q_{1/2})_{1-2} = (0.07)(2.5715) = 0.18 \text{ psi}$$

9. For a normally impinged plate, enter Figure 85 with $(\frac{X}{R_j}) = 26.8$ and $(q_{1/2})_{1-2} = 0.18$ and calculate RMS pressure at the stagnation point.
10. For an inclined plate, proceed as in the case of a circular nozzle to obtain RMS pressure at the stagnation point.

c. Fluctuating Pressures - Power Spectrum Characteristics

The calculation of spectral quantities $f_{1/2}$ and n on a flat plate is performed as follows:

Normal Impingement:

The stagnation point expressions in 1 through 4 below apply to both round and daisy nozzles.

1. Compute $S_{1/2}^*$ for a daisy nozzle (or $S_{1/2}$ for a round nozzle) at the stagnation point of a normally impinged flat plate for a specified X/D from:

$$\left[(S_{1/2}^*)_{\beta=90^\circ} \right]_{\text{stag.pt.}} = \left[(f_{1/2})_{\beta=90^\circ} \right]_{\text{stag.pt.}} \left(\frac{D^*}{V_j} \right) = .7285 - .047 \left(\frac{X}{D_{\text{eq}}} \right)$$

where $D^* = D_j$ and $D_{\text{eq}} = D_j$ for round nozzle

and $D^* = D_{\text{eq}} \sqrt{\Omega}$ for daisy nozzle

($\Omega = 3.845$ for the tested daisy nozzle)

(See Figure 89)

2. Compute $(f_{1/2})_{\beta=90^\circ}$ at the stagnation point from:

$$\left[(f_{1/2})_{\beta=90^\circ} \right]_{\text{stag.pt.}} = \left[(S_{1/2}^*)_{\beta=90^\circ} \right]_{\text{stag.pt.}} \left(\frac{V_j}{D^*} \right)$$

3. Compute $n_{\beta=90^\circ}^c$ at the stagnation point from:

$$(n_{\beta=90^\circ}^c)_{\text{stag.pt.}} = \Omega \left\{ 7.373 \left[(S_{1/2}')_{\beta=90^\circ} \right]_{\text{stag.pt.}} + 1.029 \right\}$$

$$\text{where } \left[(S_{1/2}')_{\beta=90^\circ} \right]_{\text{stag.pt.}} = \left[(f_{1/2})_{\beta=90^\circ} \right]_{\text{stag.pt.}} \left(\frac{D_e}{V_j} \right)$$

($D_e = D_j$ and $\Omega = 1$ for round nozzle)

(See Figure 90)

4. For non-isothermal jet impingement, calculate (n) from:

$$(n_{\beta=90^\circ}^h)_{\text{stag.pt.}} = (n_{\beta=90^\circ}^c)_{\text{stag.pt.}} \sqrt{T_{Tj}/T_{T\infty}}$$

The following expressions pertain only to the round nozzle:

5. Compute $(f_{1/2})_{\text{max}}$ along the centerline chord from:

$$\left[(f_{1/2})_{\text{max}} \right]_{\beta=90^\circ} = \left\{ 1.295 + 1.875 \times 10^{-3} \left| \left(\frac{x}{R_j} \right) - 12 \right|^2 \right\} \left[(f_{1/2})_{\beta=90^\circ} \right]_{\text{stag.pt.}}$$

(See Figure 91)

6. Compute $(f_{1/2})_{\beta=90^\circ}$ at the desired distance (r) from the stagnation point from:

$$(f_{1/2})_{\beta=90^\circ} = (1/4) \left\{ 3 + \sin \left[\left(\frac{r/R_j}{2.5} - 1 \right) \pi \right] \right\} \left[(f_{1/2})_{\text{max}} \right]_{\beta=90^\circ}$$

(See Figure 92)

7. Compute $n_{\beta=90^\circ}$ at the desired distance (r) from the stagnation point from:

$$n_{\beta=90^\circ} = \lambda \left[.265 + \frac{1.47}{1 + (3.551) \sqrt{(r/R_j)^3}} \right] \left[(n)_{\text{stag.pt.}} \right]_{\beta=90^\circ}$$

where λ is:

$$\lambda = (1.084) \sqrt{(r/R_j)(\chi/R_j)} \left[1 - (1/3) \sqrt{r/R_j} e^{-5(r/R_j)^3} \right]$$

NOTE: Use $(n_{\beta=90^\circ})^h_{\text{stag.pt.}}$ to obtain $n^h_{\beta=90^\circ}$

(See Figure 93)

Oblique impingement:

1. Compute $(S_{\frac{1}{2}\beta})$ at the stagnation point from:

$$\left[(S_{\frac{1}{2}\beta}) \right]_{\text{stag.pt.}} = \left[(S_{\frac{1}{2}\beta=90^\circ}) \right]_{\text{stag.pt.}} \sqrt{\sin \beta}$$

2. Compute $(f_{\frac{1}{2}\beta})_{\text{stag.pt.}}$ from:

$$\left[(f_{\frac{1}{2}\beta}) \right]_{\text{stag.pt.}} = \left[(S_{\frac{1}{2}\beta}) \right]_{\text{stag.pt.}} \left(\frac{V_j}{D_j} \right)$$

3. Compute $(n_\beta)_{\text{stag.pt.}}$ from:

$$(n_\beta)_{\text{stag.pt.}} = (n_{\beta=90^\circ})_{\text{stag.pt.}} \sqrt{\sin \beta}$$

Note: Use $(n^h_{\beta=90^\circ})_{\text{stag.pt.}}$ to obtain $(n^h_\beta)_{\text{stag.pt.}}$

4. Along the centerline chord at a downstream distance (r)

$$n_{\beta=50^\circ} = (n_{\beta=50^\circ})_{\text{stag.pt.}} [a(r/R_j)^2 - 4a(r/R_j) + 1]$$

where $a = 0.0119 (\chi/R_j) - 0.106$ and $\chi/R_j \geq 14$ (See Figure 94)

5. Along the centerline chord, compute $\left[(f_{\frac{1}{2}\beta=50^\circ}) \right]_{\text{max}}$ from:

$$\left[(f_{\frac{1}{2}\beta=50^\circ}) \right]_{\text{max}} = \frac{[.011 (\chi/R_j) + 1.272] \left[(f_{\frac{1}{2}\beta=50^\circ}) \right]_{\text{stag.pt.}}}{\sqrt{1 + M_j^2}}$$

For $M_j < 0.74$

(See Figure 95)

6. Compute $(f_{1/2})_{\beta=50^\circ}$ at the desired chordwise downstream distance (r) from the stagnation point from:

$$(f_{1/2})_{\beta=50^\circ} = \left[.85 + .15 \cos \left\{ \left| \frac{(r/R_j) - 1}{.7} \right| \frac{\pi}{2} \right\} \right] \left[(f_{1/2})_{\beta=50^\circ} \right]_{\max}$$

For $M \leq 0.74$

(See Figure 96)

- d. heat Transfer to a Flat Plate

1. Compute the velocity gradient at the stagnation point from:

$$\left(\frac{dV_e}{dr} \right)_{r=0} = 1.13 \frac{V_{\infty}}{r_{1/2}}$$

2. Calculate the stagnation point heat transfer coefficient from a laminar jet to a normal plate from:

$$(h_{1am})_{\beta=90^\circ} = \frac{(q_{1am})_{\beta=90^\circ}}{T_{T_{\infty}} - T_w} = \left[\frac{C_p}{\sqrt{2 Pr}} \right] \sqrt{(\rho \mu)_{\infty}} \left(\frac{dV_e}{dr} \right)_{r=0} (T_{T_{\infty}} - T_w)$$

3. Extend the stagnation point heat transfer result of laminar jets from a normal plate to an oblique plate by:

$$(h_{1am})_{\beta} = (h_{1am})_{\beta=90^\circ} \sqrt{\sin \beta}$$

Note that this correction for oblique impingement has to be verified experimentally before it can be used confidently.

4. Calculate the stagnation point heat transfer coefficient of a turbulent jet to an oblique plate from:

$$h_{\beta} = (h_{1am})_{\beta} f \left(\frac{\lambda}{D_j} \right)$$

where $f \left(\frac{\lambda}{D_j} \right)$ is a correction factor to be obtained from Figure 97

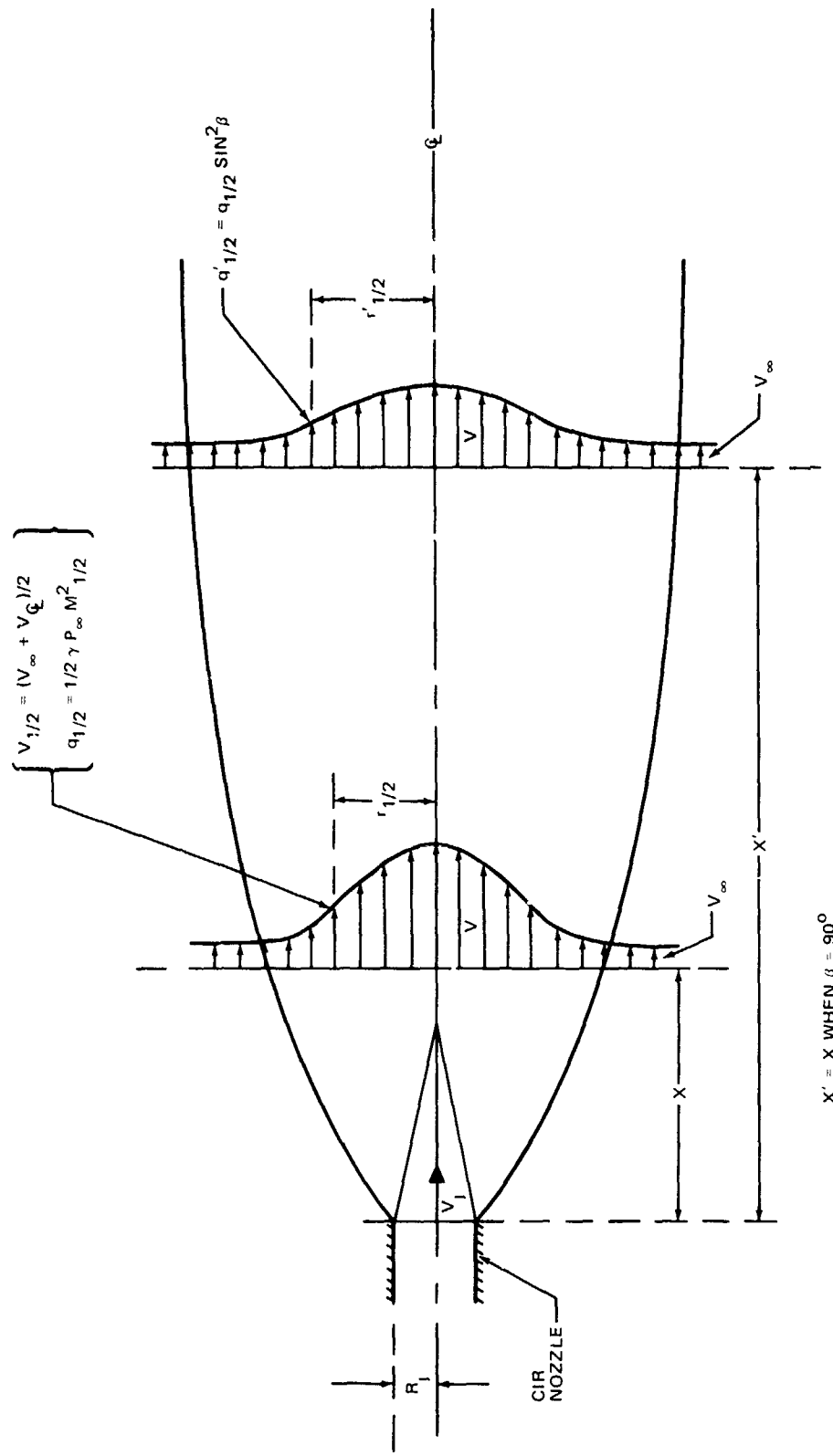
which is a reproduction of Figure 25 of Reference 1 - Part 2.

5. Further away from the stagnation point $[(r/r_{1/2}) \geq 1.8]$, obtain the heat transfer coefficient from Figure 98 which is a reproduction of Figure 34 of Reference 1 - Part 2.

In view of the fact that there is no heat transfer data given in Reference 1 for oblique impingement, assume that Step 5 also applies to oblique impingement.

6. Select the larger of h from Steps 4 and 5 as the proper local heat transfer coefficient on the plate.
7. At distances far from the stagnation point $[(r/r_{1/2}) \geq 10]$, compute the heat transfer coefficient for both normal and oblique impingement from:

$$Nu = \frac{hr}{k} = .12 (Re_{1/2})^{0.8}$$



X' = X WHEN $\beta = 90^\circ$

FIGURE 83. SUBMERGED SUBSONIC JET

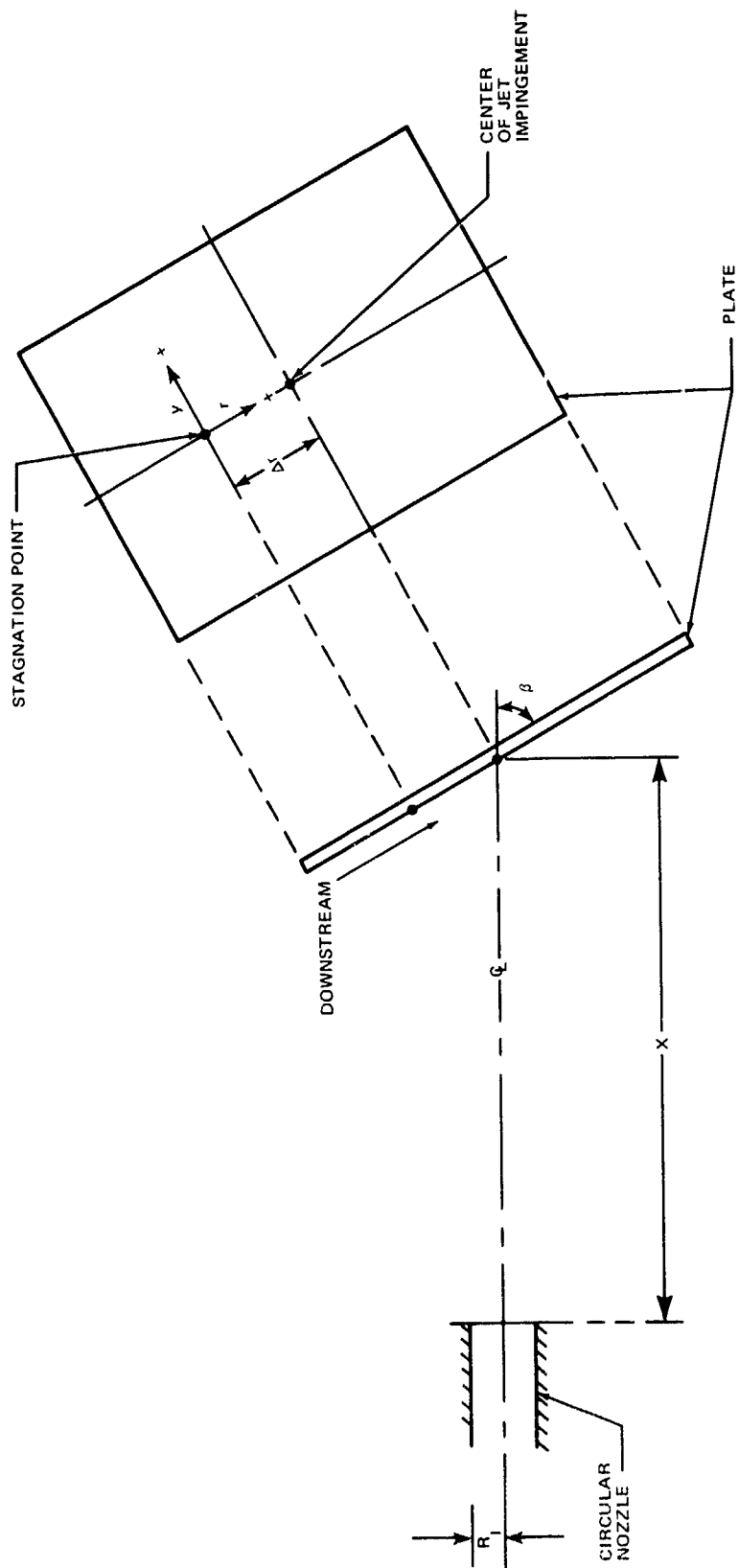


FIGURE 84. IMPINGEMENT TEST SCHEMATIC

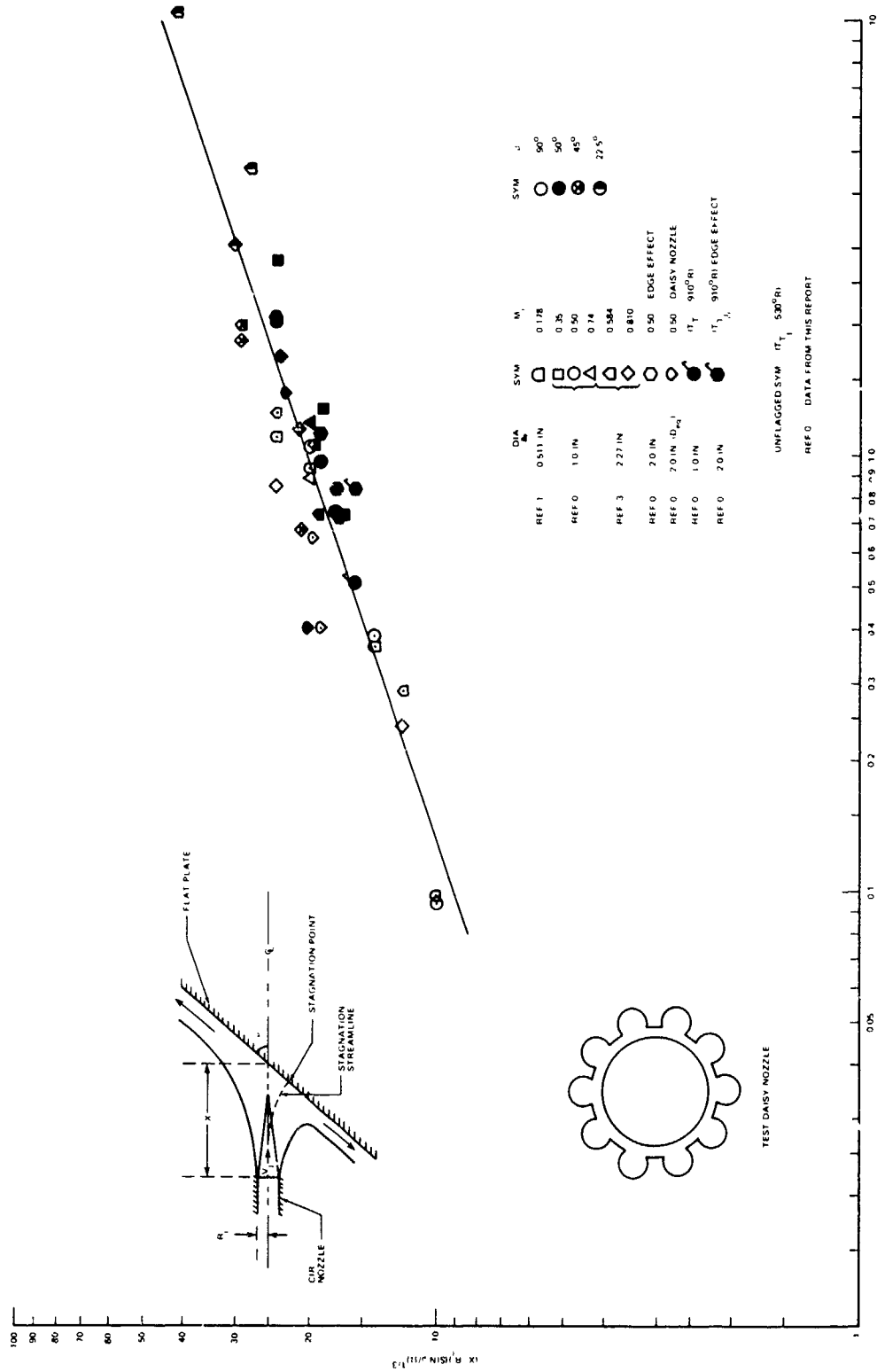


FIGURE B5 STAGNATION POINT RMS PRESSURE COEFFICIENT ON THE SURFACE OF A FLAT PLATE SUBMERGED IN A SUBSONIC JET

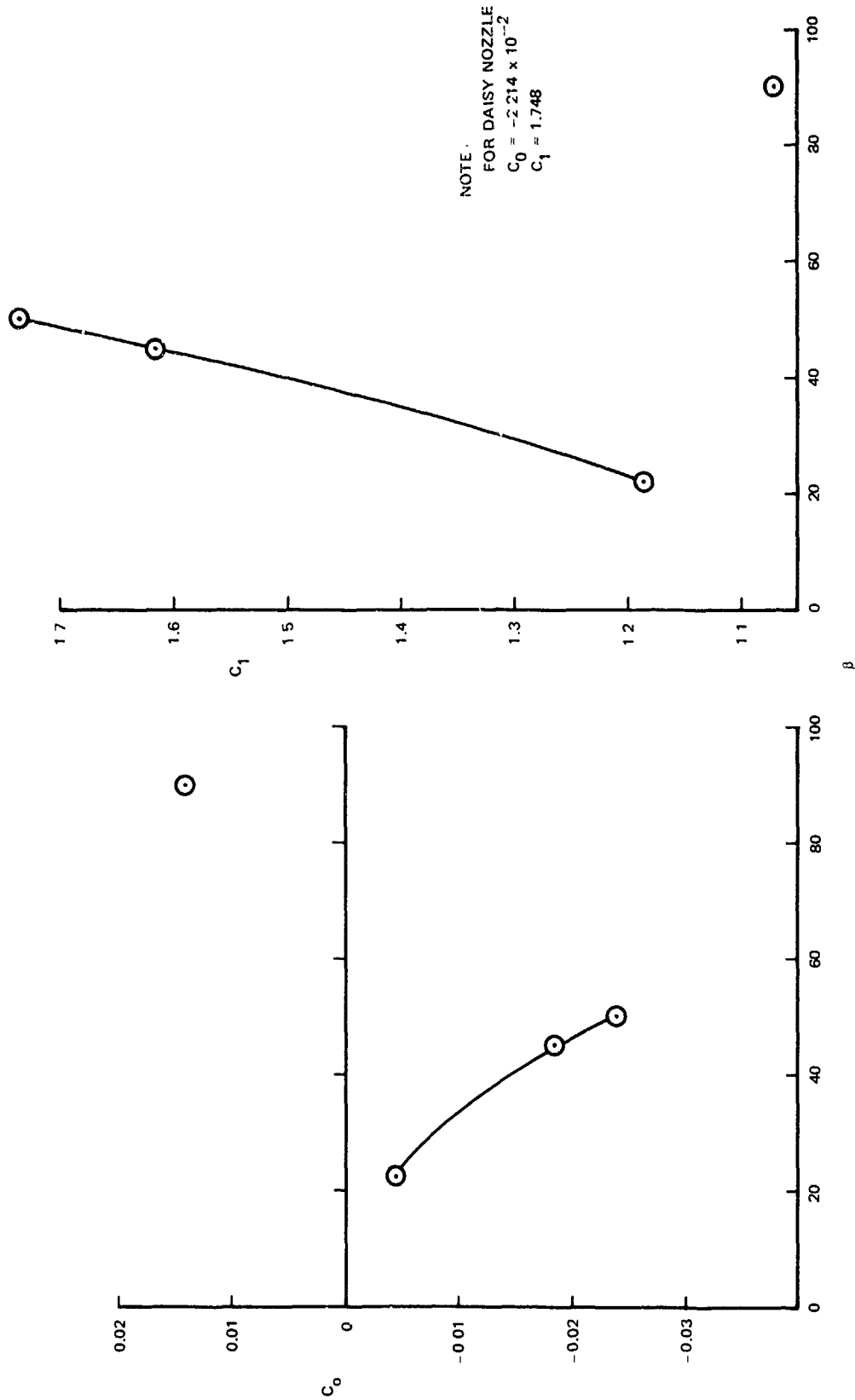


FIGURE 86. COEFFICIENTS FOR CHORDWISE DISTRIBUTION OF RMS LEVEL VERSUS PLATE INCLINATION ANGLE FOR FLAT PLATE

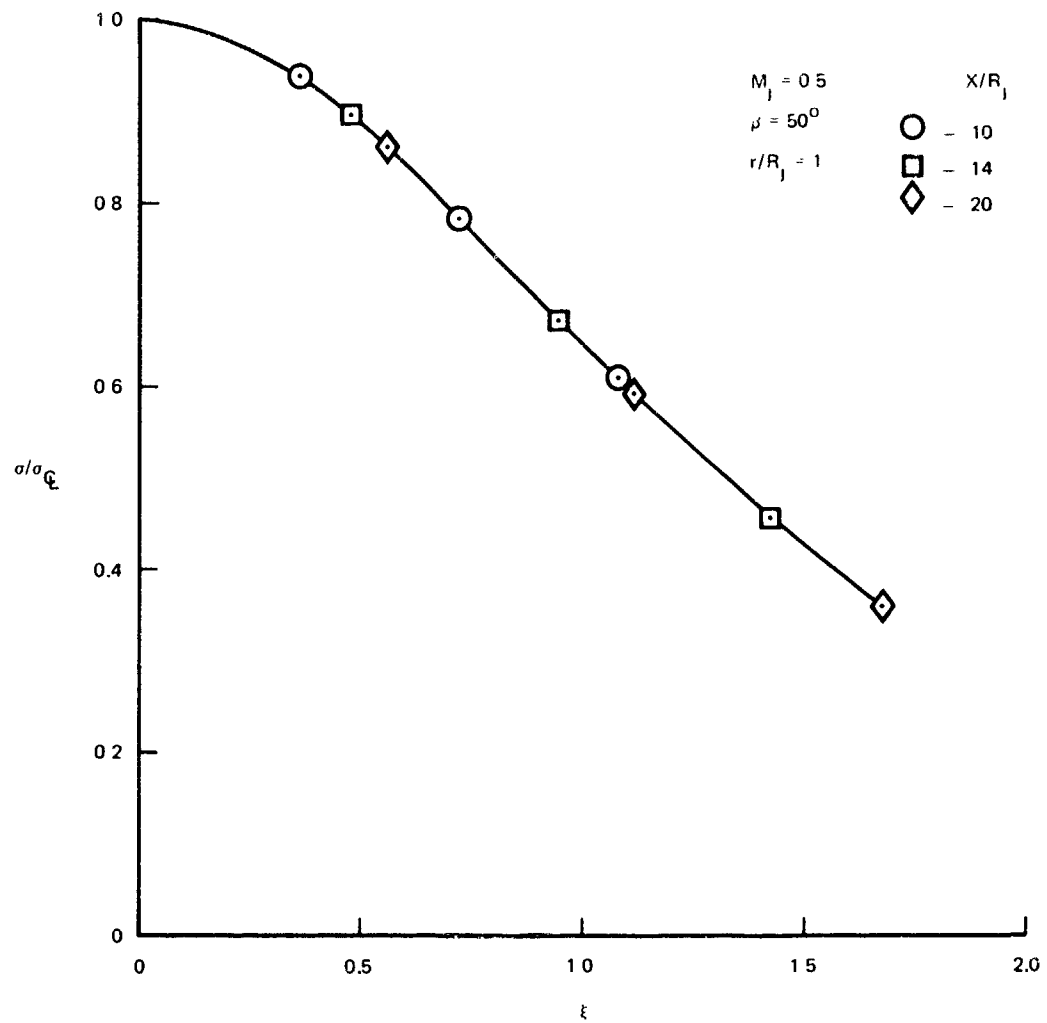


FIGURE 87. SPANWISE DISTRIBUTION OF RMS LEVEL ON INCLINED FLAT PLATE AT A SPECIFIED CHORDWISE LOCATION

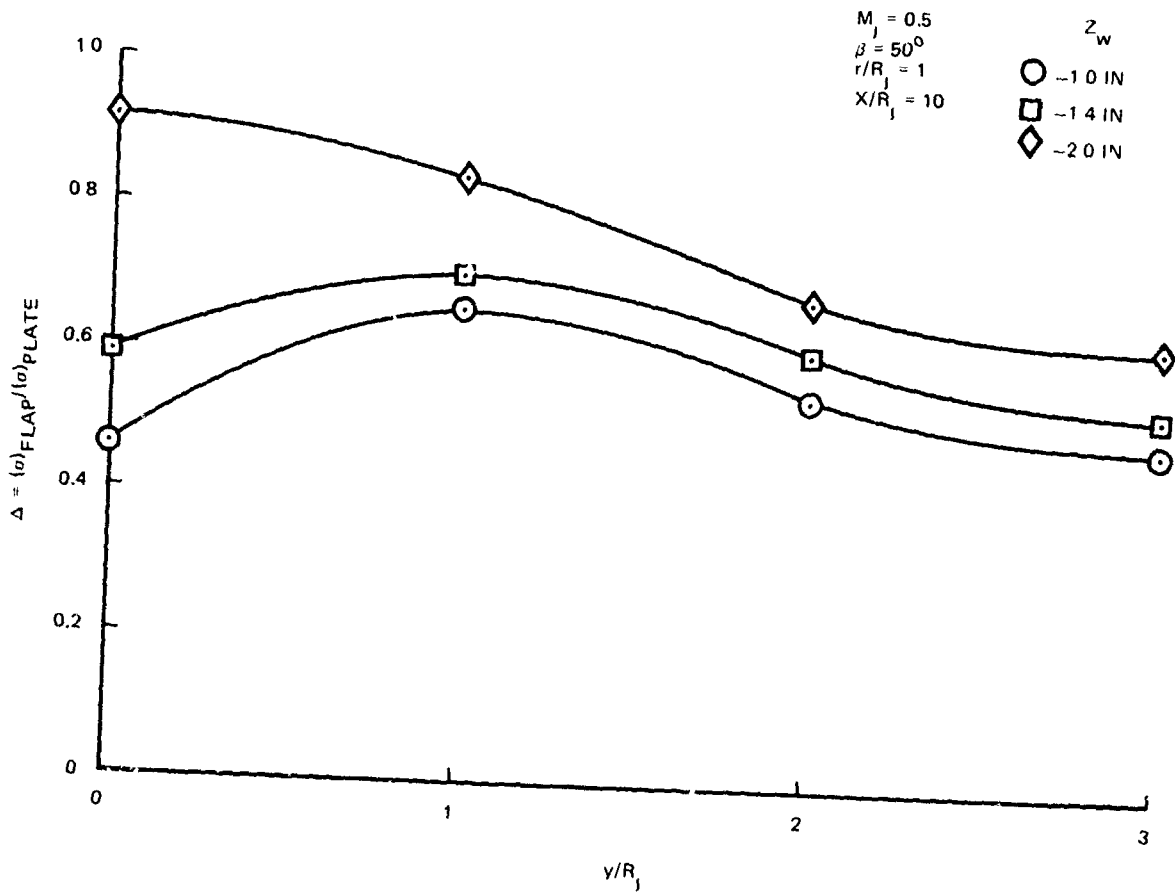


FIGURE 88. CORRECTION RELATIONSHIP FOR SPANWISE DISTRIBUTED RMS
 LEVELS BETWEEN FLAT PLATE AND AFT FLAP LOWER SURFACE AT
 $\beta = 50^\circ$

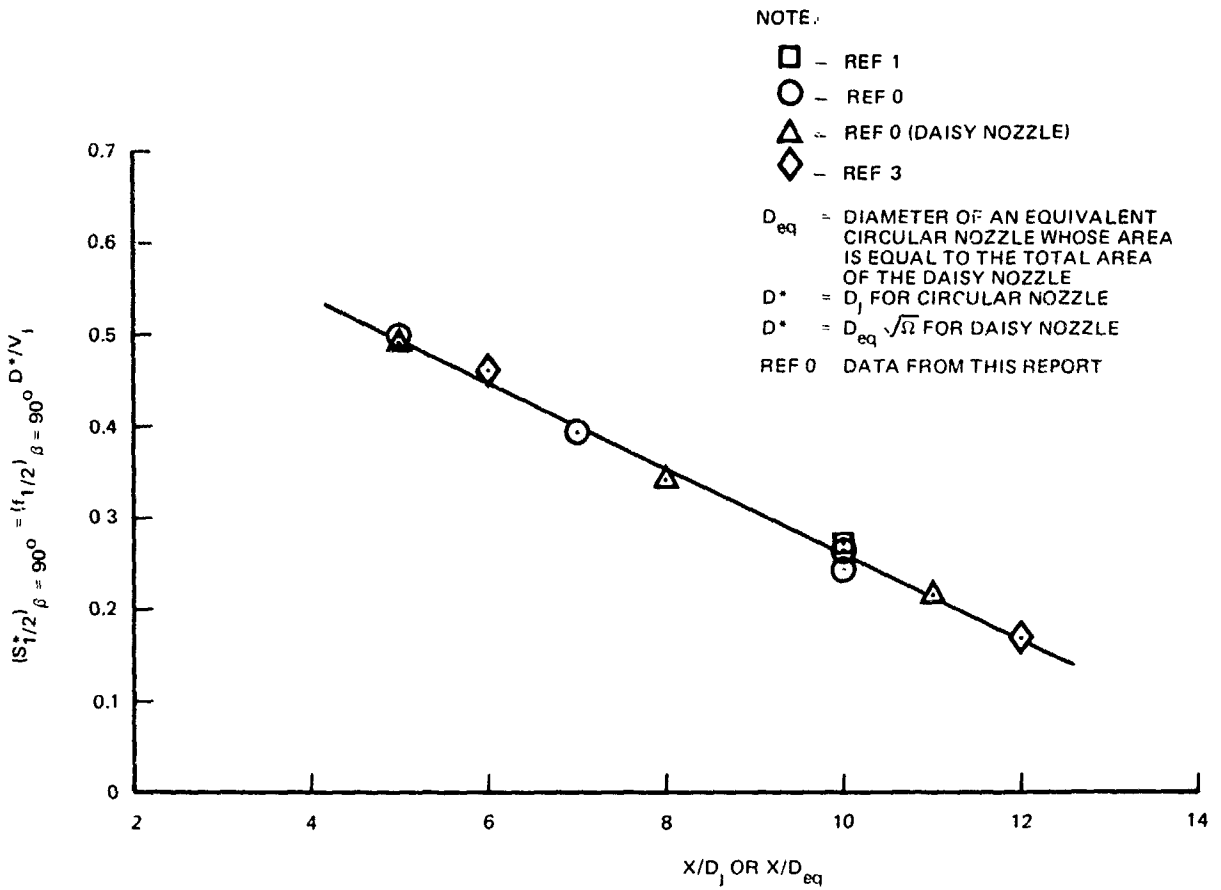


FIGURE 89. CORRECTED SPECTRUM STROUHAL NUMBER VERSUS IMPINGEMENT DISTANCE FOR NORMALLY IMPINGED FLAT PLATE AT STAGNATION POINT

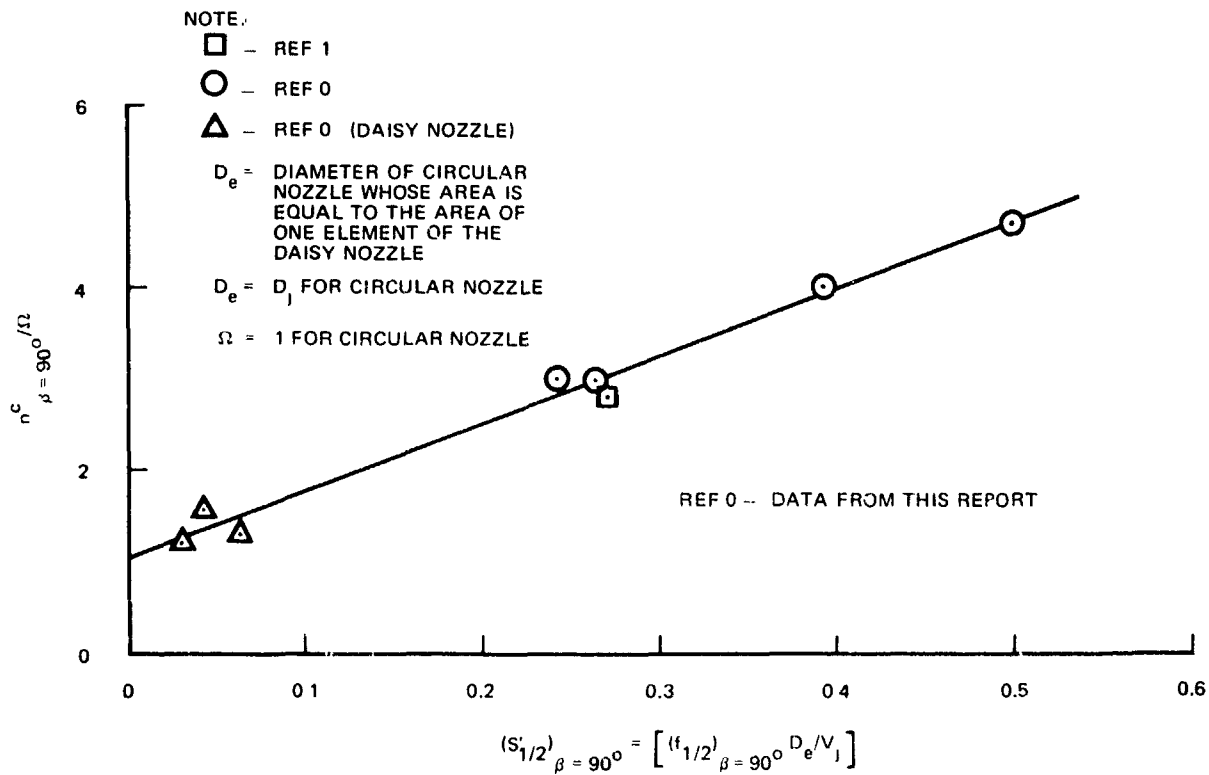


FIGURE 90. SPECTRUM ROLLOFF EXPONENT VERSUS STROUHAL NUMBER FOR NORMALLY IMPINGED FLAT PLATE AT STAGNATION POINT

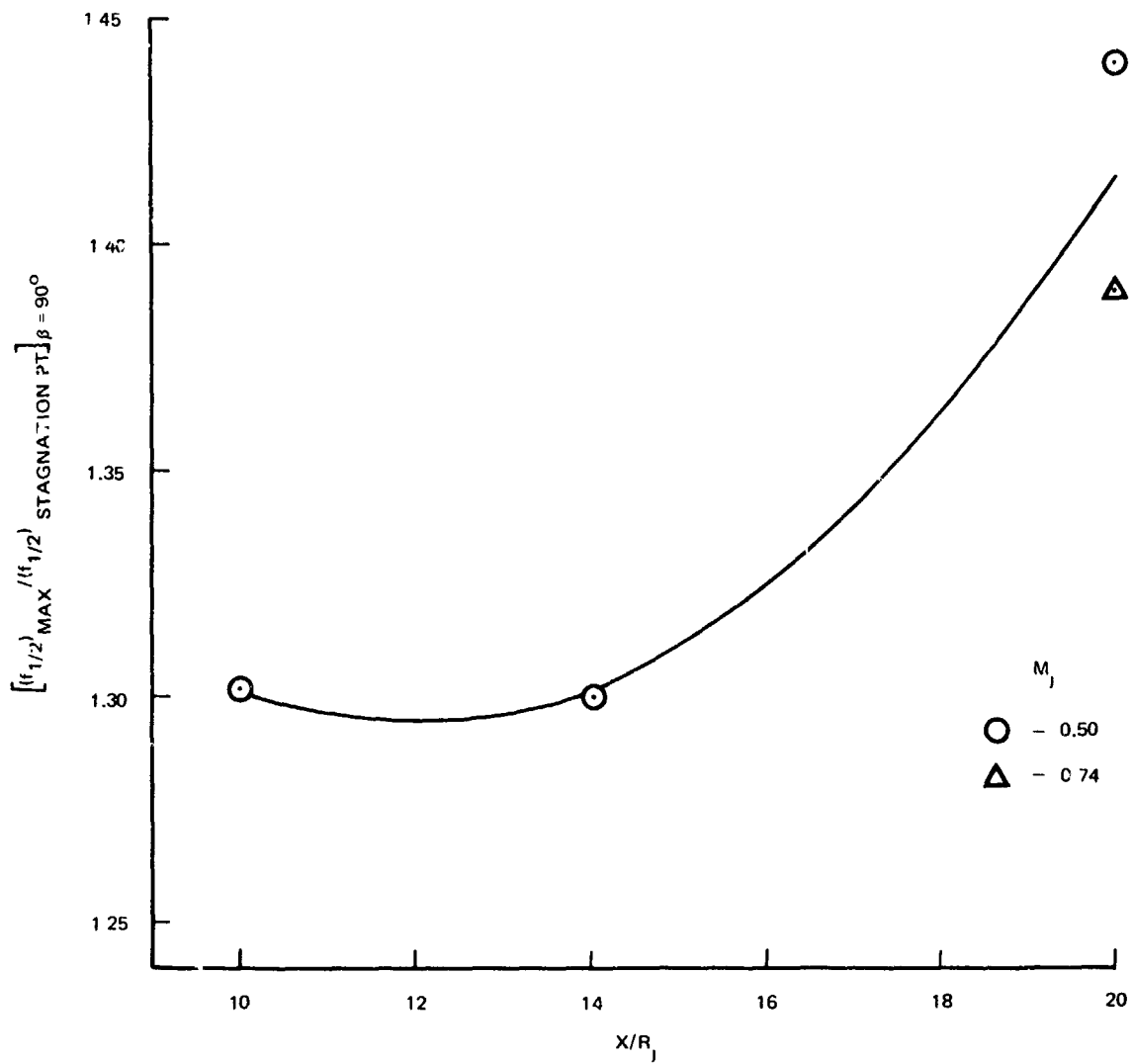


FIGURE 91. CHORDWISE MAXIMUM HALF-POWER FREQUENCY VERSUS IMPINGEMENT DISTANCE FOR NORMALLY IMPINGED FLAT PLATE

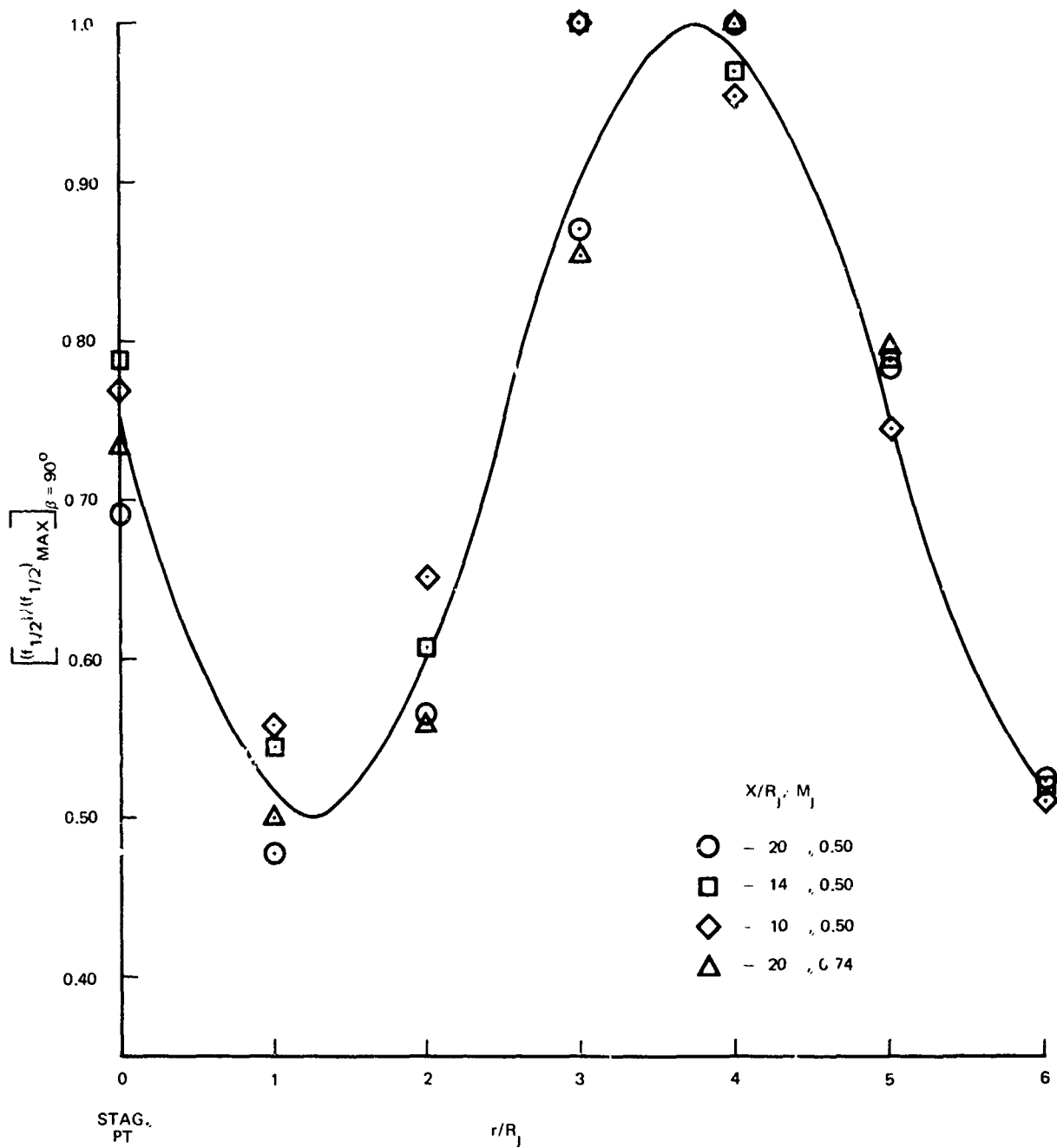


FIGURE 92. CHORDWISE DISTRIBUTION OF SPECTRUM HALF-POWER FREQUENCY ON NORMALLY IMPINGED FLAT PLATE

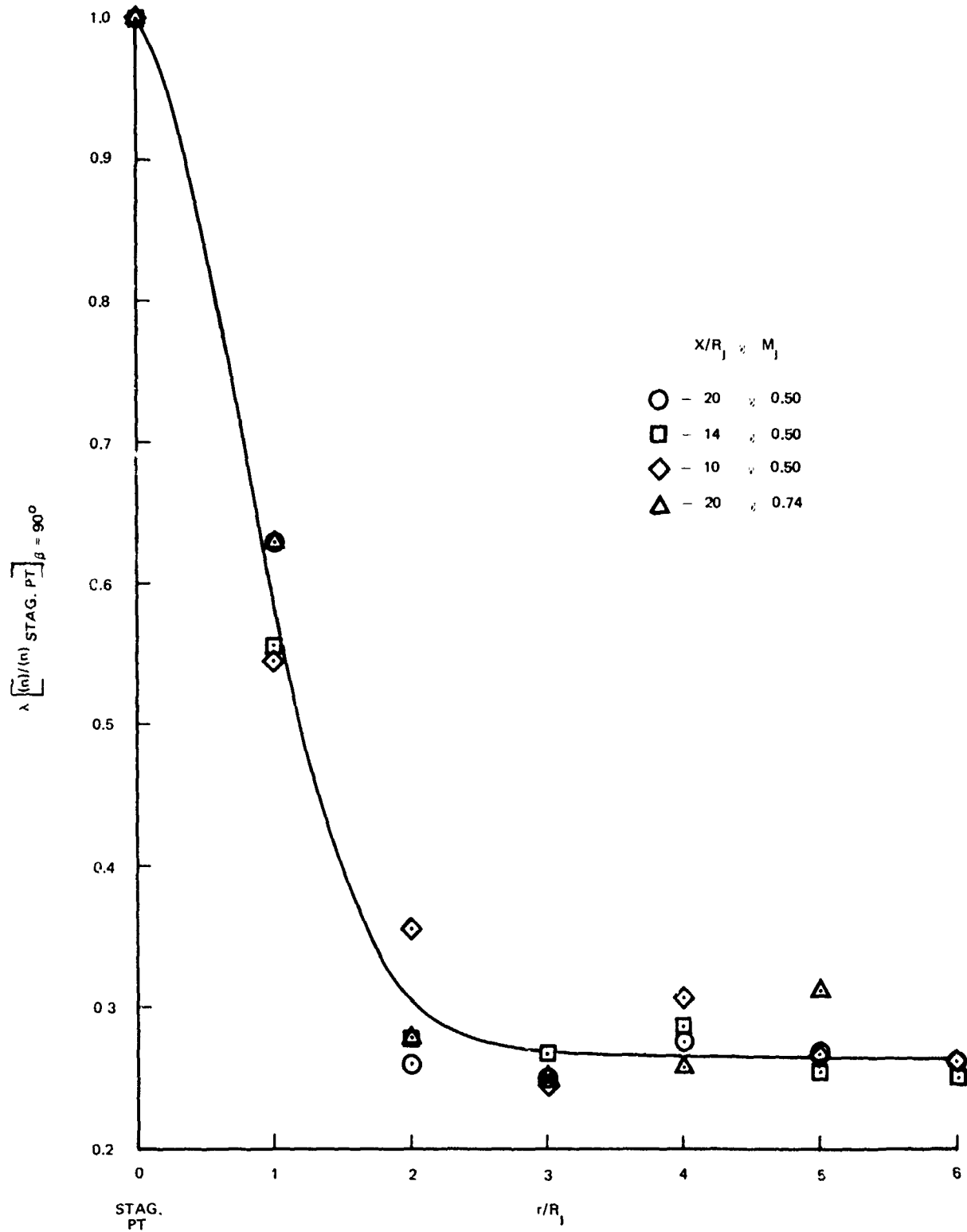


FIGURE 93. CHORDWISE DISTRIBUTION OF SPECTRUM ROLLOFF EXPONENT ON NORMALLY IMPINGED FLAT PLATE

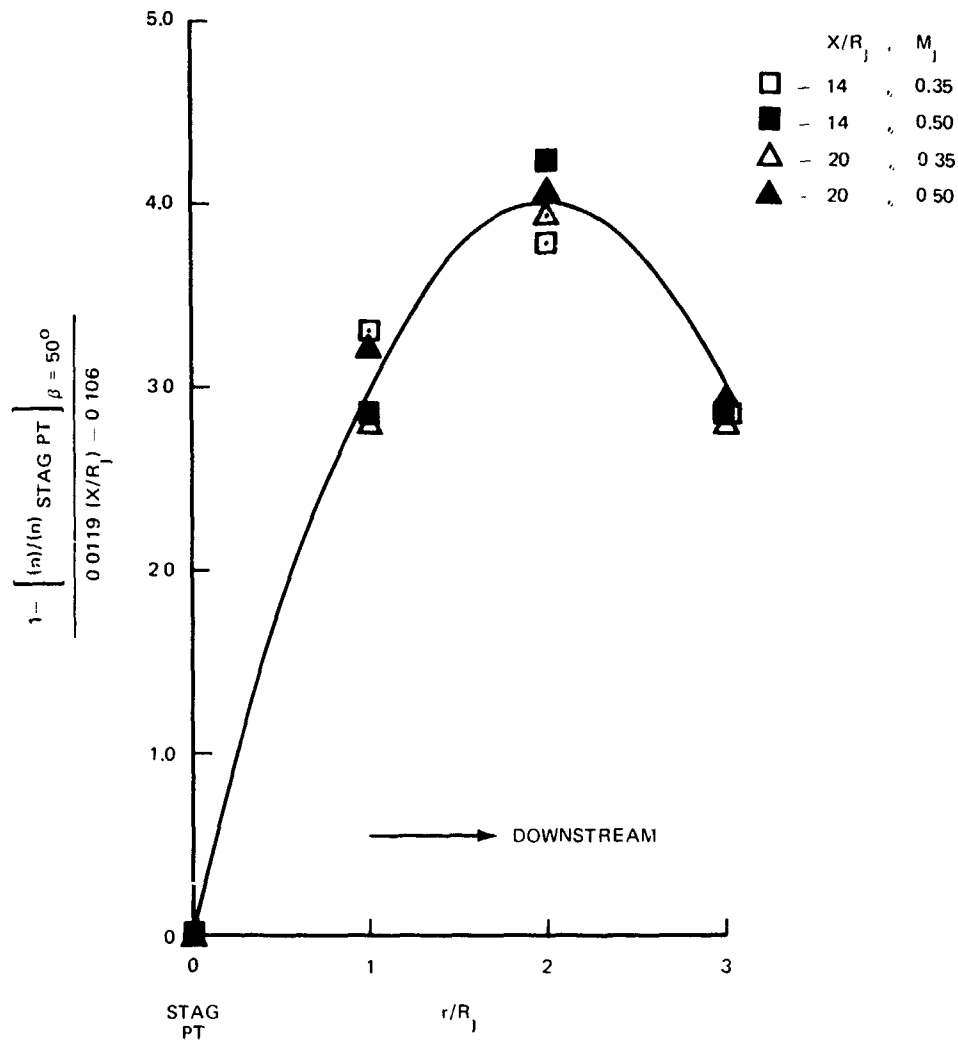


FIGURE 94. CHORDWISE DISTRIBUTION FOR SPECTRUM ROLLOFF EXPONENT ON INCLINED FLAT PLATE

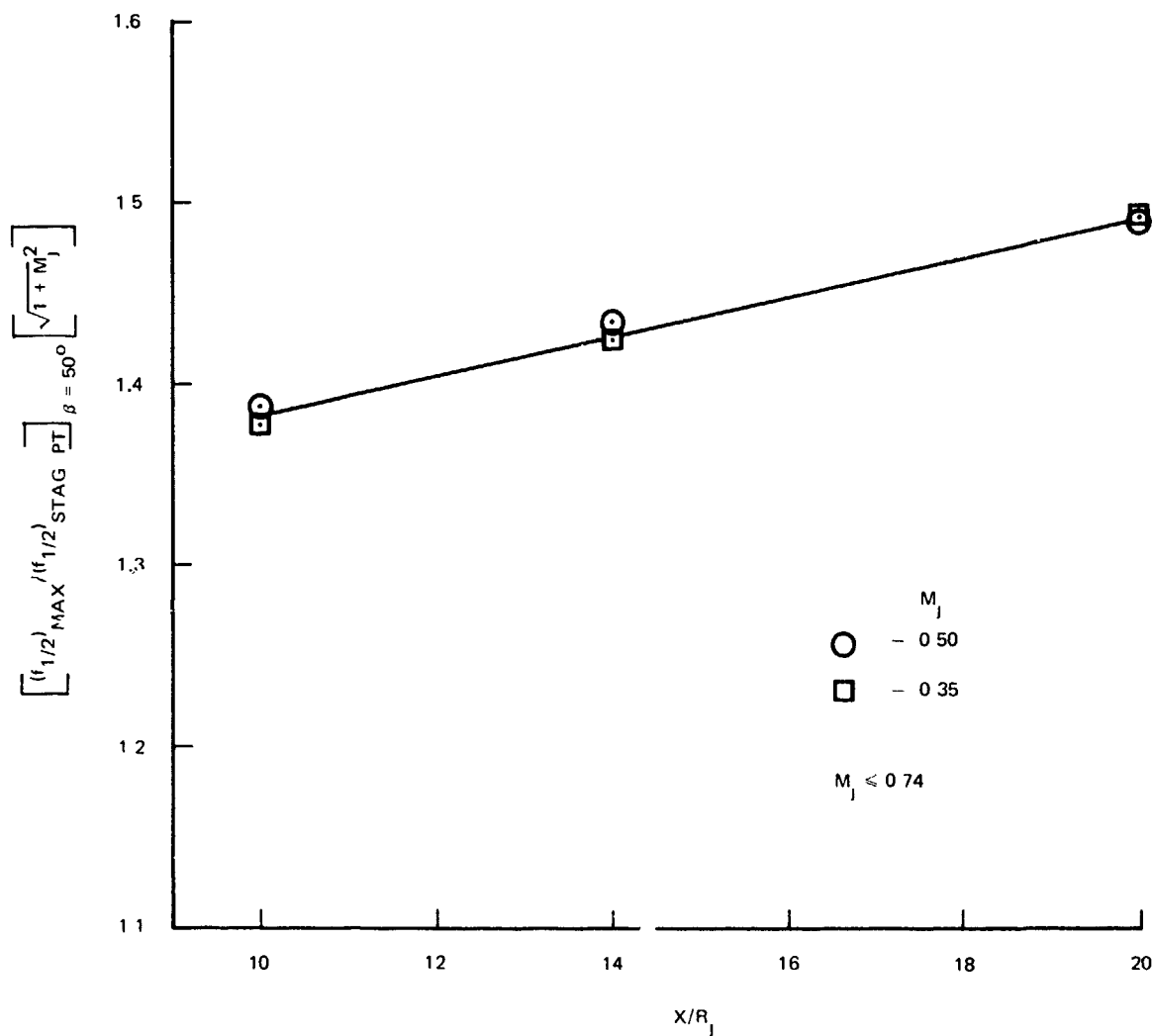


FIGURE 95. CHORDWISE MAXIMUM HALF-POWER FREQUENCY VERSUS IMPINGEMENT DISTANCE FOR INCLINED FLAT PLATE

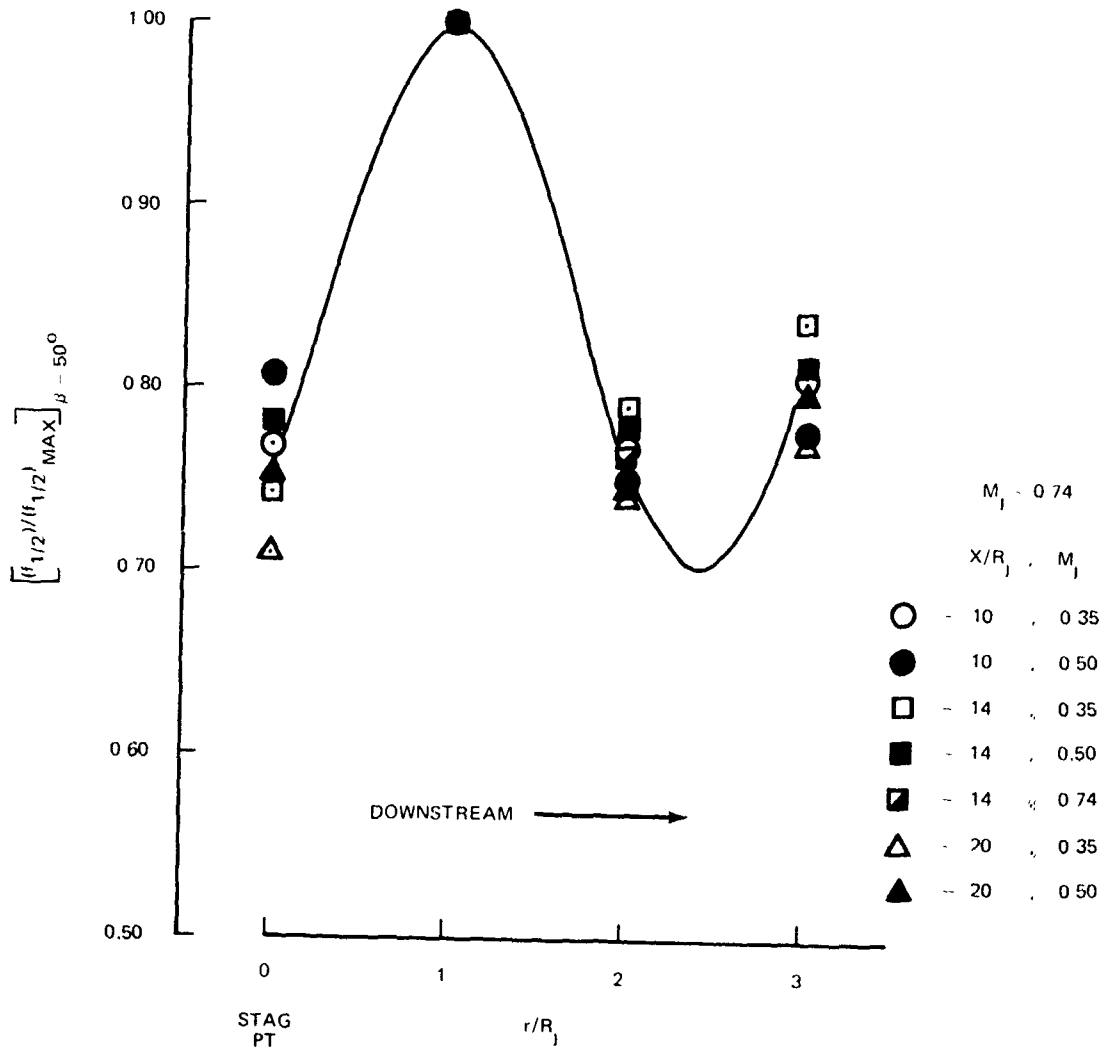


FIGURE 96. CHORDWISE DISTRIBUTION OF SPECTRUM HALF-POWER FREQUENCY ON AN INCLINED FLAT PLATE

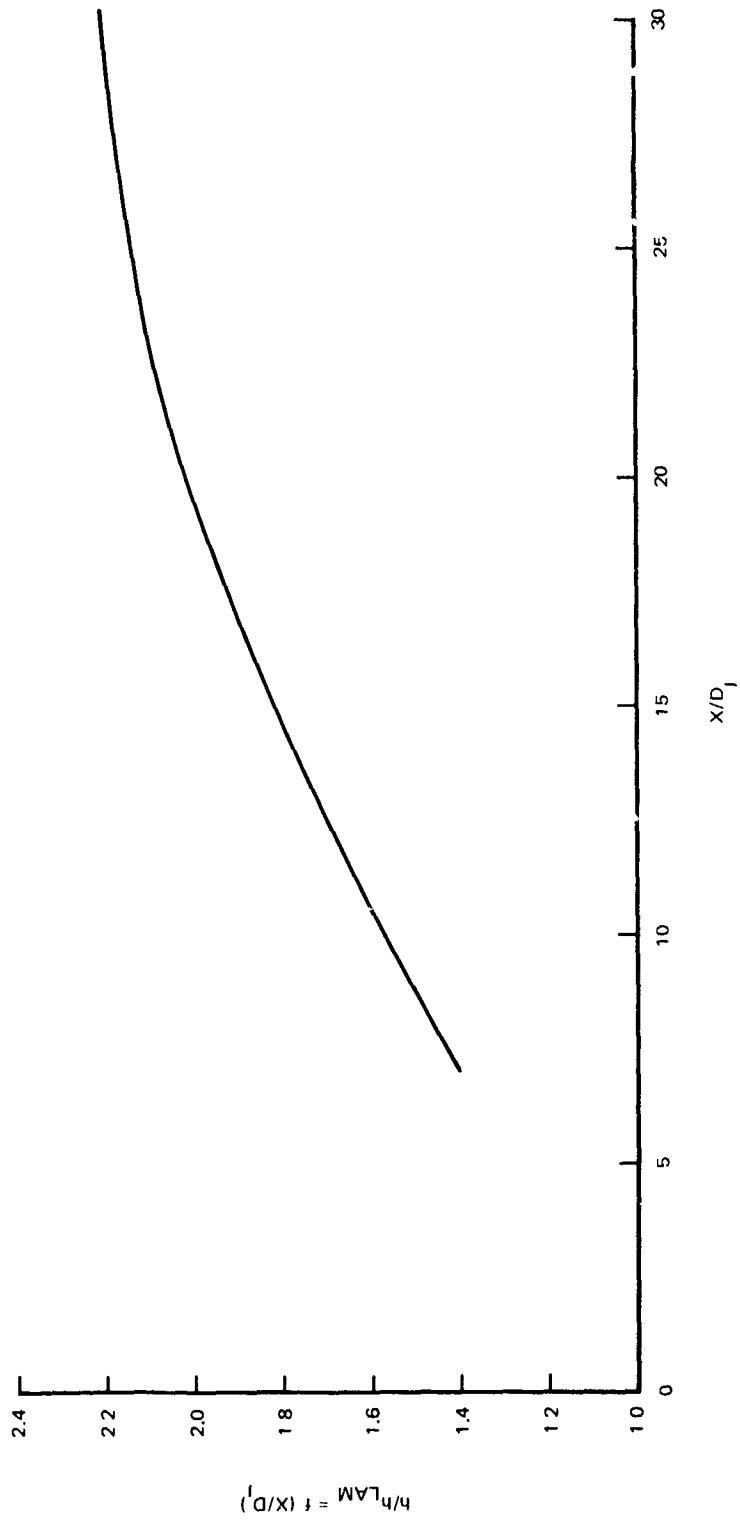


FIGURE 97. RATIO OF TURBULENT HEAT TRANSFER TO THAT PREDICTED BY LAMINAR THEORY AT THE STAGNATION POINT OF THE IMPINGING JET.

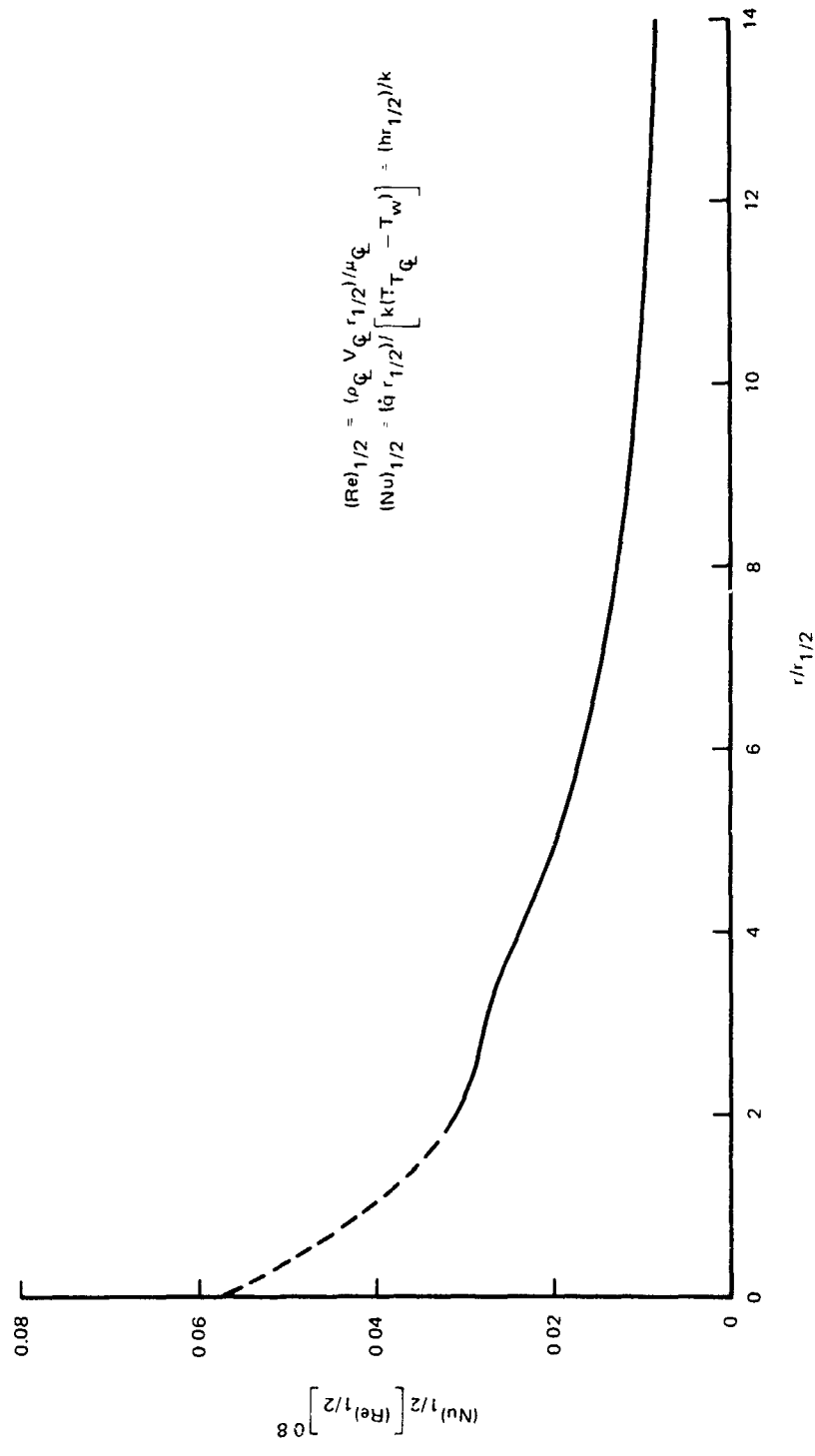


FIGURE 98. DISTRIBUTION OF TURBULENT HEAT TRANSFER COEFFICIENT FOR ALL REYNOLDS NUMBERS

SECTION VI

CONCLUSIONS

The previously discussed test program and results are intended to enhance understanding of the environment produced on externally blown flaps of STOL vehicles. In the test program, flat plates and specimens simulating under and over-the-wing blown flap configurations were exposed to jet flow. Although static pressures were obtained on all test specimens and temperatures measured on the flat plate, the major attention of the study was given to the characteristics of the fluctuating pressures produced on the surfaces. Involved in the considerations of the fluctuating pressures were (a) effects of parametric variations, (b) applicability of the results of the simplified models to the wing-flaps configuration and (c) normalizations which provide a basis for a prediction method.

1. PARAMETRIC VARIATIONS

Five categories of parameters were investigated in the test program: (a) jet Mach number, (b) total temperature of jet, (c) nozzle configuration, (d) relative position between nozzle and specimen and (e) deflection angle at downstream edge of specimen. The large coherent structures shed from the nozzle exit are modified in various degrees when changes in the test conditions are selected from these categories. The parametric variations do not significantly alter the shedding frequency of the coherent structures but do affect their development. The following conclusions derived from these variations are specifically relevant within the limits applied to the parameters in the test program.

a. Jet Mach Number Effects

The following fluctuating pressure characteristics are insensitive to variations in the jet Mach number M_j : (1) rolloff exponent n of the power spectrum, (2) Strouhal numbers $S_p = f_p D/V_j$ and $S_{1/2} = f_{1/2} D/V_j$ based on frequencies f_p and $f_{1/2}$ at the peak and half-power point locations of the power spectrum and (3) the maximum value, ρ_m , of the narrow

band correlation spectrum. The RMS level of the fluctuating pressure and the static pressure at any surface location can be scaled to M_j^2 or to the jet dynamic pressure q_j .

b. Jet Temperature Effects

Changing the temperature of the jet affects the entrainment and hence the spreading of the jet. Increases in the RMS levels, except at the stagnation point, result from the spreading. The primary effect of temperature variation was a noticeable reduction in the power spectrum rolloff exponent n . The effect of temperature on the maximum of the narrow band correlation spectrum, ρ_m , was not significant.

c. Nozzle Configuration Effects

The lobed nozzle enhances mixing in comparison to the round nozzle and, as a consequence, a more rapid decay in the jet velocity occurs downstream of the nozzle. This condition is reflected in considerably reduced RMS levels and static pressures on the exposed surfaces. In addition, the lobed nozzle Strouhal numbers $f_p D_{eq}/V_j$ and $f_{1/2} D_{eq}/V_j$ are greatly reduced with respect to the corresponding round nozzle values. The maximum values, ρ_m , of the correlation spectra are not significantly sensitive to the differences between the tested round and lobed nozzles. The rolloff exponent n of the power spectrum is relatively insensitive to the nozzle configuration except for flat plate cases where it becomes considerably larger for the lobed nozzle.

d. Effects of Relative Position Between Nozzle and Specimen

The RMS levels of the fluctuating pressure and the static pressure levels are significantly affected by position changes. The Strouhal number $S_{1/2} = f_{1/2} D_j/V_j$ tends to decrease when the separation in positions between nozzle and specimen is increased. The rolloff exponent n of the power spectrum is not appreciably affected by position changes. The maximum value, ρ_m , of the narrow band correlation spectrum has the same tendency as the Strouhal number $S_{1/2}$.

e. Effects of Trailing Edge Deflection Angle

This category is concerned with the curved plate and wing-flaps configurations. The considerations in this category must take into account the curvature of the specimen in attaining the trailing edge deflection. For the OBF curved plate, an increase in trailing edge deflection was produced by adding an extension which maintained the curvature of the trailing portion of the plate. The static pressures on the original portion of the plate are insignificantly affected by the deflection angle while the fluctuation pressure characteristics are only moderately changed.

In the case of the UBF curved plate, an increase in trailing edge deflection was accompanied by an increase in the curvature of the bend. This produced significant changes in the static pressures and fluctuating pressure characteristics except for the rolloff exponent n . Similar results occurred for the wing-flaps model.

2. RELATIONS BETWEEN SPECIMENS

In order to compare results found on the flat plate, UBF curved plates and wing-flaps model, a correspondence between locations on the different models must be established. A useful origin of reference on the flat plate or on a flap is the stagnation point. For the purpose of comparison, the reference origin for the UBF curved plates is the location of maximum RMS pressure. Distances from the origin for each specimen are scaled to the nozzle diameter. Only locations downstream of the origin are candidate for comparison since the stagnation point on a flap will be close to the leading edge.

A correspondence is also required between the different specimens with respect to their configuration variables. The limited number of values used for these variables in the test program provides a relatively inflexible basis for making comparisons. The results for a flap with a deflection angle of 50° , for instance, are compared to those of a flat plate with $\beta = 50^\circ$ and a UBF curved plate with $\beta_{TE} = 50^\circ$. Considering comparisons of configurations having a common type of nozzle, other

correspondences are: vertical clearance distance Z_w/D for wing-flaps model set equal to Z_{LE}/D for the UBF curved plate and longitudinal impingement distance X_F/D for the flaps set equal to (or nearly equal to) X_S/D for the UBF curved plate and X_I/D for the flat plate.

a. Static Pressures - Flat Plate and UBF Configurations

The peak magnitudes of the static pressures show only a small difference between comparable flat plate and UBF curved plate cases (irrespective of Z_{LE}/D). The static pressure at the stagnation point of the aft flap is considerably larger but diminishes to approximately the same level of the peaks of the other specimens as the center of the chord is approached. For the round nozzle, the dropoff of the static pressures in the spanwise direction is rapid for all specimens; at one diameter from the center of impingement the level is only 5 to 20 percent of the center-line value. The spanwise static pressure distribution for the daisy nozzle exhibits a significantly slower rate of decay.

b. Fluctuating Pressures - Flat Plate and UBF Configurations

The relation of maximum RMS pressures between flat and UBF curved plate cases depends on the value of Z_{LE}/D for the latter. The smallest difference occurs when $Z_{LE}/D = 1.0$. The fluctuating pressure pickups on the aft flaps are approximately $1/2 D$ downstream from the stagnation point. Comparing corresponding locations on the specimens, the maximum RMS levels on the flaps are in reasonably close agreement to those of the UBF curved plate. In the spanwise direction, the maximum RMS levels generally occur no more than $1/2 D$ from the center of impingement.

The maximum values of the Strouhal numbers $S_p = f_p D/V_j$ for the peaks of the power spectra typically tend to occur no more than $1 D$ spanwise from the center of impingement for the different specimens. For comparable configurations, the maximum values have relatively small differences and, for round nozzles, a value of 0.3 appears to be representative.

The peak amplifications, P , of the power spectra are close to unity or small near the reference origin for all specimens. The values of P increase with spanwise location attaining a maximum value beyond $1/2 D$ from the center of impingement. The rolloff exponents n are almost constant in magnitude for the different specimens with a representative value of 2 for round nozzles.

Strouhal numbers $S_m = f_m D / V_j$ for the maxima of the narrow band correlation spectra tend, for round nozzles, to be near 0.3 at locations on the specimens sufficiently removed from a stagnation point but no more than $1/2 D$ from the center of impingement in the spanwise direction. The values of S_m decrease beyond $1/2 D$. The maxima, L_m , of the narrow band correlation length spectra are typically less than $1 D$ in the spanwise direction for locations on the specimens near the center of impingement. The values of L_m generally increase with spanwise distance from the center of impingement. For the different specimens, the local narrow band convection speed $V_c(f)$ is typically an increasing function with frequency. The convection speed for the specimens at a Strouhal number of 0.3 is near $0.6 V_j$.

c. Wing-Flaps Upper Surface Characteristics

The following is a description of the fluctuating pressure characteristics on the upper surface of the flaps in relation to those on the lower surface. The RMS levels on the upper surfaces are of the same order of magnitude as those on the lower surfaces for nozzle positions in which the vertical clearance, Z_w/D , of the jet centerline from the UBF wing is under 0.7. With increasing Z_w/D , the upper surface RMS levels tend to fall significantly below the lower surface values. The bandwidths of the power spectra on the upper surfaces of the flaps, as measured by the half-power frequency $f_{1/2}$ or Strouhal number $S_{1/2} = f_{1/2} D / V_j$, are comparable to those on the lower surfaces at corresponding spanwise locations. The upper surface power spectra exhibit small peak amplifications, P , and a slower growth of peakedness with increasing spanwise location. The rolloff exponents, n , on the upper surfaces tend to be closer to unity than to the value of 2 on the lower surfaces. Although

the differences are not excessive, the maxima, L_m , of the narrow band correlation length spectra are typically smaller on the upper surfaces in the spanwise direction and between flaps.

d. OBF Characteristics

The ratio of the peak RMS level to the dynamic pressure, q_j , has an uppermost value for the round nozzle of about 0.13 for the UBF configurations and flat plate cases. The corresponding value for the daisy nozzle is 0.04. The maximum value found in the OBF cases (with lip extension) for the ratio of RMS level to q_j is about 0.085. The maximum RMS values in the OBF cases tend to occur on chordlines located near the lateral edges of the nozzle exit.

The Strouhal numbers $S_p = f_p D_{eq} / V_j$, where D_{eq} is the diameter of a round nozzle with the same exit area as the OBF nozzle, are comparable in magnitude to those obtained for the other specimens with the round nozzle. The values of S_p tend to be uniform over the highly curved, trailing portion of the plate to spanwise locations at least $1 \frac{1}{2} D_{eq}$ from the center of the jet. A representative value of S_p in this region is 0.3. S_p is greater than 0.3 in the leading portion of the plate.

The rolloff exponents n tend to be between 3 and 4 near the exit, but are close to a value of 2 in the trailing portion of the plate. The value of n tends to be fairly constant in the spanwise direction to at least $1 \frac{1}{2} D_{eq}$ from the center of the jet. The peak amplifications, P , of the power spectra in the leading portion of the plate are more pronounced than any found for the other specimens. These amplifications drop rapidly toward unity for positions approaching the trailing edge. The peakedness tends to remain at about the same magnitude for spanwise locations at least $1 \frac{1}{2} D_{eq}$ from the center of the jet.

The Strouhal numbers $S_m = f_m D_{eq} / V_j$ for the maxima of the narrow band correlation spectra are typically greater than 0.3 except near the trailing edge. The values of S_m diminish away from the centerline in the spanwise direction. The maxima, L_m , of the narrow band correlation length

spectra tend to be of the order of $1/D_{eq}$ in the spanwise direction. The values of L_m decrease away from the center of the jet. In the chordwise direction, the values of L_m are the largest of all the tested specimens.

3. METHODOLOGY

The study indicates that simple specimens provide data that can be adapted to UBF wing-flaps configurations through appropriate adjustments. The extent of the adjustment is a basis for deciding on the usefulness of the simple specimens. Comparing the flat and UBF curved plates, the results from the flat plate generally appear to be closer to the trends found for the wing-flaps model. A clear indication that the flat plate is suitable was shown in the study by demonstrating a relationship between the spanwise distribution of RMS levels in the impingement region on the flat plate and the spanwise distribution on the lower surface of a flap. The flat plate is also a preferable model because the impinging jet forms a stagnation point on its surface, permitting a common origin of reference between the flap and flat plate.

The concept behind the prediction methodology was to find appropriate quantities for non-dimensionalization of a fluctuating pressure characteristic which would minimize the data scatter about the mean trend. Candidates were only those quantities whose magnitudes were known from measurement or could be obtained from analysis. The scope of the study limited the selection to steady quantities in the free jet.

After selecting a quantity, it was also necessary to establish the location of the quantity in the free jet. The free jet quantity which best non-dimensionalized the stagnation point RMS level was $q_{1/2}$, the dynamic pressure at the half-velocity point. In the case of normal impingement on a plate at a distance X from the nozzle exit, $q_{1/2}$ was taken at the same distance X in the free jet. For the stagnation point half-power frequency, $f_{1/2}$, the best quantities to use were at the nozzle exit; namely, the velocity of the jet V_j and the nozzle diameter D .

For oblique impingement, a well-defined transformation procedure was developed for locating the appropriate $q_{1/2}$. Since the RMS level at the stagnation point is lower on the inclined plate ($\beta < 90^\circ$), the $q_{1/2}$ for non-dimensionalization must come from a location $X' > X$. The location X' was found to be where the dynamic pressure, $q_{1/2}(X') = q_{1/2}(X) \cdot \sin^2 \beta$. The oblique case is by this means transformed to a normally impinged case with the plate at an apparent location X' .

Transformations as involved as that described above are not always necessary. In the case of oblique impingement, the Strouhal numbers $S_{1/2} = f_{1/2} D / V_j$ and rolloff exponents n at the stagnation point are obtained from the normal impingement results by simply multiplying by $\sqrt{\sin \beta}$. The use of transformations, however, broaden the foundation of the methodology. This need for transformations is best seen when comparing results from such diverse nozzle configurations as those exemplified by the round and lobed nozzles. The RMS levels from the lobed nozzle are far below those from the round nozzle. The quantity used for nondimensionalization, $q_{1/2}$, must be taken at considerably different locations in the free jet for the two nozzles. The transformation required to find the corresponding locations was defined in the study.

APPENDIX A
DETAIL TEST CASES

1. FLAT PLATE - ROUND NOZZLE ($D_j = 1''$) - COLD JET

TEST CASE	T_j/T_a	M_j	X_I/D_j	β (DEG)
A	1.0	.50	10	25
B	1.0	.50	10	50
C	1.0	.50	10	90
D	1.0	.50	5.27	25
E	1.0	.50	5	50
F	1.0	.50	5	90
G	1.0	.50	7	25
H	1.0	.50	7	50
I	1.0	.50	7	90
J	1.0	.35	10	50
K	1.0	.35	5	50
L	1.0	.35	7	50
M	1.0	.74	7	50
N	1.0	.74	5.27	25
\emptyset	1.0	.74	10	90

2. FLAT PLATE - ROUND NOZZLE ($D_j = 1''$) - HOT JET

TEST CASE	T_j/T_a	M_j	X_I/D_j	β (DEG)
A	1.7	.46	10	50
B	1.7	.46	7	50
C	1.7	.46	5	50

DETAIL TEST CASES CONT'D

3. FLAT PLATE EDGE - ROUND NOZZLE ($D_j = 2''$)

TEST CASE	T_j/T_a	M_j	X_I/D_j	β (DEG)
A	1.0	.50	5	50
B	1.0	.50	7	50
C	1.7	.50	5	50
D	1.0	.50	10	50

4. FLAT PLATE - DAISY NOZZLE ($D_{eq} = 2''$)

TEST CASE	T_j/T_a	M_j	X_I/D_{eq}	β (DEG)
A	1.0	.50	5	50
B	1.0	.50	8	50
C	1.0	.50	11	50
D	1.0	.50	5	25
E	1.0	.50	8	25
F	1.0	.50	11	25
G	1.0	.50	5	90
H	1.0	.50	8	90
I	1.0	.50	11	90

5. UBF CURVED PLATE - $\beta_{TE} = 50^\circ$ - DAISY NOZZLE ($D_{eq} = 2''$)

TEST CASE	T_j/T_a	M_j	Z_{LE}/D_{eq}	X_{LE}/D_{eq}
A	1.0	.5	1.0	0
B	1.7	.5	1.0	0
C	1.0	.5	1.0	1.5

DETAIL TEST CASES CONT'D

5. CONT'D. UBF CURVED PLATE - $\beta_{TE} = 50^\circ$ -
 ROUND NOZZLE ($D_j = 2''$)

TEST CASE	T_j/T_a	M_j	Z_{LE}/D_j	X_{LE}/D_j
D	1.0	.50	.7	0
E	1.0	.50	1.0	0
F	1.7	.50	.7	0
G	1.0	.50	.7	1.5
H	1.0	.74	.7	0
I	1.0	.35	.7	0
J	1.7	.35	.7	1.5

6. UBF CURVED PLATE - $\beta_{TE} = 25^\circ$ - ROUND NOZZLE ($D_j = 2''$)

TEST CASE	T_j/T_a	M_j	Z_{LE}/D_j	X_{LE}/D_j
A	1.0	.5	.7	0
B	1.0	.5	1.0	0
C	1.0	.74	.7	0
D	1.0	.35	.7	0

7. WING-FLAPS MODEL - $\beta_f/\beta_a = 5^\circ/25^\circ$ -
 ROUND NOZZLE ($D_j = 2''$)

TEST CASE	T_j/T_a	M_j	Z_w/D_j	X_{LE}/D_j
A	1.0	.50	.7	0
B	1.0	.50	1.0	0

DETAIL TEST CASES CONT'D

8. WING-FLAPS MODEL - $\beta_f/\beta_a = 30^\circ/50^\circ$ -
 ROUND NOZZLE ($D_j = 2''$)

TEST CASE	T_j/T_a	M_j	Z_w/D_j	X_{LE}/D_j
A	1.0	.5	.7	0
B	1.0	.5	1.0	0
C	1.0	.5	.7	1.5
D	1.0	.5	.5	0
E	1.0	.74	.7	0

8. CONT'D. WING-FLAPS MODEL - $\beta_f/\beta_a = 30^\circ/50^\circ$ -
 DAISY NOZZLE ($D_{eq} = 2''$)

TEST CASE	T_j/T_a	M_j	Z_w/D_{eq}	X_{LE}/D_{eq}
F	1.0	.50	1.0	0
G	1.0	.74	1.0	0

9. OBF CURVED PLATE -
 $\beta_{TE} = 70^\circ$ -
 WITH LIP EXTENSION

TEST CASE	T_j/T_a	M_j
A	1.0	.50
B	1.87	.50
C	1.0	.74

10. OBF CURVED PLATE -
 $\beta_{TE} = 70^\circ$ -
 NO LIP EXTENSION

TEST CASE	T_j/T_a	M_j
A	1.0	.5

DETAIL TEST CASES CONT'D

11. OBF CURVED PLATE -
 $\beta_{TE} = 40^\circ$ -
 WITH LIP EXTENSION

12. OBF CURVED PLATE -
 $\beta_{TE} = 40^\circ$ -
 NO LIP EXTENSION

TEST CASE	T_j/T_a	M_j	TEST CASE	T_j/T_a	M_j
A	1.0	.5	A	1.0	.5
B	1.87	.5			
C	1.0	.74			
D	1.0	.35			

13. FLAT PLATE - DAISY NOZZLE ($D_{eq} = 2''$) - HOT JET

TEST CASE	T_j/T_a	M_j	X_I/D_{eq}	β (DEG)
A	1.7	0.5	5	50

13. CONT'D. FLAT PLATE - ROUND NOZZLE ($D_j = 2''$)
 HOT JET

TEST CASE	T_j/T_a	M_j	X_I/D_j	β (DEG)
B	1.7	0.5	10	50
C	1.7	0.5	5	25
D	1.7	0.5	5	50
E	1.7	0.5	5	90
F	1.7	0.5	7	50
G	1.7	0.74	5	50

APPENDIX B
LABORATORY DESCRIPTION

The floor plan of the Jet Noise Laboratory at the University of Southern California (USC) is shown in Figure B-1.

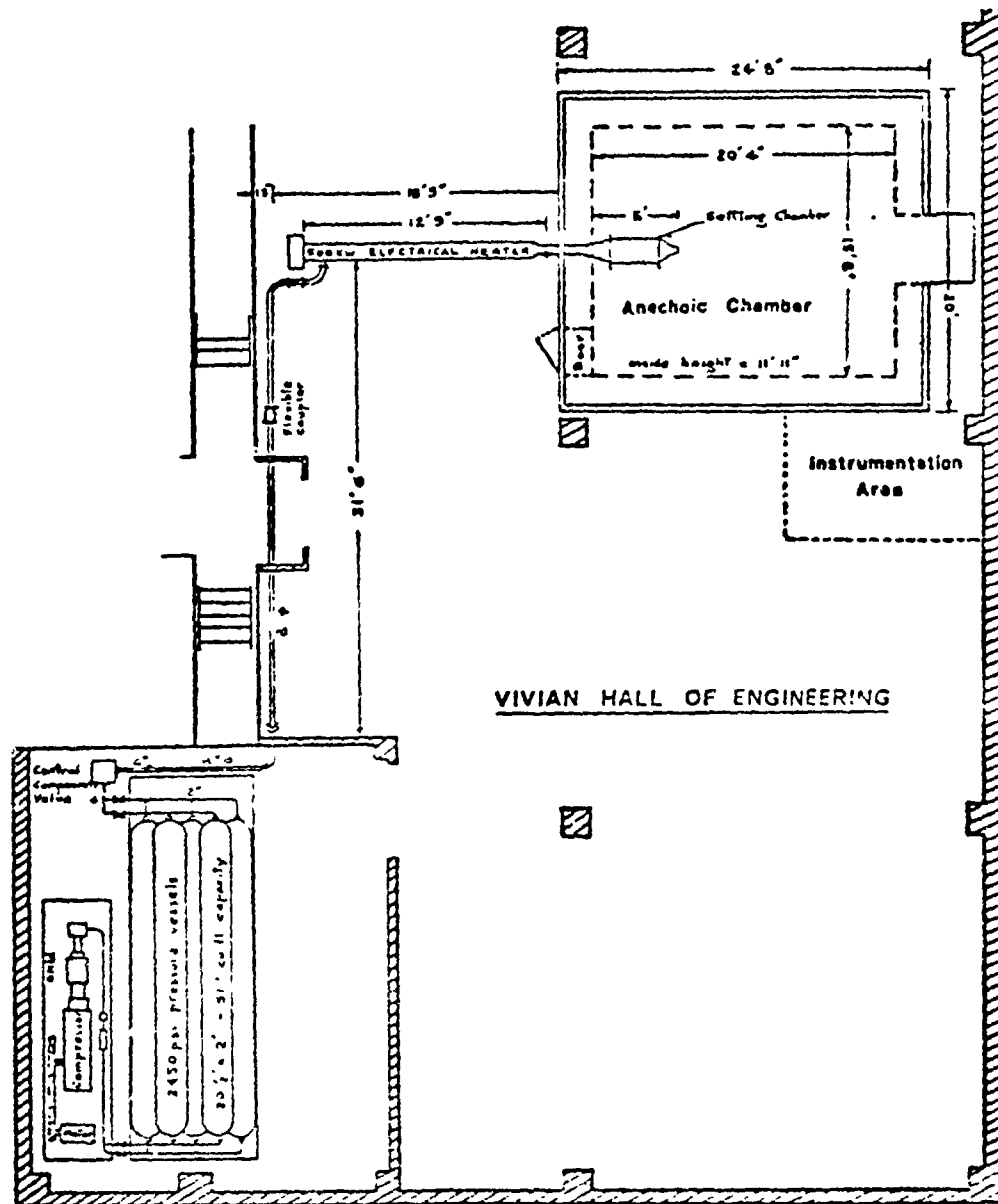


Figure B-1. Jet Noise Facilities at USC

The laboratory includes an air supply system, an anechoic chamber and an instrumentation area. The air supply system provides the prescribed flow conditions. The anechoic chamber serves to maintain a testing environment free from extraneous external effects. The instrumentation area contains recording, playback and data processing capability.

1. AIR SUPPLY SYSTEM

The air supply system, Figure B-1, consists of a 75 HP, 2500 psi, 142 SCFM, 3-stage Chicago pneumatic air compressor which supplies air to five 51.1 cu. ft. storage vessels. The compressor pumps the air through a desiccant to provide dry air with a dewpoint of -48°F . The pressure vessels may be connected as a group of two, three or five.

2. VALVE AND CONTROLLER

The air flow from the pressure vessels is controlled by a low-noise, self-drag valve built by Control Components, Inc. of Irvine, California. The valve is capable of passing 6.8 lb./sec. and is designed for operating pressure ratios of 10 to 30. The valve is opened by a Moore 3-15 psi positioner which receives a pneumatic pressure signal from a Honeywell Batch-0-Line controller, Model RY704P1-(93), operated manually. Regulation is normally better than $\pm 3\%$ in gauge pressure.

3. HEATER

The air may be heated prior to entering the settling chamber by a 500 KW Hynes Radi-Fin electric heater. This heater operates from 480 volt, 3-phase electric power and is controlled by a 500 KVA SCR phase-angle power-control package made by Crydom Controls. The heater rests in a casing of Type 304 stainless steel and is 12-3/4" OD by 15 ft. long. It is capable of heating flows from 0.1 lb/sec. at 10 psig to 117 lb/sec. at 250 psig and can regulate temperature from 70° to 900°F .

The heater is anchored at its downstream end where it joins to the settling chamber. The other end is mounted on wheels to allow for thermal expansion. In the 40 feet of 8-inch pipe connecting the valve and the heater, a flexible coupling has been installed to accommodate any movement due to expansion.

4. SETTLING CHAMBER

The settling chamber, Figure B-2, is immediately downstream of the heater. The diffuser has a total included angle of 28 degrees and area ratio of 4.934 and is fitted with screens to prevent flow separation. To reduce turbulence, five screens and a 4 inch layer of steel wool are installed inside the 16-15/16" diameter settling chamber. The turbulence level downstream of the last screen has been measured to be 0.4%. The settling chamber has a downstream extension reducing its diameter to 10.466 in. ID.

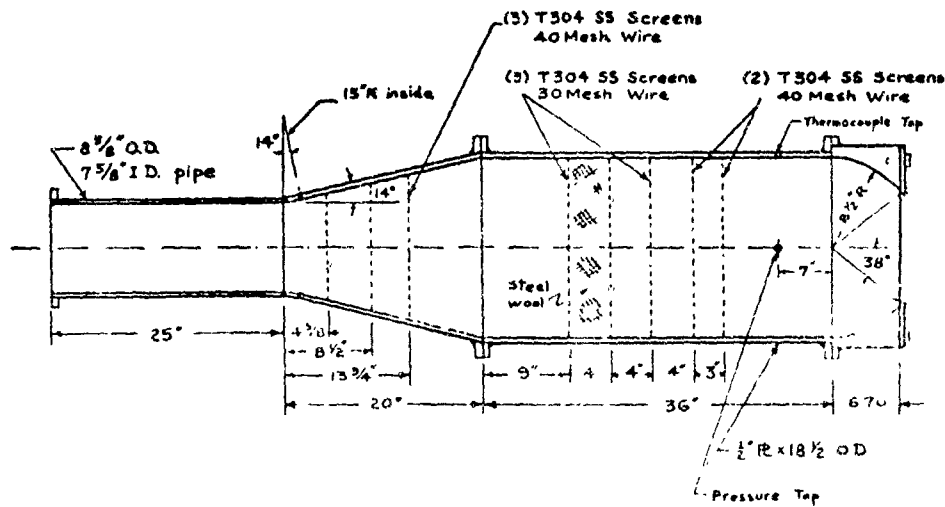


Figure B-2. Settling Chamber

Located upstream of the exit of the settling chamber, as seen in Figure B-2, are holes which provide access for measuring temperature and pressure in the settling chamber. A type J thermocouple and a Validyne DP 15 TL variable reluctance pressure transducer are used for the monitoring. The transducer has interchangeable diaphragms making it useful over an extremely wide range: 1 PSID full scale to 3000 PSID full scale. Running at Mach 0.9, the estimated uncertainty in measuring the settling chamber pressure is .04 psi.

5. ANECHOIC CHAMBER

The anechoic chamber at USC was designed and built by Eckel Industries, Inc. of Cambridge, Massachusetts. The walls, ceiling and floor of this chamber are covered by 24" x 24" panels on each of which are mounted three fiberglass wedges (see photograph in Figure B-3). The interior measures 15' 8" wide by 20' 4" long by 11' 11" high. (Measurements are to tips of wedges). Eight inches above the floor wedges is a cable floor on which one may walk. An elevation view providing a cross section of the anechoic chamber is shown in Figure B-4. The position of the center of the nozzle exit is indicated in this figure.



Figure B-3. Interior of Anechoic Chamber

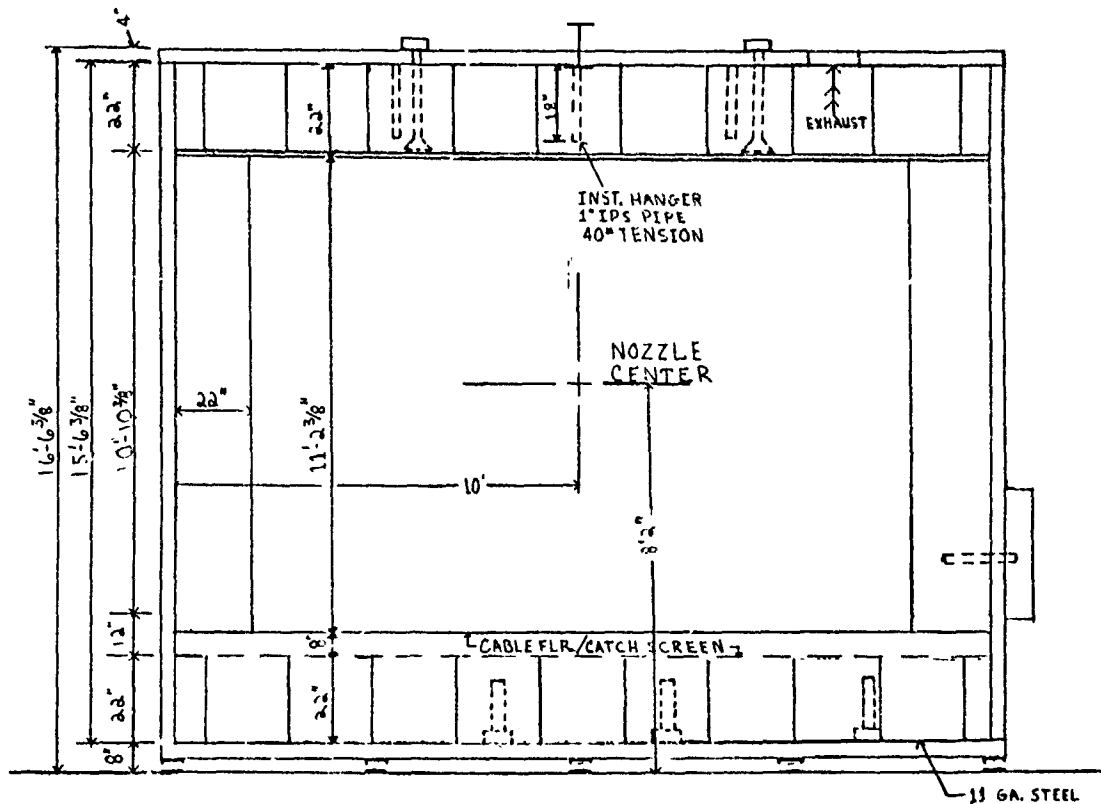


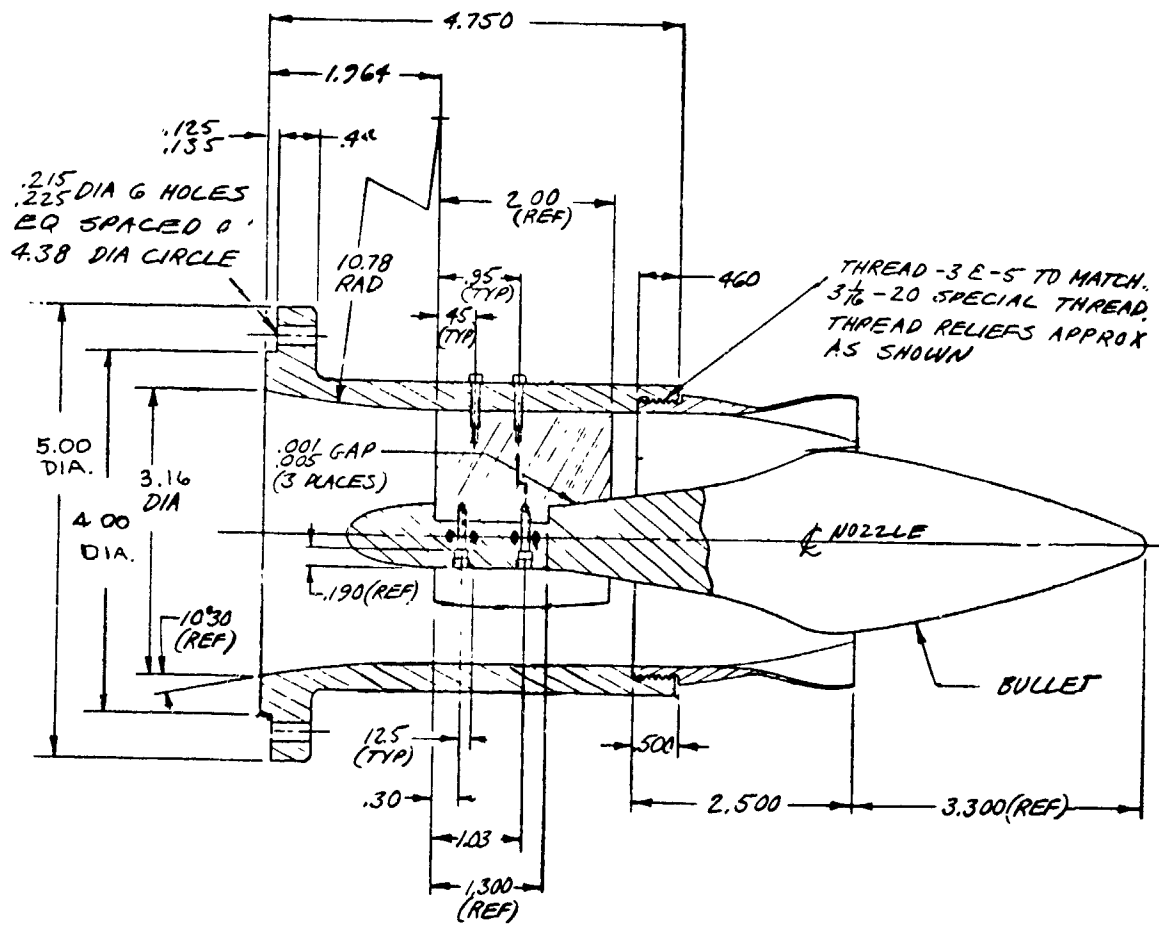
Figure B-4. Elevation through Anechoic Chamber

The entire chamber is mounted on heavy coiled springs for isolation from vibration. The chamber was designed for an acoustic low frequency cut-off of 150 Hz.

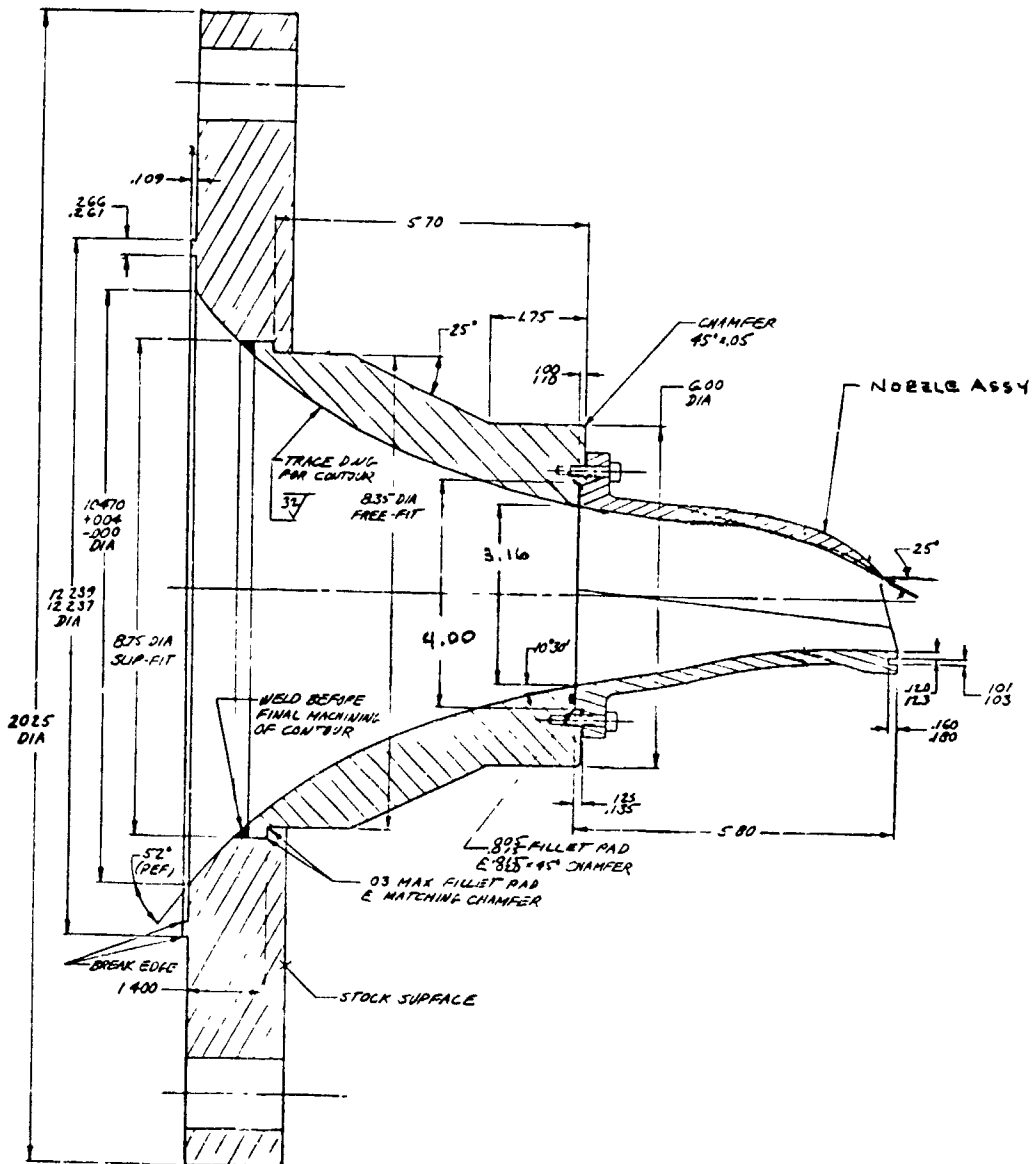
Two studies have been made to verify that the jet inside the anechoic chamber behaves like a free jet and is not overly influenced by recirculation. In the first test a 1/10 scale model was built of plexiglas. Using water and a dye, it was found that the jet's spreading rate was the same as that of a jet in free space. In the second study velocity profiles for a two-inch subsonic jet were compared to profiles obtained by other researchers. Excellent agreement was found.

APPENDIX C
NOZZLE DETAILS

1.0 LOBED NOZZLE DETAILS



2.0 OBF NOZZLE AND CONTRACTION SECTION DETAILS



APPENDIX D

INSTRUMENTATION LOCATIONS IN TEST SPECIMENS

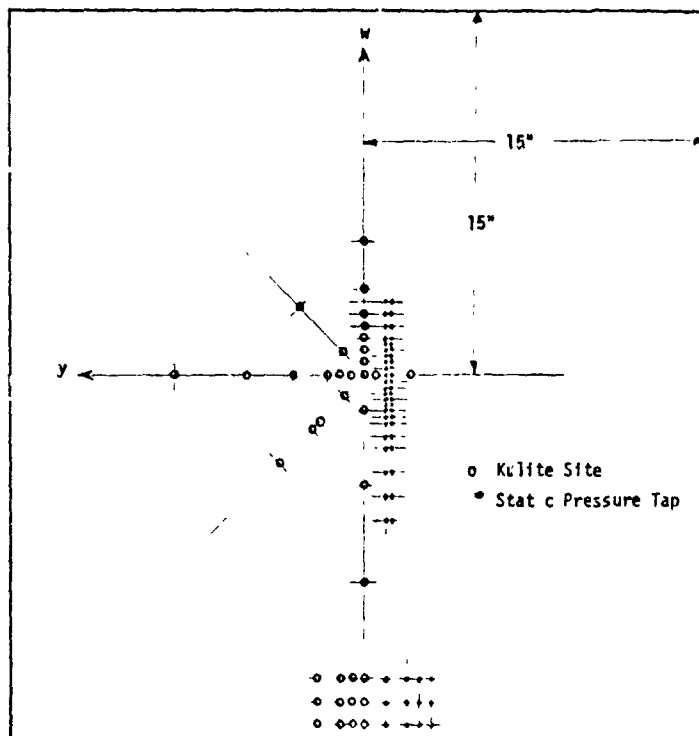
1.0 STATIC AND FLUCTUATING PRESSURE MEASURING PLATE

a. Coordinates of Static Taps:

Vertical Lines

y (in.)	
-1.0	-1.25

w (in.)
-6.0
-5.0
-4.0
-3.0
-2.5
-2.0
-1.75
-1.5
-1.25
-1.0
-0.75
-0.5
-0.25
0.0
0.25
0.5
0.75
1.0
1.25
1.5
2.0
2.5
3.0



Edge Array

y (in.)			
-1.0	-2.0	-2.5	-3.0

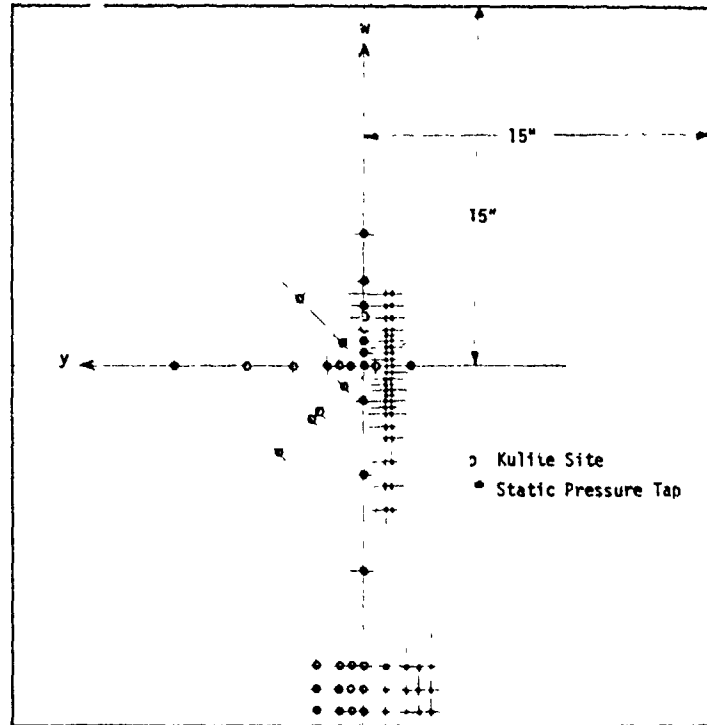
w (in.)
-12.5
-13.5
-14.5

1.0 STATIC AND FLUCTUATING PRESSURE MEASURING PLATE (cont'd.)

b. Coordinates of Fluctuating Pressure Sites:

Vertical Line

y = 0.0
w (in.)
-5.5
-3.5
-3.0
-2.5
-2.0
-1.5
-1.0
-0.5
0.0
1.5
4.5
8.5



Horizontal Line

w = 0.0
y (in.)
-2.0
-0.5
0.0
0.5
1.0
1.5
3.0
5.0
8.5

Edge Array

y (in.)			
0.0	0.5	1.0	2.0
w (in.)			
-12.5			
-13.5			
-14.5			

Diagonals

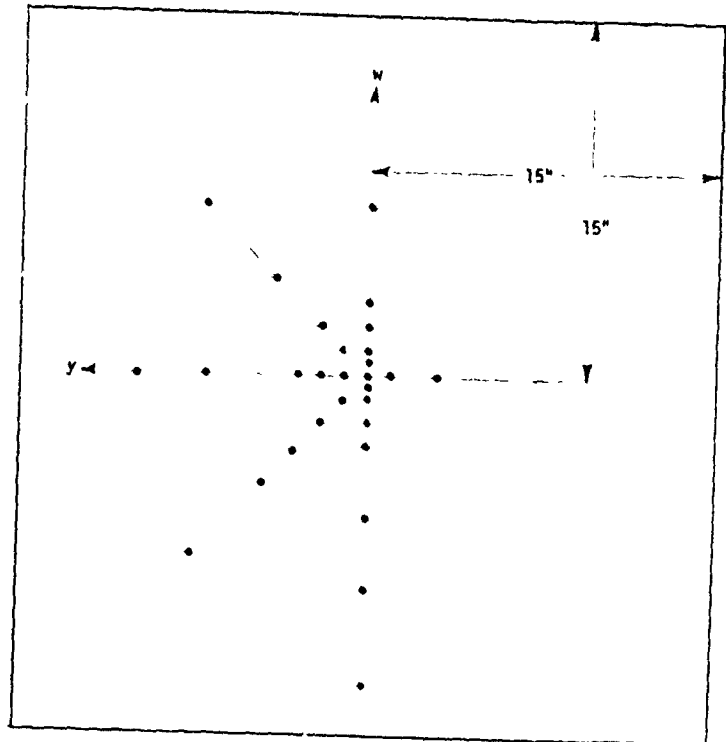
y (in.)	w (in.)
0.53	-0.53
1.44	-1.44
1.76	-1.76
2.83	-2.83
0.71	0.71
2.12	2.12

2.0 THERMOCOUPLE PLATE

Thermocouple Locations

Horizontal Line

w = 0.0
y (in.)
-3.0
-1.0
1.0
2.0
3.0
7.0
10.0



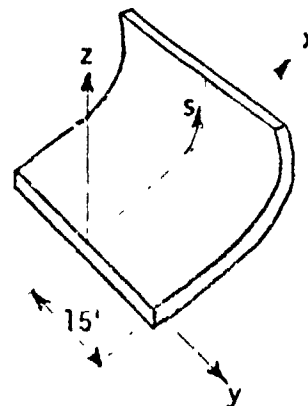
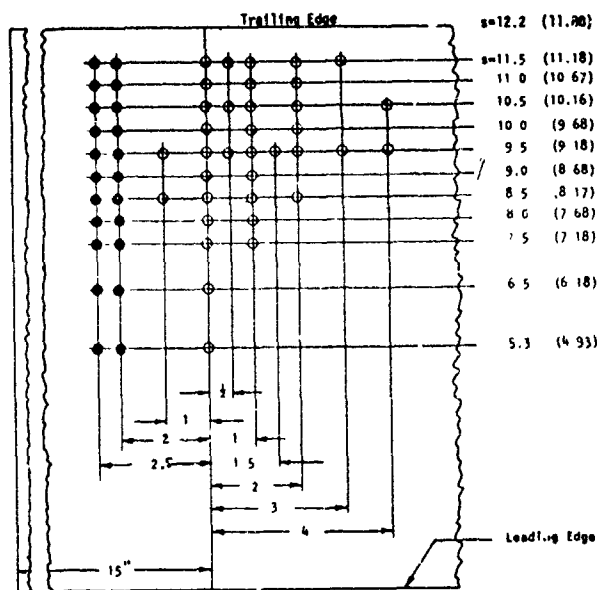
Diagonals

y (in.)	w (in.)
1.06	-1.06
2.12	-2.12
3.18	-3.18
4.60	-4.60
7.42	-7.42
1.06	1.06
2.12	2.12
3.89	3.89
6.72	6.72

Vertical Line

y = 0.0
w (in.)
-13.0
-9.0
-6.0
-3.0
-2.0
-1.0
-0.5
0.0
0.5
1.0
2.0
3.0
7.0

3.0 UBF CURVED PLATES



Coordinate Systems (x, y, z) and (s, y) Attached to Plate

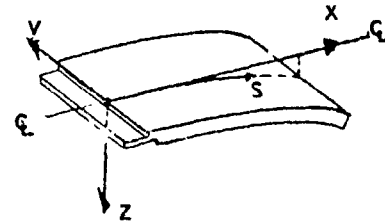
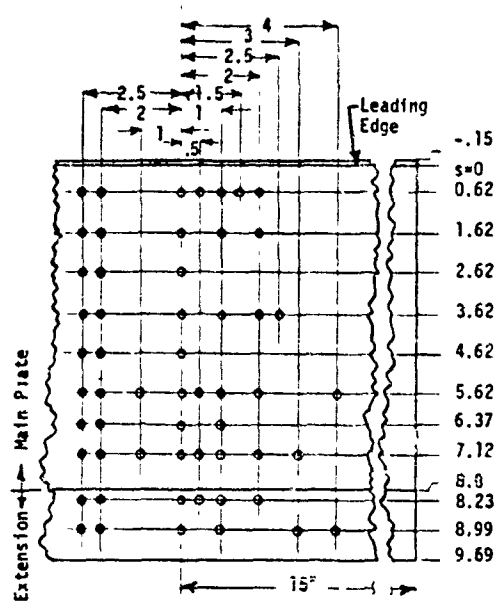
- Fluctuating Pressure Site
- Static Pressure Tap

Developed Surface of Curved Plates

Fluctuating and Static Pressure Locations on UBF Curved Plates

50° Plate			25° Plate		
s (in.)	x (in.)	z (in.)	s (in.)	x (in.)	z (in.)
5.3	5.30	0.0	4.93	4.93	0.0
6.5	6.46	0.01	6.18	6.18	0.01
7.5	7.44	0.16	7.18	7.18	0.10
8.0	7.92	0.30	7.68	7.65	0.18
8.5	8.39	0.478	8.17	8.11	0.27
9.0	8.84	0.70	8.68	8.60	0.39
9.5	9.27	0.96	9.18	9.08	0.53
10.0	9.67	1.25	9.68	9.55	0.68
10.5	10.05	1.58	10.16	10.02	0.86
11.0	10.39	1.94	10.67	10.48	1.06
11.5	10.71	2.33	11.18	10.93	1.27

4.0 OBF CURVED PLATES



Coordinate Systems (x, y, z) and (s, y) Attached to OBF Plate

- Fluctuating Pressure Site
- Static Pressure Tap

Developed Surface of Curved Plates

Fluctuating and Static Pressure Locations on OBF Curved Plates

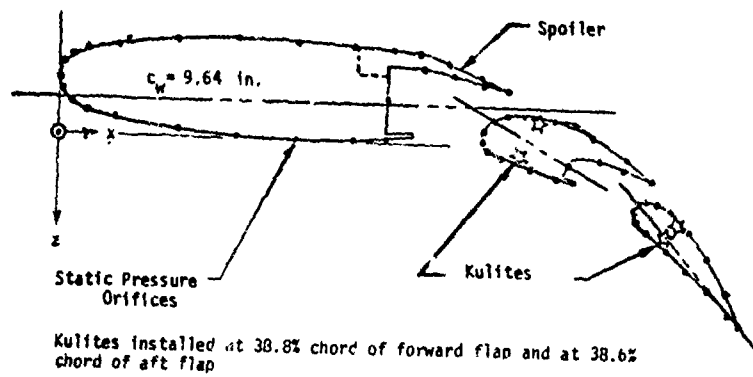
Main Plate

s (in.)	x (in.)	z (in.)
0.62	0.52	0.0
1.62	1.62	0.06
2.62	2.62	0.16
3.62	3.60	0.31
4.62	4.59	0.51
5.62	5.56	0.75
6.37	6.28	0.99
7.12	6.96	1.33

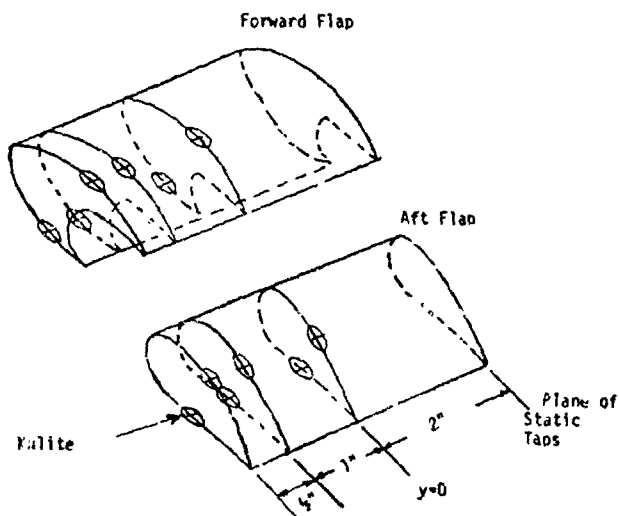
Trailing Edge Extension

s (in.)	x (in.)	z (in.)
8.23	7.80	2.05
8.99	8.17	2.09

5.0 WING-FLAPS MODEL



Surface	Fluctuating Pressure Pickup Location			
	$\beta_f/\beta_a = 30^\circ/50^\circ$		$\beta_f/\beta_a = 5^\circ/25^\circ$	
	x (in.)	z (in.)	x (in.)	z (in.)
Fwd Flap-Lower Surface	7.7	0.3	7.3	0.3
Aft Flap-Lower Surface	10.0	1.8	9.7	0.7



APPENDIX E

GEOMETRIC CENTER OF IMPINGEMENT

The locations of the geometric centers of impingement for all flat plate cases are given in Section III-2. Specifying the geometric center on a flat plate is necessary for relating any position on the plate surface to the center of the nozzle exit. For the UBF curved plates and wing-flaps model, the geometric center does not have as significant a role. It is, however, worthwhile to give the geometric centers for these last mentioned specimens in order to provide a more complete geometric description of the test set-ups.

1. UBF CURVED PLATES

The dimensions given in Figure 14 are sufficient to determine the geometric centers for all the UBF curved plate cases listed in Appendix A. Performing the necessary calculations, the locations of the geometric centers are as follows:

TABLE E-1

IMPINGEMENT CENTERS - UBF CURVED PLATES

CONFIGURATION		IMPINGEMENT CENTER LOCATION			
$x_{LE} = 0$					
β_{TE}	z_{LE}	x_I	z_I	s_I	s_I^*
25°	1.4	11.2	1.4	11.40	.50
	2.0	(12.45)	(2.0)	(12.85)	(-.95)
50°	1.4	9.8	1.4	10.15	2.05
	2.0	10.4	2.0	10.95	1.25

The distances x_I , z_I and s_I given in inches in Table E-1 for the

centers of impingement are based on the x, y, z, s coordinate system defined in Appendix D-3. The lateral or spanwise positions of the impingement centers are at $y = 0$. The distance s_I is measured from the leading edge along the centerline chord on the exposed surface. A complementary distance s_I^* is also presented in the table and gives the distance upstream on the surface from the trailing edge to the impingement center.

For the case $\beta_{TE} = 25^\circ$ and $Z_{LE} = 2.0$, the centerline of the jet does not intercept the plate. The values given within parentheses are those that would result if the straight trailing edge of the plate were sufficiently extended (s_I^* is still measured from the actual trailing edge and is negative downstream).

Referenced in terms of the nozzle coordinates, the geometric centers of impingement in the X, Y, Z system are $X (= X_S \text{ in Figure 4}) = X_{LE} + x_I$, $Y = 0, Z = 0$.

2. WING-FLAPS MODEL

The positions of the fluctuating pressure pick-ups on the wing-flaps model are given in Appendix D-5. These positions are referenced to a system of coordinates x, y, z attached to the test specimen. Table E-2 gives the locations of the impingement centers for the wing-flaps model in terms of these coordinates and others to be subsequently defined.

For each configuration in Table E-2, four dimensions in inches are given to locate the centers of impingement. (The spanwise positions are at $y = 0$). The distances x_I and z_I have the same meaning as previously used for the UBF curved plates. The other two dimensions, s_{fI} and s_{aI} , denote the distances to the center of impingement measured along the centerline chord from origins at the pickup positions on the lower surfaces of the forward and aft flaps, respectively. Positive values for these distances are in the downstream direction from their origins.

The center of impingement fell on the forward flap in only one case.

TABLE E-2

IMPINGEMENT CENTERS - WING-FLAPS MODEL

CONFIGURATION		IMPINGEMENT CENTER LOCATION				
$X_{LE} = 0$						
β_f/β_a	Z_w	FLAP	x_I	z_I	s_{fI}	s_{aI}
5°/25°	1.0	AFT	10.4	1.0		0.8
	1.4	(BELOW)	(11.3)	(1.4)		(1.8)
	2.0	(BELOW)	(12.6)	(2.0)		(3.2)
30°/50°	1.0	FWD	9.0	1.0	1.5	
	1.4	AFT	9.7	1.4		-0.5
	2.0	AFT	10.2	2.0		0.3

For the case in which $\beta_f/\beta_a = 30^\circ/50^\circ$ and $Z_w = 1.4$, the negative value for s_{aI} indicates that the center of impingement on the aft flap occurs upstream of the pickup position. The distances within parentheses for the impingement centers in two of the $\beta_f/\beta_a = 5^\circ/25^\circ$ cases designate the values that would occur if the aft flap reference line were extended downstream.

Referenced in terms of the nozzle coordinates, the geometric centers of impingement in the X, Y, Z system are

$$X(=X_F \text{ in Figure 1}) = X_{LE} + x_I, Y = 0, Z = 0.$$

APPENDIX F
ACOUSTIC RESONANCE STUDY

It was known prior to the test program that a phenomena termed 'acoustic resonance' can arise when a subsonic jet impinges on an object in its path. This resonance produces a noticeable spike in the power spectrum of a fluctuating pressure pickup on the exposed surface of the object. Power spectra have been acquired in which this spike is a dominating feature containing a large share of the total power in the spectrum.

From the work in Reference 9 , a necessary condition for acoustic resonance is that an object such as a flat plate must intercept the potential core of the free jet. For the round nozzles used in the test program, this indicates that the distance of the object from the nozzle exit must be less than 6 diameters. It was found by Douglas Aircraft that even when the jet is turned, as is the case for the wing-flaps model, acoustic resonance can be produced if the flaps still intercept the potential core of the free jet.

The following features of acoustic resonance have been reported by Reference 9 :

- (a) The Mach number must be greater than 0.5 or the resonance doesn't occur.
- (b) This cutoff Mach number increases with the temperature of the jet.
- (c) The dominance of the resonance increases with inclination angle, β , of the plate.
- (d) If f_R is the frequency at which the 'spike' in the power spectrum appears, the maximum value for the Strouhal No. $S_R = f_R D_j / V_j$ is approximately 0.8.
- (e) The Strouhal No. S_R diminishes with increasing jet Mach No. and is relatively insensitive to the plate position for $\lambda_1 / D_j > 3$.

- (f) An object projecting into the jet at the nozzle exit, such as a nail, will reduce the intensity of the resonance or even suppress it to a level that is not discernible.

It was desired in the test program to avoid acoustic resonance. (The only test intentionally run to produce resonance was Case 8E listed in Appendix A.) For this purpose, a short study was conducted prior to the test program to determine the boundaries on the parameter levels at which resonance occurs. The results of this study can be compared with those of Reference 9 to determine the extent of agreement. A close agreement would permit using the broader conclusions established in Reference 9.

Flat plate, cold jet tests were performed for the resonance study using round nozzles. The results of these tests are summarized in the following table:

TABLE F-1
ACOUSTIC RESONANCE RESULTS

JET M_j	PLATE		ACOUSTIC RESONANCE	
	X_I/D_j	β	OCCURRENCE	STROUHAL NUMBER, S_R
0.9	3	90°	Yes	0.39
0.9	6	90°	Yes	0.39
0.9	6 1/2	90°	No	
0.9	7	90°	No	
0.72	6	90°	Yes (Weak)	0.57
0.5	5	90°	No	
0.9	3	41°	Yes	0.41
0.9	3	33°	No	

In the table, it is seen that the Strouhal Number, S_R , is not sensitive to the plate position, X_I/D_j , or to the inclination angle of the plate, β . The magnitude of S_R , however, does diminish with increasing Mach No., M_j . All these results are in agreement with Reference 9.


It is seen in Table F-1 that the resonance, although weak, can occur for $X_I/D_j = 6$. This position is slightly beyond the potential core. The resonance boundary for β appears to be near 33° . That is, resonance will not occur for plate inclinations less than 33° , irrespective of the values for M_j and X_I/D_j . The Mach No. at which resonance occurs is above $M_j = 0.5$. A refined determination of the Mach No. boundary was not performed.

Tests were also conducted to verify that the resonance can be suppressed. An extension was attached at the exit end of the 1" diameter round nozzle and four threaded holes, separated 90° apart, were placed in the extension near the new exit. A screw was put into each hole so that its tip projected inside the nozzle to a distance of about 1/16 inch. The resonance was barely noticeable in this case. Leaving the holes open on both ends or leaving the holes open at the inner surface and sealing at the outer surface had no effect in reducing the resonance.

A study conducted by Douglas Aircraft on the wing-flaps model showed that the Strouhal number at which resonance occurs is affected by the dimension Z_w , the distance between the jet centerline and the lower surface of the wing. Using a landing approach flap setting ($\beta_f/\beta_a = 30^\circ/50^\circ$) and having $Z_w/D_j = 0.65$ where $D_j = 3"$, it was found that $S_R = .58$ for $M_j = 0.74$. (Approximately the same result was found for test program case 8E in which $Z_w/D_j = 0.7$ and $M_j = 0.74$.) When Z_w/D_j was reduced to 0.5, the value for S_R increased to 0.78.

APPENDIX G

TEMPERATURE MEASUREMENTS


The transient temperature tests conducted in the test program are described in Section III-2. Temperature measurements were made only on the flat plate. The following tables give results for the 7 cases listed in Category 13 of Appendix A. The numerical values of the parameters are given with each table. The tables are laid-out in two-dimensions with the plate's two centerlines indicated. The center of jet impingement on the plate, denoted by , is located for all cases at the intersection of the two centerlines. The results are shown in the tables in their proper spatial relation to each other. Dimensions consistent with those given in Appendix D-2 are placed in the tables for defining the locations at which measurements are specified.


The typical temperature as a function of time is discussed in Section II-5. Values of two characteristics of the time history T_e in $^{\circ}\text{R}$ and t_r in seconds, are given in the tables. The rise time is enclosed in parentheses.


Samples showing actual time histories of the measured temperatures are given in Figure G-1. The location of the thermocouple measuring the temperature for each time history is designated in the figure by w and y in the plate coordinate system.


TABLE G-1
 TEMPERATURE MEASUREMENT RESULTS
 FLAT PLATE - DAISY NOZZLE ($D_{eq} = 2''$)

TEST CASE	T_j/T_a	M_j	X/D	θ	RESULT TYPE
13A	1.7	0.5	5	50°	Equilibrium Temperature (°R) (Rise Time) sec


 621.1 (3.64)


 629.5 (4.68)


 623.0 (3.16)


 683.1 (3.08)

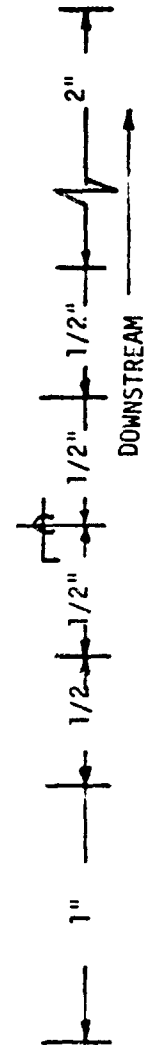
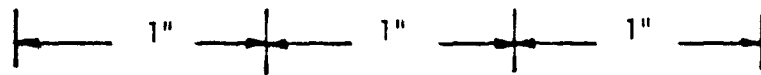


TABLE G-2
 TEMPERATURE MEASUREMENT RESULTS
 FLAT PLATE - ROUND NOZZLE (D = 2")

TEST CASE	T_j/T_a	M_j	X/D	θ	RESULT TYPE
13B	1.7	0.5	10	50°	Equilibrium Temperature (°R) (Rise Time) sec

ϕ
 646.3 | (3.04)

+ + + +
 670.5 | (3.6)

\bullet 667.5 | (3.0)
 659.3 | (3.0)

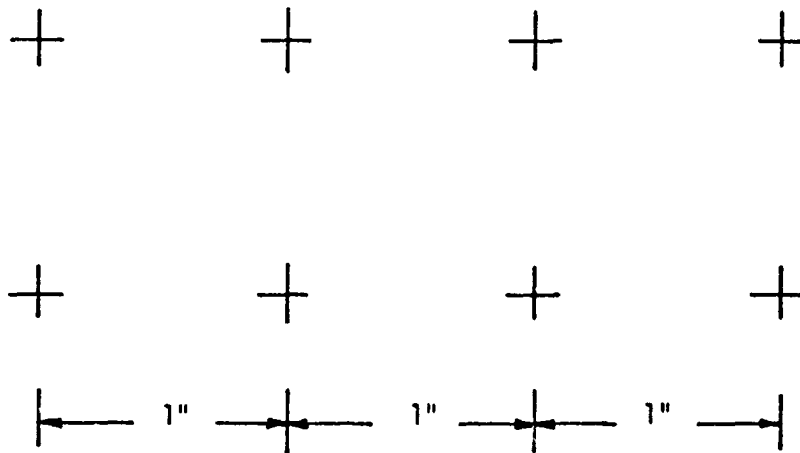


TABLE G-3
 TEMPERATURE MEASUREMENT RESULTS
 FLAT PLATE - ROUND NOZZLE (D = 2")

TEST CASE	T_j/T_a	M_j	X/D	β	RESULT TYPE
13C	1.7	0.5	5	25°	Equilibrium Temperature (°R) (Rise Time) sec

ϕ
 719.2 | (3.0)

+

+

+

+

+

685 | (2.4)

679.9 | (2.92)

+

+

700.0 | (3.08)

+

678.0 | (2.4)

+

+

+

+

621.2 | (2.6)

+

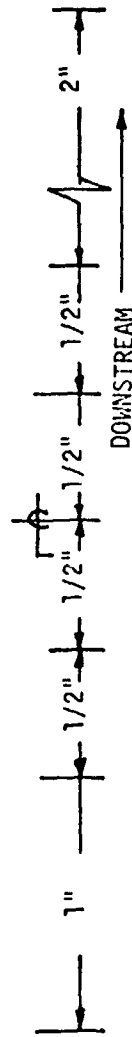
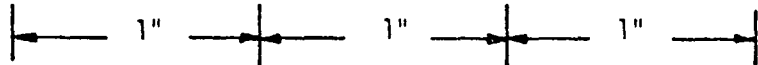


TABLE G-4
 TEMPERATURE MEASUREMENT RESULTS
 FLAT PLATE - ROUND NOZZLE (D = 2")

TEST CASE	T_j/T_a	M_j	X/D	β	RESULT TYPE
13D	1.7	0.5	5	50°	Equilibrium Temperature (°R) (Rise Time) sec

ϕ
 735.0 | (2.72)

+
 729.0 | (3.36)

\bullet 723.5 | (3.2)
 731.6 | (3.52)

+
 678.0 | (2.92)

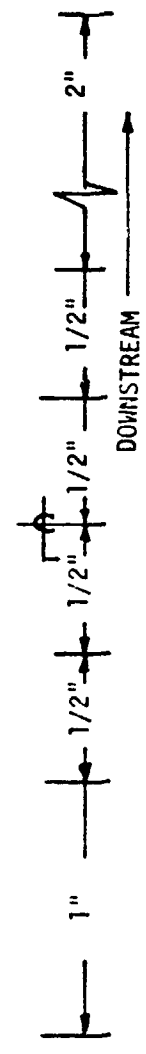
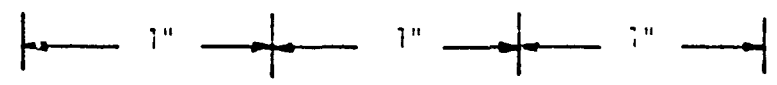


TABLE G-5
 TEMPERATURE MEASUREMENT RESULTS
 FLAT PLATE - ROUND NOZZLE (D = 2")

TEST CASE	T_j/T_a	M_j	X/D	β	RESULT TYPE
13E	1.7	0.5	5	90°	Equilibrium Temperature (°R) (Rise Time) sec

¢
 699.5 | (2.76)

758. | (2.88)

762.5 | (4.08)

807.5 | (3.32)

774.3 | (3.64)

768.0 | (3.74)

759.1 | (3.0)

762.5 | (3.0)

769.0 | (4.2)

767.5 | (3.68)

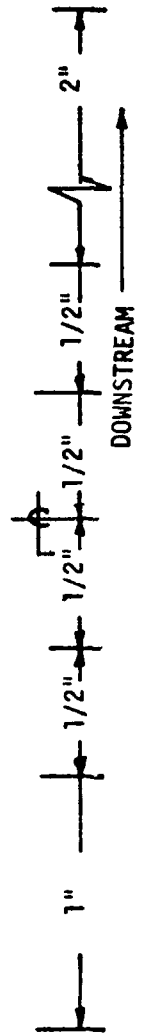
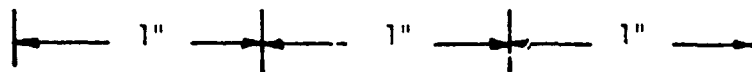


TABLE G-6
 TEMPERATURE MEASUREMENT RESULTS
 FLAT PLATE - ROUND NOZZLE (D = 2")

TEST CASE	T_j/T_a	M_j	X/D	β	RESULT TYPE
13F	1.7	0.5	7	50°	Equilibrium Temperature (°R) (Rise Time) sec

⊘
 696.5 (2.4)

+

715.5 (3.1)

⊙

704.2 (2.92)

721.7 (3.7)

+

+

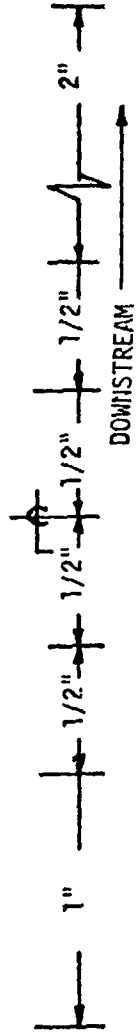
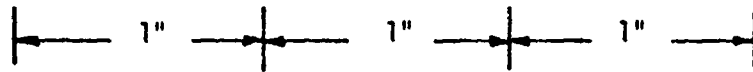
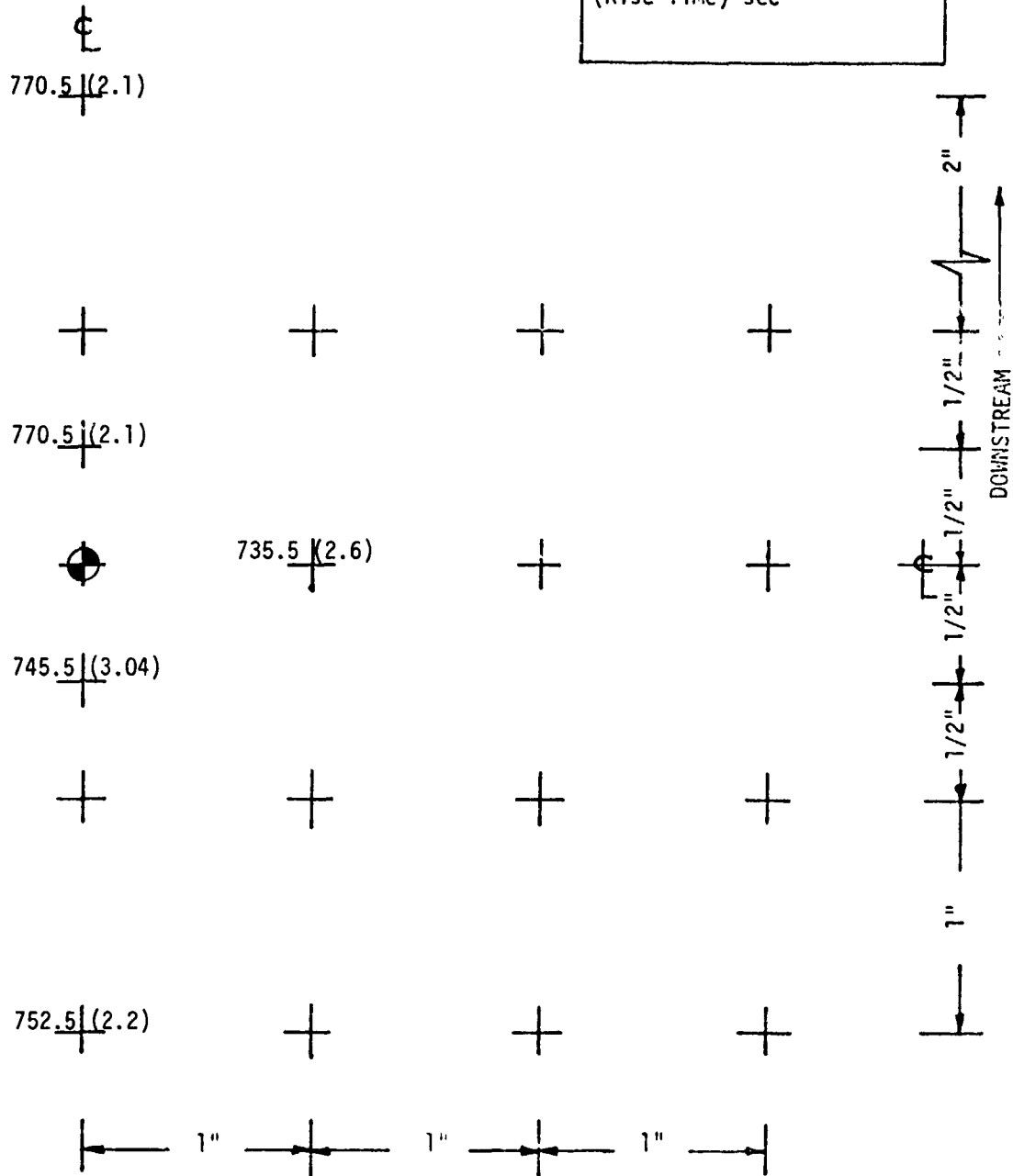
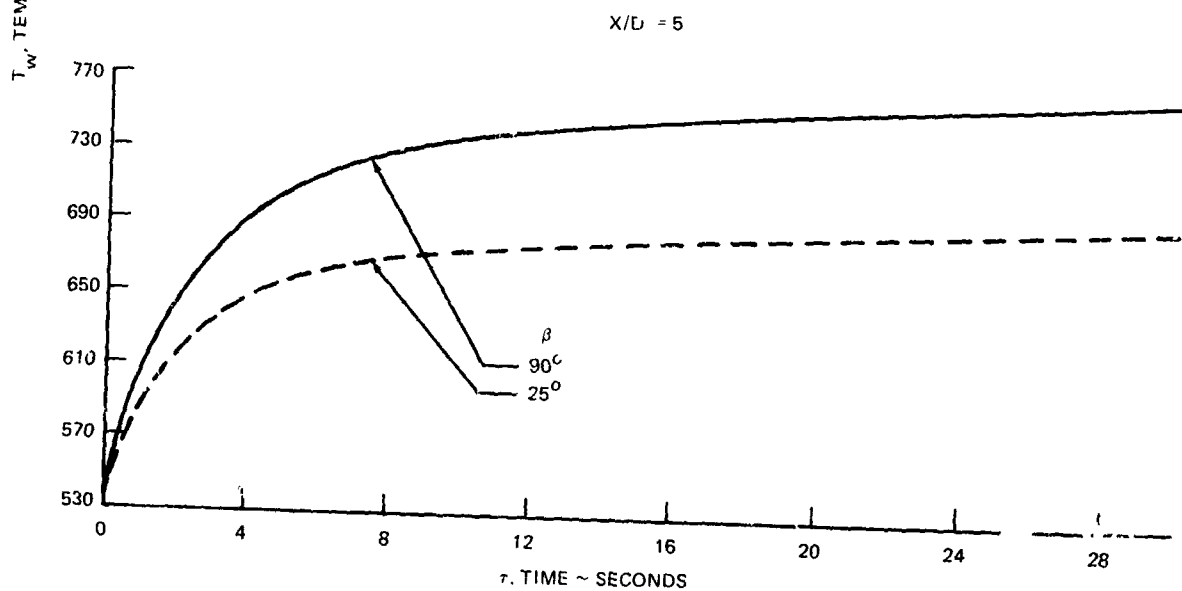
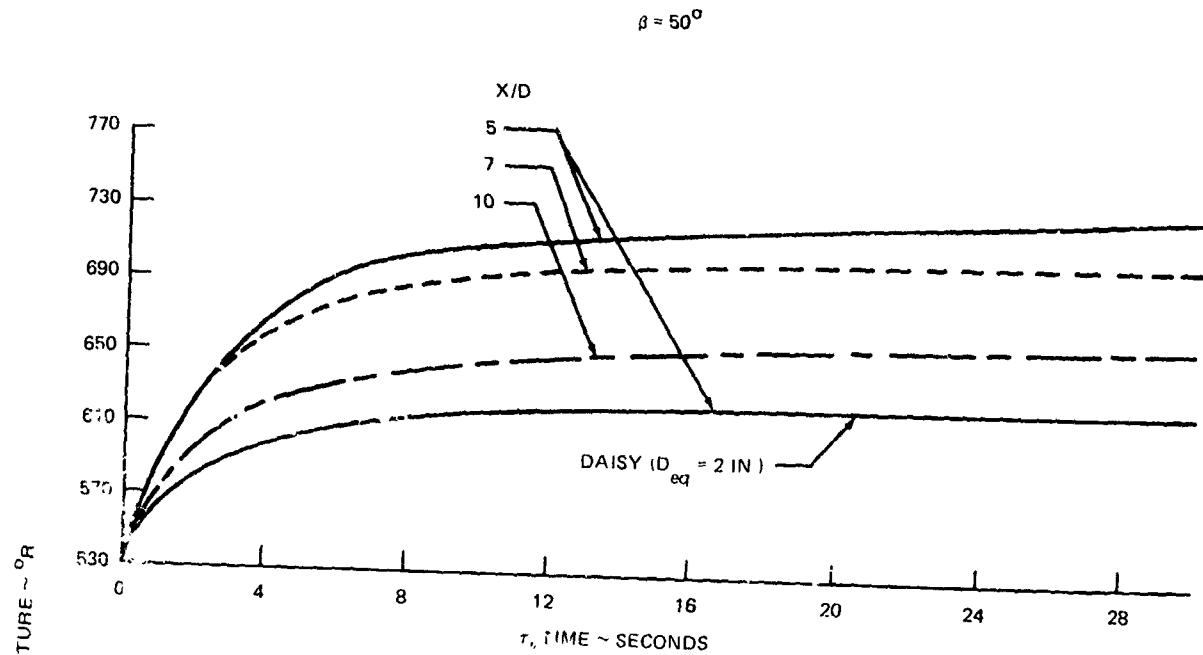


TABLE G-7
 TEMPERATURE MEASUREMENT RESULTS
 FLAT PLATE - ROUND NOZZLE (D = 2")

TEST CASE	T_j/T_a	M_j	X/D	β	RESULT TYPE
13G	1.7	0.74	5	50°	Equilibrium Temperature (°R) (Rise Time) sec





UNLESS NOTED, ROUND NOZZLE ($D_j = 2 \text{ IN}$), HOT JET ($T_j/T_a = 1.7$), $M_j = 0.5$,
 $v/R_j = 0$, $w/R_j = 0.5$

FIGURE G-1. TRANSIENT TEMPERATURE MEASUREMENTS

APPENDIX H

STATIC PRESSURE MEASUREMENTS

The surface static pressures are obtained along the chords of the various specimens. The following plots exhibit many of the measured chordwise distributions and cover the four types of specimens in the test program. The 'y' or offset distance of the chordline from the span center is indicated on each plotted curve. The static pressures are in psig and designated by p_s .

For the flat plate, round nozzle cases the static pressure distributions were originally obtained only as relative magnitudes. The maximum or stagnation value of each of these static pressure distributions was determined by calculating free jet total pressure on the centerline at the location, X , of the plate and using the information presented in Figures 15 and 18 of Reference 1 (Part 1). If $(P_T)_\phi$ is the indicated total pressure in the free jet at the plate position, then the stagnation pressure level p_s^* was estimated from $p_s^* = [(P_T)_\phi - P_a] \sin^2 \beta$, where β is the inclination angle of the plate and P_a = ambient air pressure = 14.7 psi.

The origin of each chordwise distribution of static pressures on the flat plate is the center of impingement. Distances in inches from the origin are denoted by r_1 and are positive in the downstream direction. The origin for data from the curved plates (UBF and OBF) is the leading edge of the plates. The distances in inches downstream from the leading edge are designated by 's'.

Static pressure distributions on the flap surfaces of the wing-flaps model are shown in Figure H-5. This data was obtained using a 3 inch round nozzle with $X_{LE} = 1$ inch and $Z_w = 1.9$ inches.

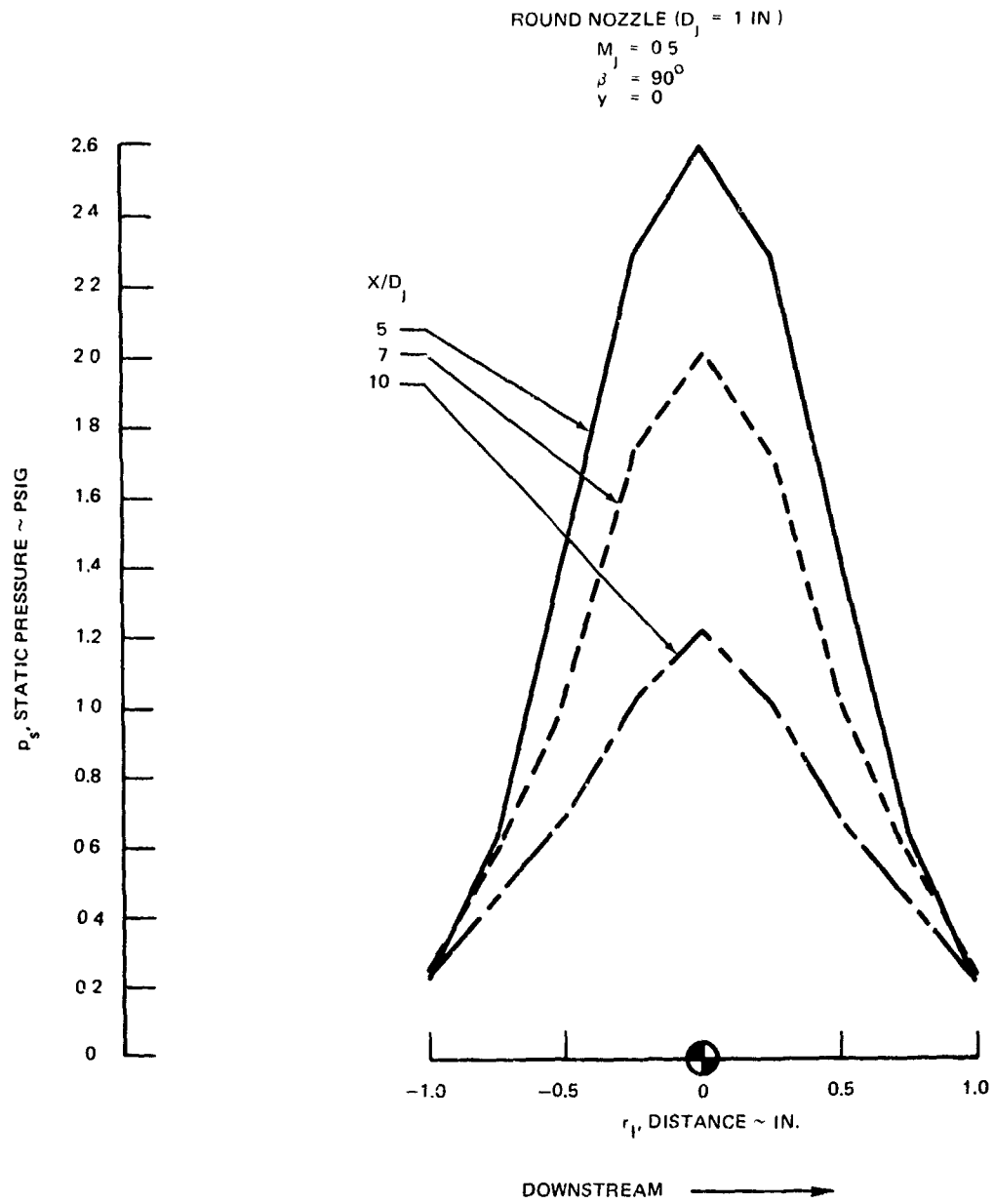


FIGURE H-1. STATIC PRESSURE MEASUREMENTS – FLAT PLATE – ROUND NOZZLE

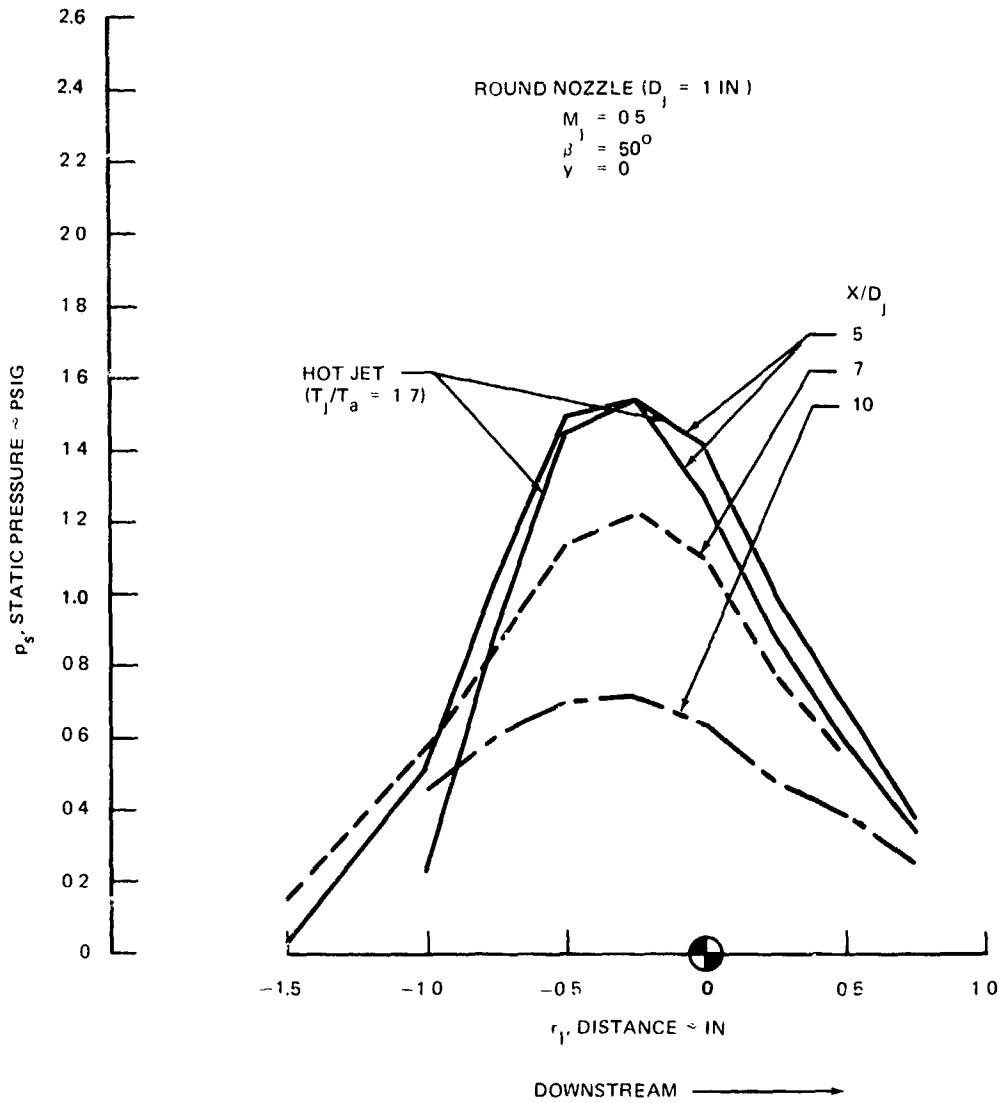


FIGURE H-1. CONTINUED

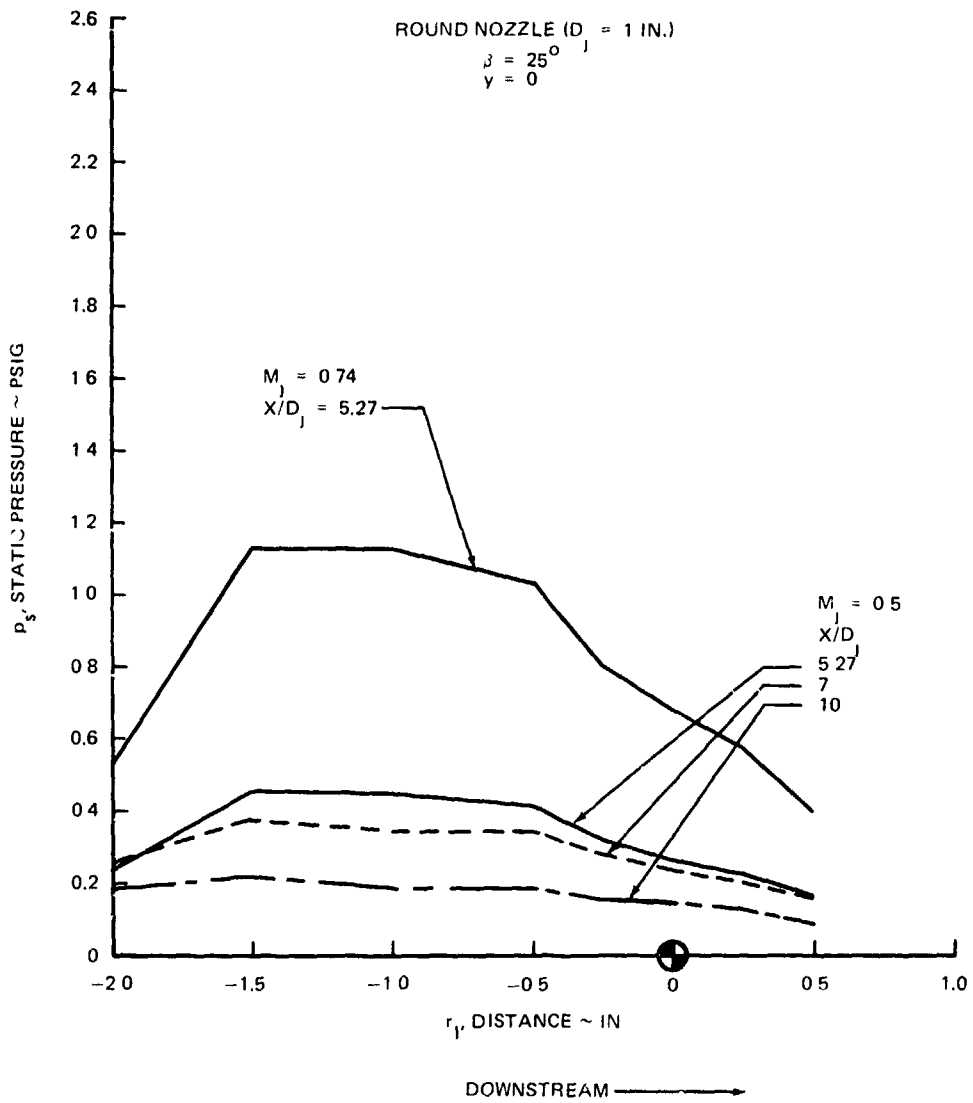


FIGURE H-1. CONTINUED

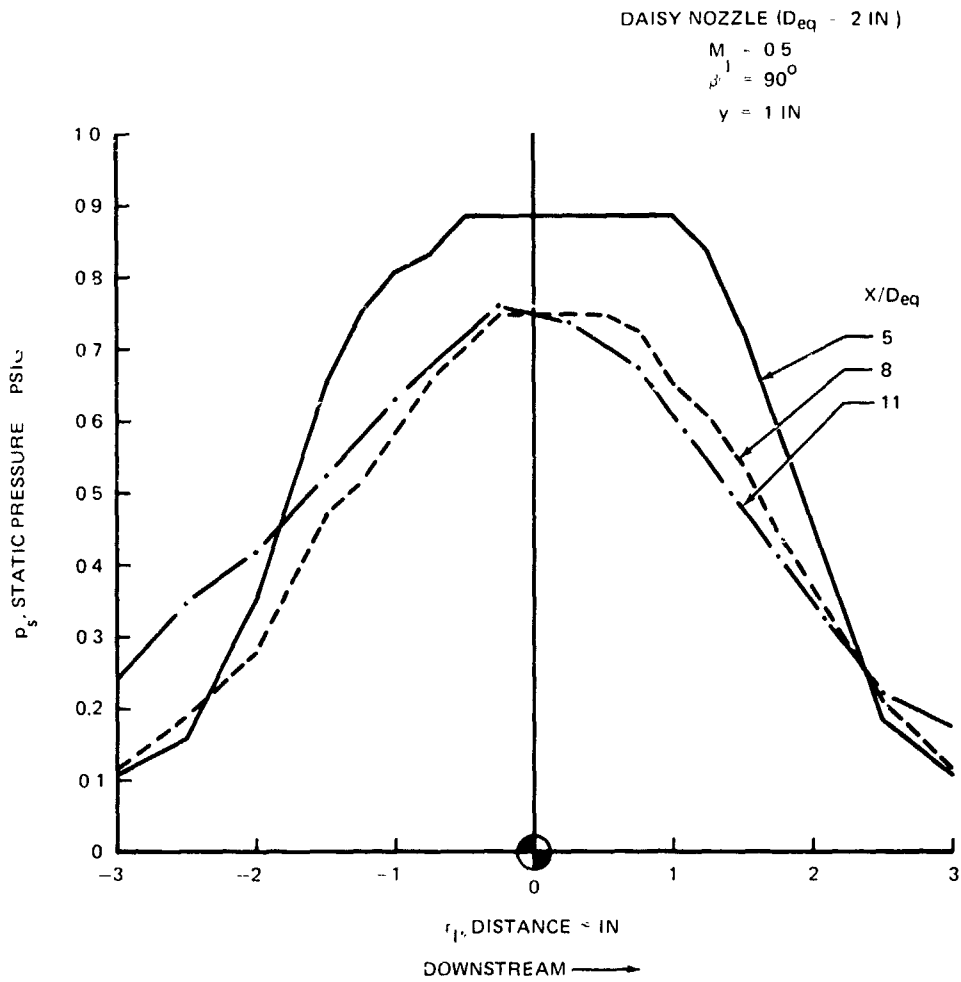


FIGURE H-2. STATIC PRESSURE MEASUREMENTS - FLAT PLATE - DAISY NOZZLE

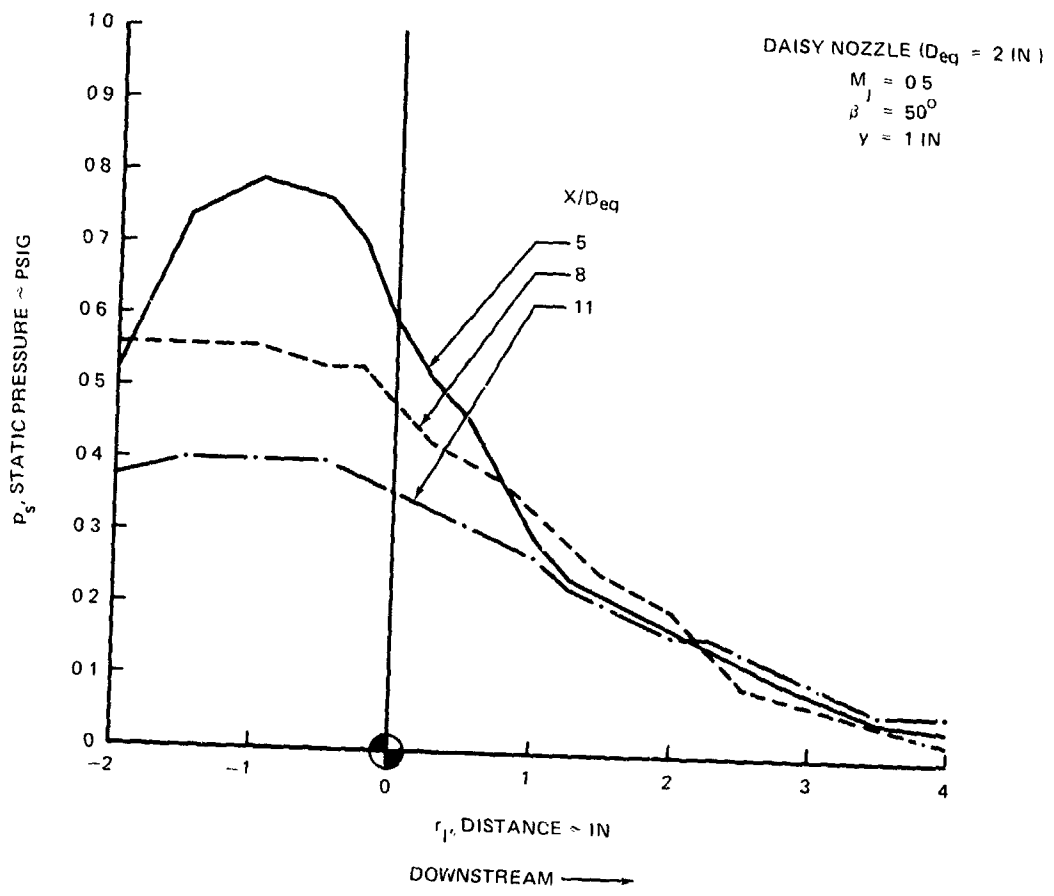


FIGURE H-2, CONTINUED

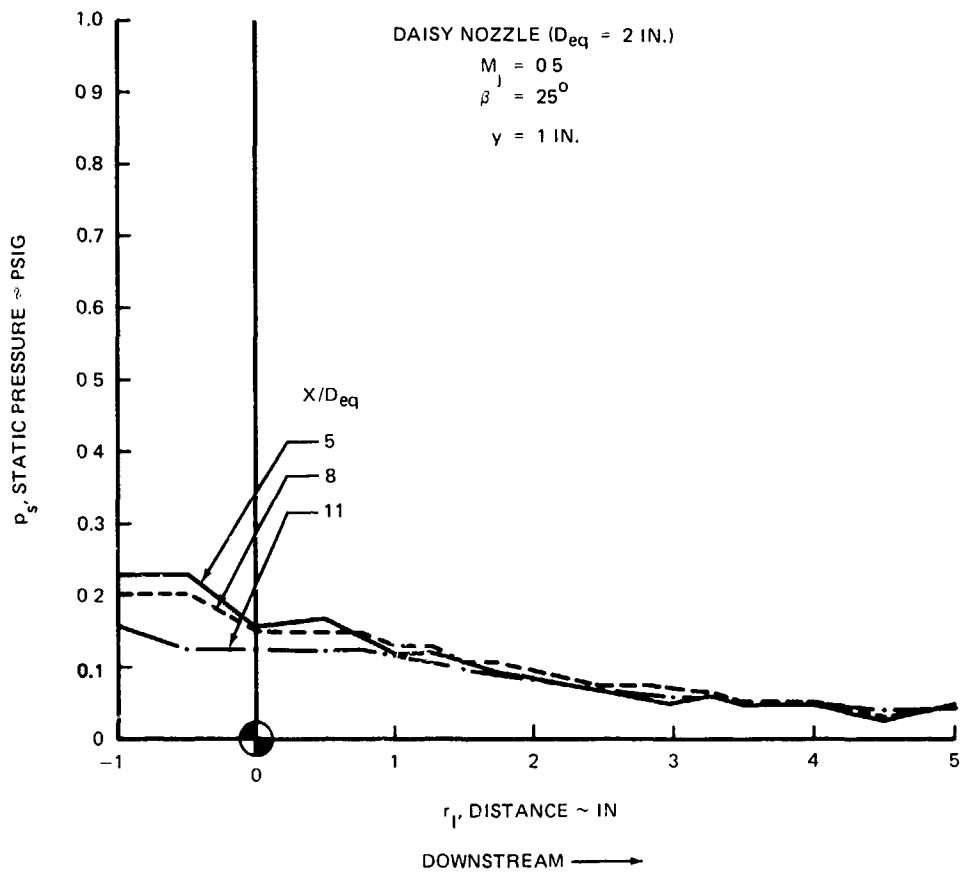
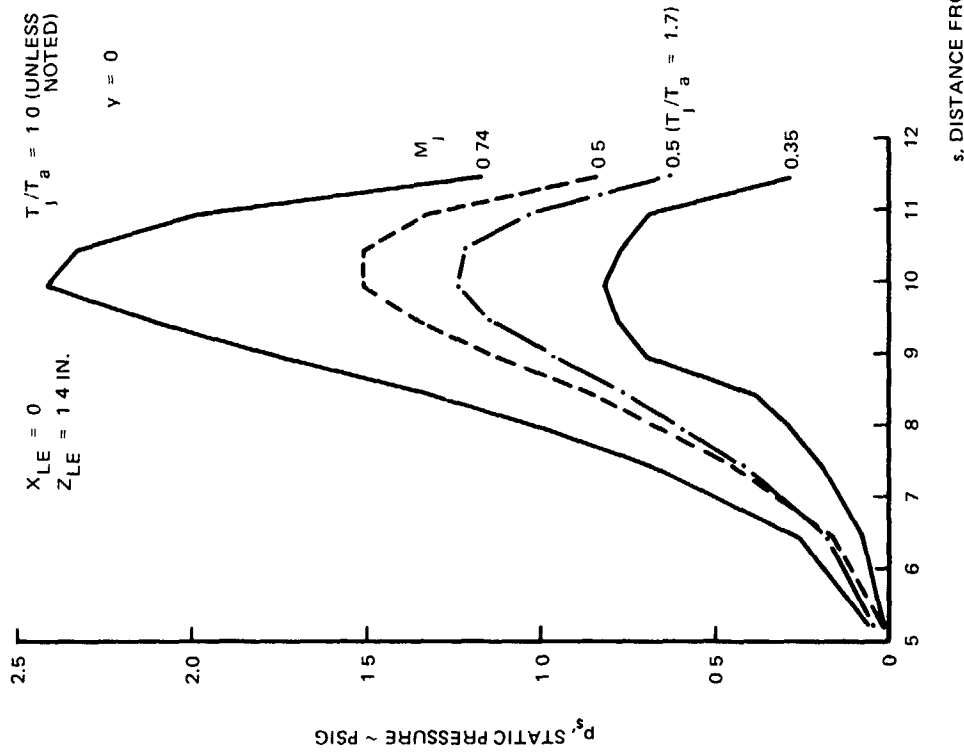


FIGURE H-2. CONTINUED

ROUND NOZZLE (D_j = 2 IN.)
 $\beta_{TE} = 50^\circ$



ROUND NOZZLE (D_j = 2 IN.)
 $\beta_{TE} = 50^\circ$

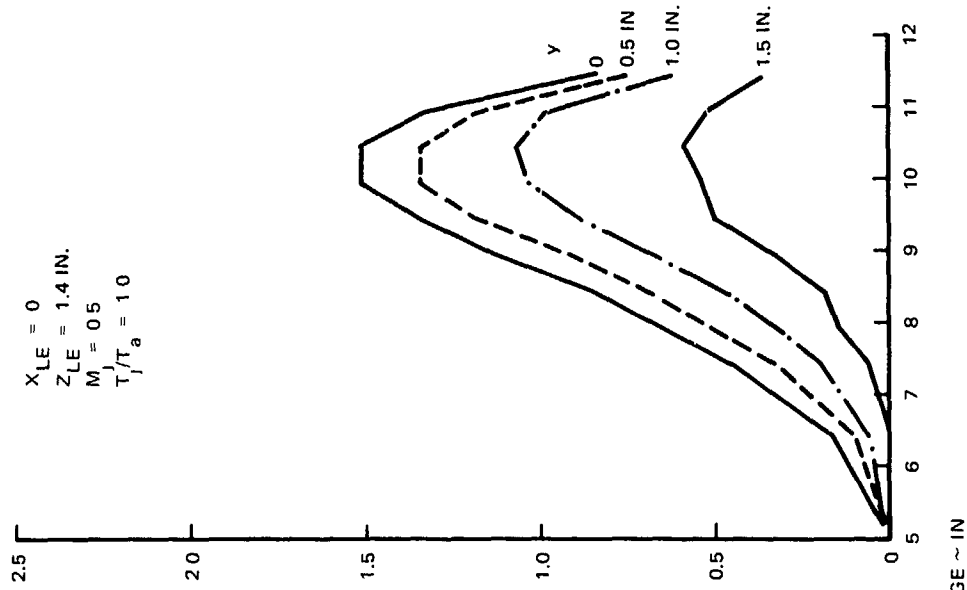
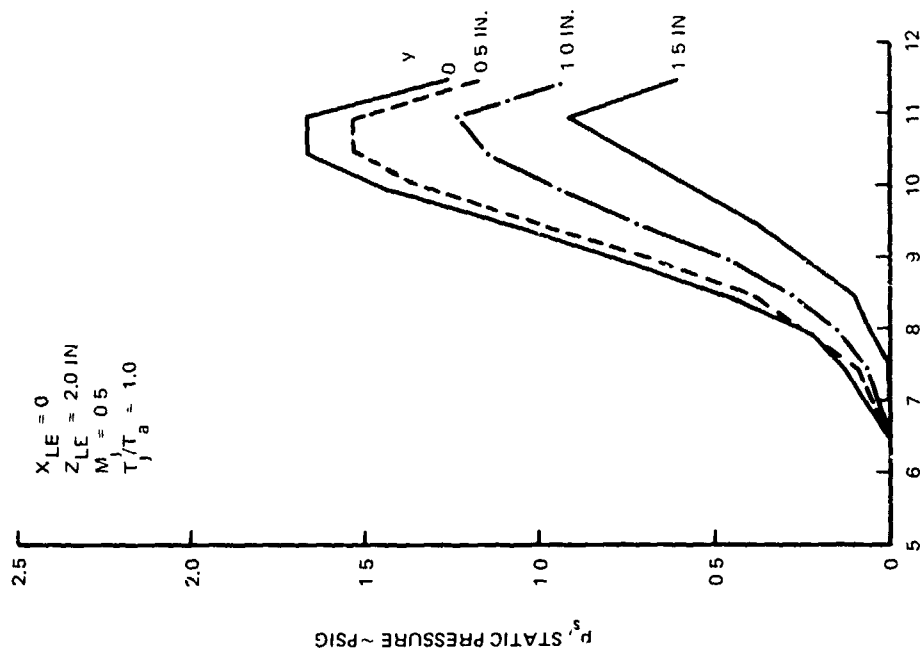
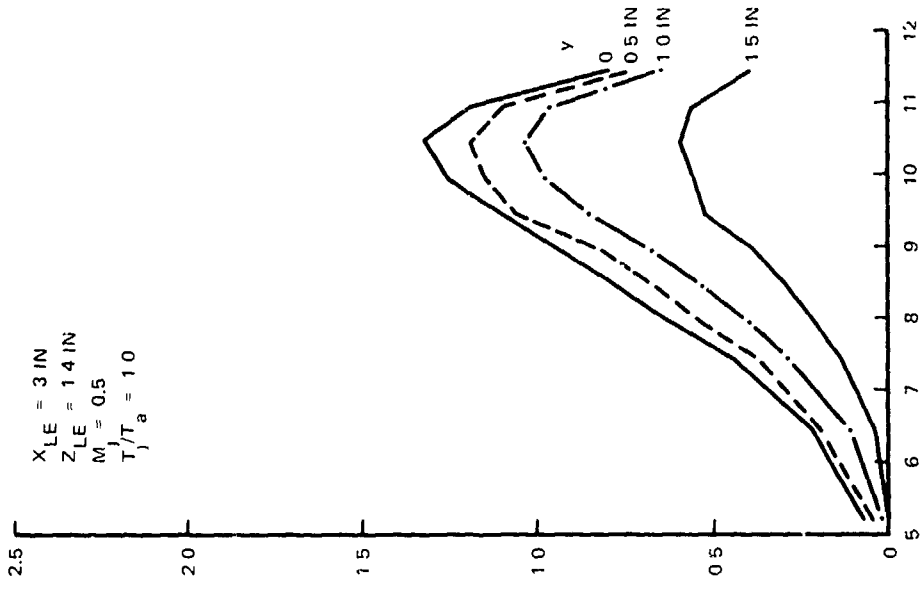


FIGURE H-3. STATIC PRESSURE MEASUREMENTS - UBF CURVED PLATES

ROUND NOZZLE ($D_j = 2$ IN)
 $\beta_{TE} = 50^\circ$



ROUND NOZZLE ($D_j = 2$ IN)
 $\beta_{TE} = 50^\circ$

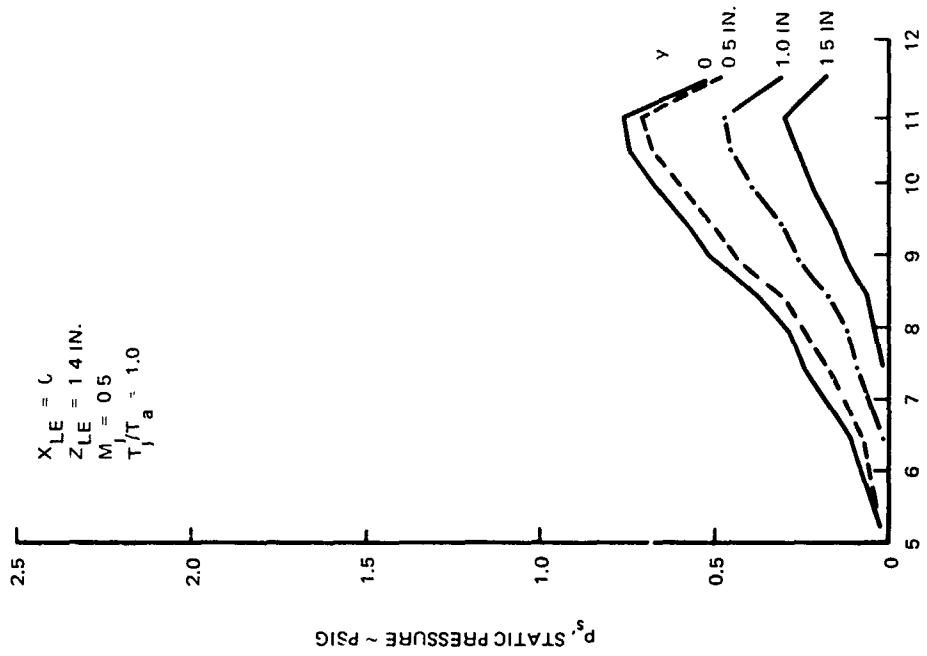


s, DISTANCE FROM LEADING EDGE ~ IN

FIGURE H-3. CONTINUED

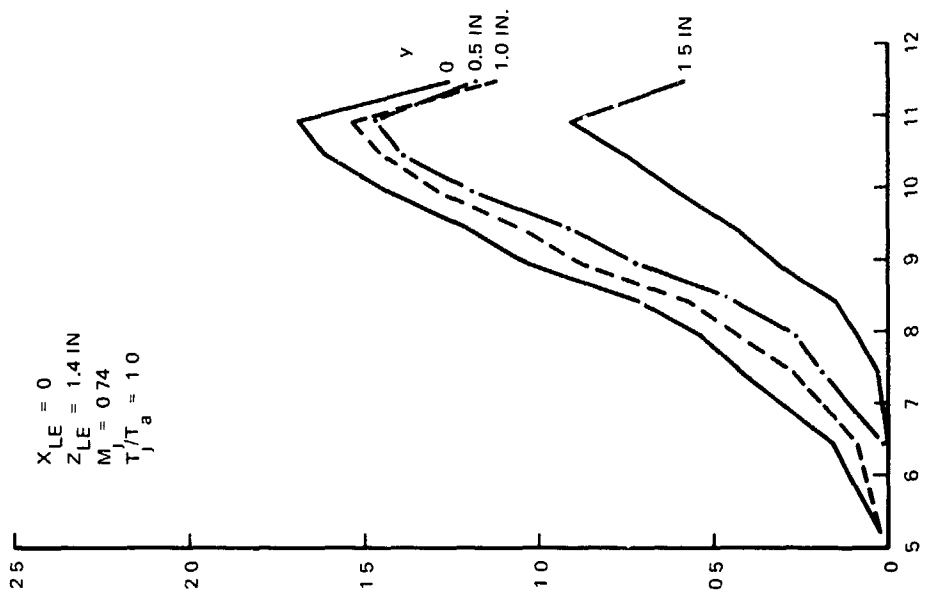
ROUND NOZZLE (D_j = 2 IN)

$\beta_{TE} = 25^\circ$



ROUND NOZZLE (D_j = 2 IN)

$\beta_{TE} = 25^\circ$



s, DISTANCE FROM LEADING EDGE ~ IN.

FIGURE H-3. CONTINUED

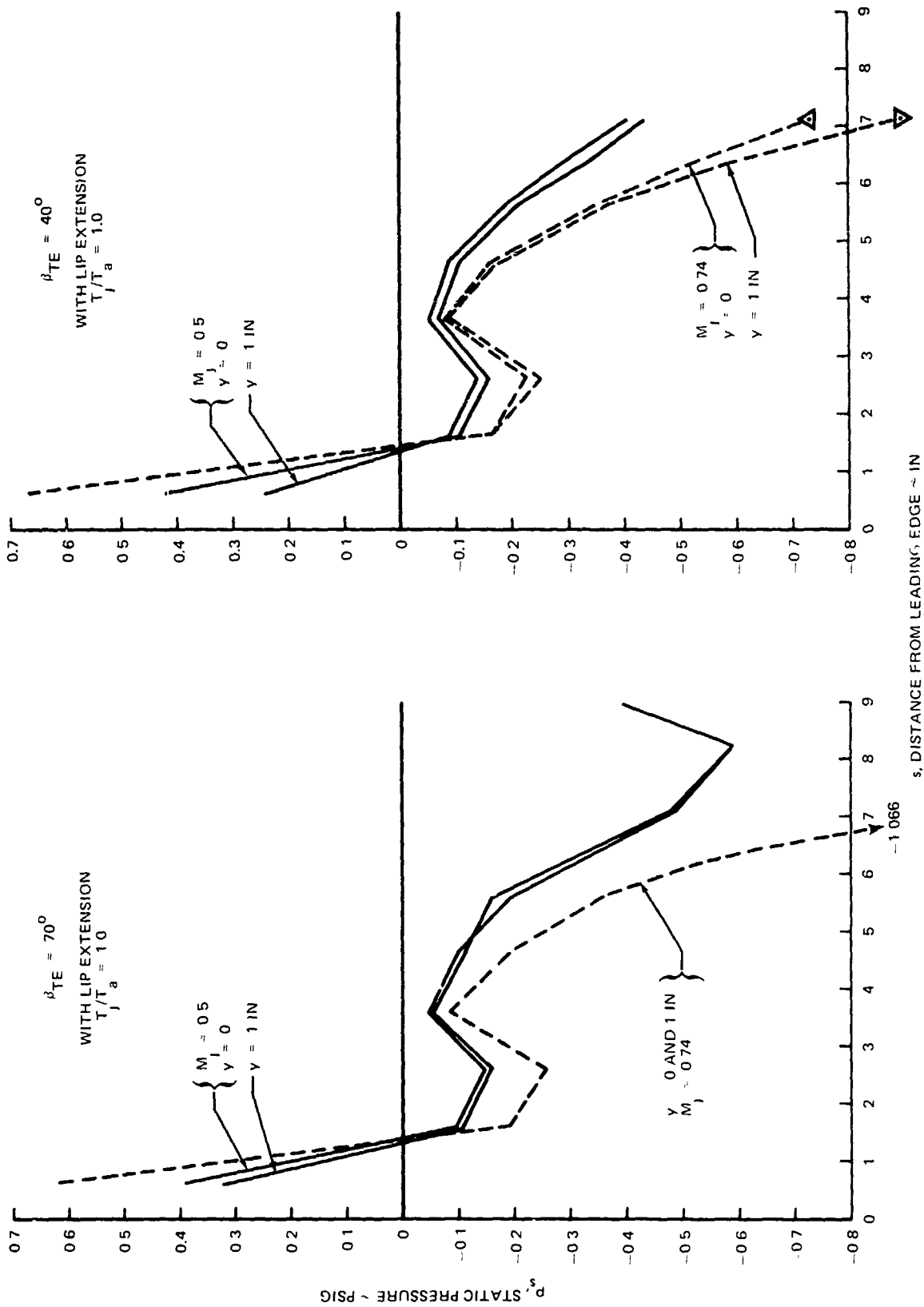


FIGURE H-4. STATIC PRESSURE MEASUREMENTS -- JBF CURVED PLATES

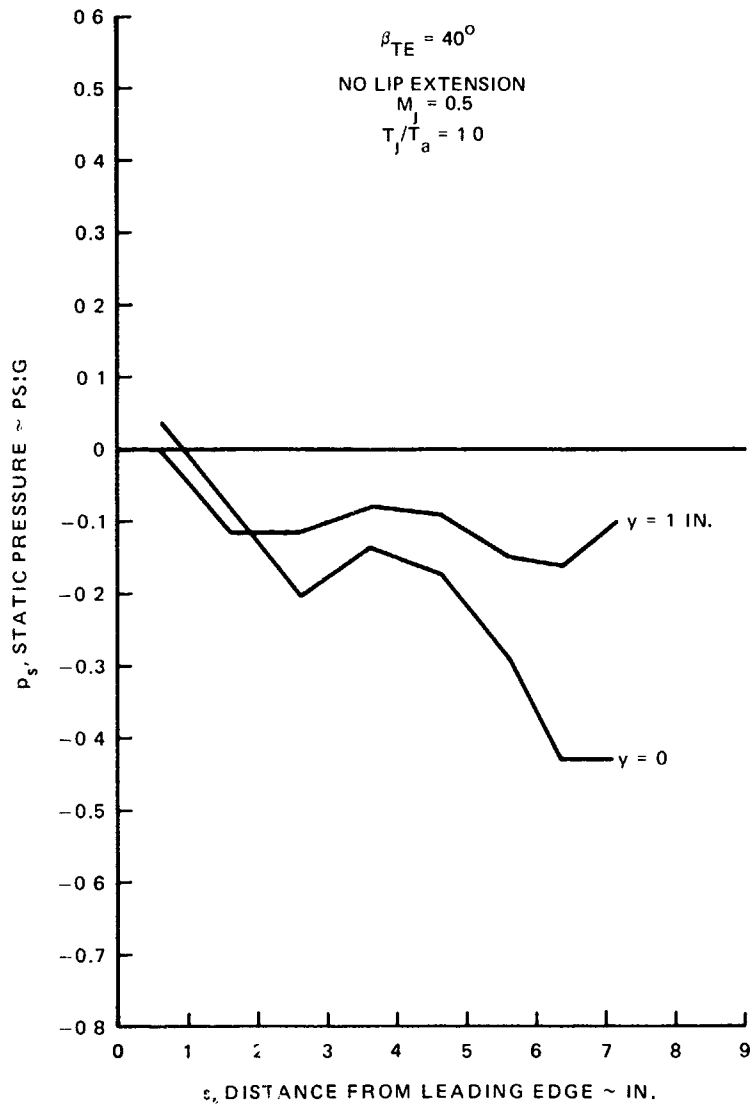


FIGURE H-4. CONTINUED

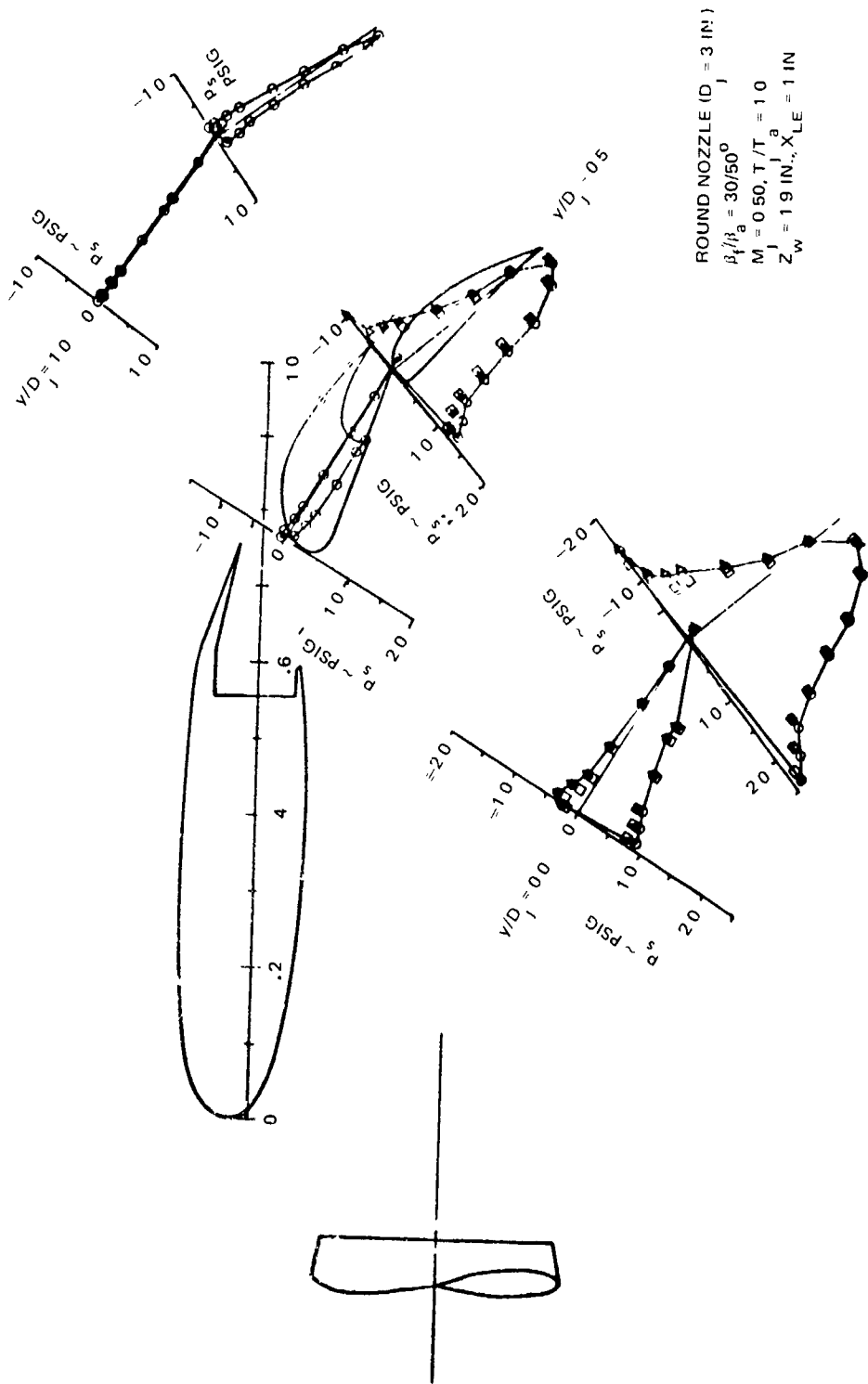


FIGURE H-5. STATIC PRESSURE MEASUREMENTS - WING-FLAPS MODEL

APPENDIX I


FLUCTUATING PRESSURE TRENDS

The surface fluctuating pressure characteristics determined from the test program are more completely reported in Appendix J. A major portion of the tabulated data found in Appendix J is plotted in the following figures to more clearly exhibit trends in the data. The plots show six different characteristics of the fluctuating pressures: (1) overall RMS level, (2) half power frequency, $f_{1/2}$, (3) rolloff exponent of the power spectrum, n , (4) peak amplification, P , of power spectrum, (5) maximum correlation length, L_m (which occurs at frequency f_m), and (6) convection speed V_{cm} at frequency f_m . (See definitions of these quantities in Section II-5).

In the following plots, these fluctuating pressure characteristics are expressed in simple non-dimensional forms as (1) RMS/q_j , (2) $f_{1/2} \times D_j/V_j$, (3) n , (4) P , (5) L_m/D_j and (6) V_{cm}/V_j . The quantities introduced for non-dimensionalizing are the nozzle diameter, D_j , the jet dynamic pressure, q_j , and the jet exit velocity V_j . The quantity q_j is related to the jet Mach No. M_j by $q_j = \gamma P_a M_j^2 / 2$, where $\gamma = 1.4$ and P_a = ambient air pressure = 14.7 psi for test location. The velocity V_j is obtained from M_j and the jet total temperature T_j by the relation $V_j = 49 \times M_j \sqrt{T_j / (1 + .2M_j^2)}$.

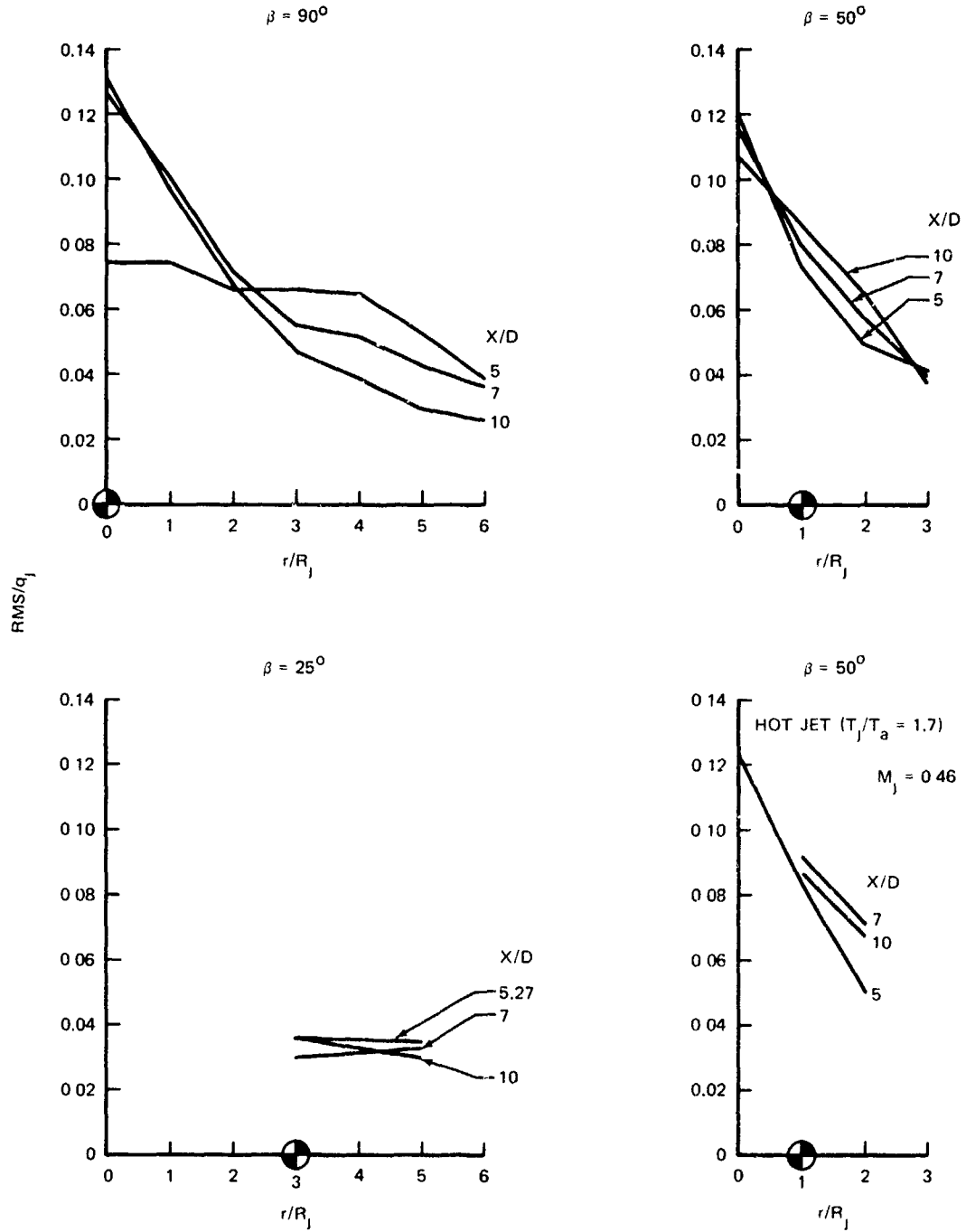
Plots are given for all four test specimens. For each of the non-dimensional characteristics, chordwise (i.e., streamwise) distributions are shown for flat plate and curved plate (UBF and OBF) cases and spanwise distributions for flat plate and wing-flaps cases. The origin for spanwise distributions is at the center of span for all specimens. The distance from the center is specified by y/R_j (where $R_j = D_j/2$) or y/R_{eq} . The latter applies to the lobed and OBF nozzles; the radius R_{eq} is that of a round nozzle having the same exit area. For both of these nozzles R_{eq} is 1 inch.

The origin to which each chordwise distribution is referenced on the

flat plate is taken near to the stagnation point; i.e., the static pressure port giving maximum static pressure (see plots in Appendix H). Specifically, the origin was taken at 0, 1 and 3 radii upstream from the center of impingement for plate inclination angles $\beta = 90^\circ$, 50° and 25° , respectively. The location of the center of impingement is marked on the plots with the symbol .

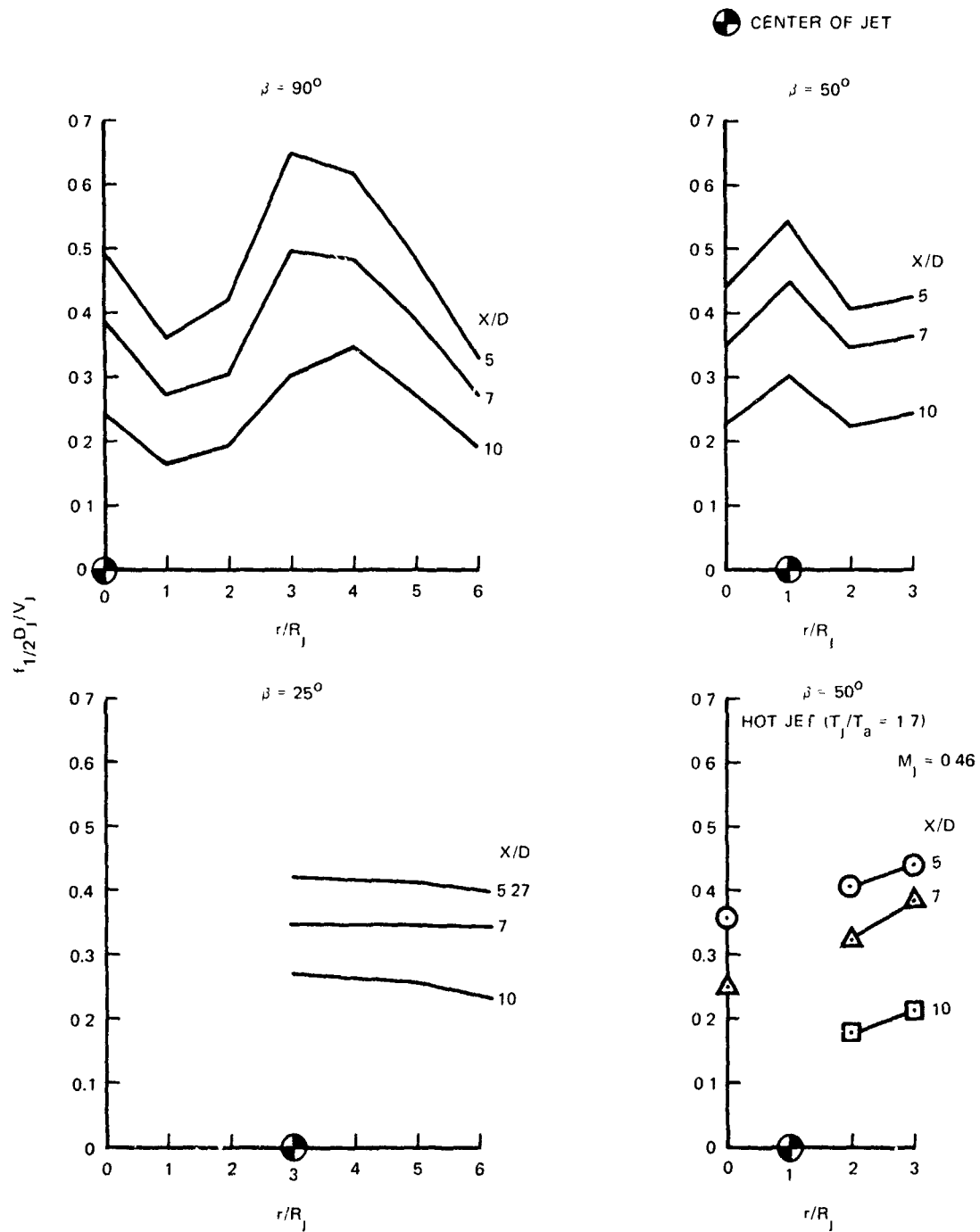
The origin for the chordwise distributions on the UBF and OBF curved plates is the leading edge of the plates. Distances from the leading edge are designated by s/R_j or s/R_{eq} .

● CENTER OF JET



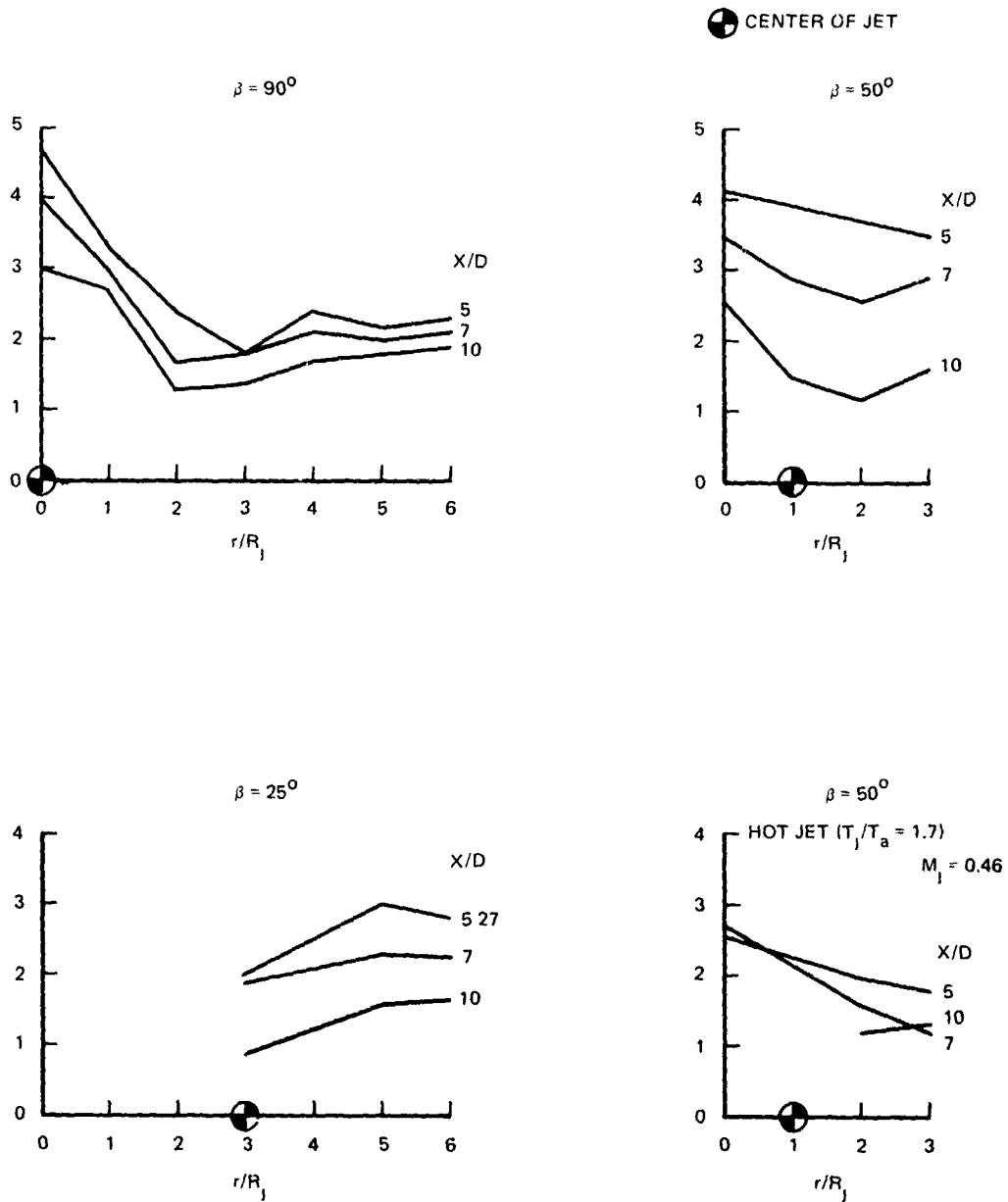
UNLESS NOTED ROUND NOZZLE ($D_j = 1$ IN), COLD JET ($T_j/T_a = 1$), $M_j = 0.5$, $v/R_j = 0$

FIGURE I-1. TREND DATA FOR RMS LEVEL ALONG CENTERLINE CHORD — FLAT PLATE CONFIGURATION



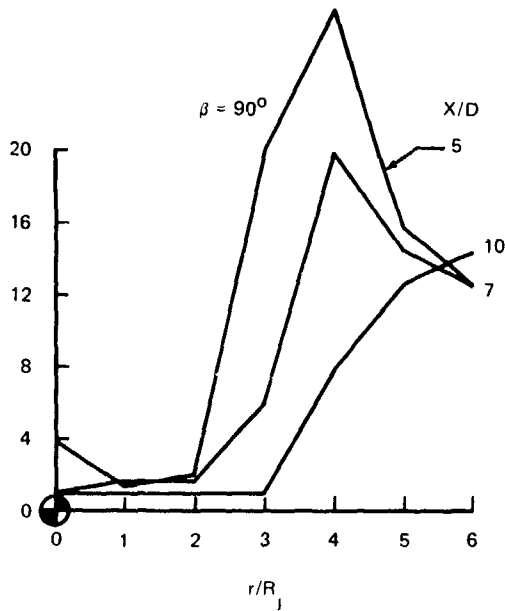
UNLESS NOTED ROUND NOZZLE ($D_j = 1$ IN.), COLD JET ($T_j/T_a = 1$), $M_j = 0.5$, $v/R_j = 0$

FIGURE I-2. TREND DATA FOR SPECTRUM HALF POWER FREQUENCY ALONG CENTERLINE CHORD - FLAT PLATE CONFIGURATION

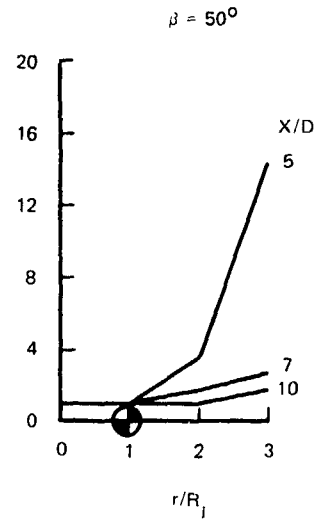


UNLESS NOTED: ROUND NOZZLE ($D_j = 1$ IN.), COLD JET ($T_j/T_a = 1$), $M_j = 0.5$, $y/R_j = 0$

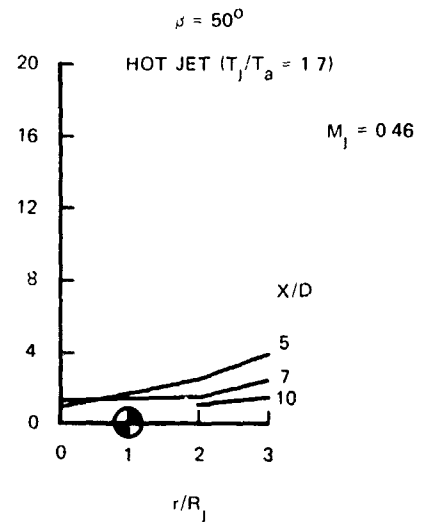
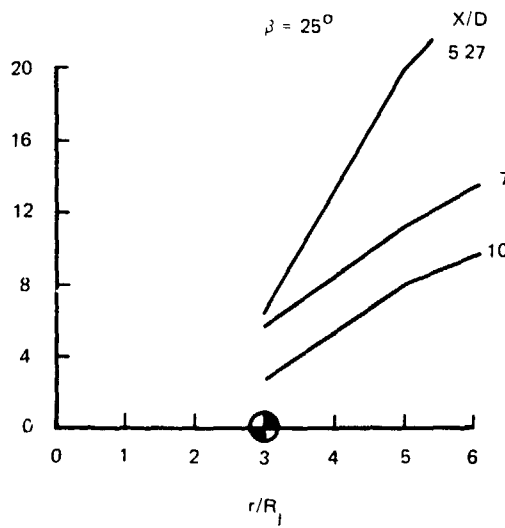
FIGURE I-3. TREND DATA FOR SPECTRUM ROLLOFF EXPONENT ALONG CENTERLINE CHORD - FLAT PLATE CONFIGURATION



● CENTER OF JET



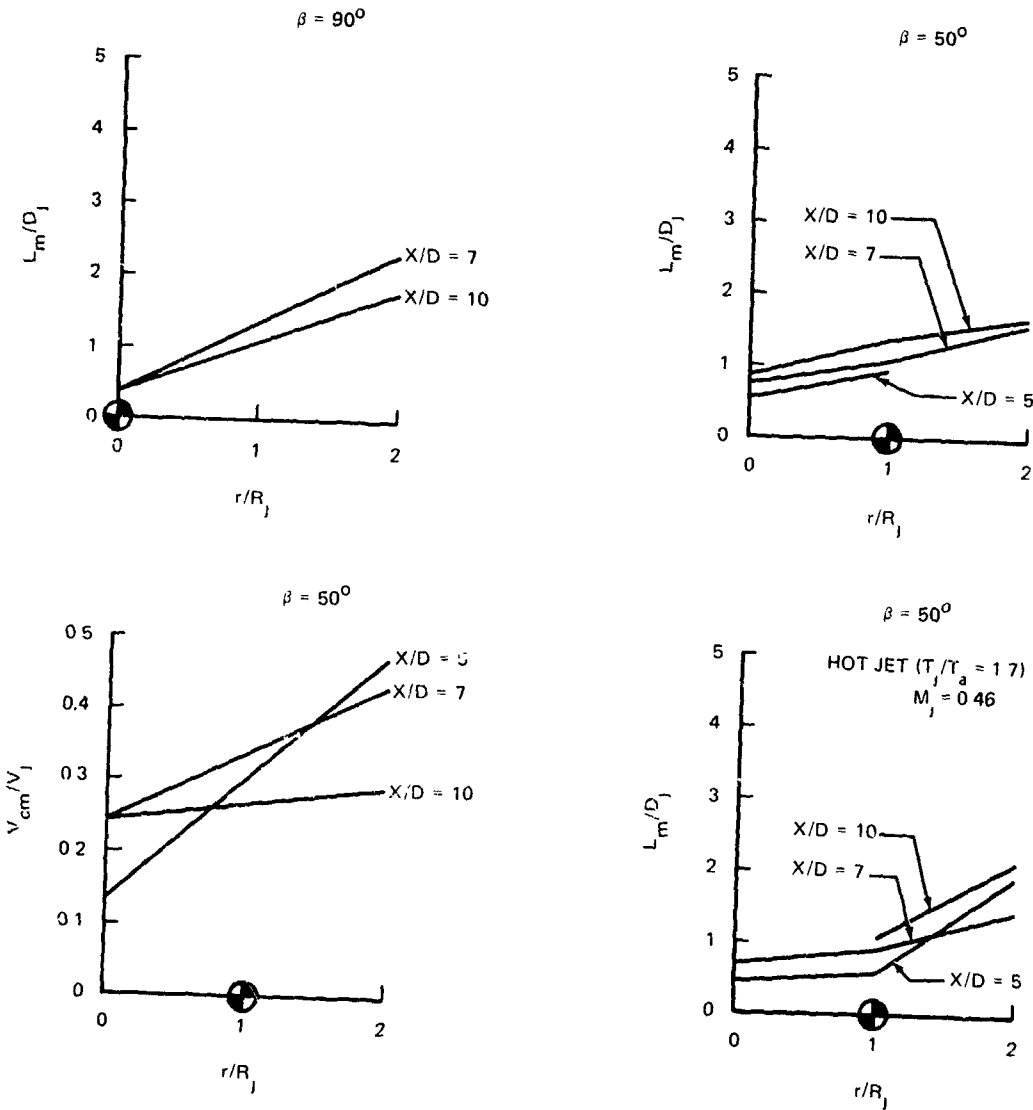
P



UNLESS NOTED ROUND NOZZLE ($D_j = 1$ IN.), COLD JET ($T_j/T_a = 1$), $M_j = 0.5$, $v/R_j = 0$

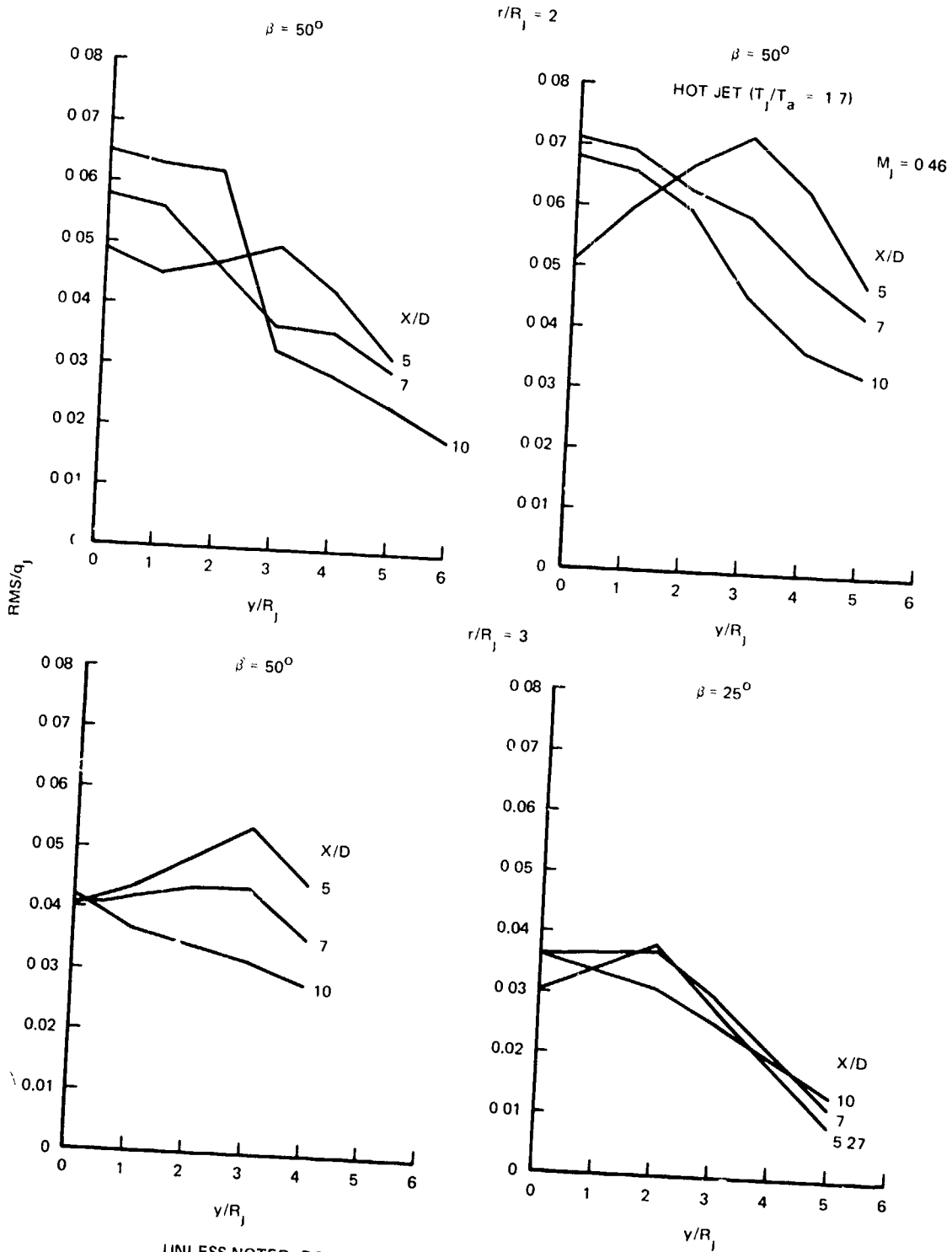
FIGURE I-4. TREND DATA FOR SPECTRUM PEAK AMPLIFICATION ALONG CENTERLINE CHORD - FLAT PLATE CONFIGURATION

⊕ CENTER OF JET



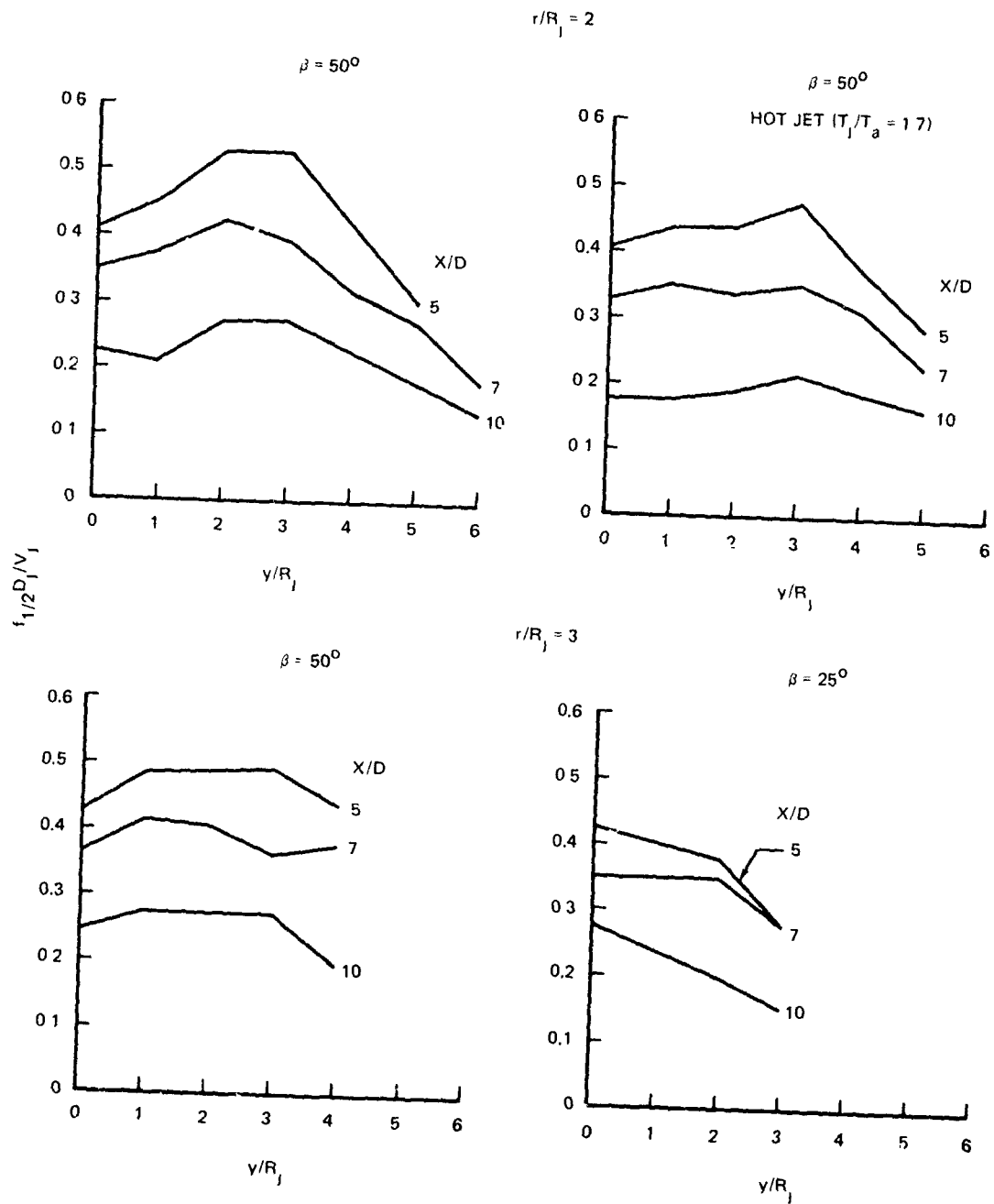
UNLESS NOTED ROUND NOZZLE ($D_j = 1$ IN), COLD JET ($T_j/T_a = 1$), $M_j = 0.5$, $v/R_j = 0$

FIGURE 1-5. TREND DATA FOR CORRELATION LENGTHS AND CONVECTION SPEEDS ALONG CENTERLINE CHORD - FLAT PLATE CONFIGURATION



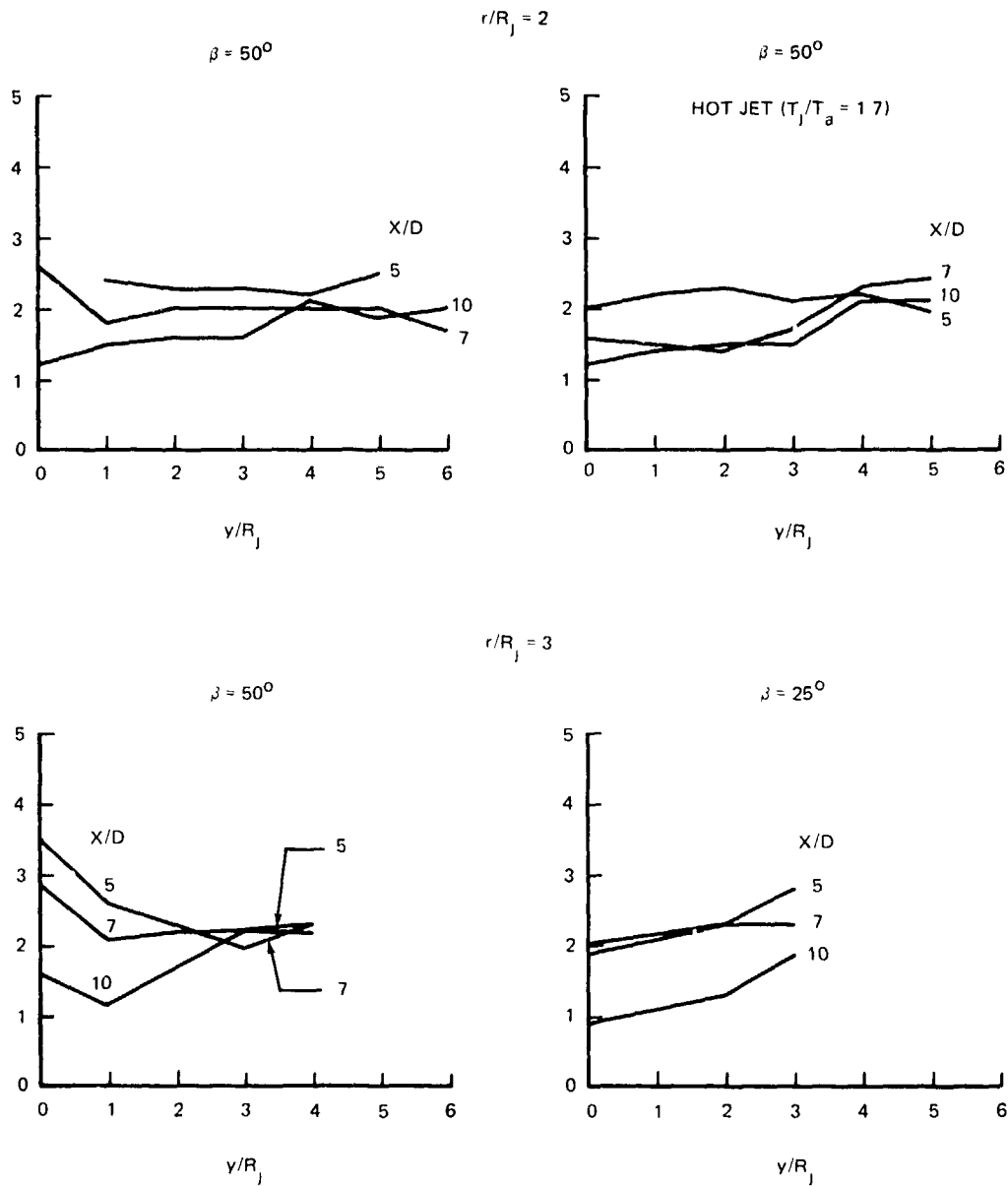
UNLESS NOTED ROUND NOZZLE ($D_j = 1$ IN.), COLD JET ($T_j/T_a = 1$), $M_j = 0.5$

FIGURE I-6. TREND DATA FOR RMS LEVEL ALONG SPAN LINES - FLAT PLATE CONFIGURATION



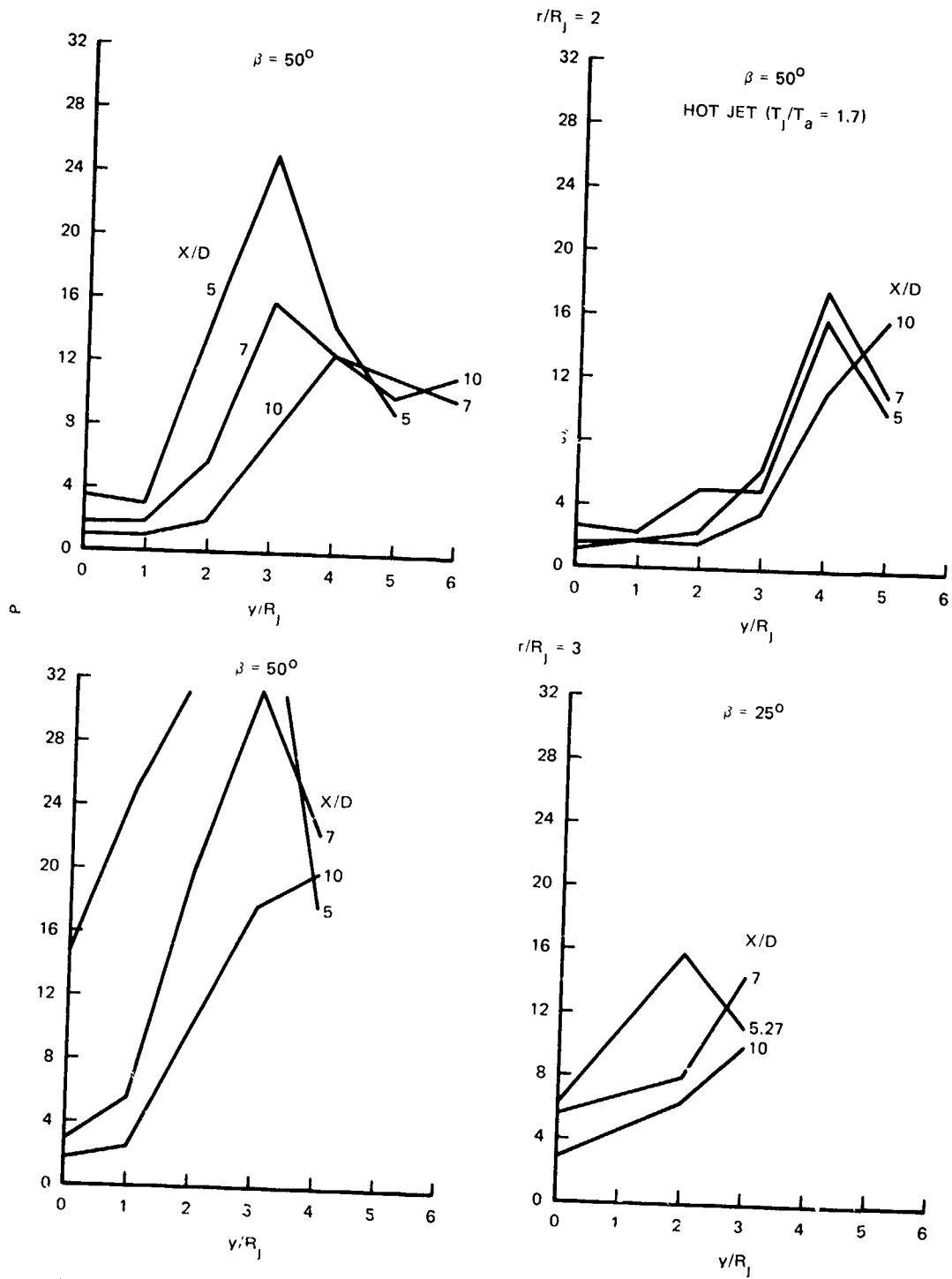
UNLESS NOTED ROUND NOZZLE ($D_j = 1$ IN.), COLD JET ($T_j/T_a = 1$), $M_j = 0.5$

FIGURE I-7. TREND DATA FOR SPECTRUM HALF POWER FREQUENCY ALONG SPAN LINES - FLAT PLATE CONFIGURATION



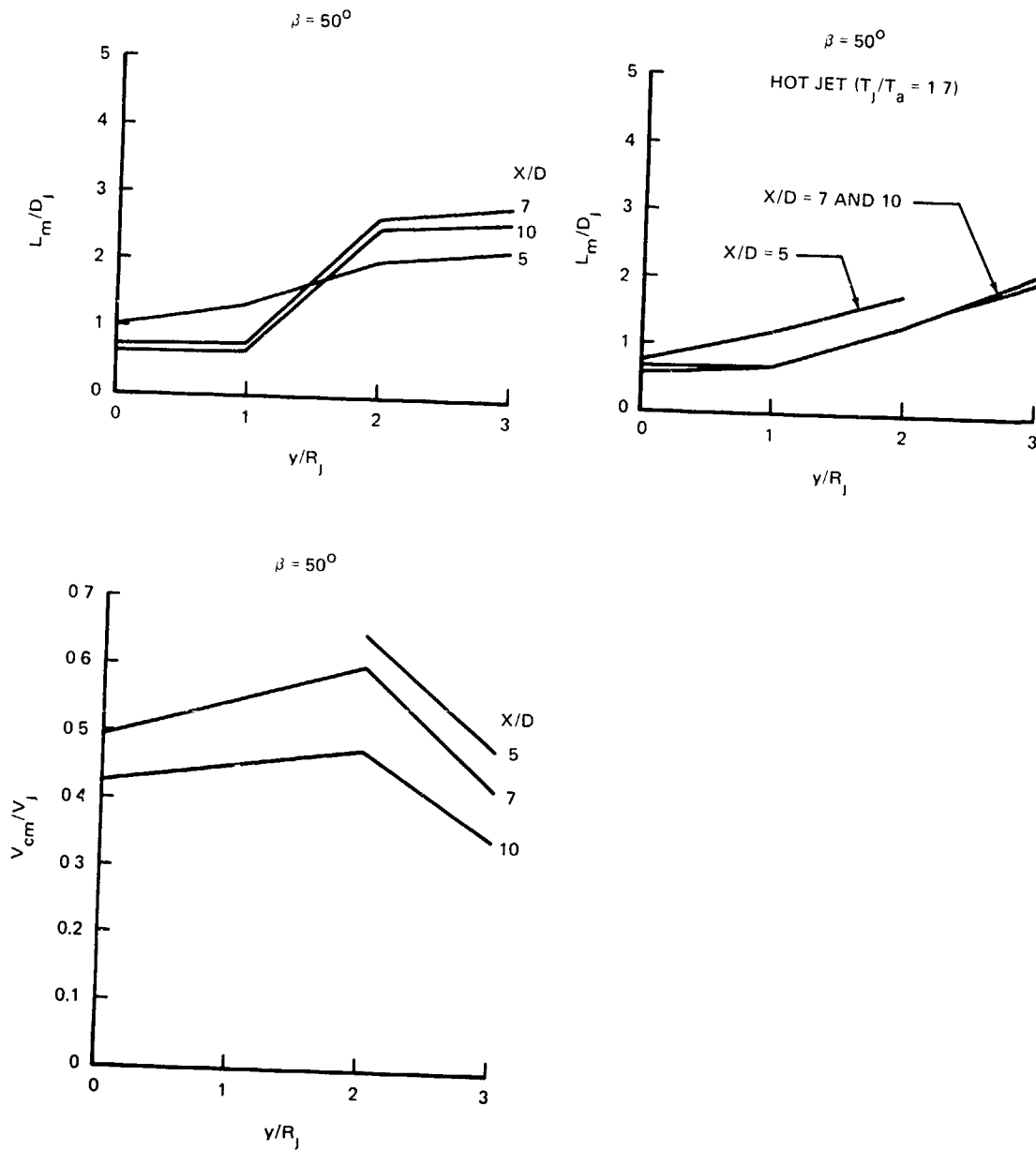
UNLESS NOTED · ROUND NOZZLE ($D_j = 1$ IN), COLD JET ($T_j/T_a = 1$), $M_j = 0.5$

FIGURE I-8. TREND DATA FOR SPECTRUM ROLLOFF EXPONENT ALONG SPAN LINES – FLAT PLATE CONFIGURATION



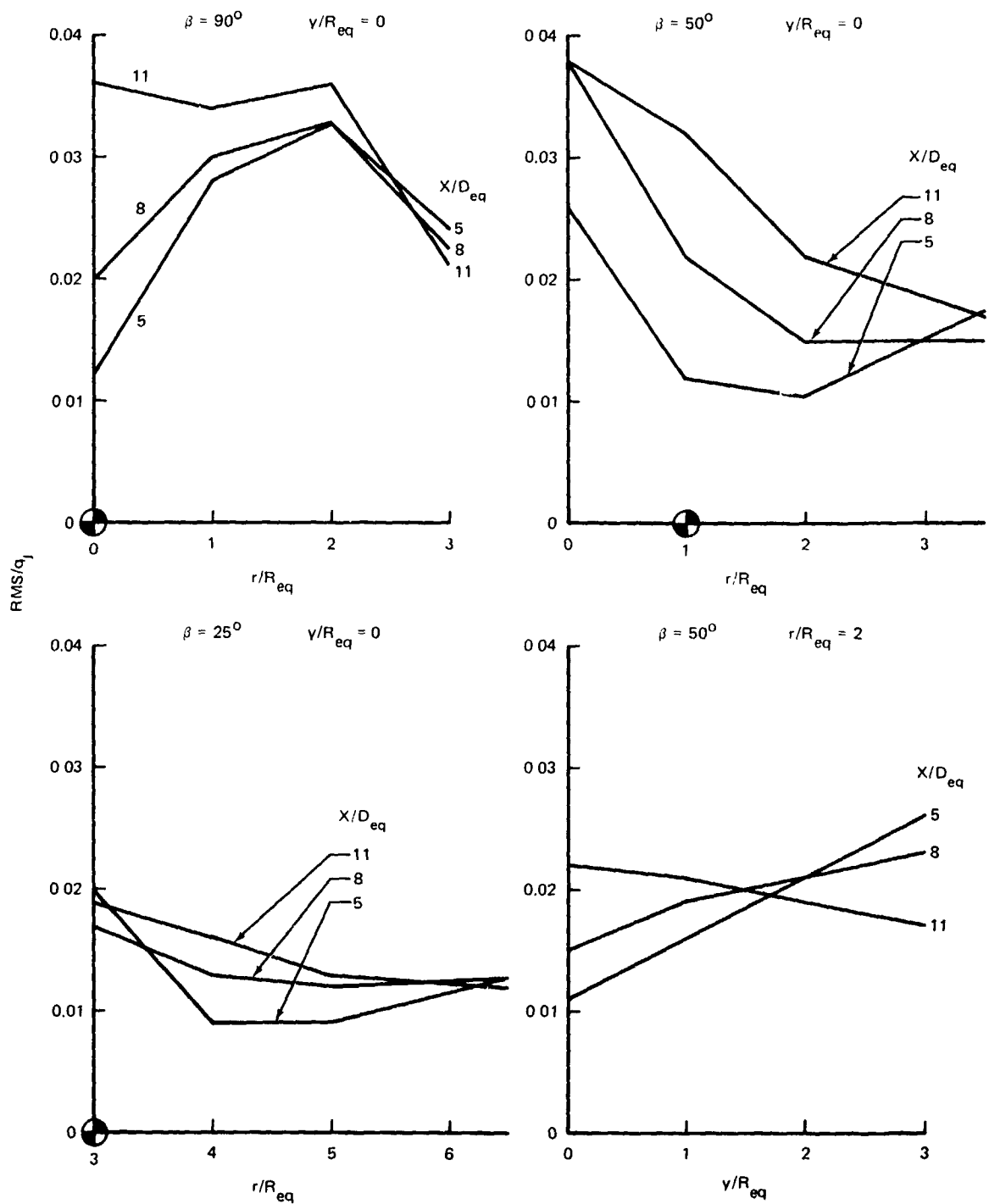
UNLESS NOTED ROUND NOZZLE ($D_j = 1$ IN.), COLD JET ($T_j/T_a = 1$), $M_j = 0.5$

FIGURE I-9. TREND DATA FOR SPECTRUM PEAK AMPLIFICATION ALONG SPAN LINES -- FLAT PLATE CONFIGURATION



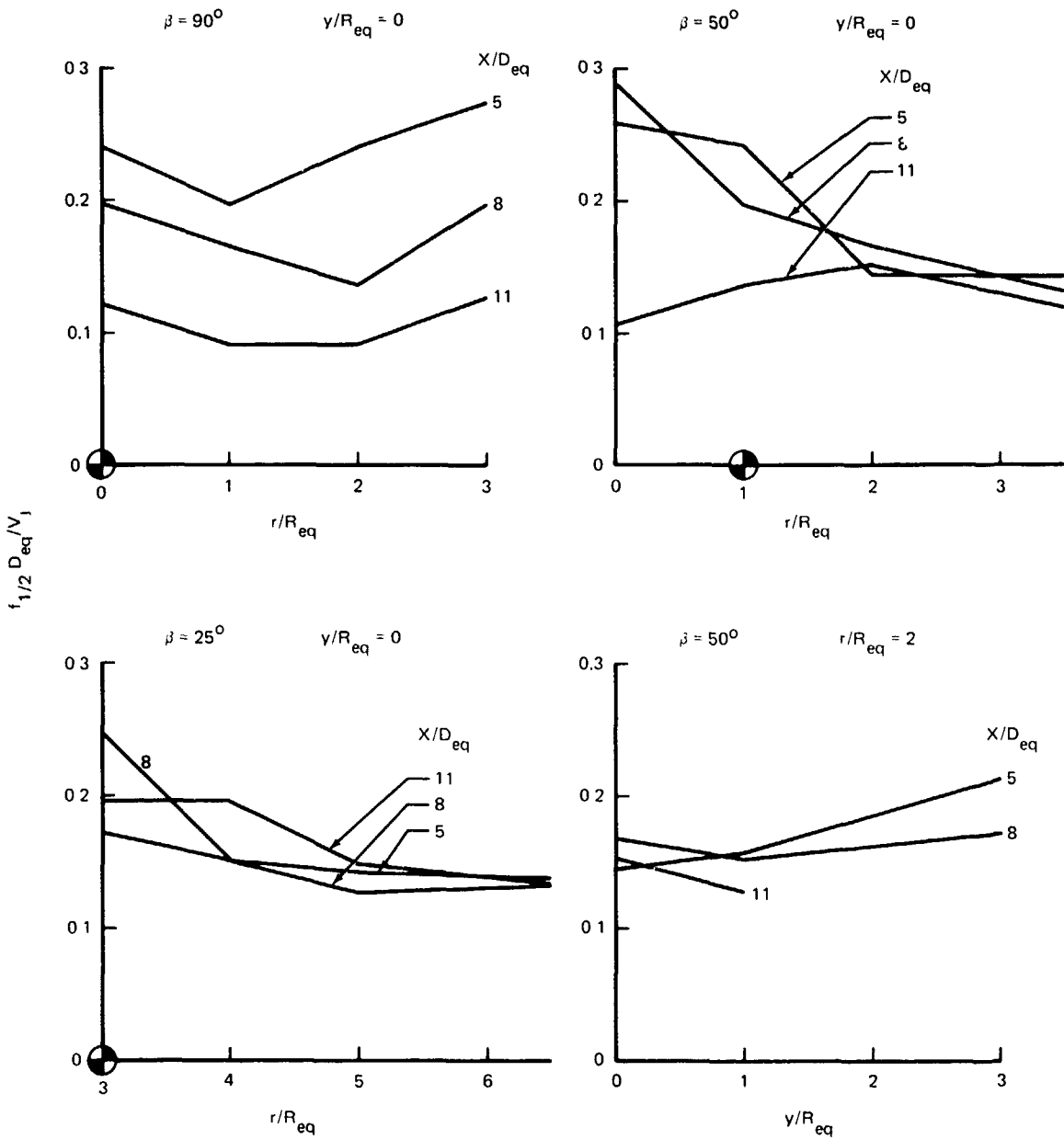
UNLESS NOTED ROUND NOZZLE ($D_j = 1$ IN.), COLD JET ($T_j/T_a = 1$), $M_j = 0.5$, $r/R_j = 2$

FIGURE I-10. TREND DATA FOR CORRELATION LENGTHS AND CONVECTION SPEEDS ALONG SPAN LINES - FLAT PLATE CONFIGURATION



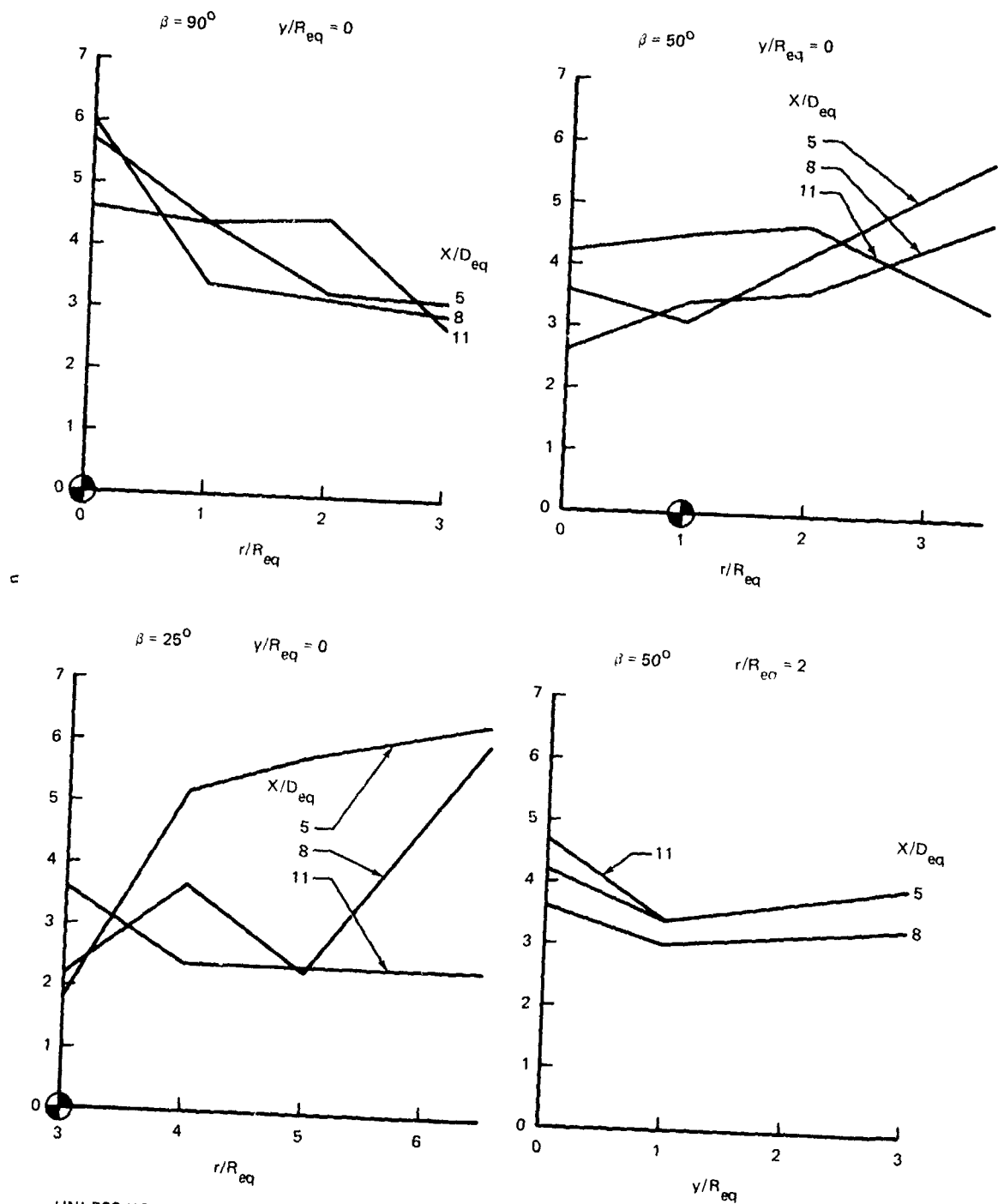
UNLESS NOTED · DAISY NOZZLE ($D_{eq} = 2$ IN.), COLD JET ($T_j/T_a = 1$), $M_j = 0.5$

FIGURE I-11. TREND DATA FOR RMS LEVEL - FLAT PLATE CONFIGURATION - DAISY NOZZLE



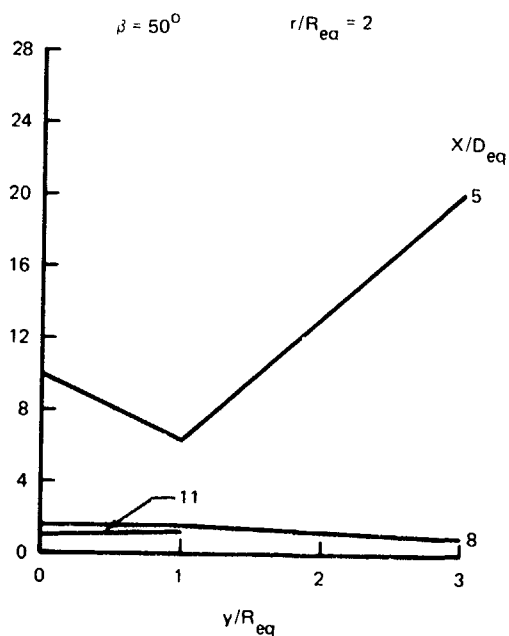
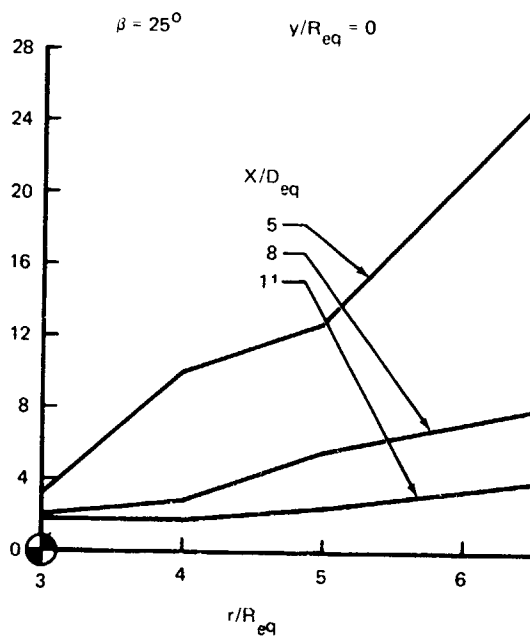
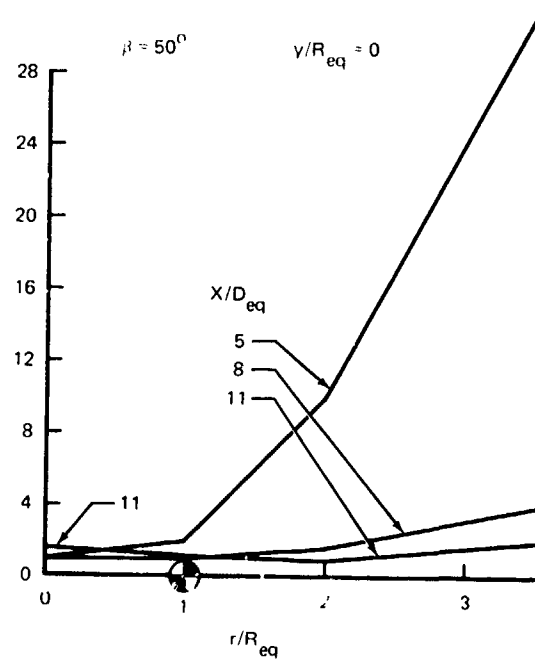
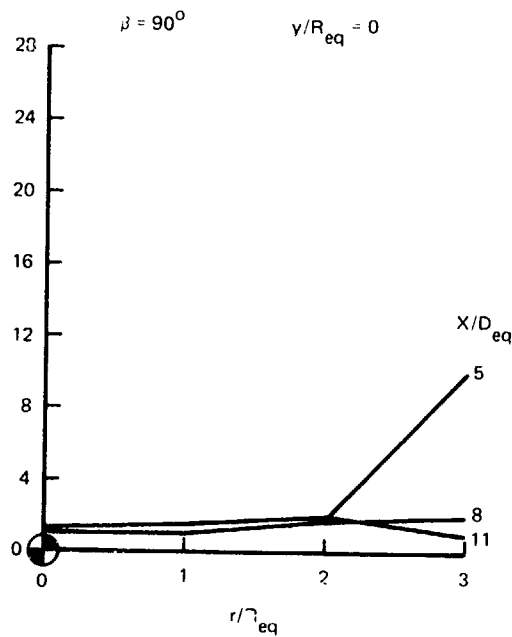
UNLESS NOTED DAISY NOZZLE ($D_{eq} = 2$ IN.), COLD JET ($T_j/T_a = 1$), $M_j = 0.5$

FIGURE I-12. TREND DATA FOR SPECTRUM HALF POWER FREQUENCY - FLAT PLATE CONFIGURATION - DAISY NOZZLE



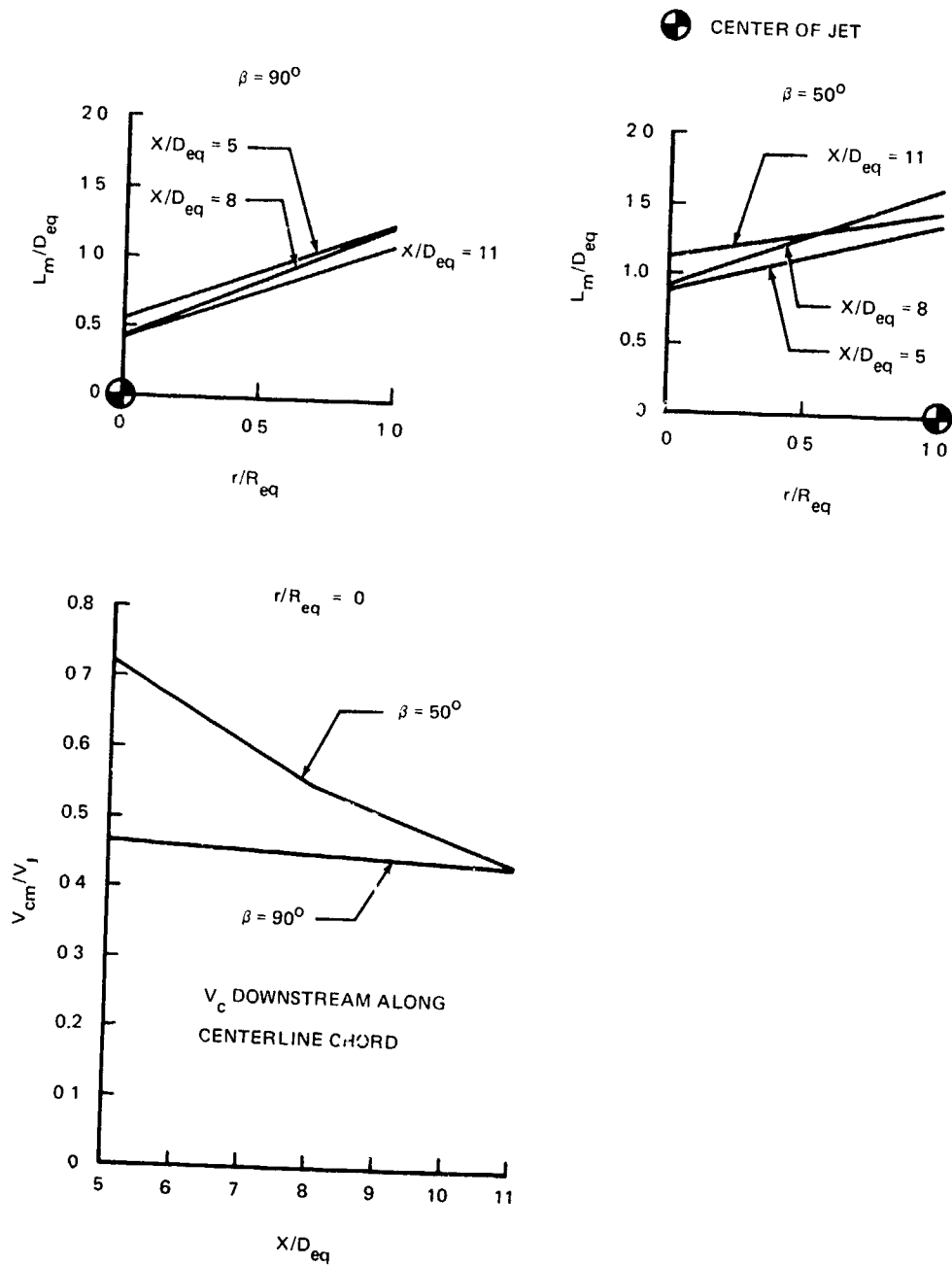
UNLESS NOTED DAISY NOZZLE ($D_{eq} = 2$ IN), COLD JET ($T_1/T_2 = 1$), $M_1 = 0.5$

FIGURE I-13. TREND DATA FOR SPECTRUM ROLLOFF EXPONENT - FLAT PLATE CONFIGURATION - DAISY NOZZLE



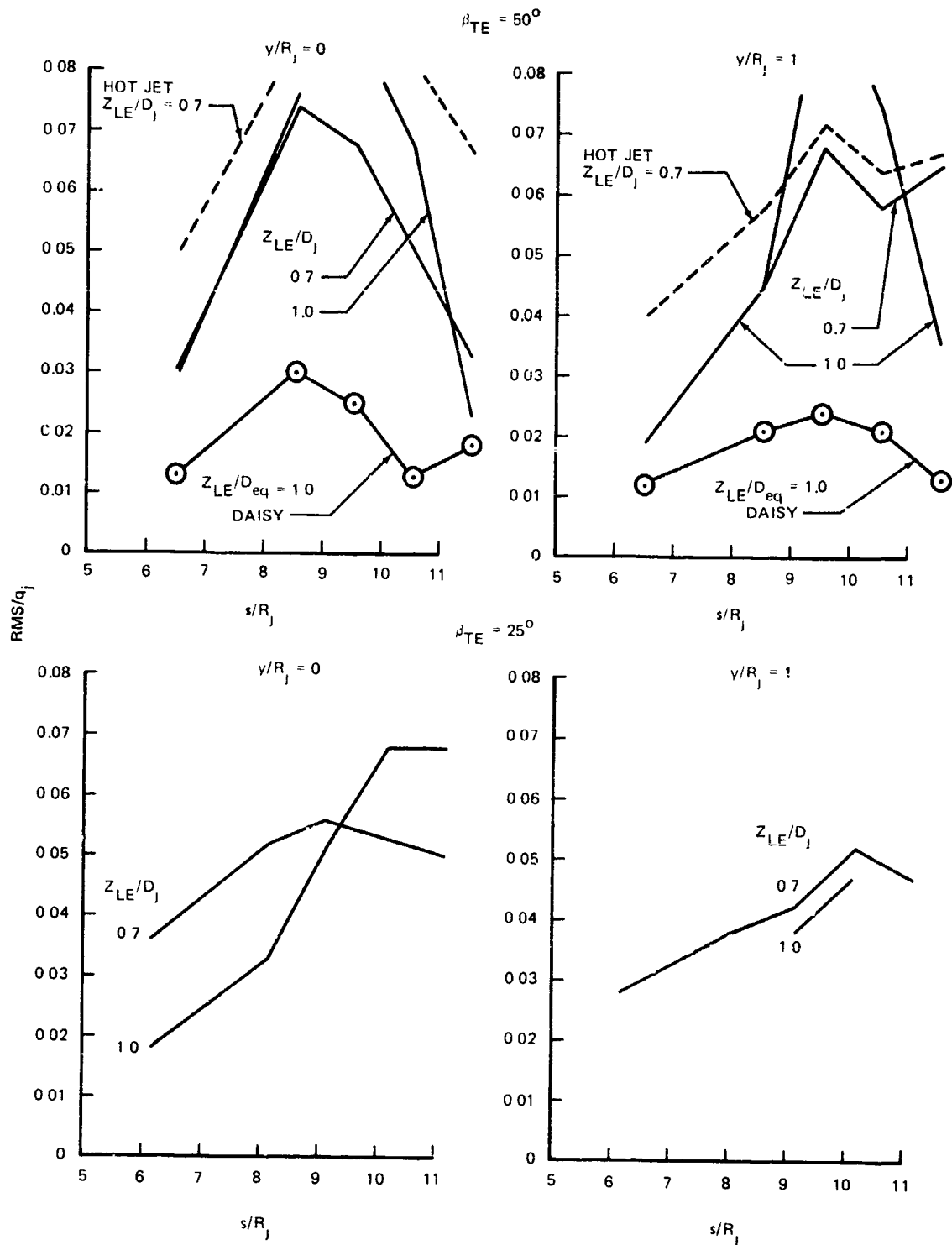
UNLESS NOTED. DAISY NOZZLE ($D_{eq} = 2$ IN.), COLD JET ($T_j/T_a = 1$), $M_j = 0.5$

FIGURE I-14. TREND DATA FOR SPECTRUM PEAK AMPLIFICATION - FLAT PLATE CONFIGURATION - DAISY NOZZLE



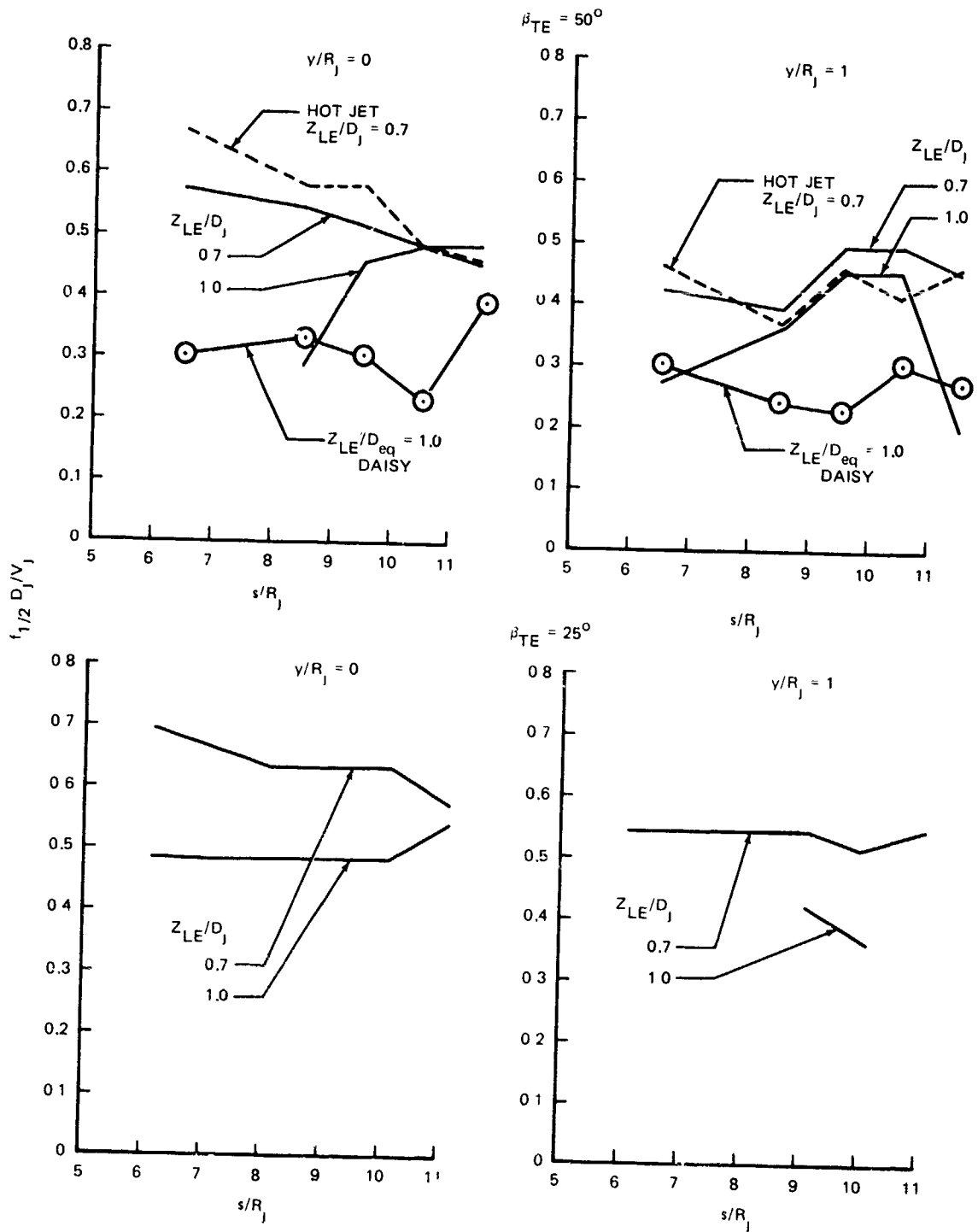
UNLESS NOTED DAISY NOZZLE ($D_{eq} = 2$ IN.), COLD JET ($T_j/T_a = 1$), $M_j = 0.5$, $r/R_{eq} = 0$

FIGURE I-15. TREND DATA FOR CORRELATION LENGTHS AND CONVECTION SPEEDS - FLAT PLATE CONFIGURATION - DAISY NOZZLE



UNLESS NOTED ROUND NOZZLE ($D_j = 2$ IN.), COLD JET ($T_j/T_a = 1$), $M_j = 0.5$, $X_{LE}/D_j = 0$

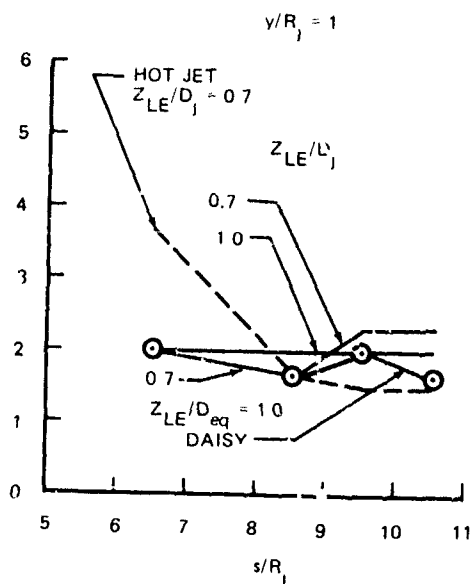
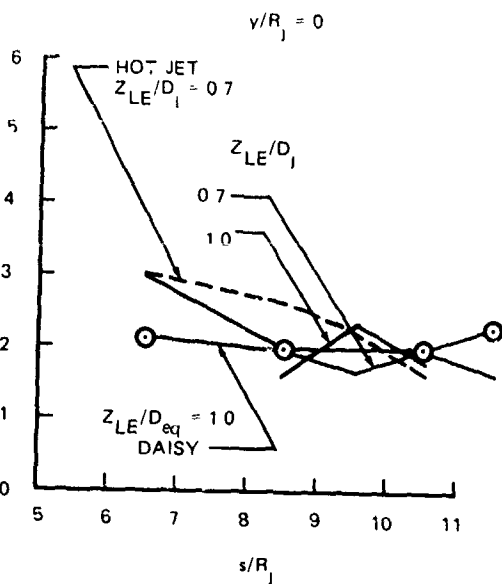
FIGURE I-16. TREND DATA FOR RMS LEVEL - UBF CURVED PLATE CONFIGURATION



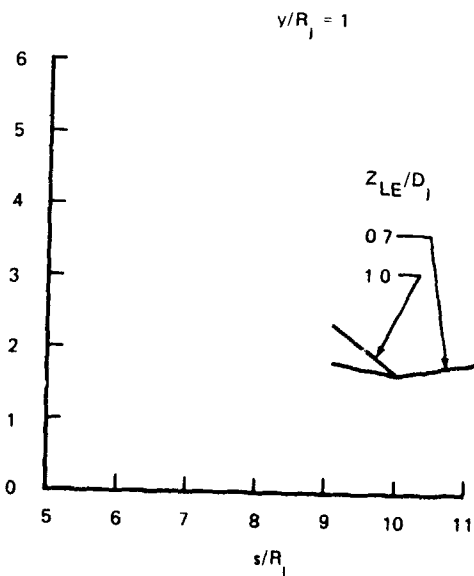
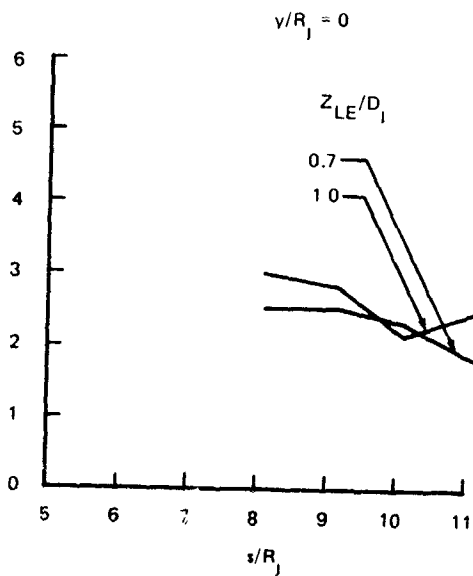
UNLESS NOTED ROUND NOZZLE ($D_j = 2$ IN.) COLD JET ($T_j/T_a = 1$), $M_j = 0.5$, $X_{LE}/D_j = 0$

FIGURE I-17. TREND DATA FOR SPECTRUM HALF POWER FREQUENCY - UBF CURVED PLATE CONFIGURATION.

$\beta_{TE} = 50^\circ$



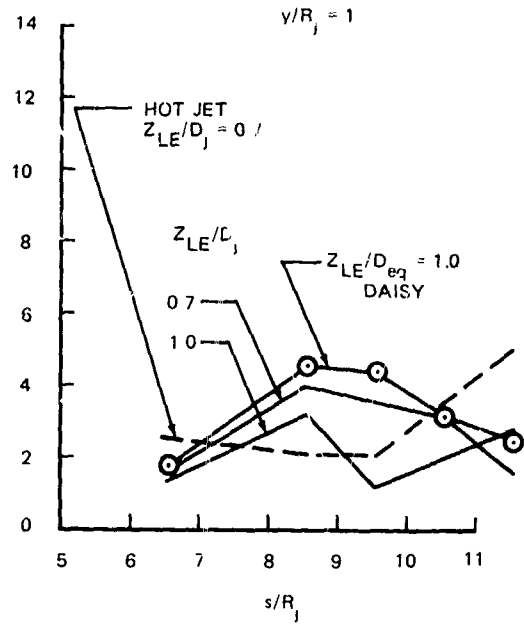
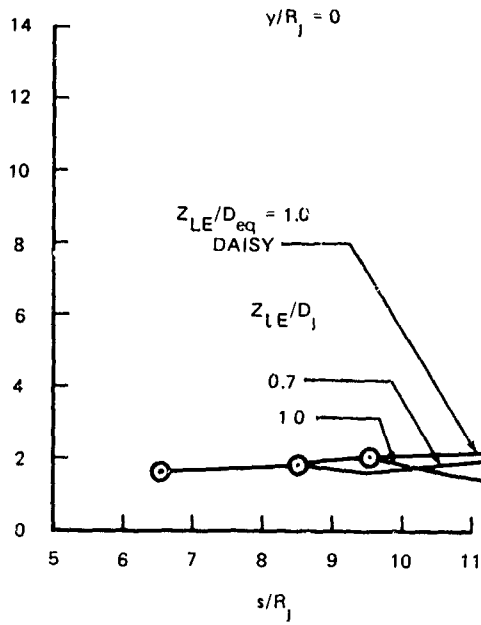
$\beta_{TE} = 25^\circ$



UNLESS NOTED: ROUND NOZZLE ($D_j = 2$ IN.), COLD JET ($T_j/T_a = 1$), $M_j = 0.5$, $X_{LE}/D_j = 0$

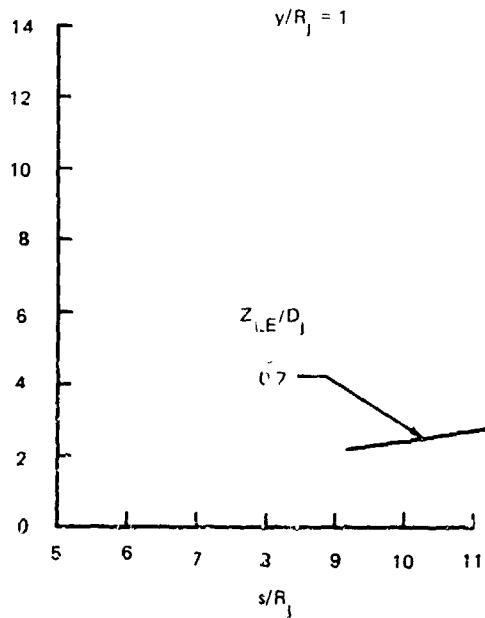
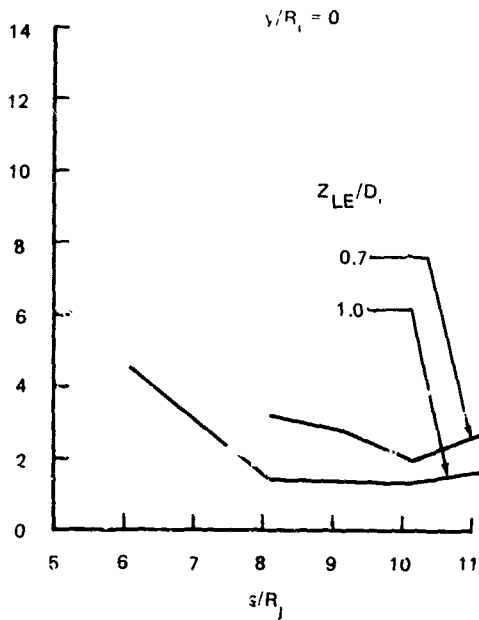
FIGURE I-18. TREND DATA FOR SPECTRUM ROLLOFF EXPONENT - UBF CURVED PLATE CONFIGURATION

$\beta_{TE} = 50^\circ$



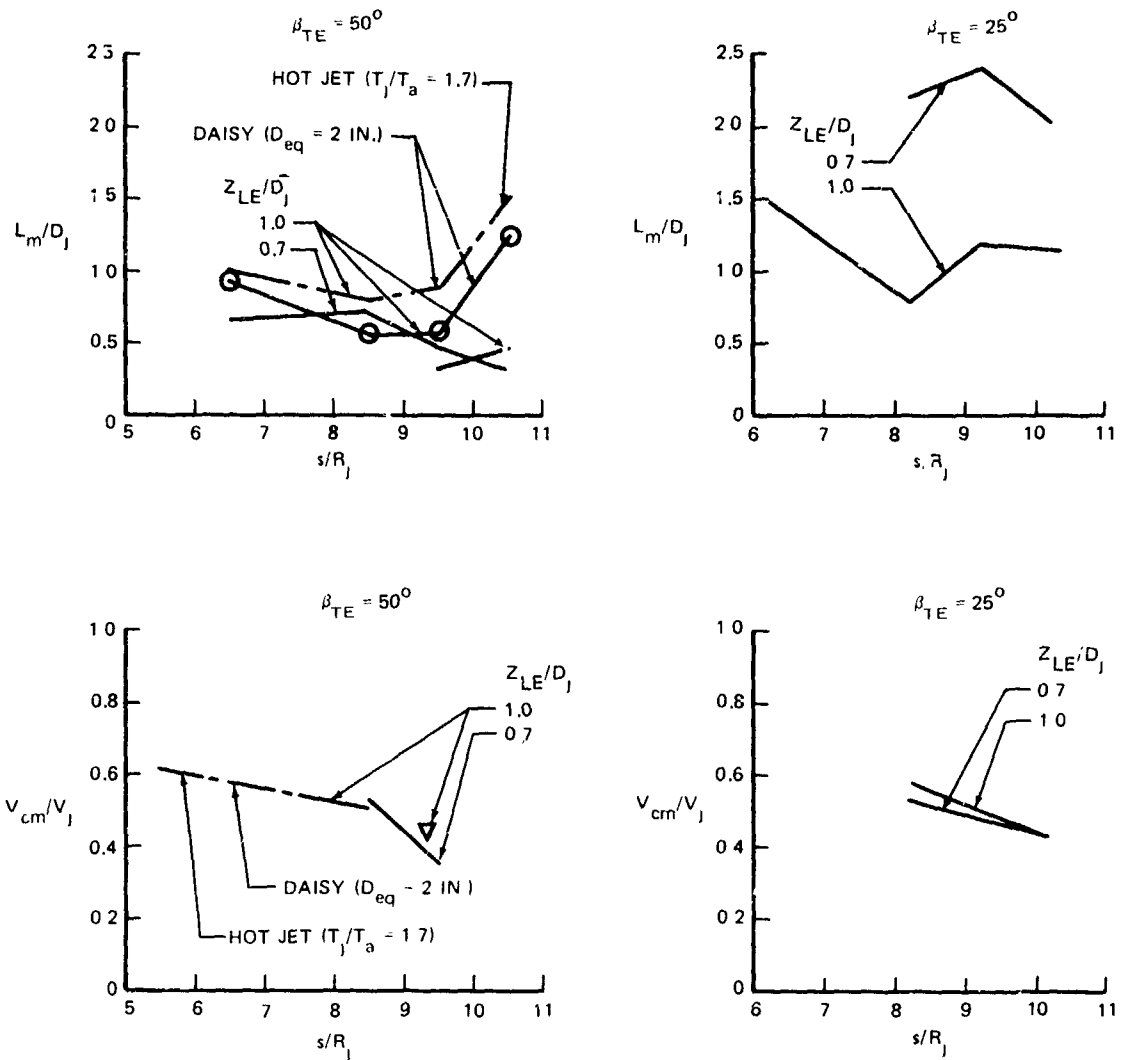
L

$\beta_{TE} = 25^\circ$



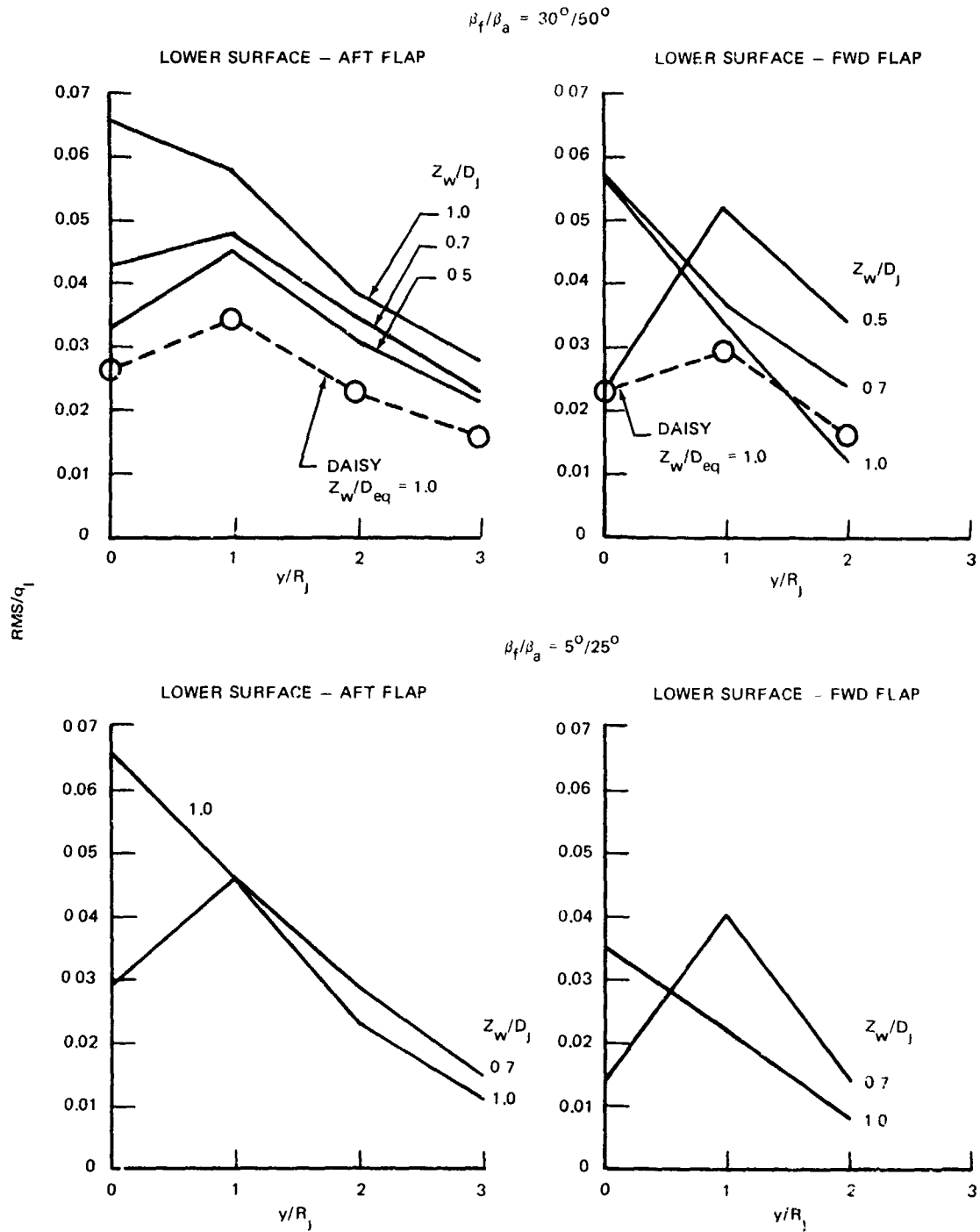
UNLESS NOTED - ROUND NOZZLE ($D_j = 2$ IN), COLD JET ($T_j/T_a = 1$), $M_j = 0.5$, $X_{LE}/D_j = 0$

FIGURE I-19. TREND DATA FOR SPECTRUM PEAK AMPLIFICATION - UBF CURVED PLATE CONFIGURATION



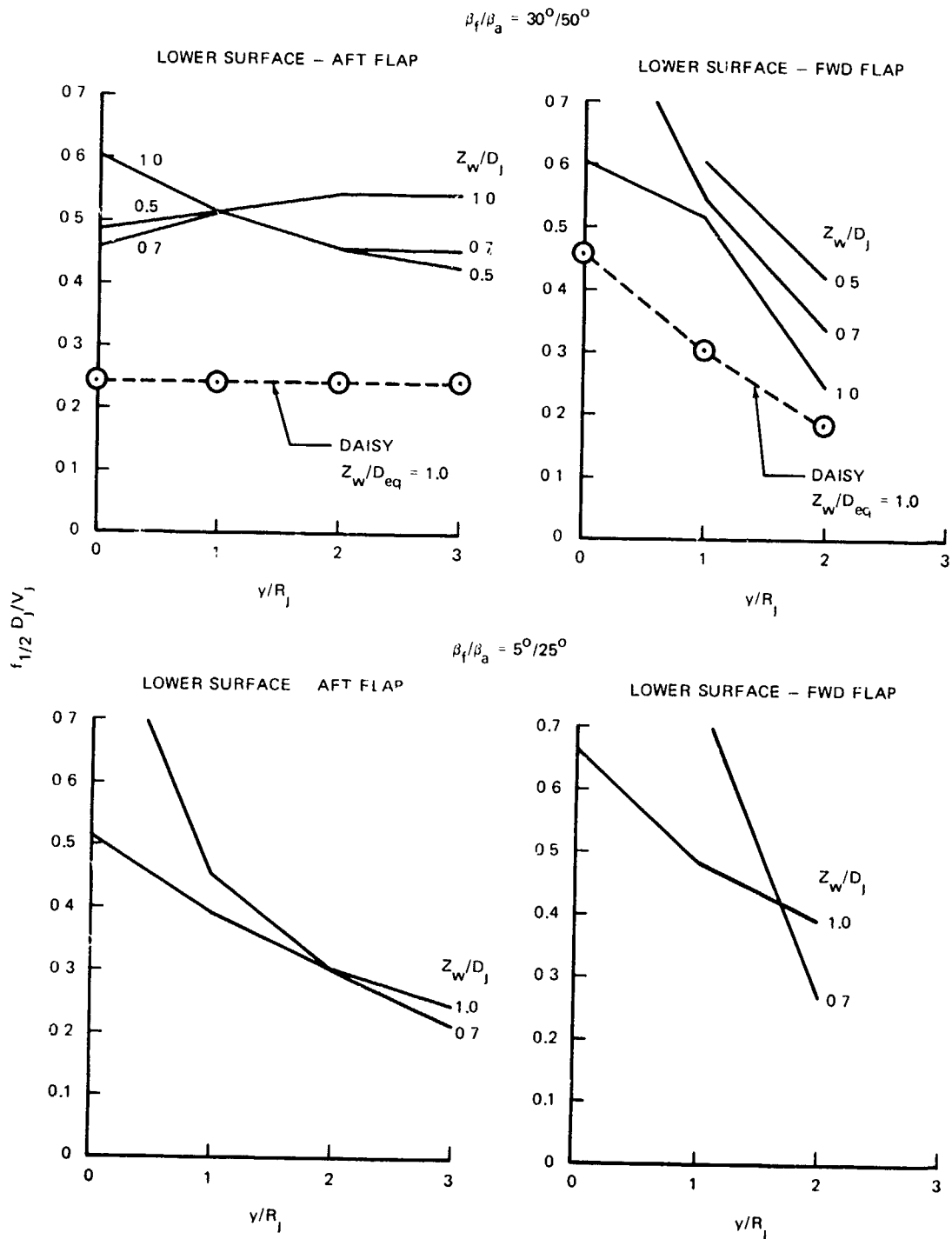
UNLESS NOTED ROUND NOZZLE ($D_j = 2$ IN.), COLD JET ($T_j/T_a = 1$), $M_j = 0.5$, $X_{LE}/D_j = 0$, $v/R_j = 0$

FIGURE I-20. TREND DATA FOR CORRELATION LENGTHS AND CONVECTION SPEEDS - UBF CURVED PLATE CONFIGURATION



UNLESS NOTED: ROUND NOZZLE ($D_j = 2$ IN.), COLD JET ($T_j/T_a = 1$), $M_j = 0.5$, $X_{LE}/D_j = 0$

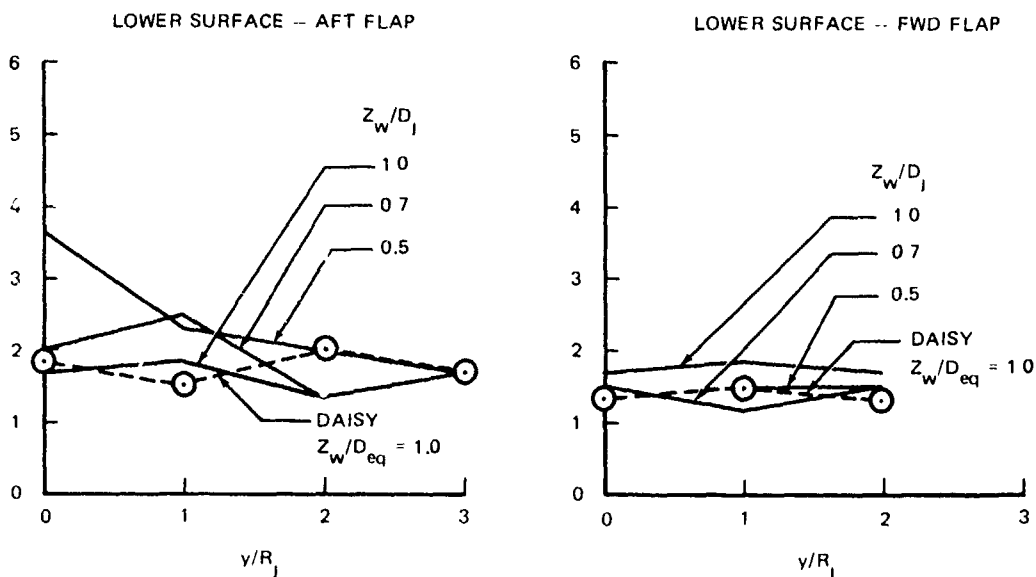
FIGURE I-21. TREND DATA FOR RMS LEVEL - WING-FLAPS CONFIGURATION



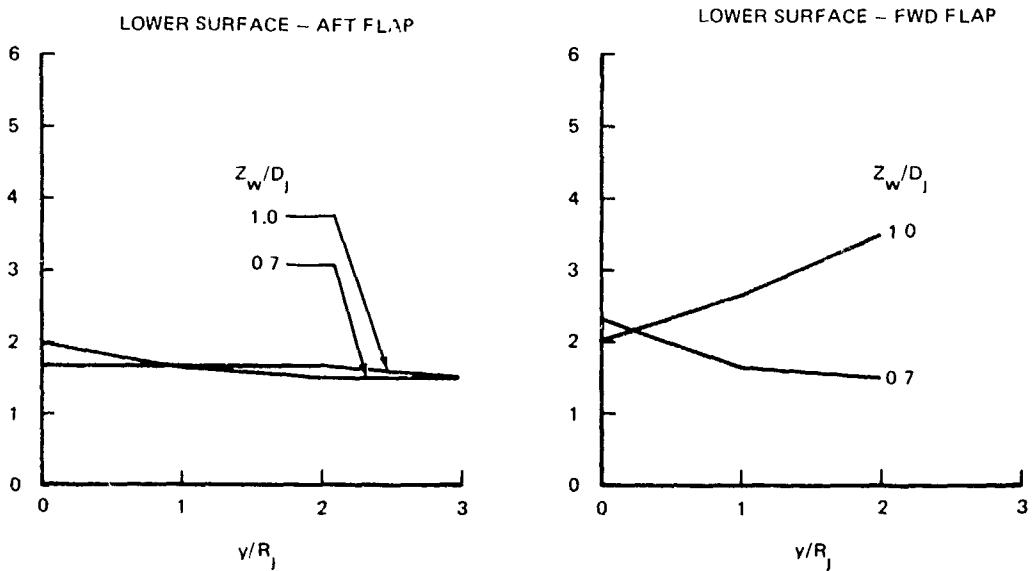
UNLESS NOTED - ROUND NOZZLE ($D_j = 2$ IN), COLD JET ($T_j/T_a = 1$), $M_j = 0.5$, $X_{LE}/D_j = 0$

FIGURE I-22. TREND DATA FOR SPECTRUM HALF POWER FREQUENCY - WING-FLAPS CONFIGURATION

$$\beta_f / \beta_a = 30^\circ / 50^\circ$$



$$\beta_f / \beta_a = 5^\circ / 25^\circ$$

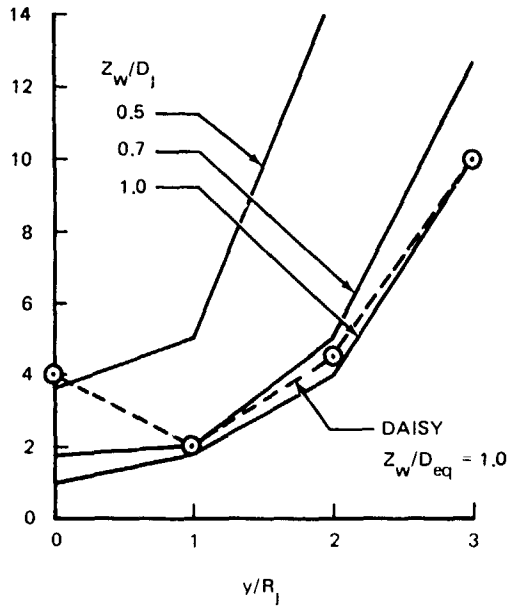


UNLESS NOTED: ROUND NOZZLE ($D_j = 2$ IN.), COLD JET ($T_j/T_a = 1$), $M_j = 0.5$, $X_{LE}/D_j = 0$

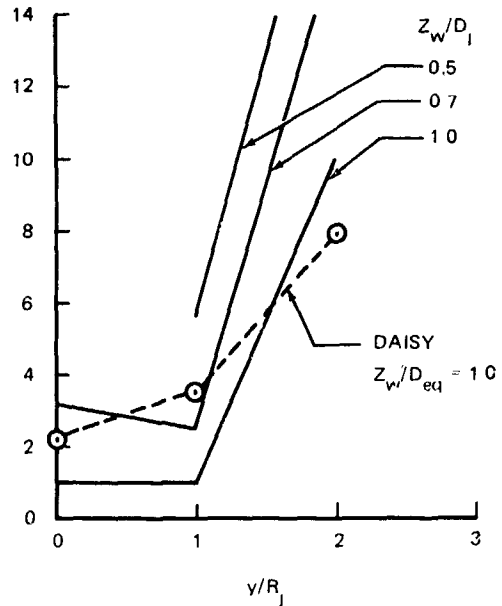
FIGURE I-23. TREND DATA FOR SPECTRUM ROLLOFF EXPONENT -- WING-FLAPS CONFIGURATION

$$\beta_f/\beta_a = 30^\circ/50^\circ$$

LOWER SURFACE – AFT FLAP

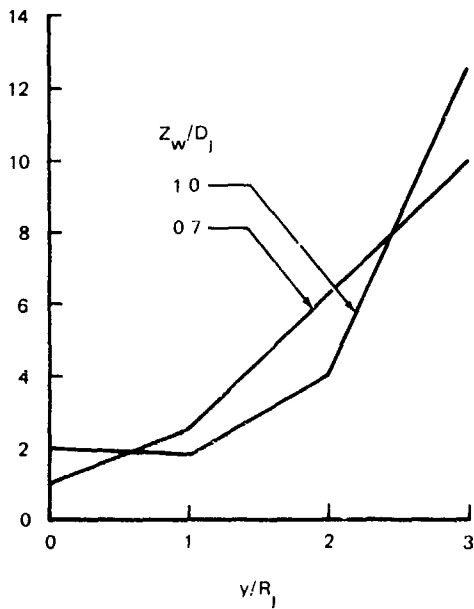


LOWER SURFACE – FWD FLAP

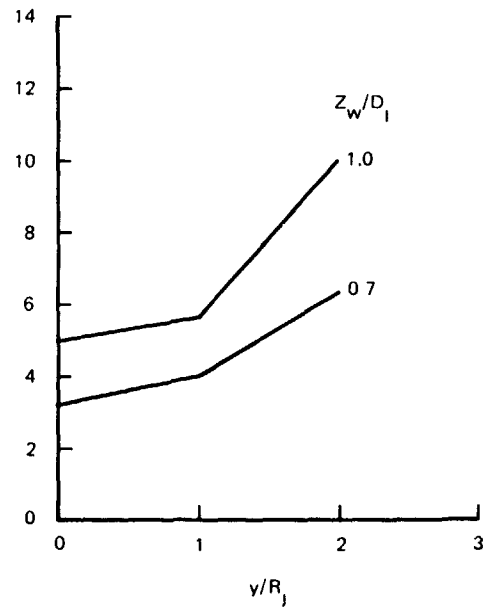


$$\beta_f/\beta_a = 5^\circ/25^\circ$$

LOWER SURFACE – AFT FLAP

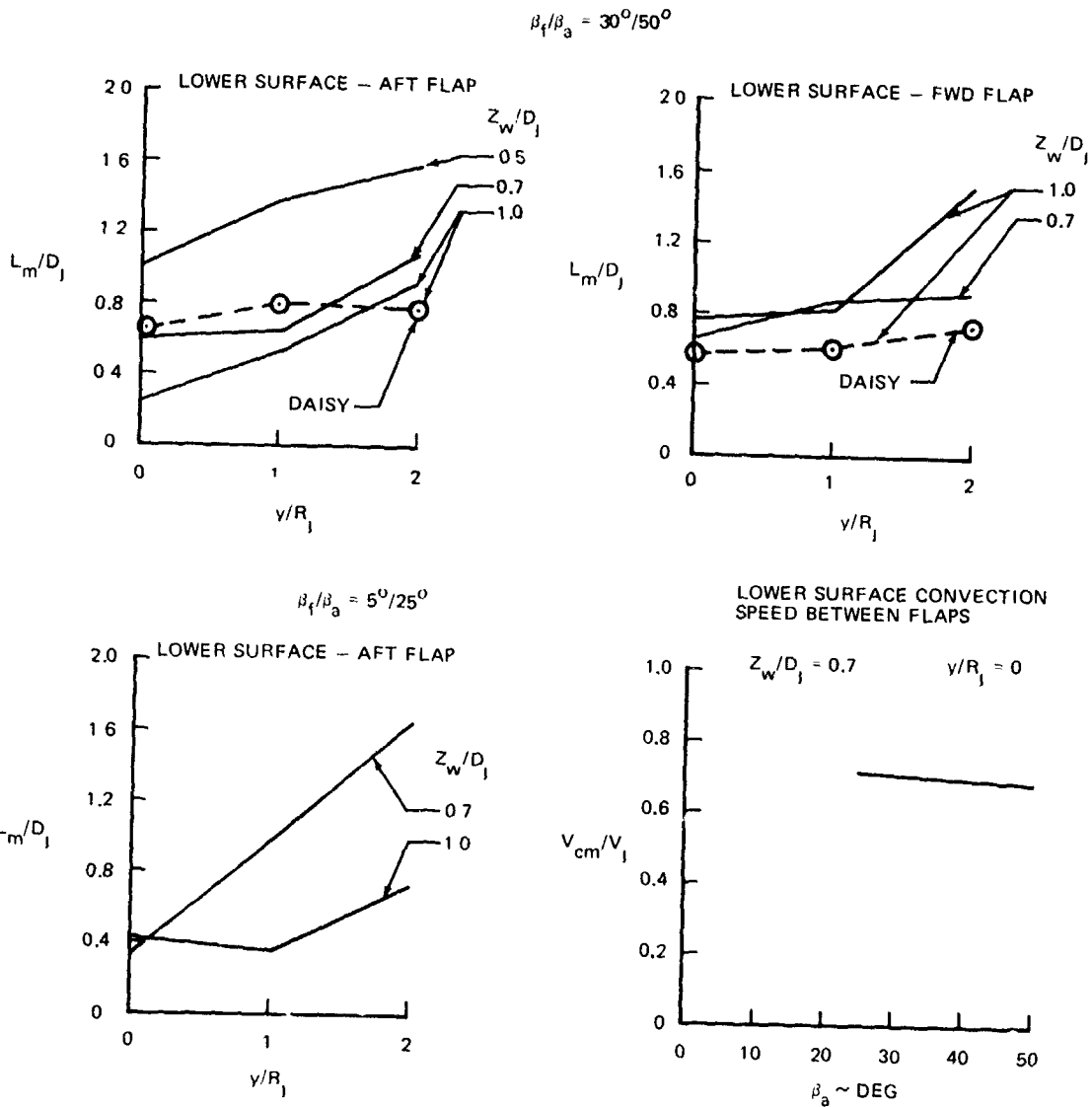


LOWER SURFACE – FWD FLAP



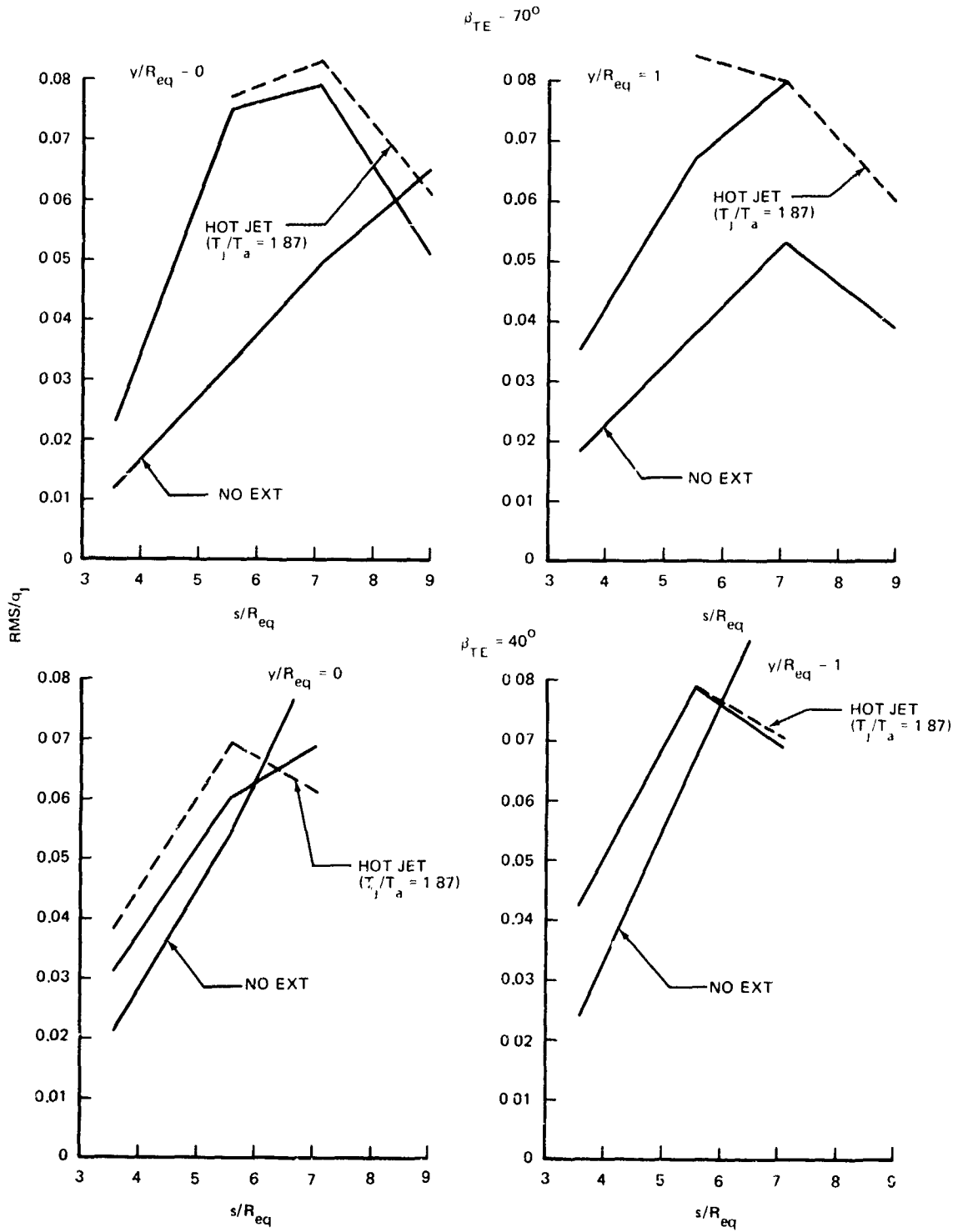
UNLESS NOTED ROUND NOZZLE ($D_j = 2$ IN.), COLD JET ($T_j/T_a = 1$), $M_j = 0.5$, $X_{LE}/D_j = 0$

FIGURE I-24. TREND DATA FOR SPECTRUM PEAK AMPLIFICATION – WING-FLAPS CONFIGURATION



UNLESS NOTED ROUND NOZZLE ($D_j = 2$ IN.), COLD JET ($T_j/T_a = 1.0$), $M_j = 0.5$, $X_{LE}/D_j = 0$

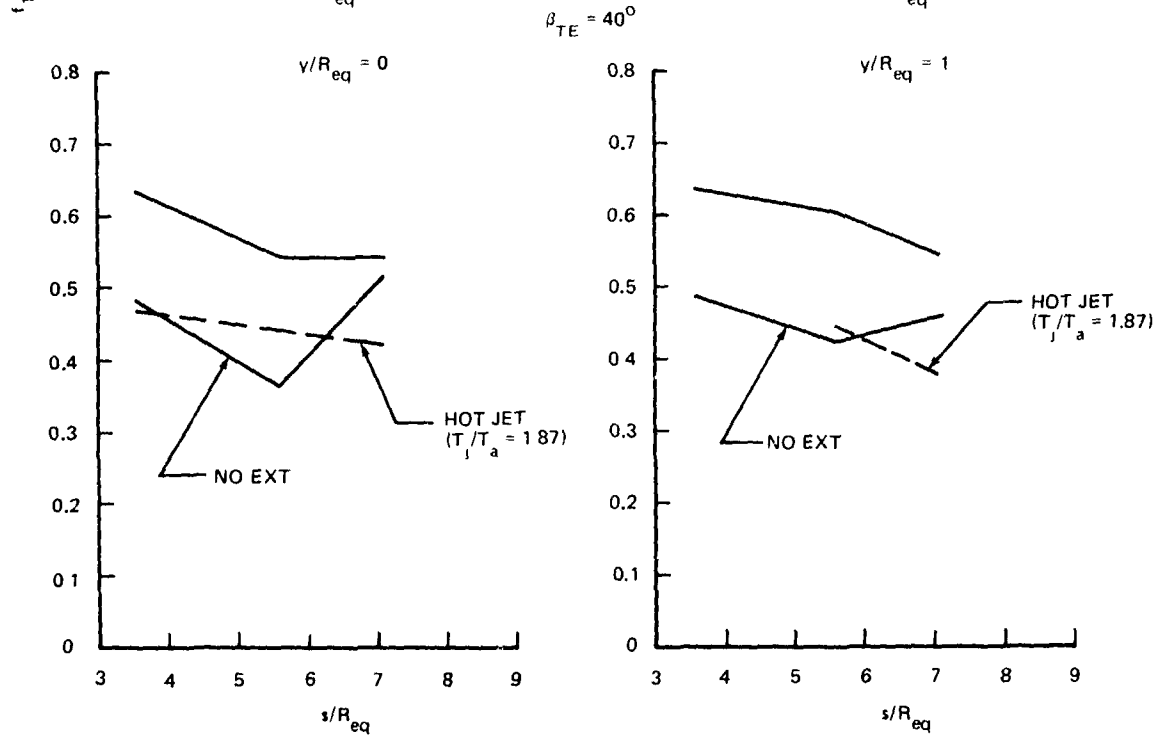
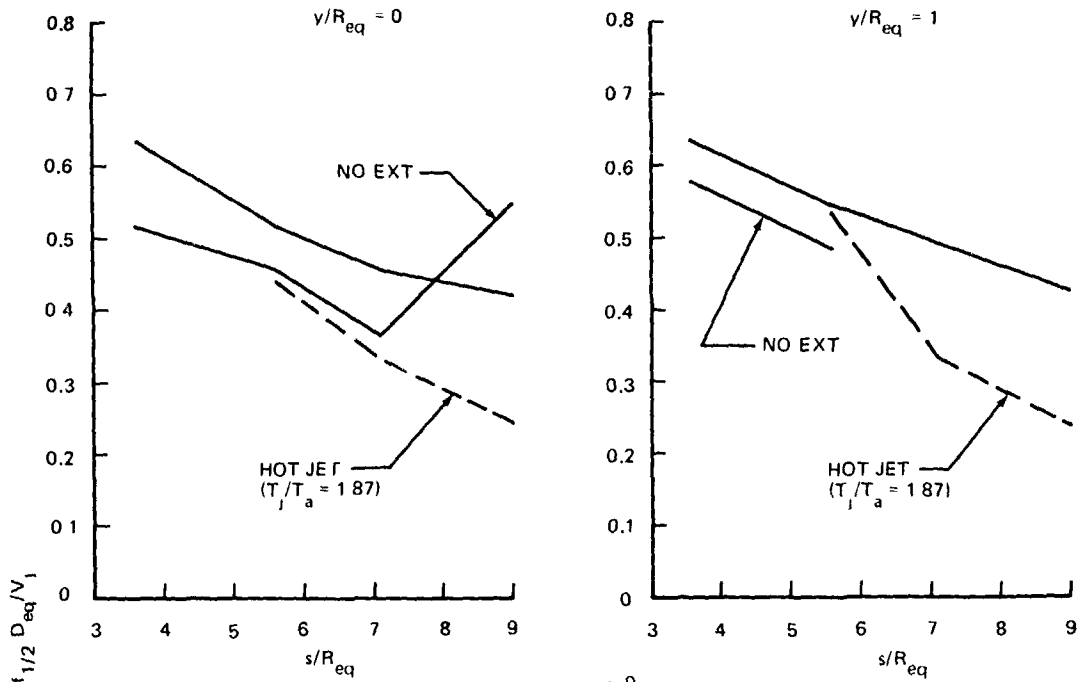
FIGURE I-25. TREND DATA FOR CORRELATION LENGTHS AND CONVECTION SPEEDS - WING-FLAPS CONFIGURATION



UNLESS NOTED: LIP EXTENDED, COLD JET ($T_j/T_a = 1$), $M_j = 0.5$, $D_{eq} = 2$ IN

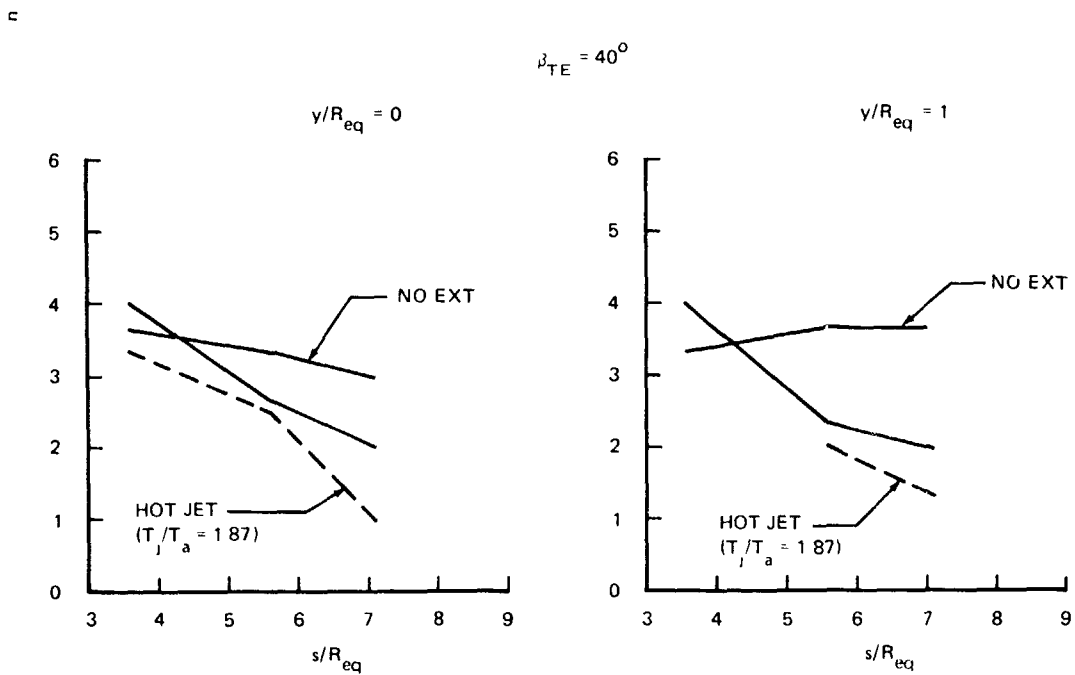
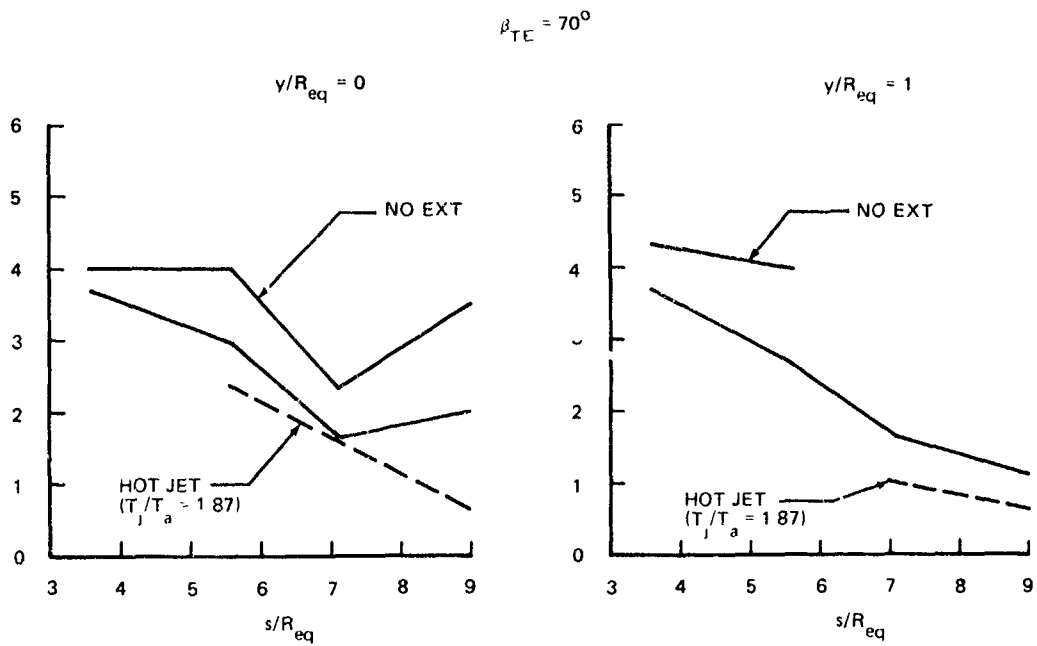
FIGURE I-26. TREND DATA FOR RMS LEVEL - OBF CURVED PLATE CONFIGURATION

$\beta_{TE} = 70^\circ$



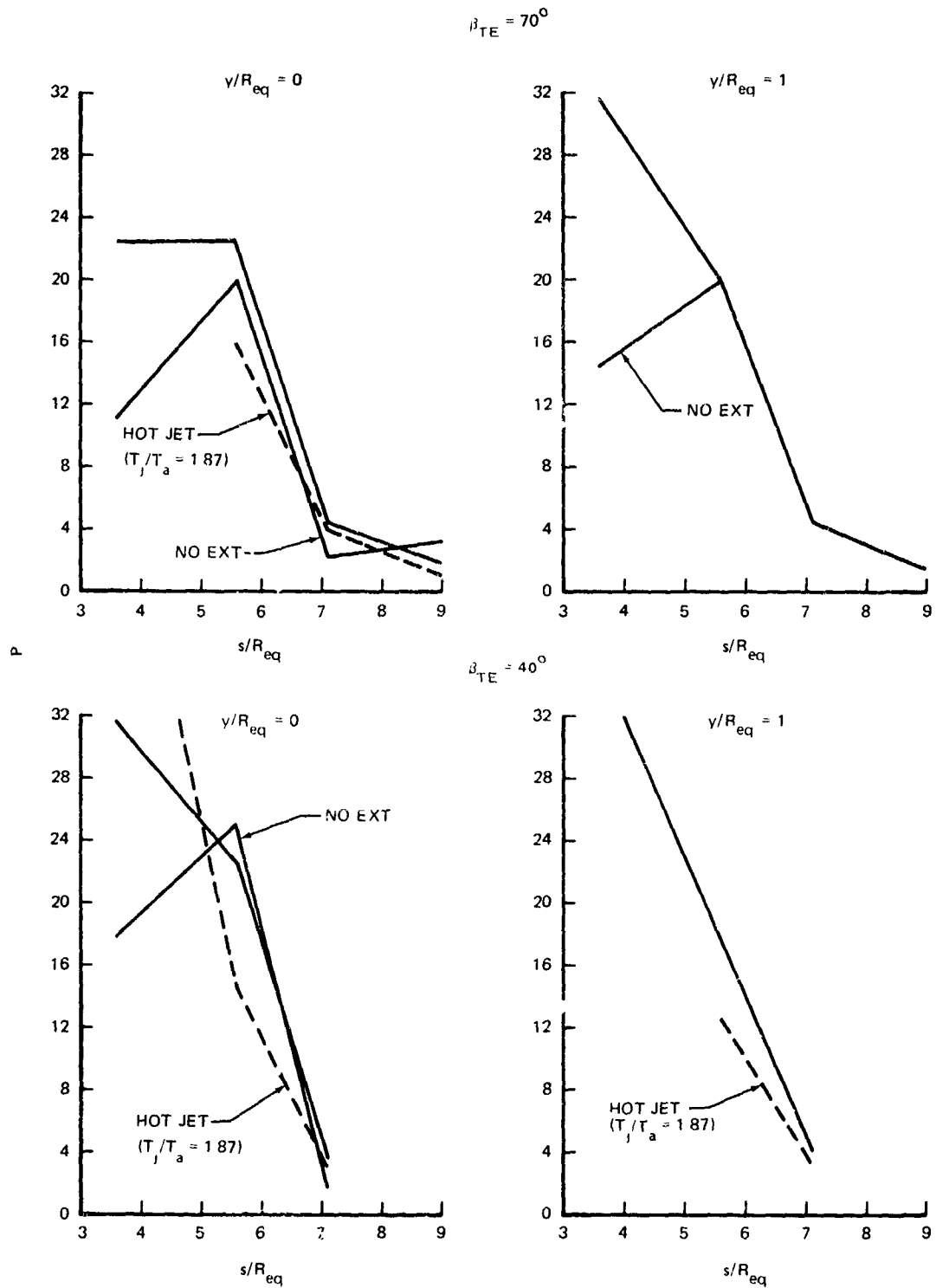
UNLESS NOTED LIP EXTENDED, COLD JET ($T_j/T_a = 1$), $M_j = 0.5$, $D_{eq} = 2$ IN

FIGURE I-27. TREND DATA FOR SPECTRUM HALF POWER FREQUENCY – OBF CURVED PLATE CONFIGURATION



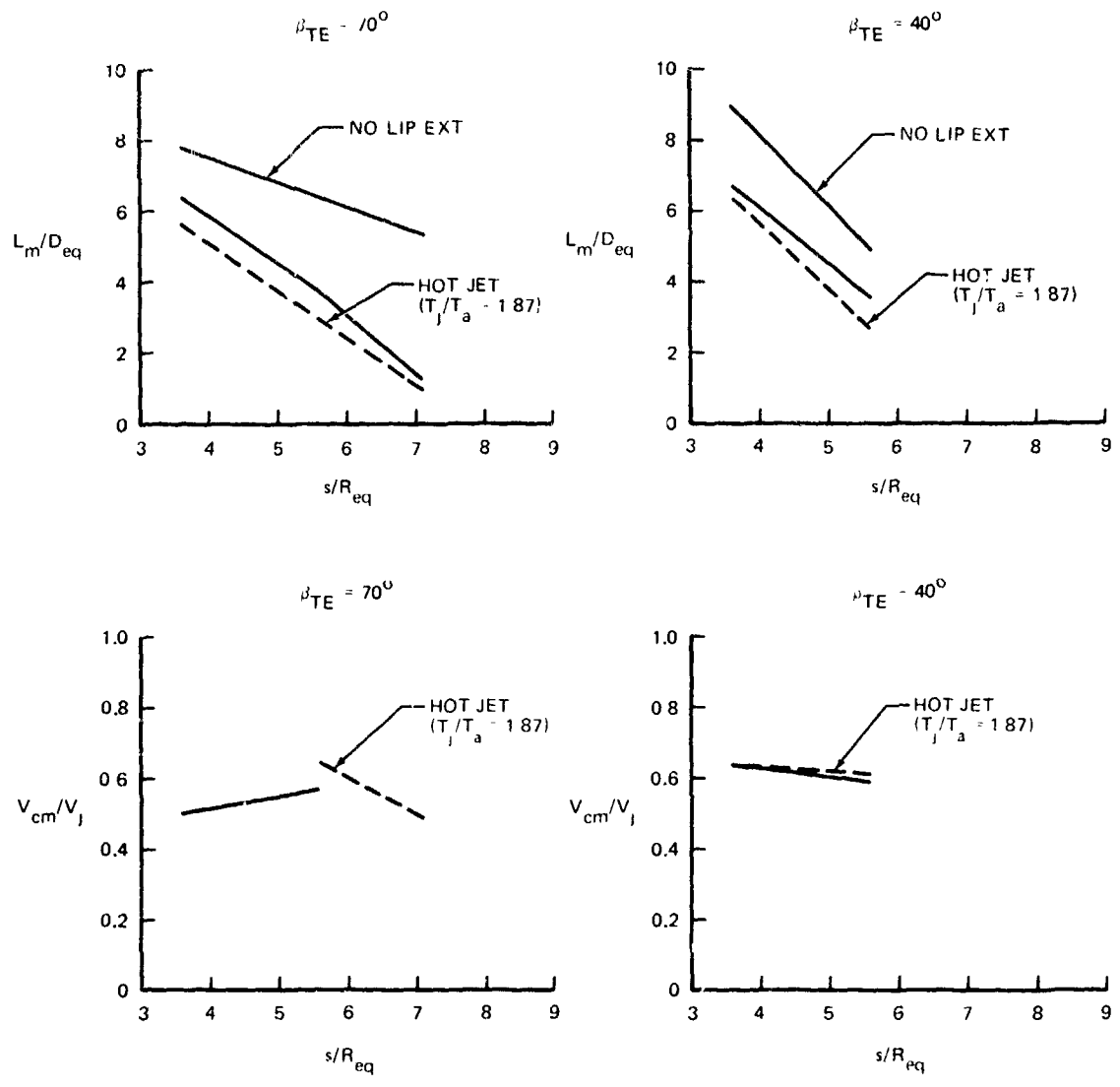
UNLESS NOTED · LIP EXTENDED, COLD JET ($T_j/T_a = 1$), $M_j = 0.5$, $D_{eq} = 2$ IN.

FIGURE I-28. TREND DATA FOR SPECTRUM ROLLOFF EXPONENT – OBF CURVED PLATE CONFIGURATION



UNLESS NOTED. LIP EXTENDED, COLD JET ($T_j/T_a = 1$), $M_j = 0.5$, $D_{eq} = 2$ IN

FIGURE I-29. TREND DATA FOR SPECTRUM PEAK AMPLIFICATION - OBF CURVED PLATE CONFIGURATION




UNLESS NOTED LIP EXTENDED, COLD JET ($T_j/T_a = 1$), $M_j = 0.5$, $y/R_{eq} = 0$, $D_{eq} = 2$ IN.

FIGURE i-30. TREND DATA FOR CORRELATION LENGTHS AND CONVECTION SPEEDS - OBF CURVED PLATE CONFIGURATION

APPENDIX J

TABLATIONS OF FLUCTUATING PRESSURE MEASUREMENTS

The surface fluctuating pressure data obtained in the test program are presented in the following set of tables. There is a table for each test case listed in Appendix A for categories 1 through 12. The tables are laid-out in two-dimensions showing the results in proper spatial relation to each other. Dimensions consistent with those given in Appendix D are provided in the tables for defining the locations at which measurements are specified. The values for the test parameters are displayed in the table for the case. Also stated in each table are the types of presented results and their units. In the flat plate tables, the location of the center of impingement is marked by the symbol .

Data is given for seven different characteristics of the fluctuating pressures. These characteristics are (1) overall RMS level, (2) power spectrum half-power frequency, $f_{1/2}$, (3) power spectrum rolloff exponent, n , (4) peak amplification of power spectrum, P , (5) maximum correlation length, L_m , (6) frequency at which L_m occurs, f_m and (7) convection speed, V_{cm} , at frequency f_m . The seven properties are separated into two groups with the first four in one and the last three in the other. The quantity associated with a tabulated numerical value is identified from the manner in which the value is bracketed. In the first group the RMS value has no bracketing, while $f_{1/2}$, n and P are, respectively, contained within parentheses, brackets and braces. The value L_m has no bracketing in the second group, while f_m and the convection speed are shown within parentheses and brackets, respectively.

From the definitions of the test results given in Section II-5, it will be noted that a separation distance Δ is required in determining L_m and the convection speed. The values presented for these quantities are typically based on using $\Delta = R_j$, the radius of the nozzle exit. At a few locations an * indicates $\Delta = 2R_j$ and ** designates that $\Delta = 1/2 R_j$.

The correlation lengths and convection speeds originate from the location at which their values are given. These quantities are directed from the originating location either downstream chordwise or outward spanwise (i.e., directed away from the span center).

Correlation lengths and convection speeds between flaps for the wing-flaps model are from the pickup on the forward flap downstream to the corresponding pickup on the aft flap. The separation distances used in obtaining these results are $\Delta = 2.5''$ and $2.7''$ between the corresponding lower and upper surface locations, respectively. These distances pertain to both flap settings tested in the program; i.e., $\beta_f/\beta_a = 30^\circ/50^\circ$ and $5^\circ/25^\circ$.

Maximum correlations, ρ_m , between corresponding locations on opposite surfaces of the same flap are given for the wing-flaps model in Table J-64. (See definition of ρ_m in Section II-5). The frequency f_m at which the maximum correlation occurs is also shown in the table. The location associated with each ρ_m value is specified by noting the flap (forward or aft) containing the pickups and the distance from the center of the span, denoted by 'y' in inches. Explanation of the case designations in the table are found in Appendix A.

TABLE J-1
 PRESSURE MEASUREMENT RESULTS
 FLAT PLATE - ROUND NOZZLE (D = 1")

TEST CASE	T_j/T_a	M_j	X/D	θ	RESULT TYPE
1A	1	0.5	10	25°	RMS (psi) (half-power freq.) KHZ [rolloff exponent] {peak amplification}

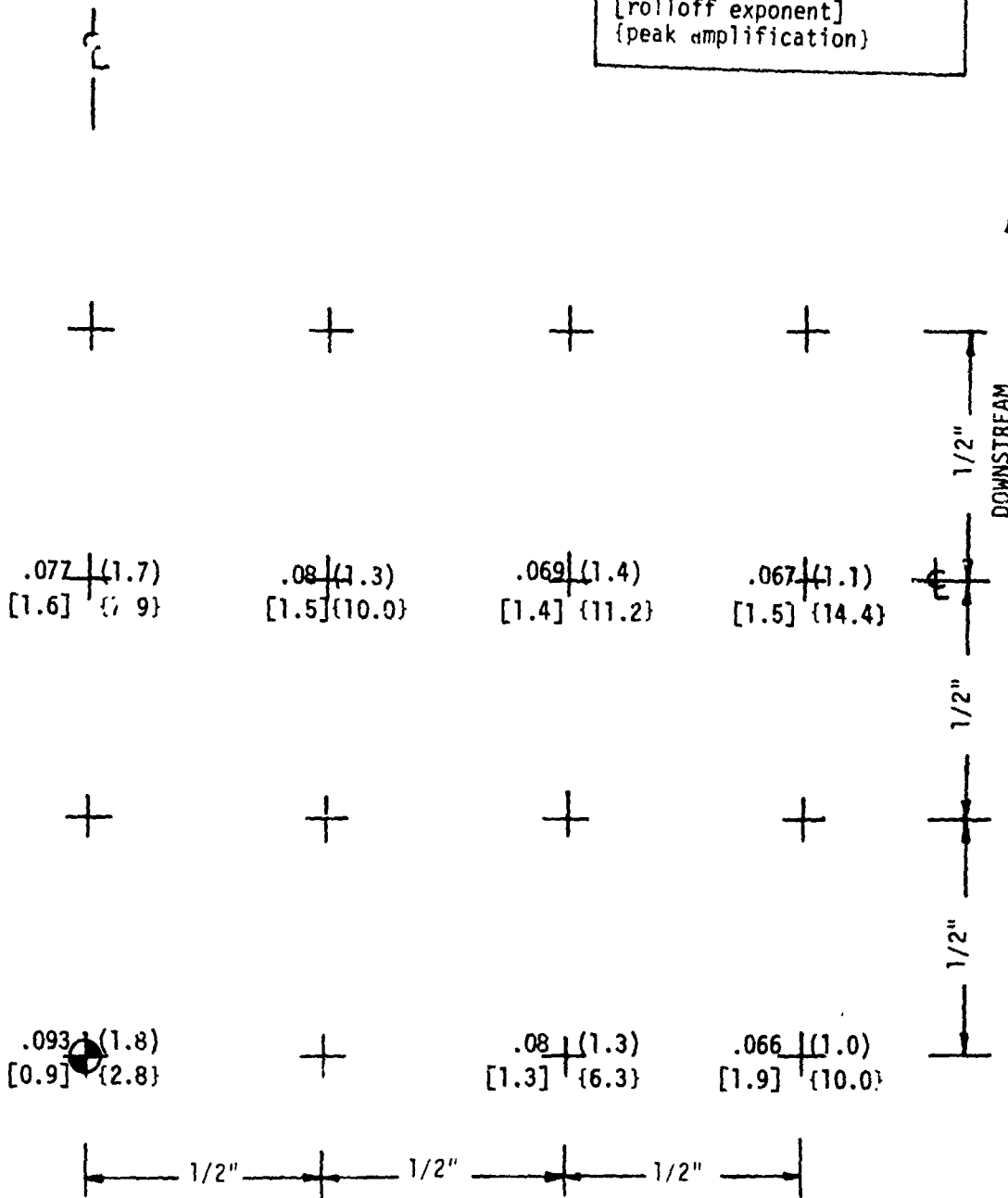


TABLE J-1 (CONT'D)
 PRESSURE MEASUREMENT RESULTS
 FLAT PLATE - ROUND NOZZLE (D = 1")

TEST CASE	T_j/T_a	M_j	X/D	β	RESULT TYPE
1A	1.0	0.5	10	25°	Max. Correlation Length (in) (Freq. at Maximum, f_m) KHZ [Convection Speed at f_m] fps

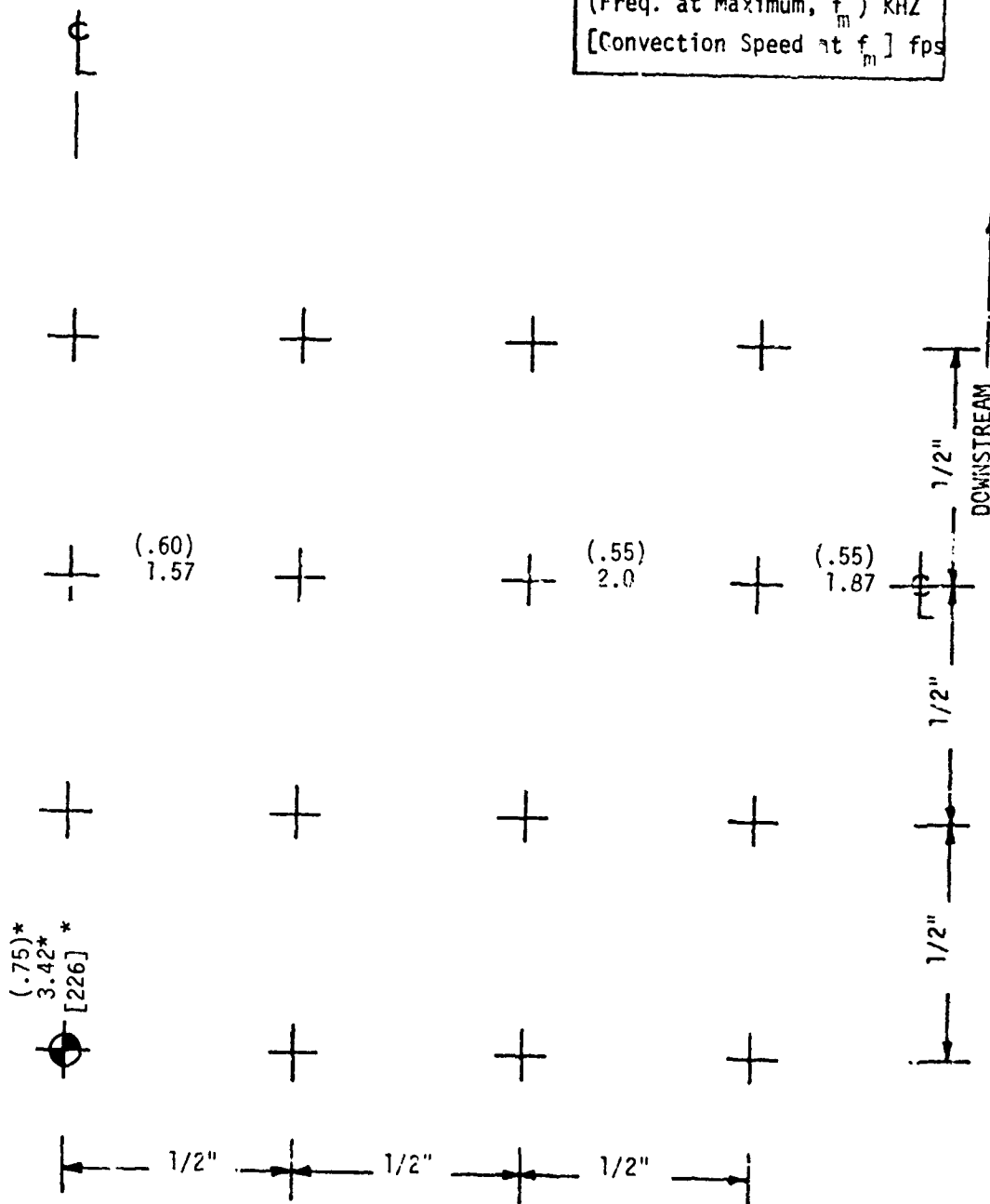


TABLE J-2
 PRESSURE MEASUREMENT RESULTS
 FLAT PLATE - ROUND NOZZLE (D = 1")

TEST CASE	T_j/T_a	M_j	X/D	ϵ	RESULT TYPE
7B	1.0	0.5	10	50°	RMS (psi) (half-power freq.) KHZ [rolloff exponent] peak amplification

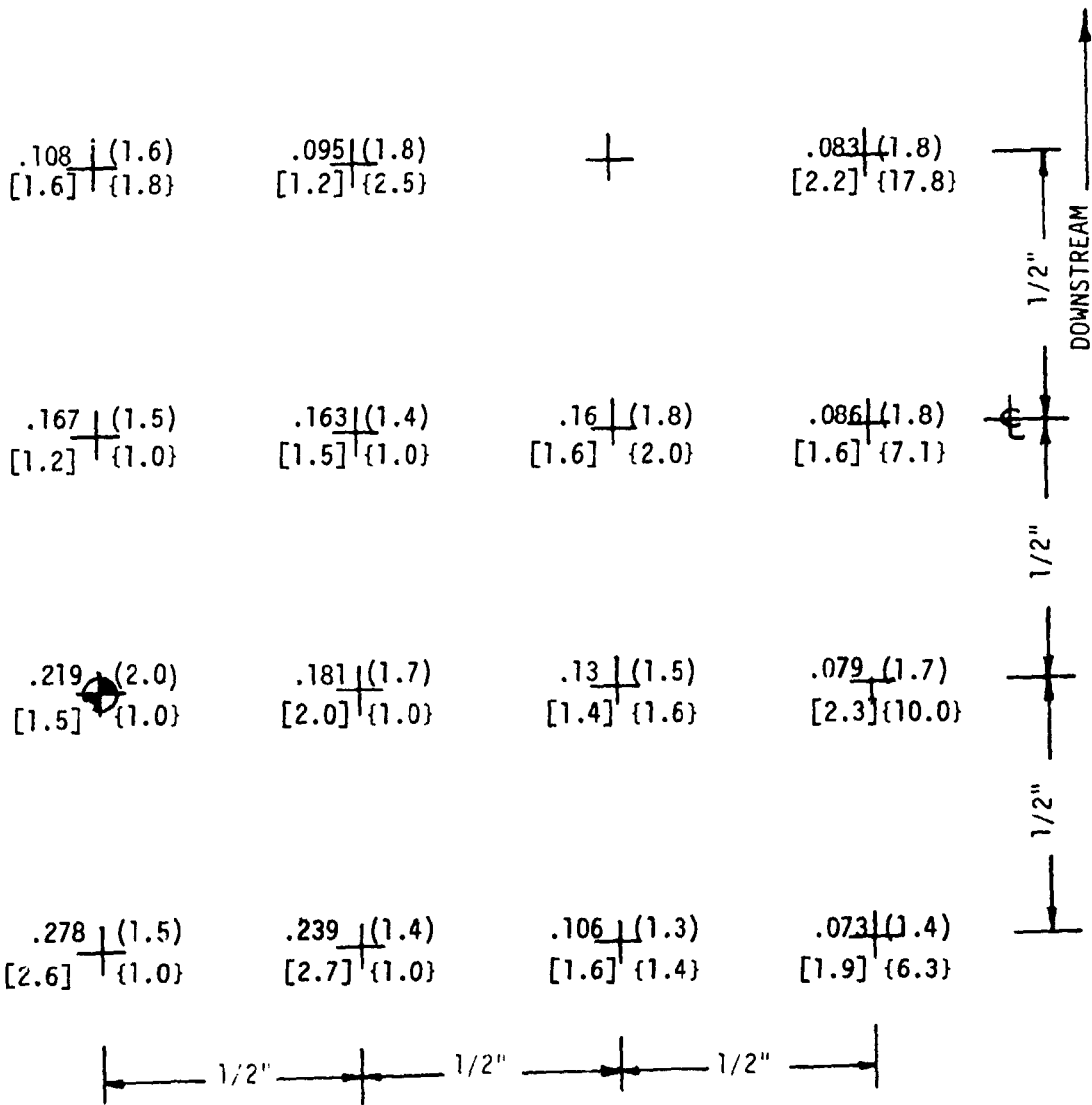


TABLE J-2 (CONT'D)
 PRESSURE MEASUREMENT RESULTS
 FLAT PLATE - ROUND NOZZLE (D = 1")

TEST CASE	T_j/T_a	M_j	X/D	β	RESULT TYPE
1B	1.0	0.5	10	50°	Max. Correlation Length (in) (Freq. at Maximum, f_m) KHZ [Convection Speed at f_m] fps

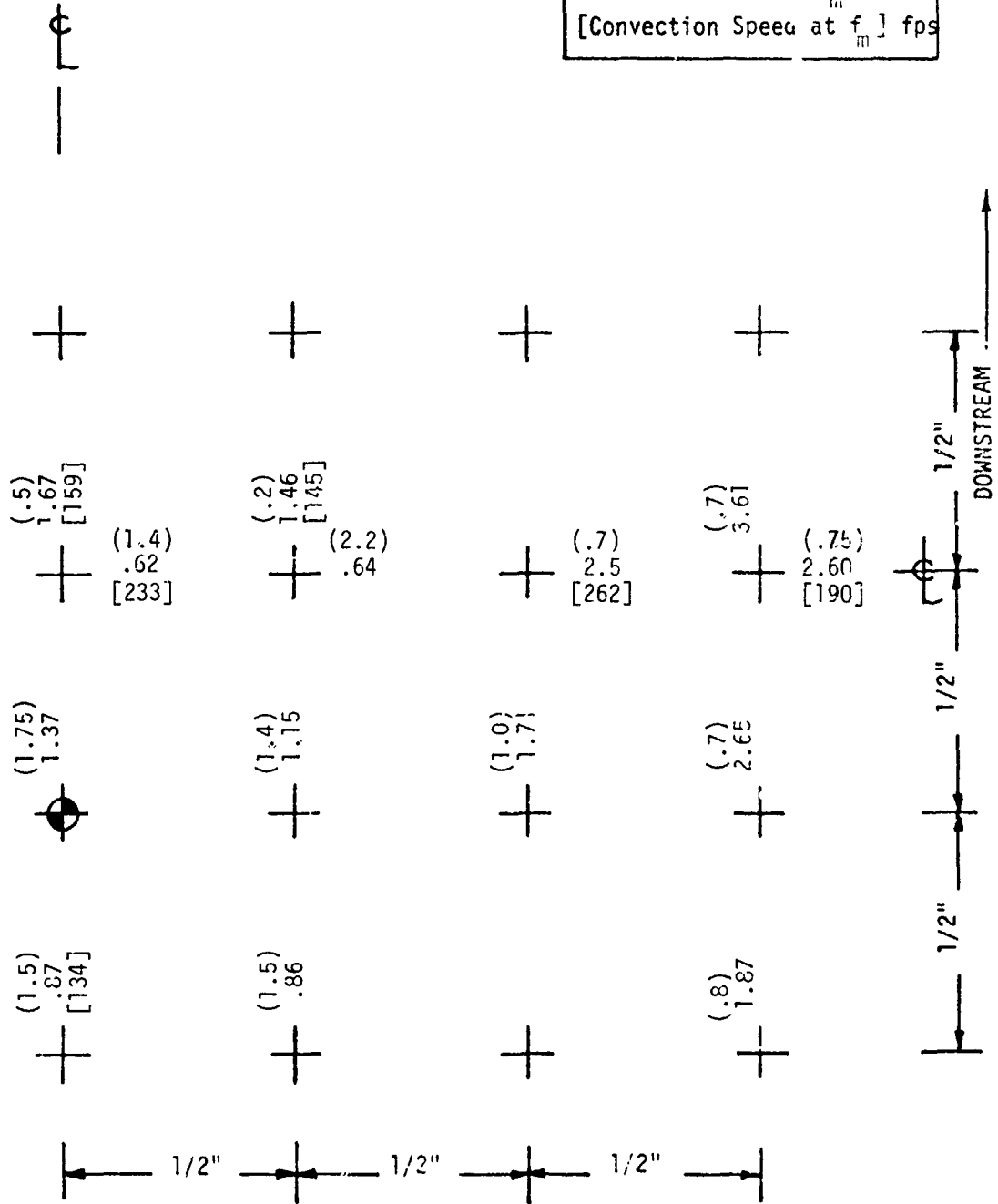


TABLE J-3
 PRESSURE MEASUREMENT RESULTS
 FLAT PLATE - ROUND NOZZLE (D = 1")

TEST CASE	T_j/T_a	M_j	x/D	β	RESULT TYPE
1C	1.0	.50	10	90°	RMS (psi) (half-power freq.) KHZ [rolloff exponent] (peak amplification)

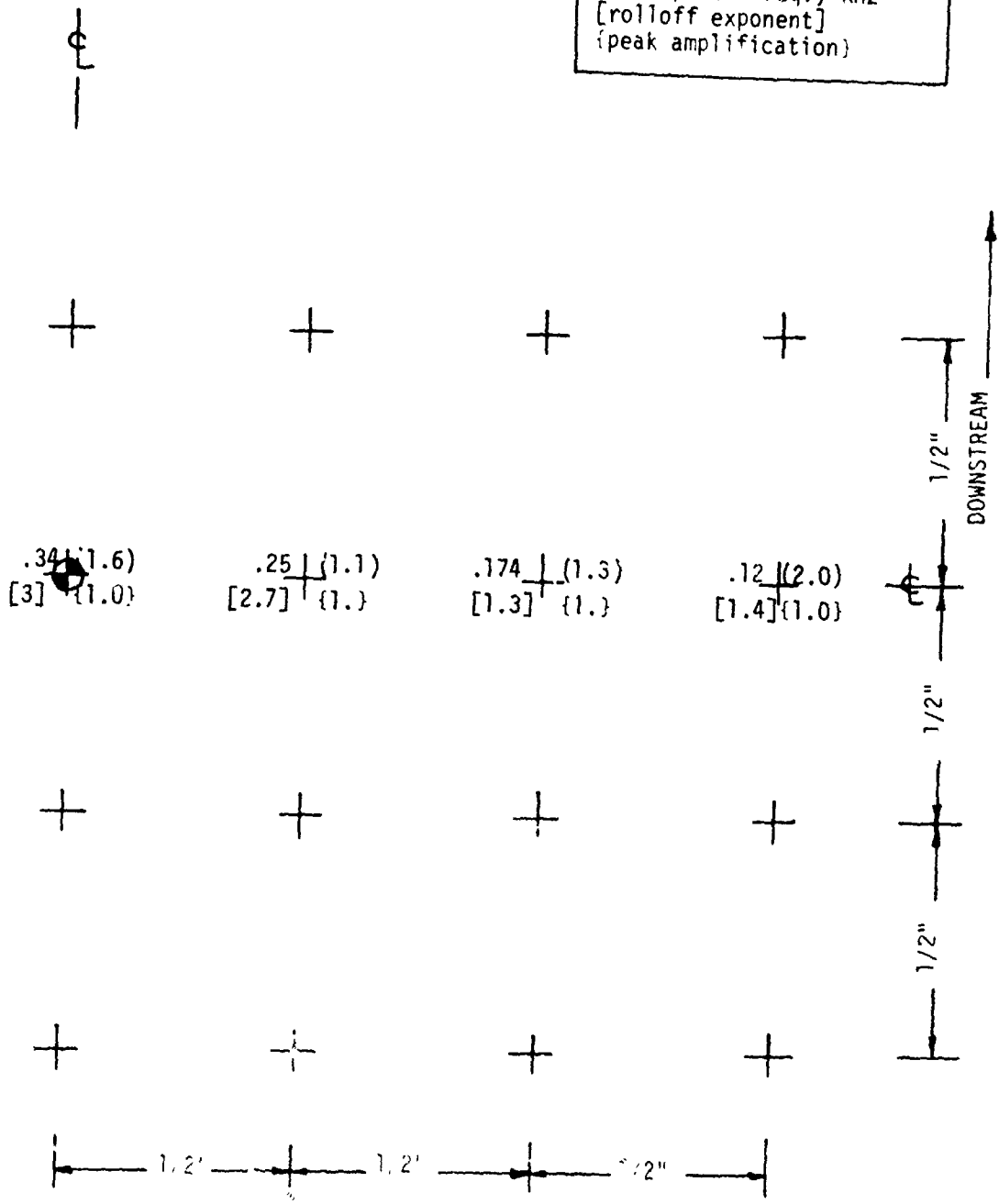


TABLE J-3 (CONT'D)
 PRESSURE MEASUREMENT RESULTS
 FLAT PLATE - ROUND NOZZLE (D = 1")

TEST CASE	T_j/T_a	i_j	X/D	β	RESULT TYPE
1C	1.0	0.5	10	90°	Max. Correlation Length (in) (Freq. at Maximum, f_m) KHZ [Convection Speed at f_m] fps

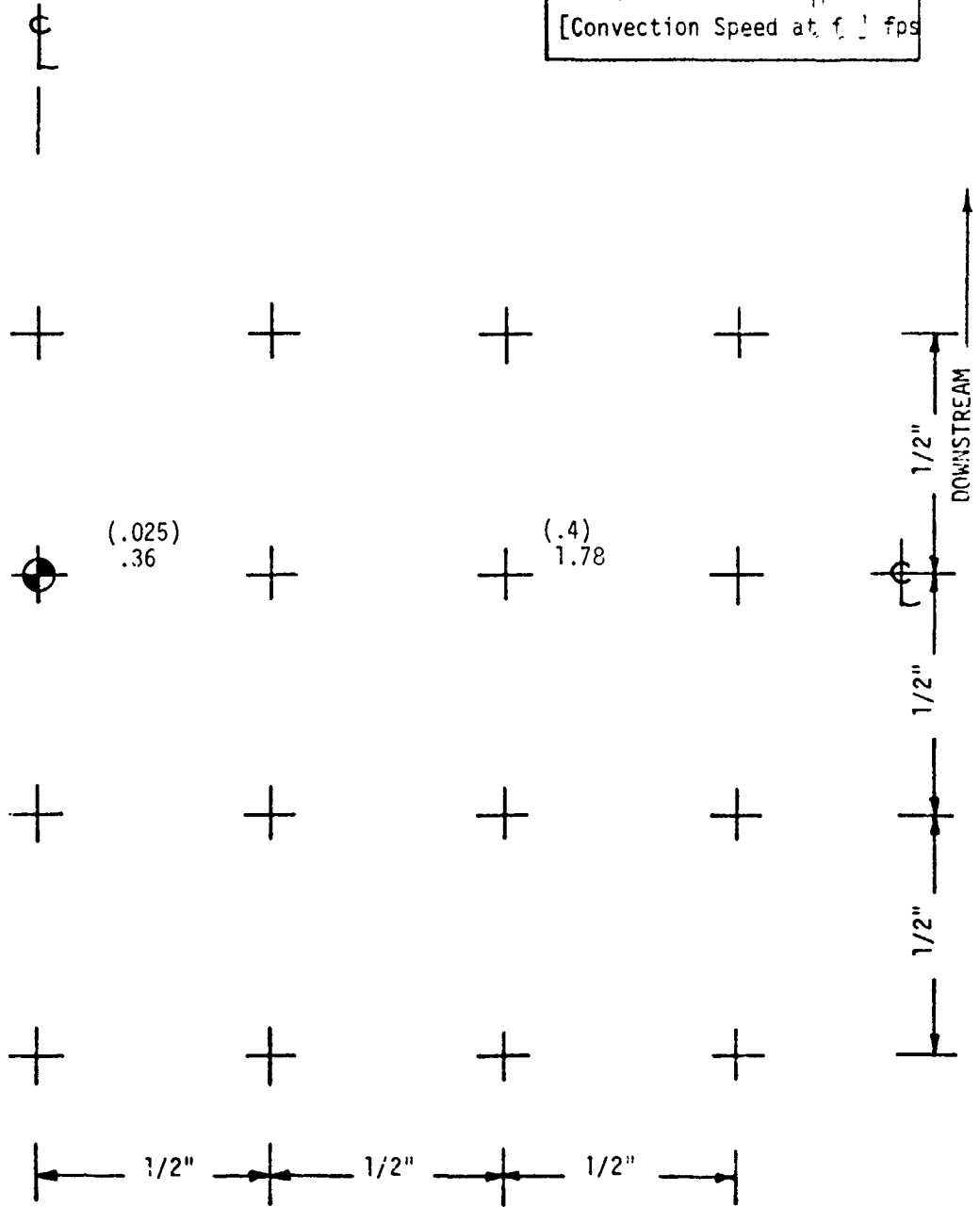


TABLE J-4
 PRESSURE MEASUREMENT RESULTS
 FLAT PLATE - ROUND NOZZLE (D = 1")

TEST CASE	T_j/T_a	M_j	X/D	β	RESULT TYPE
1D	1.0	0.5	5.27	25°	RMS (psi) (half-power freq.) KHZ [rolloff exponent] {peak amplification}

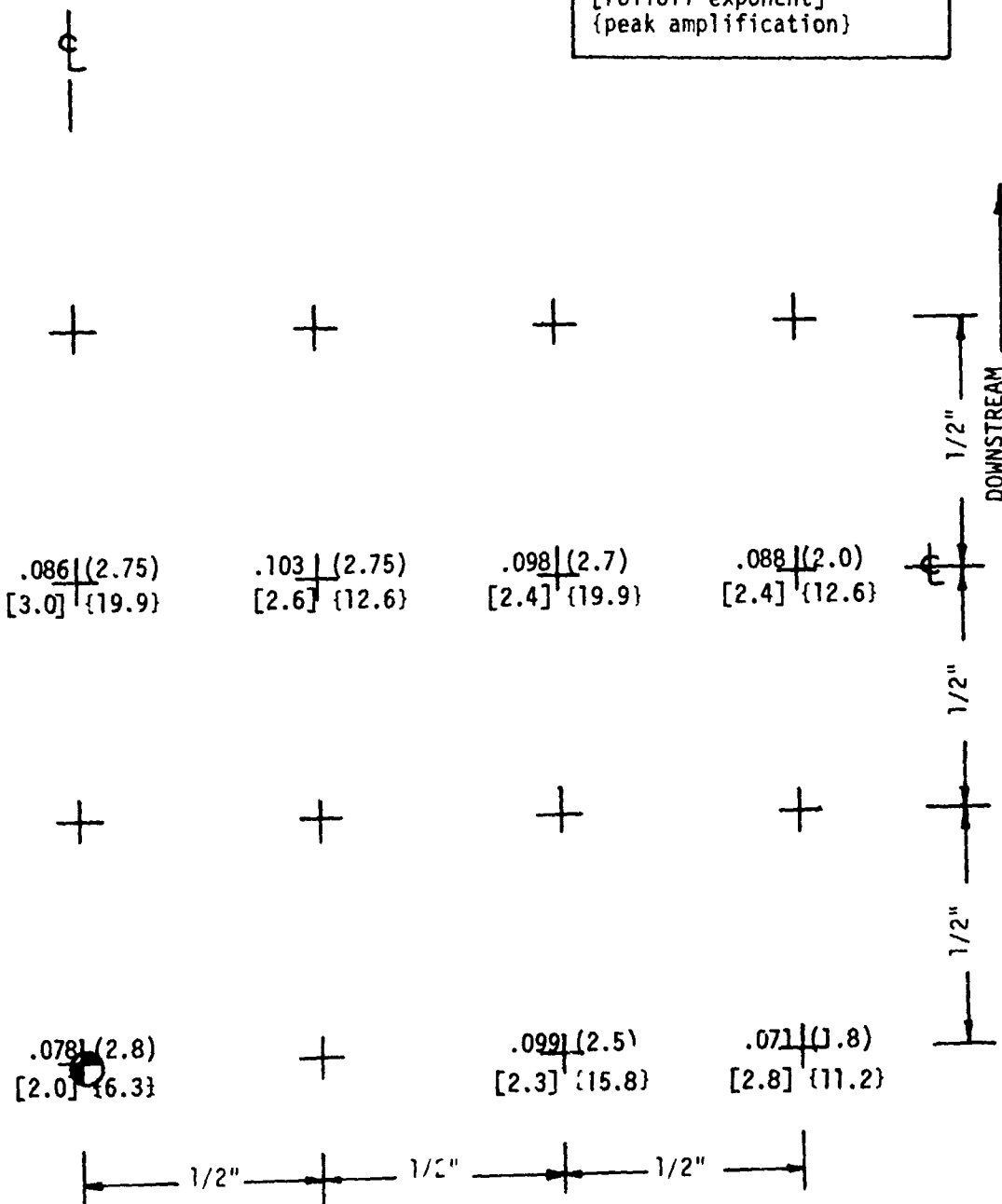


TABLE J-4 (CONT'D)
 PRESSURE MEASUREMENT RESULTS
 FLAT PLATE - ROUND NOZZLE (D = 1")

TEST CASE	T_j/T_a	M_j	X/D	θ	RESULT TYPE
1D	1.0	0.5	5.27	25°	Max. Correlation Length (in) (Freq. at Maximum, f_m) KHZ [Convection Speed at f_m] fps

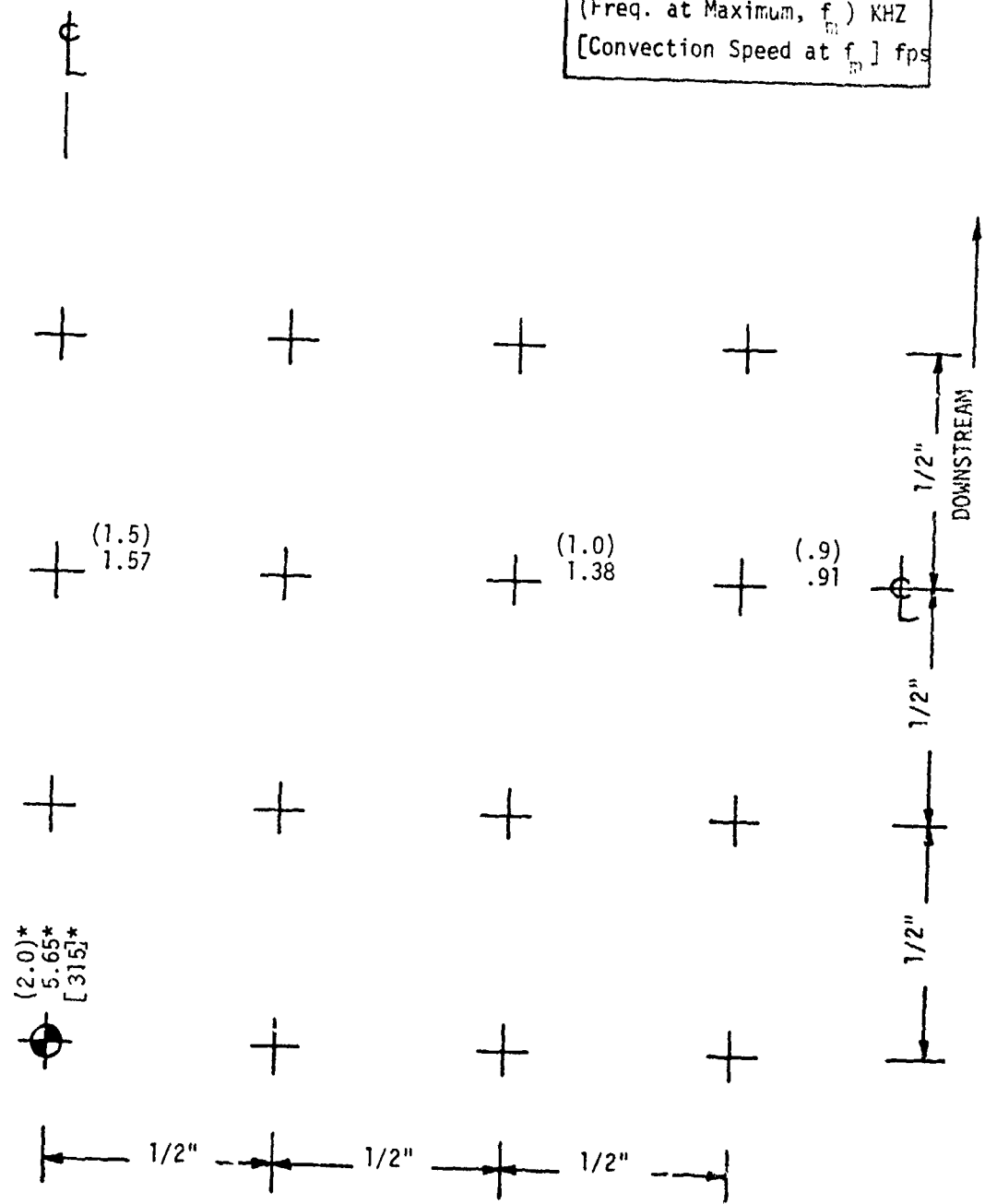


TABLE J-5
 PRESSURE MEASUREMENT RESULTS
 FLAT FLATE - ROUND NOZZLE (D = 1")

TEST CASE	T_j/T_a	M_j	X/D	ϵ	RESULT TYPE
1E	1.0	0.5	5	50°	RMS (psi) (half-power freq.) KHZ [rolloff exponent] (peak amplification)

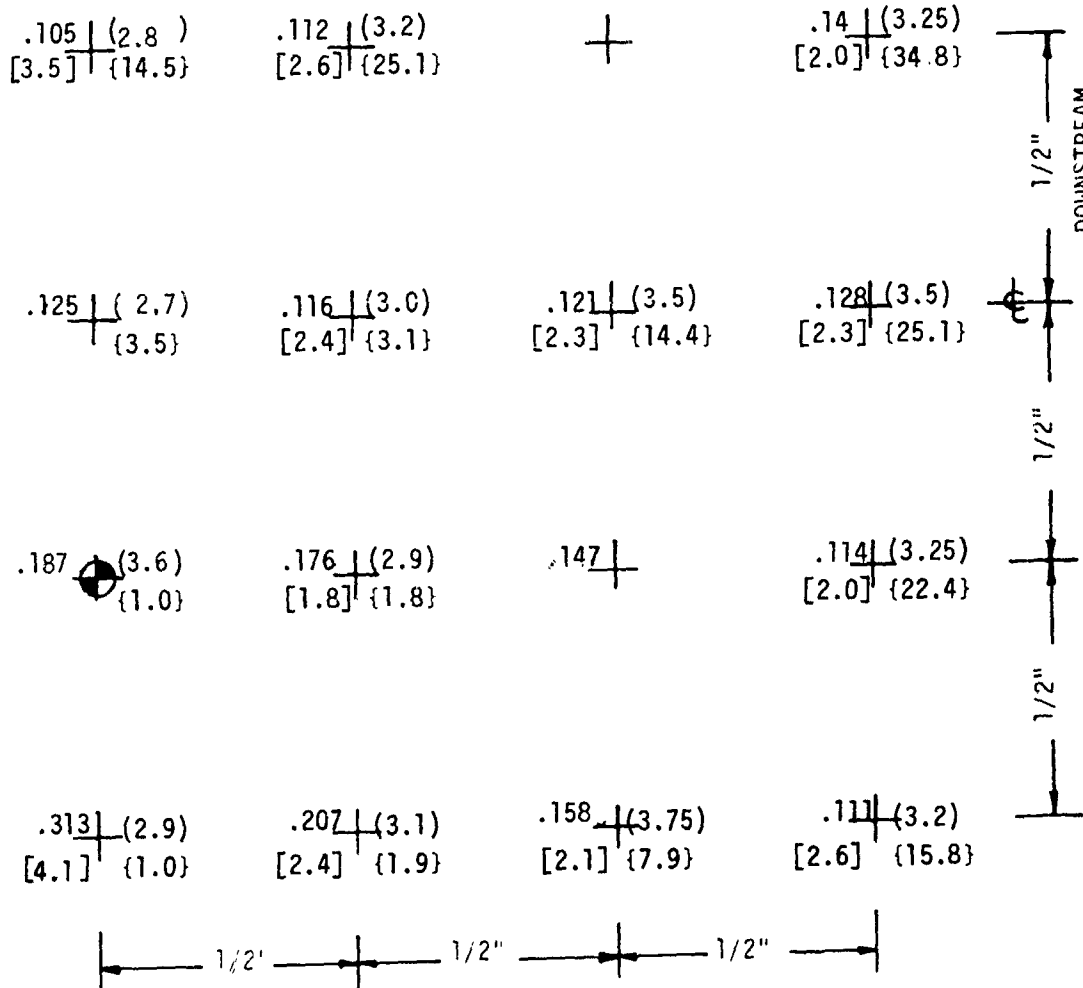
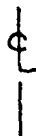


TABLE J-5 (CONT'D)
 PRESSURE MEASUREMENT RESULTS
 FLAT PLATE - ROUND NOZZLE (D = 1")

TEST CASE	T_j/T_a	M_j	X/D	β	RESULT TYPE
1E	1.0	0.5	5	50°	Max. Correlation Length (in) (Freq. at Maximum, f_m) KHZ [Convection Speed at f_m] fps

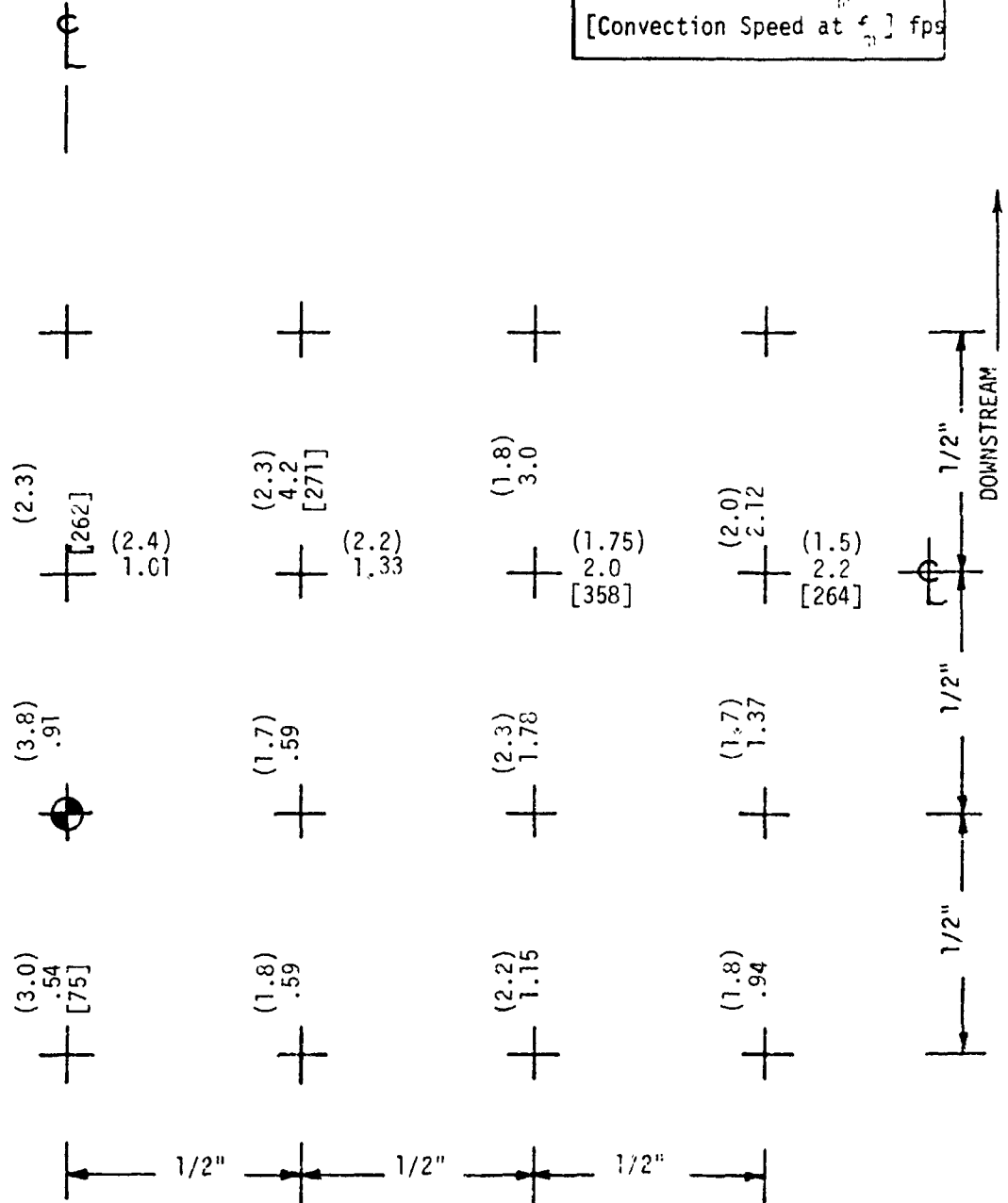


TABLE J-6
 PRESSURE MEASUREMENT RESULTS
 FLAT PLATE - ROUND NOZZLE (D = 1")

TEST CASE	T_j/T_a	M_j	X/D	β	RESULT TYPE
1F	1.0	.50	5	90°	RMS (psi) (half-power freq.) KHZ [rolloff exponent] {peak amplification}

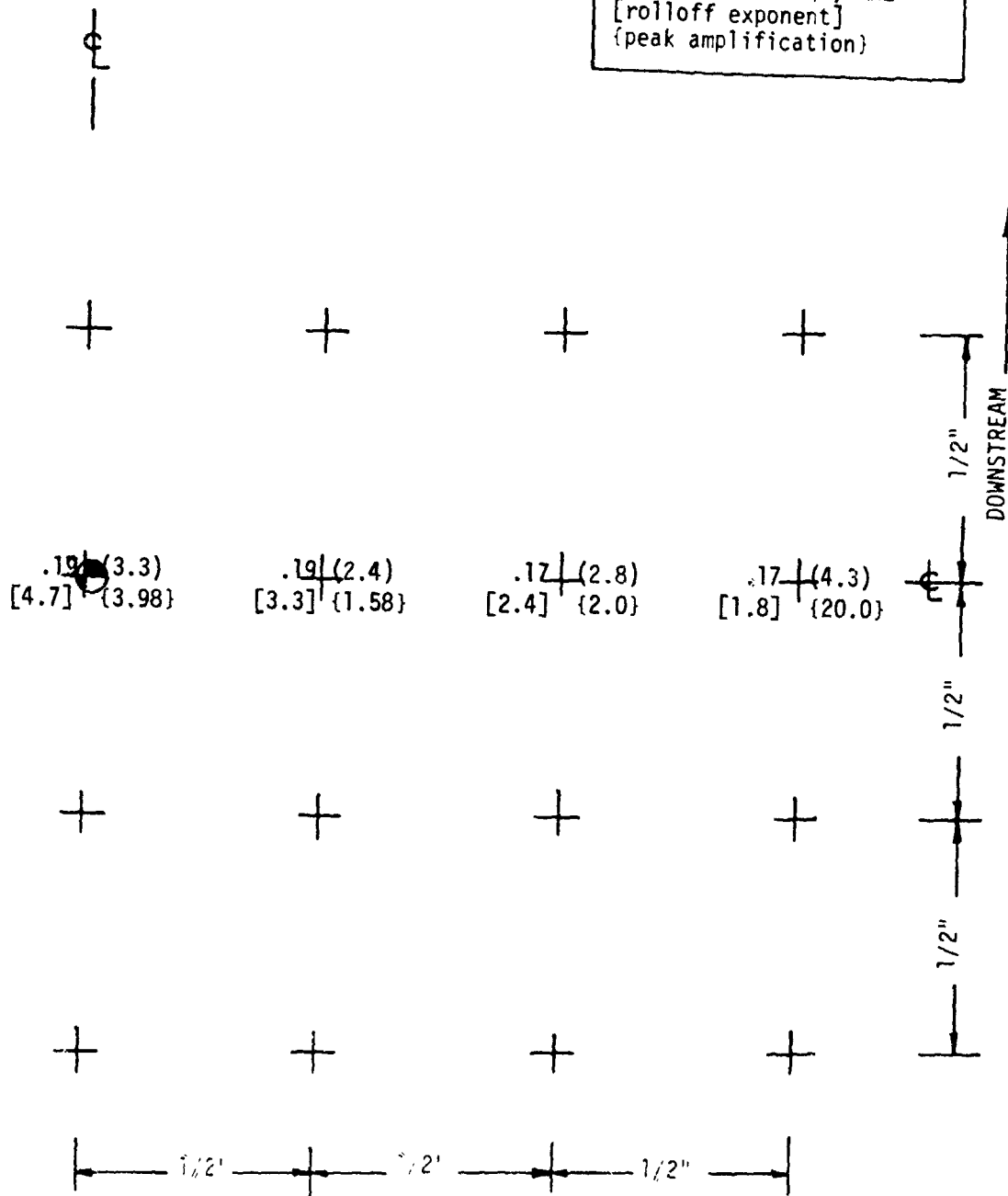


TABLE J-6 (CONT'D)
 PRESSURE MEASUREMENT RESULTS
 FLAT PLATE - ROUND NOZZLE (D = 1")

TEST CASE	T_j/T_a	M_j	X/D	β	RESULT TYPE
1F	1.0	0.5	5	90°	Max. Correlation Length (in) (Freq. at Maximum, f_m) KHZ [Convection Speed at f_m] fps

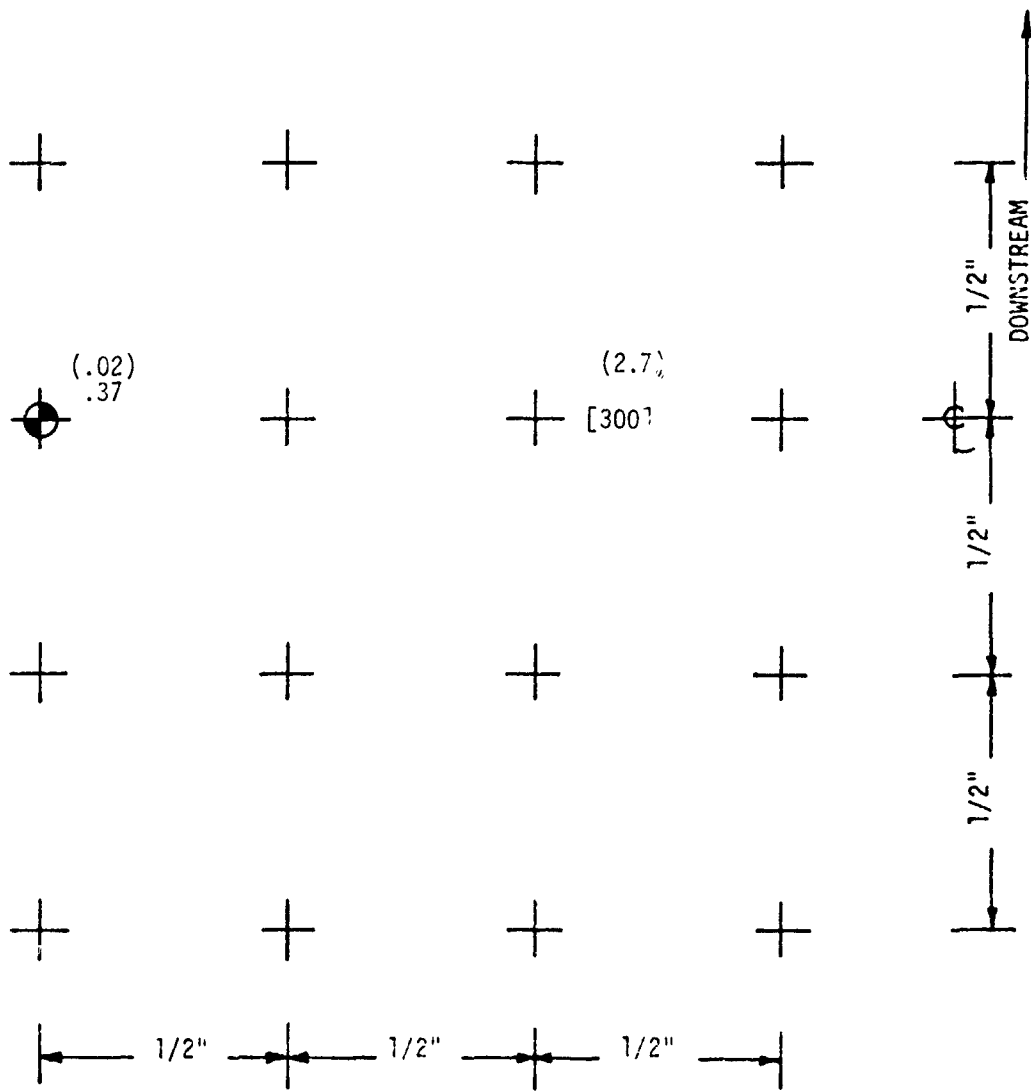
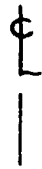


TABLE J-7
 PRESSURE MEASUREMENT RESULTS
 FLAT PLATE - ROUND NOZZLE (D = 1")

TEST CASE	T_j/T_a	M_j	X/D	β	RESULT TYPE
1G	1.0	0.5	7	25°	RMS (psi) (half-power freq.) KHZ [rolloff exponent] {peak amplification}

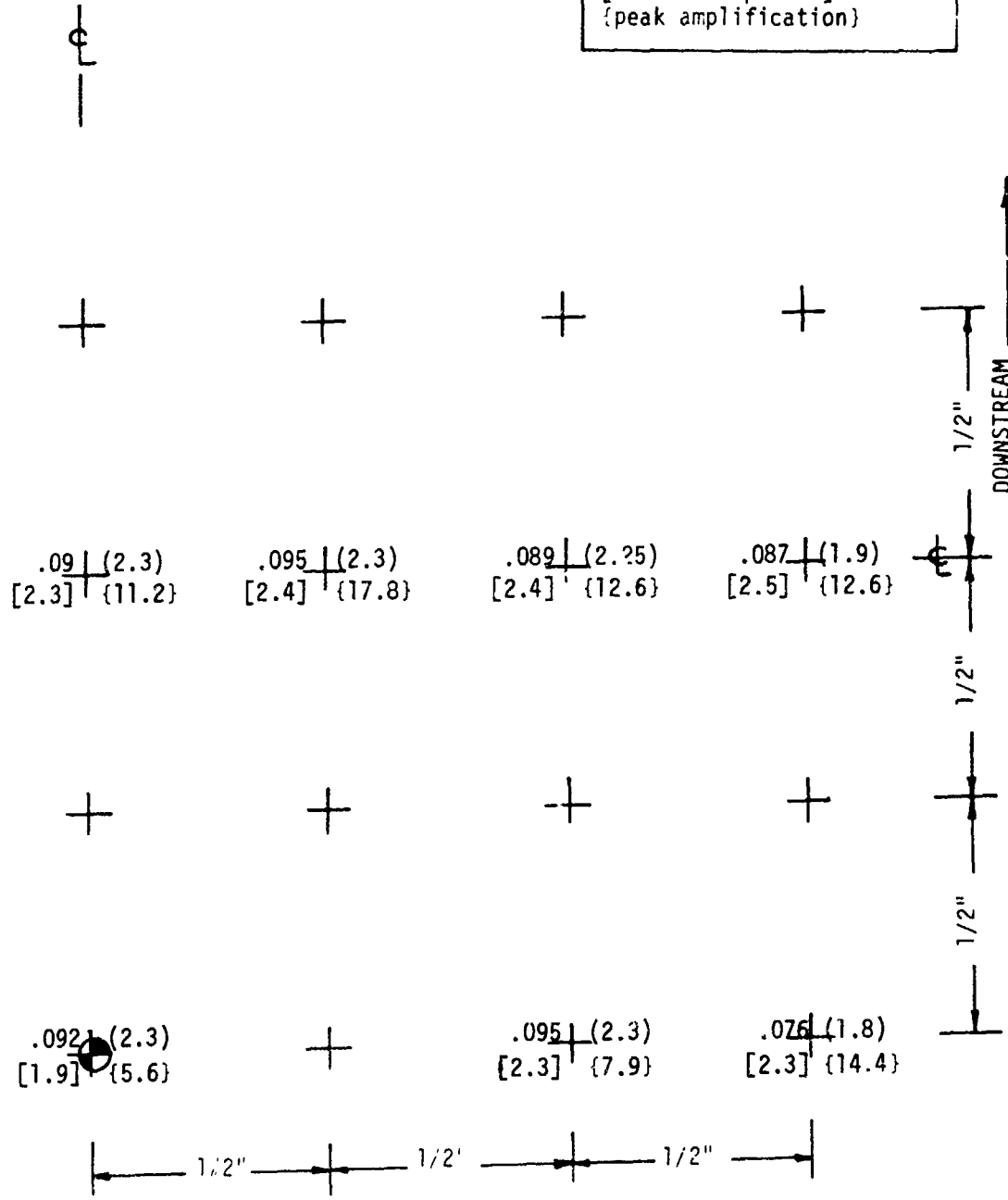


TABLE J-7 (CONT'D)
 PRESSURE MEASUREMENT RESULTS
 FLAT PLATE - ROUND NOZZLE (D = 1")

TEST CASE	T_j/T_a	M_j	X/D	θ	RESULT TYPE
1G	1.0	0.5	7	25°	Max. Correlation Length (in) (Freq. at Maximum, f_m) KHZ [Convection Speed at f_m] fcs

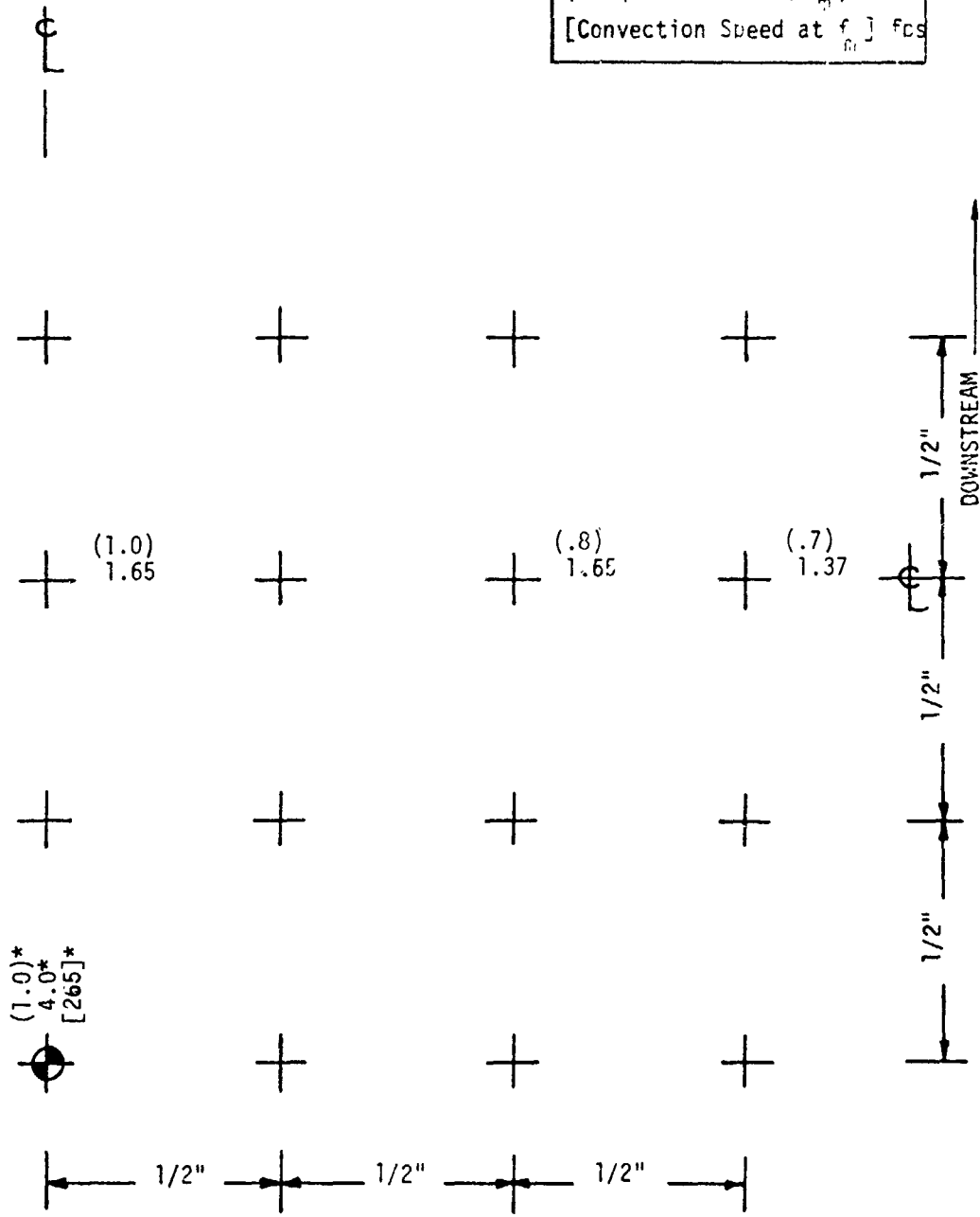
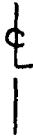


TABLE J-8
 PRESSURE MEASUREMENT RESULTS
 FLAT PLATE - ROUND NOZZLE (D = 1")

TEST CASE	T_j/T_a	M_j	X/D	β	RESULT TYPE
11"	1.0	0.5	7	50°	RMS (psi) (half-power freq.) KHZ [rolloff exponent] (peak amplification)

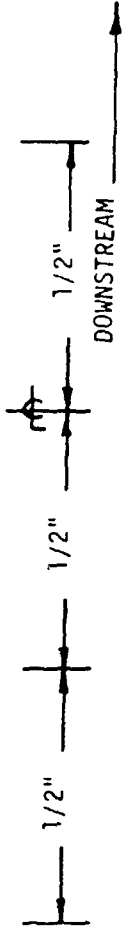


.104 (2.4)
 [2.9] (2.8)

.107 (2.75)
 [2.1] (5.6)

.112 (2.7)
 [2.2] (19.9)

.112 (2.4)
 [2.2] (31.6)



.148 (2.3)
 [2.6] (1.8)

(2.5)
 [1.8] (1.9)

(2.8)
 [2.0] (5.6)

.095 (2.6)
 [2.0] (15.9)

.205 (2.95)
 [2.9] (1.0)

.183 (2.5)
 [1.9] (1.6)

.138 (2.6)
 [1.8] (2.8)

.093 (2.7)
 [2.0] (19.9)

.307 (2.3)
 [3.5] (1.0)

.243 (1.9)
 [2.3] (2.0)

.153 (2.7)
 [1.8] (1.8)

.088 (2.3)
 [2.1] (15.8)

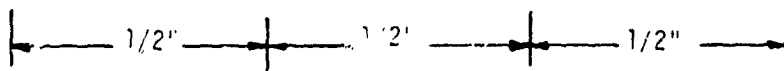


TABLE J-9
 PRESSURE MEASUREMENT RESULTS
 FLAT PLATE - ROUND NOZZLE (D = 1")

TEST CASE	T_j/T_a	M_j	X/D	β	RESULT TYPE
1I	1	.5	7	90°	RMS (psi) (half-power freq.) KHZ [rolloff exponent] [peak amplification]

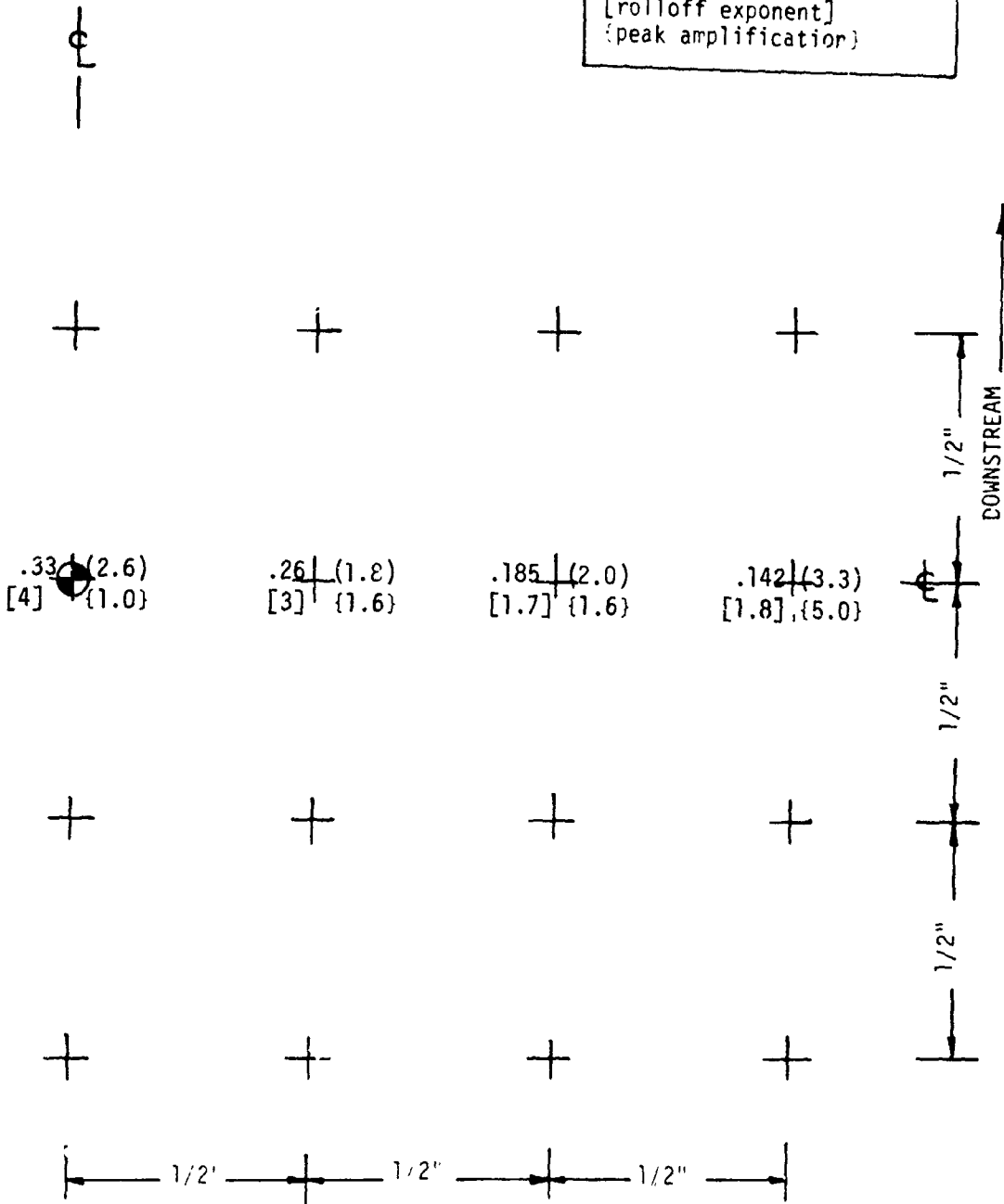


TABLE J-9 (CONT'D)
 PRESSURE MEASUREMENT RESULTS
 FLAT PLATE - ROUND NOZZLE (D = 1")

TEST CASE	T_j/T_a	M_j	X/D	β	RESULT TYPE
11	1.0	0.5	7	90°	Max. Correlation Length (in) (Freq. at Maximum, f_m) KHZ [Convection Speed at f_m] fps

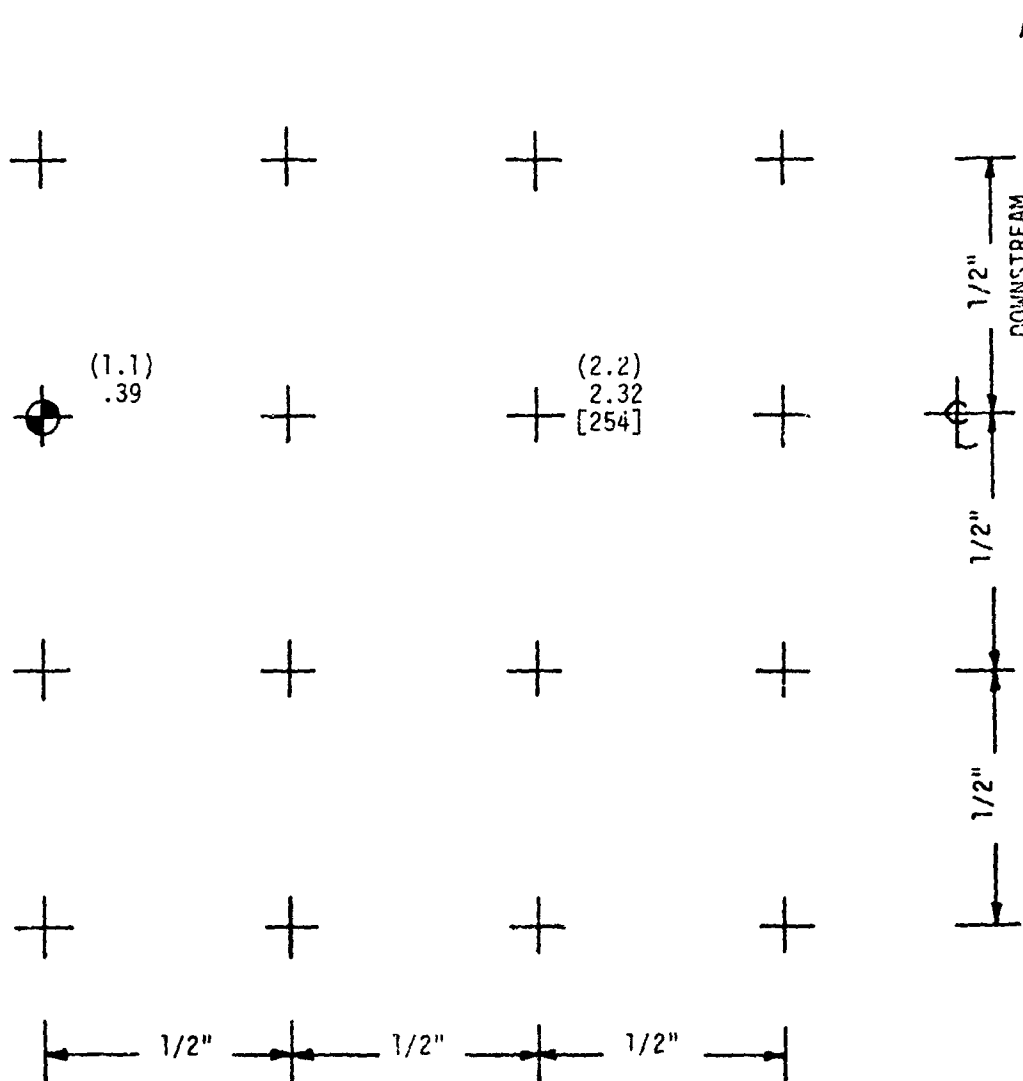
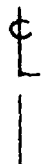


TABLE J-10
 PRESSURE MEASUREMENT RESULTS
 FLAT PLATE - ROUND NOZZLE (D = 1")

TEST CASE	T_j/T_a	M_j	X/D	β	RESULT TYPE
1J	1.0	0.35	10	50°	RMS (psi) (half-power freq.) KHZ [rolloff exponent] (peak amplification)

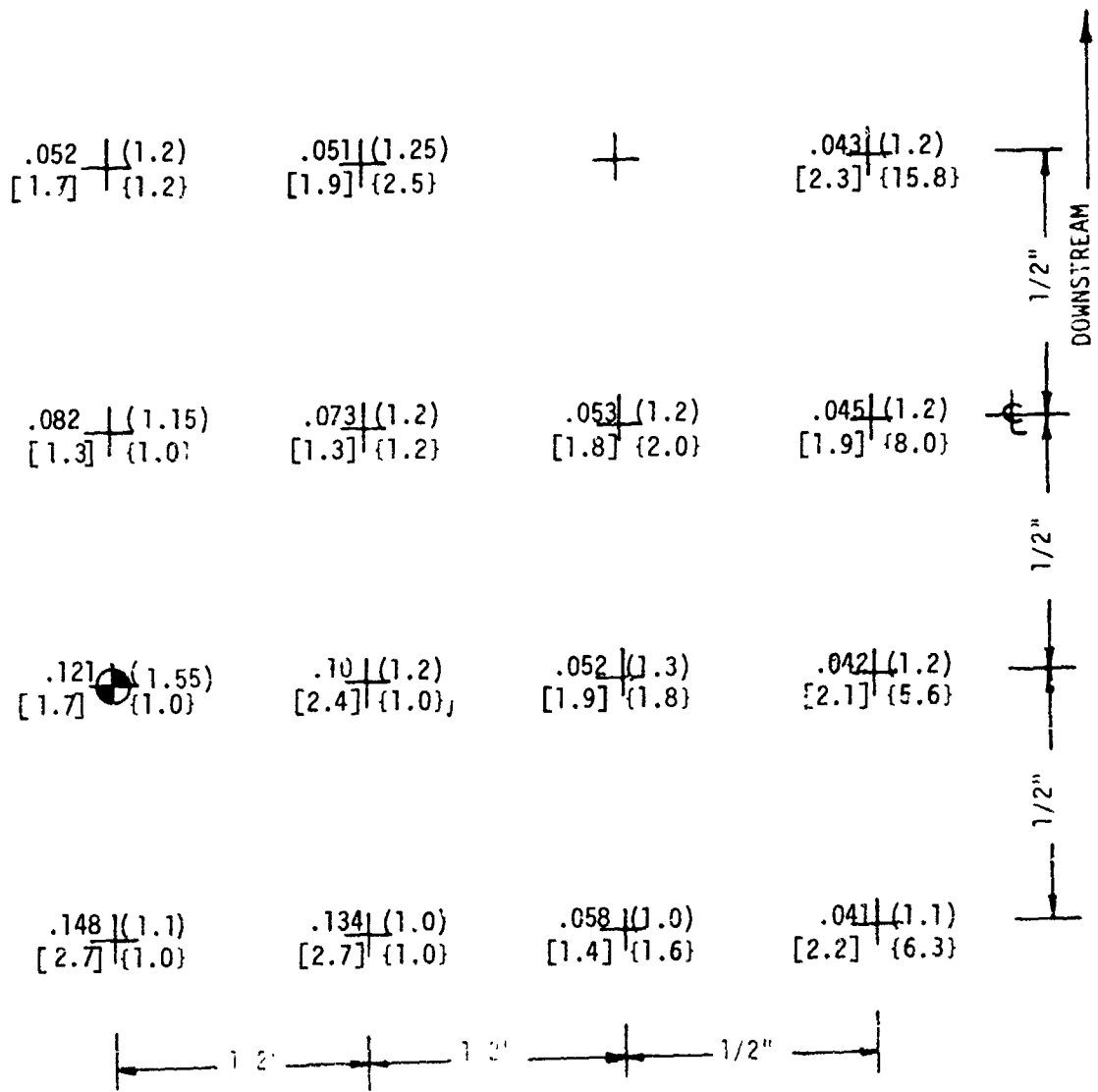


TABLE J-10 (CONT'D)
 PRESSURE MEASUREMENT RESULTS
 FLAT PLATE - ROUND NOZZLE (D = 1")

TEST CASE	T_j/T_a	M_j	X/D	β	RESULT TYPE
1J	1.0	0.35	10	50°	Max. Correlation Length (in) (Freq. at Maximum, f_m) KHZ [Convection Speed at f_m] fps

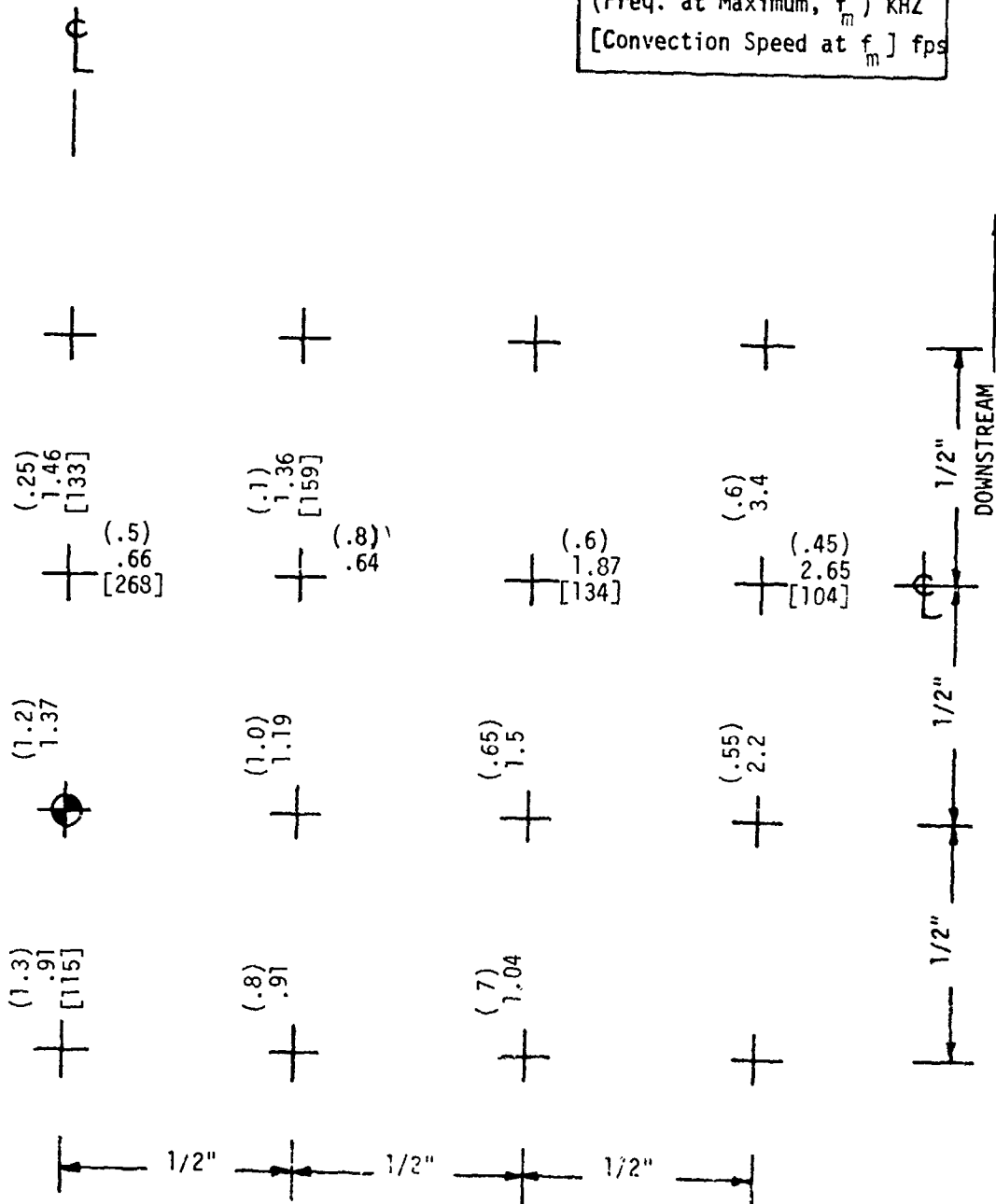


TABLE J-11
 PRESSURE MEASUREMENT RESULTS
 FLAT PLATE - ROUND NOZZLE (D = 1")

TEST CASE	T_j/T_a	M_j	X/D		RESULT TYPE
1K	1.0	0.35	5	50°	RMS (psi) (half-power freq.) KHZ [rolloff exponent] (peak amplification)

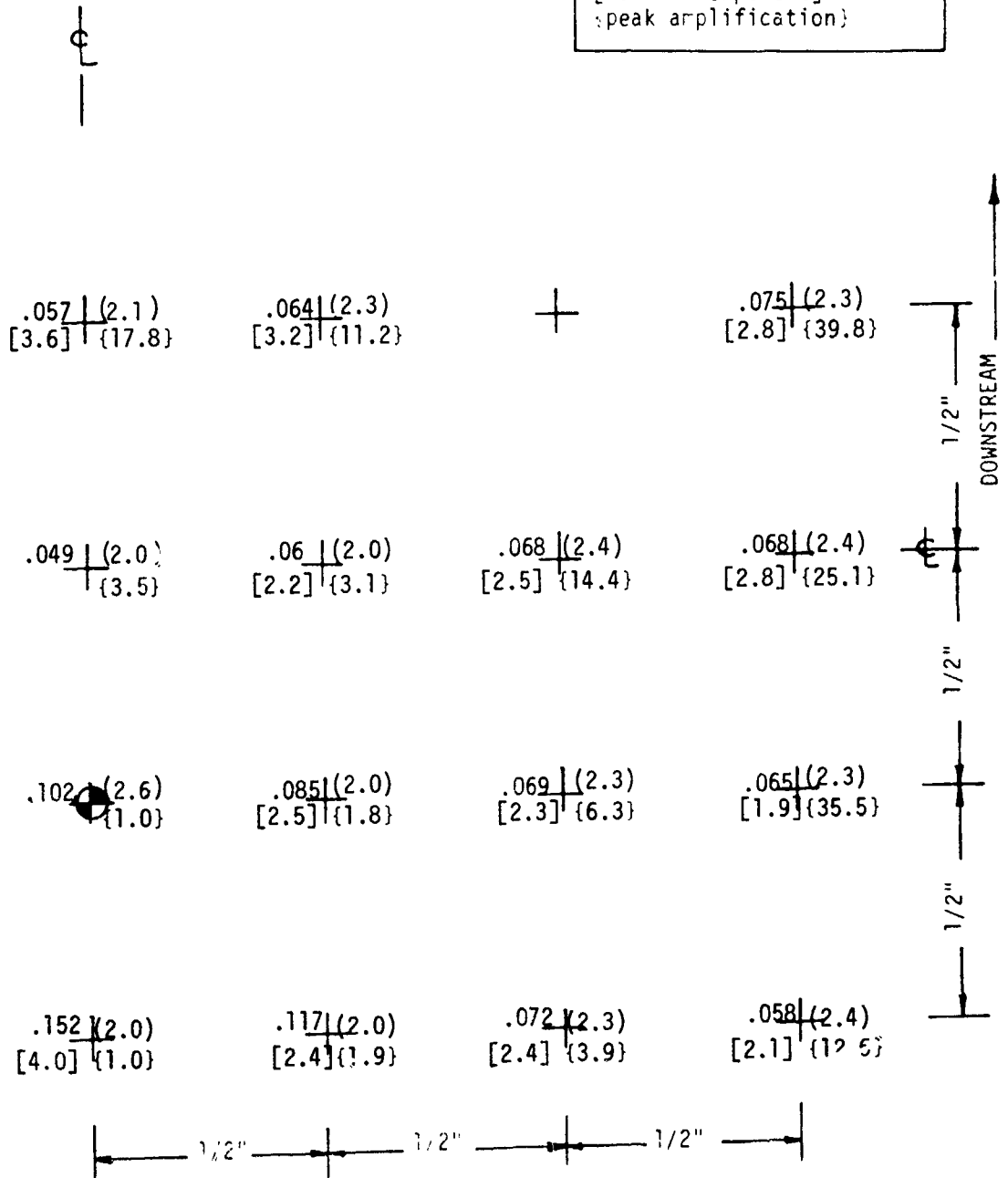


TABLE J-11 (CONT'D)
 PRESSURE MEASUREMENT RESULTS
 FLAT PLATE - ROUND NOZZLE (D = 1")

TEST CASE	T_j/T_a	M_j	X/D	β	RESULT TYPE
1K	1.0	.35	5	50°	Max. Correlation Length (in) (Freq. at Maximum, f_m) KHZ [Convection Speed at f_m] fps

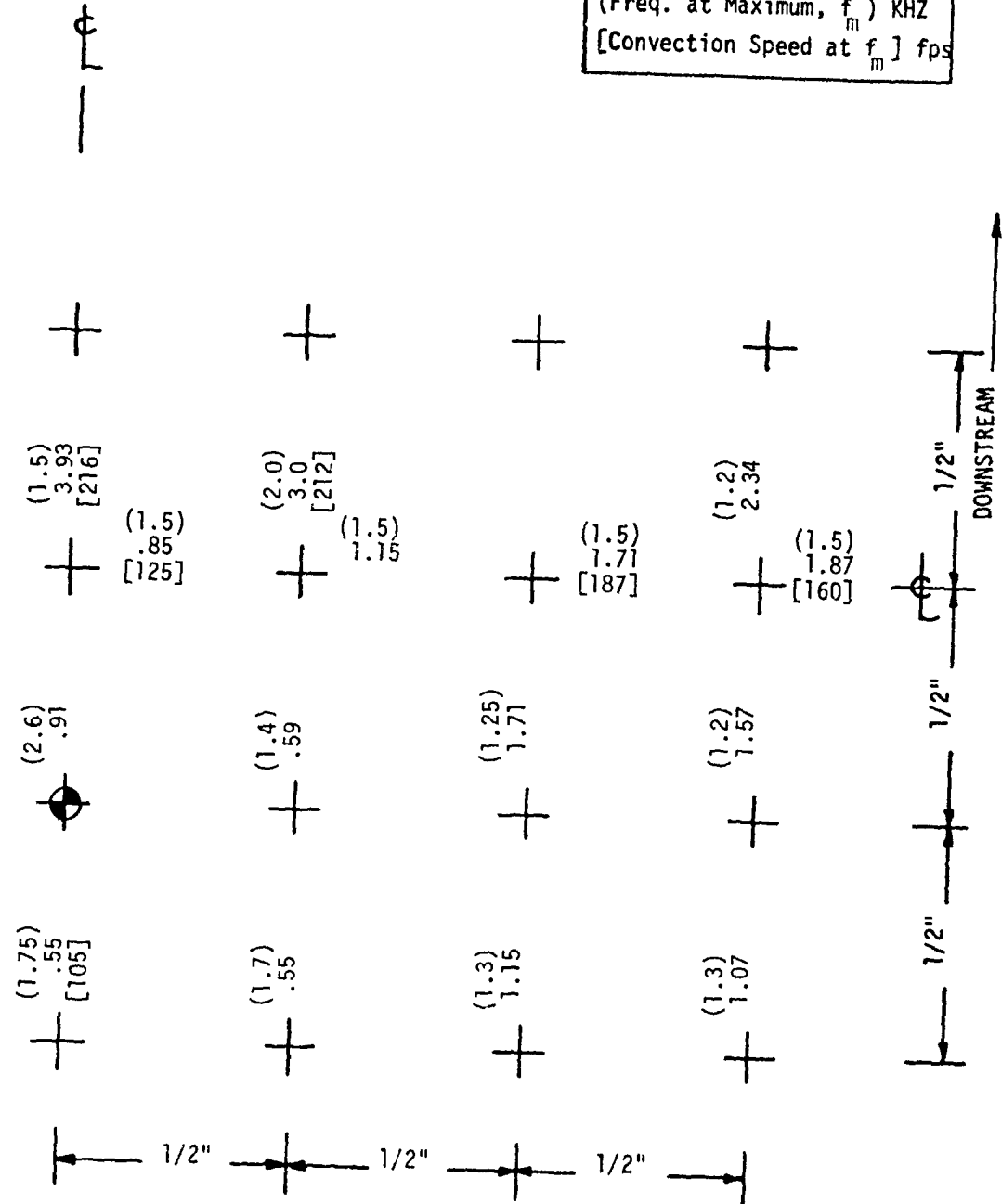
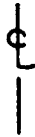


TABLE J-12
 PRESSURE MEASUREMENT RESULTS
 FLAT PLATE - ROUND NOZZLE (D = 1")

TEST CASE	T_j/T_a	M_j	X/D	β	RESULT TYPE
1L	1.0	0.35	7	50°	RMS (psi) (half-power freq.) KHZ [rolloff exponent] {peak amplification}



.056 | (1.8)
[2.9] | {2.8}

.057 | (2.0)
[2.3] | {4.0}



.057 | (1.7)
[2.9] | {31.6}



.071 | (1.7)
[2.7] | {1.8}

.069 | (1.6)
[2.3] | {1.8}

.055 | (1.8)
[1.6] | {5.6}

.053 | (1.8)
[1.9] | {15.8}



.11 | (2.15)
[2.8] | {1.0}

.095 | (1.6)
[2.0] | {1.6}

.075 | (1.9)
[1.7] | {2.8}

.053 | (1.9)
[2.1] | {15.8}



.166 | (1.6)
[3.5] | {1.0}

.128 | (1.4)
[2.4] | {1.9}

.079 | (1.8)
[1.8] | {2.2}

.048 | (1.7)
[2.2] | {15.9}

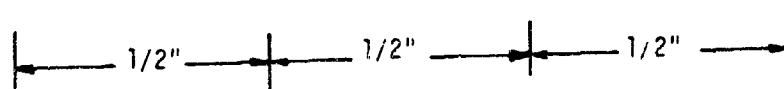
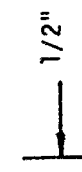


TABLE J-12 (CONT'D)
 PRESSURE MEASUREMENT RESULTS
 FLAT PLATE - ROUND NOZZLE (D = 1")

TEST CASE	r_j/r_a	M_j	X/D	β	RESULT TYPE
1L	1.0	0.35	7	50°	Max. Correlation Length (in) (Freq. at Maximum, f_m) KHZ [Convection Speed at f_m] ft/ps

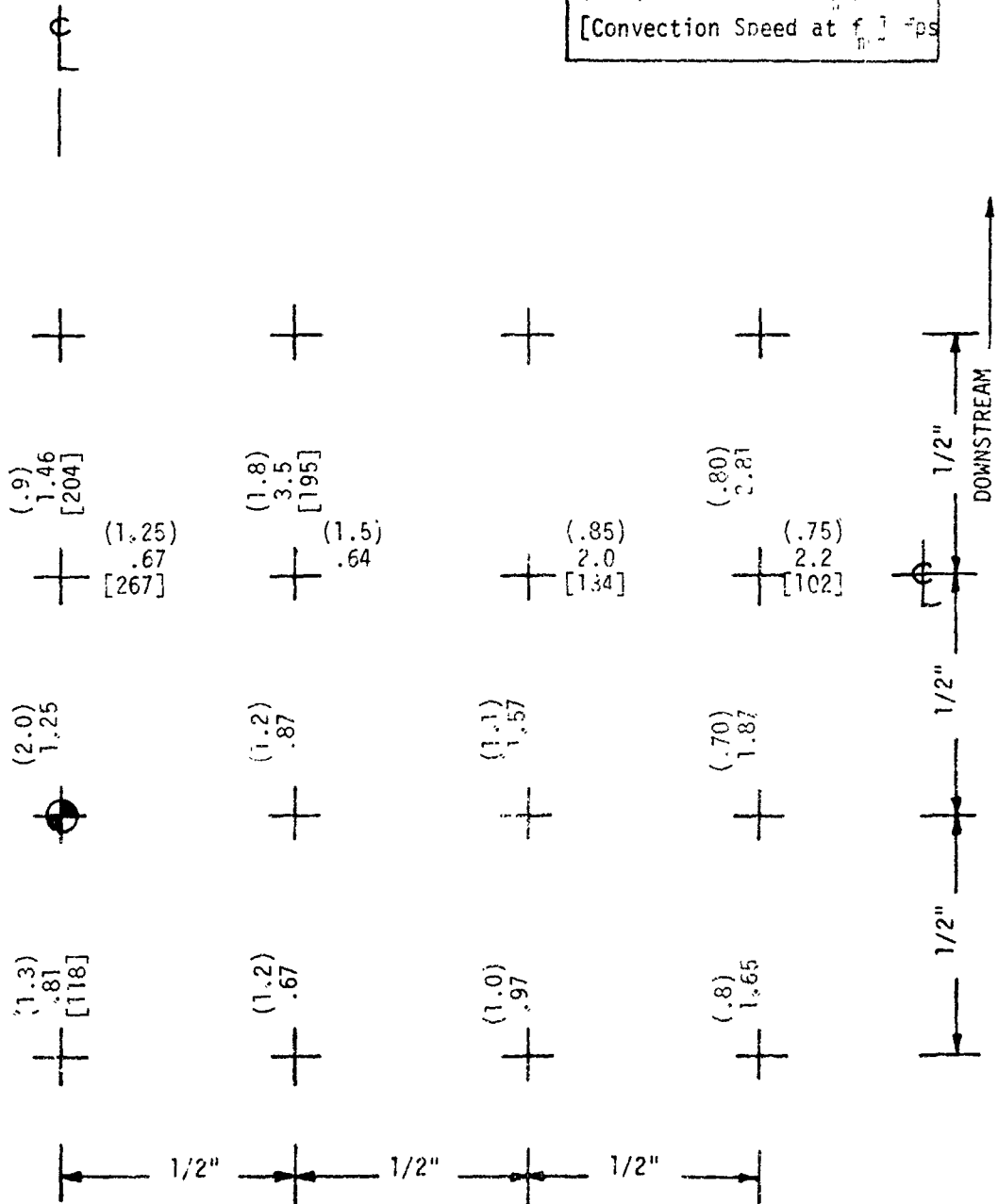


TABLE J-13
 PRESSURE MEASUREMENT RESULTS
 FLAT PLATE - ROUND NOZZLE (D = 1")

TEST CASE	T_j/T_a	M_j	X/D	β	RESULT TYPE
1M	1.0	0.74	7	50°	RMS (psi) (half-power freq.) KHZ [rolloff exponent] {peak amplification}

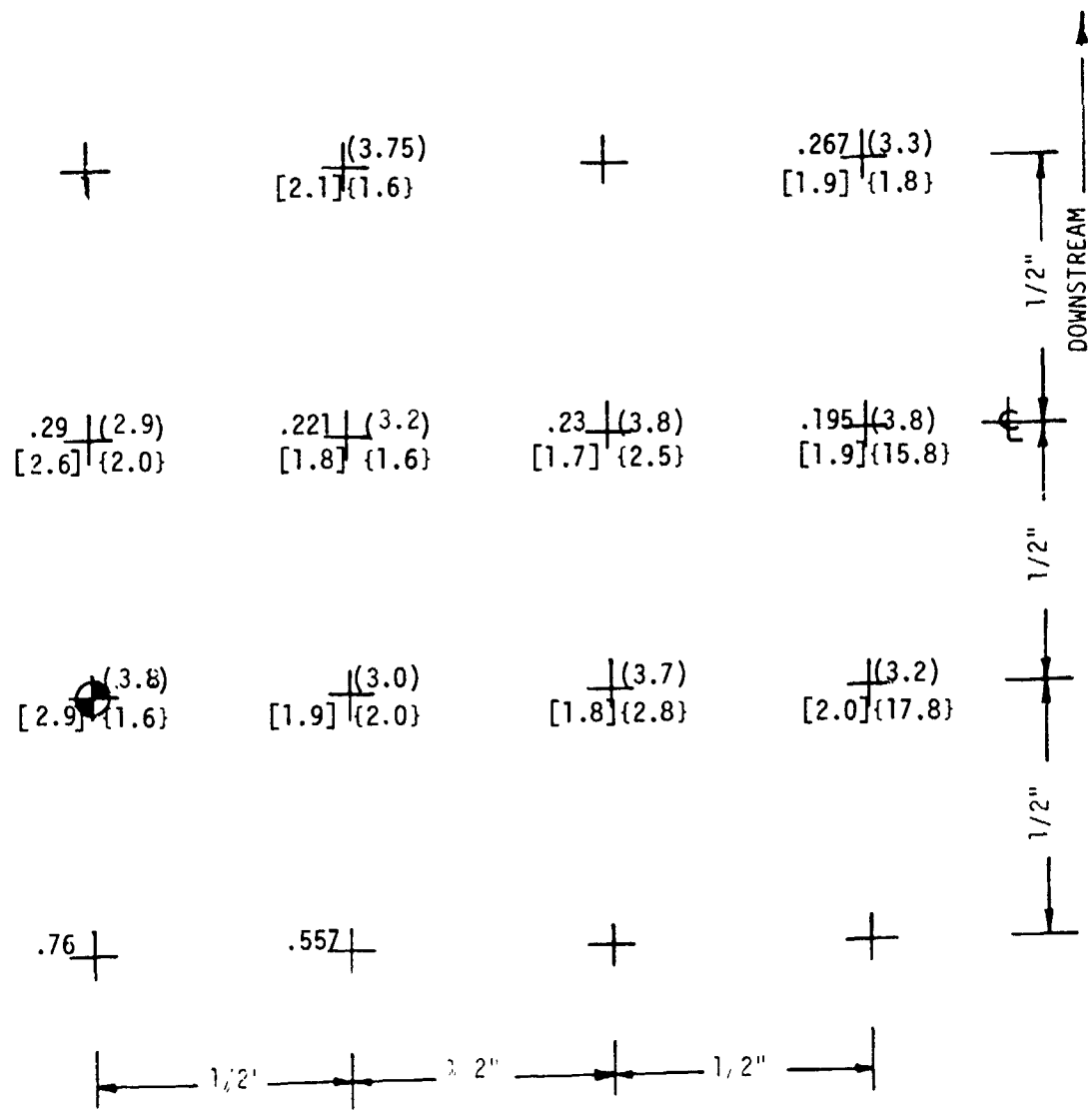


TABLE J-13 (CONT'D)
 PRESSURE MEASUREMENT RESULTS
 FLAT PLATE - ROUND NOZZLE (D = 1")

TEST CASE	T_j/T_a	M_j	X/D	β	RESULT TYPE
1M	1.0	0.74	7	50°	Max. Correlation Length (in) (Freq. at Maximum, f_m) KHZ [Convection Speed at f_m] fps

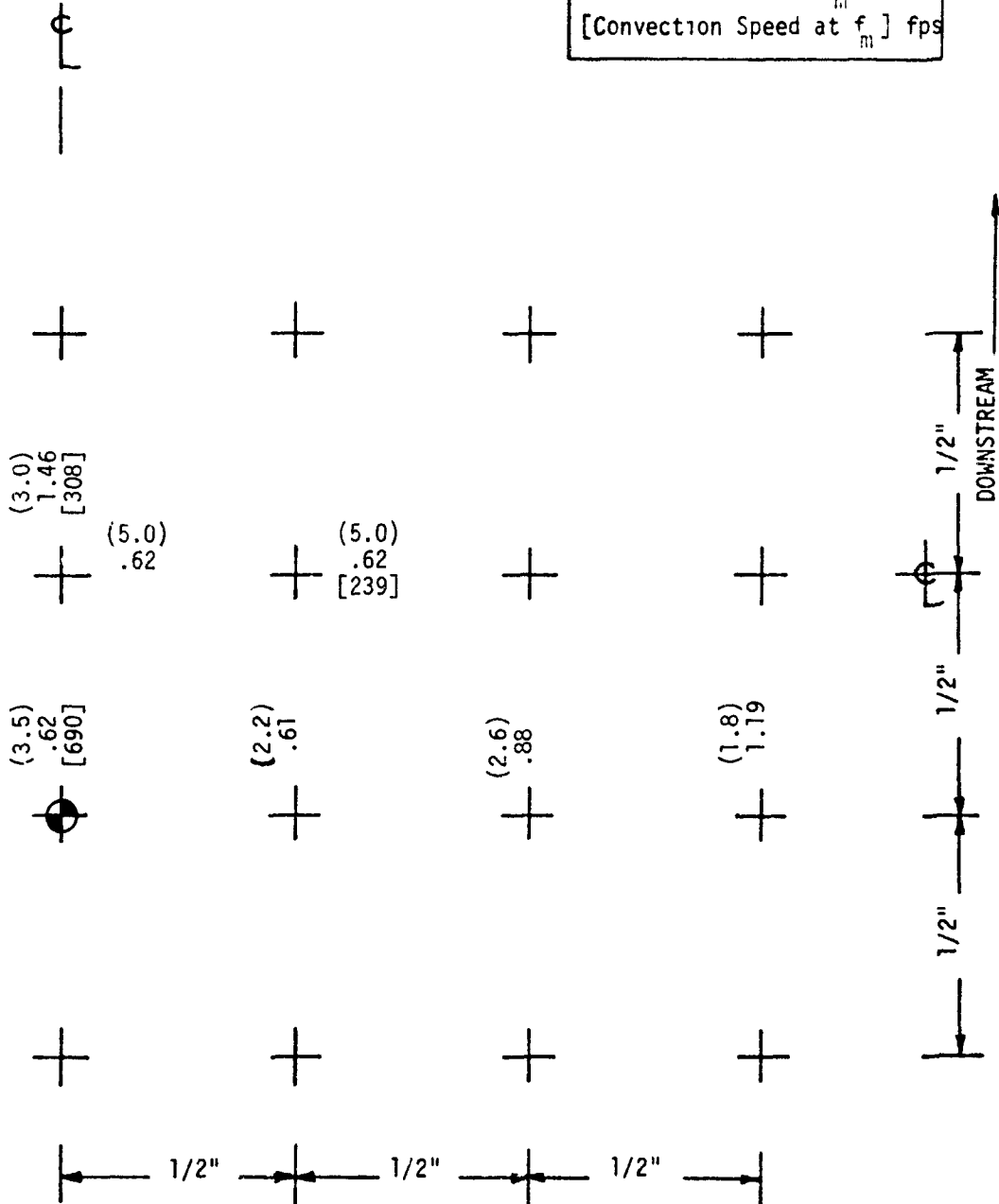


TABLE J-14
 PRESSURE MEASUREMENT RESULTS
 FLAT PLATE - ROUND NOZZLE (D = 1")

TEST CASE	T_j/T_a	M_j	X/D	ϵ	RESULT TYPE
1N	1.0	0.74	5.27	25°	RMS (psi) (half-power freq.) KHZ [rolloff exponent] {peak amplification}

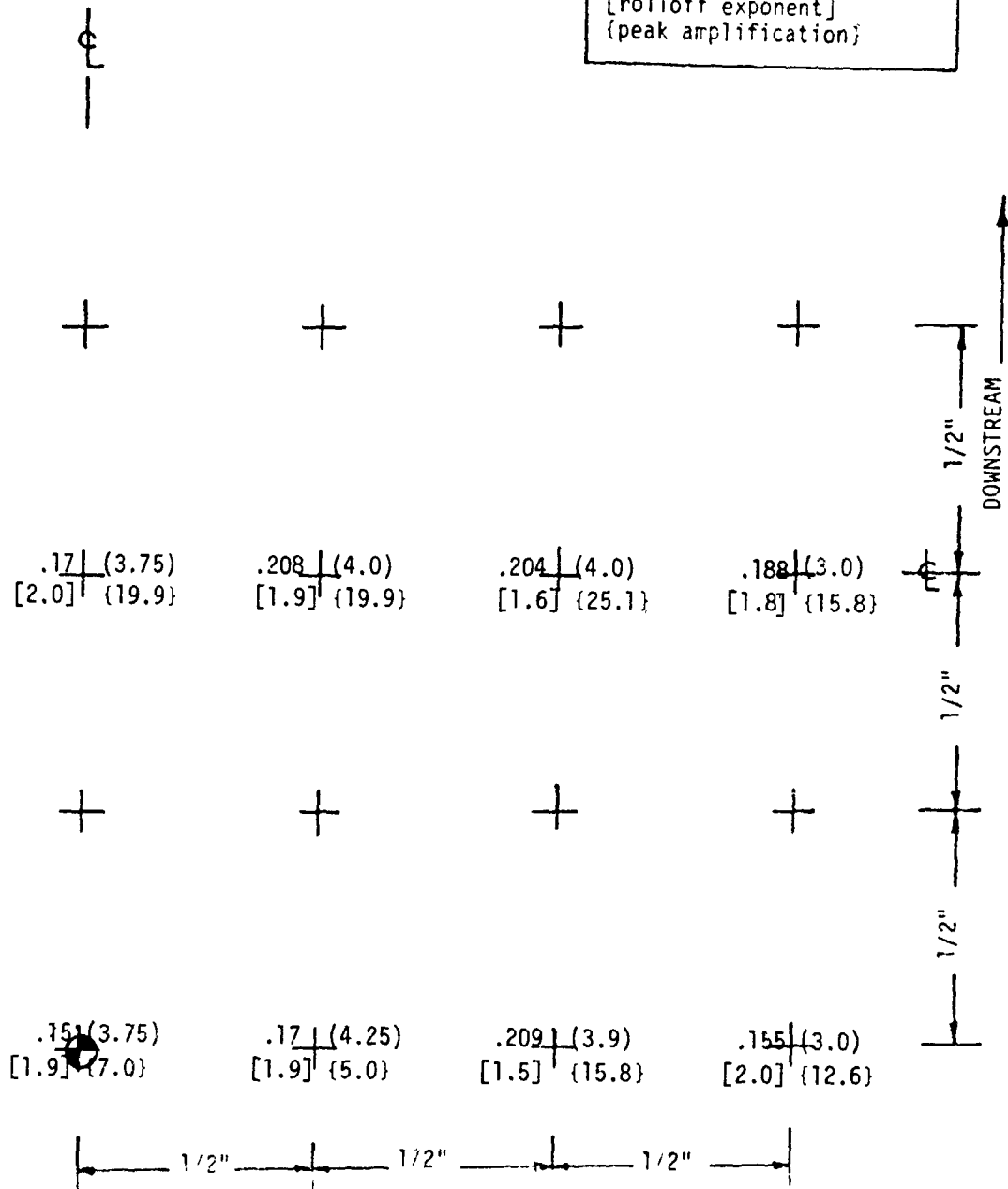


TABLE J-14 (CONT'D)
 PRESSURE MEASUREMENT RESULTS
 FLAT PLATE - ROUND NOZZLE (D = 1")

TEST CASE	T_j/T_a	M_j	X/D	β	RESULT TYPE
1N	1.0	0.74	5.27	25°	Max. Correlation Length (in) (Freq. at Maximum, f_m) KHZ [Convection Speed at f_m] fps

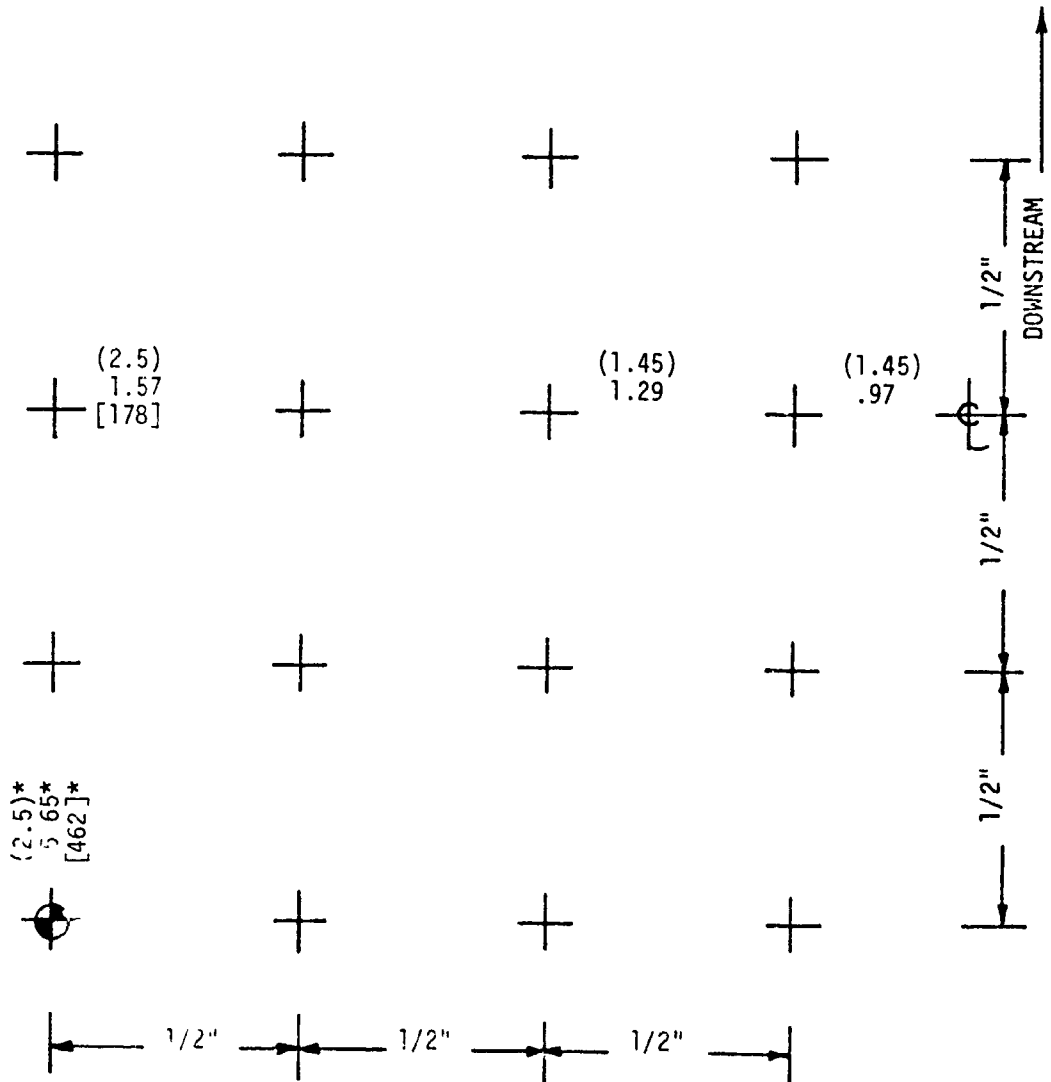
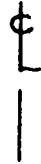


TABLE J-15
 PRESSURE MEASUREMENT RESULTS
 FLAT PLATE - ROUND NOZZLE (D = 1")

TEST CASE	T_j/T_a	M_j	X/D	β	RESULT TYPE
10	1.0	.74	10	90°	RMS (psi) (half-power freq.) KHZ [rolloff exponent] {peak amplification}

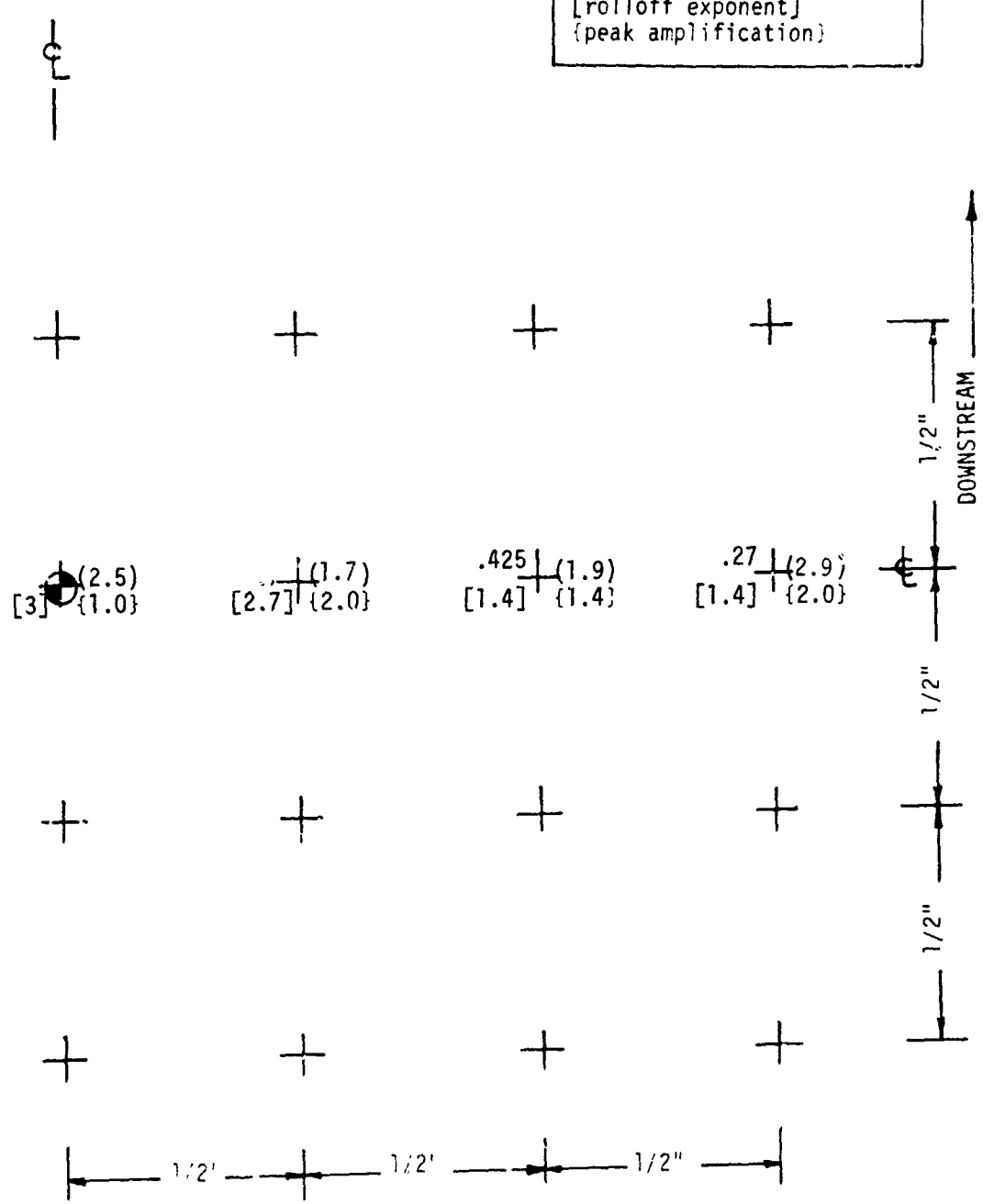


TABLE J-15 (CONT'D)
 PRESSURE MEASUREMENT RESULTS
 FLAT PLATE - ROUND NOZZLE (D = 1")

TEST CASE	T_j/T_a	U_j	X/D	ϵ	RESULT TYPE
10	1.0	0.74	10	90°	Max. Correlation Length (in) (Freq. at Maximum, f_r) KHZ [Convection Speed at f_r] fps

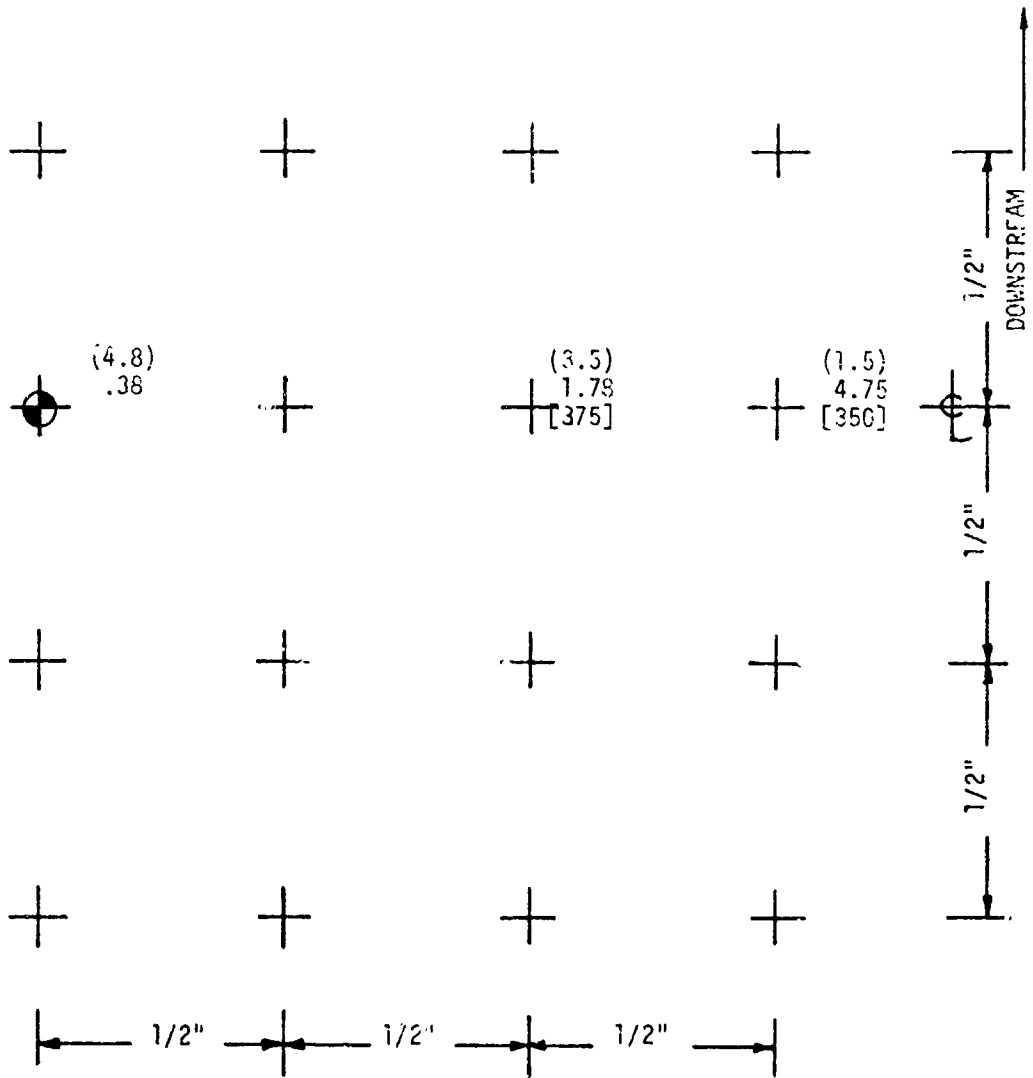
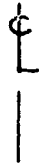


TABLE J-16
 PRESSURE MEASUREMENT RESULTS
 FLAT PLATE - ROUND NOZZLE (D = 1")

TEST CASE	T_j/T_a	M_j	X/D	β	RESULT TYPE
2A	1.7	0.46	10	50°	RMS (psi) (half-power freq.) KHZ [rolloff exponent] {peak amplification}

⊕
|

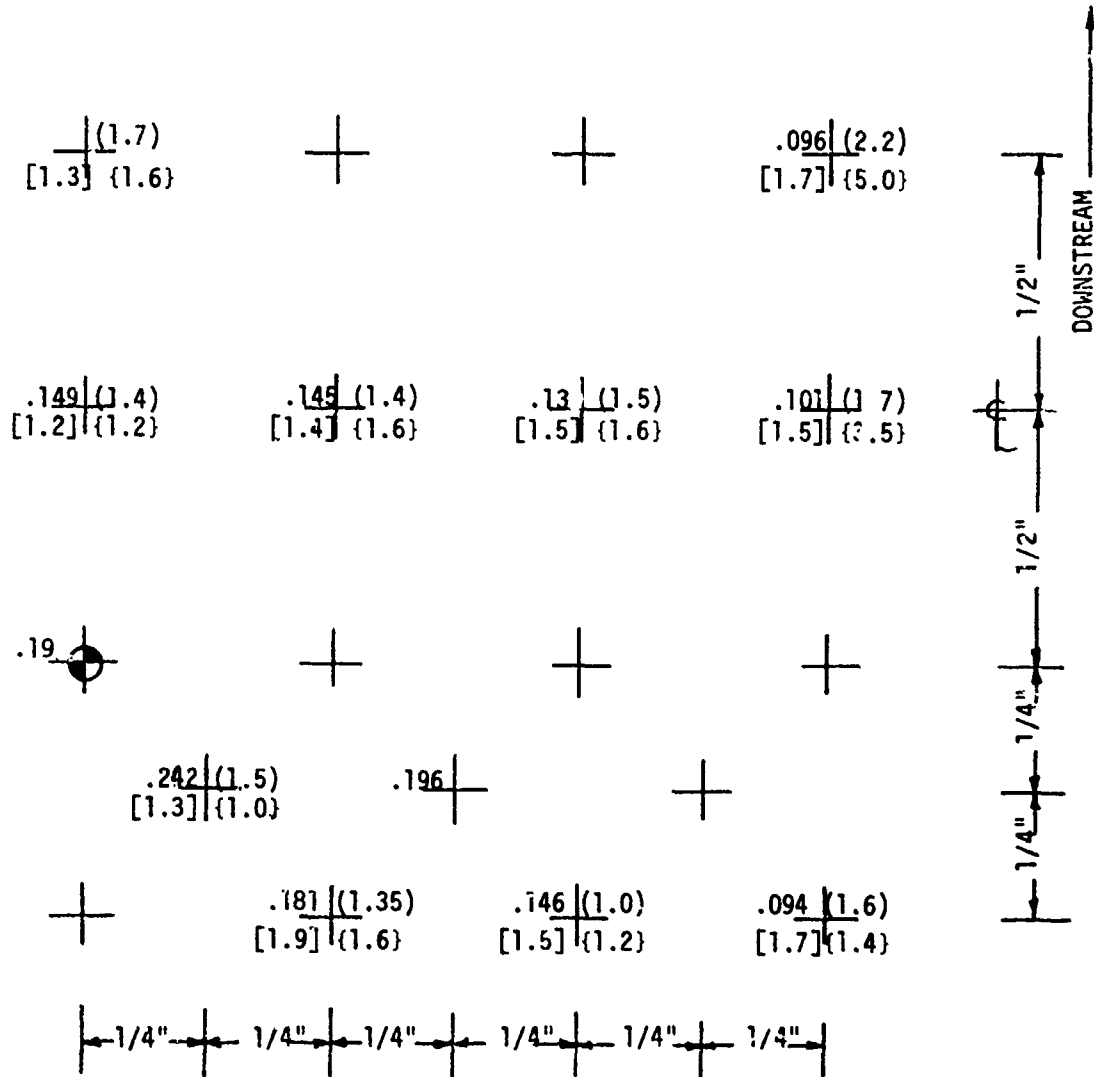


TABLE J-16 (CONT'D)
 PRESSURE MEASUREMENT RESULTS
 FLAT PLATE - ROUND NOZZLE (D = 1")

TEST CASE	\bar{T}_j/T_a	M_j	X/D	β	RESULT TYPE
2A	1.7	0.46	10	50°	Max. Correlation Length (in) (Freq. at Maximum, f_m) KHZ [Convection Speed at f_m] fps

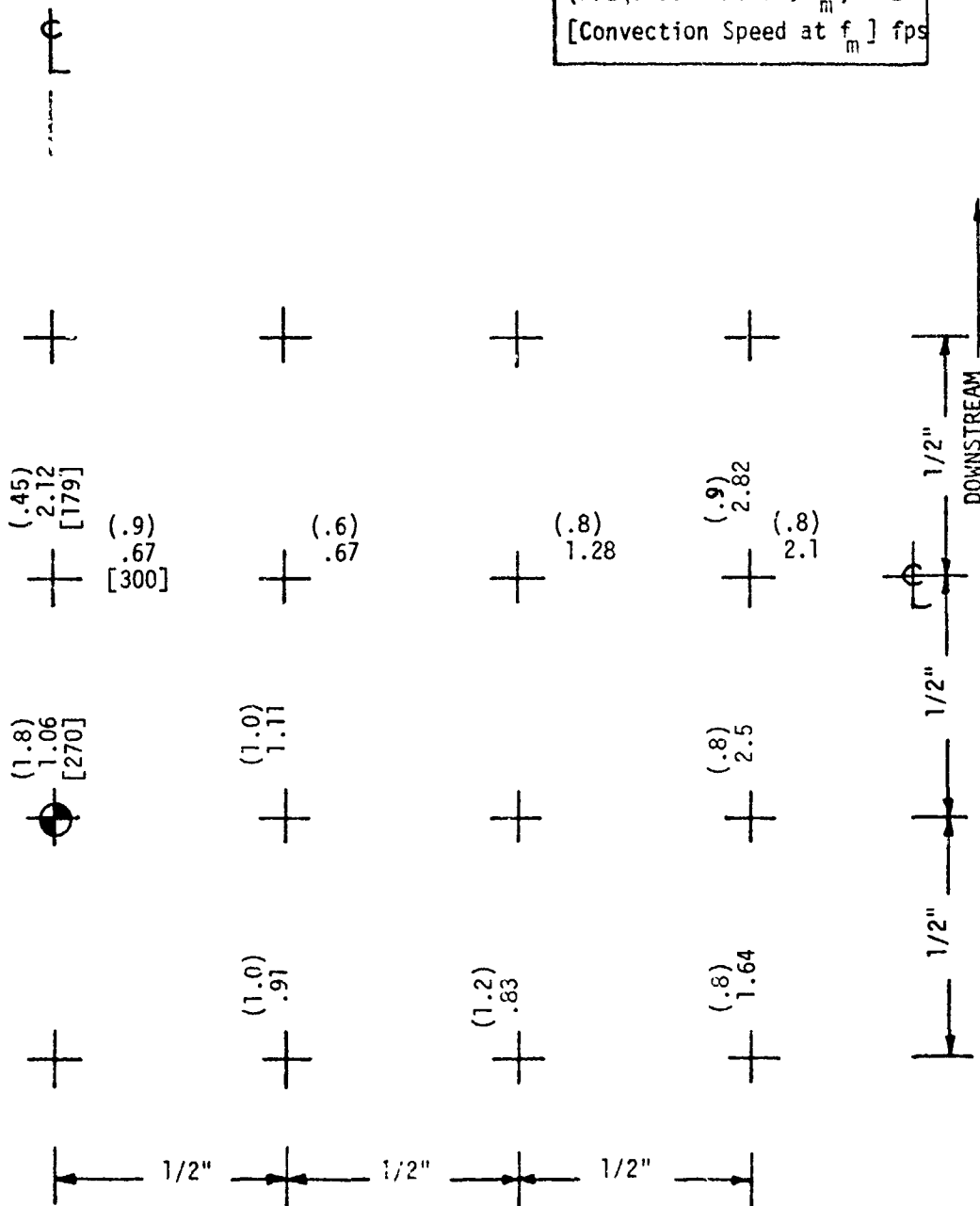


TABLE J-17
 PRESSURE MEASUREMENT RESULTS
 FLAT PLATE - ROUND NOZZLE (D = 1")

TEST CASE	T_j/T_a	M_j	X/D	β	RESULT TYPE
2B	1.7	0.46	7	50°	RMS (psi) (half-power freq.) KHZ [roll-off exponent] (peak amplification)

|
 ⊕
 |

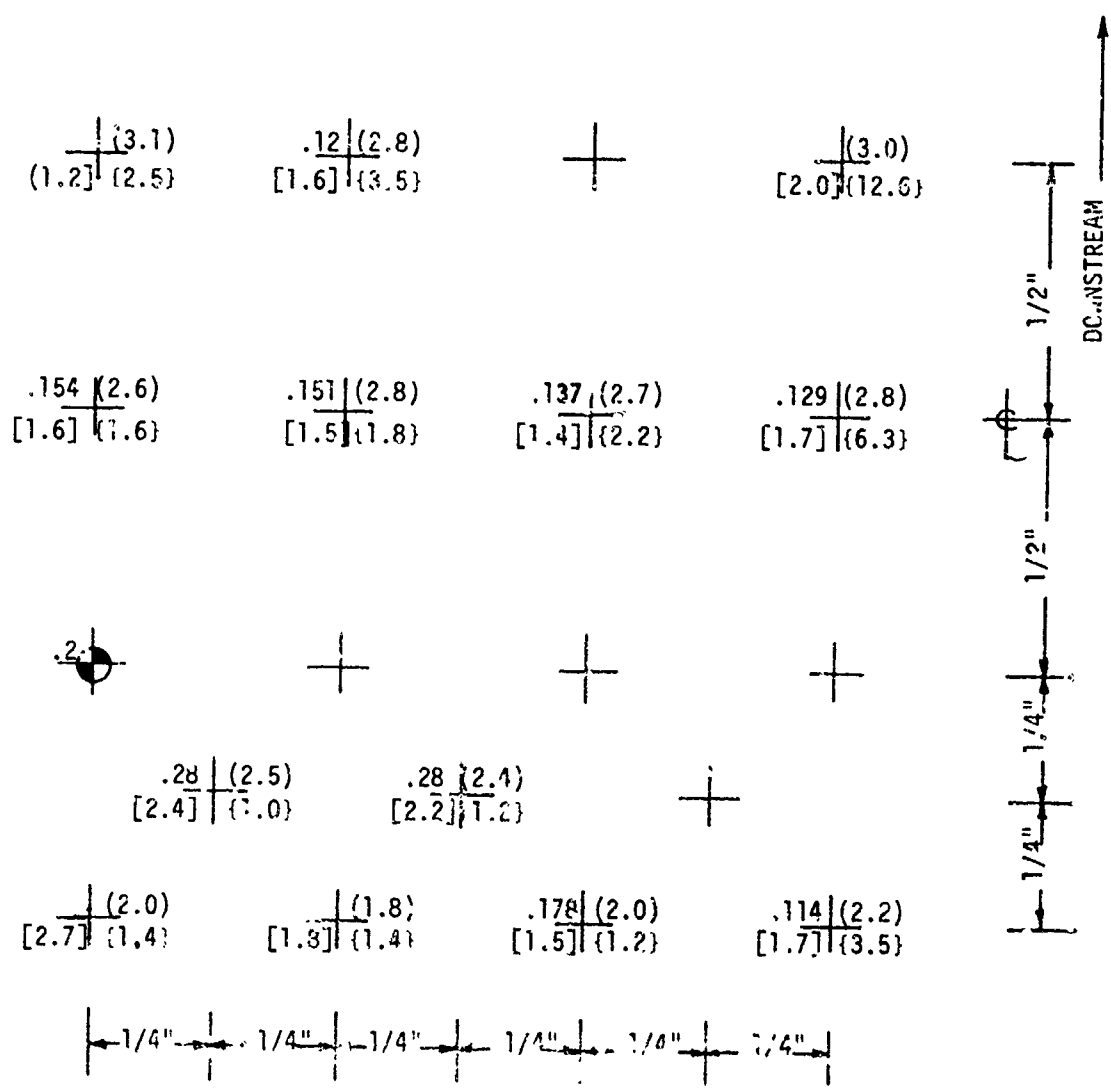


TABLE J-17 (CONT'D)
 PRESSURE MEASUREMENT RESULTS
 FLAT PLATE - ROUND NOZZLE (D = 1")

TEST CASE	T_j/T_a	M_j	X/D	ρ	RESULT TYPE
2B	1.7	0.46	7	50°	Max. Correlation Length (in) (Freq. at Maximum, f_m) KHZ [Convection Speed at f_m] fps

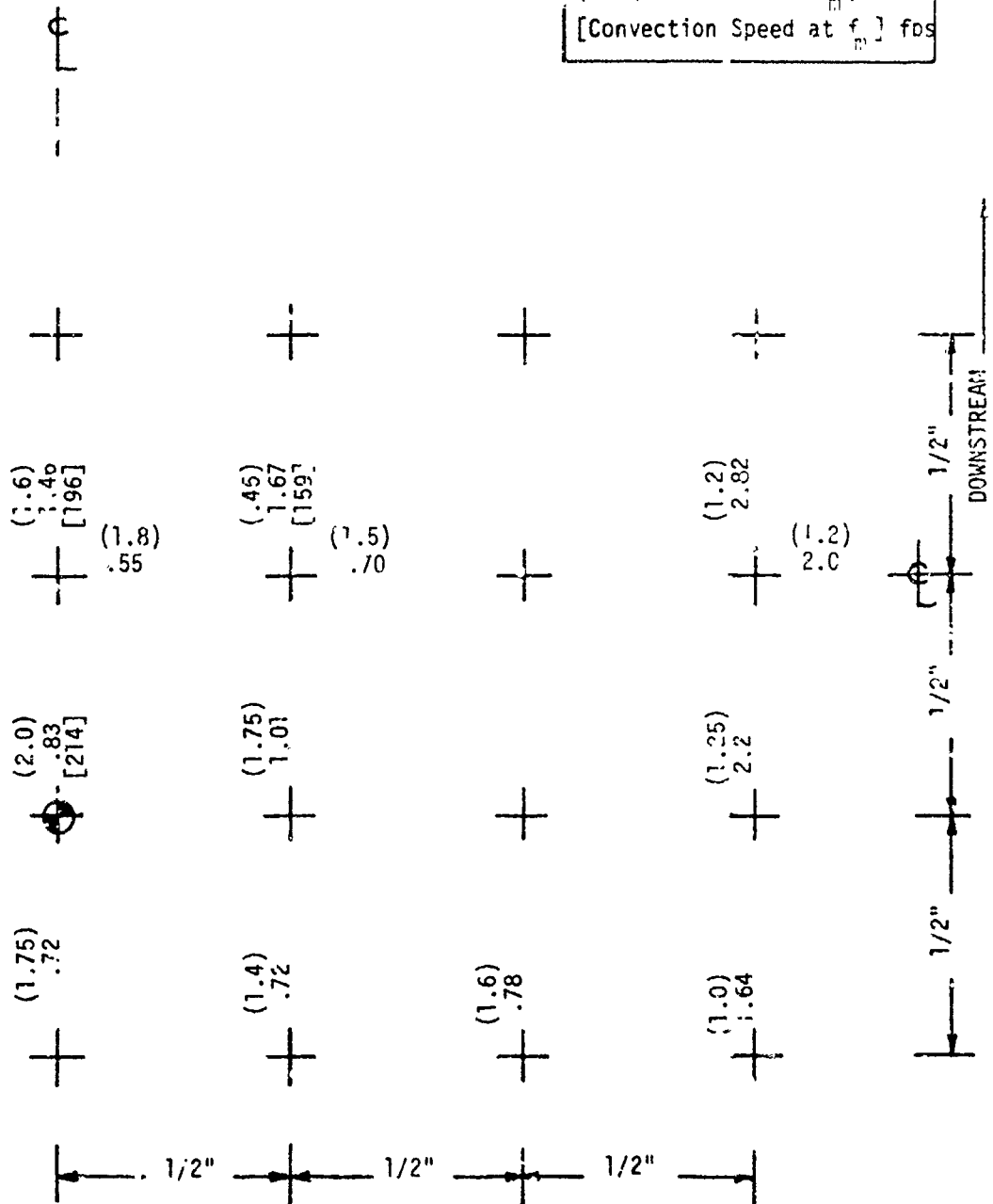


TABLE J-18
PRESSURE MEASUREMENT RESULTS
FLAT PLATE - ROUND NOZZLE (D = 1")

TEST CASE	T_j/T_a	M_j	X/D	β	RESULT TYPE
2C	1.7	0.46	5	50°	RMS (psi) (half-power freq.) KHZ [rolloff exponent] (peak amplification)

⊕
|

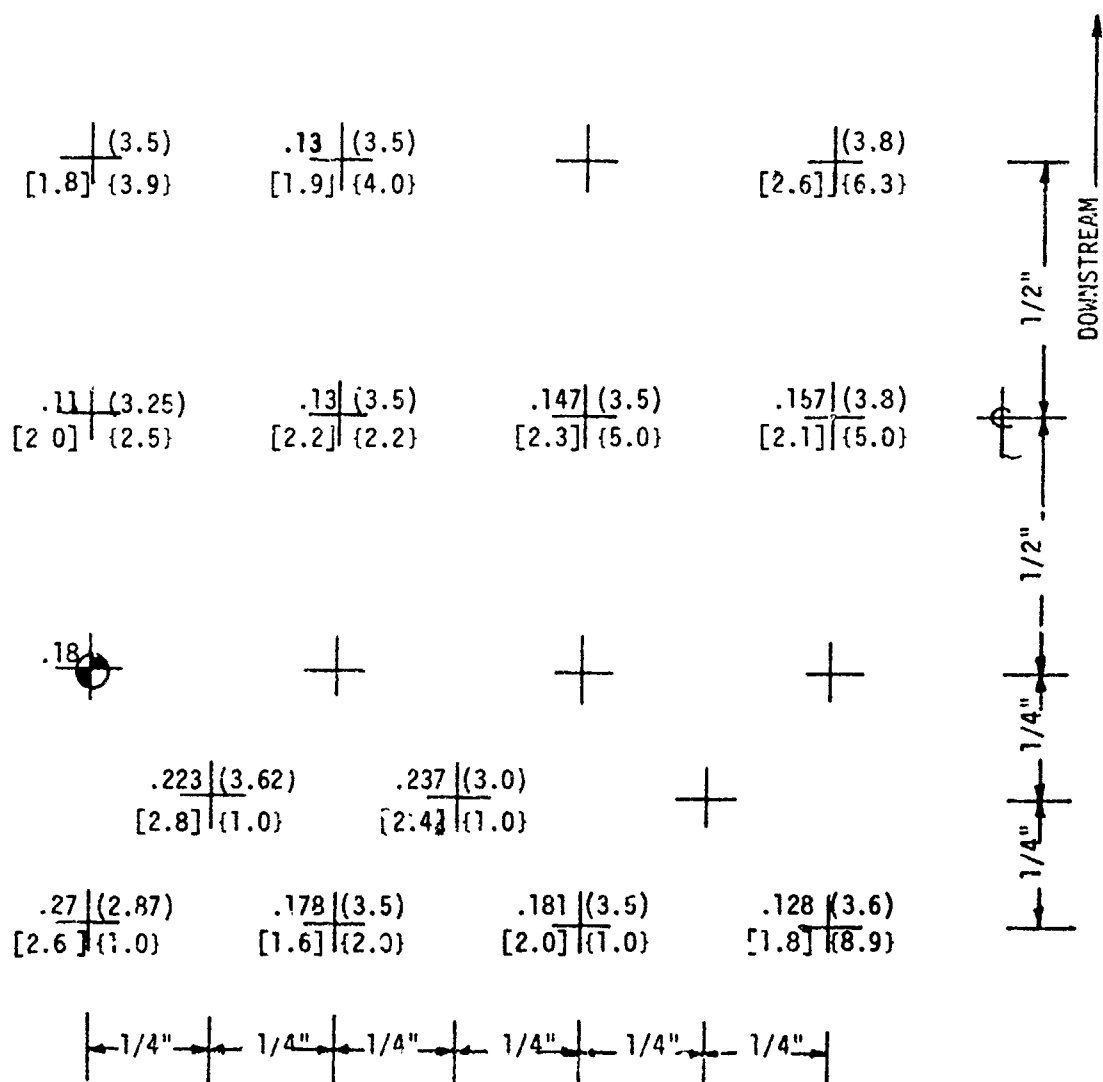


TABLE J-18 CONT'D)
 PRESSURE MEASUREMENT RESULTS
 FLAT PLATE - ROUND NOZZLE (D = 1")

TEST CASE	Γ_j/T_a	M_j	X/D	β	RESULT TYPE
2C	1.7	0.46	5	50°	Max. Correlation Length (in) (Freq. at Maximum, f_m) KHZ [Convection Speed at f_m] fps

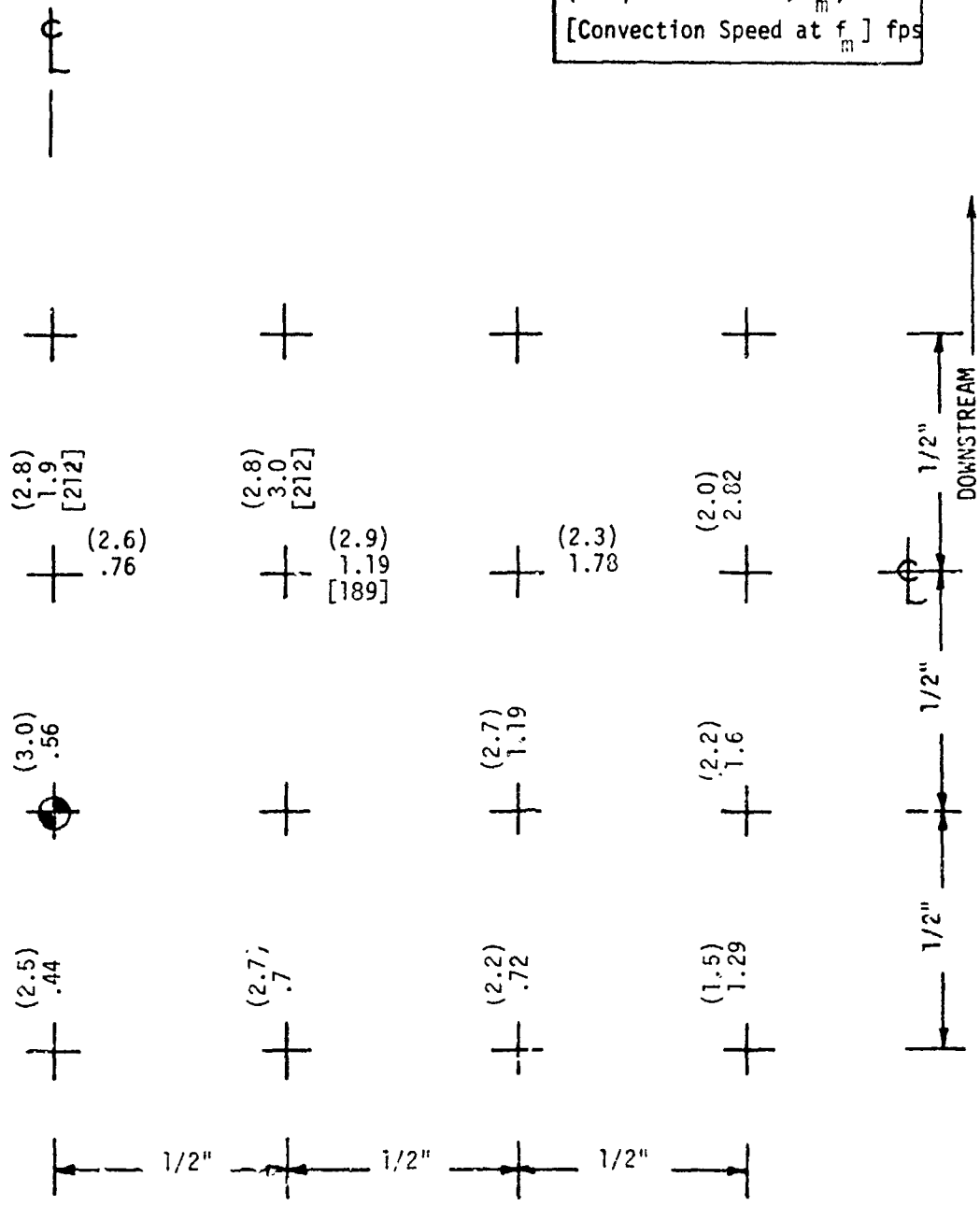


TABLE J-19
 PRESSURE MEASUREMENT RESULTS
 FLAT PLATE - ROUND NOZZLE (D = 2")

TEST CASE	T_j/T_a	M_j	X/D	β	RESULT TYPE
3A	1.0	0.5	5	50°	RMS (psi) (half-power freq.) KHZ [rolloff exponent] (peak amplification)

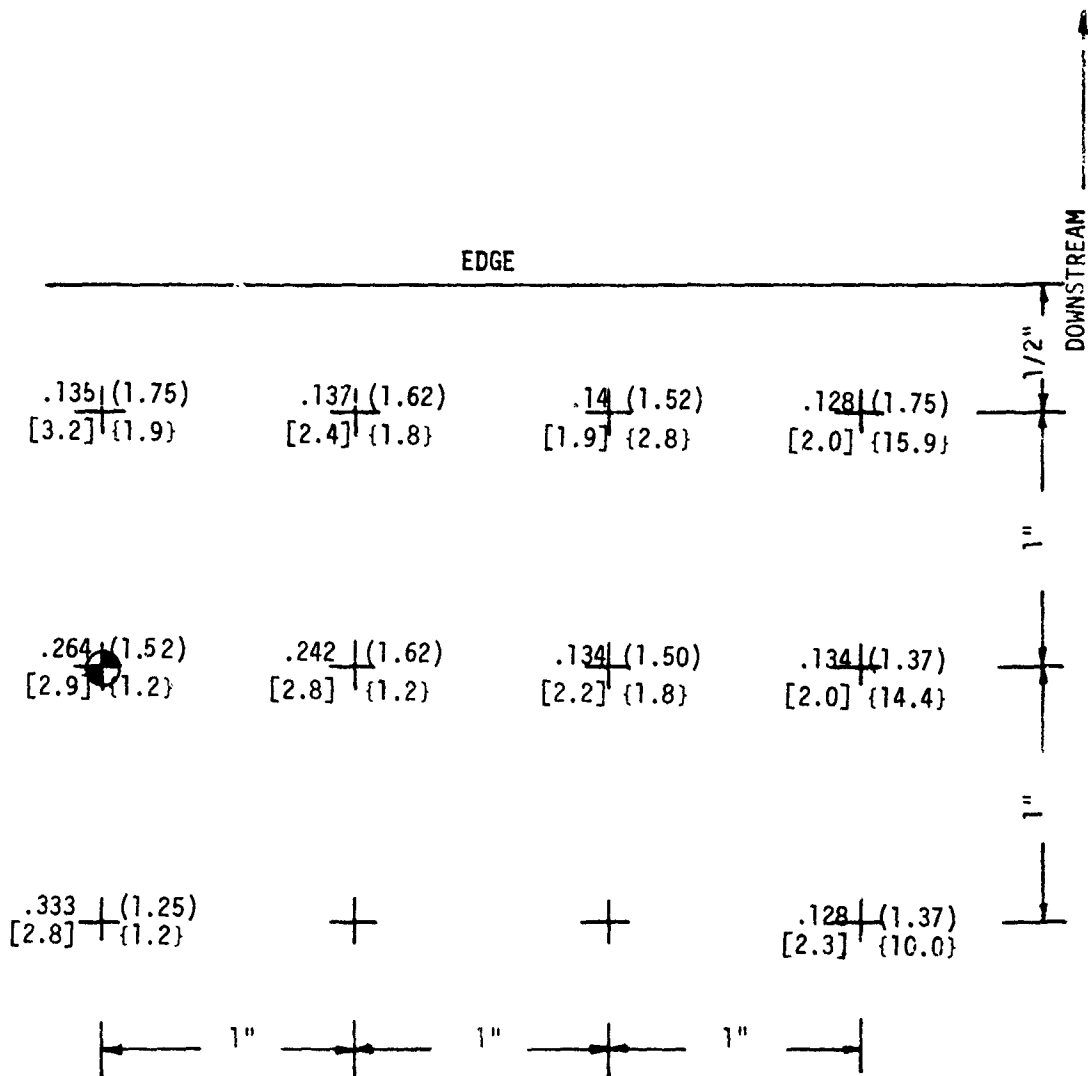


TABLE J-19 (CONT'D)
 PRESSURE MEASUREMENT RESULTS
 FLAT PLATE - ROUND NOZZLE (D = 2")

TEST CASE	T_j/T_a	M_j	X/D	β	RESULT TYPE
3A	1.0	0.5	5	50°	Max. Correlation Length (in) (Freq. at Maximum, f_m) KHZ [Convection Speed at f_m] fps

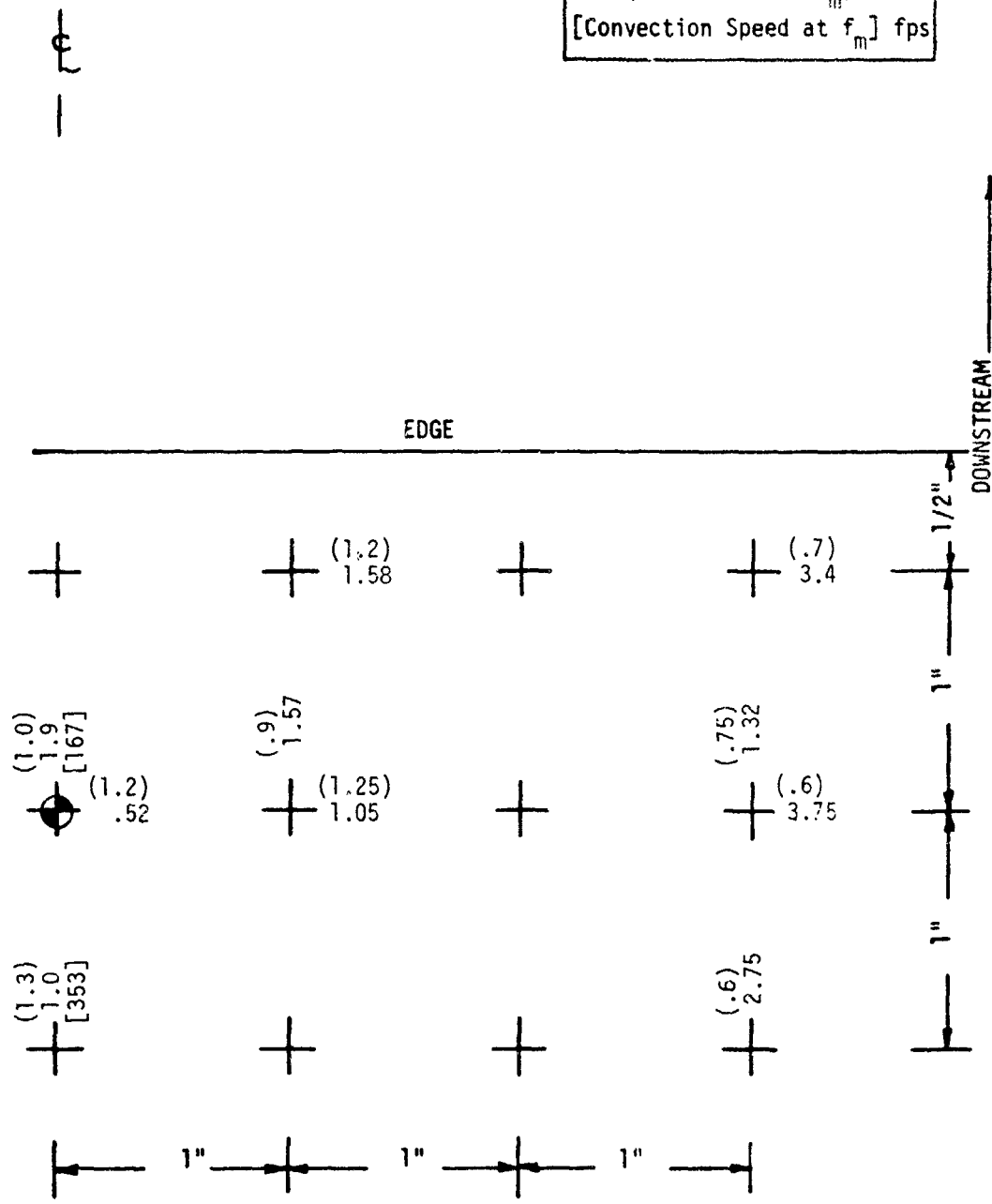


TABLE J-20
 PRESSURE MEASUREMENT RESULTS
 FLAT PLATE - ROUND NOZZLE (D = 2")

TEST CASE	T_j/T_a	M_j	X/D	ρ	RESULT TYPE
3B	1.0	0.5	7	50°	RMS (psi) (half-power freq.) KHZ [rolloff exponent] (peak amplification)

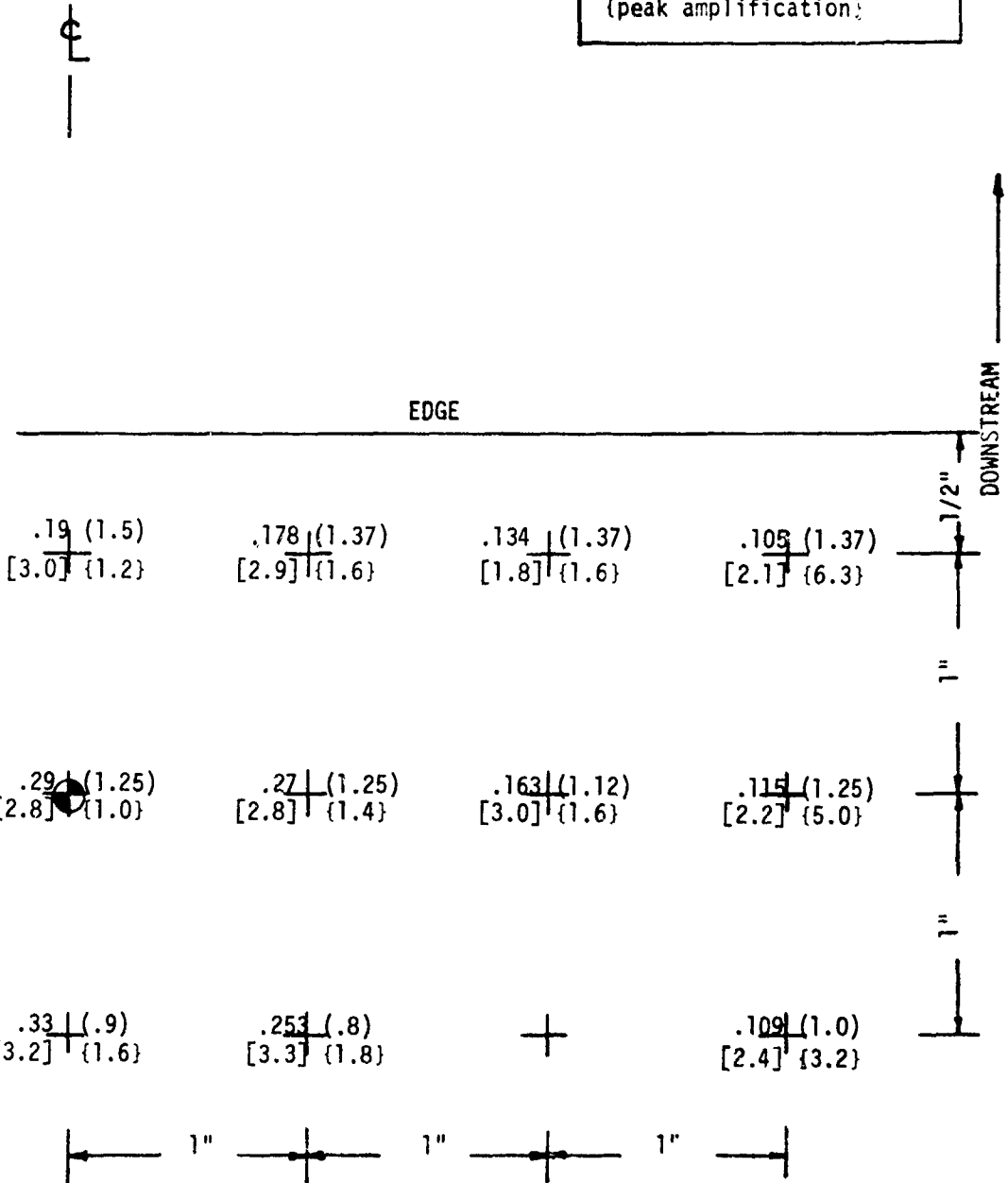


TABLE J-20 (CONT'D)
 PRESSURE MEASUREMENT RESULTS
 FLAT PLATE - ROUND NOZZLE (D = 2")

TEST CASE	T_j/T_a	M_j	X/D	β	RESULT TYPE
3B	1.0	0.5	7	50°	Max. Correlation Length (in) (Freq. at Maximum, f_m) KHZ [Convection Speed at f_m] fps

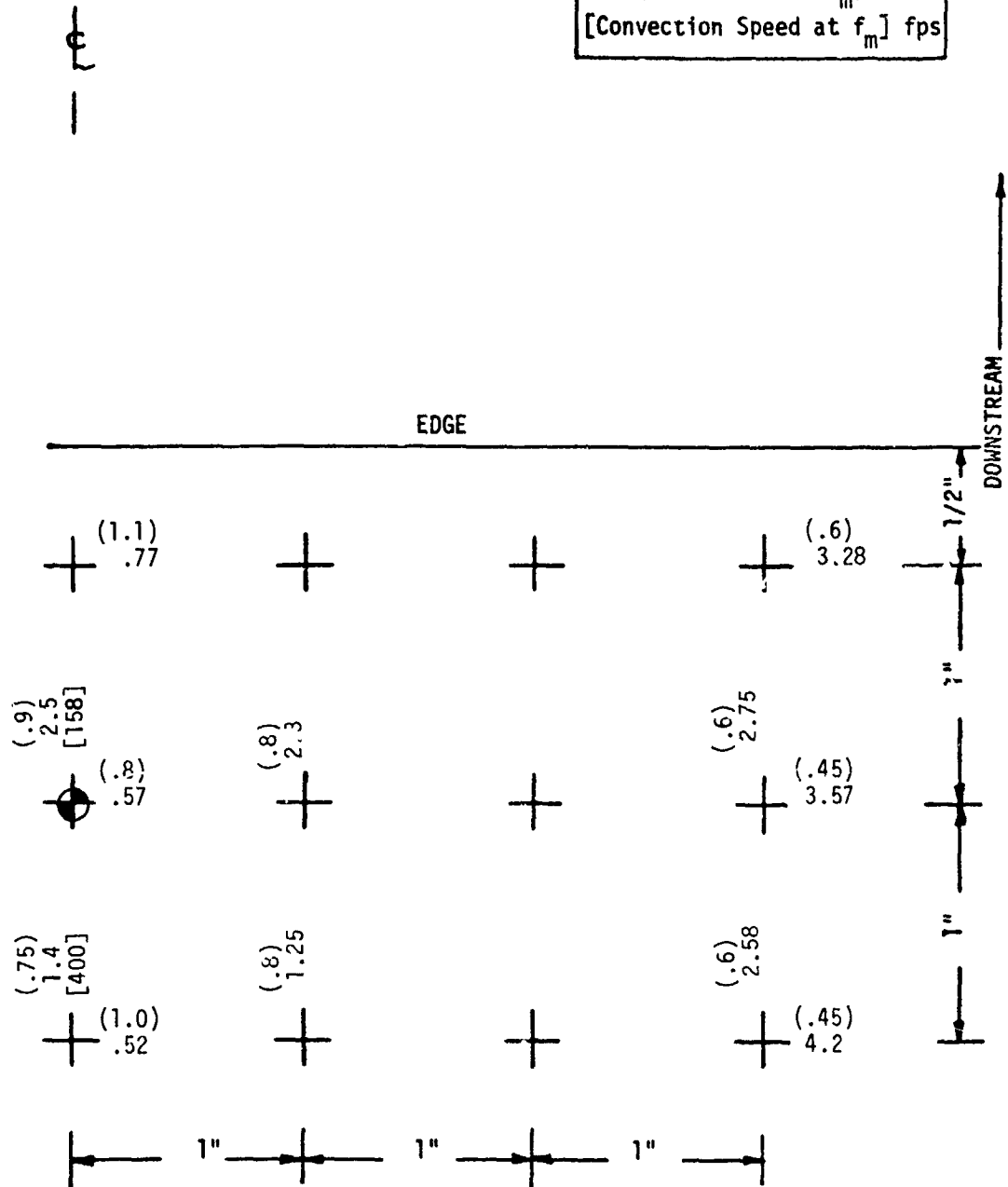


TABLE J-21
 PRESSURE MEASUREMENT RESULTS
 FLAT PLATE - ROUND NOZZLE (D = 2")

TEST CASE	T_j/T_a	M_j	X/D	β	RESULT TYPE
3C	1.7	0.5	5	50°	RMS (psi) (half-power freq.) KHZ [rolloff exponent] (peak amplification)

⊕
|

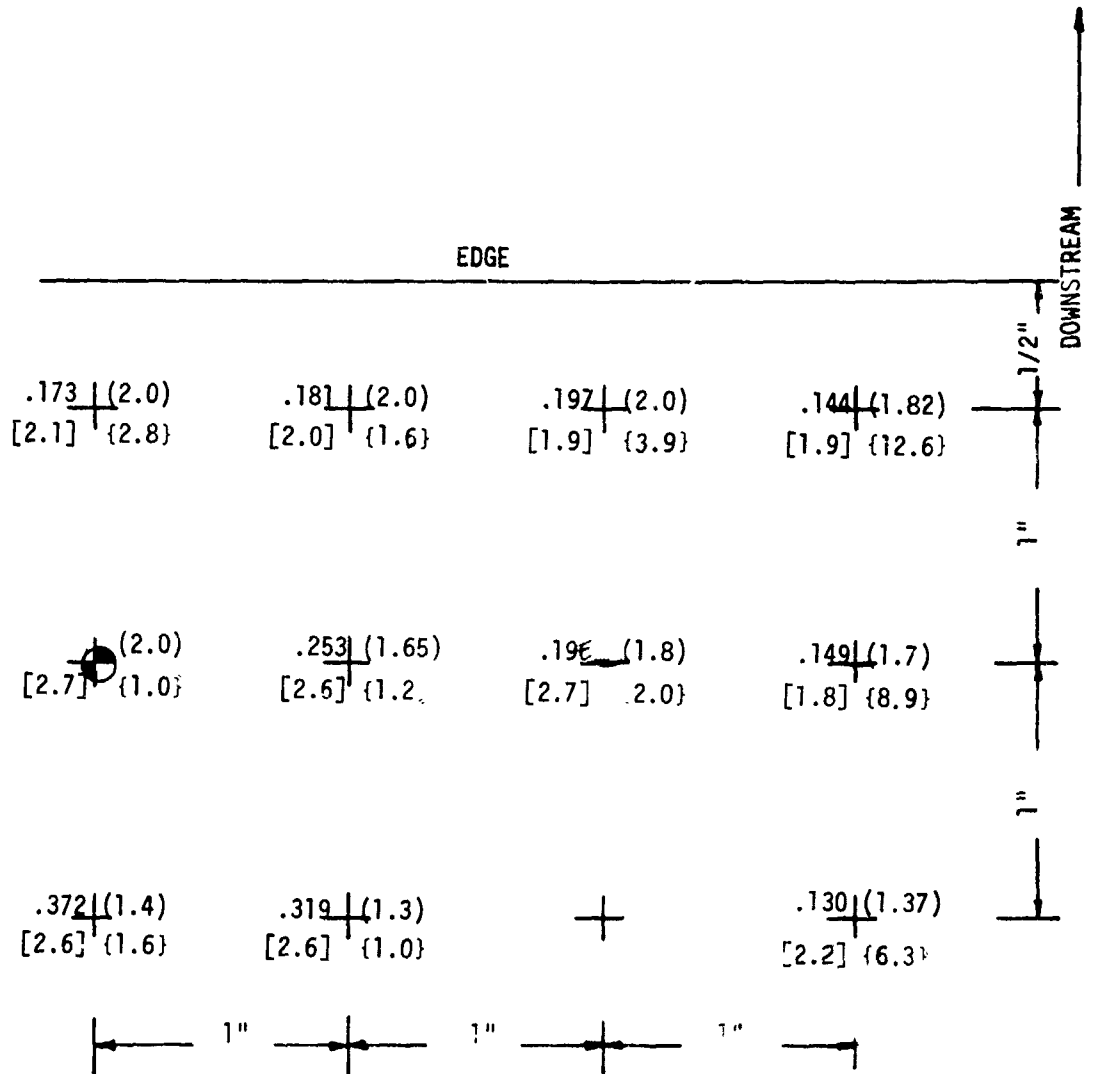


TABLE J-21 (CONT'D)
 PRESSURE MEASUREMENT RESULTS
 FLAT PLATE - ROUND NOZZLE (D = 2")

TEST CASE	T_j/T_a	M_j	X/D	β	RESULT TYPE
3C	1.7	0.5	5	50°	Max. Correlation Length (in) (Freq. at Maximum, f_m) kHz [Convection Speed at f_m] fps

⊕
|

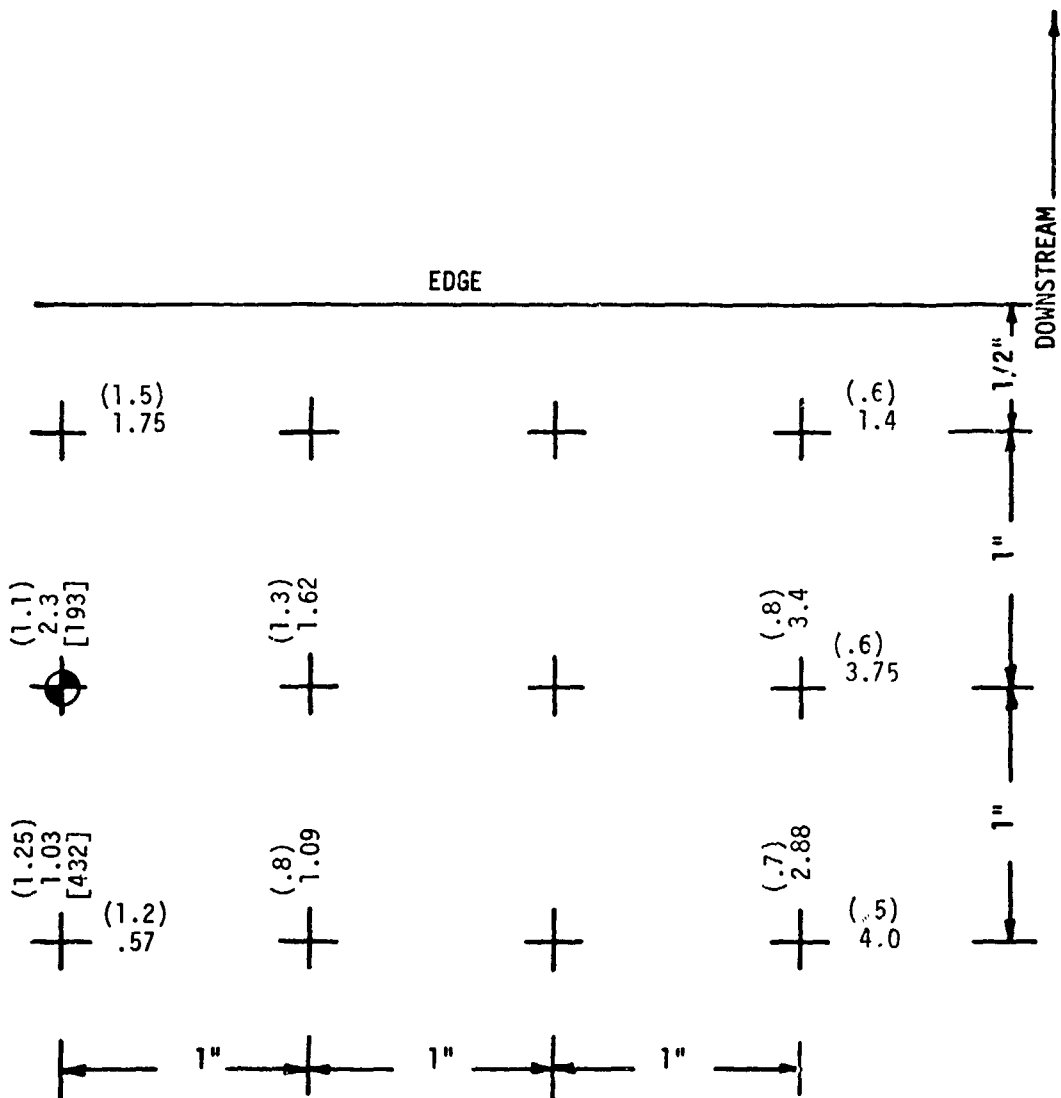


TABLE J-22
 PRESSURE MEASUREMENT RESULTS
 FLAT PLATE - ROUND NOZZLE (D = 2")

TEST CASE	T_j/T_a	M_j	X/D	β	RESULT TYPE
3D	1.0	0.5	10	50°	RMS (psi) (half-power freq.) KHZ [rolloff exponent] {peak amplification}

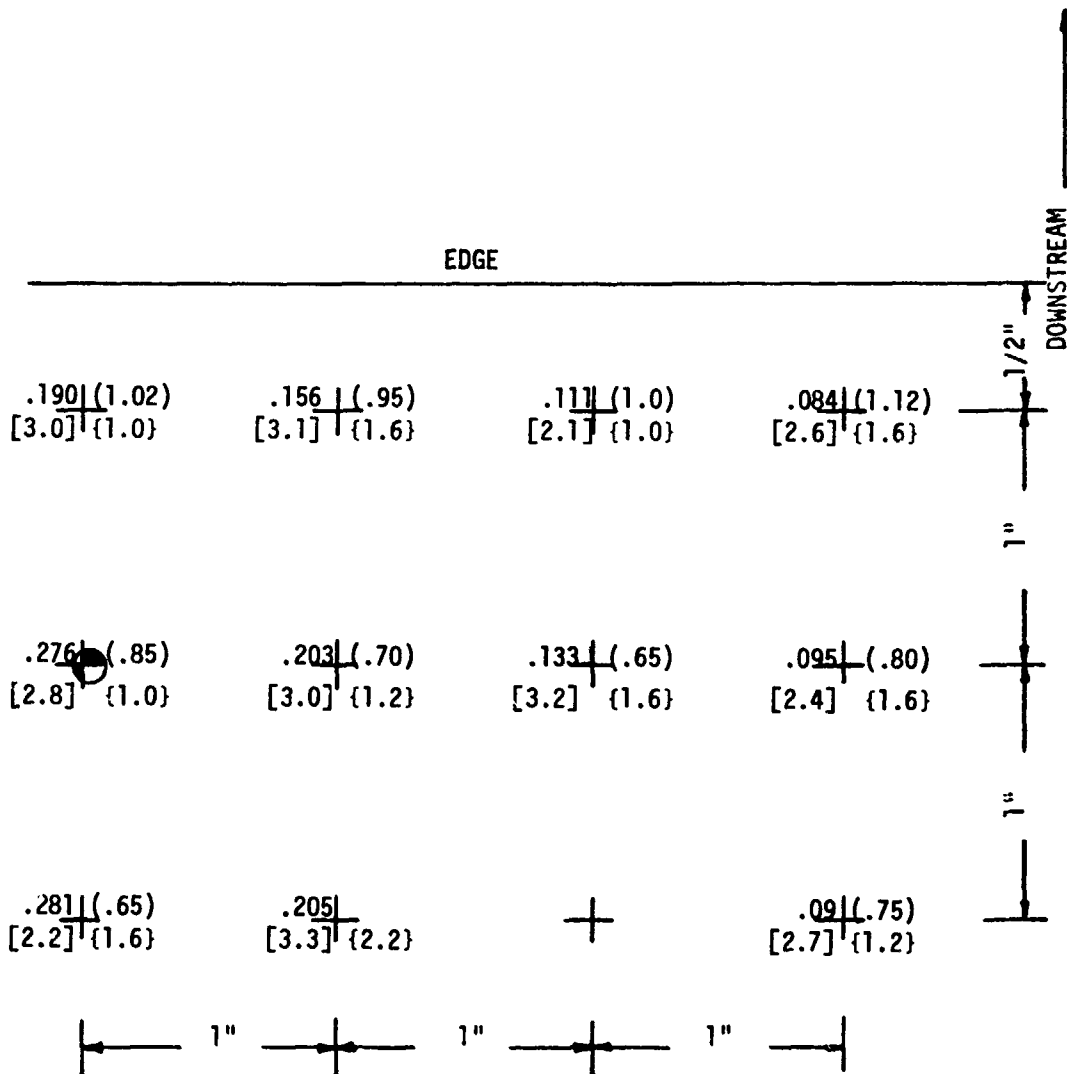


TABLE J-22 (CONT'D)
 PRESSURE MEASUREMENT RESULTS
 FLAT PLATE - ROUND NOZZLE (C = 2")

TEST CASE	T_j/T_a	M_j	X/D	β	RESULT TYPE
3D	1.0	0.5	10	50°	Max. Correlation Length (in) (Freq. at Maximum, f_m) KHZ [Convection Speed at f_m] fps

ε
|

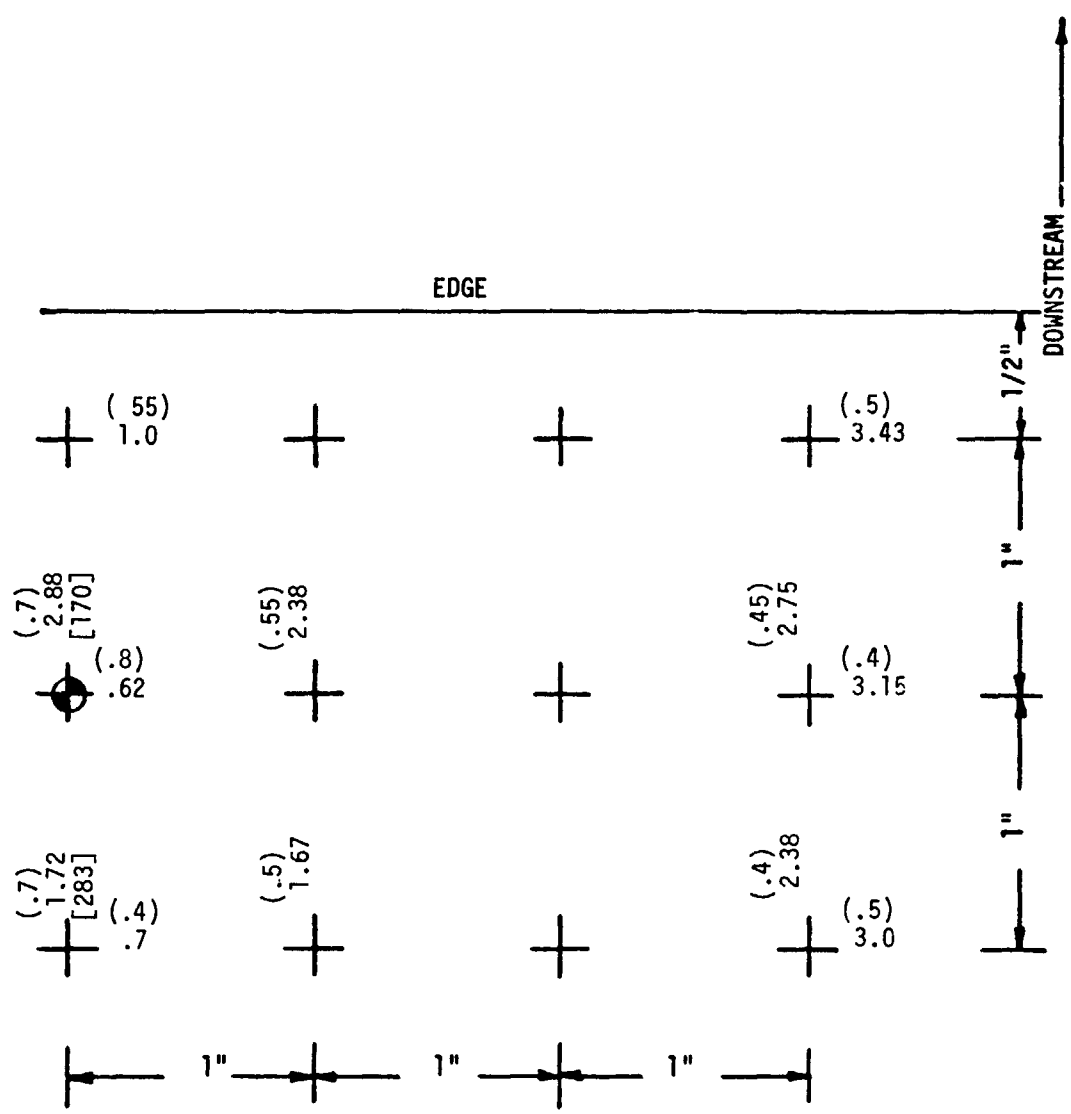


TABLE J-23
 PRESSURE MEASUREMENT RESULTS
 FLAT PLATE - DAISY NOZZLE ($C_{eq} = 2"$)

TEST CASE	T_j/T_a	M_j	X/D_{eq}	β	RESULT TYPE
4A	1	.5	5	50°	RMS (psi) (half-power freq.) KHZ [roll off exponent] {peak amplification}

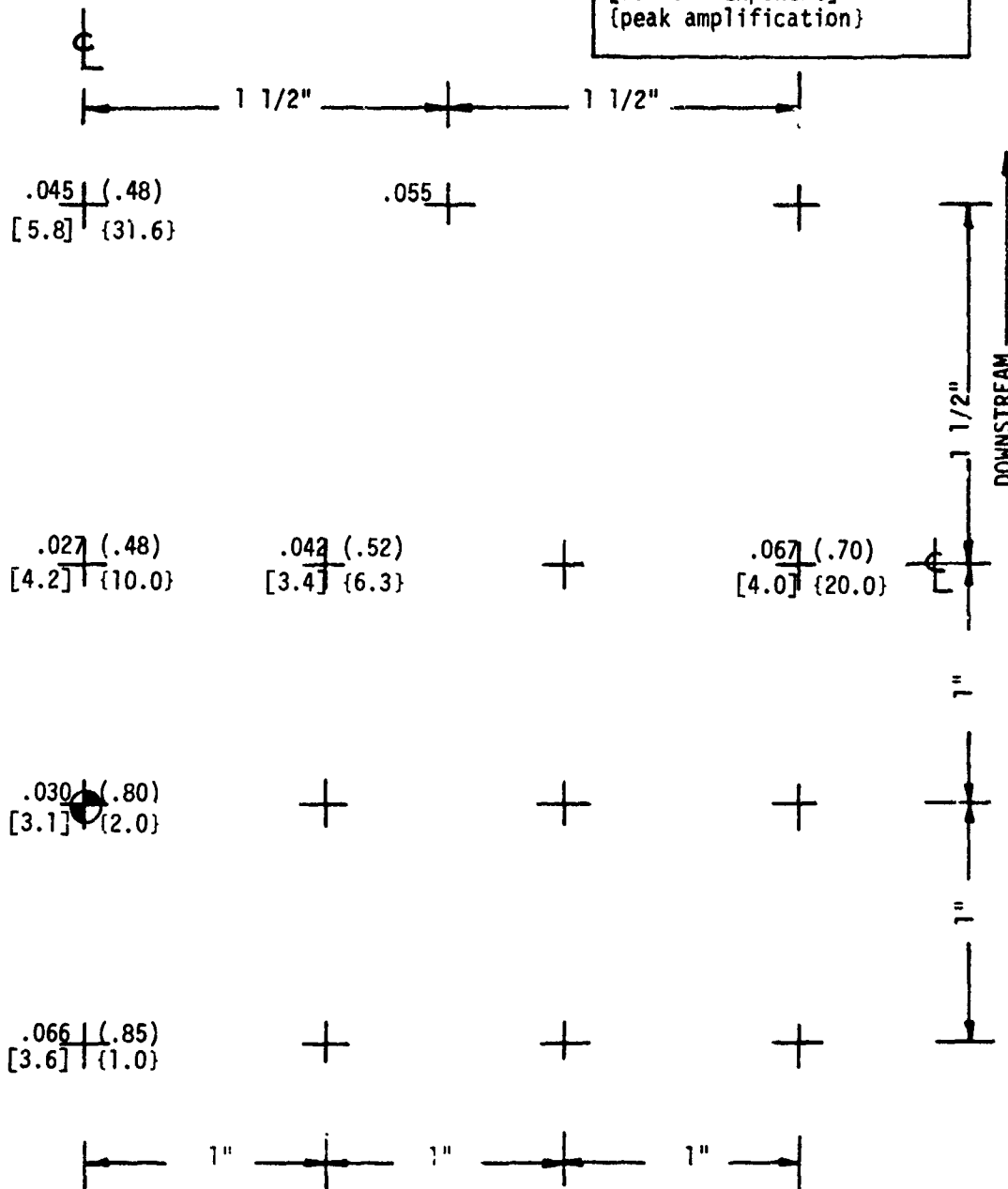


TABLE J-23 (CONT'D)
 PRESSURE MEASUREMENT RESULTS
 FLAT PLATE - DAISY NOZZLE ($D_{eq} = 2"$)

TEST CASE	T_j/T_a	M_j	X/D_{eq}	β	RESULT TYPE
4A	1.0	0.5	5	50°	Max. Correlation Length (in) (Freq. at Maximum, f_m) KHZ [Convection Speed at f_m] fps

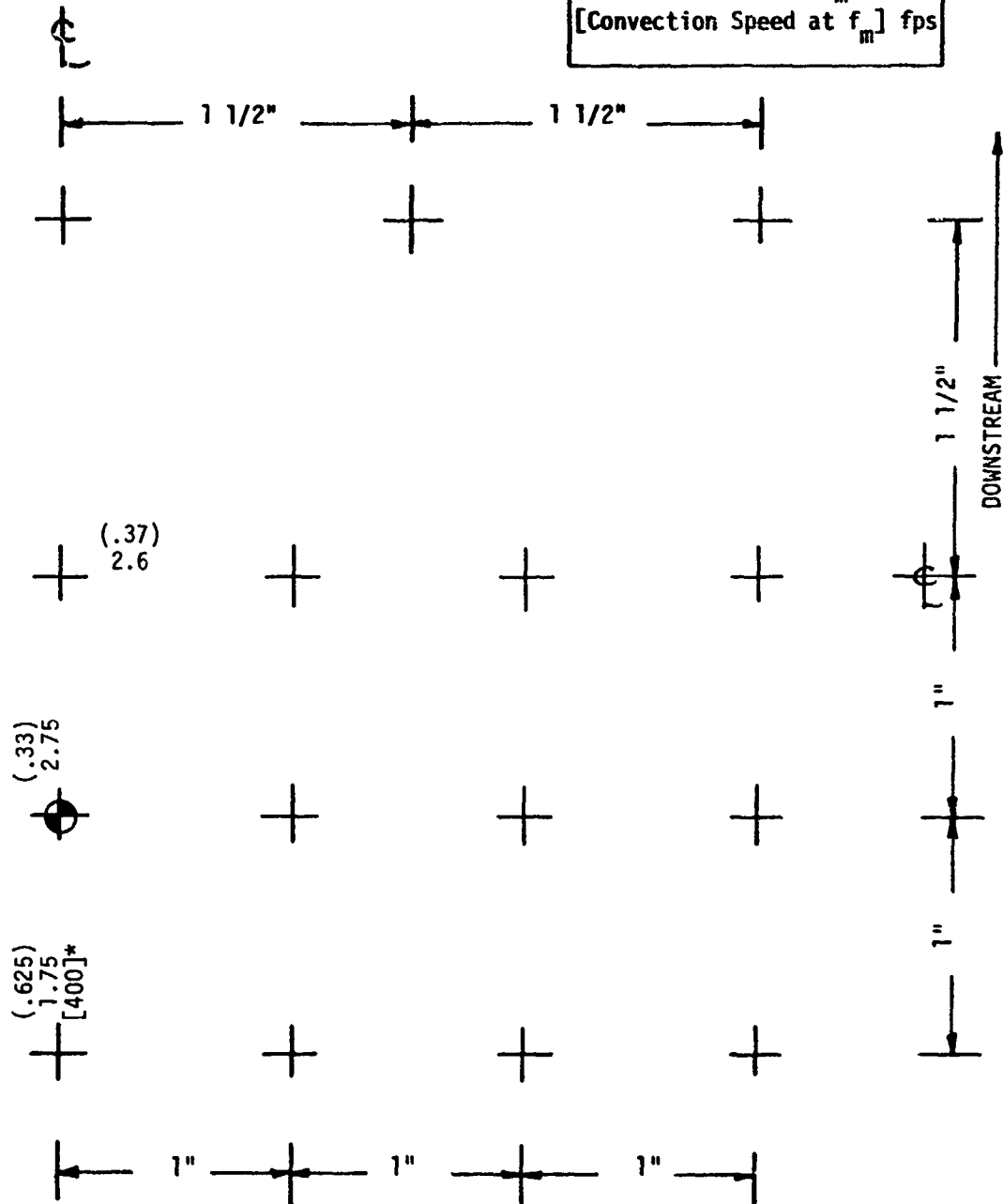


TABLE J-24
 PRESSURE MEASUREMENT RESULTS
 FLAT PLATE - DAISY NOZZLE ($L_{eq} = 2''$)

TEST CASE	T_j/T_a	M_j	X/D_{eq}	β	RESULT TYPE
4B	1	.5	8	50°	RMS (psi) (half-power freq.) KHZ [rolloff exponent] {peak amplification}

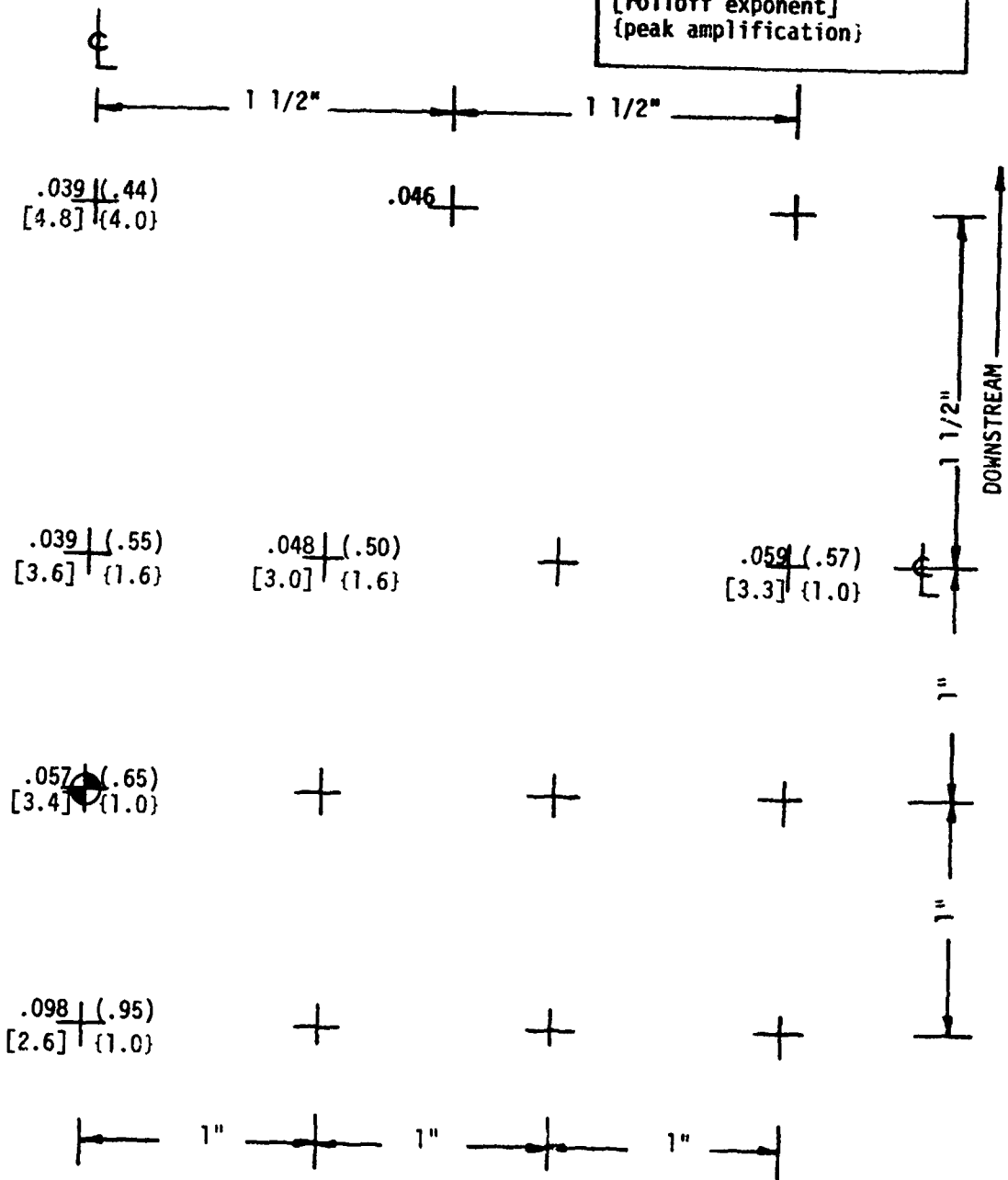


TABLE J-24 (CONT'D)
 PRESSURE MEASUREMENT RESULTS
 FLAT PLATE - DAISY NOZZLE ($D_{eq} = 2''$)

TEST CASE	T_j/T_a	M_j	X/D_{eq}	β	RESULT TYPE
4B	1.0	0.5	8	50°	Max. Correlation Length (in) (Freq. at Maximum, f_m) KHZ [Convection Speed at f_m] fps

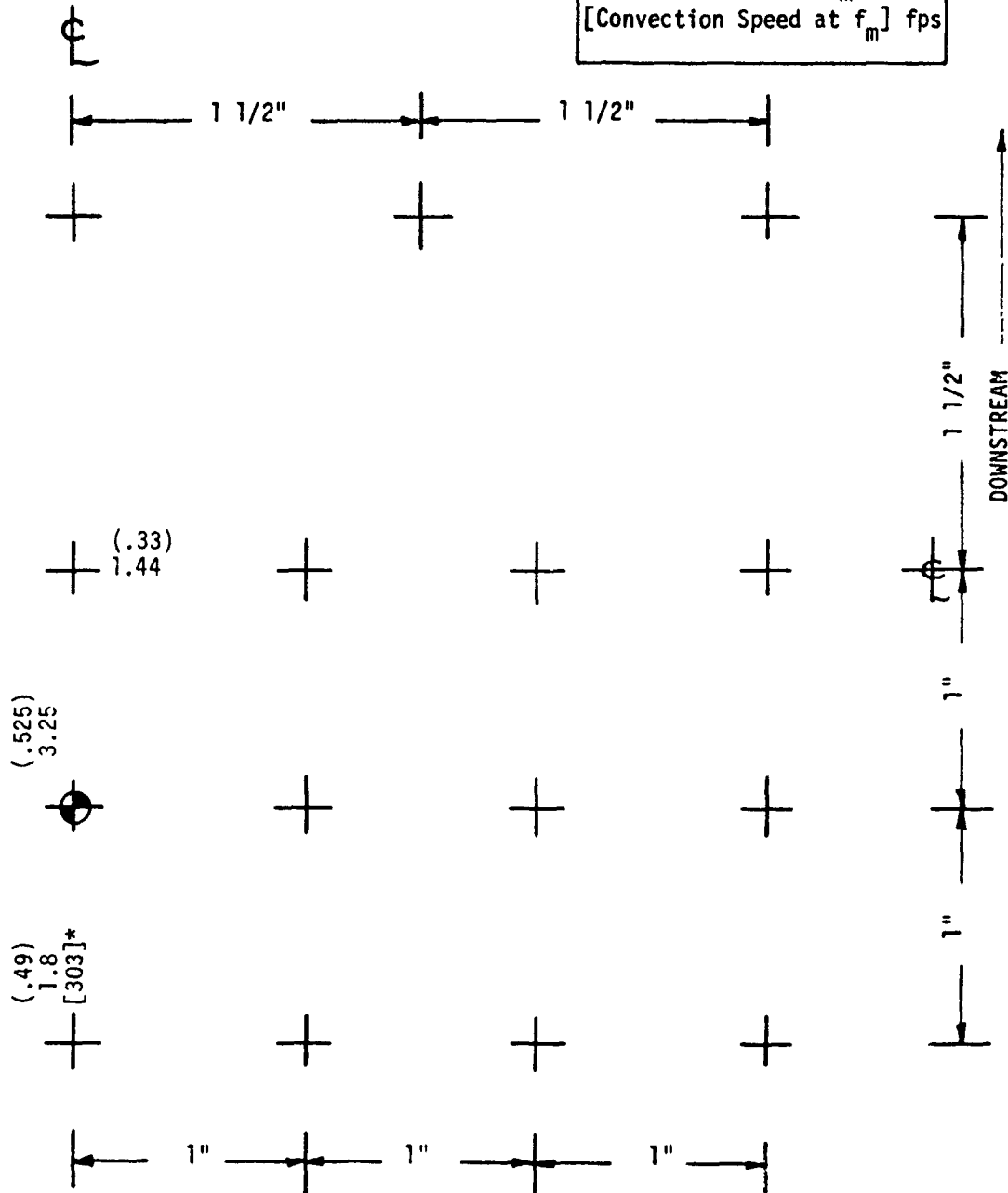


TABLE J-25
 PRESSURE MEASUREMENT RESULTS
 FLAT PLATE - DAISY NOZZLE ($C_{eq} = 2''$)

TEST CASE	T_j/T_a	M_j	X/D_{eq}	β	RESULT TYPE
4C	1	.5	11	50°	RMS (psi) (half-power freq.) KHZ [rolloff exponent] {peak amplification}

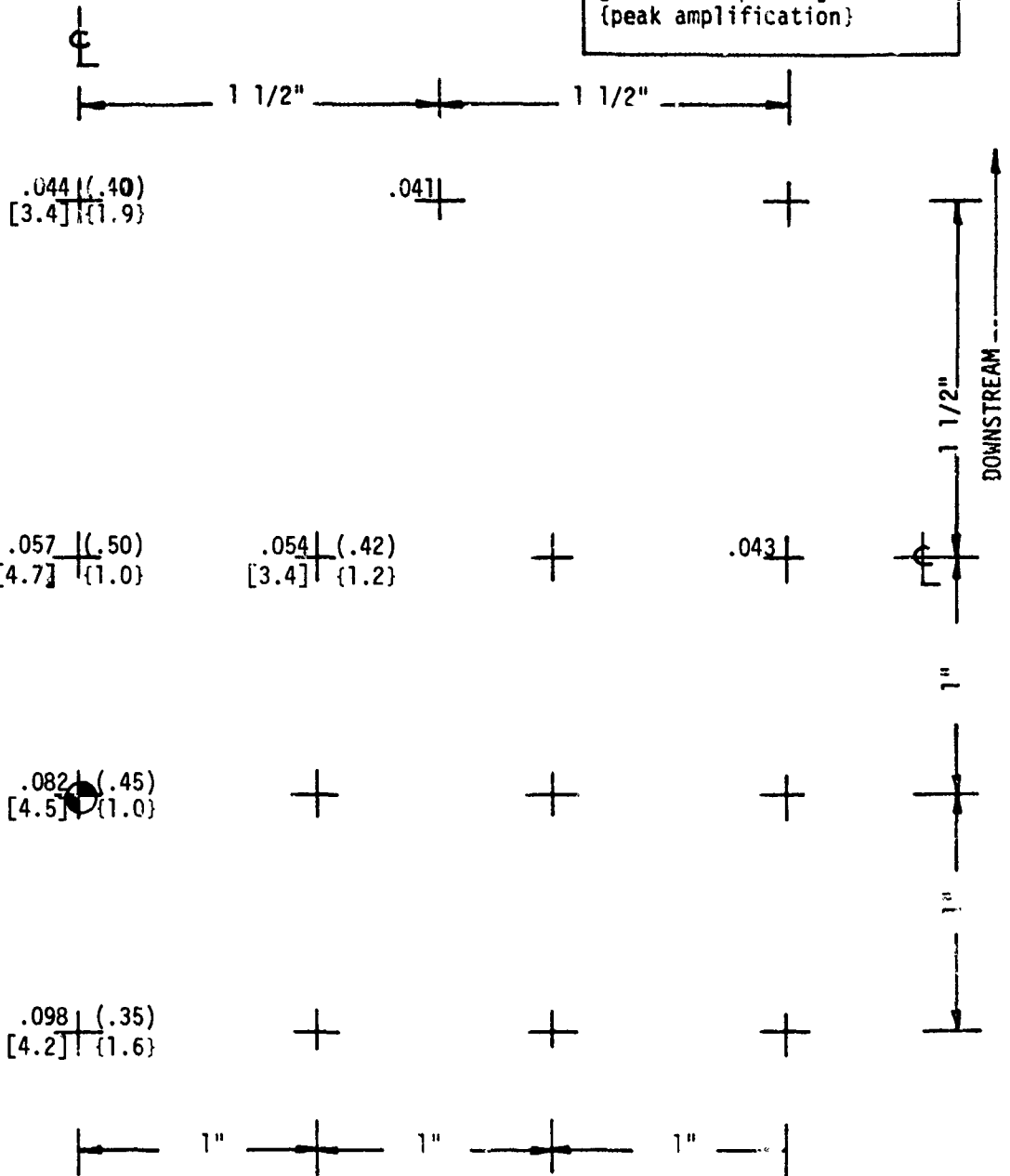


TABLE J-25 (CONT'D)
 PRESSURE MEASUREMENT RESULTS
 FLAT PLATE - DAISY NOZZLE ($D_{eq} = 2'$)

TEST CASE	T_j/T_a	M_j	X/D_{eq}	β	RESULT TYPE
4C	1.0	0.5	11	50°	Max. Correlation Length (in) (Freq. at Maximum, f_m) KHZ [Convection Speed at f_m] fps

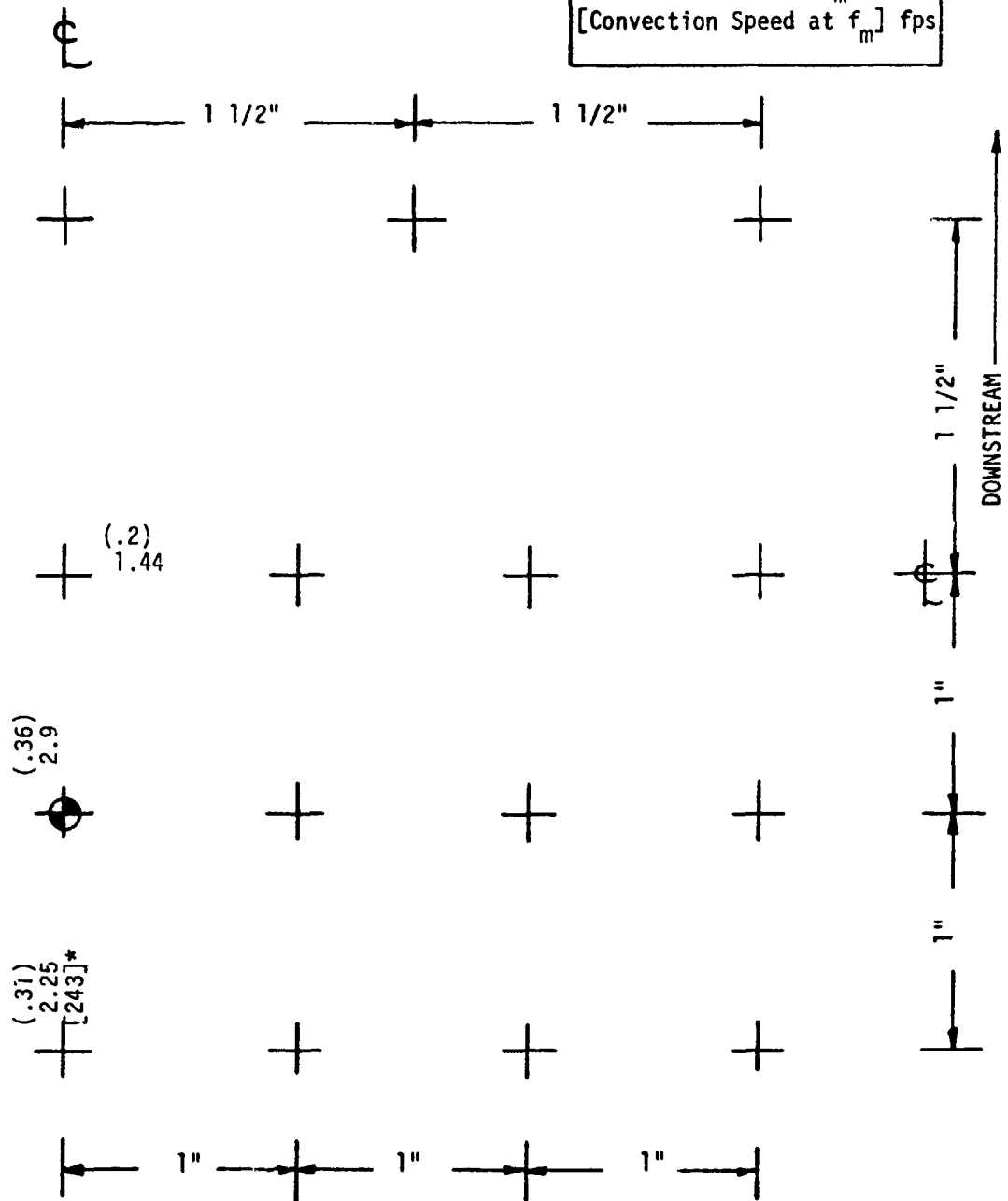


TABLE J-26
 PRESSURE MEASUREMENT RESULTS
 FLAT PLATE - DAISY NOZZLE ($C_{eq} = 2''$)

TEST CASE	T_j/T_a	M_j	X/D_{eq}	β	RESULT TYPE
4D	1	.5	5	25°	RMS (psi) (half-power freq.) KHZ [rolloff exponent] (peak amplification)

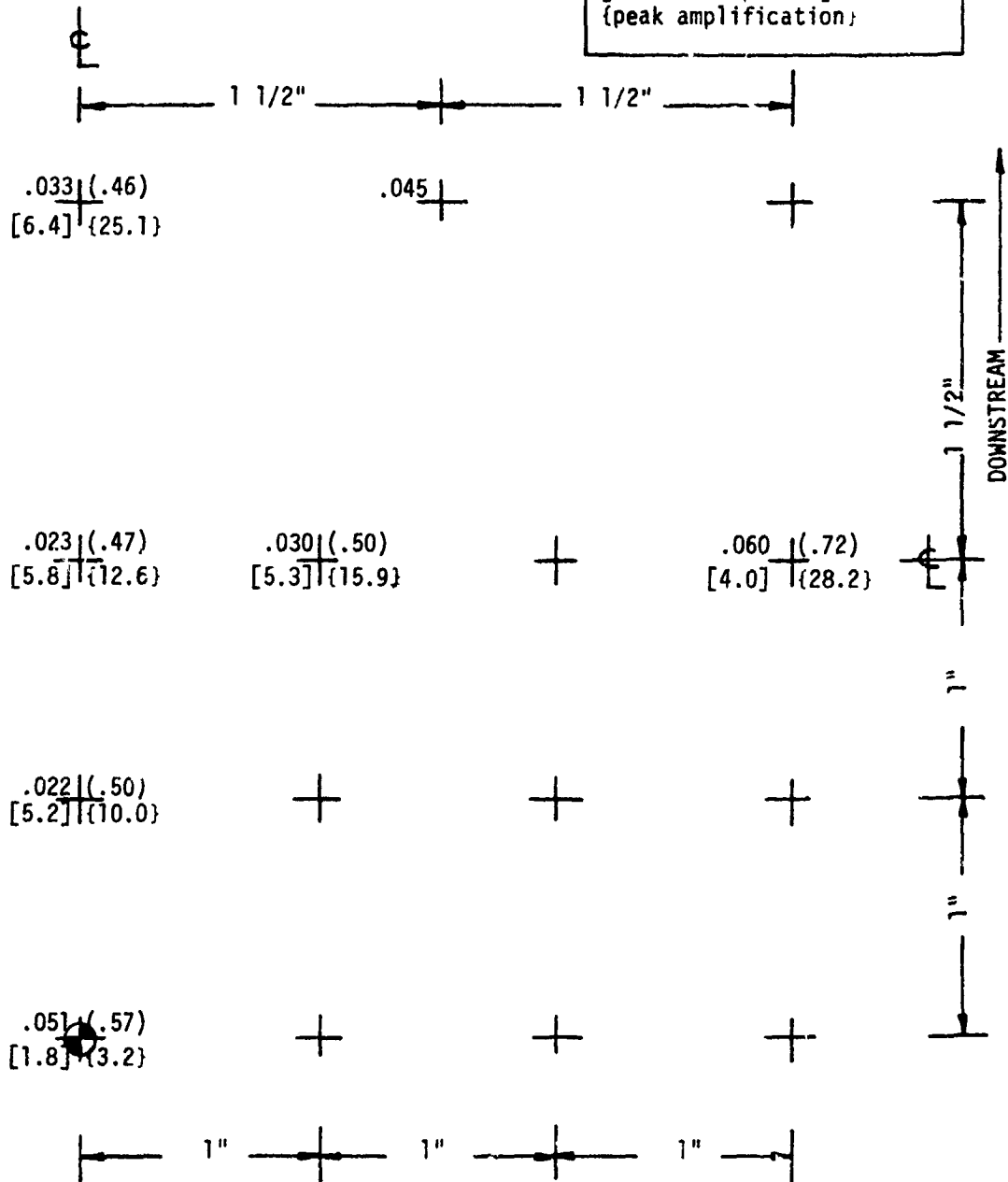


TABLE J-26 (CONT'D)

PRESSURE MEASUREMENT RESULTS

FLAT PLATE - DAISY NOZZLE ($D_{eq} = 2''$)

TEST CASE	T_j/T_a	M_j	X/D_{eq}	β	RESULT TYPE
4D	1.0	0.5	5	25°	Max. Correlation Length (in) (Freq. at Maximum, f_m) KHZ [Convection Speed at f_m] fps

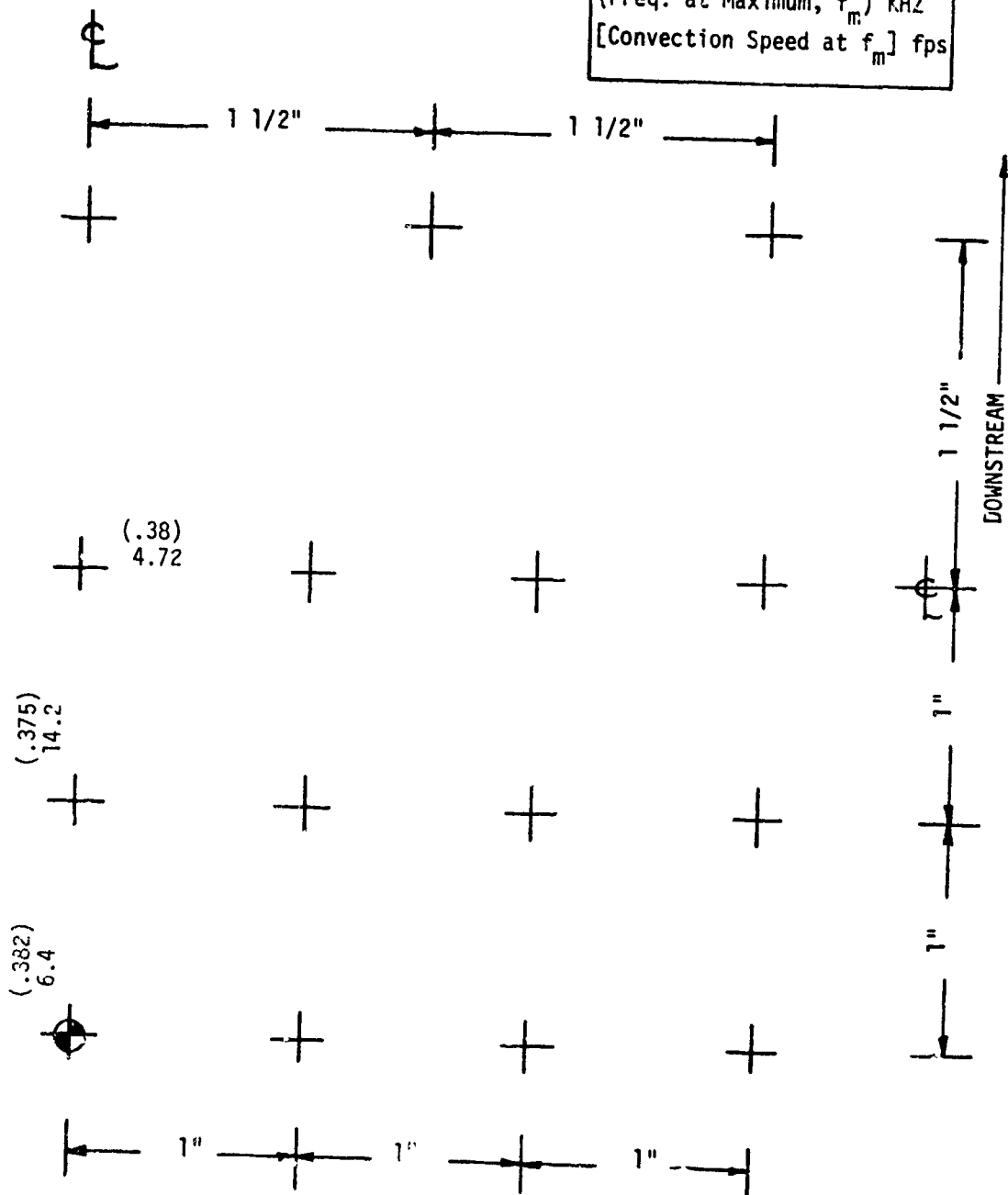


TABLE J-27
 PRESSURE MEASUREMENT RESULTS
 FLAT PLATE - DAISY NOZZLE ($C_{eq} = 2''$)

TEST CASE	T_j/T_a	M_j	X/D_{eq}	β	RESULT TYPE
4E	1	.5	8	25°	RMS (psi) (half-power freq.) KHZ [rolloff exponent] {peak amplification}

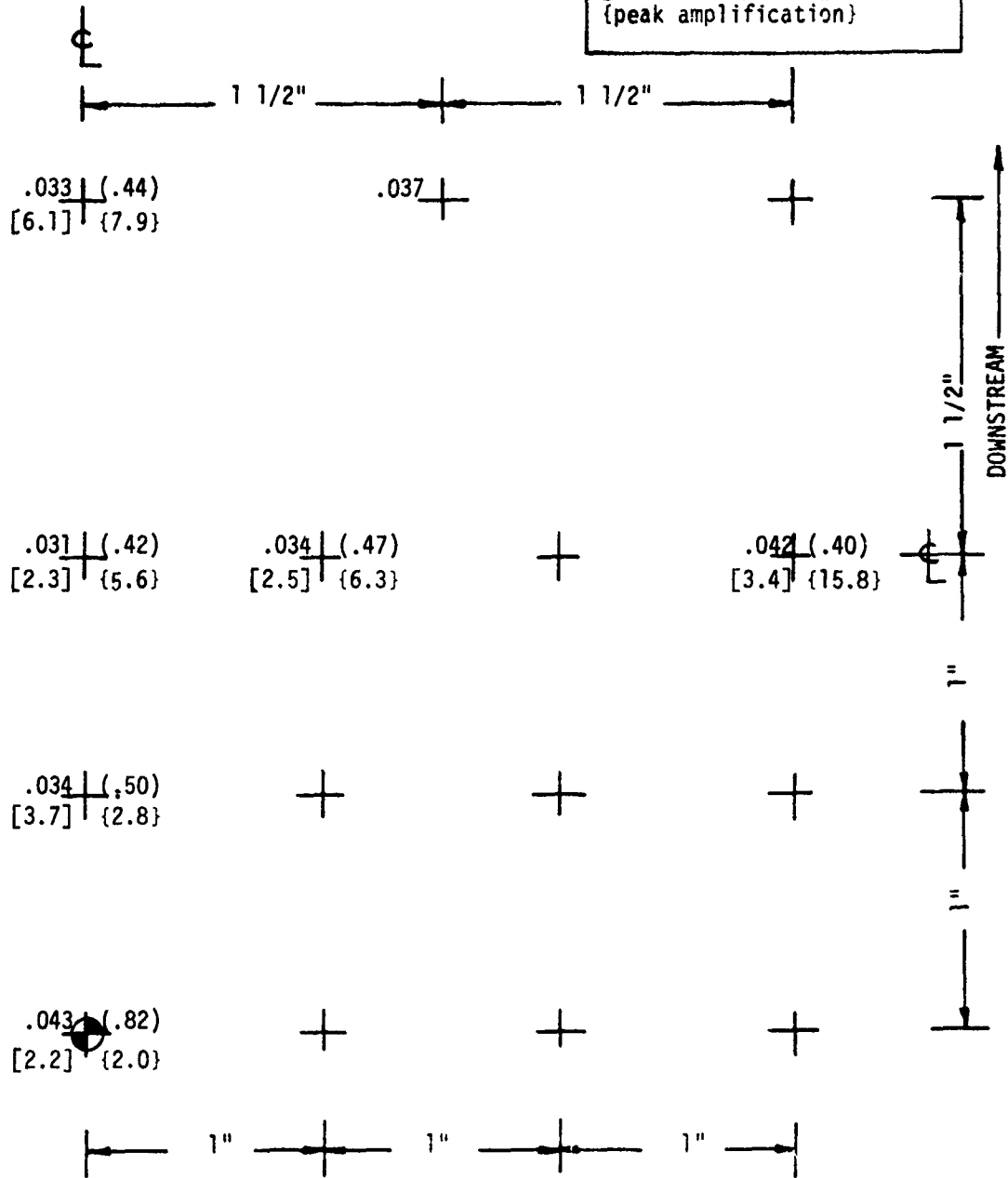


TABLE J-27 (CONT'D)
 PRESSURE MEASUREMENT RESULTS
 FLAT PLATE - DAISY NOZZLE ($D_{eq} = 2"$)

TEST CASE	T_j/T_a	M_j	X/D_{eq}	β	RESULT TYPE
4E	1.0	0.5	8	25°	Max. Correlation Length (in) (Freq. at Maximum, f_m) KHz [Convection Speed at f_m] fps

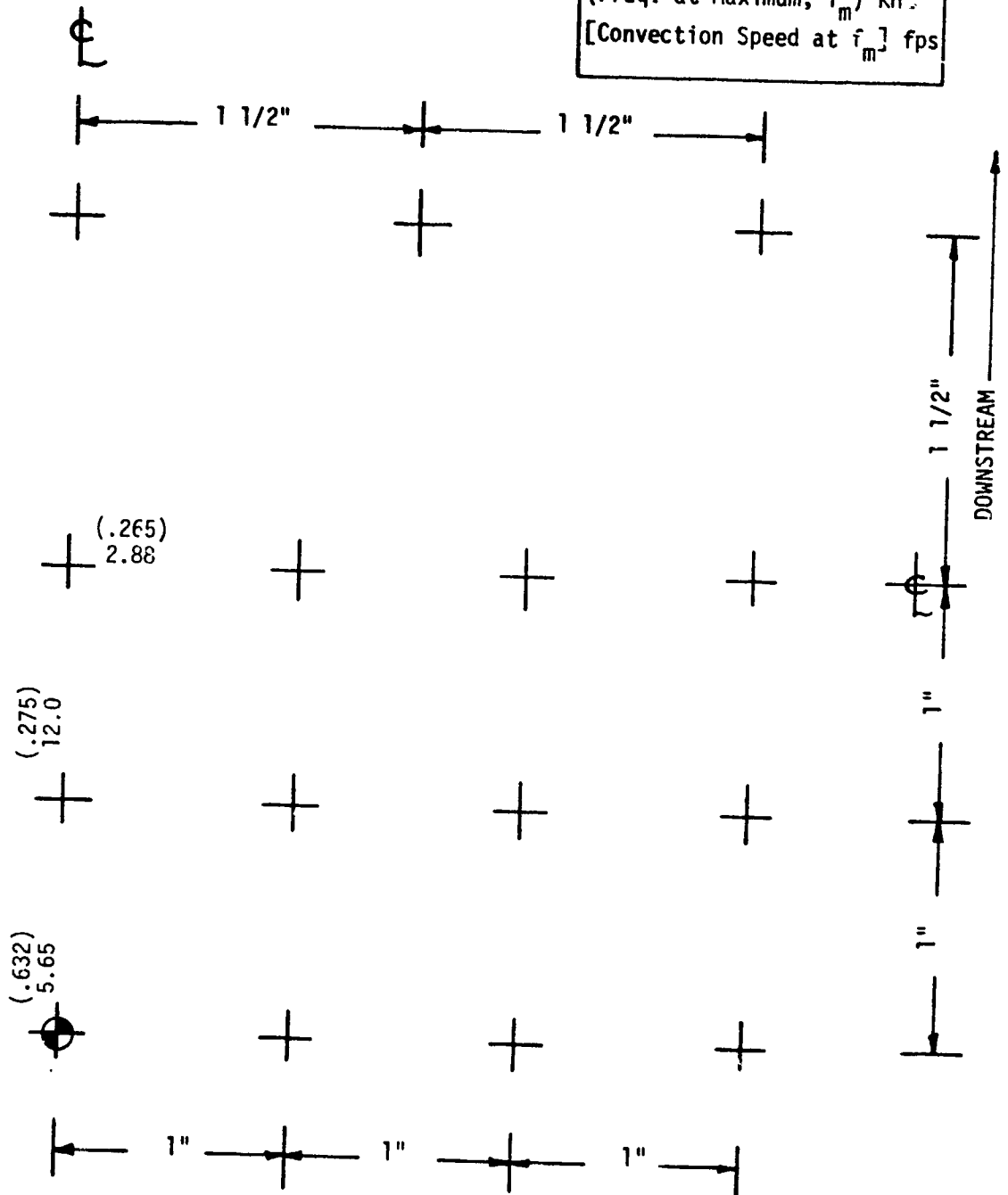


TABLE J-28
 PRESSURE MEASUREMENT RESULTS
 FLAT PLATE - DAISY NOZZLE ($C_{eq} = 2''$)

TEST CASE	T_j/T_a	M_j	X/D_{eq}	β	RESULT TYPE
4F	1	.5	11	25°	RMS (psi) (half-power freq.) KHZ [rolloff exponent] {peak amplification}

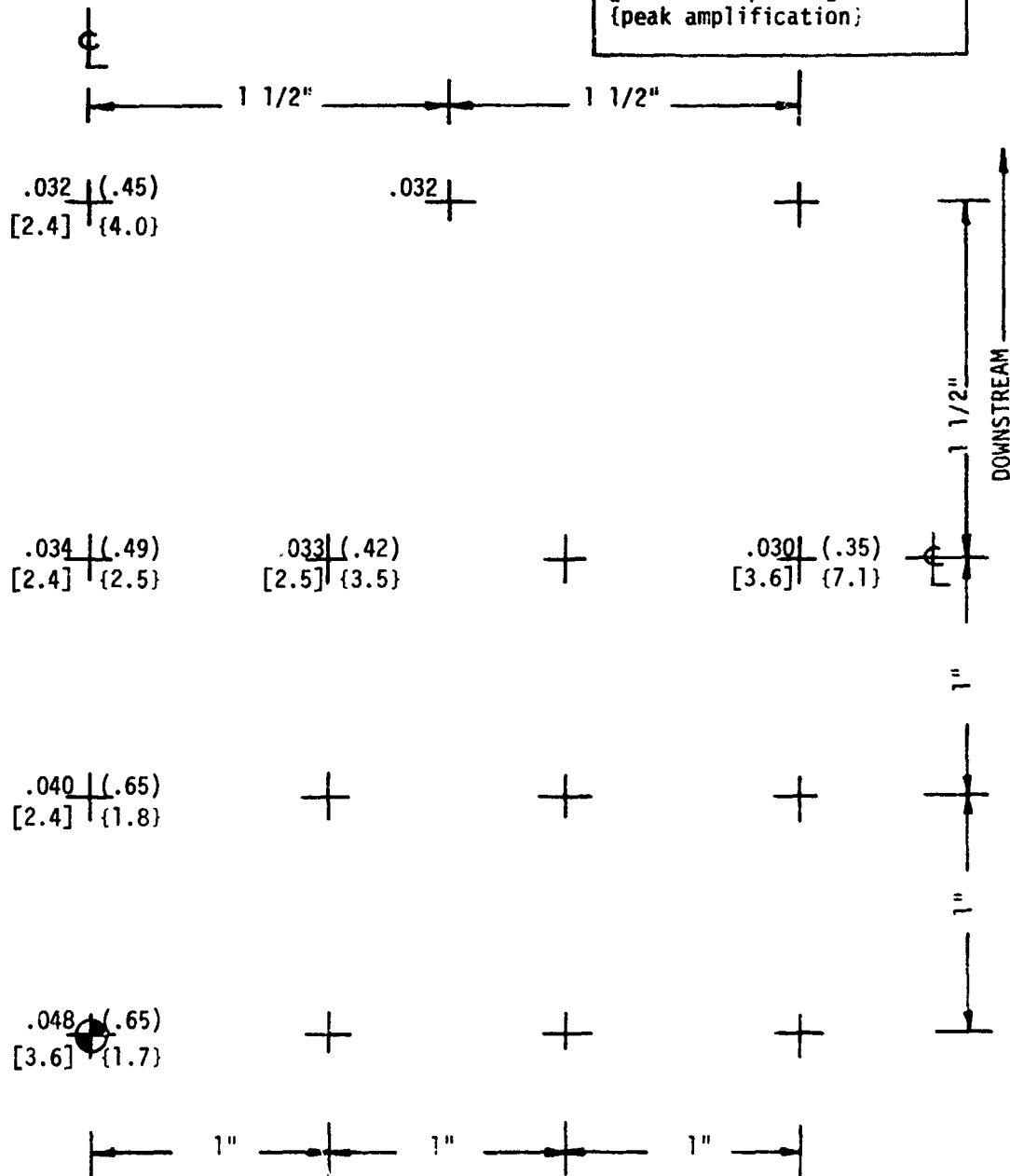


TABLE J-28 (CONT'D)
 PRESSURE MEASUREMENT RESULTS
 FLAT PLATE - DAISY NOZZLE ($D_{eq} = 2'$)

TEST CASE	T_j/T_a	M_j	λ/D_{eq}	β	RESULT TYPE
4F	1.0	0.5	11	25°	Max. Correlation Length (in) (Freq. at Maximum, f_m) KHZ [Convection Speed at f_m] fps

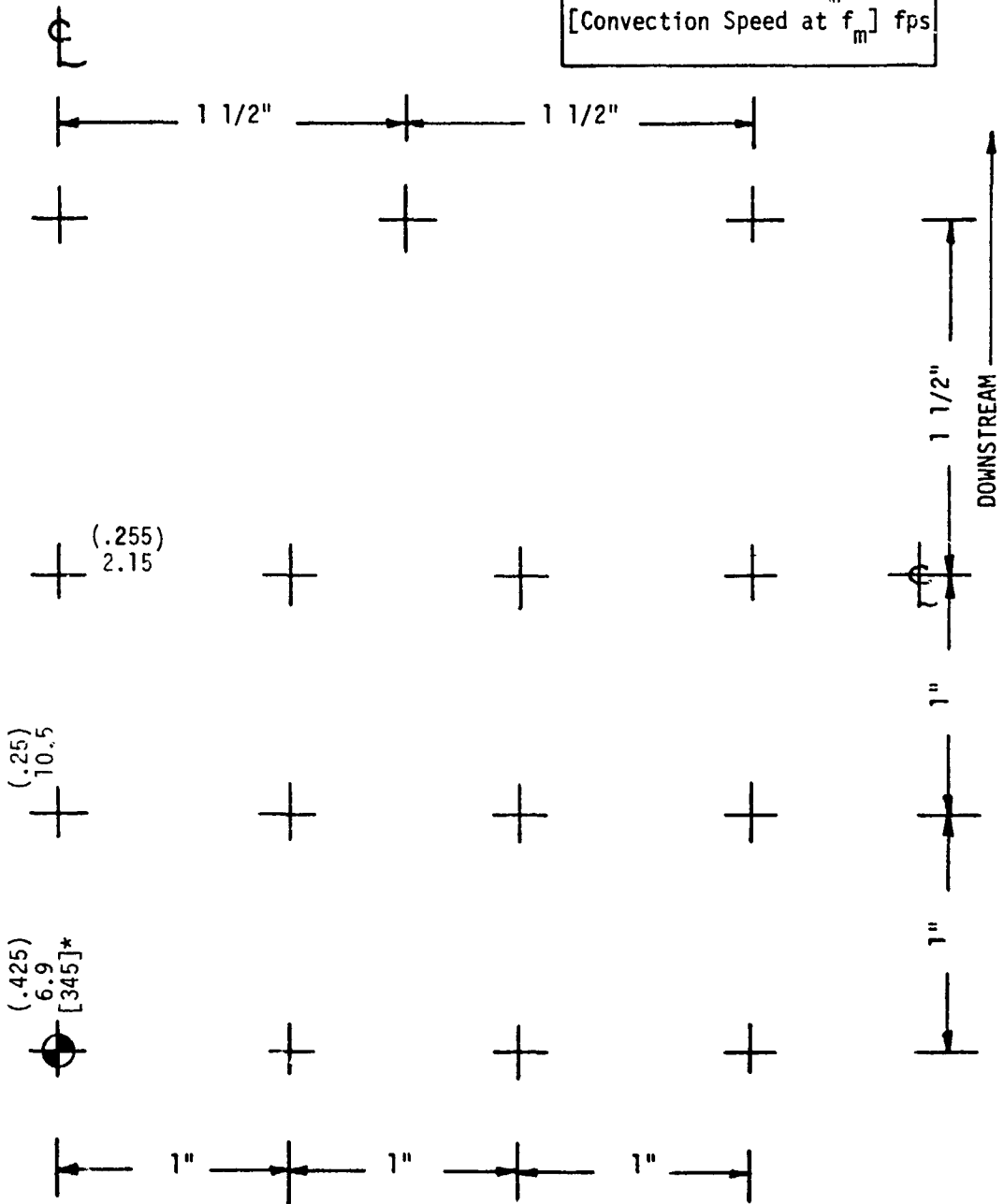


TABLE J-29
 PRESSURE MEASUREMENT RESULTS
 FLAT PLATE - DAISY NOZZLE ($D_{eq} = 2"$)

TEST CASE	T_j/T_a	M_j	X/D_{eq}	β	RESULT TYPE
4G	1	.5	5	90°	RMS (psi) (half-power freq.) KHZ [rolloff exponent] {peak amplification}

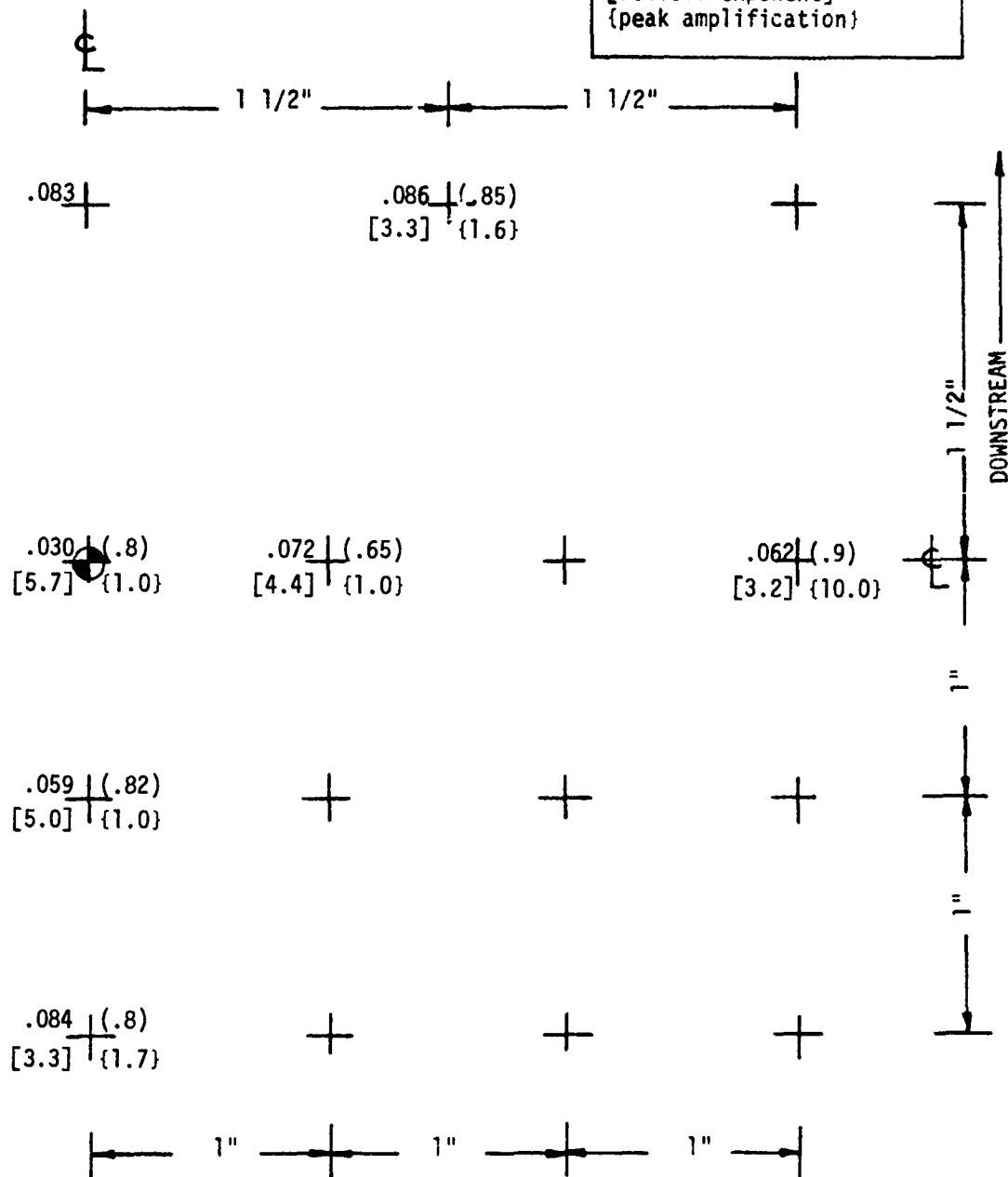


TABLE J-29 (CONT'D)
 PRESSURE MEASUREMENT RESULTS
 FLAT PLATE - DAISY NOZZLE ($D_{eq} = 2''$)

TEST CASE	T_j/T_a	M_j	X/D_{eq}	β	RESULT TYPE
4G	1.0	0.5	5	90°	Max. Correlation Length (in) (Freq. at Maximum, f_m) KHZ [Convection Speed at f_m] fps

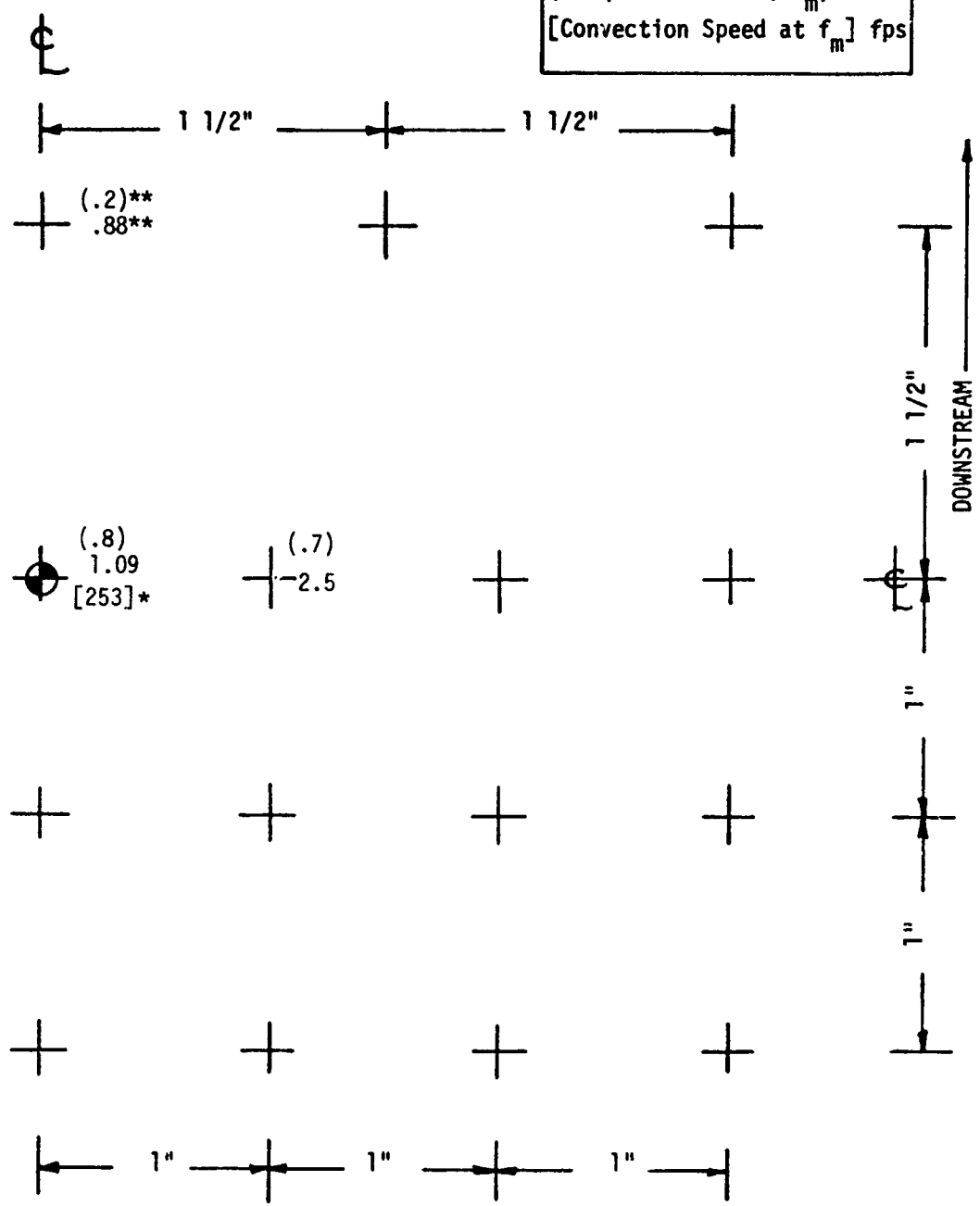


TABLE J-30
 PRESSURE MEASUREMENT RESULTS
 FLAT PLATE - DAISY NOZZLE ($C_{eq} = 2''$)

TEST CASE	T_j/T_a	M_j	X/D_{eq}	β	RESULT TYPE
4H	1	.5	8	90°	RMS (psi) (half-power freq.) KHZ [rolloff exponent] (peak amplification)

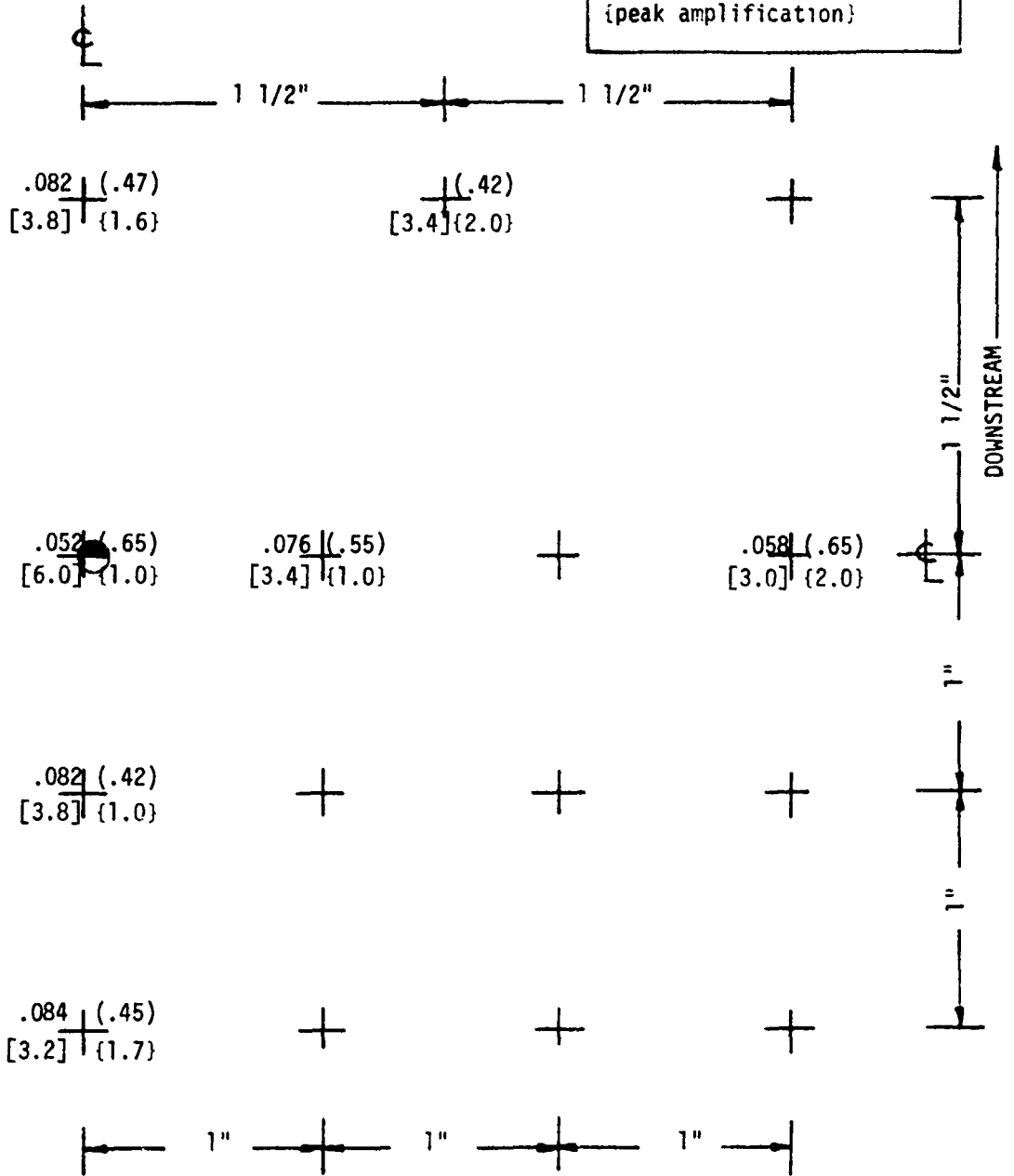


TABLE J-30 (CONT'D)
 PRESSURE MEASUREMENT RESULTS
 FLAT PLATE - DAISY NOZZLE ($D_{eq} = 2'$)

TEST CASE	T_j/T_a	M_j	X/D_{eq}	β	RESULT TYPE
4H	1.0	0.5	8	90°	Max. Correlation Length (in) (Freq. at Maximum, f_m) KHZ [Convection Speed at f_m] fps

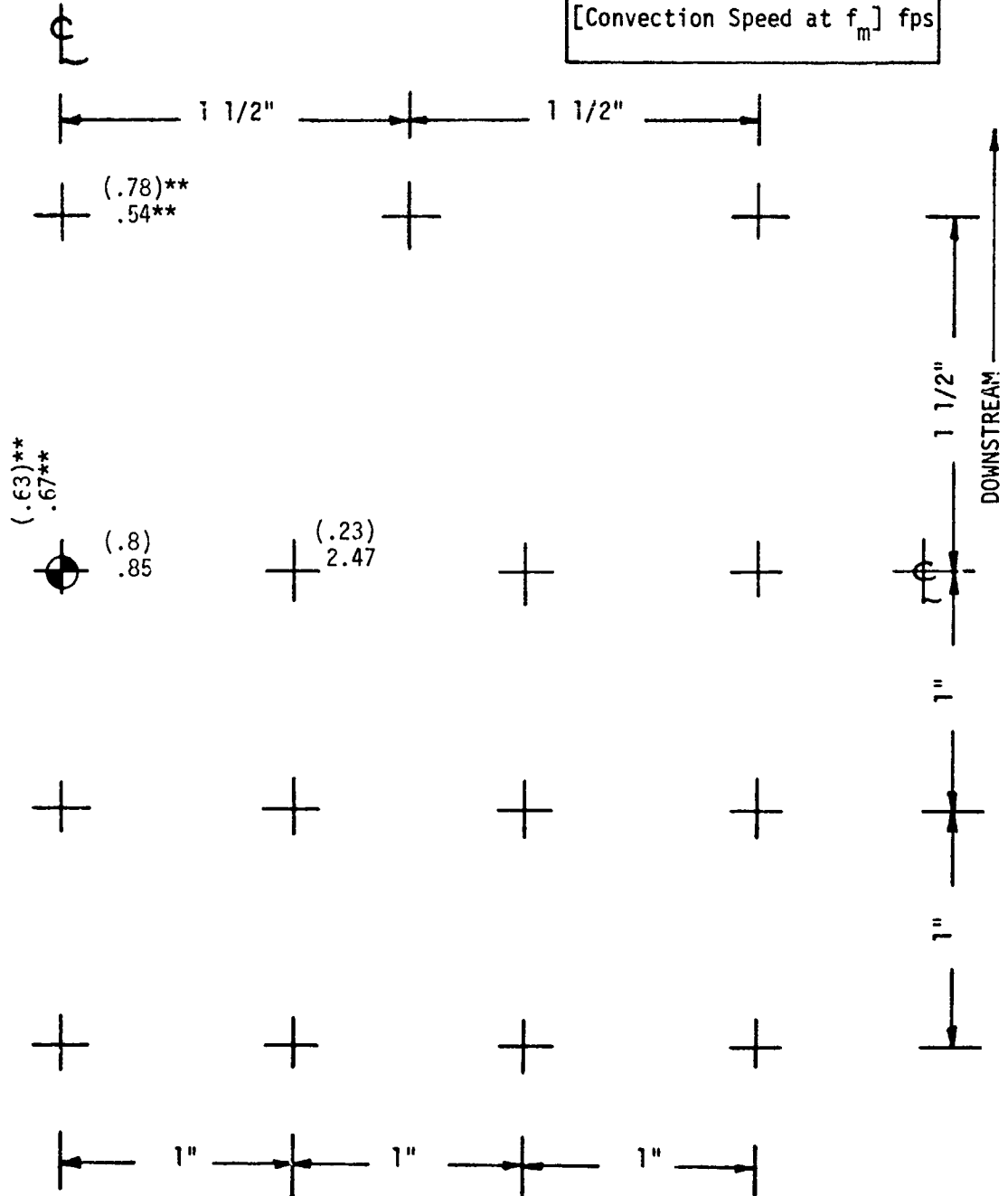


TABLE J-31
 PRESSURE MEASUREMENT RESULTS
 FLAT PLATE - DAISY NOZZLE ($C_{eq} = 2''$)

TEST CASE	T_j/T_a	M_j	X/D_{eq}	β	RESULT TYPE
4I	1	.5	11	90°	RMS (psi) (half-power freq.) KHZ [rolloff exponent] {peak amplification}

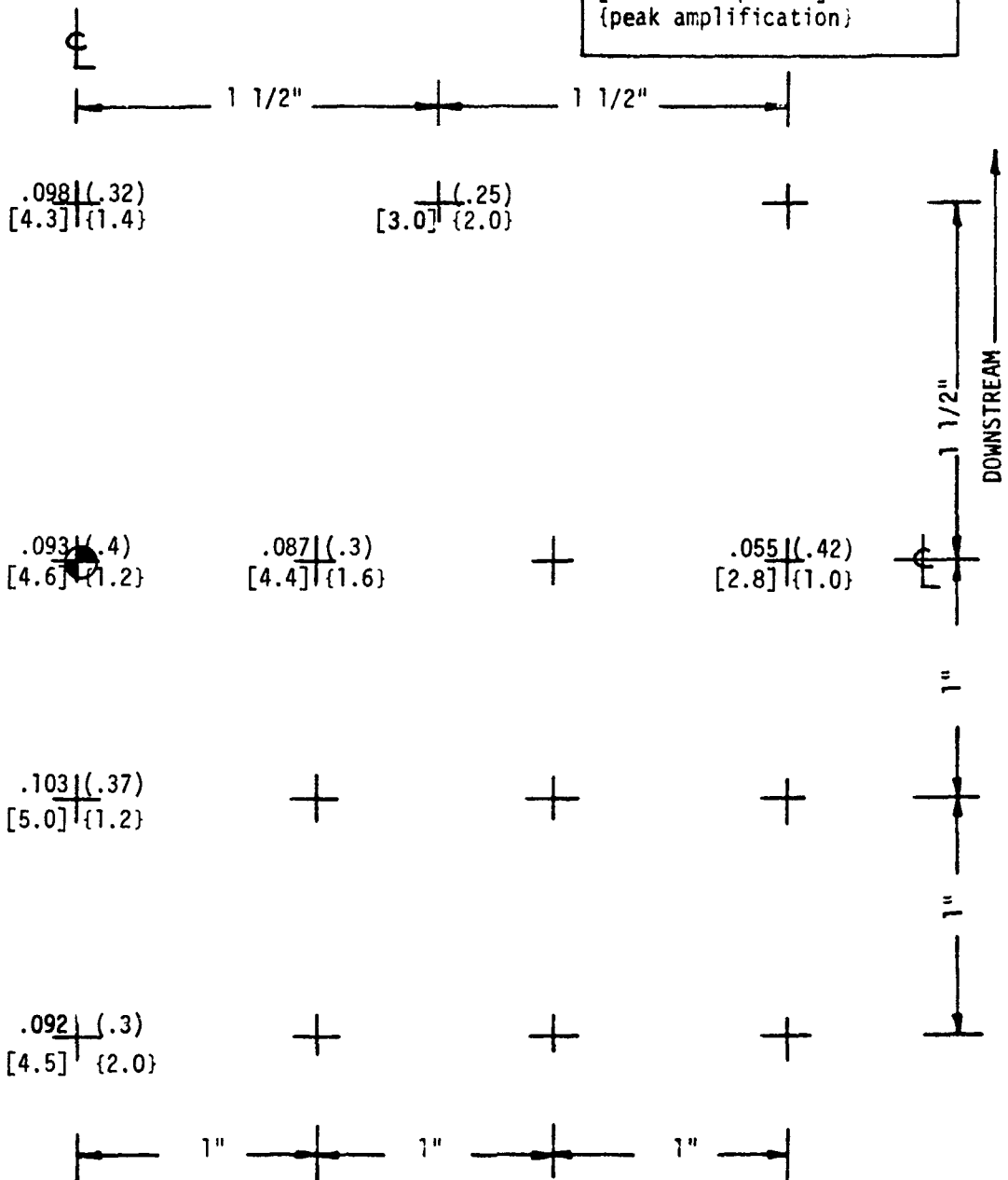


TABLE J-31 (CONT'D)
 PRESSURE MEASUREMENT RESULTS
 FLAT PLATE - DAISY NOZZLE ($D_{eq} = 2"$)

TEST CASE	T_j/T_a	M_j	X/D_{eq}	β	RESULT TYPE
4I	1.0	0.5	11	90°	Max. Correlation Length (in) (Freq. at Maximum, f_m) KHZ [Convection Speed at f_m] fps

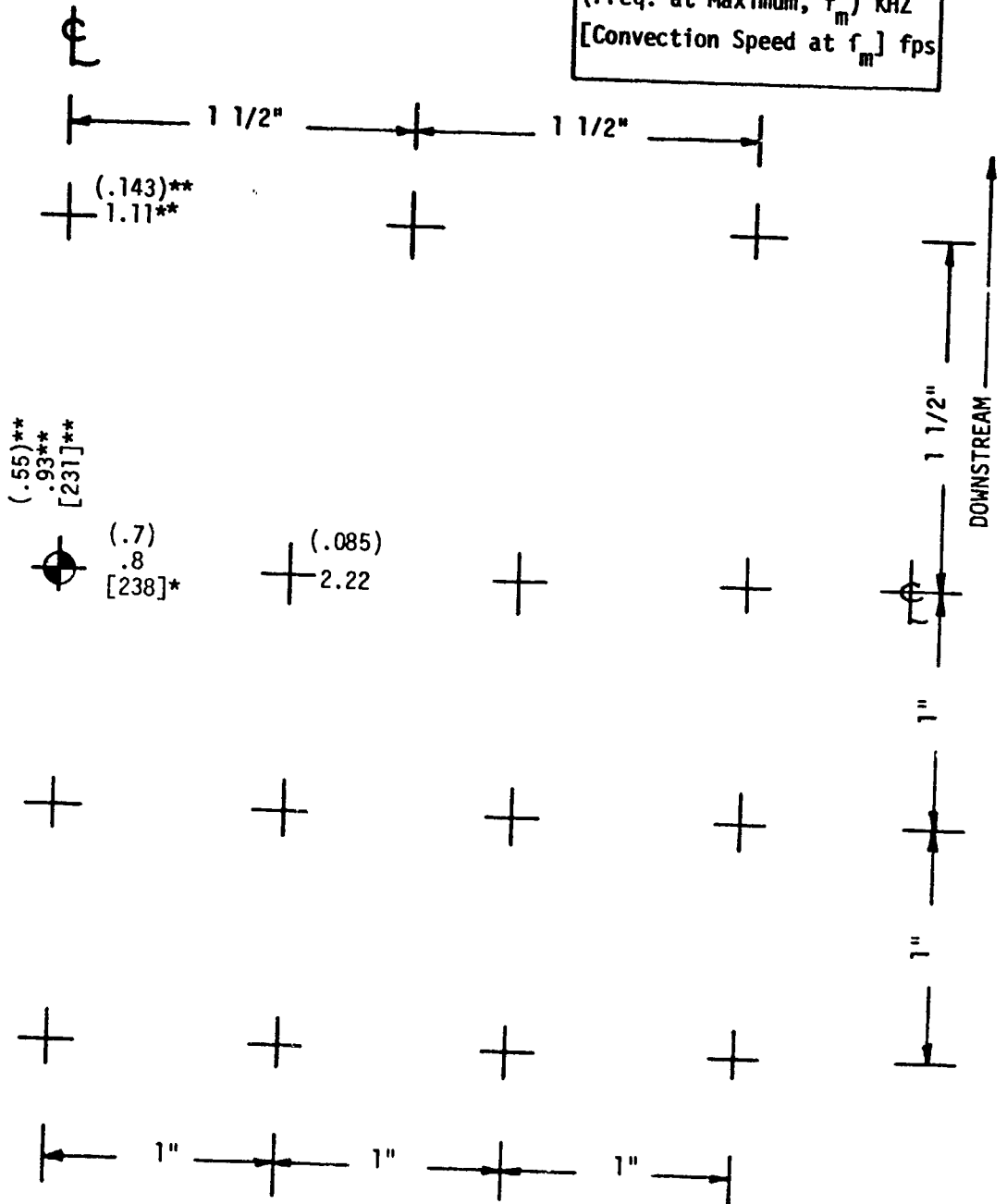


TABLE J-32
 PRESSURE MEASUREMENT RESULTS
 UBF CURVED PLATE-DAISY NOZZLE ($D_{eq} = 2"$)

TEST CASE	T_j/T_a	M_j	Z_{LE}	β_{TE}	X_{LE}	RESULT TYPE
5A	1	.5	2.0	50°	0	RMS (psi) (half-power freq) KHZ [rollcfff exponent] {peak amplification}

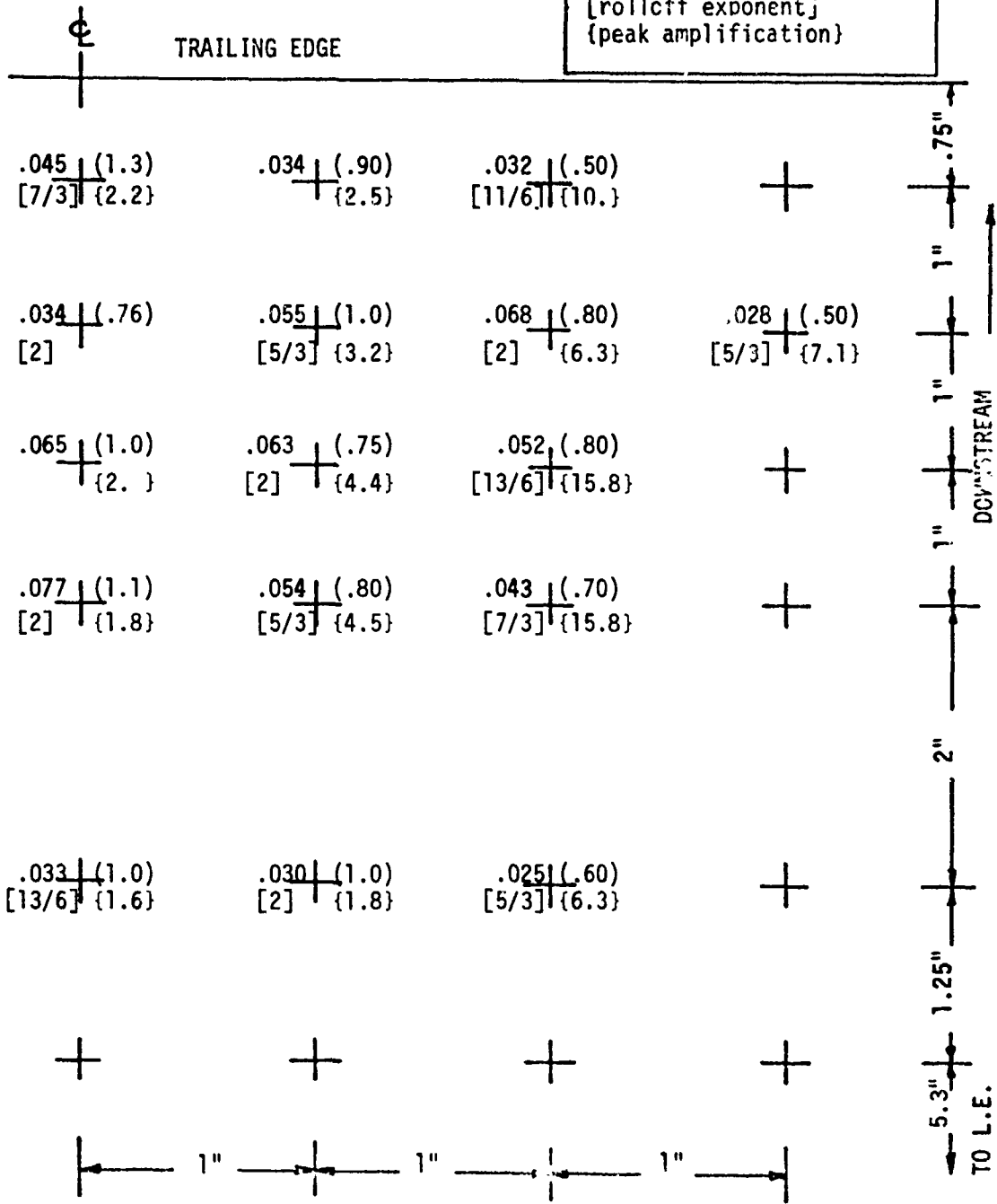


TABLE J-32 (CONT'D)
 PRESSURE MEASUREMENT RESULTS
 UBF CURVED PLATE-DAISY NOZZLE ($D_{eq} = 2''$)

TEST CASE	T_j/T_a	M_j	Z_{LE}	β_{TE}	X_{LE}	RESULT TYPE
5A	1.0	0.5	2.0	50°	0	Max. Correlation Length (in) (Freq. at Maximum, f_m) KHZ [Convection Speed at f_m] fps

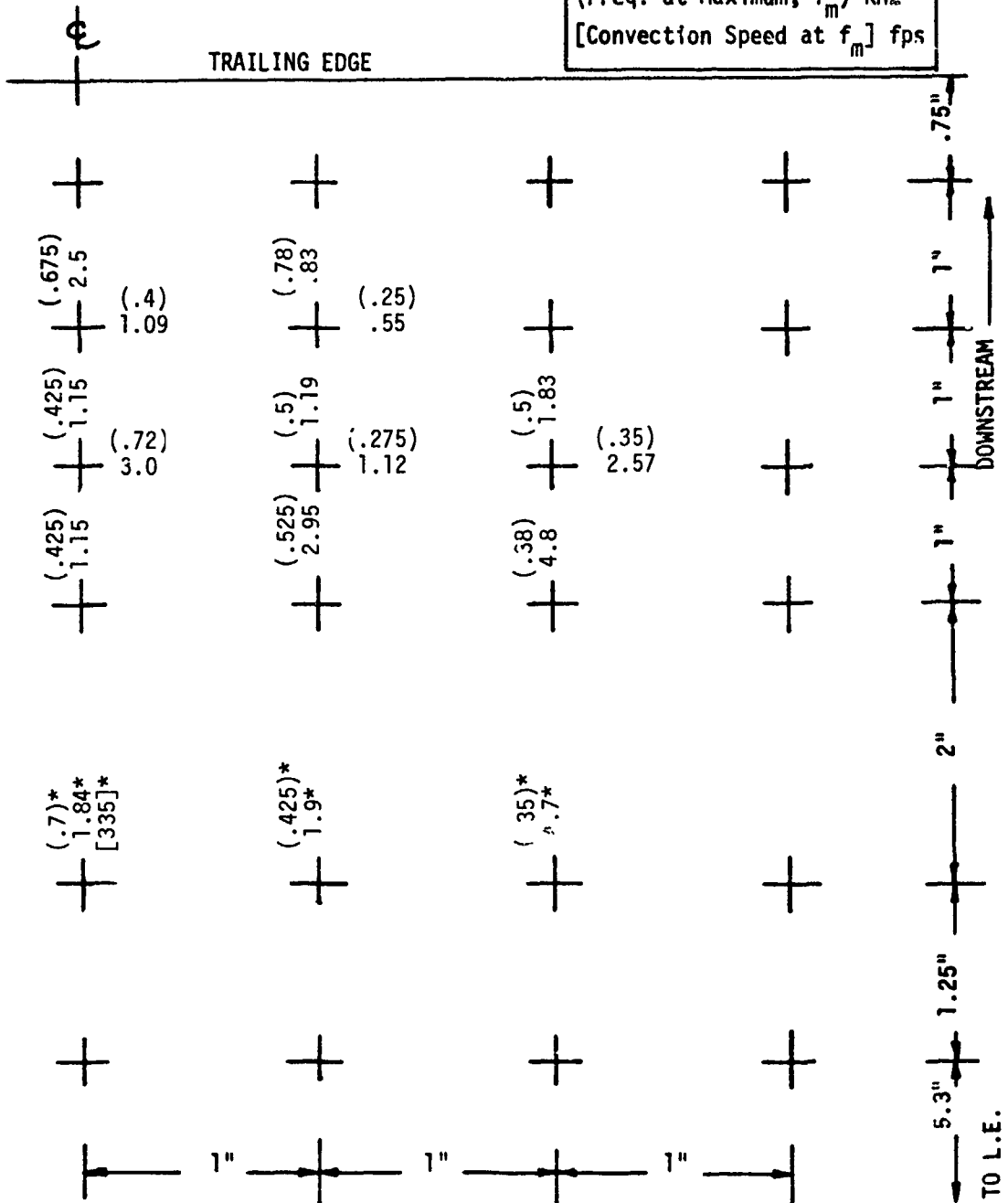


TABLE J-33
 PRESSURE MEASUREMENT RESULTS
 UBF CURVED PLATE-DAISY NOZZLE ($D_{eq} = 2"$)

TEST CASE	T_j/T_a	M_j	Z_{LE}	β_{TE}	X_{LE}	RESULT TYPE
5B	1.7	.5	2.0	50°	0	RMS (psi) (half-power freq) KHZ [rolloff exponent] {peak amplification}

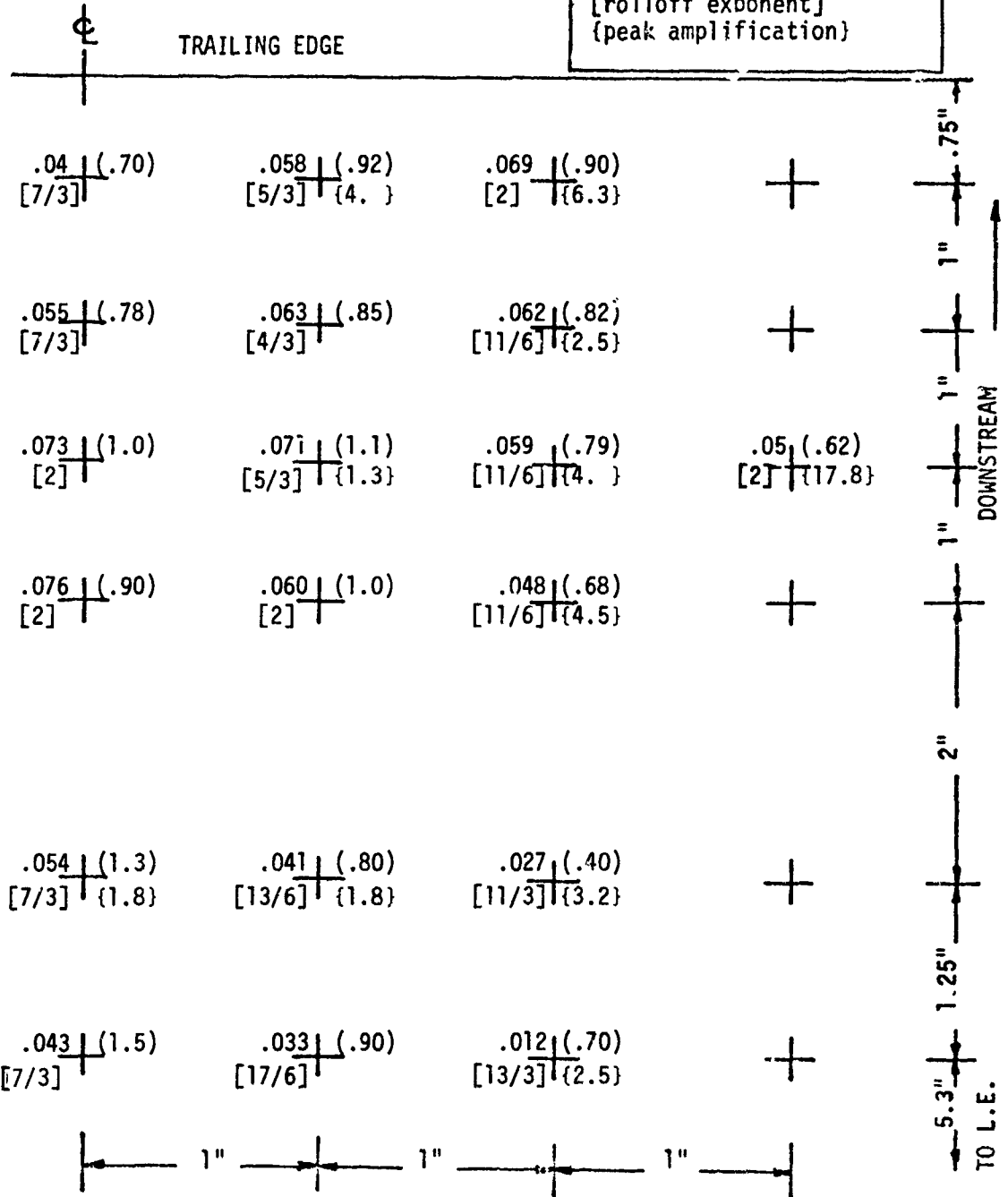


TABLE J-33 (CONT'D)
 PRESSURE MEASUREMENT RESULTS
 UBF CURVED PLATE-DAISY NOZZLE ($D_{eq} = 2"$)

TEST CASE	T_j/T_a	M_j	Z_{LE}	β_{TE}	χ_{LE}	RESULT TYPE
5B	1.7	0.5	2.0	50°	0	Max. Correlation Length (in) (Freq. at Maximum, f_m) KHZ [Convection Speed at f_m] fps

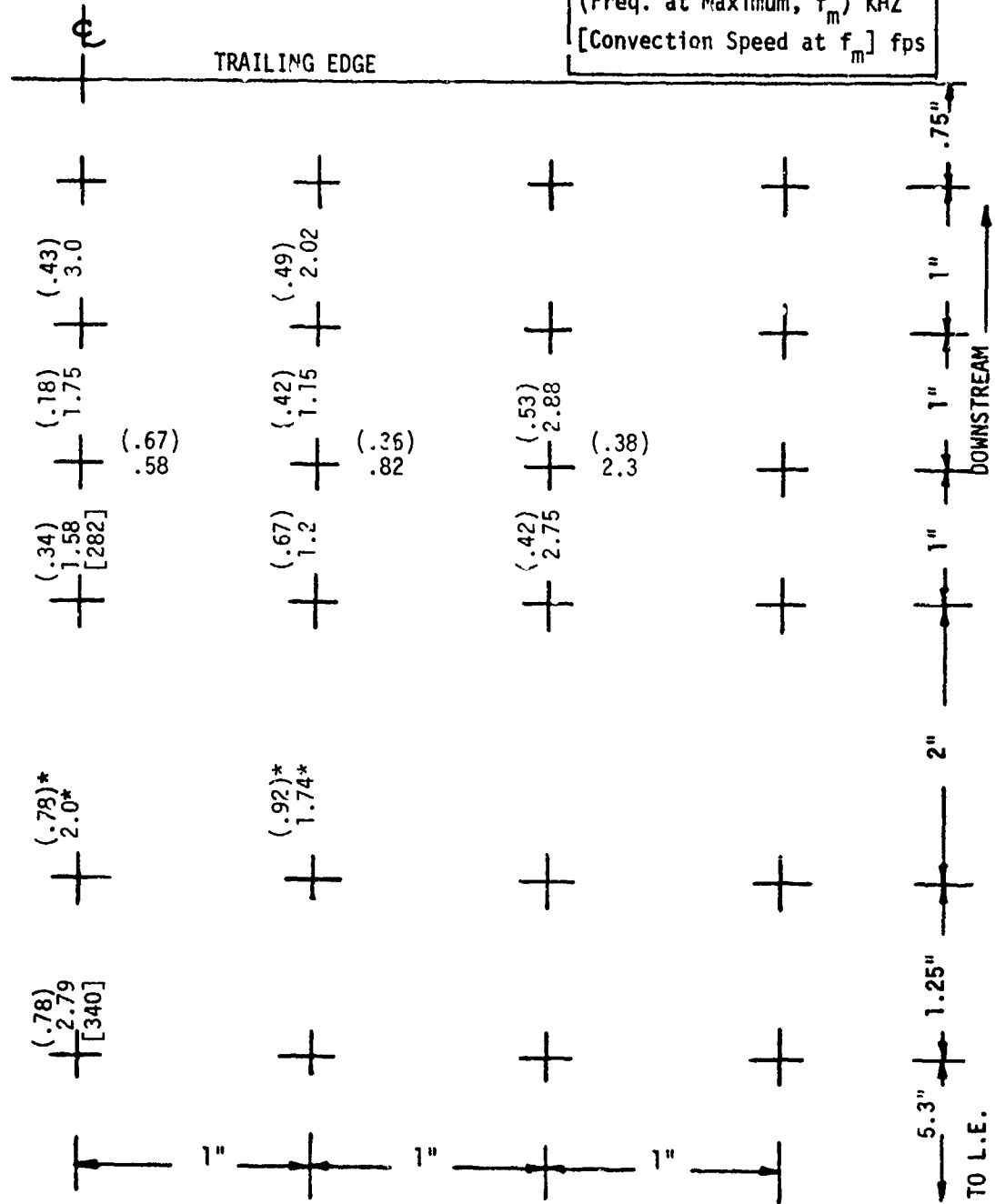
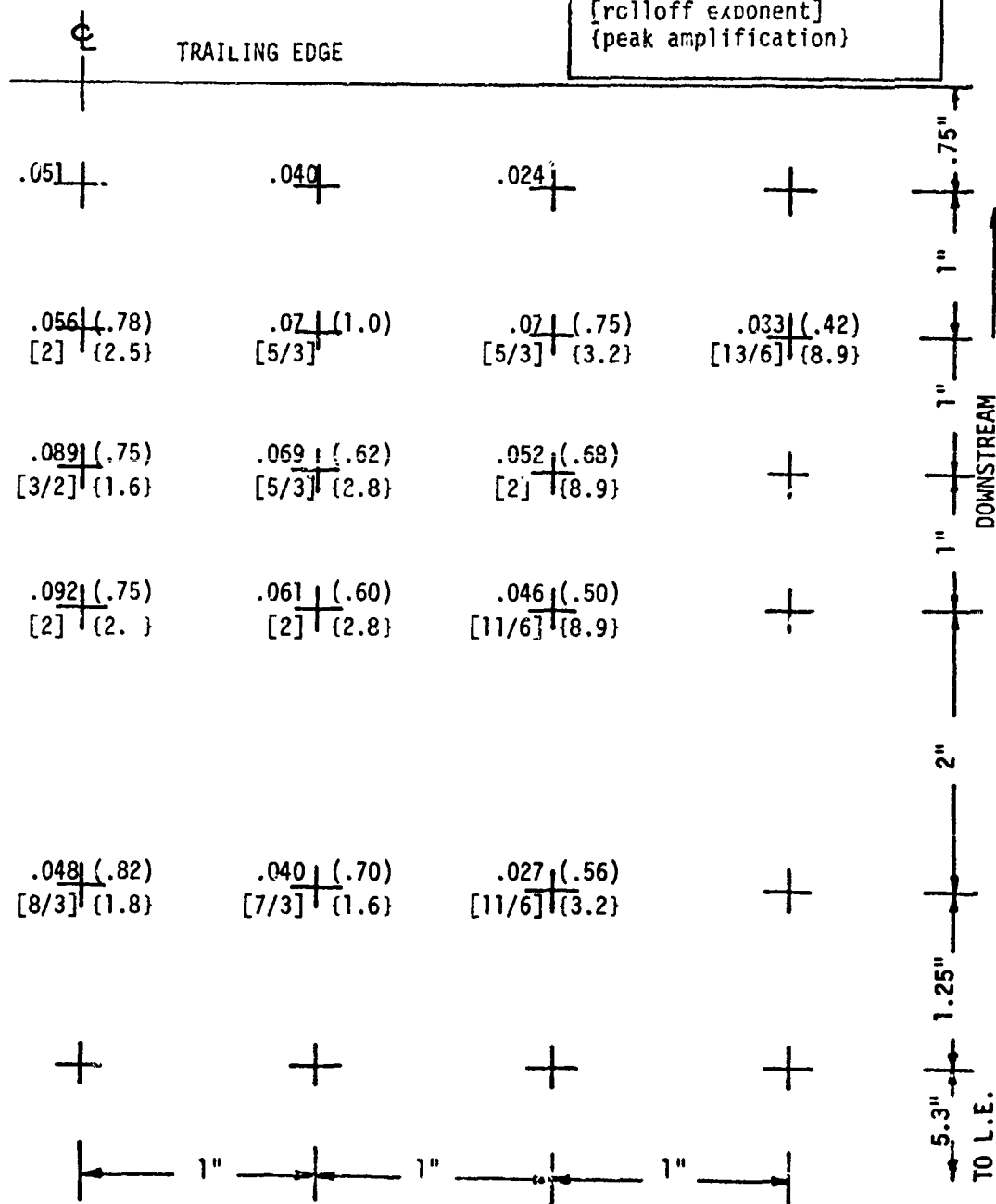


TABLE J-34
 PRESSURE MEASUREMENT RESULTS
 UBF CURVED PLATE-DAISY NOZZLE ($D_{eq} = 2"$)

TEST CASE	T_j/T_a	M_j	Z_{LE}	β_{TE}	X_{LE}	RESULT TYPE
5C	1	.5	2.0	50°	3	RMS (psi) (half-power freq) KHZ [rolloff exponent] {peak amplification}



.051	.040	.024	+
.056 (.78) [2] {2.5}	.07 (1.0) [5/3]	.07 (.75) [5/3] {3.2}	.033 (.42) [13/6] {8.9}
.089 (.75) [3/2] {1.6}	.069 (.62) [5/3] {2.8}	.052 (.68) [2] {8.9}	+
.092 (.75) [2] {2. }	.061 (.60) [2] {2.8}	.046 (.50) [11/6] {8.9}	+
.048 (.82) [8/3] {1.8}	.040 (.70) [7/3] {1.6}	.027 (.56) [11/6] {3.2}	+
+	+	+	+

TABLE J-34 (CONT'D)
 PRESSURE MEASUREMENT RESULTS
 UBF CURVED PLATE-DAISY NOZZLE ($D_{eq} = 2''$)

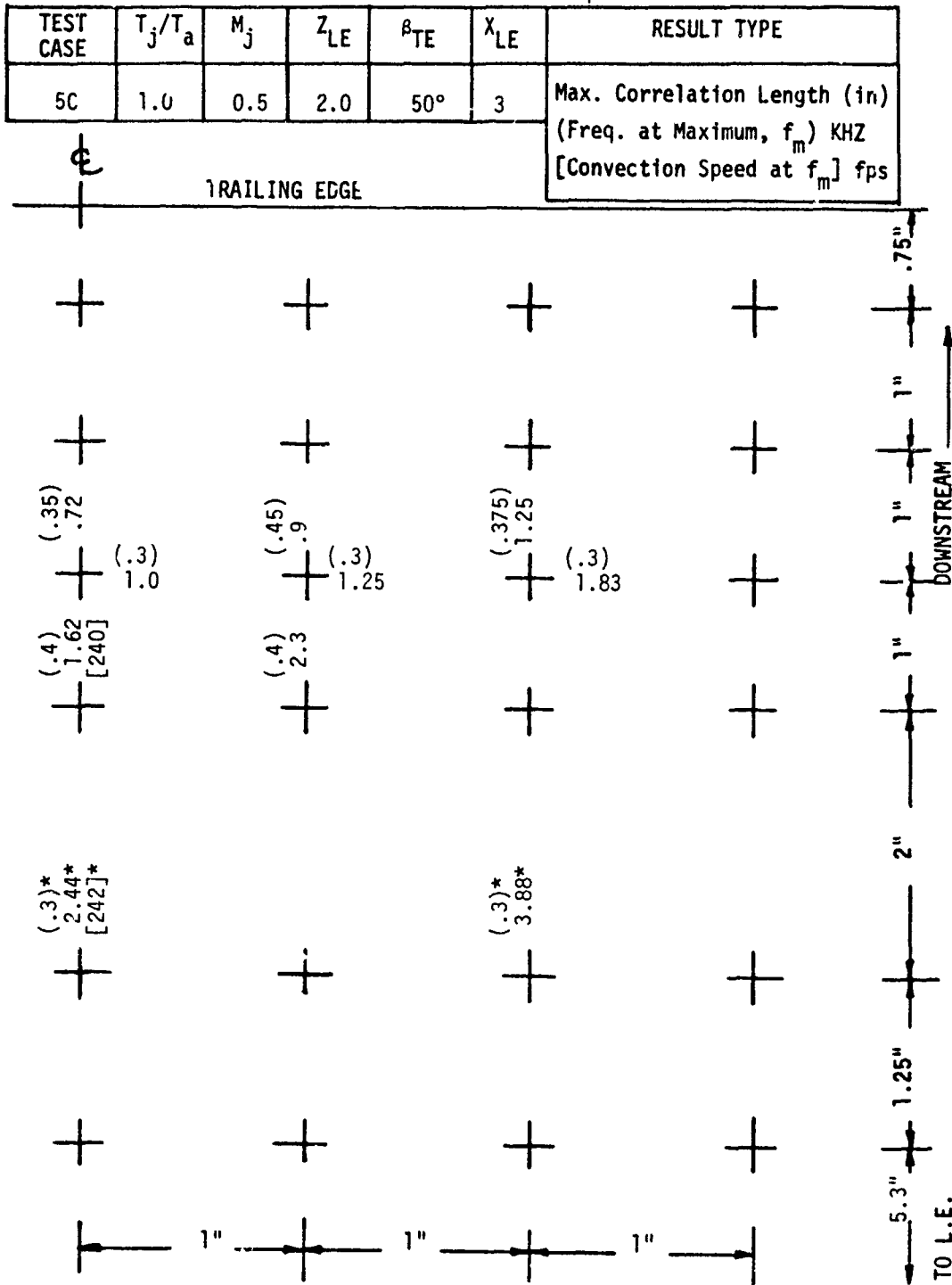


TABLE J-35

PRESSURE MEASUREMENT RESULTS
UBF CURVED PLATE-ROUND NOZZLE (D = 2")

TEST CASE	T_j/T_a	M_j	Z_{LE}	β_{TE}	X_{LE}	RESULT TYPE
5D	1	.5	1.4	50°	0	RMS (psi) (half-power freq) KHZ [rolloff exponent] {peak amplification}

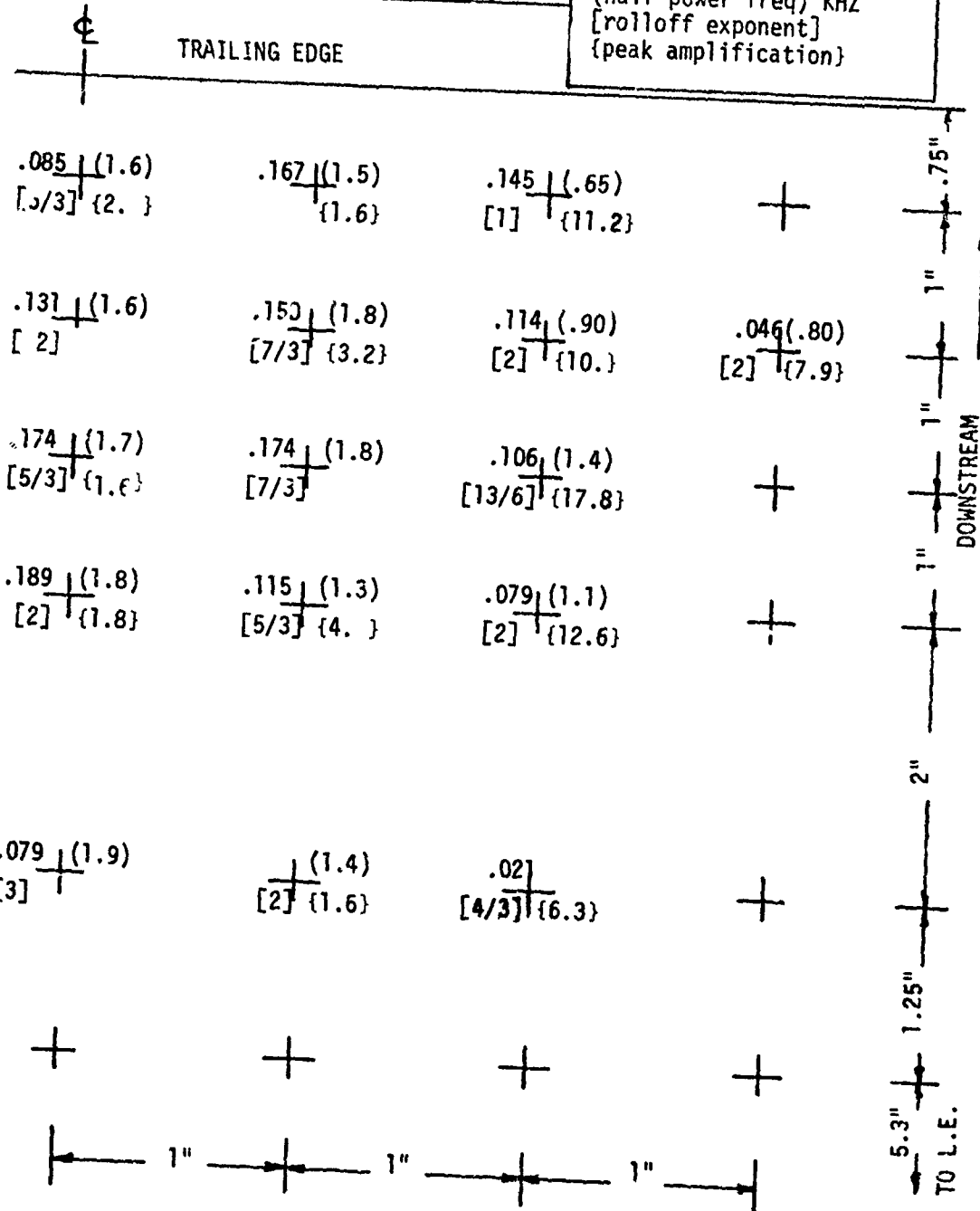


TABLE J-35 (CONT'D)
 PRESSURE MEASUREMENT RESULTS
 UBF CURVED PLATE - ROUND NOZZLE (D = 2")

TEST CASE	T_j/T_a	M_j	Z_{LE}	β_{TE}	X_{LE}	RESULT TYPE
5D	1.0	0.5	1.4	50°	0	Max. Correlation Length (in) (Freq. at Maximum, f_m) KHZ [Convection Speed at f_m] fps

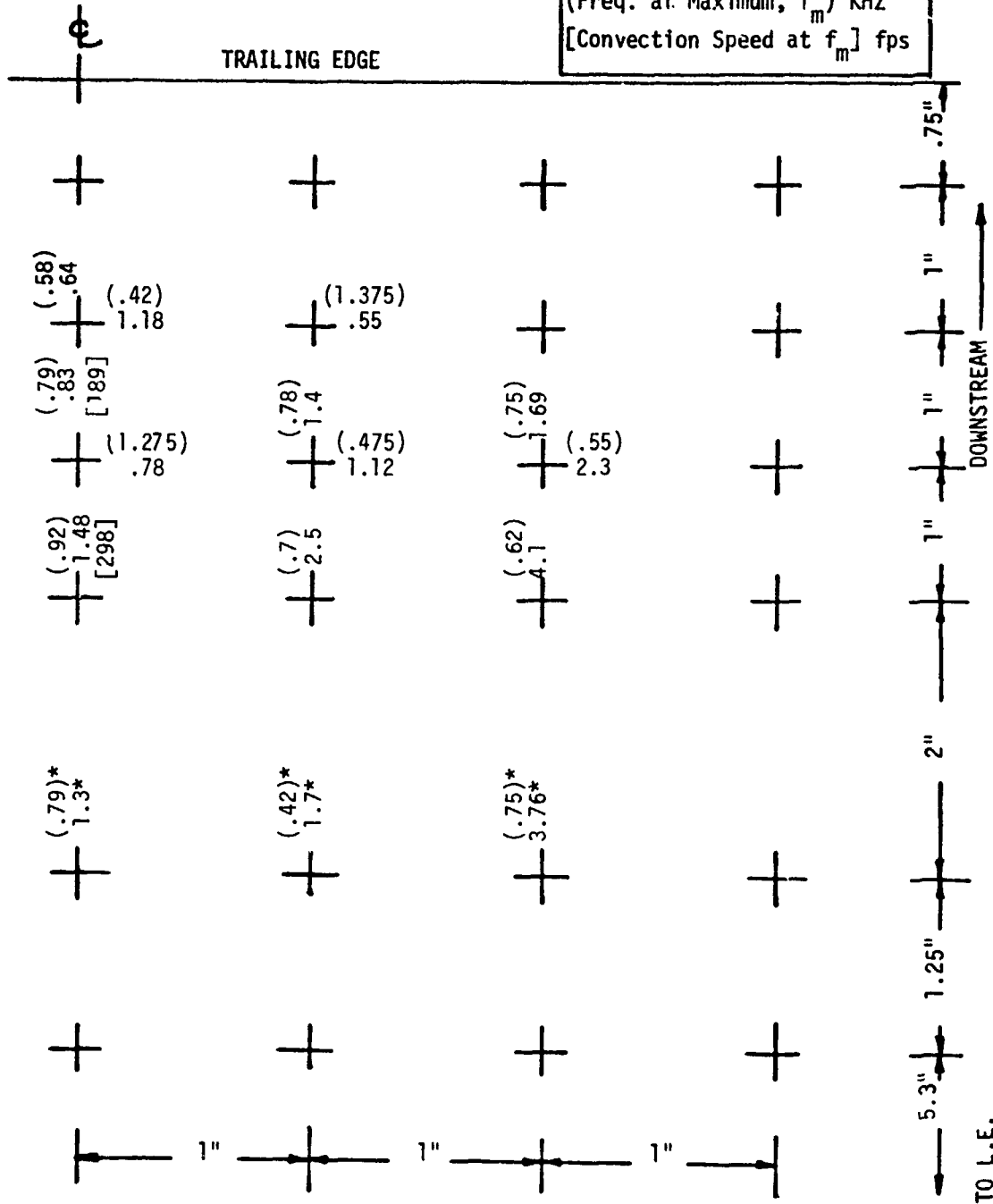


TABLE J-36

PRESSURE MEASUREMENT RESULTS
UBF CURVED PLATE-ROUND NOZZLE (D = 2")

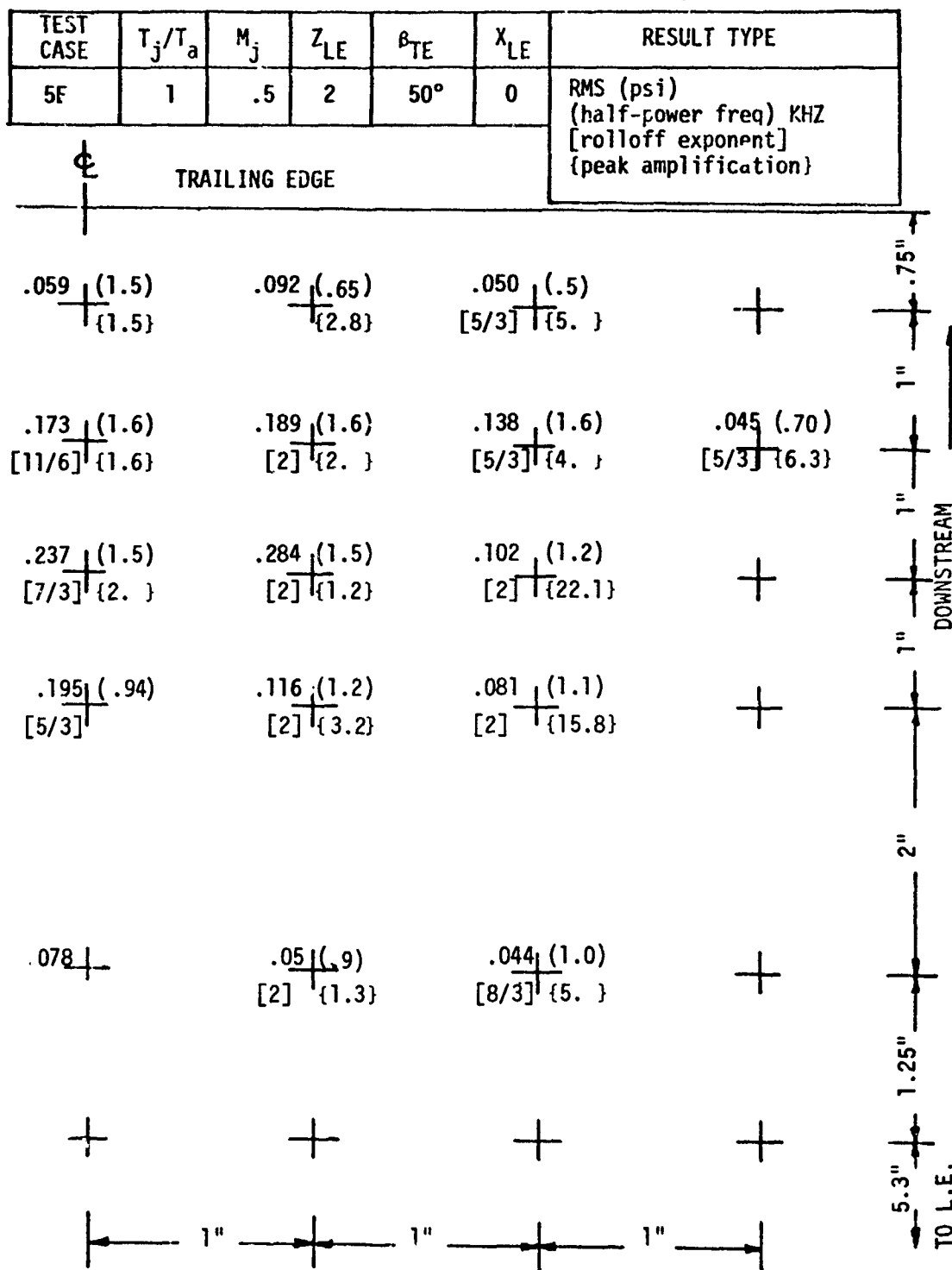


TABLE J-36 (CONT'D)
 PRESSURE MEASUREMENT RESULTS
 UBF CURVED PLATE - ROUND NOZZLE (D = 2")

TEST CASE	T_j/T_a	M_j	Z_{LE}	β_{TE}	X_{LE}	RESULT TYPE
5E	1.0	0.5	2.0	50°	0	Max. Correlation Length (in) (Freq. at Maximum, f_m) KHZ [Convection Speed at f_m] fps

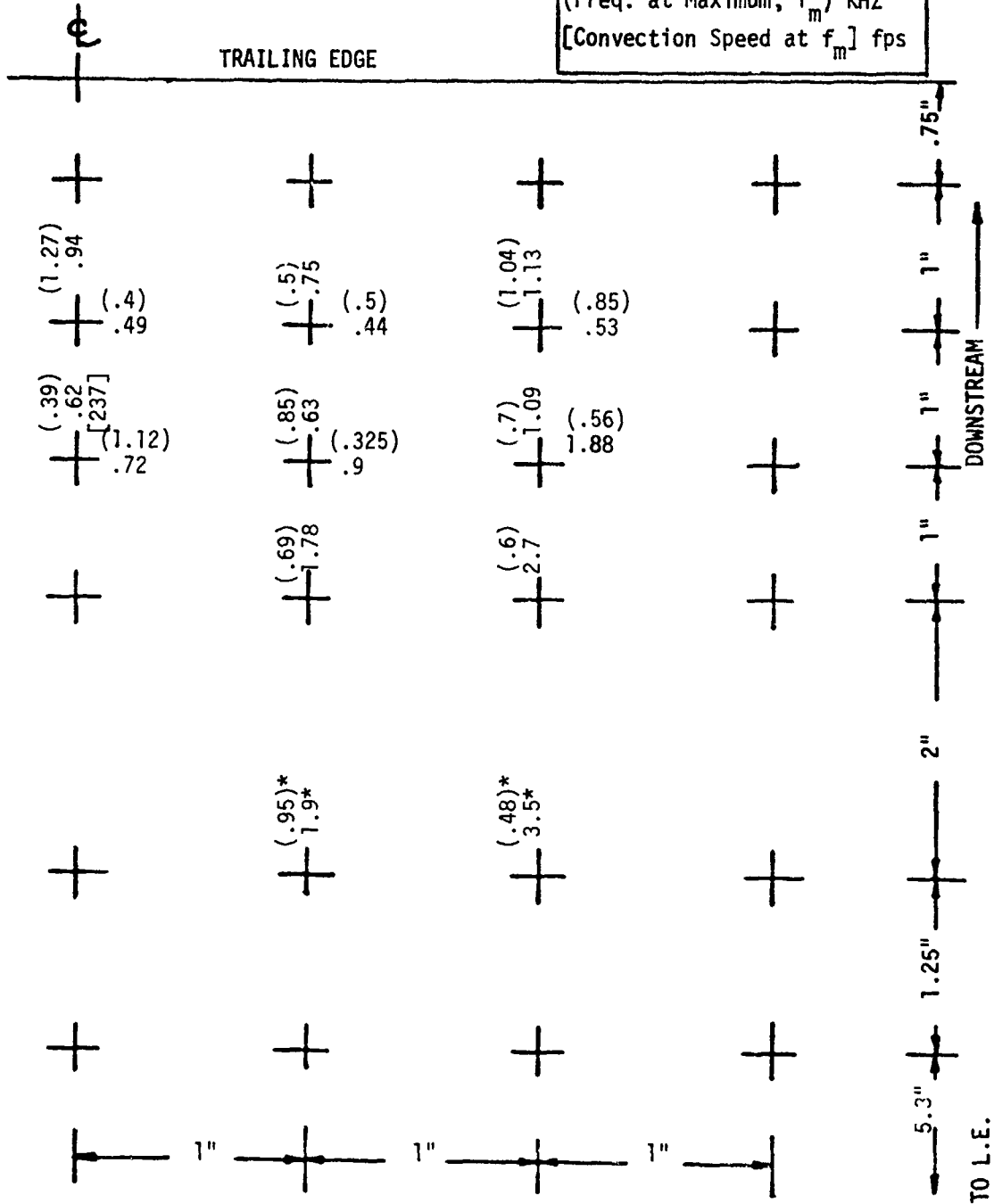


TABLE J-37
 PRESSURE MEASUREMENT RESULTS
 UBF CURVED PLATE-ROUND NOZZLE (D = 2")

TEST CASE	T_j/T_a	M_j	Z_{LE}	β_{TE}	X_{LE}	RESULT TYPE
5F	1.7	.5	1.4	50°	0	RMS (psi) (half-power freq) KHZ [rolloff exponent] {peak amplification}

TRAILING EDGE

.173 (2.0) +	.173 (2.0) + {5.0}	.157 (2.0) + [2] {17.8}	+	.75"
.183 (2.1) + [5/3]	.165 (1.8) + [3/2]	.125 (1.8) + [11/6] {3.5}	+	1"
.251 (2.5) + [7/3]	.186 (2.0) + [3/2] {2. }	.111 (1.5) + [2] {7.9}	.08 (1.2) + [13/6] {12.6}	1"
.222 (2.5) + [8/3]	.150 (1.6) + [5/3] {2. }	.084 (1.4) + [7/3] {7.1}	+	1"
.130 (2.9) + [3] {3.2}	.102 (2.0) + [11/3] {2.5}	.035 (.60) + [10/3] {13.5}	+	2"
.109 (3.4) + [3]	.078 (2.3) + [5] {2. }	.021 +	+	1.25"
				5.3" TO L.E.

TABLE J-37 (CONT'D)
 PRESSURE MEASUREMENT RESULTS
 UBF CURVED PLATE - ROUND NOZZLE (D = 2")

TEST CASE	T_j/T_a	M_j	Z_{LE}	β_{TE}	X_{LE}	RESULT TYPE
5F	1.7	0.5	1.4	50°	0	Max. Correlation Length (in) (Freq. at Maximum, f_m) KHZ [Convection Speed at f_m] fps

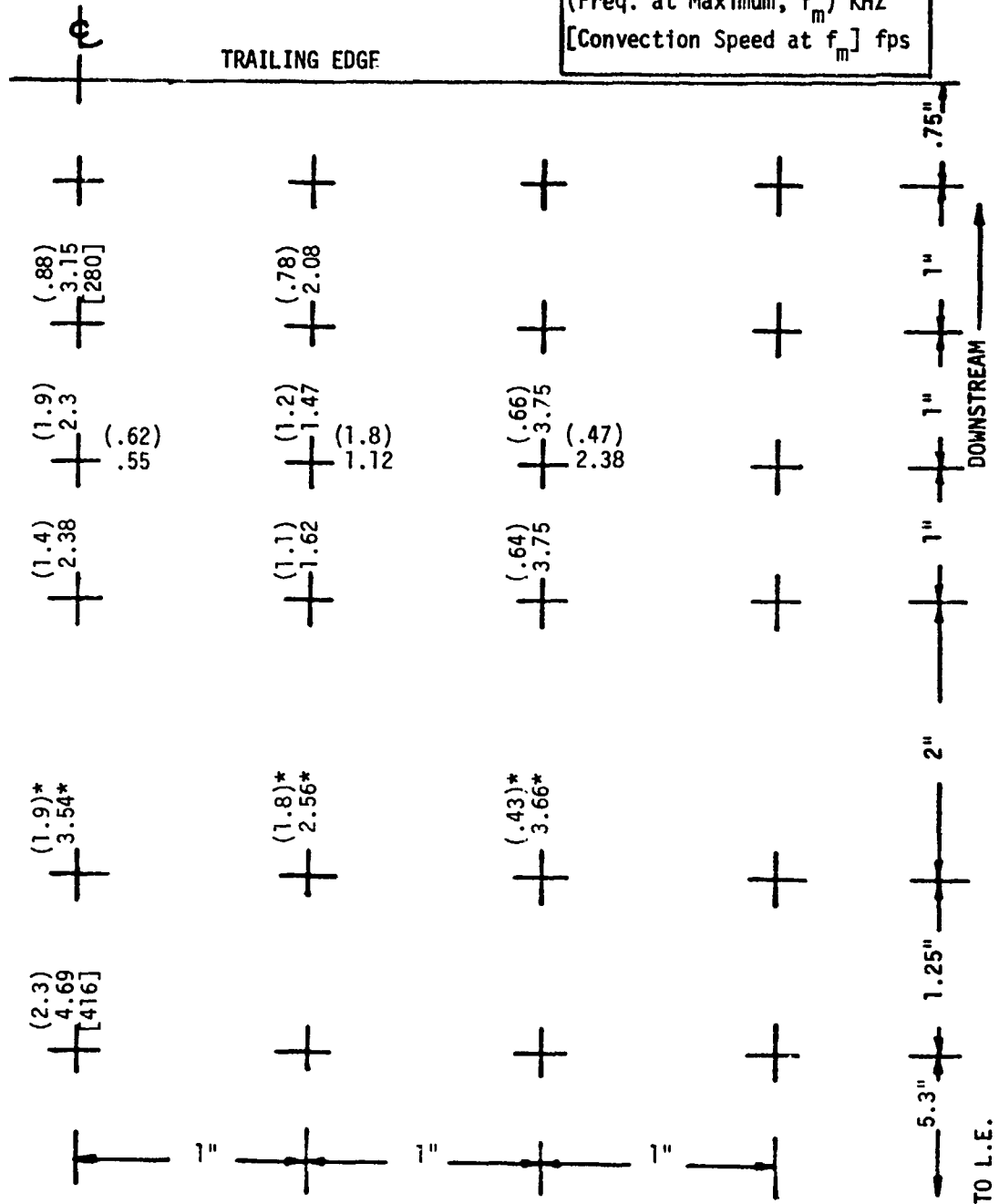


TABLE J-38

PRESSURE MEASUREMENT RESULTS
UBF CURVED PLATE-ROUND NOZZLE (D = 2")

TEST CASE	T_j/T_a	M_j	Z_{LE}	β_{TE}	X_{LE}	RESULT TYPE
5G	1	.5	1.4	50°	3	RMS (psi) (half-power freq) KHZ [rolloff exponent] {peak amplification}

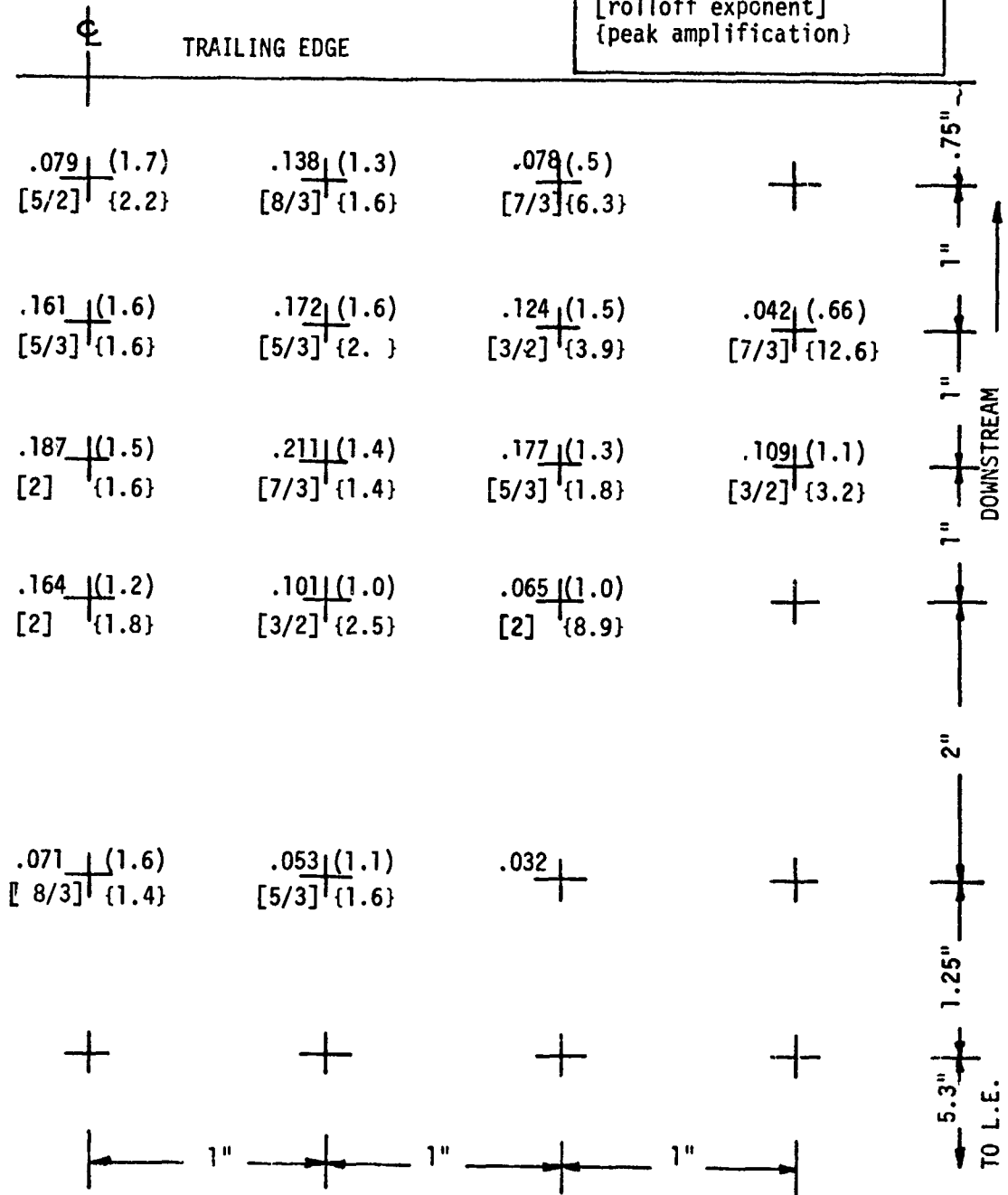


TABLE J-38 (CONT'D)
 PRESSURE MEASUREMENT RESULTS
 UBF CURVED PLATE - ROUND NOZZLE (D = 2")

TEST CASE	T_j/T_a	M_j	Z_{LE}	β_{TE}	X_{LE}	RESULT TYPE
5G	1.0	0.5	1.4	50°	3	Max. Correlation Length (in) (Freq. at Maximum, f_m) KHZ [Convection Speed at f_m] fps

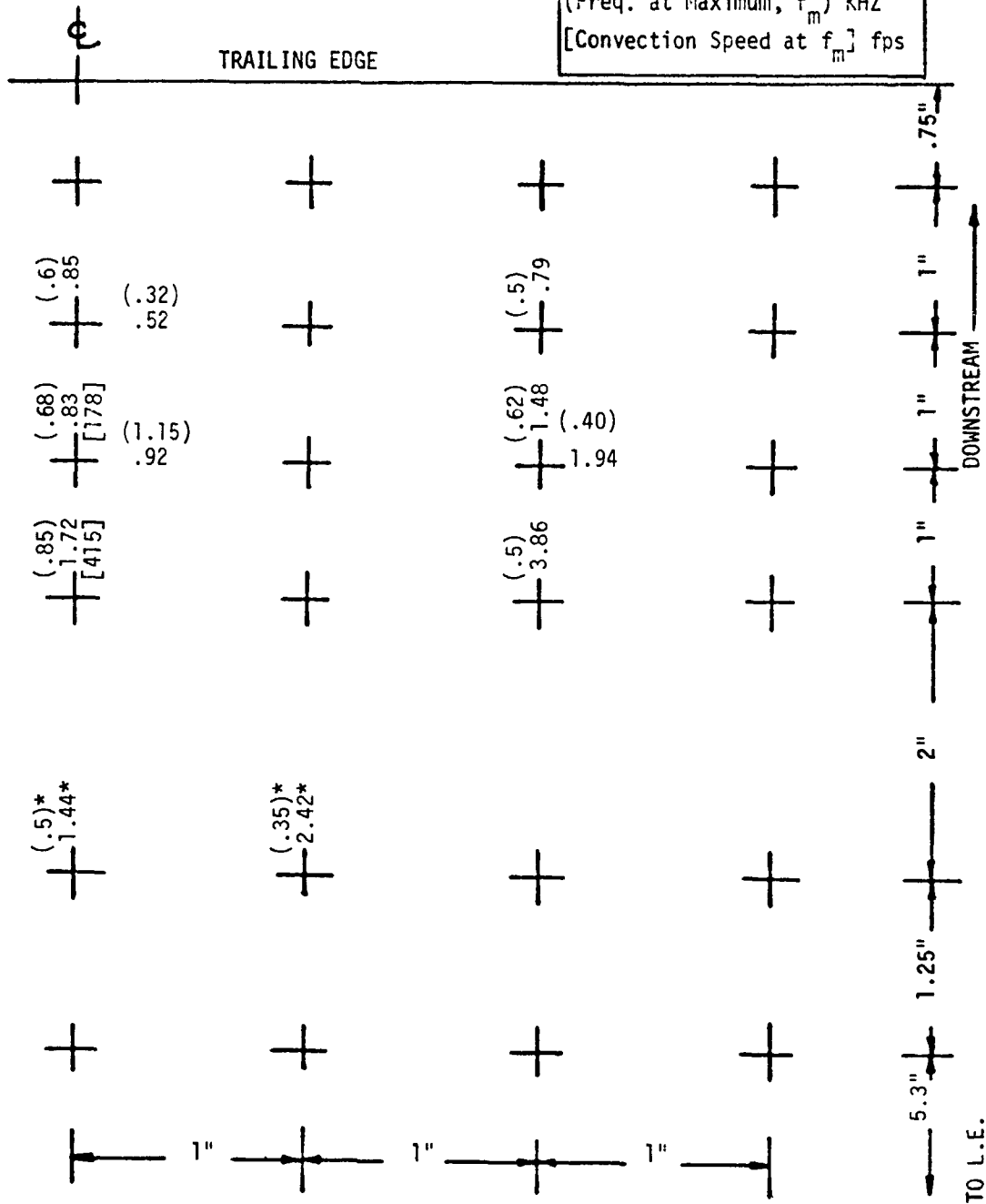


TABLE J-39
 PRESSURE MEASUREMENT RESULTS
 UBF CURVED PLATE-ROUND NOZZLE (D = 2")

TEST CASE	T_j/T_a	M_j	Z_{LE}	β_{TE}	X_{LE}	RESULT TYPE
5H	1	.74	1.4	50°	0	RMS (psi) (half-power freq) KHZ [rolloff exponent] {peak amplification}

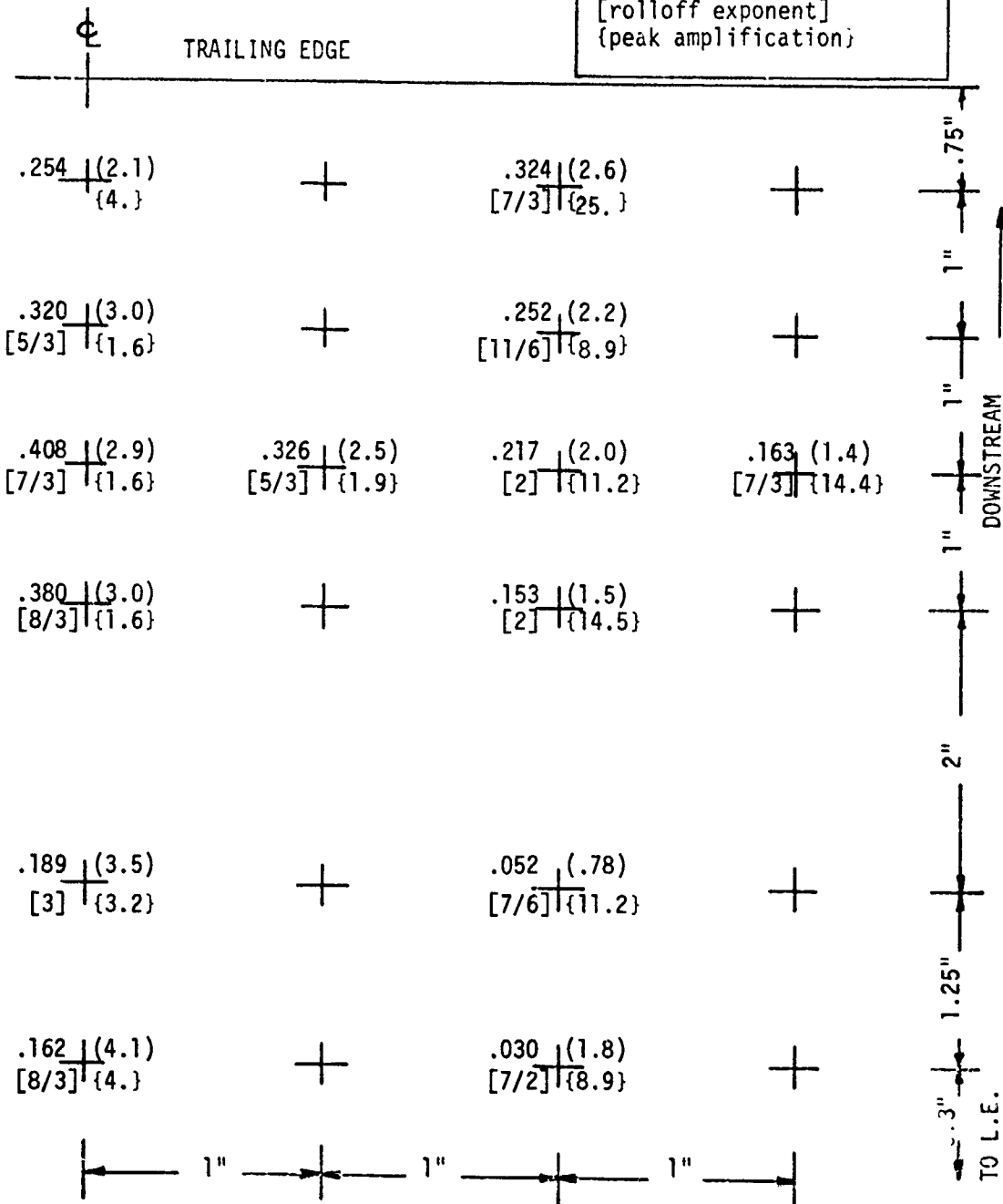


TABLE J-39 (CONT'D)
 PRESSURE MEASUREMENT RESULTS
 UBF CURVED PLATE - ROUND NOZZLE (D = 2")

TEST CASE	T_j/T_a	M_j	Z_{LE}	β_{TE}	X_{LE}	RESULT TYPE
5H	1.0	0.74	1.4	50°	0	Max. Correlation Length (in) (Freq. at Maximum, f_m) KHZ [Convection Speed at f_m] fps

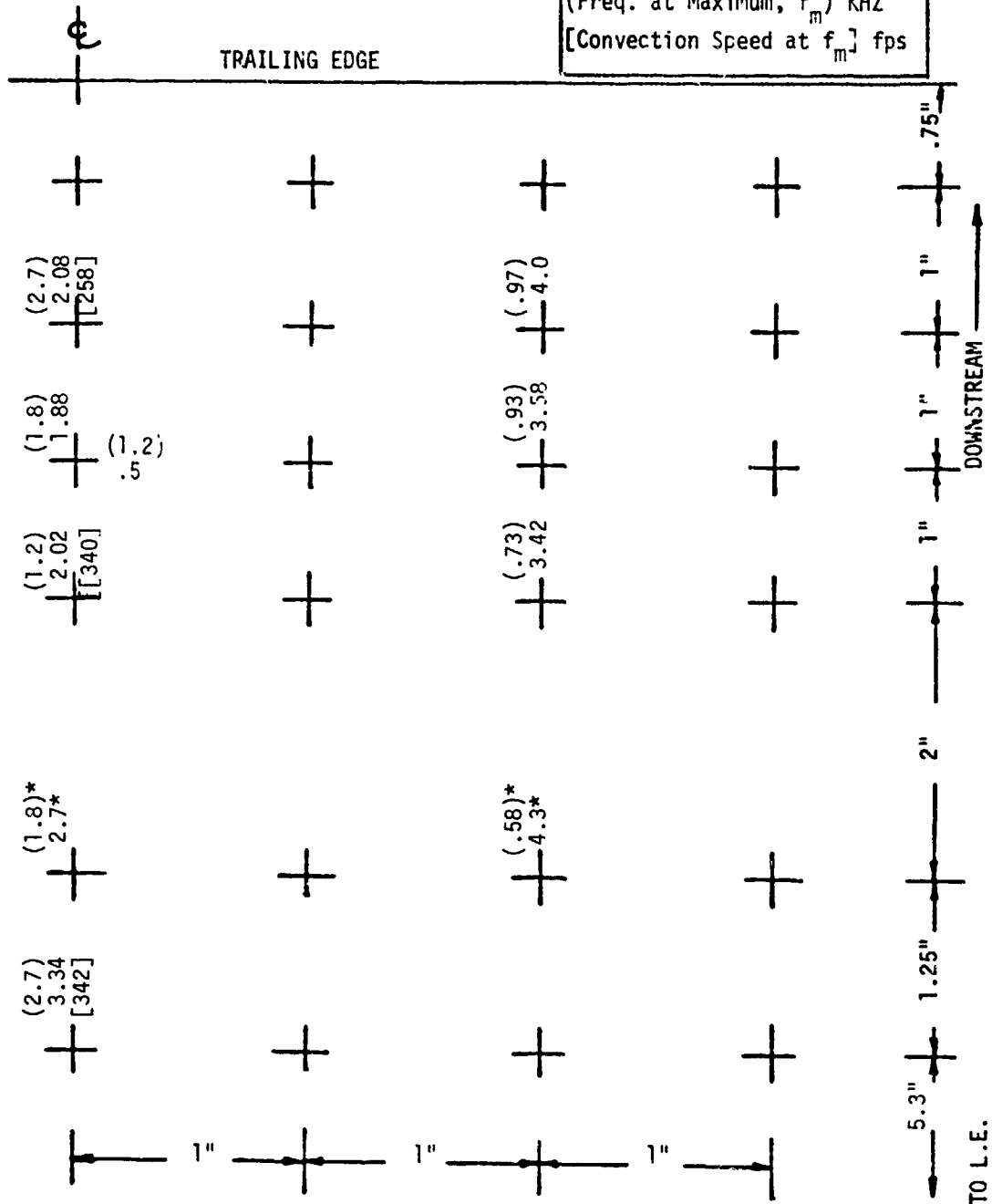


TABLE J-40

PRESSURE MEASUREMENT RESULTS

UBF CURVED PLATE-ROUND NOZZLE (D = 2")

TEST CASE	T_j/T_a	M_j	Z_{LE}	β_{TE}	X_{LE}	RESULT TYPE
5I	1	.35	1.4	50°	0	RMS (psi) (half-power freq) KHZ [rolloff exponent] {peak amplification}

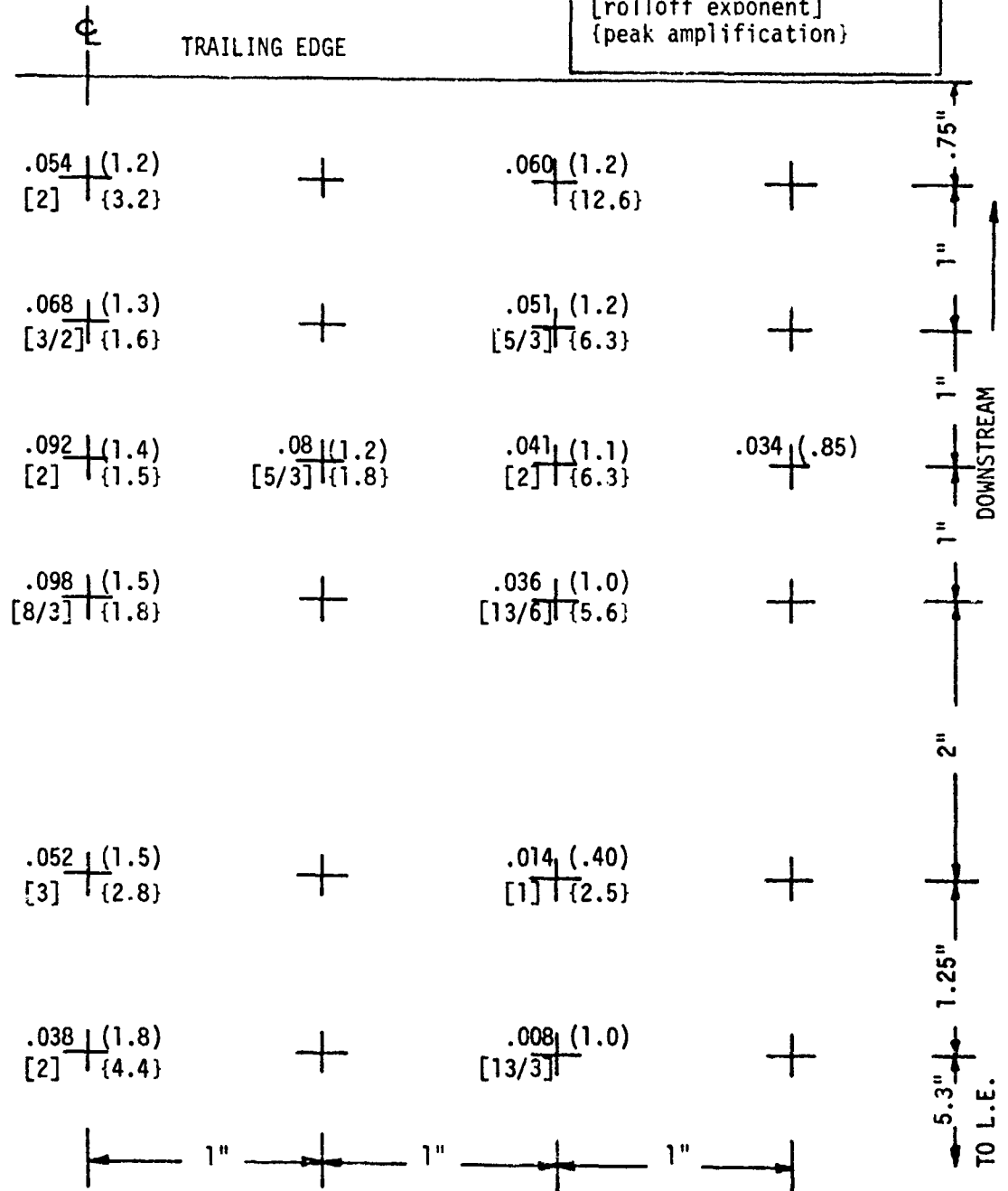


TABLE J-40 (CONT'D)
 PRESSURE MEASUREMENT RESULTS
 UBF CURVED PLATE - ROUND NOZZLE (D = 2")

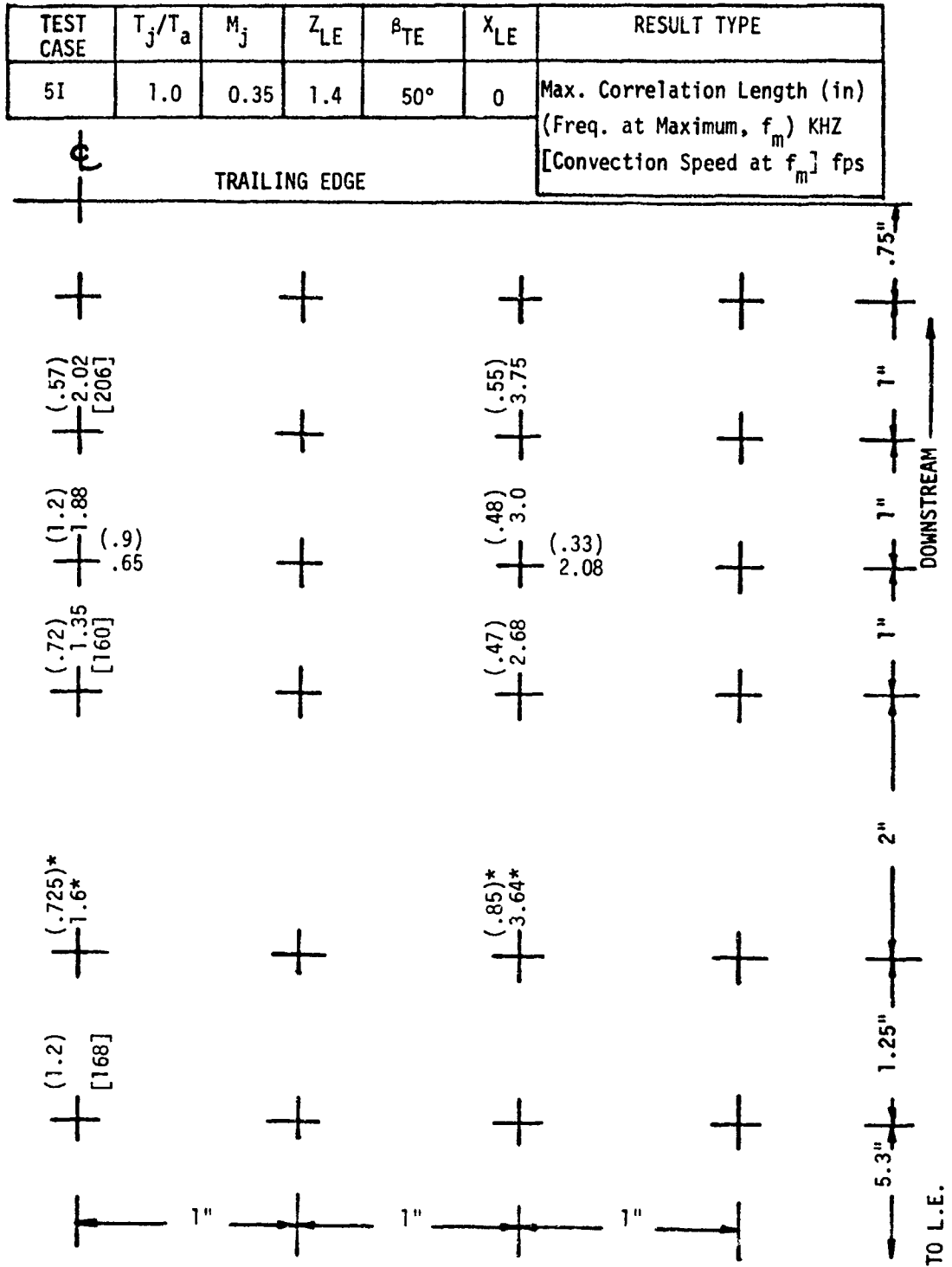


TABLE J-41
 PRESSURE MEASUREMENT RESULTS
 UBF CURVED PLATE-ROUND NOZZLE (D = 2")

TEST CASE	T_j/T_a	M_j	Z_{LE}	β_{TE}	X_{LE}	RESULT TYPE
5J	1	.35	1.4	50°	3	RMS (psi) (half-power freq) KHZ [rolloff exponent] {peak amplification}

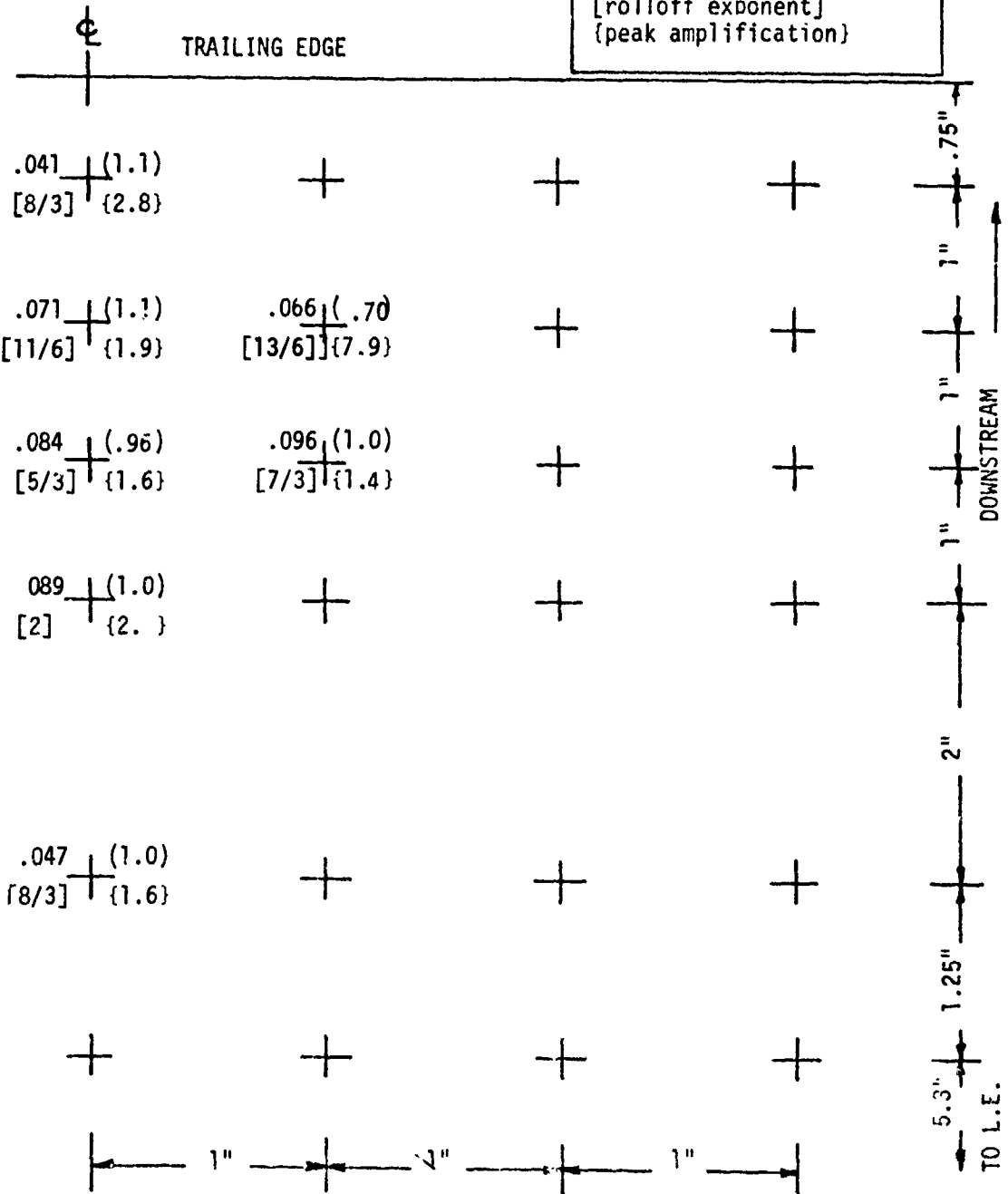


TABLE J-41 (CONT'D)
 PRESSURE MEASUREMENT RESULTS
 UBF CURVED PLATE - ROUND NOZZLE (D = 2")

TEST CASE	T_j/T_a	M_j	Z_{LE}	β_{TE}	X_{LE}	RESULT TYPE
5J	1.0	0.35	1.4	50°	3	Max. Correlation Length (in) (Freq. at Maximum, f_m) KHZ [Convection Speed at f_m] fps

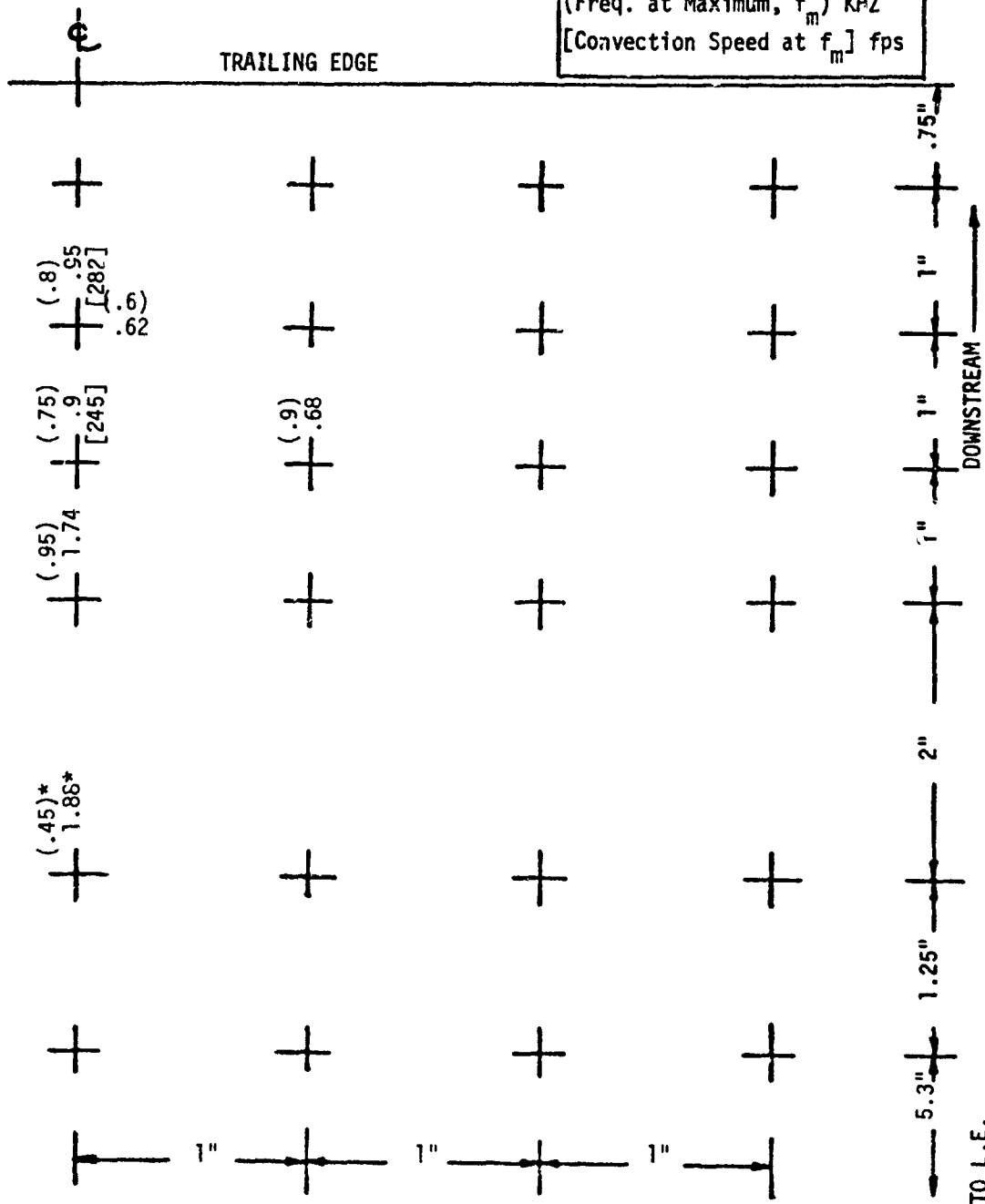


TABLE J-42
 PRESSURE MEASUREMENT RESULTS
 UBF CURVED PLATE-ROUND NOZZLE (D = 2")

TEST CASE	T_j/T_a	M_j	Z_{LE}	β_{TE}	X_{LE}	RESULT TYPE
6A	1	.5	1.4	25°	0	RMS (psi) (half-power freq) KHZ [rolloff exponent] {peak amplification}

TRAILING EDGE

Distance from Trailing Edge	RMS (psi)	(half-power freq) KHZ	[rolloff exponent]	{peak amplification}
0.75"	.129	(1.9)	[11/6]	{2.8}
1"	.120	(1.8)	[11/6]	{2.8}
1"	.083	(1.2)	[11/6]	{6.3}
1"	.133	(1.7)	[5/3]	{2.5}
1"	.076	(1.1)	[3/2]	{5.0}
1"	.144	(2.1)	[5/2]	{2.8}
1"	.108	(1.8)	[11/6]	{2.2}
1"	.062	(.80)	[7/3]	{6.3}
2"	.031			
1.25"	.134	(2.1)	[5/2]	{3.2}
1.25"	.097	(1.8)		
4.9"	.046	(.80)	[8/3]	{8.9}
	.093	(2.3)		
	.073	(1.8)		
	.026	(1.0)	[1.0]	

DOWNSTREAM

TO L.E.

TABLE J-42 (CONT'D)
 PRESSURE MEASUREMENT RESULTS
 UBF CURVED PLATE - ROUND NOZZLE (D = 2")

TEST CASE	T_j/T_a	M_j	Z_{LE}	β_{TE}	X_{LE}	RESULT TYPE
6A	1.0	0.5	1.4	25°	0	Max. Correlation Length (in) (Freq. at Maximum, f_m) KHZ [Convection Speed at f_m] fps

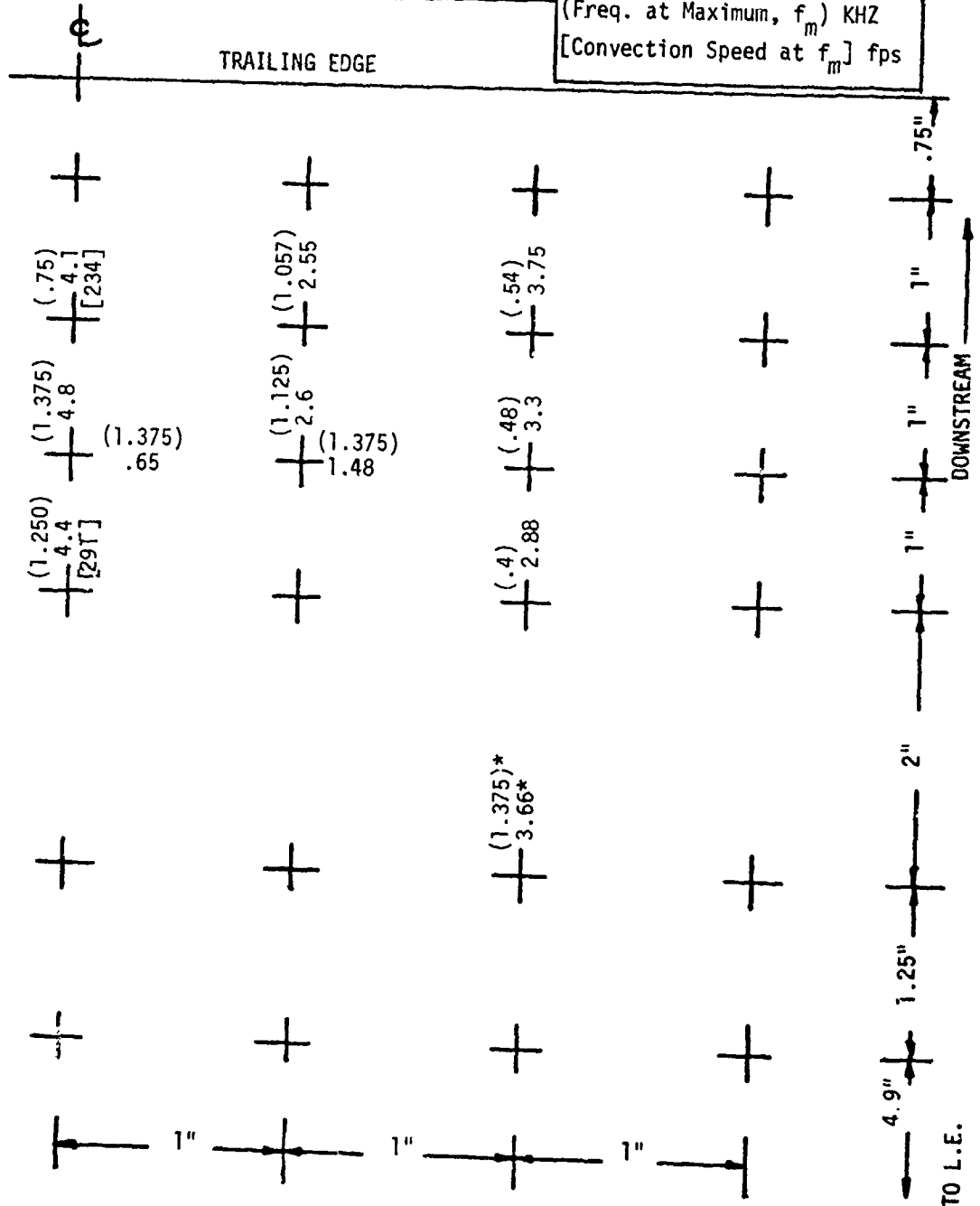


TABLE J-43

PRESSURE MEASUREMENT RESULTS

UBF CURVED PLATE-ROUND NOZZLE (D = 2")

TEST CASE	T_j/T_a	M_j	Z_{LE}	β_{TE}	χ_{LE}	RESULT TYPE
6B	1	.5	2	25°	0	RMS (psi) (half-power freq) KHZ [rolloff exponent] {peak amplification}

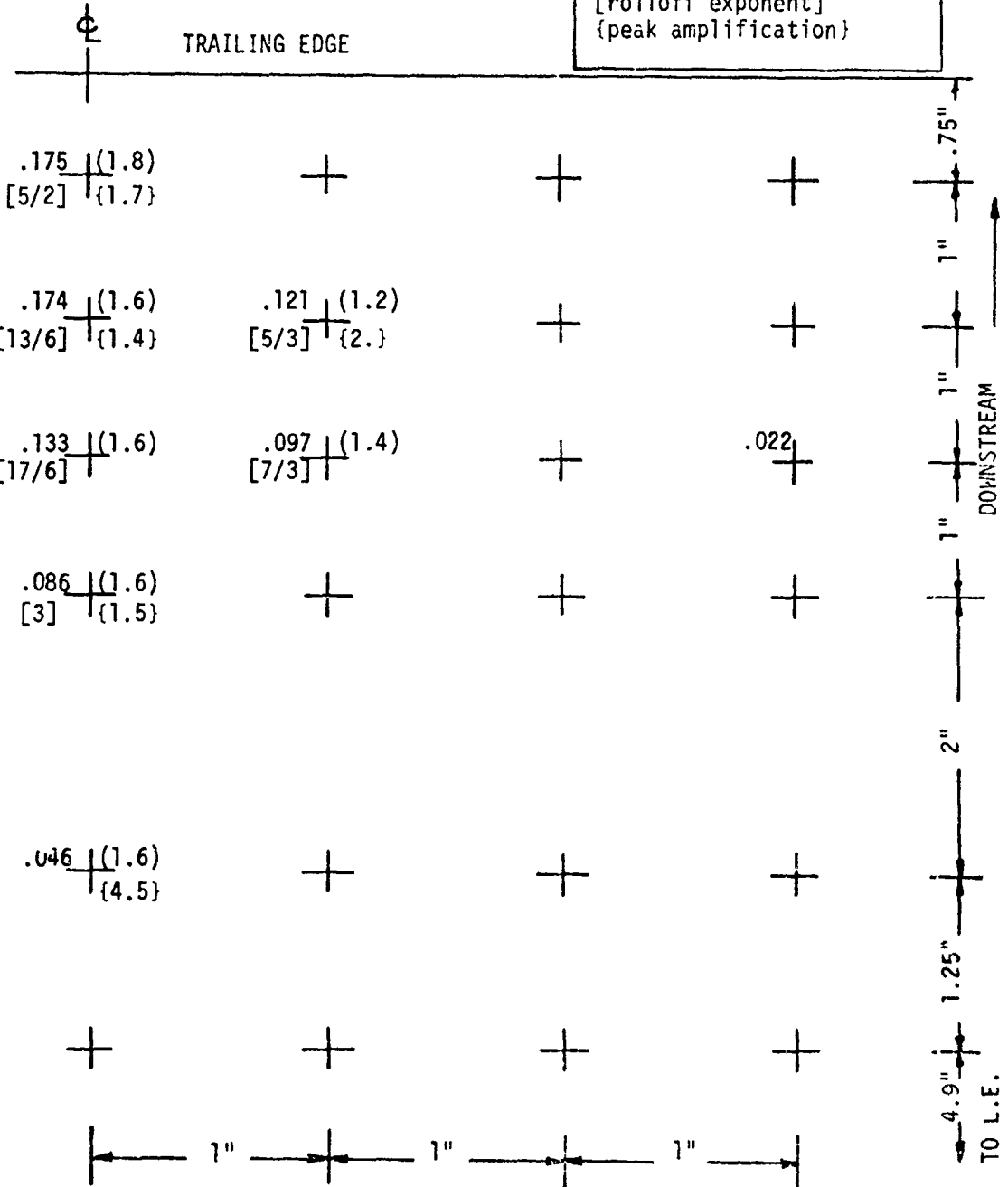


TABLE J-43 (CONT'D)
 PRESSURE MEASUREMENT RESULTS
 URF CURVED PLATE - ROUND NOZZLE (D = 2")

TEST CASE	T_j/T_a	M_j	Z_{LE}	β_{TE}	X_{LE}	RESULT TYPE
6B	1.0	0.5	2.0	25°	0	Max. Correlation Length (in) (Freq. at Maximum, f_m) KHZ [Convection Speed at f_m] fps

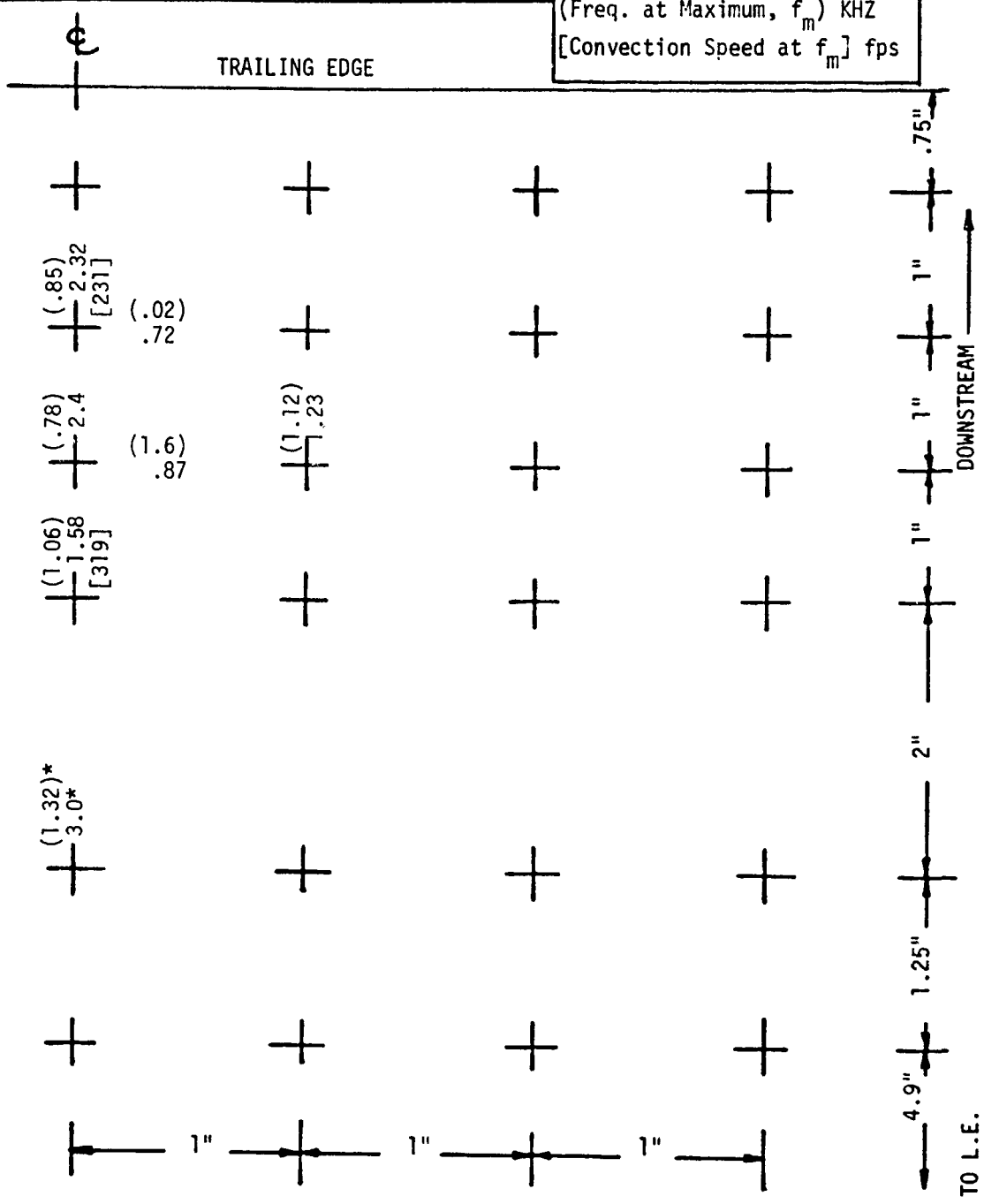


TABLE J-44

PRESSURE MEASUREMENT RESULTS
UBF CURVED PLATE-ROUND NOZZLE (D = 2")

TEST CASE	T_j/T_a	M_j	Z_{LE}	β_{TE}	X_{LE}	RESULT TYPE
6C	1	.74	1.4	25°	0	RMS (psi) (half-power freq) KHZ [rolloff exponent] {peak amplification}

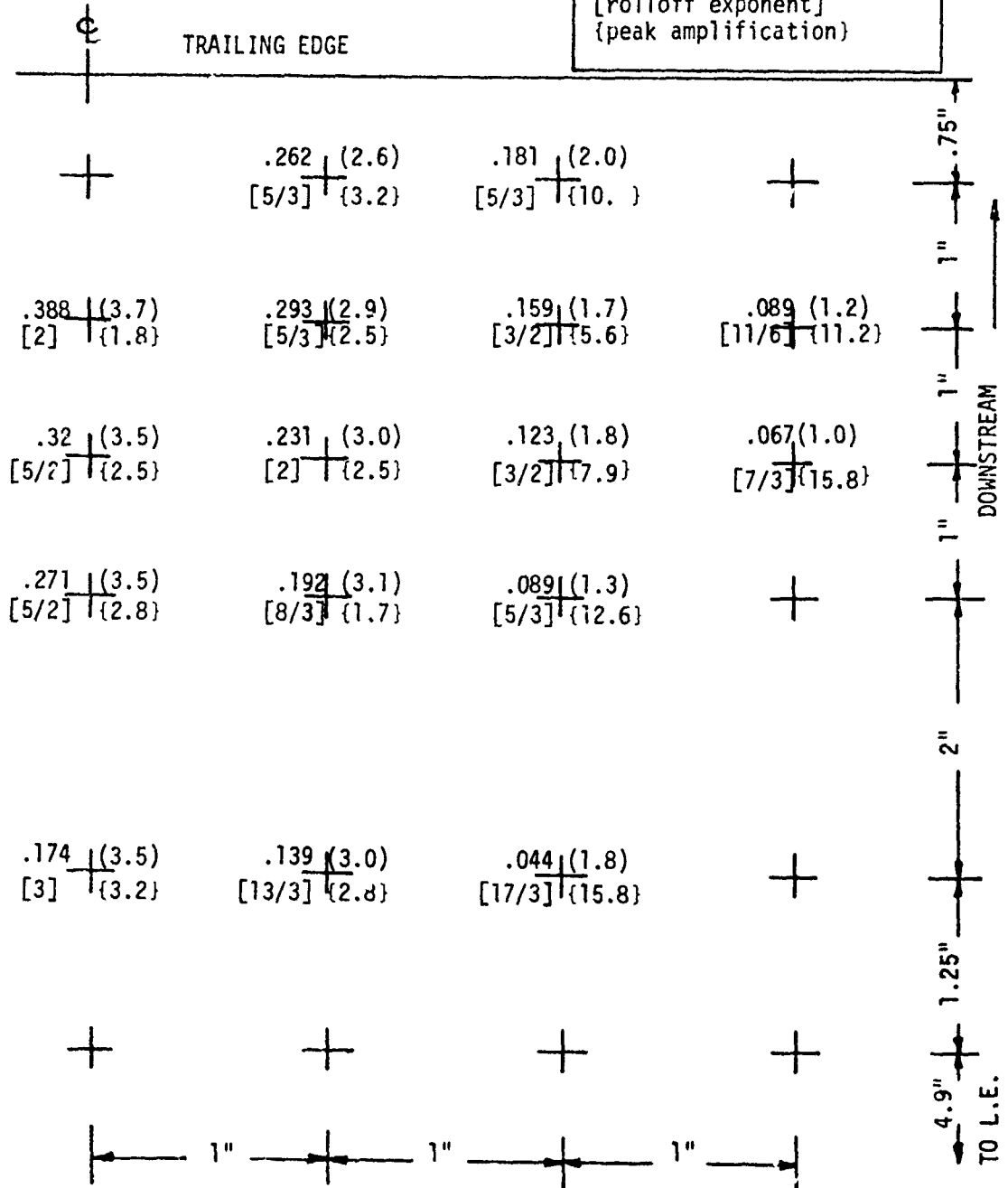


TABLE J-44 (CONT'D)
 PRESSURE MEASUREMENT RESULTS
 UBF CURVED PLATE - ROUND NOZZLE (D = 2")

TEST CASE	T_j/T_a	M_j	Z_{LE}	β_{TE}	X_{LE}	RESULT TYPE
6C	1.0	0.74	1.4	25°	0	Max. Correlation Length (in) (Freq. at Maximum, f_m) KHZ [Convection Speed at f_m] fps

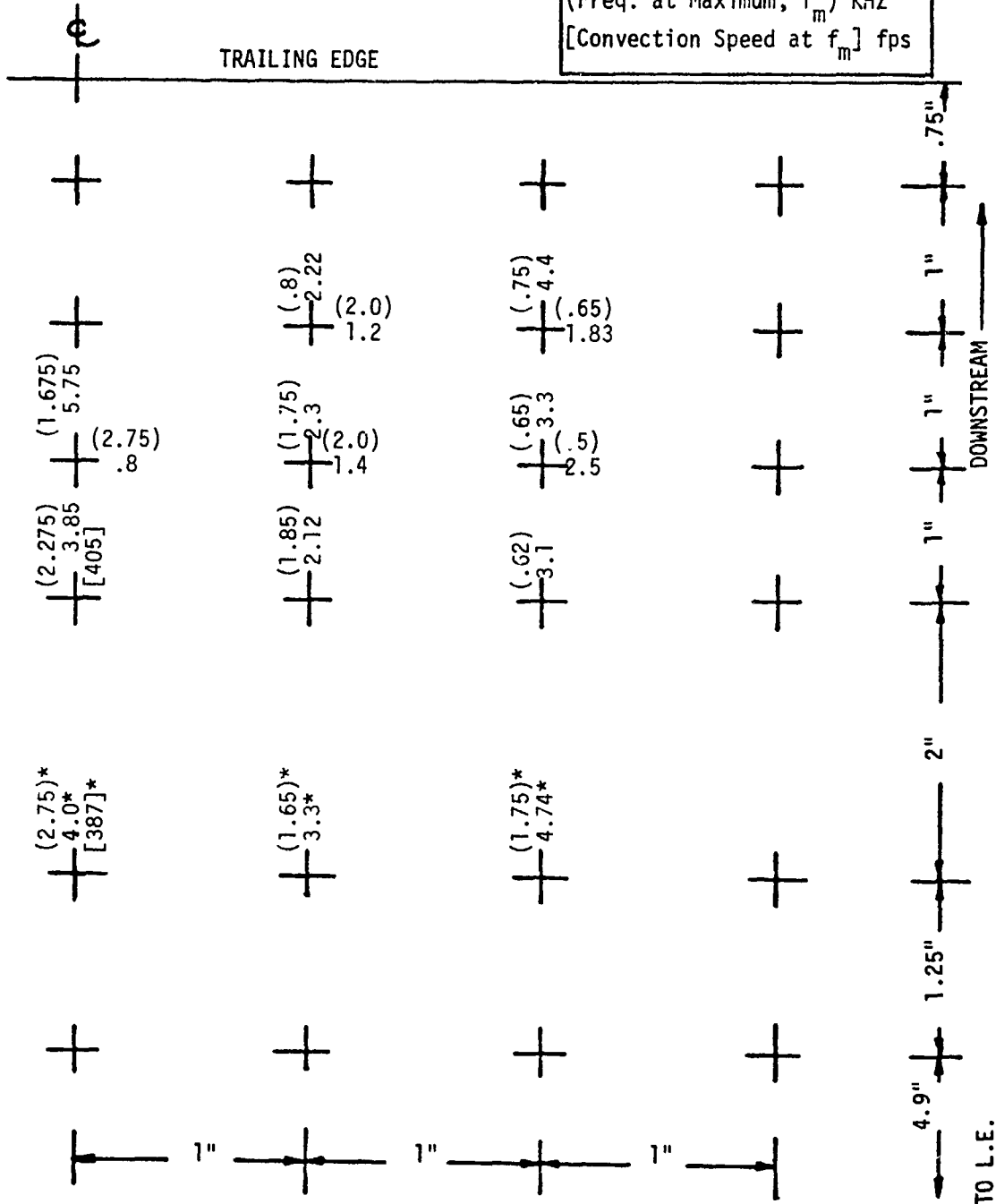


TABLE J-45
 PRESSURE MEASUREMENT RESULTS
 UBF CURVED PLATE-ROUND NOZZLE (D = 2")

TEST CASE	T _j /T _a	M _j	Z _{LE}	β _{TE}	X _{LE}	RESULT TYPE
6D	1	.35	1.4	25°	0	RMS (psi) (half-power freq) KHZ [rolloff exponent] {peak amplification}

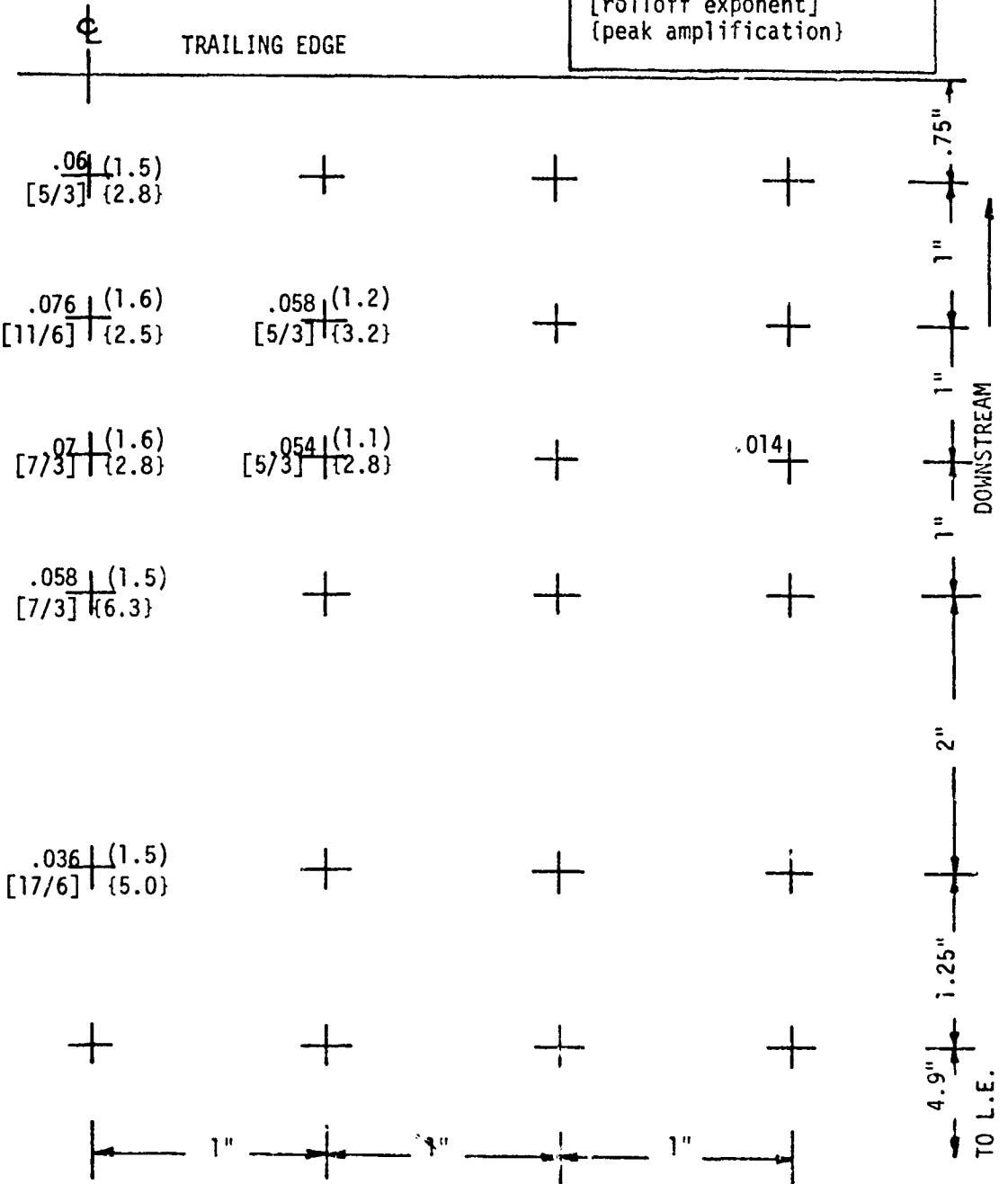


TABLE J-45 (CONT'D)
 PRESSURE MEASUREMENT RESULTS
 UBF CURVED PLATE - ROUND NOZZLE (D = 2")

TEST CASE	T_j/T_a	M_j	Z_{LE}	β_{TE}	X_{LE}	RESULT TYPE
6D	1.0	0.35	1.4	25°	0	Max. Correlation Length (in) (Freq. at Maximum, f_m) KHZ [Convection Speed at f_m] fps

TRAILING EDGE

DOWNSTREAM

TO L.E.

TABLE J-46
 PRESSURE MEASUREMENT RESULTS
 WING FLAP ROUND NOZZLE (D=2")

TEST CASE	T_j/T_a	M_j	Z_w	β_f/β_a	X_{LE}	RESULT TYPE
7A	1.0	.50	1.4	5°/25°	0	RMS (psi) (half-power freq.) KHZ [rolloff exponent] {peak amplification}

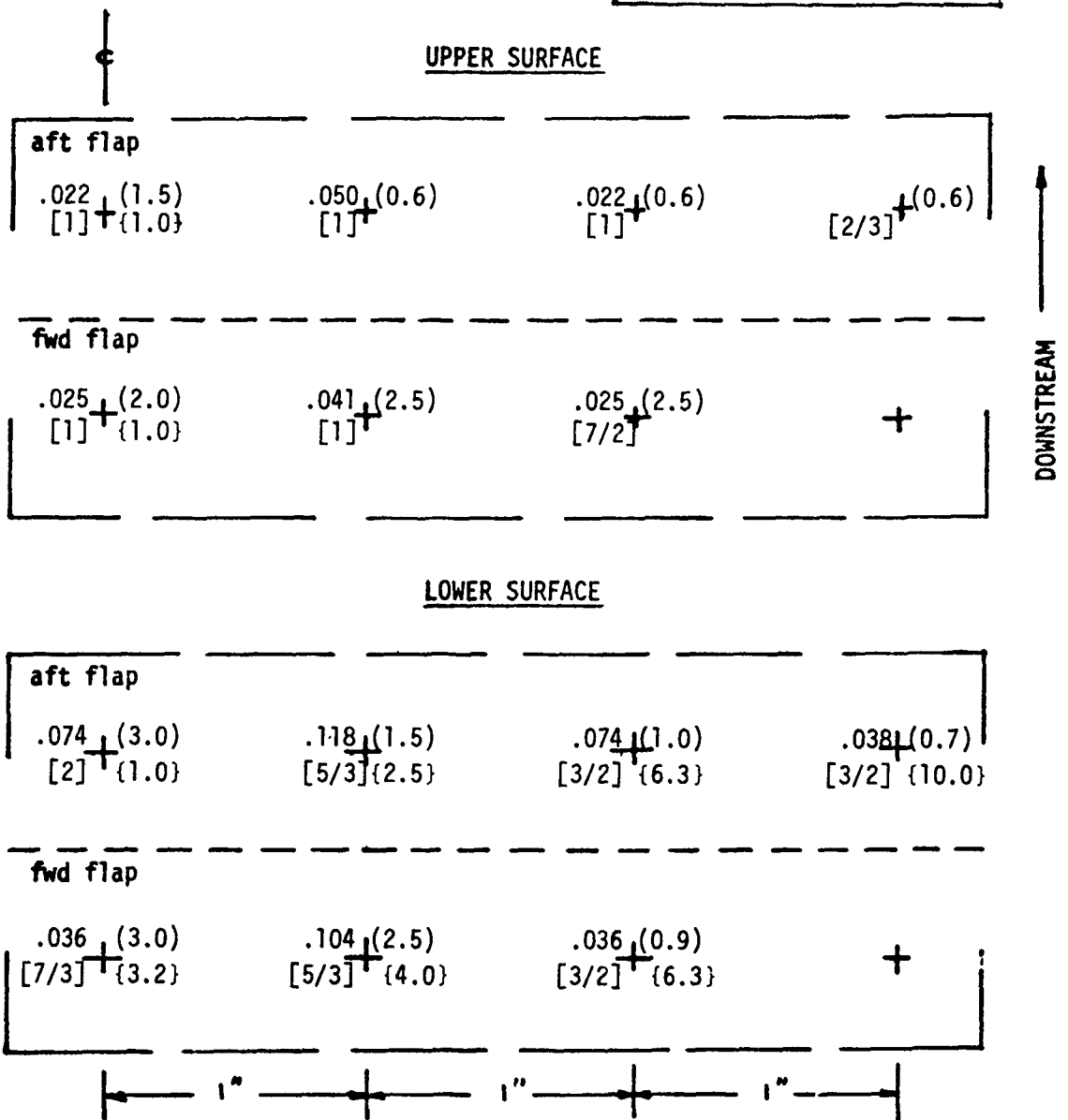


TABLE J-46 (CONT'D)
 PRESSURE MEASUREMENT RESULTS
 WING FLAP ROUND NOZZLE (D=2")

TEST CASE	T_j/T_a	M_j	Z_w	β_f/β_a	λ_{LE}	RESULT TYPE
7A	1.0	0.5	1.4	5°/25°	0	Max. Correlation Length (in) (Freq. at Maximum, f_m) KHZ [Convection Speed at f_m] fps

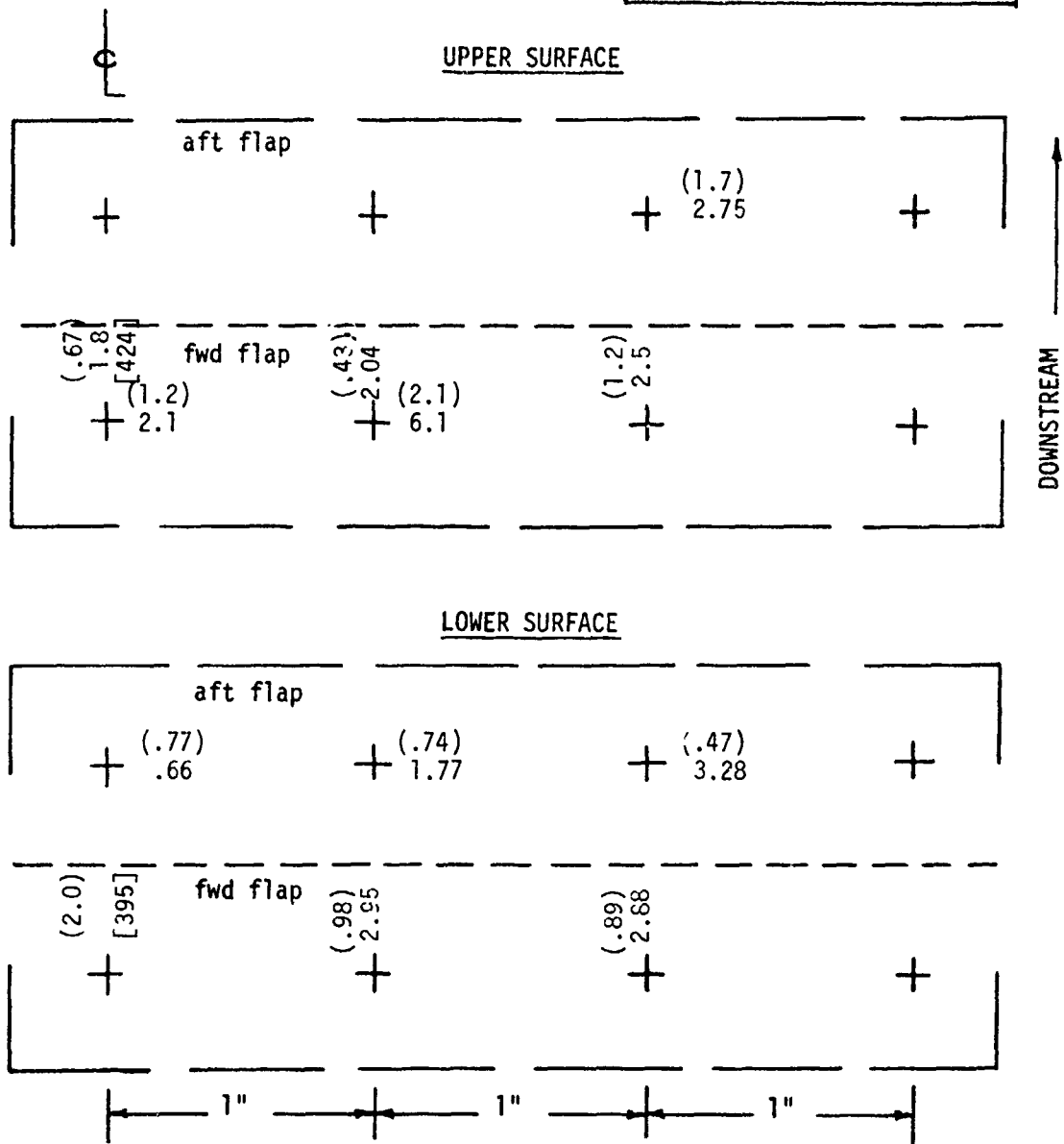


TABLE J-47
 PRESSURE MEASUREMENT RESULTS
 WING FLAP ROUND NOZZLE (D=2")

TEST CASE	T_j/T_a	M_j	Z_w	β_f/β_a	X_{LE}	RESULT TYPE
7B	1.0	.50	2.0	5°/25°	0	RMS (psi) (half-power freq.) KHZ [rolloff exponent] {peak amplification}

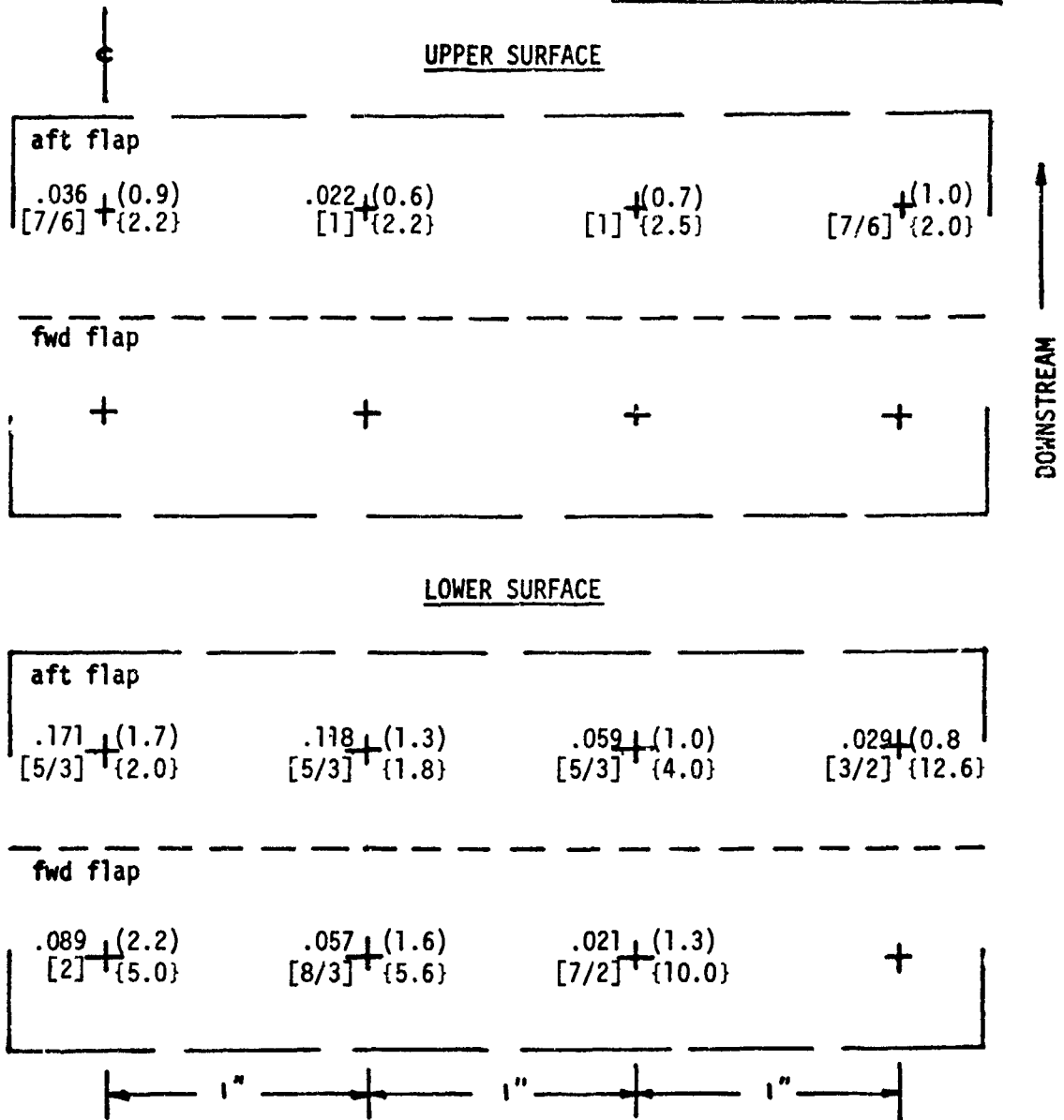


TABLE J-47 (CONT'D)
 PRESSURE MEASUREMENT RESULTS
 WING FLAP ROUND NOZZLE (D=2")

TEST CASE	T_j/\bar{T}_a	M_j	Z_w	β_f/β_a	X_{LE}	RESULT TYPE
7B	1.0	0.5	2.0	5°/25°	0	Max. Correlation Length (in) (Freq. at Maximum, f_m) KHZ [Convection Speed at f_m] fps

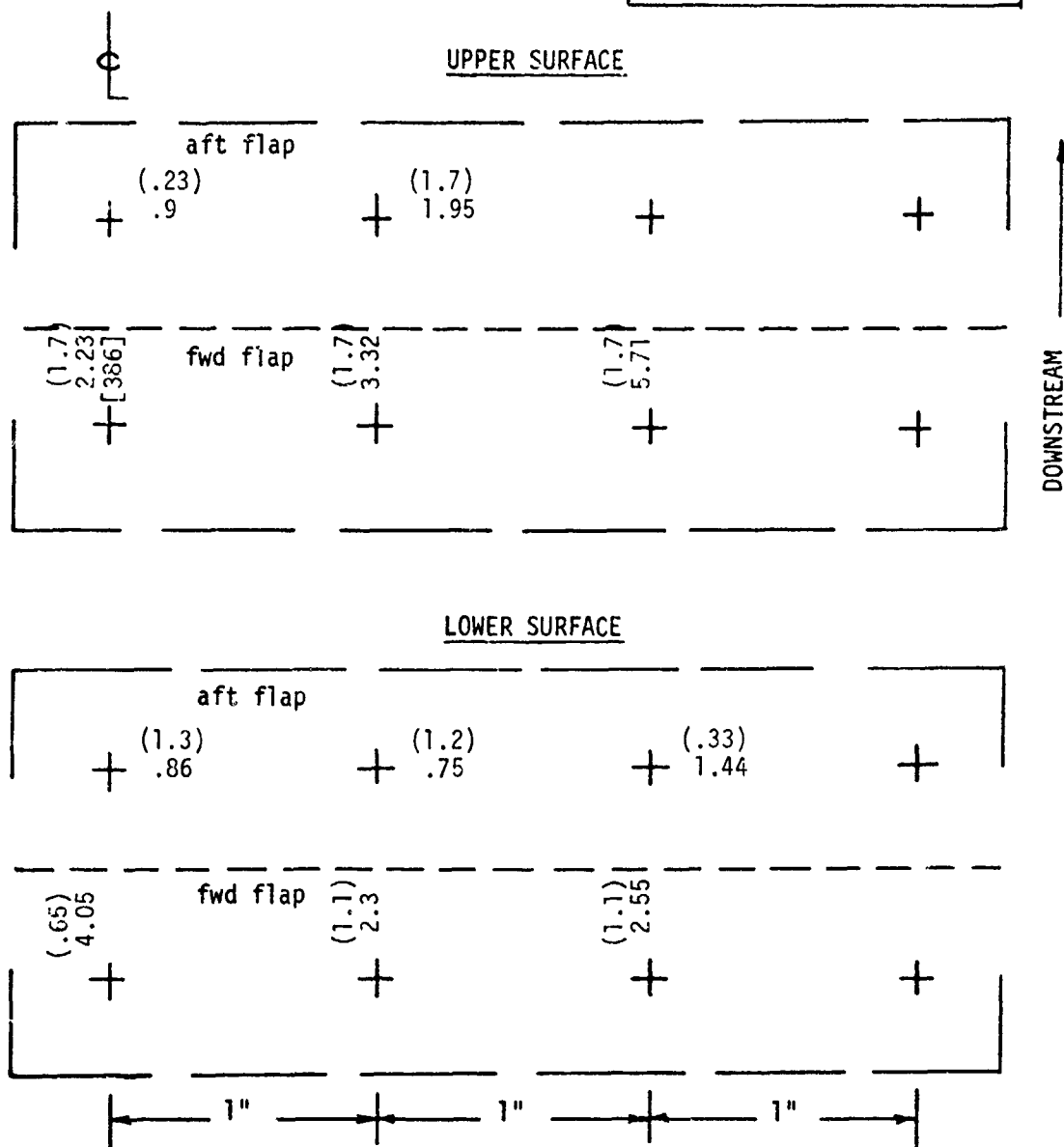


TABLE J-48
 PRESSURE MEASUREMENT RESULTS
 WING FLAP ROUND NOZZLE (D=2")

TEST CASE	T_j/T_a	M_j	Z_w	β_f/β_a	X_{LE}	RESULT TYPE
8A	1.0	.50	1.4	30°/50°	0	RMS (psi) (half-power freq.) KHZ [rolloff exponent] {peak amplification}

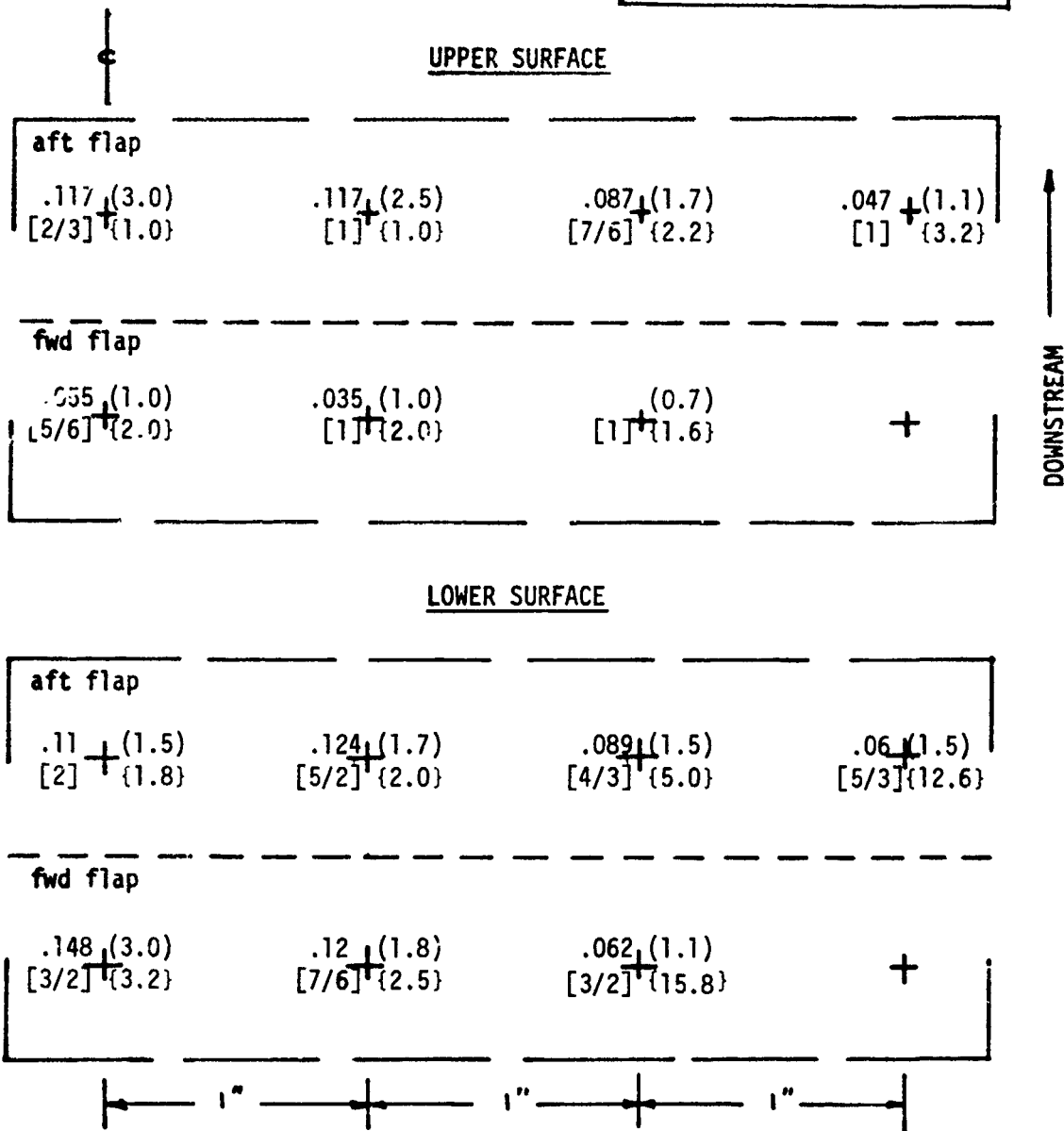


TABLE J-48 (CONT'D)
 PRESSURE MEASUREMENT RESULTS
 WING FLAP ROUND NOZZLE (D=2")

TEST CASE	T_j/T_a	M_j	Z_w	β_f/β_a	X_{LE}	RESULT TYPE
8A	1.0	0.5	1.4	30°/50°	0	Max. Correlation Length (in) (Freq. at Maximum, f_m) KHZ [Convection Speed at f_m] fps

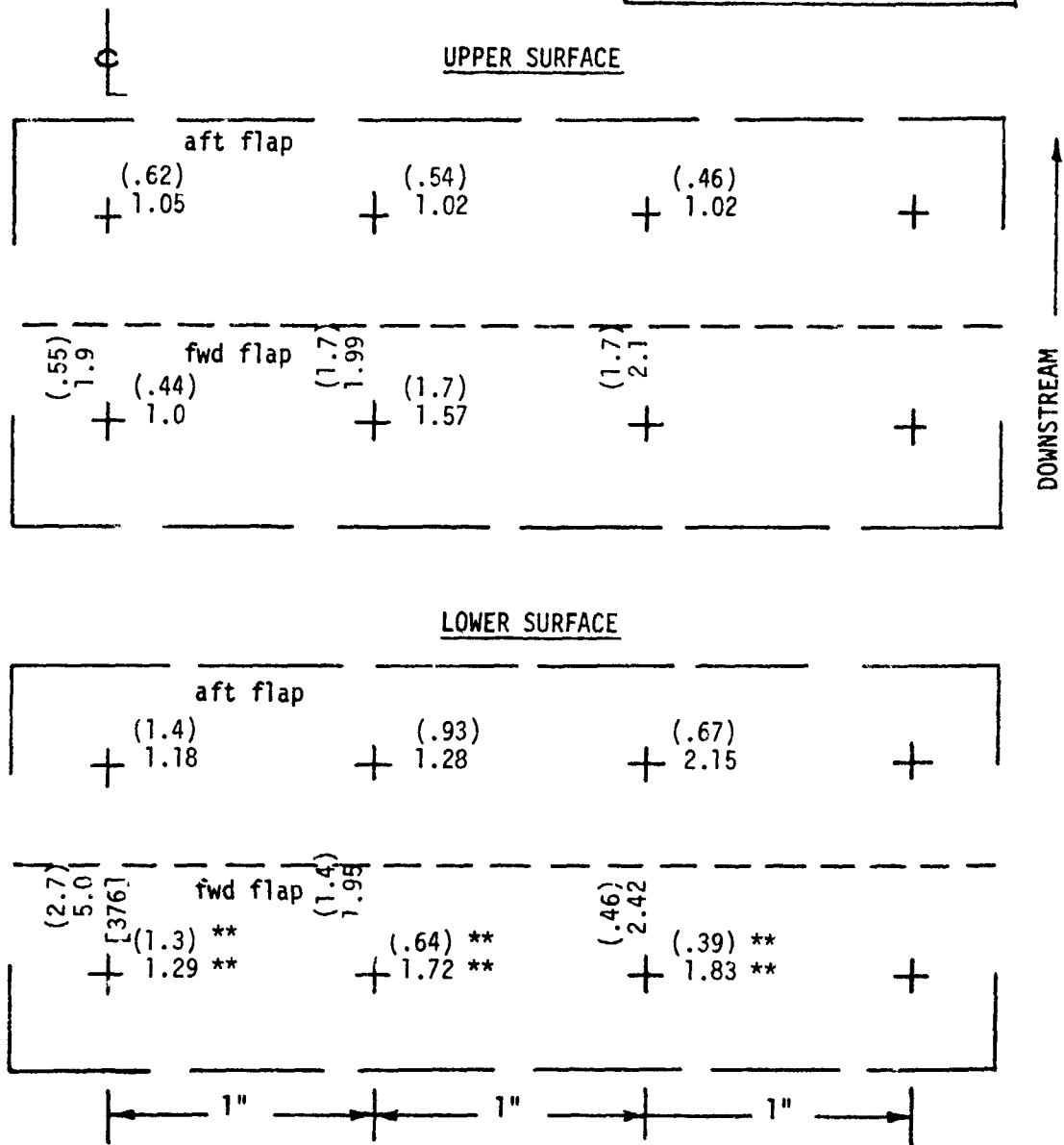


TABLE J-49
 PRESSURE MEASUREMENT RESULTS
 WING FLAP ROUND NOZZLE (D=2")

TEST CASE	T_j/T_a	M_j	Z_w	β_f/β_a	X_{LE}	RESULT TYPE
8B	1.0	.50	2.0	30°/50°	0	RMS (psi) (half-power freq.) KHZ [rolloff exponent] {peak amplification}

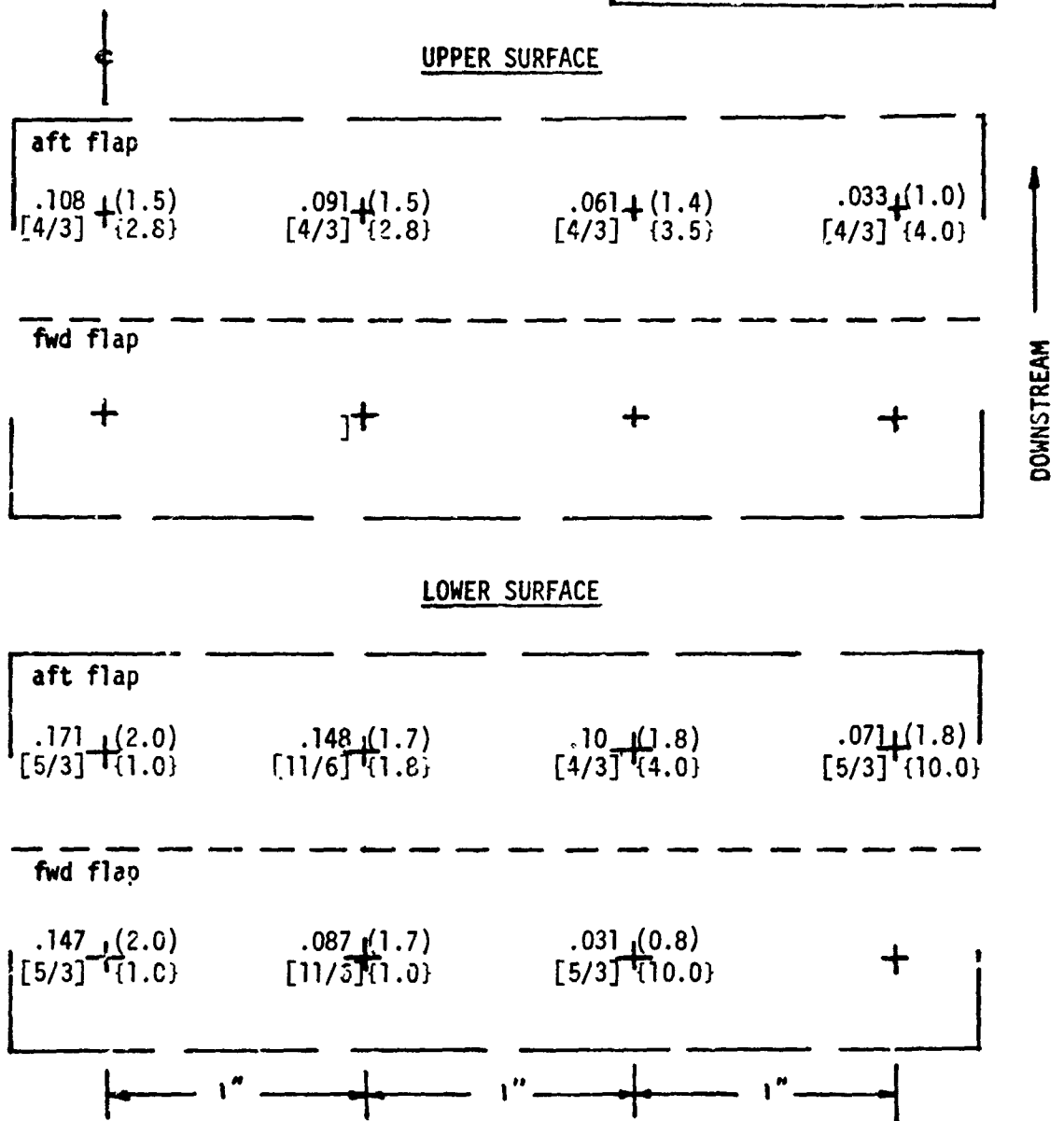


TABLE J-49 (CONT'D)

PRESSURE MEASUREMENT RESULTS
WING FLAP ROUND NOZZLE (D=2")

TEST CASE	T_j/T_a	M_j	Z_w	β_f/ϵ_d	X_{LE}	RESULT TYPE
8B	1.0	0.5	2.0	30°/50°	0	Max. Correlation Length (in) (Freq. at Maximum, f_m) KHZ [Convection Speed at f_m] fps

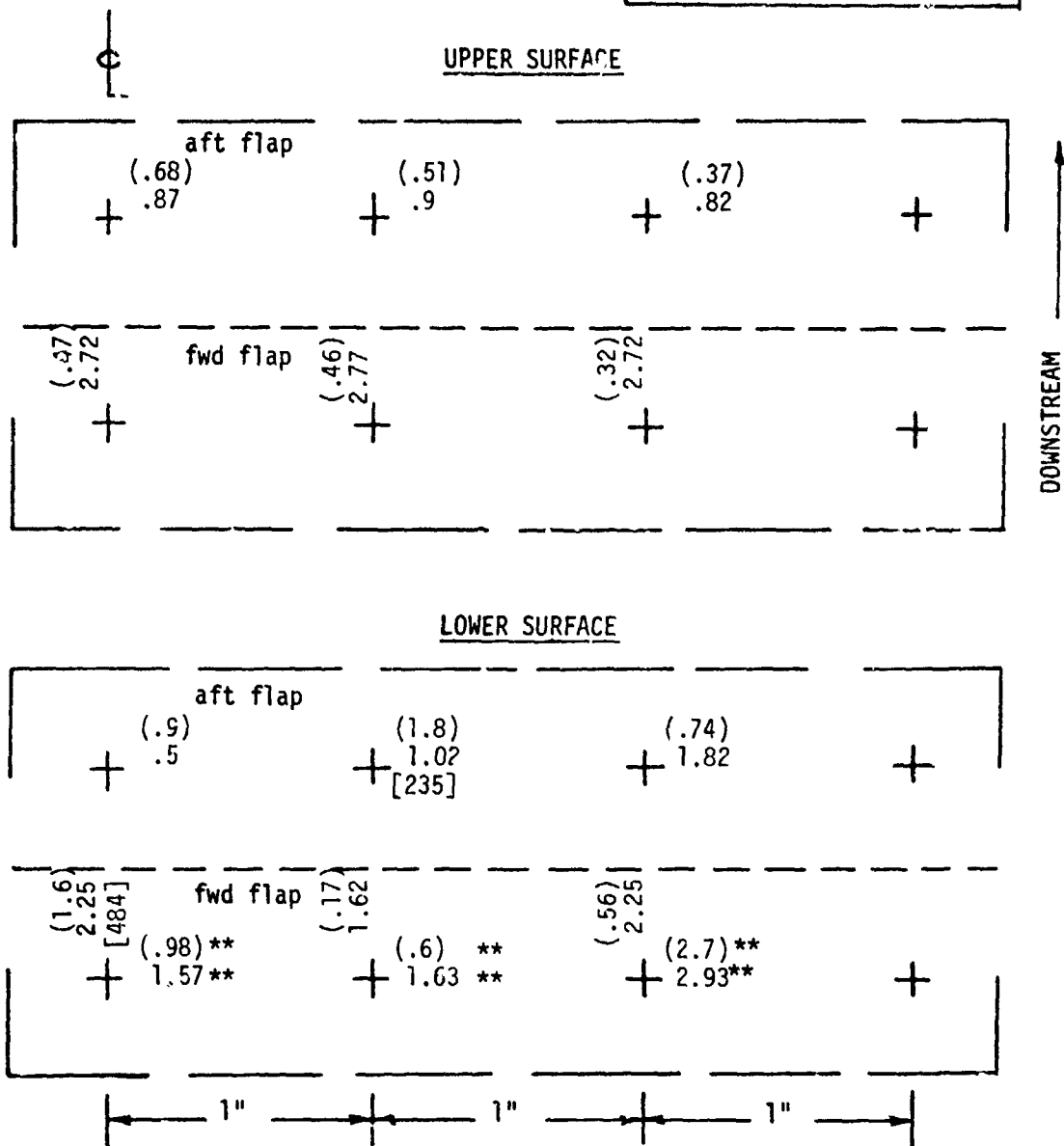


TABLE J-50
 PRESSURE MEASUREMENT RESULTS
 WING FLAP ROUND NOZZLE (D=2")

TEST CASE	T_j/T_a	M_j	Z_w	β_f/β_a	X_{LE}	RESULT TYPE
8C	1.0	.50	1.4	30°/50°	3	RMS (psi) (half-power freq.) KHZ [rolloff exponent] {peak amplification}

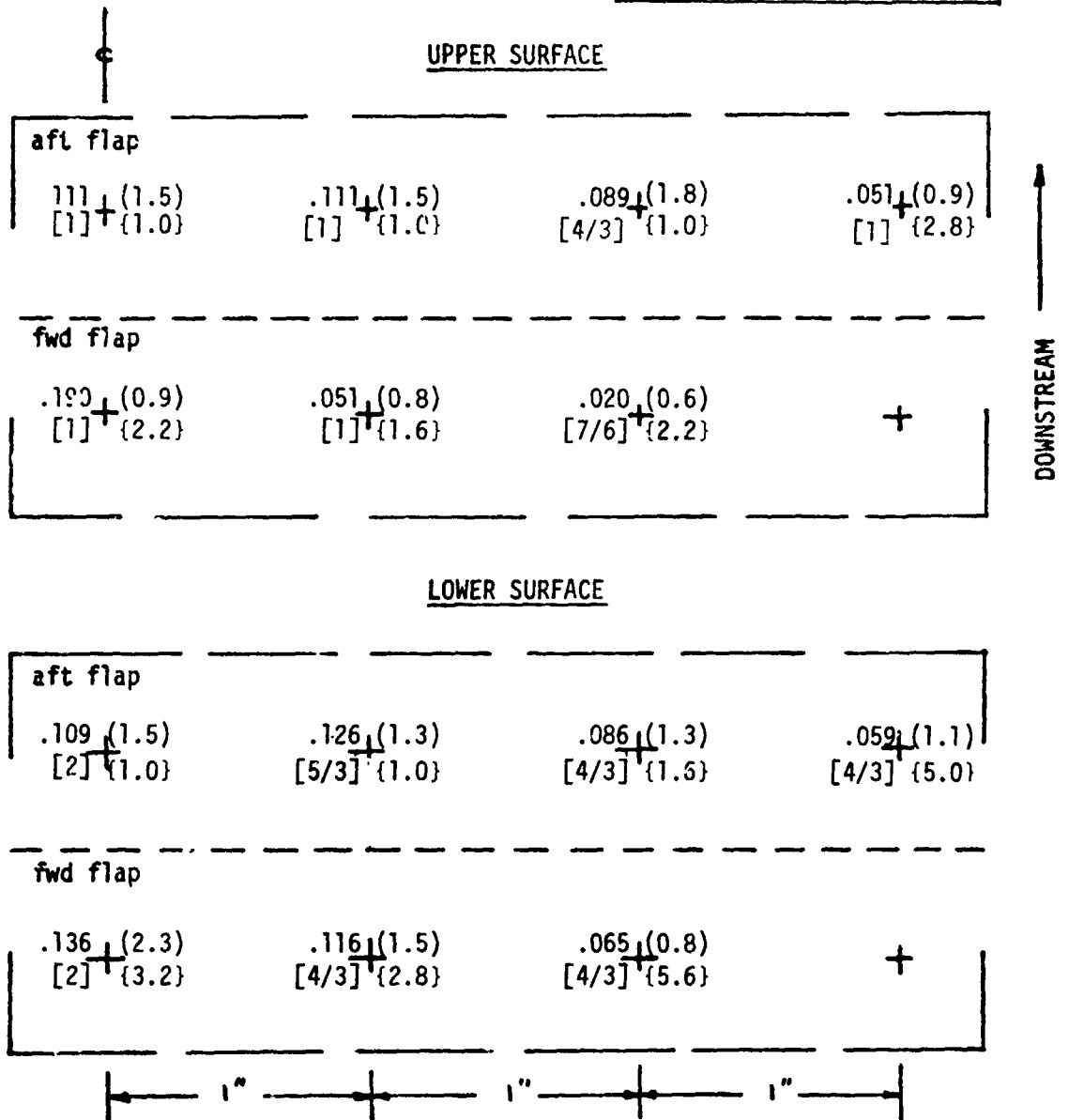


TABLE J-50 (CONT'D)

PRESSURE MEASUREMENT RESULTS
WING FLAP ROUND NOZZLE (D=2")

TEST CASE	T_j/T_a	M_j	Z_w	β_f/β_a	X_{LE}	RESULT TYPE
8C	1.0	0.5	1.4	30°/50°	3	Max. Correlation Length (in) (Freq. at Maximum, f_m) KHZ [Convection Speed at f_m] fps

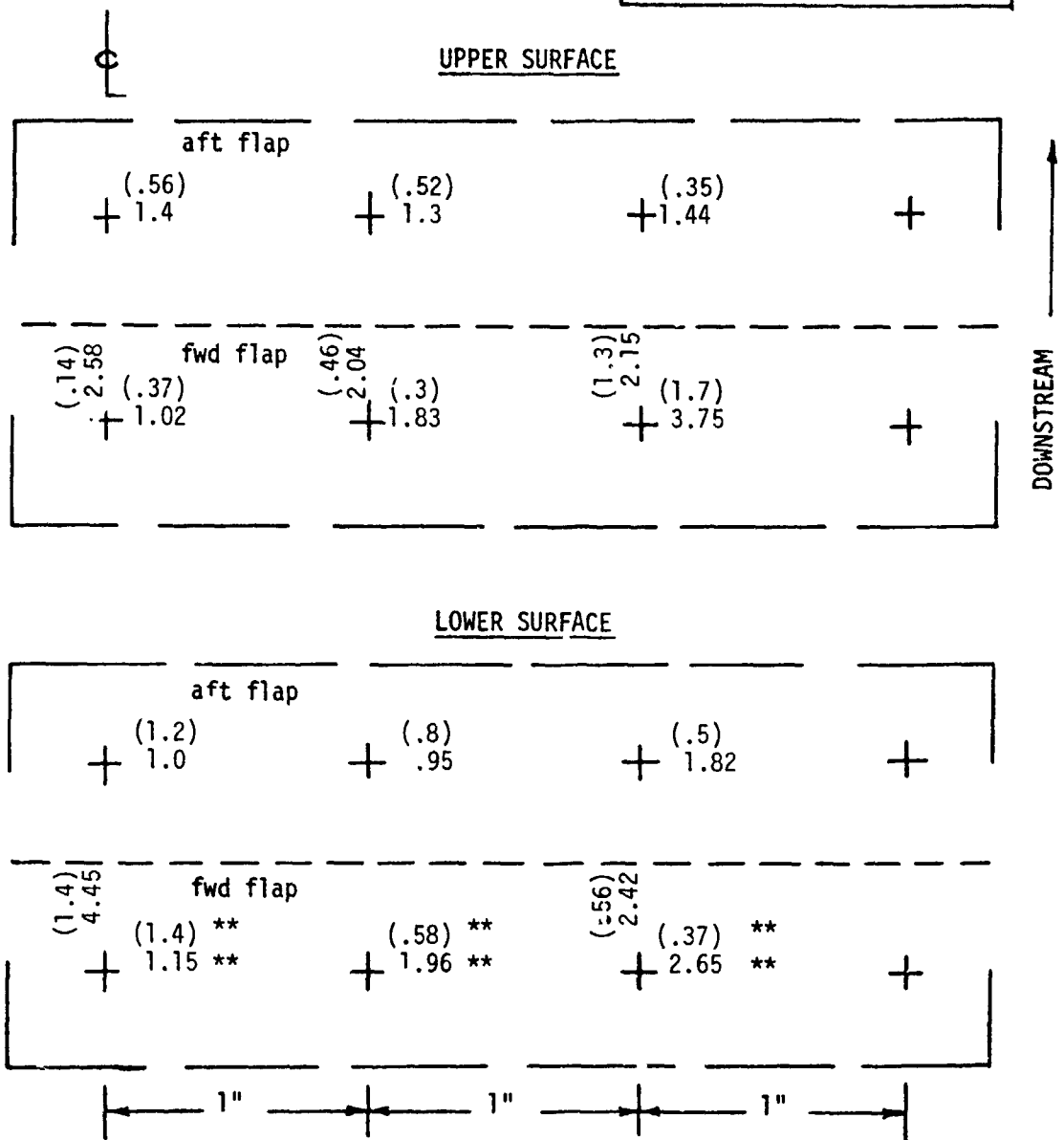


TABLE J-51
 PRESSURE MEASUREMENT RESULTS
 WING FLAP ROUND NOZZLE (D=2")

TEST CASE	T_j/T_a	M_j	Z_w	β_f/β_a	X_{LE}	RESULT TYPE
8D	1.0	.50	1.0	30°/50°	0	RMS (psi) (half-power freq.) KHZ [rolloff exponent] {peak amplification}

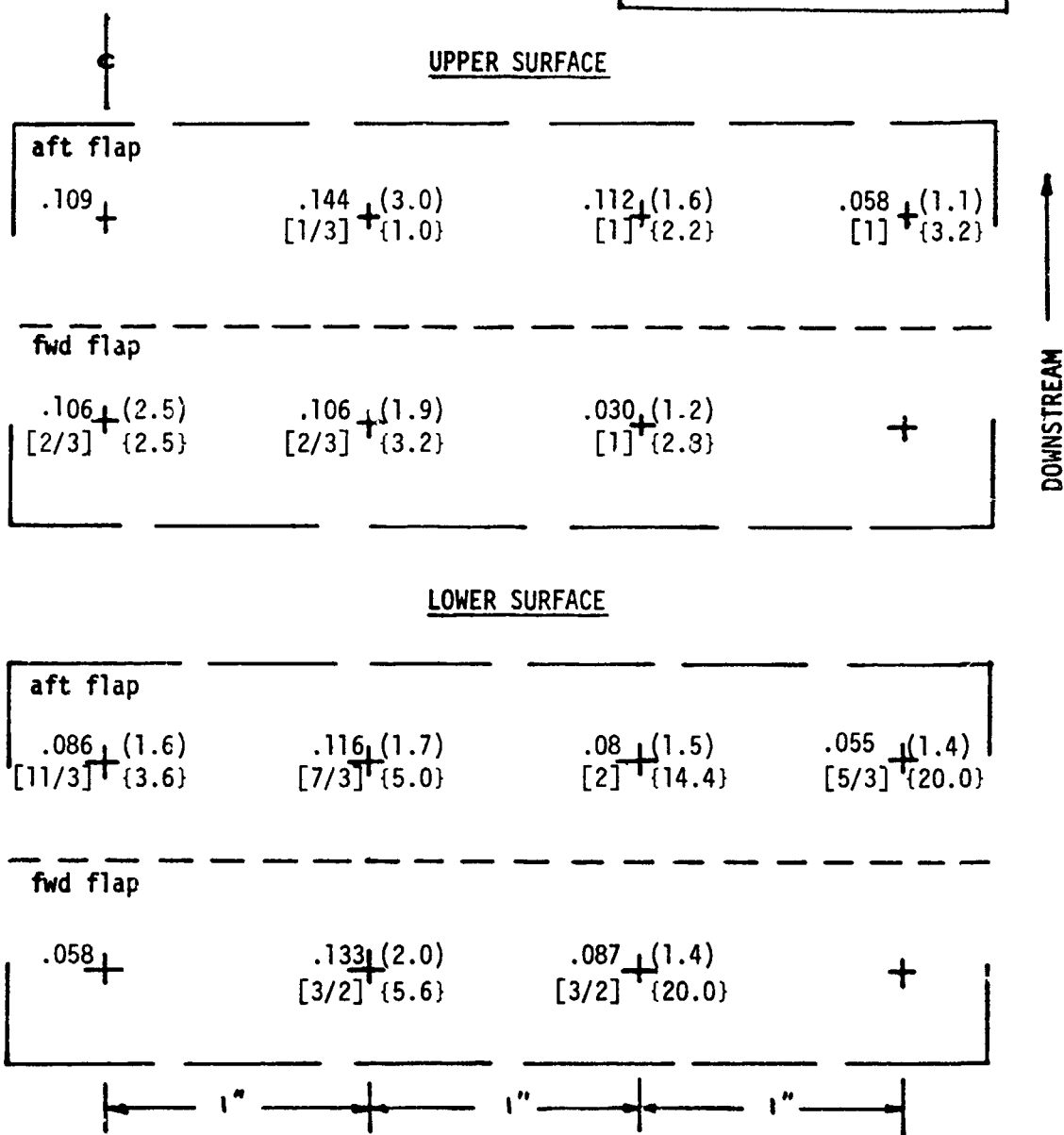


TABLE J-51 (CONT'D)
 PRESSURE MEASUREMENT RESULTS
 WING FLAP ROUND NOZZLE (D=2")

TEST CASE	T_j/T_a	M_j	Z_w	β_f/β_a	X_{LE}	RESULT TYPE
8D	1.0	0.5	1.0	30°/50°	0	Max. Correlation Length (in) (Freq. at Maximum, f_m) KHZ [Convection Speed at f_m] fps

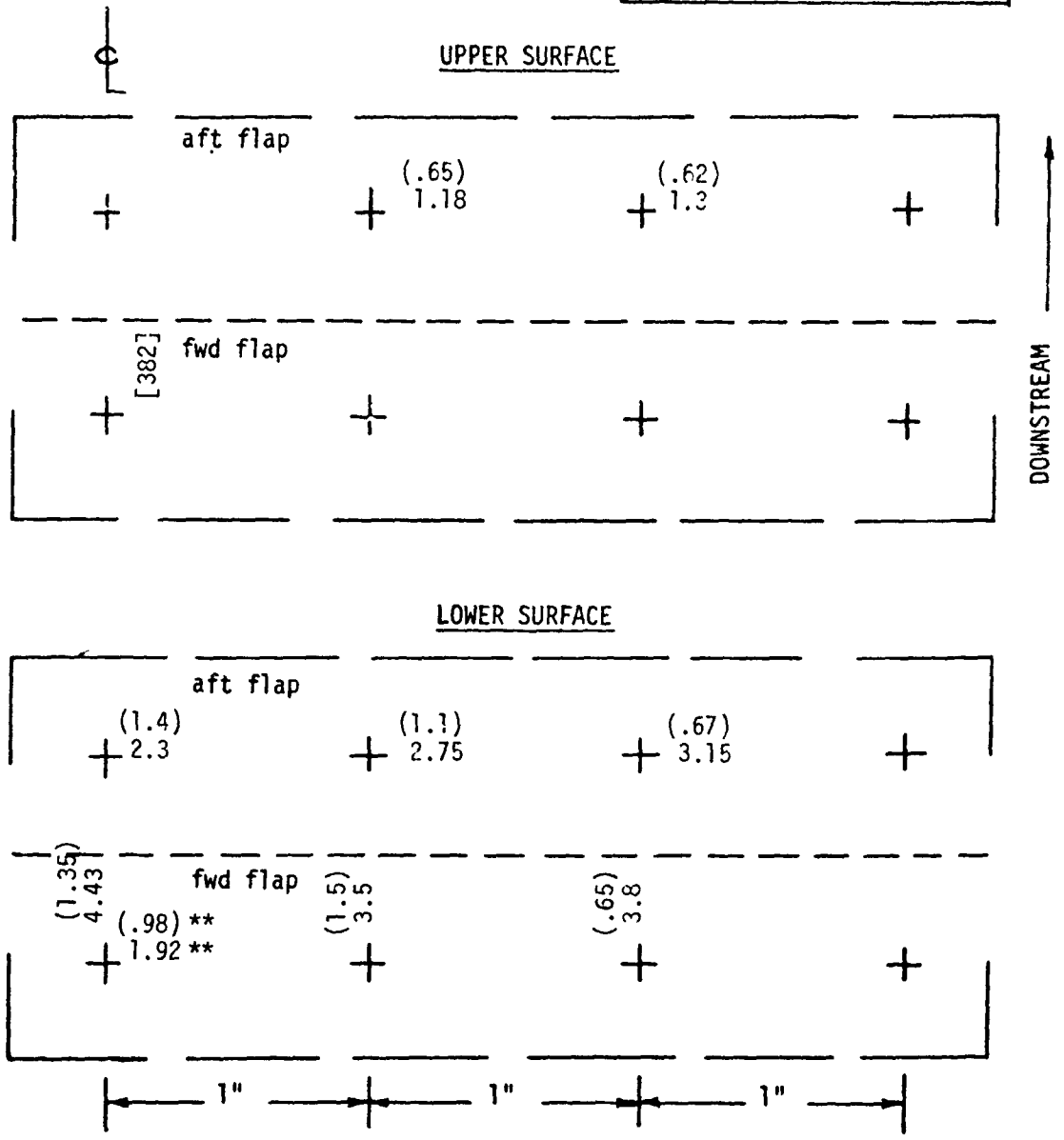


TABLE J-52
 PRESSURE MEASUREMENT RESULTS
 WING FLAP ROUND NOZZLE (D=2")

TEST CASE	T_j/T_a	M_j	Z_w	β_f/β_a	X_{LE}	RESULT TYPE
8E	1.0	.74	1.4	30°/50°	0	RMS (psi) (half-power freq.) KHZ [rolloff exponent] {peak amplification}

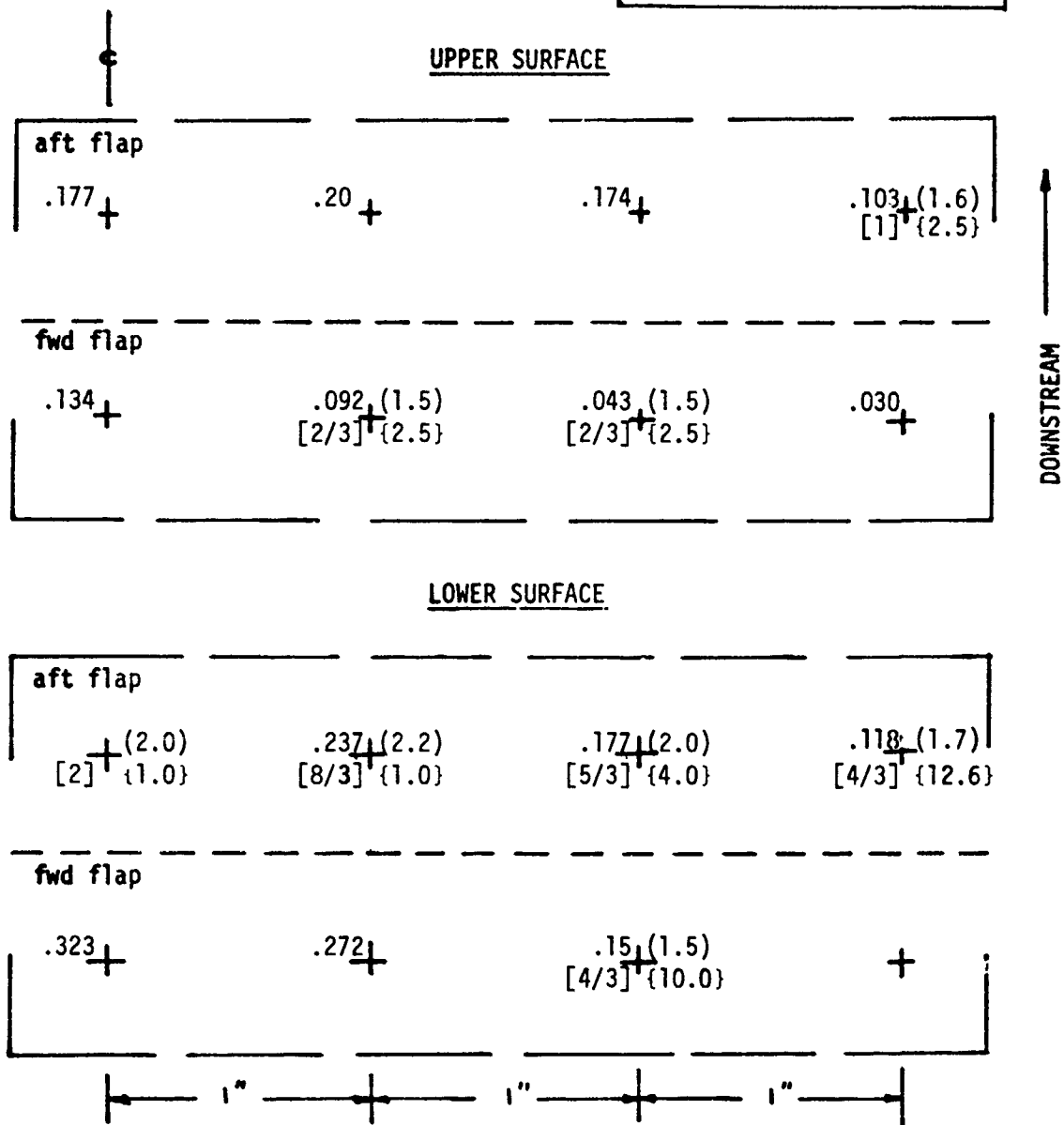


TABLE J-52 (CONT'D)
 PRESSURE MEASUREMENT RESULTS
 WING FLAP ROUND NOZZLE (D=2")

TEST CASE	T_j/T_a	M_j	Z_w	β_f/β_a	X_{LE}	RESULT TYPE
8E	1.0	0.74	1.4	30°/50°	0	Max. Correlation Length (in) (Freq. at Maximum, f_m) KHZ [Convection Speed at f_m] fps

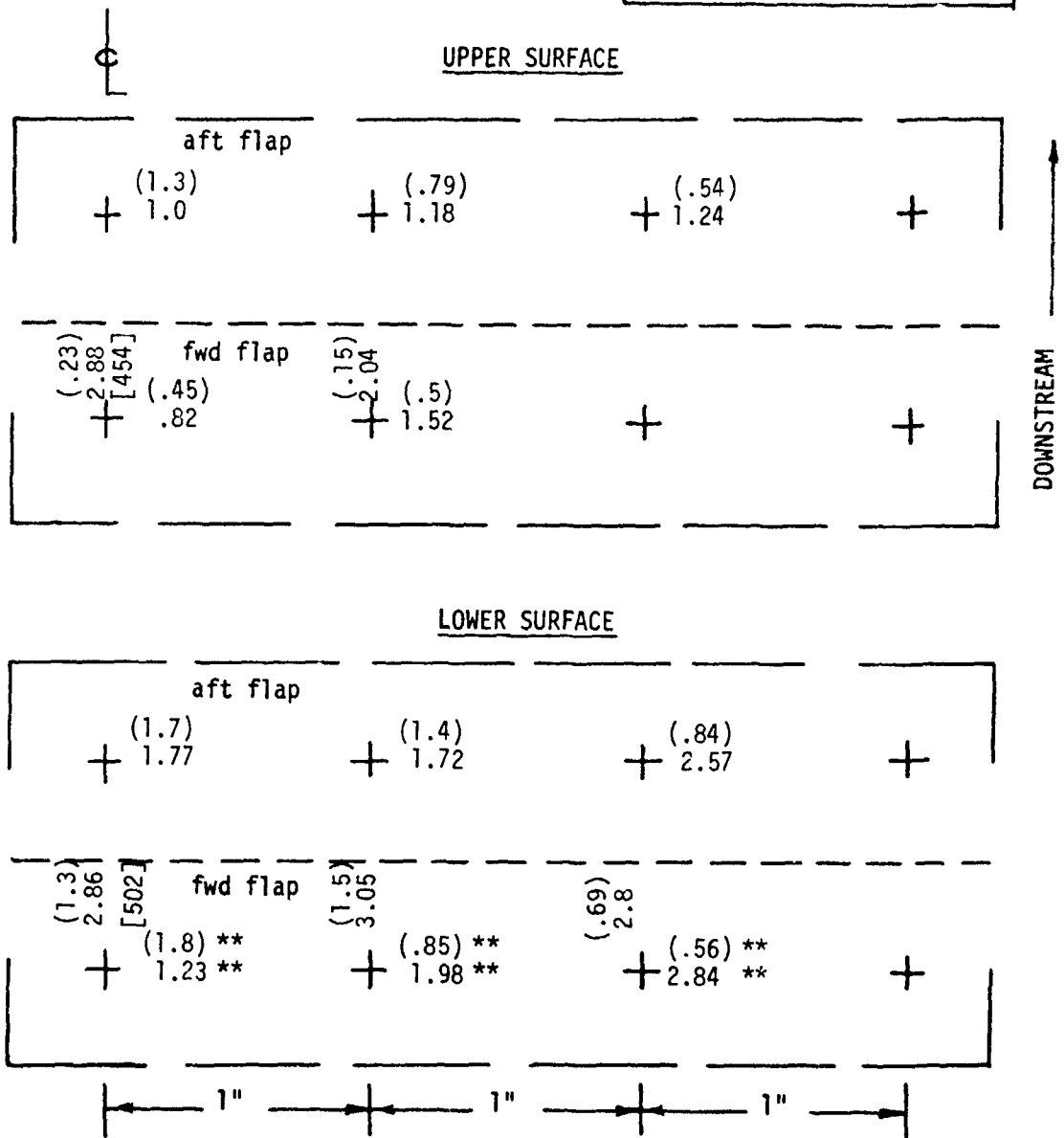


TABLE J-53
 PRESSURE MEASUREMENT RESULTS
 WING FLAP DAISY NOZZLE ($D_{eq} = 2''$)

TEST CASE	T_j/T_a	M_j	Z_w	β_f/β_a	X_{LE}	RESULT TYPE
8F	1.0	.50	2.0	30°/50°	0	RMS (psi) (half-power freq.) KHZ [rolloff exponent] {peak amplification}

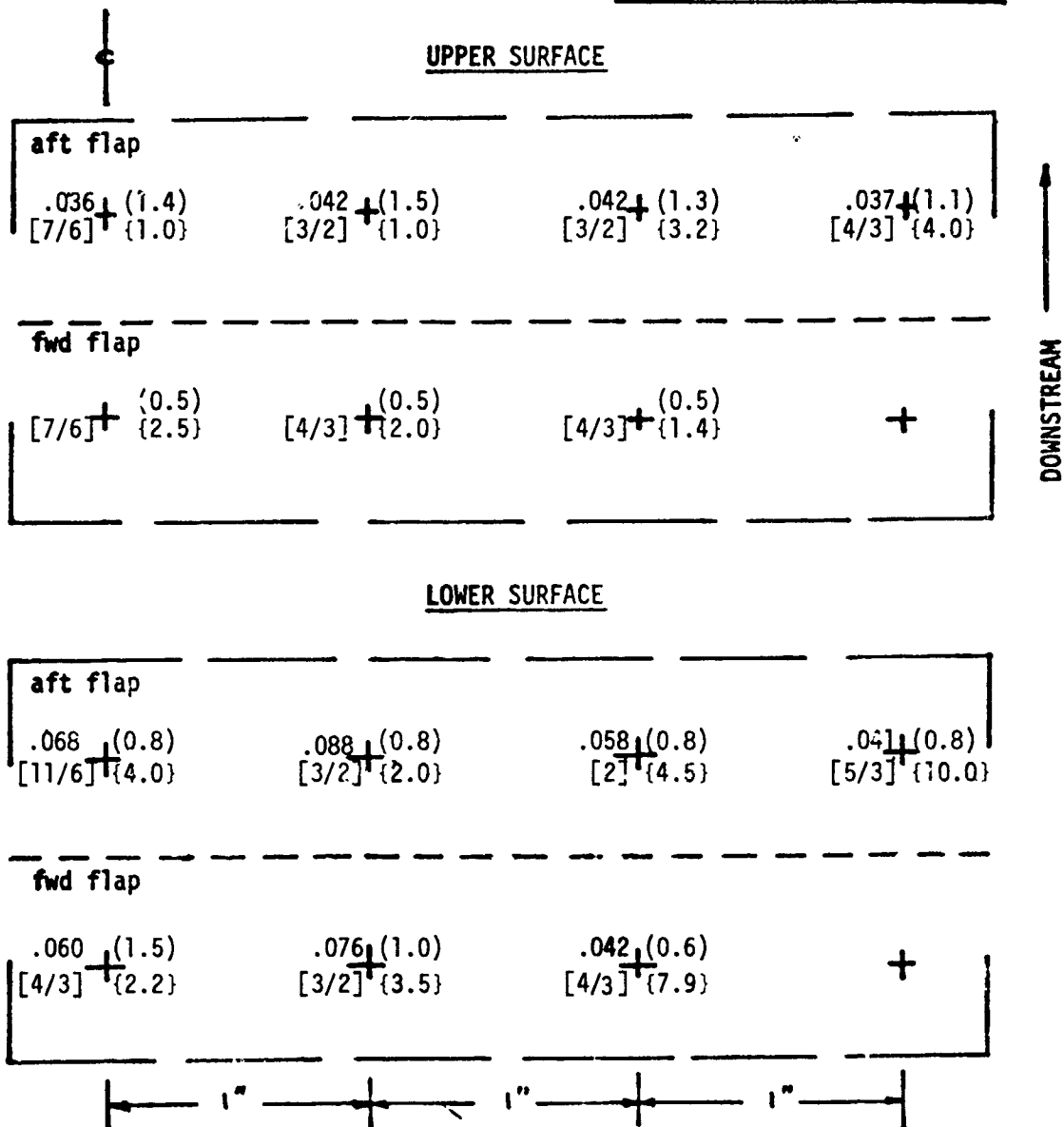


TABLE J-53 (CONT'D)
 PRESSURE MEASUREMENT RESULTS
 WING FLAP DAISY NOZZLE ($D_{eq} = 2''$)

TEST CASE	T_j/T_a	M_j	Z_w	β_f/β_a	X_{LE}	RESULT TYPE
8F	1.0	0.5	2.0	30°/50°	0	Max. Correlation Length (in) (Freq. at Maximum, f_m) KHZ [Convection Speed at f_m] fps

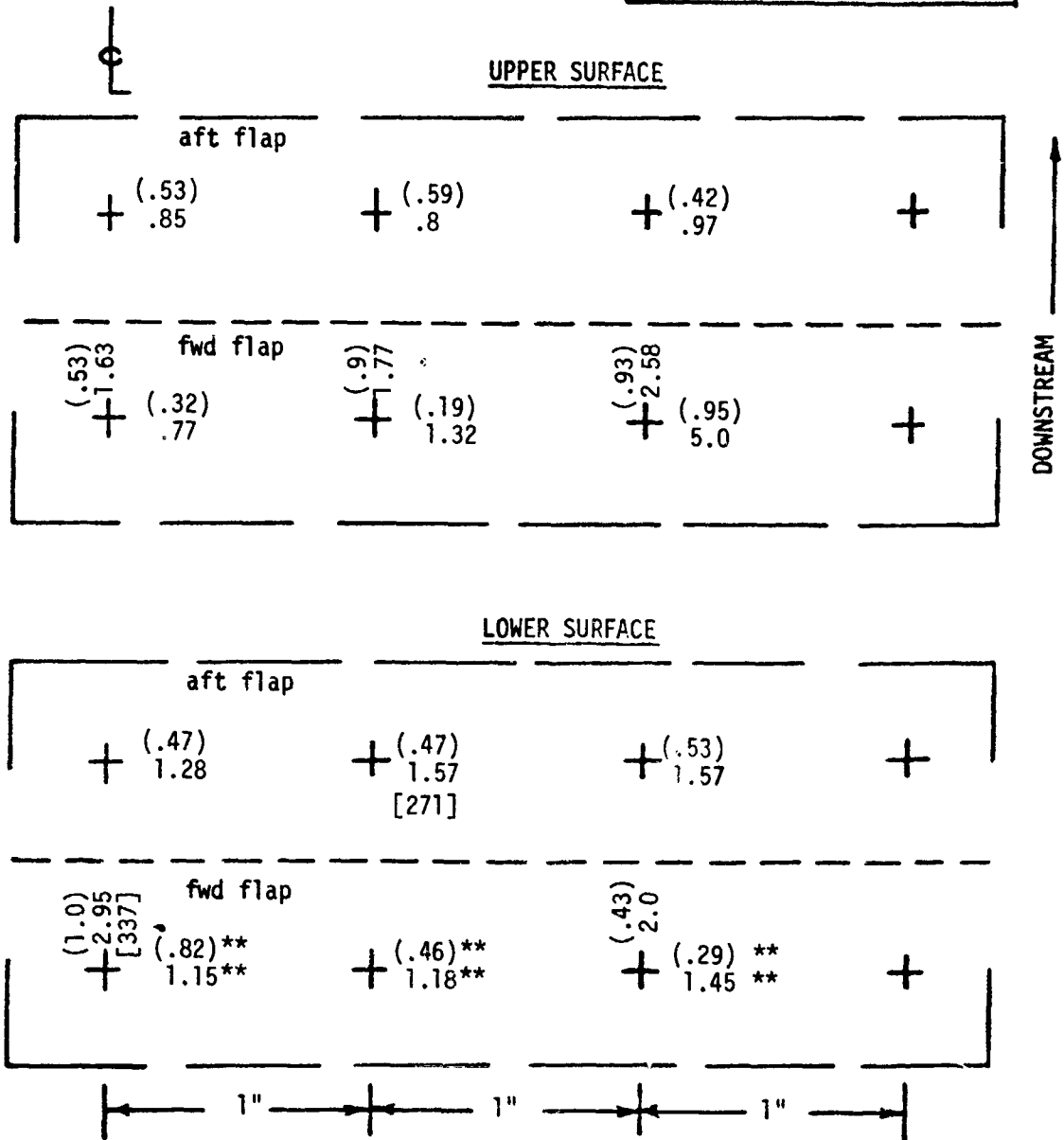


TABLE J-54
 PRESSURE MEASUREMENT RESULTS
 WING FLAP DAISY NOZZLE ($D_{eq} = 2''$)

TEST CASE	T_j/T_a	M_j	Z_w	β_f/β_a	χ_{LE}	RESULT TYPE
8G	1.0	.74	2.0	30°/50°	0	RMS (psi) (half-power freq.) KHZ [rolloff exponent] {peak amplification}

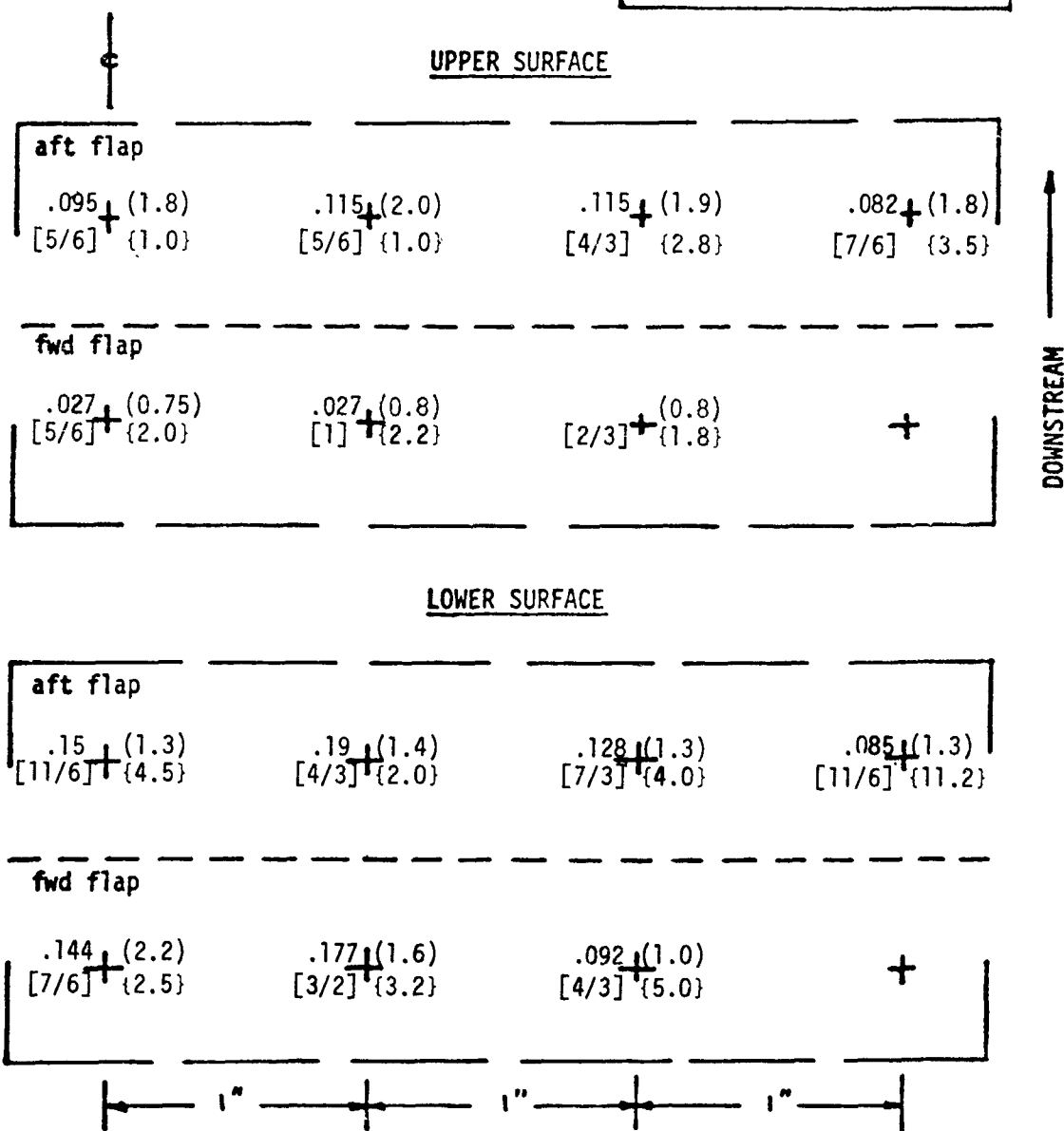


TABLE J-54 (CONT'D)

PRESSURE MEASUREMENT RESULTS
 WING FLAP DAISY NOZZLE ($D_{eq} = 2''$)

TEST CASE	T_j/T_a	M_j	Z_w	β_f/β_a	X_{LE}	RESULT TYPE
8G	1.0	0.74	2.0	30°/50°	0	Max. Correlation Length (in) (Freq. at Maximum, f_m) KHZ [Convection Speed at f_m] fps

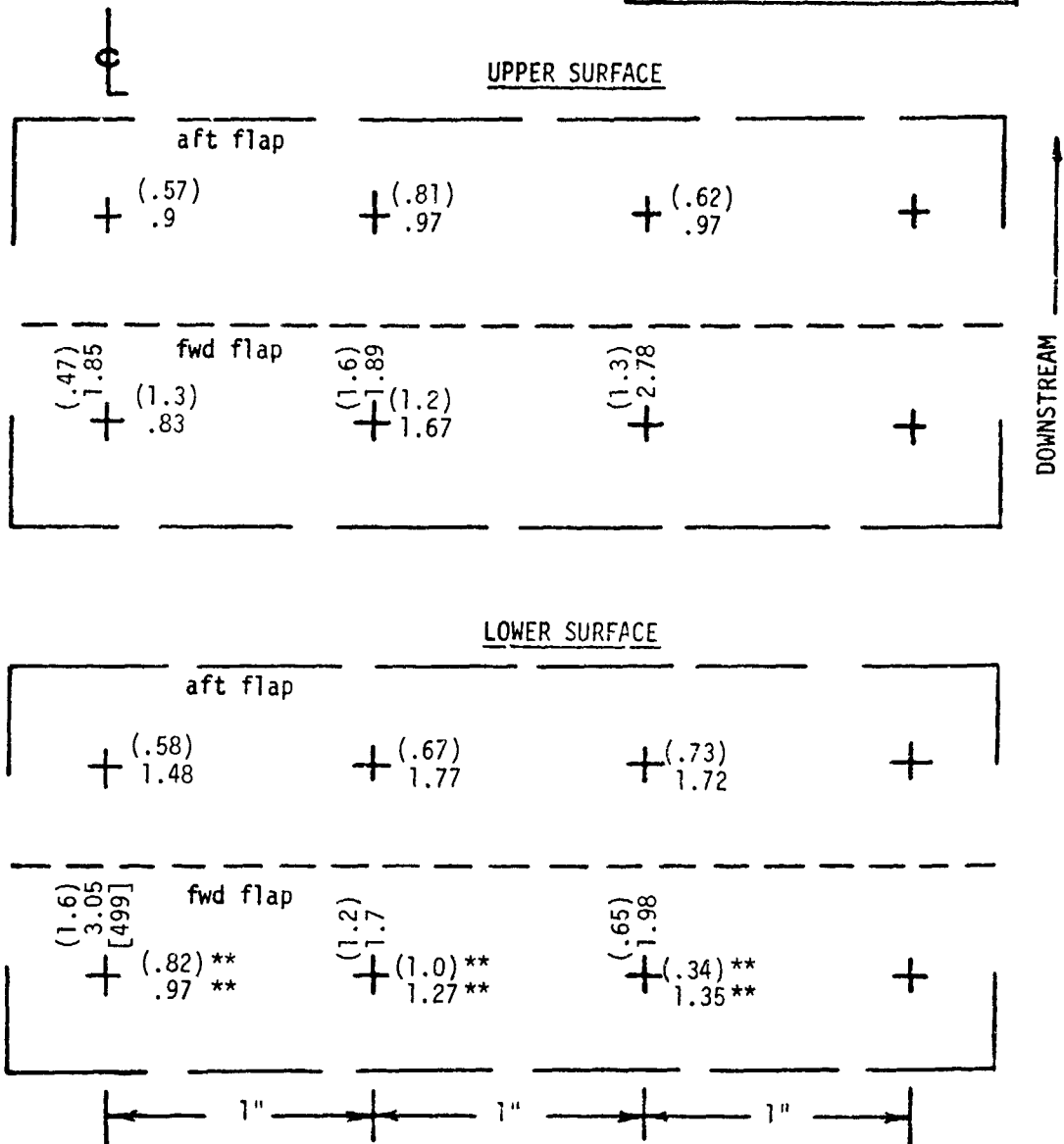


TABLE J-55
 PRESSURE MEASUREMENT RESULTS
 OBF CURVED PLATE (3.25" x 1.35" NOZZLE)

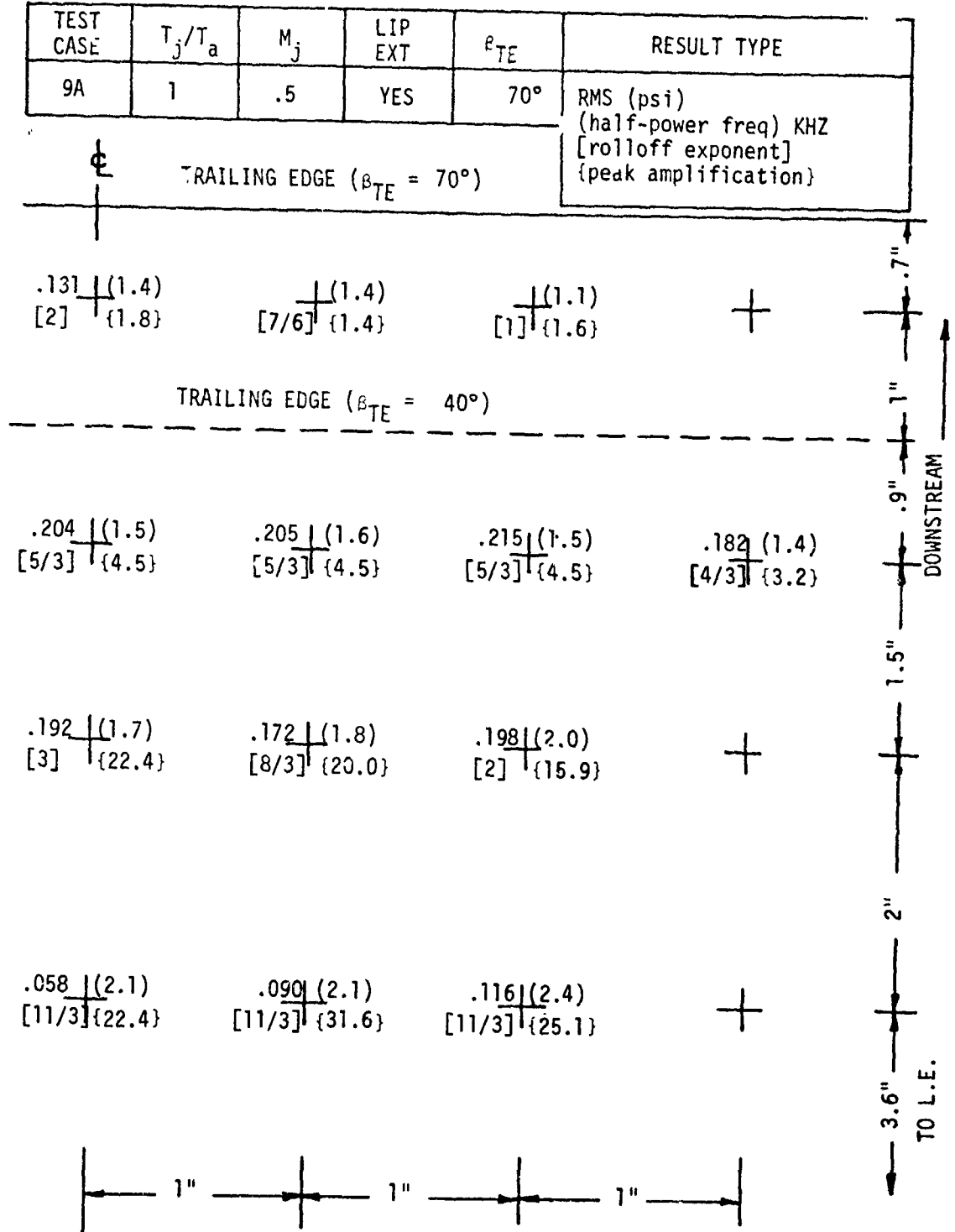


TABLE J-55 (CONT'D)
 PRESSURE MEASUREMENT RESULTS
 OBF CURVED PLATE (3.25" x 1.35" NOZZLE)

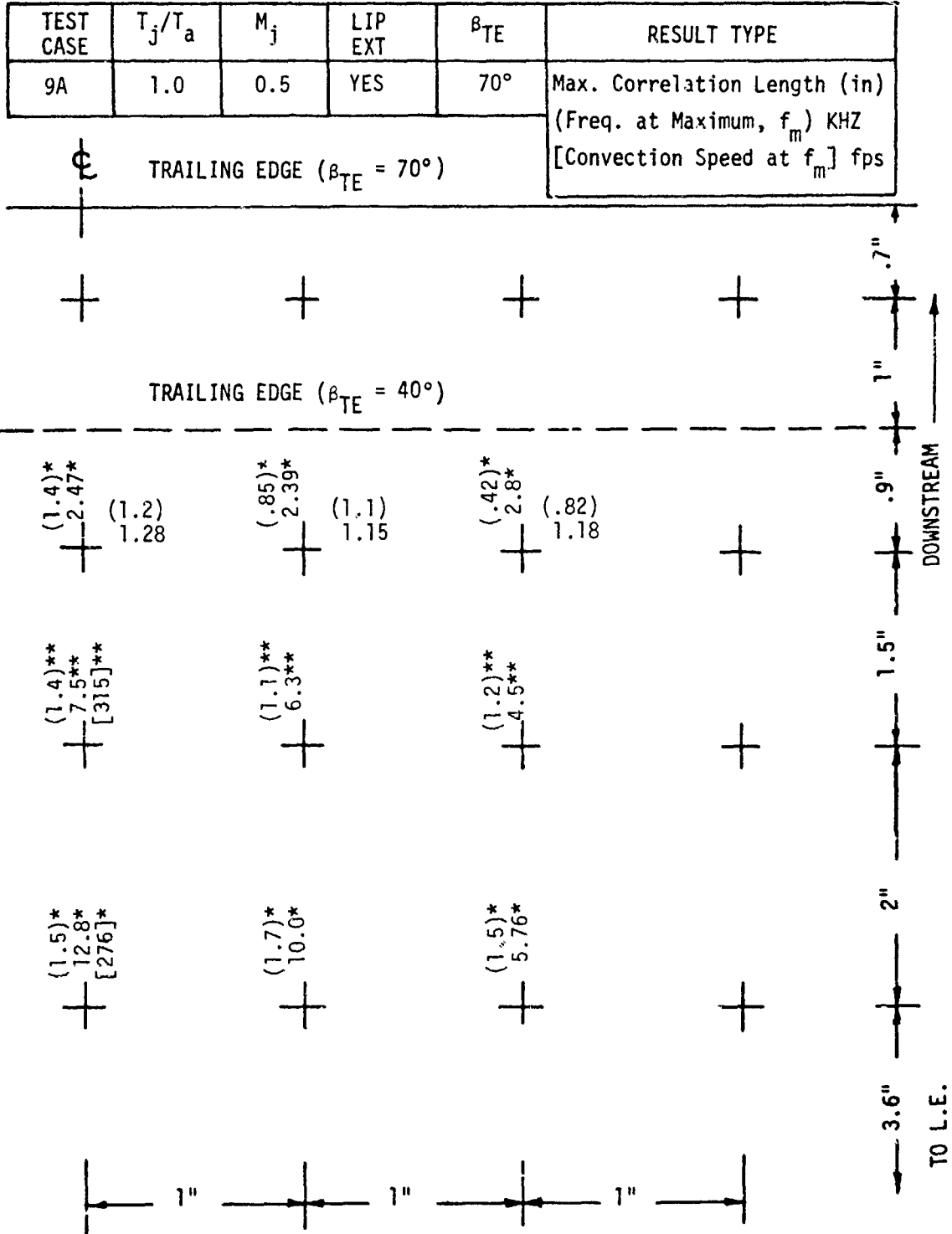


TABLE J-56
 PRESSURE MEASUREMENT RESULTS
 OBF CURVED PLATE (3.25" x 1.35" NOZZLE)

TEST CASE	T_j/T_a	M_j	LIP EXT	β_{TE}	RESULT TYPE
9B	1.87	.5	YES	70°	RMS (psi) (half-power freq) KHZ [rolloff exponent] {peak amplification}

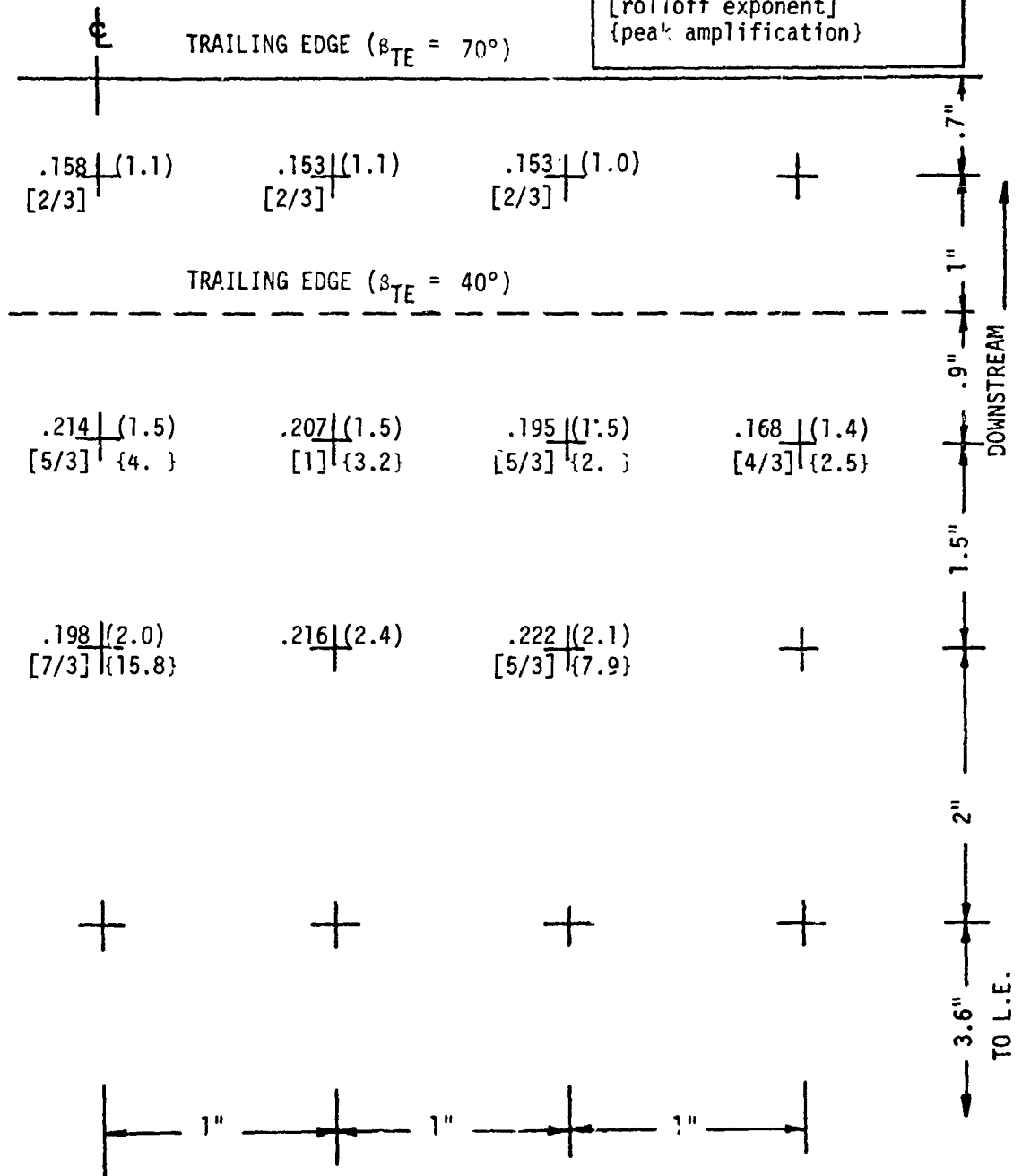


TABLE J-56 (CONT'D)
 PRESSURE MEASUREMENT RESULTS
 OBF CURVED PLATE (3.25" x 1.35" NOZZLE)

TEST CASE	T_j/T_a	M_j	LIP EXT	β_{TE}	RESULT TYPE
9B	1.87	0.5	YES	70°	Max. Correlation Length (in) (Freq. at Maximum, f_m) KHZ [Convection Speed at f_m] fps

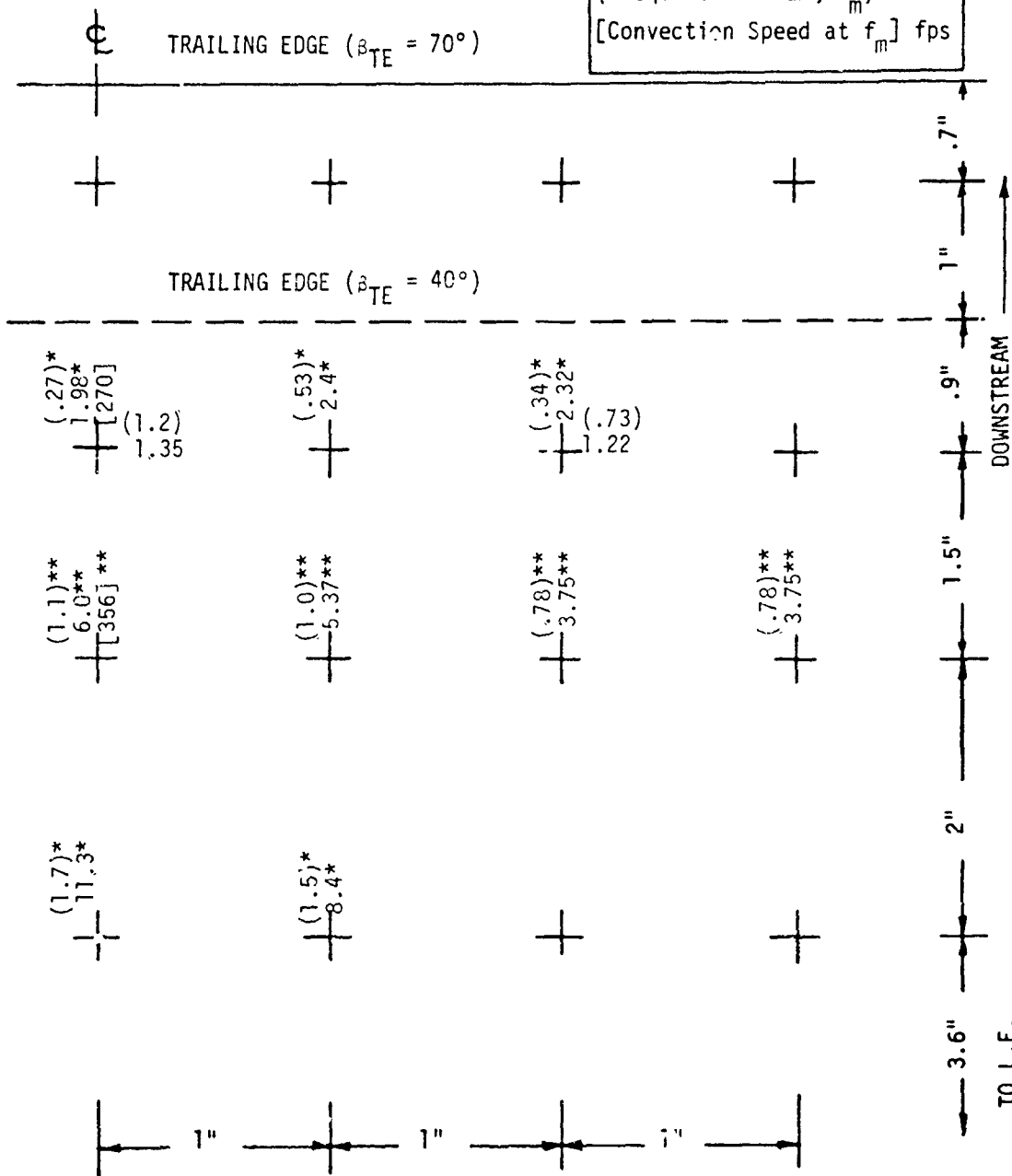


TABLE J-57
 PRESSURE MEASUREMENT RESULTS
 OBF CURVED PLATE (3.25" x 1.35" NOZZLE)

TEST CASE	T _j /T _a	M _j	LIP EXT	β _{TE}	RESULT TYPE
9C	1	.74	YES	70°	RMS (psi) (half-power freq) KHZ [rolloff exponent] {peak amplification}
⊕ TRAILING EDGE (β _{TE} = 70°)					

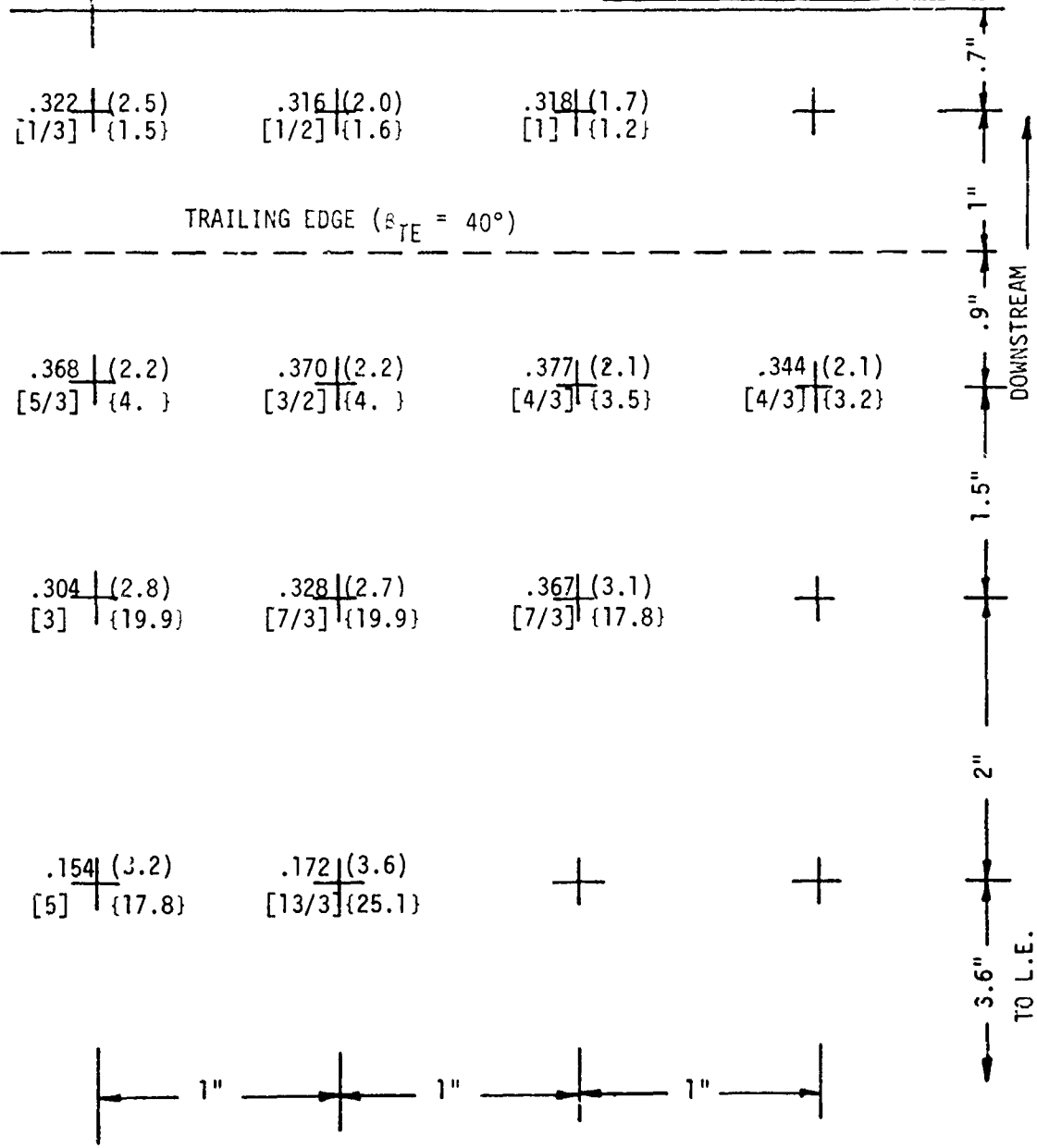


TABLE J-57 (CONT'D)
 PRESSURE MEASUREMENT RESULTS
 OBF CURVED PLATE (3.25" x 1.35" NOZZLE)

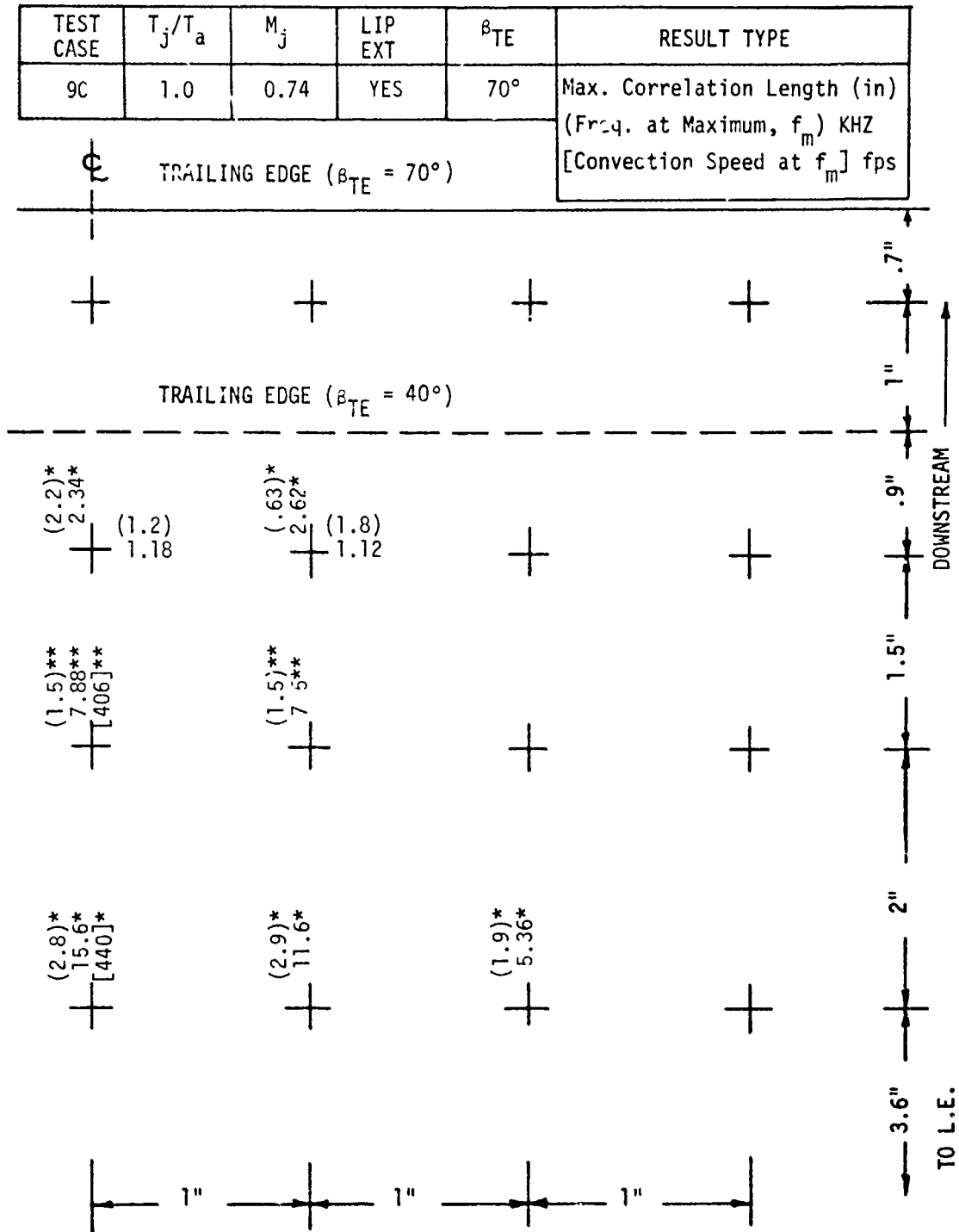


TABLE J-58
 PRESSURE MEASUREMENT RESULTS
 OBF CURVED PLATE (3.25" x 1.35" NOZZLE)

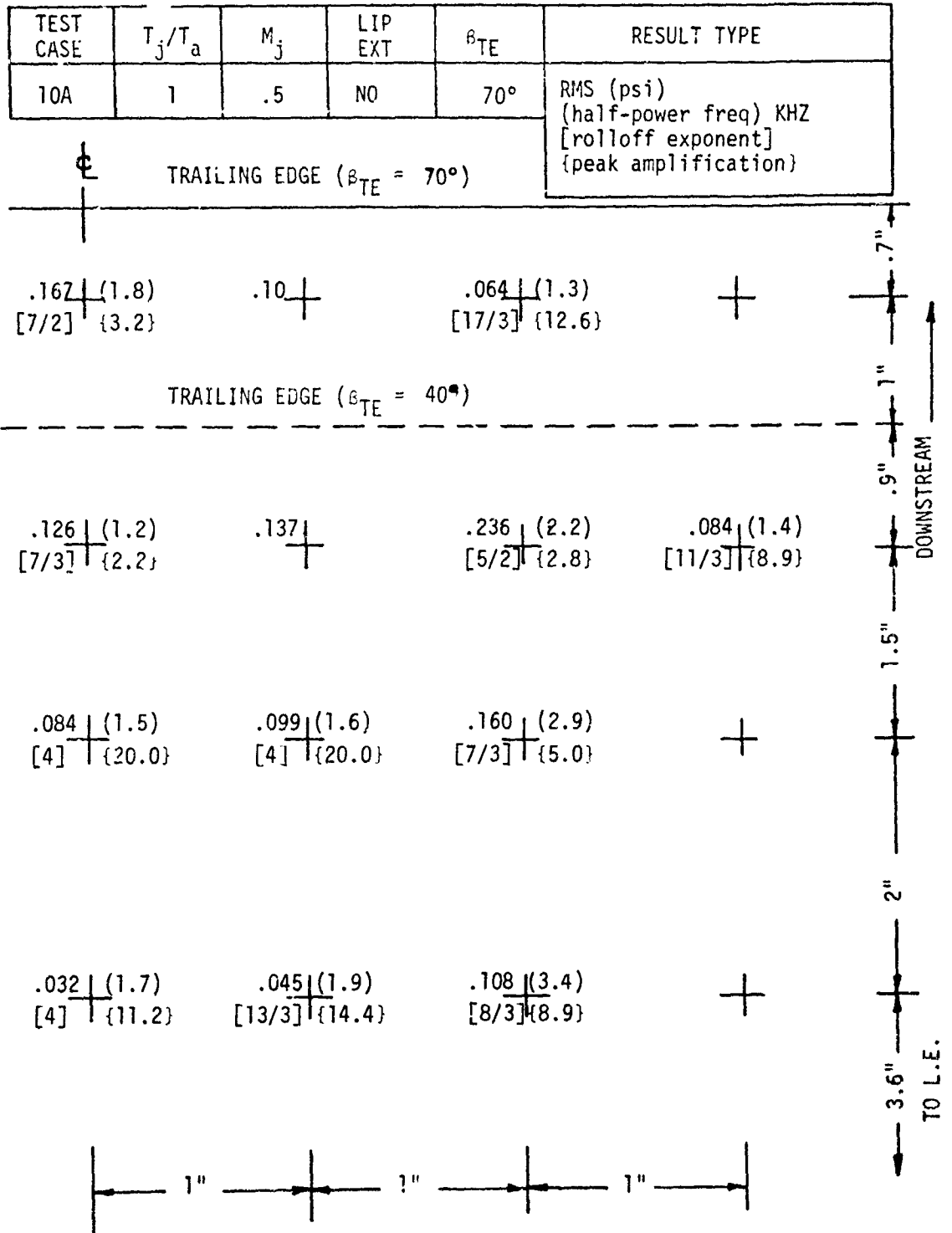


TABLE J-58 (CONT'D)

PRESSURE MEASUREMENT RESULTS
 OBF CURVED PLATE (3.25" x 1.35" NOZZLE)

TEST CASE	T_j/T_a	M_j	LIP EXT	β_{TE}	RESULT TYPE
10A	1.0	0.5	NO	70°	Max. Correlation Length (in) (Freq. at Maximum, f_m) KHZ [Convection Speed at f_m] fps

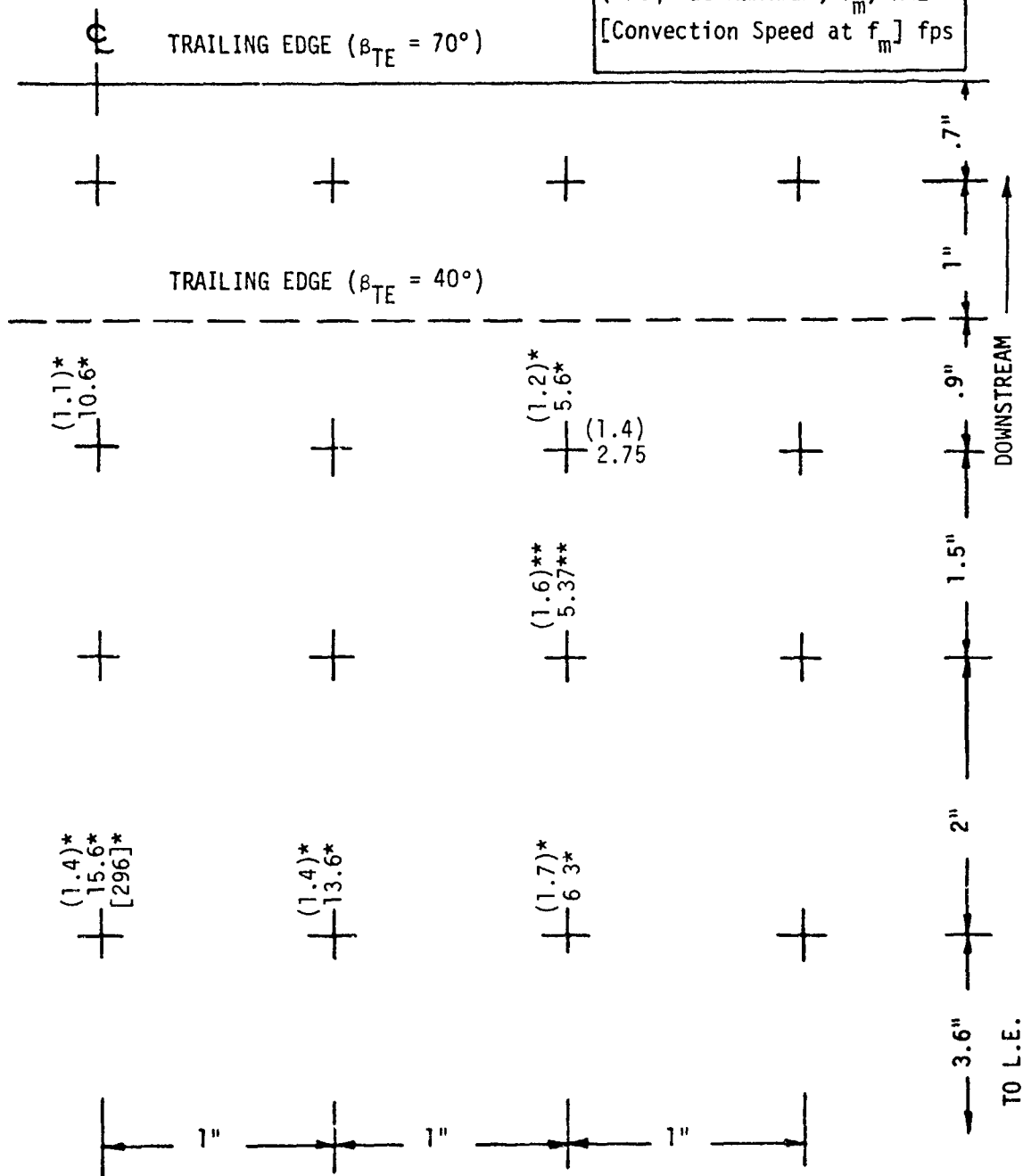


TABLE J-59
 PRESSURE MEASUREMENT RESULTS
 OBF CURVED PLATE (3.25" x 1.35" NOZZLE)

TEST CASE	T _j /T _a	M _j	LIP EXT	β _{TE}	RESULT TYPE
11A	1	.5	YES	40°	RMS (psi) (half-power freq) KHZ [rolloff exponent] {peak amplification}

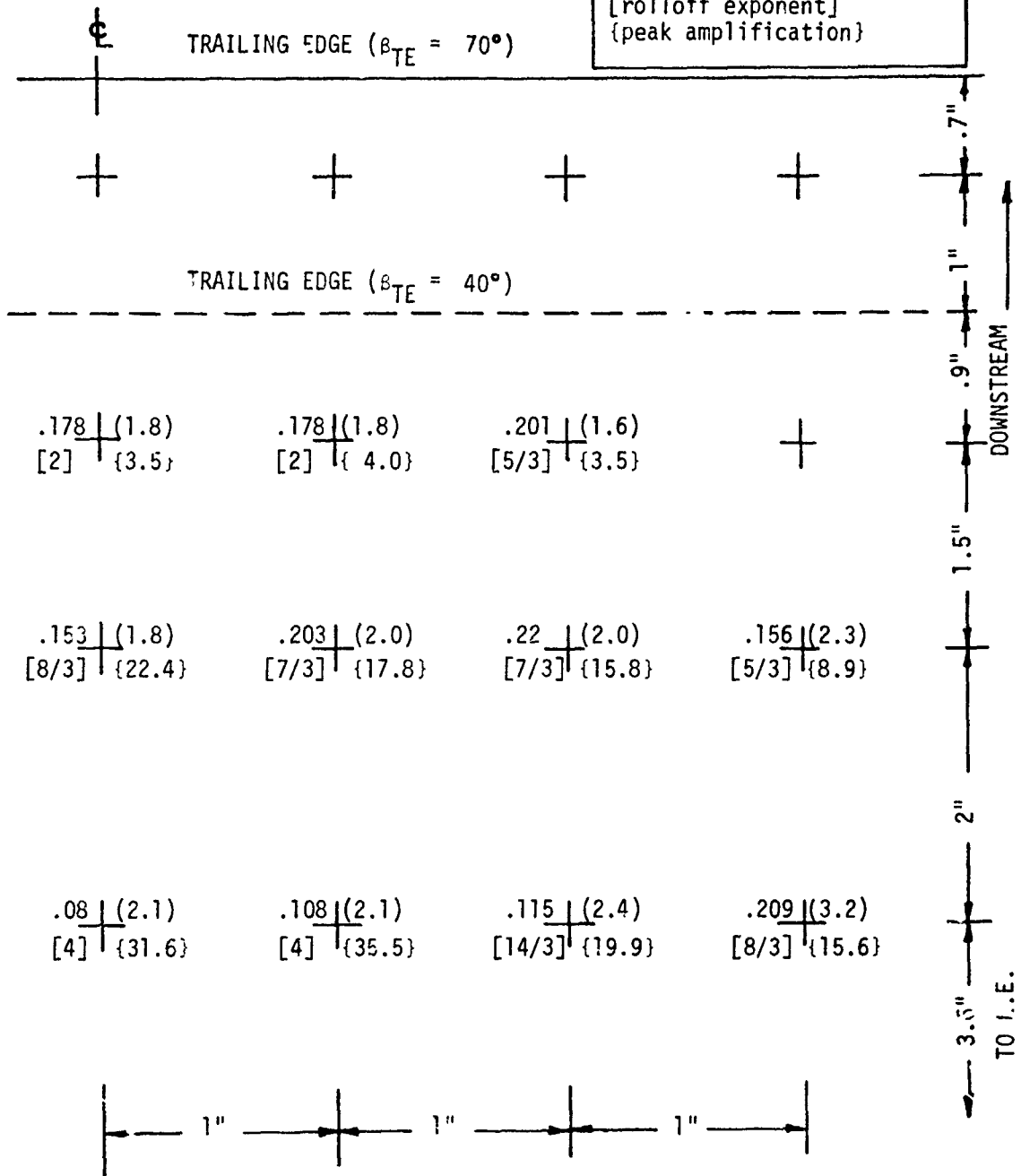


TABLE J-59 (CONT'D)
 PRESSURE MEASUREMENT RESULTS
 OBF CURVED PLATE (3.25" x 1.35" NOZZLE)

TEST CASE	T_j/T_a	M_j	LIP EXT	β_{TE}	RESULT TYPE
11A	1.0	0.5	YES	40°	Max. Correlation Length (in) (Freq. at Maximum, f_m) KHZ [Convection Speed at f_m] fps

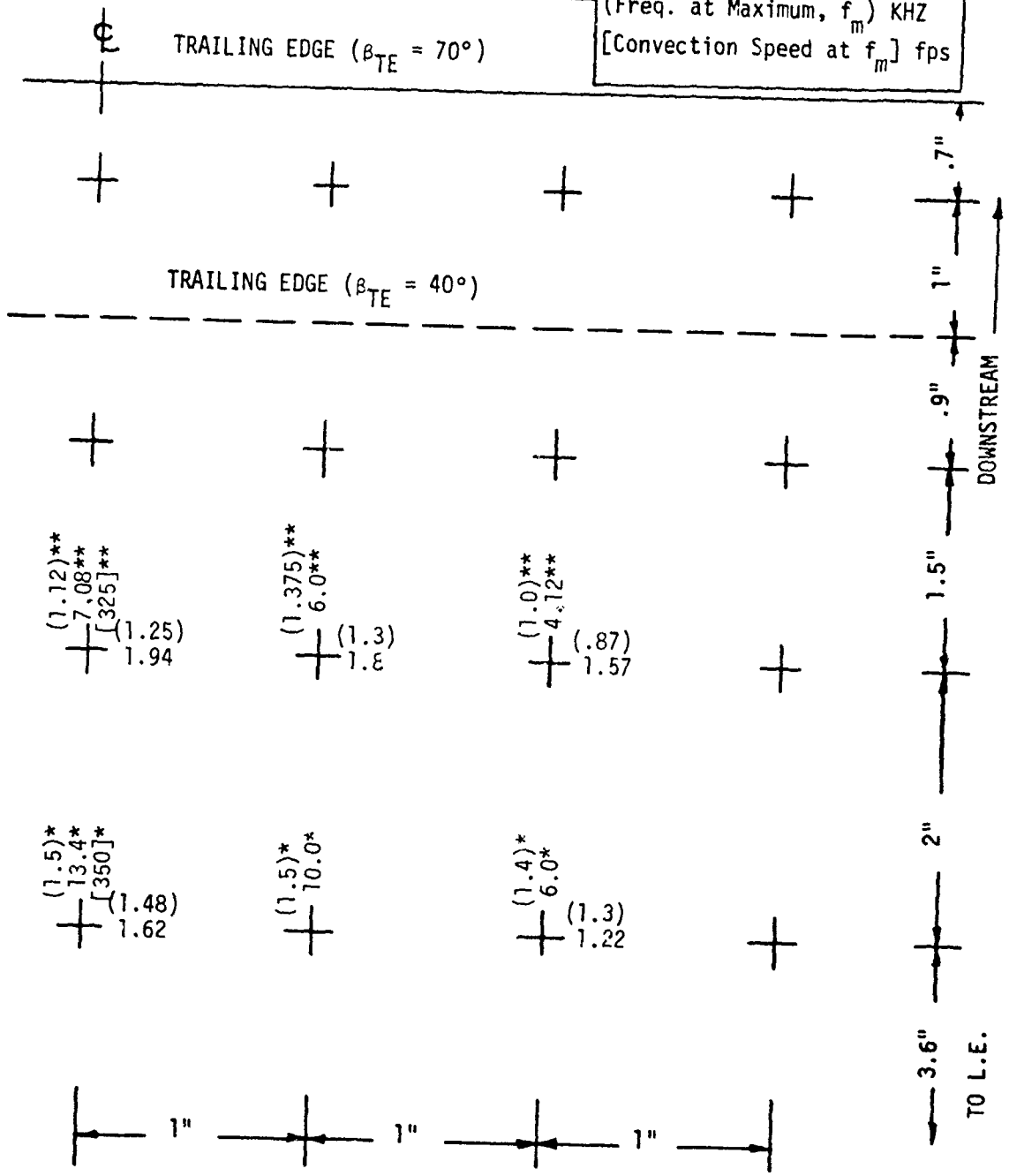


TABLE J-60

PRESSURE MEASUREMENT RESULTS

OBF CURVED PLATE (3.25" x 1.35" NOZZLE)

TEST CASE	T_j/T_a	M_j	LIP EXT	β_{TE}	RESULT TYPE
11B	1.87	.5	YES	40°	RMS (psi) (half-power freq) KHZ [rolloff exponent] {peak amplification}

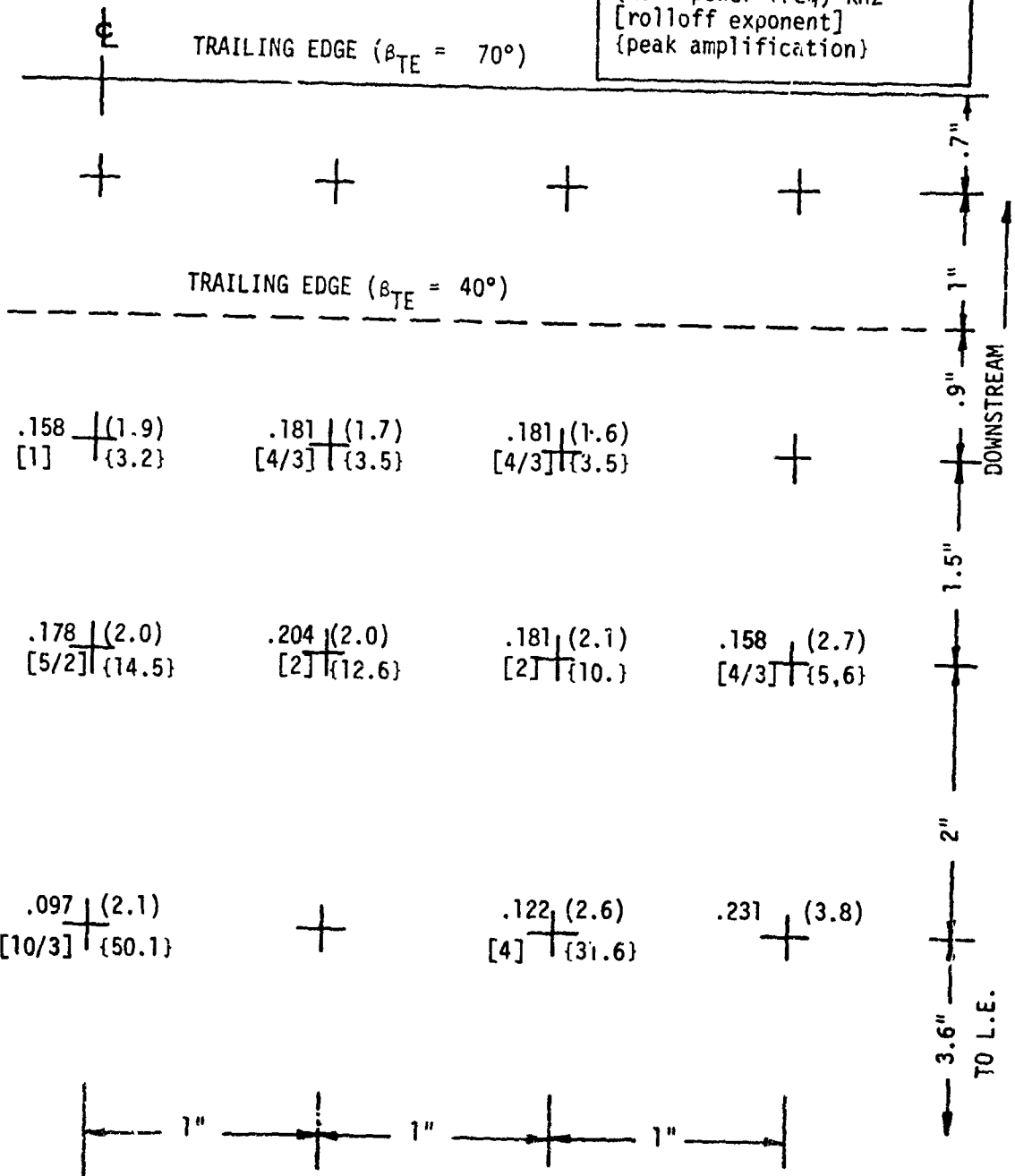


TABLE J-60 (CONT'D)
 PRESSURE MEASUREMENT RESULTS
 OBF CURVED PLATE (3.25" x 1.35" NOZZLE)

TEST CASE	T_j/T_a	M_j	LIP EXT	β_{TE}	RESULT TYPE
11B	1.87	0.5	YES	40°	Max. Correlation Length (in) (Freq. at Maximum, f_m) KHZ [Convection Speed at f_m] fps

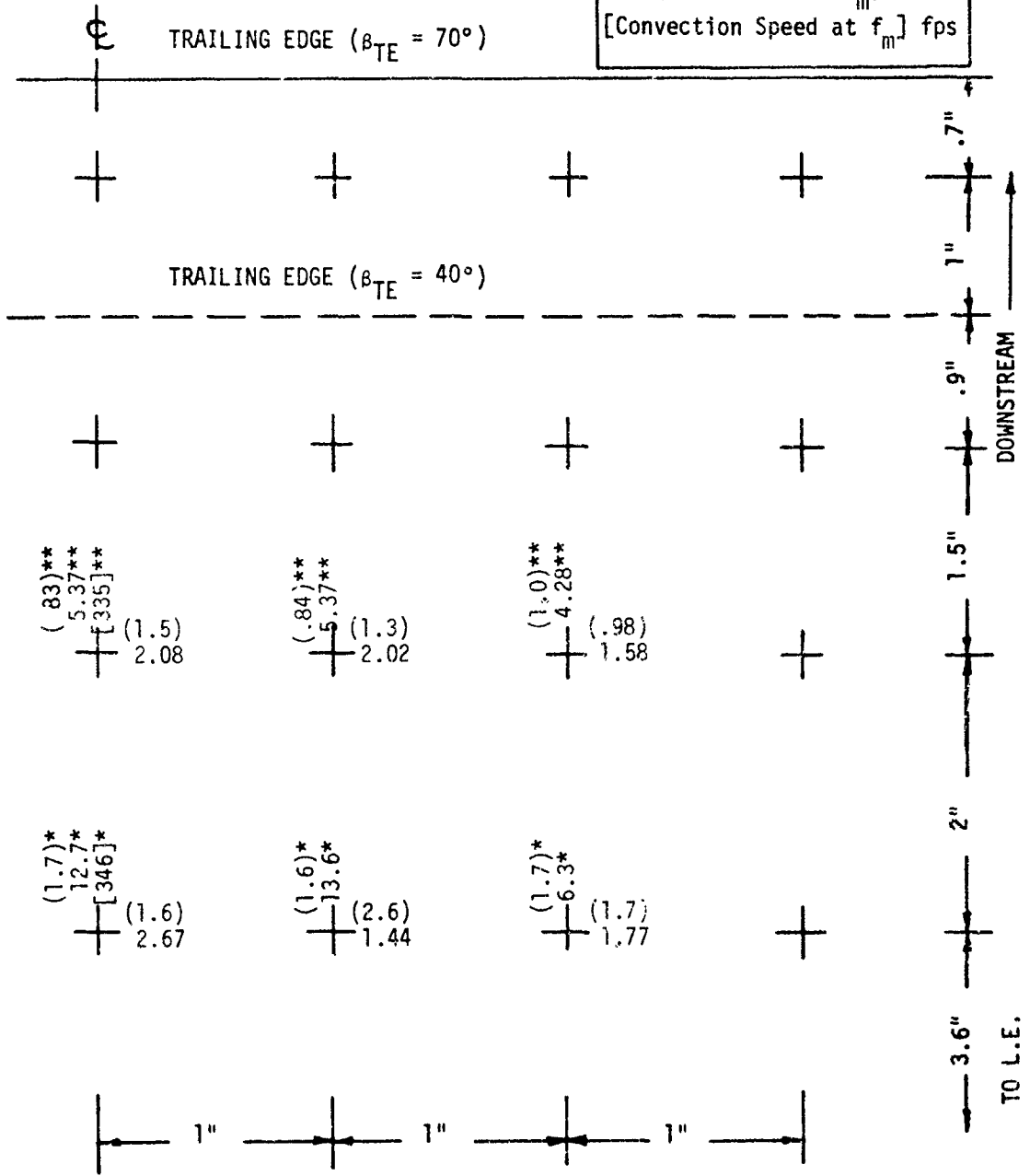


TABLE J-61
 PRESSURE MEASUREMENT RESULTS
 OBF CURVED PLATE (3.25" x 1.35" NOZZLE)

TEST CASE	T_j/T_a	M_j	LIP EXT	β_{TE}	RESULT TYPE
11C	1	.74	YES	40°	RMS (psi) (half-power freq) KHZ [rolloff exponent] {peak amplification}

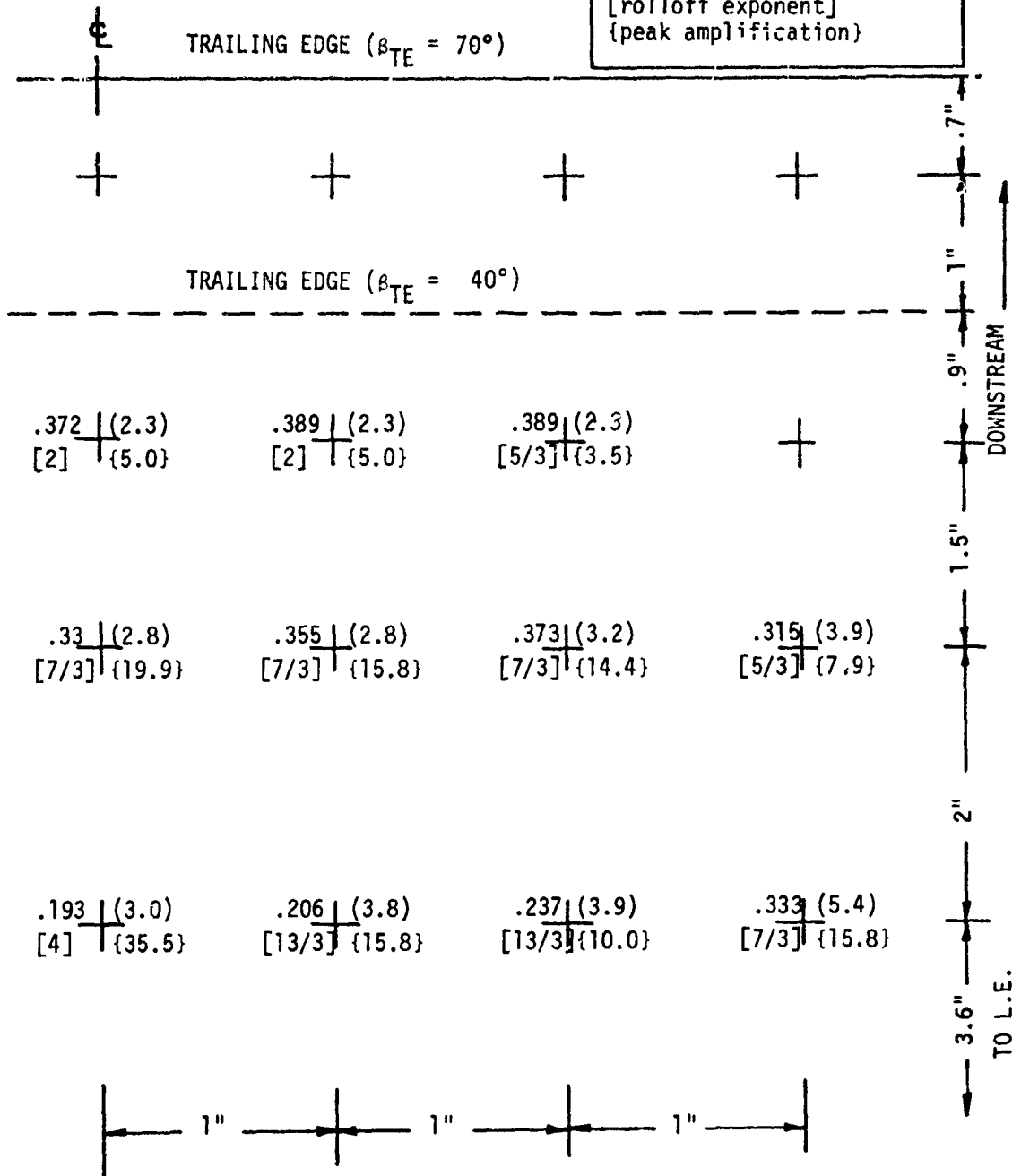


TABLE J-61 (CONT'D)

PRESSURE MEASUREMENT RESULTS
 OBF CURVED PLATE (3.25" x 1.35" NOZZLE)

TEST CASE	T_j/T_a	M_j	LIP EXT	β_{TE}	RESULT TYPE
11C	1.0	0.74	YES	40°	Max. Correlation Length (in) (Freq. at Maximum, f_m) KHZ [Convection Speed at f_m] fps

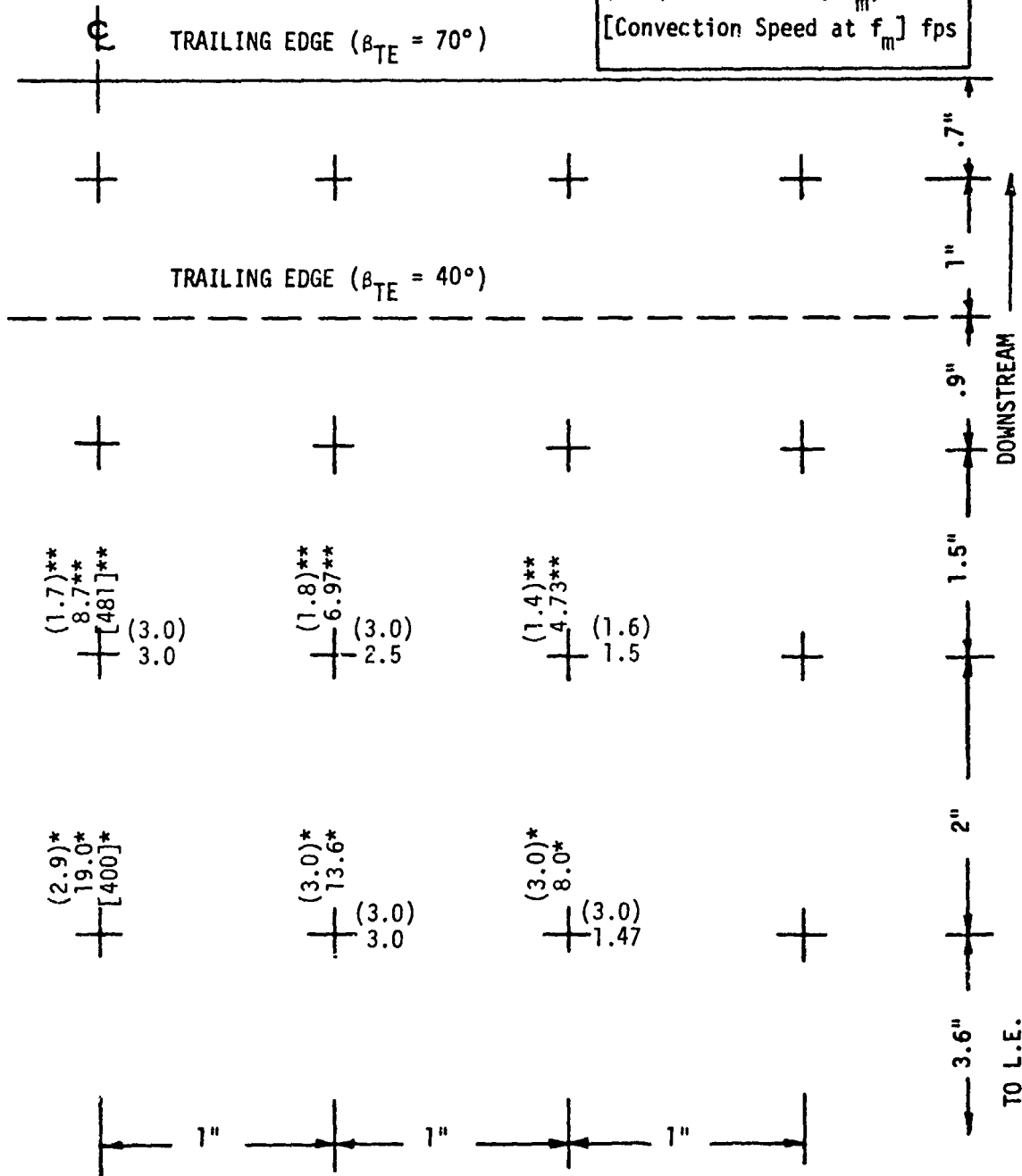


TABLE J-62

PRESSURE MEASUREMENT RESULTS
 OBF CURVED PLATE (3.25" x 1.35" NOZZLE)

TEST CASE	T_j/T_a	M_j	LIP EXT	β_{TE}	RESULT TYPE
11D	1	.35	YES	40°	RMS (psi) (half-power freq) KHZ [rolloff exponent] {peak amplification}

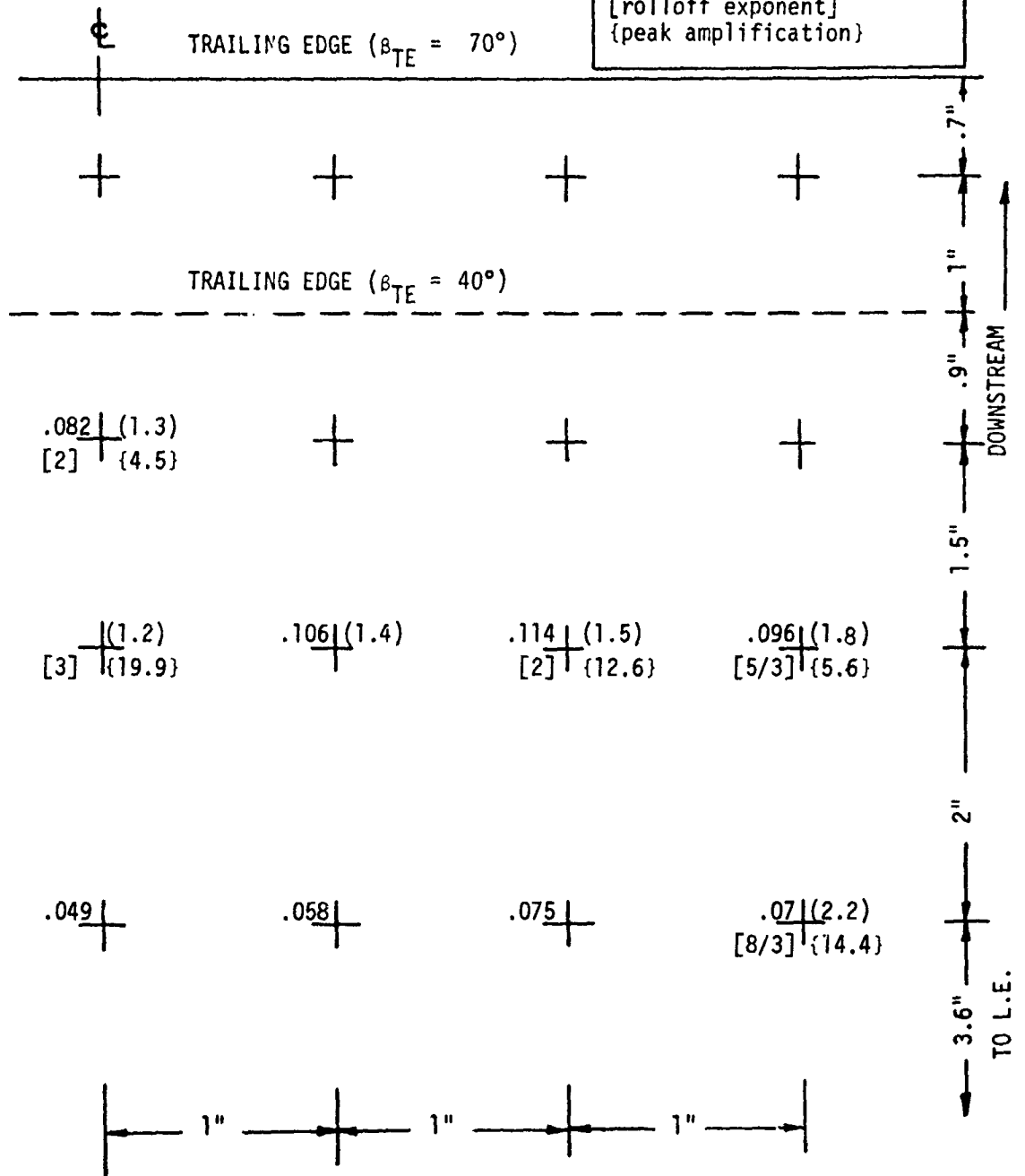


TABLE J-62 (CONT'D)
 PRESSURE MEASUREMENT RESULTS
 OBF CURVED PLATE (3.25" x 1.35" NOZZLE)

TEST CASE	T_j/T_a	M_j	LIP EXT	β_{TE}	RESULT TYPE
11D	1.0	0.35	YES	40°	Max. Correlation Length (in, (Freq. at Maximum, f_m) KHZ [Convection Speed at f_m] fps

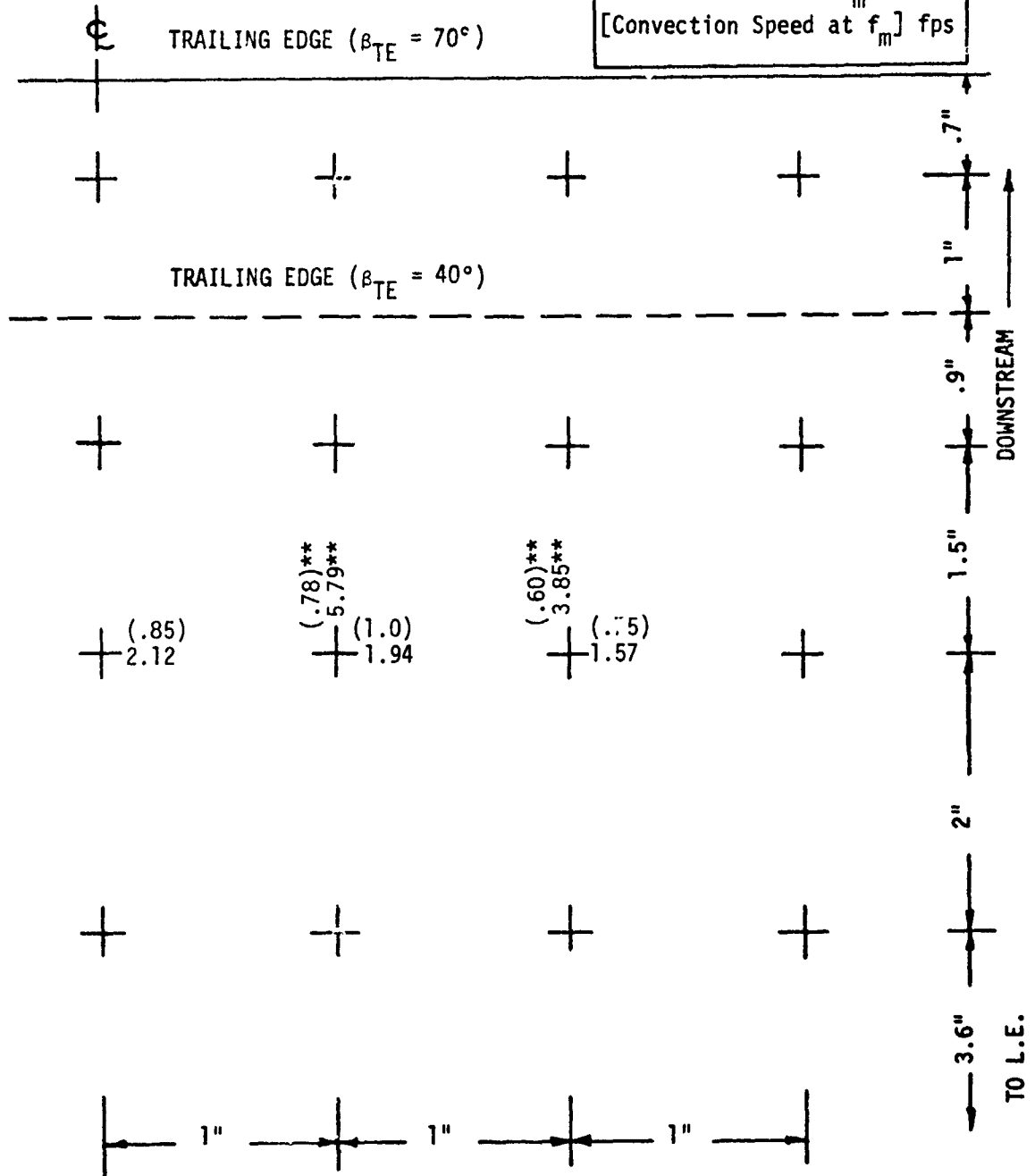


TABLE J-63
 PRESSURE MEASUREMENT RESULTS
 OBF CURVED PLATE (3.25" x 1.35" NOZZLE)

TEST CASE	T_j/T_a	M_j	LIP EXT	β_{TE}	RESULT TYPE
12A	1	.5	NO	40°	RMS (psi) (half-power freq) KHZ [rolloff exponent] {peak amplification}

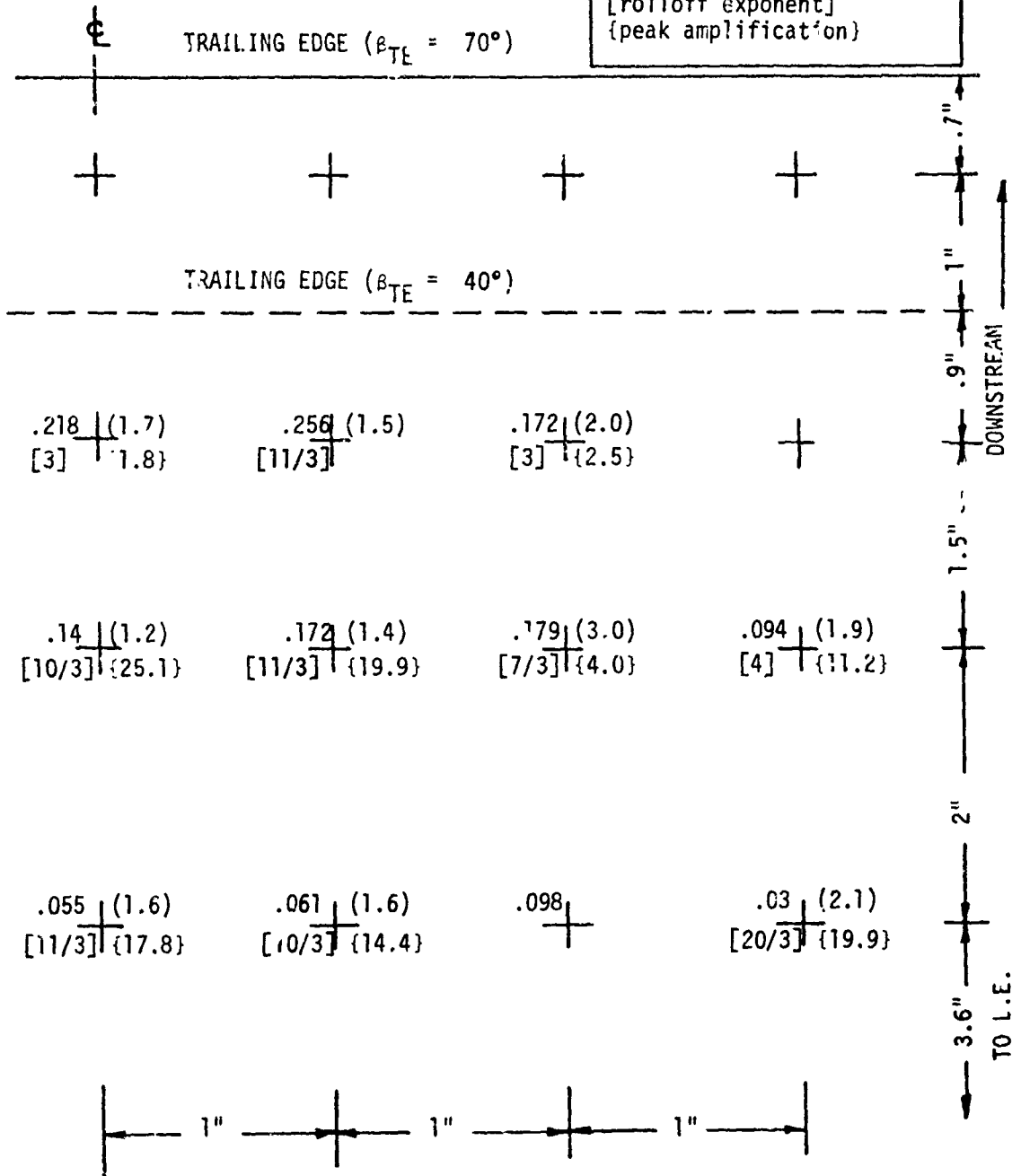


TABLE J-63 (CONT'D)
 PRESSURE MEASUREMENT RESULTS
 OBF CURVED PLATE (3.25" x 1.35" NOZZLE)

TEST CASE	T _j /T _a	M _j	LIP EXT	β _{TE}	RESULT TYPE
12A	1.0	0.5	NO	40°	Max. Correlation Length (in) (Freq. at Maximum, f _m) KHZ [Convection Speed at f _m] fps
⊕ TRAILING EDGE (β _{TE} = 70°)					

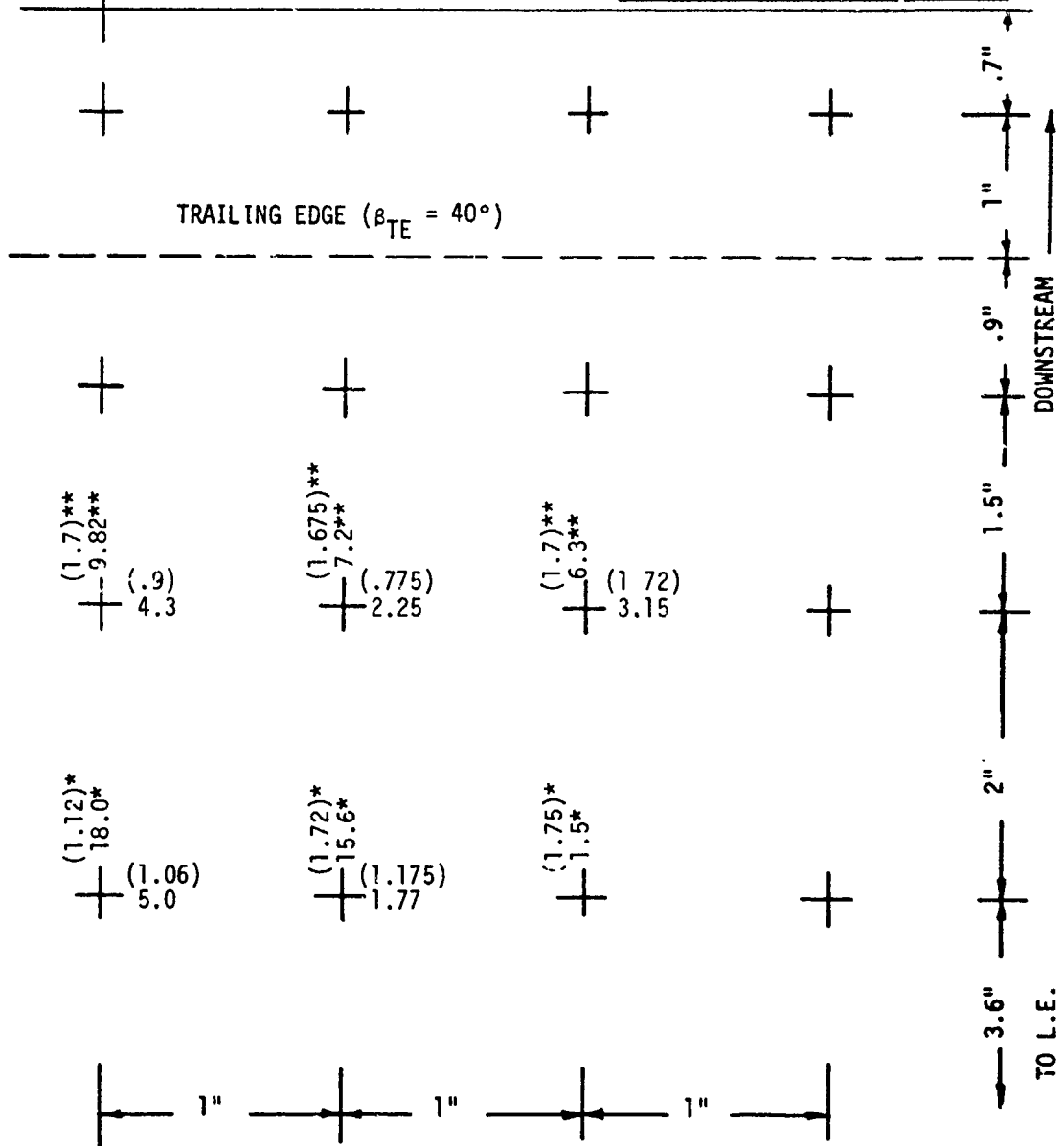


TABLE J-64

MAXIMUM CORRELATIONS ACROSS THICKNESS
OF FLAPS FOR WING-FLAPS MODEL

ROUND NOZZLE ($D_j = 2''$)

TEST CASE	FLAP LOCATION y (IN.)	FWD FLAP		AFT FLAP	
		ρ_m	f_m (KHZ)	ρ_m	f_m (KHZ)
7A	0	0.66	2.0	0.38	1.1
	1	0.5	2.1	0.35	1.4
7B	0	0.78	1.3	0.35	0.54
	1	0.69	1.7	0.27	1.3
8A	0	0.34	1.6	0.4	1.7
	1	0.23	1.1	0.35	1.1
8B	0	0.57	1.3	0.35	0.86
	1	0.38	1.5	0.25	0.73
8D	0	0.23	0.85	0.29	1.0
	1	0.18	1.6	0.38	1.9
8E	0	0.66*	2.9*	0.38	1.4
	1	0.26	1.8	0.28	1.5
LOBED (DAISY) NOZZLE ($D_{eq} = 2''$)					
8F	0	0.19	0.37	0.25	0.34
	1	0.22	0.58	0.35	0.64
8G	0	0.31	1.2	0.30	0.5
	1	0.28	1.4	0.32	0.83

* Acoustic Resonance (see Appendix F)

APPENDIX K

FREE JET PROPERTIES

The following plots exhibit properties of the free jet for a round nozzle as a function of the distance downstream of the nozzle exit. All these results were obtained by analysis using a Douglas Aircraft Company program. (Corresponding results can be found from the program described in Reference 11). The jet conditions associated with each plot are given in the labeling on the plot. The FORTRAN notation on the plots relates to mathematical notation as follows:

FORTRAN	MATHEMATICAL
HALF RADIUS	$r_{1/2}$
Q HALF	$q_{1/2}$
JET Q	q_j
MJ	M_j
TTJ	T_j or T_{Tj}
DJ	D_j
PAMB	P_a
PTJ	P_{Tj}

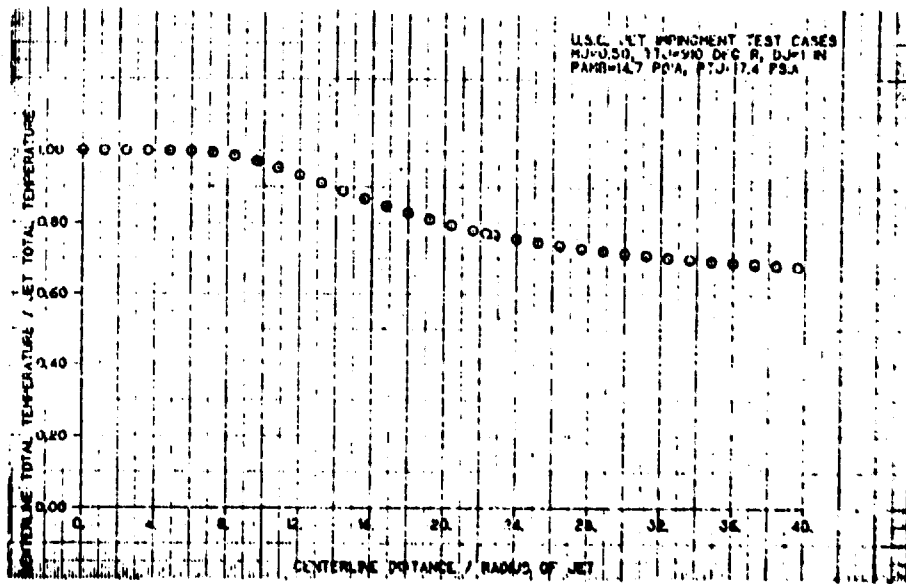
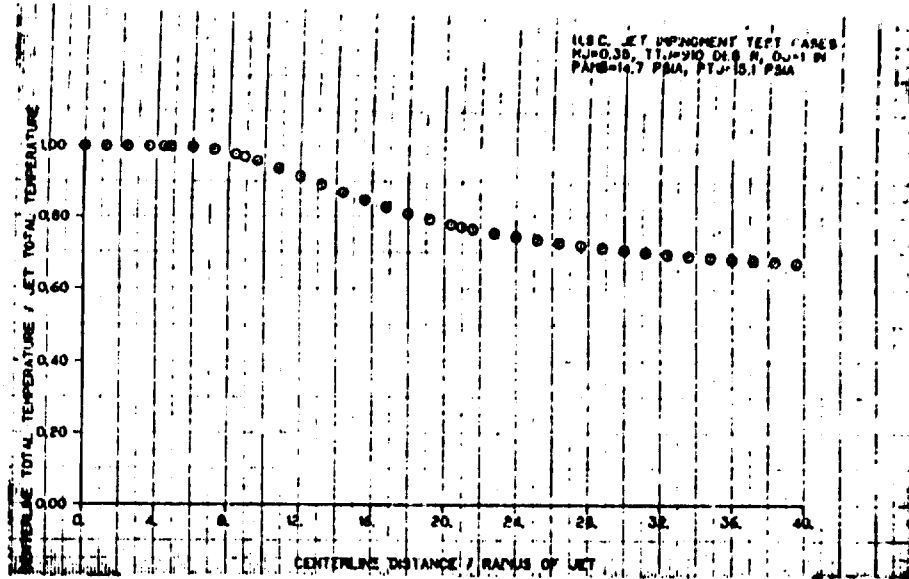


Figure K-1. Free Jet Properties - Centerline Total Temperature Versus Centerline Distance

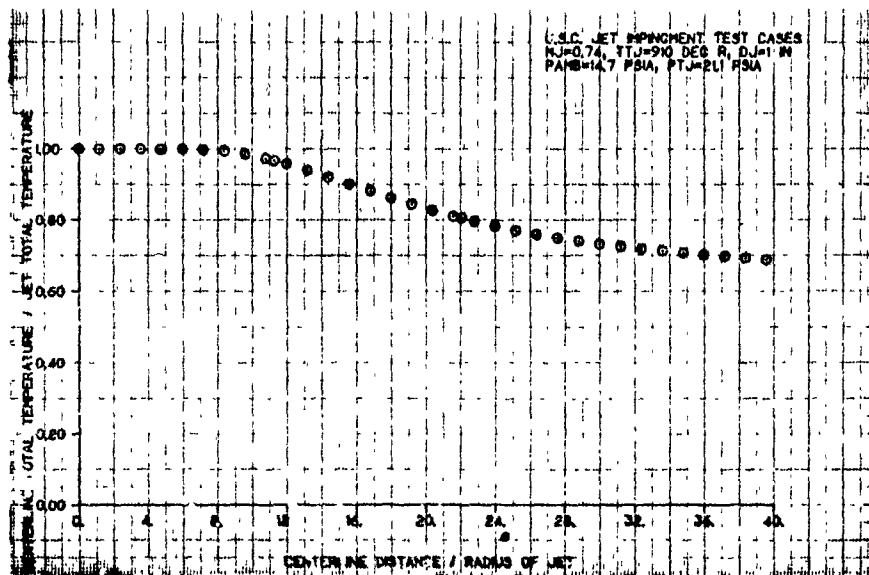


Figure K-1. Cont'd

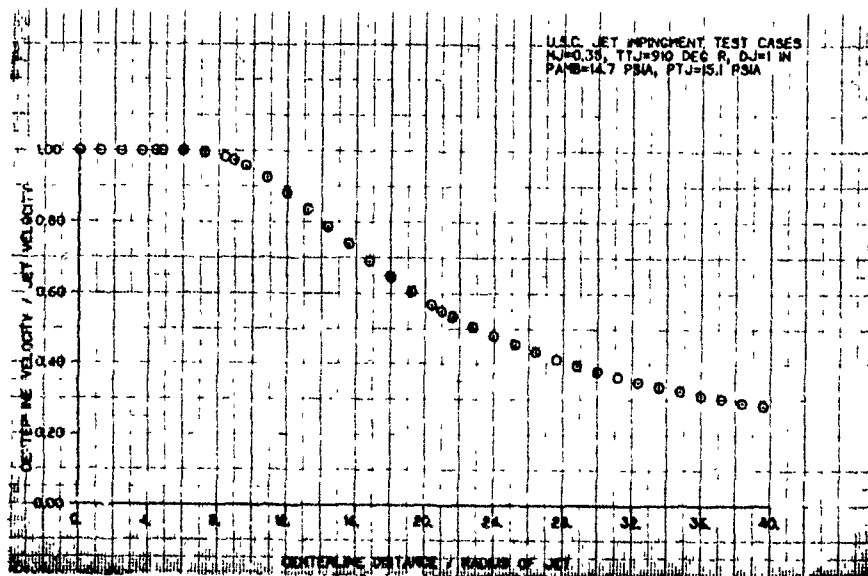
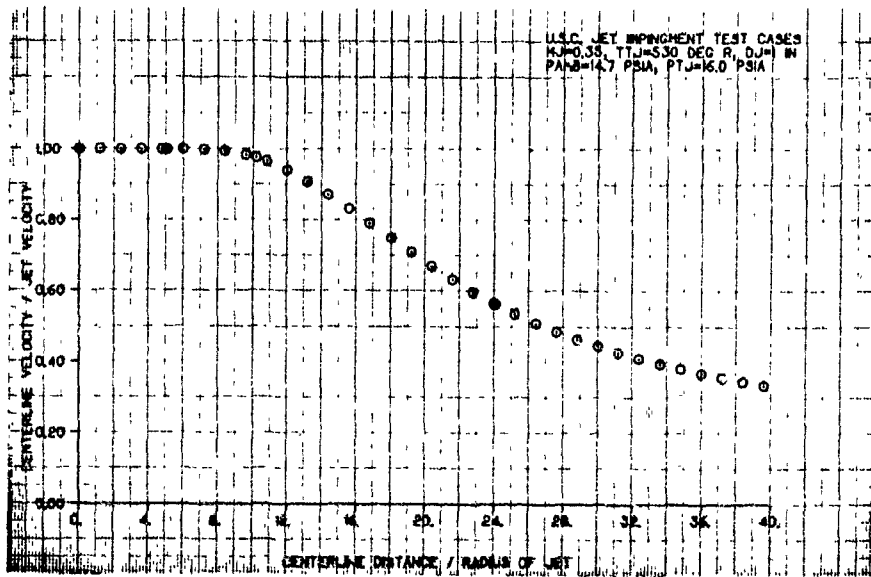


Figure K-2. Free Jet Properties - Centerline Velocity Versus Centerline Distance

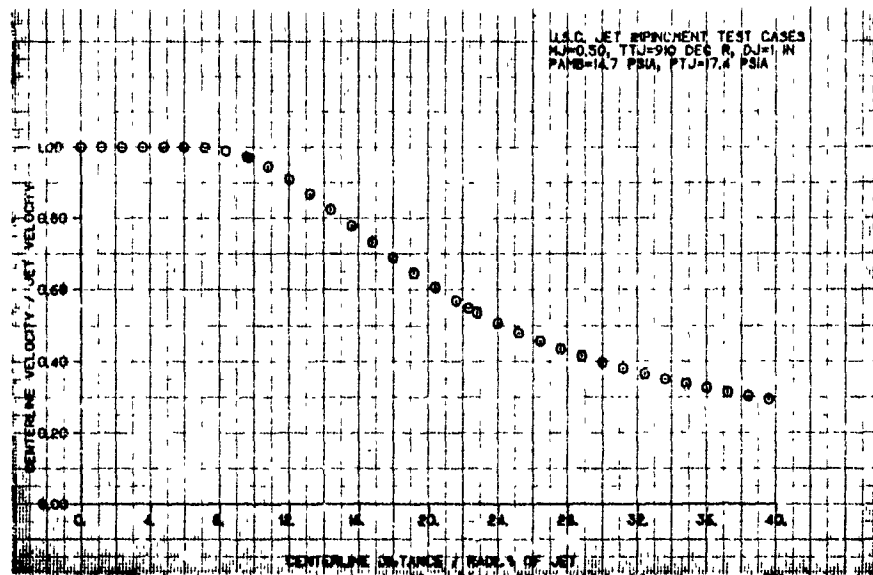
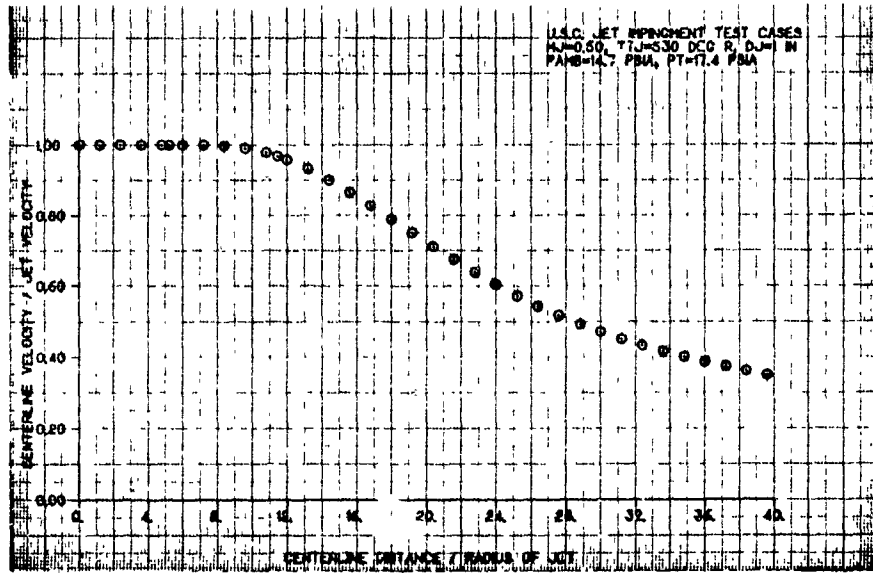


Figure K-2. Cont'd

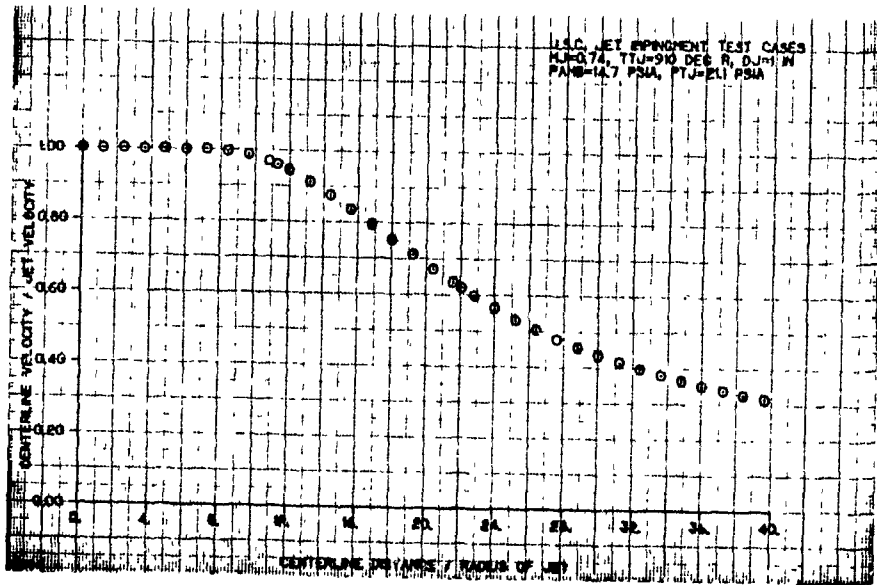
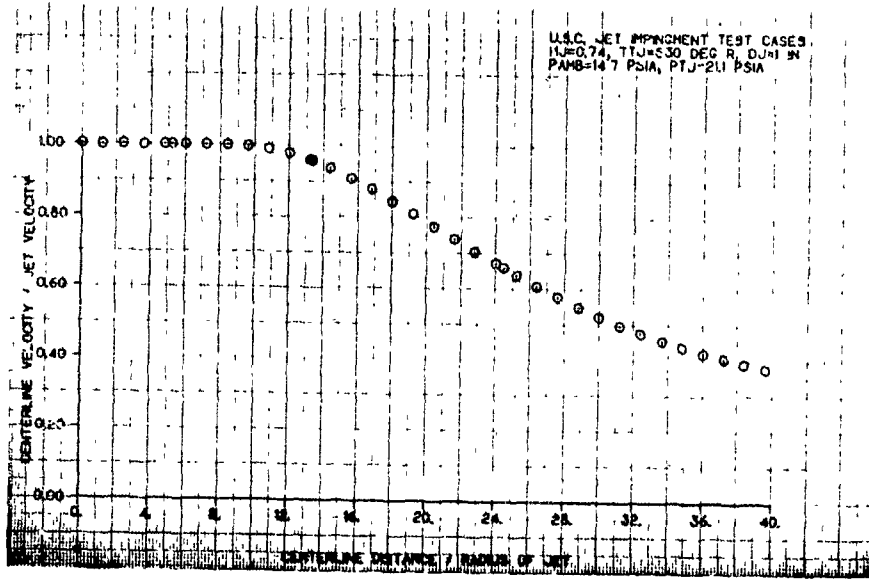


Figure K-2. Cont'd

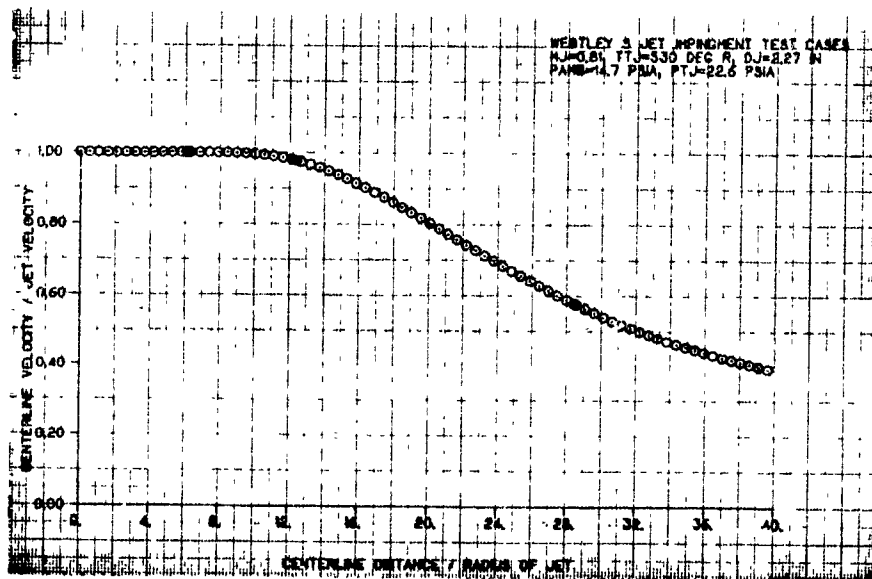
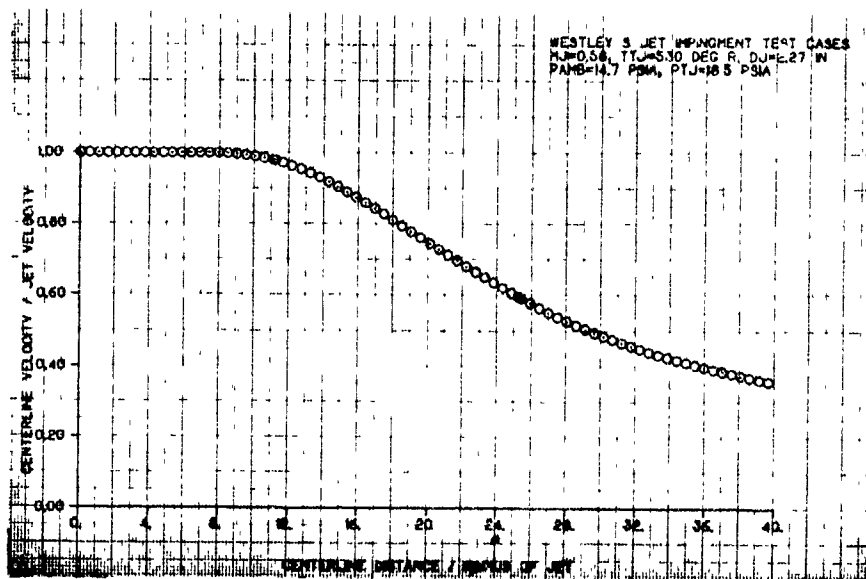


Figure K-2. Cont'd

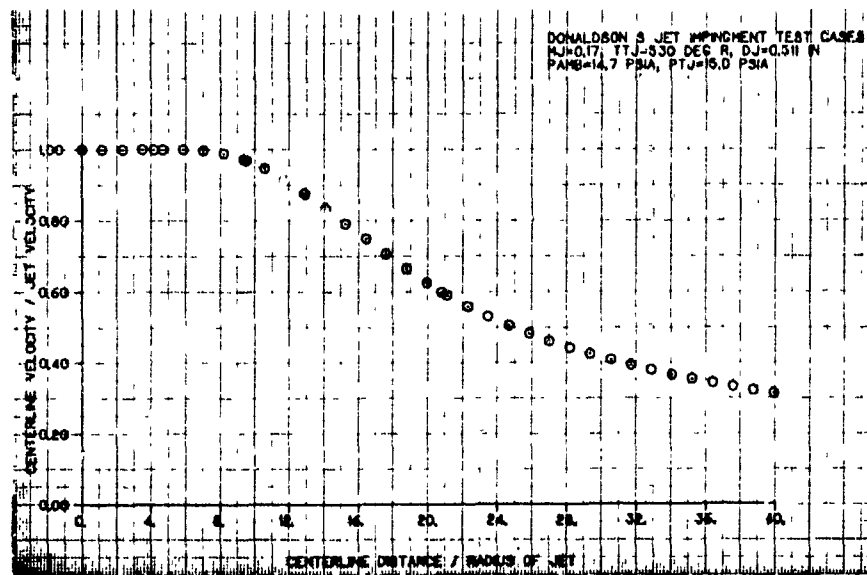


Figure K-2. Cont'd

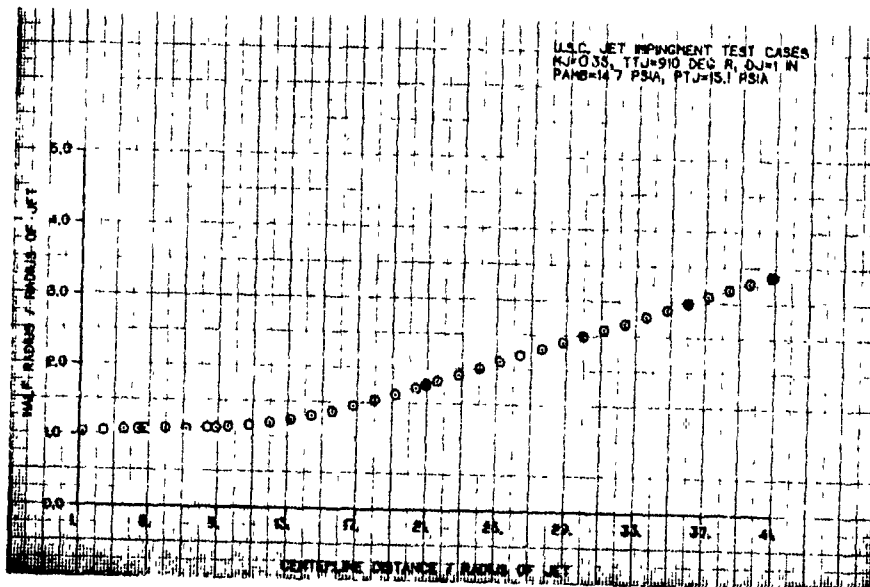
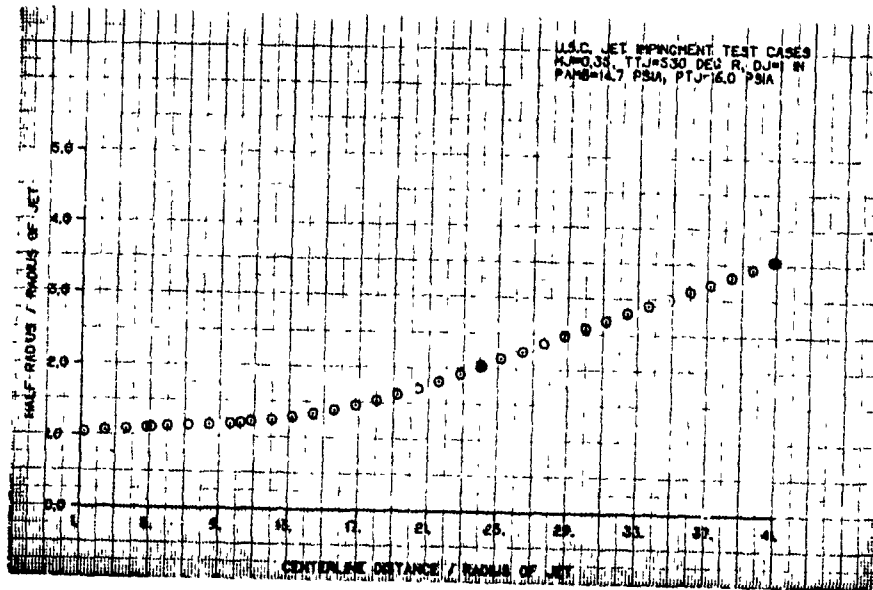


Figure K-3. Free Jet Properties - $r_{1/2}$ Versus Centerline Distance

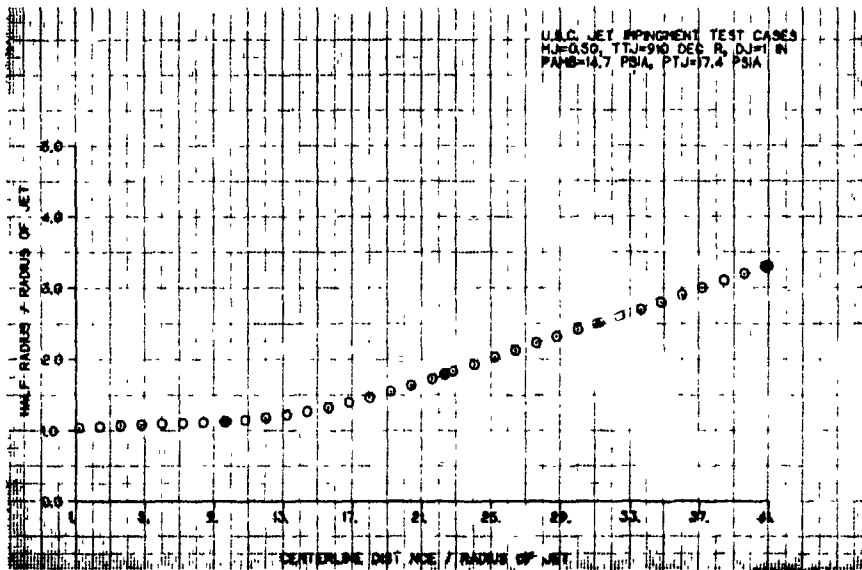
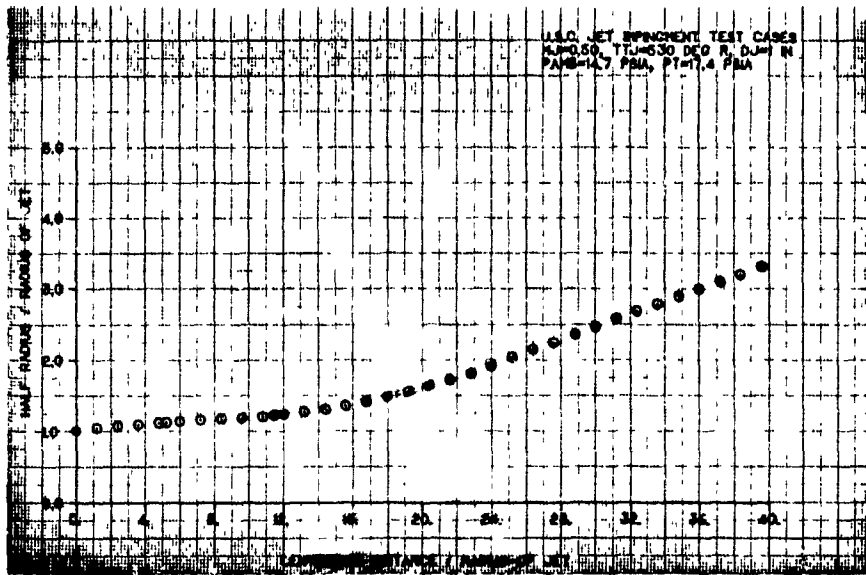


Figure K-3. Cont'd

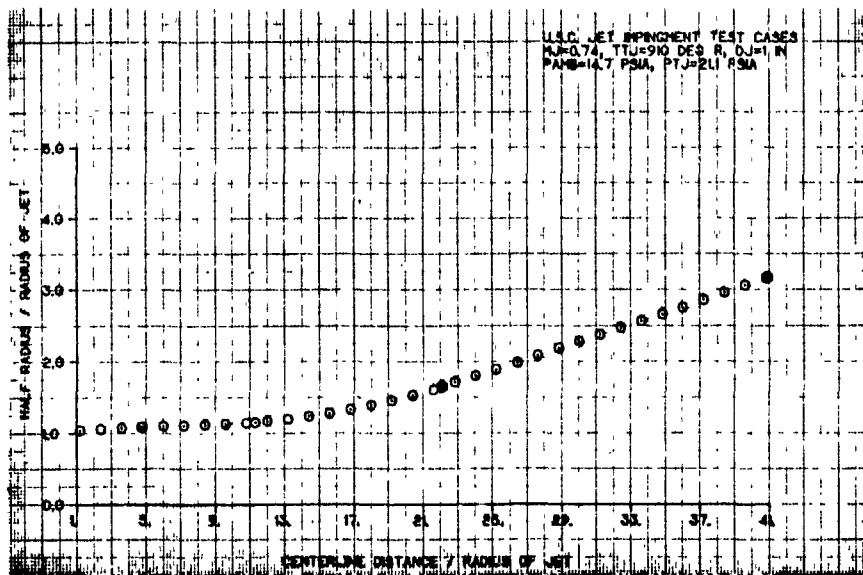
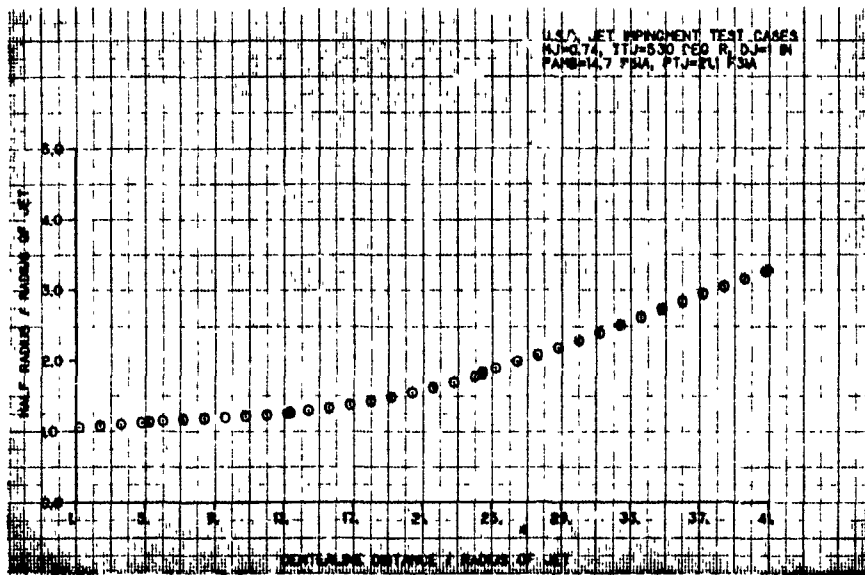


Figure K-3. Cont'd

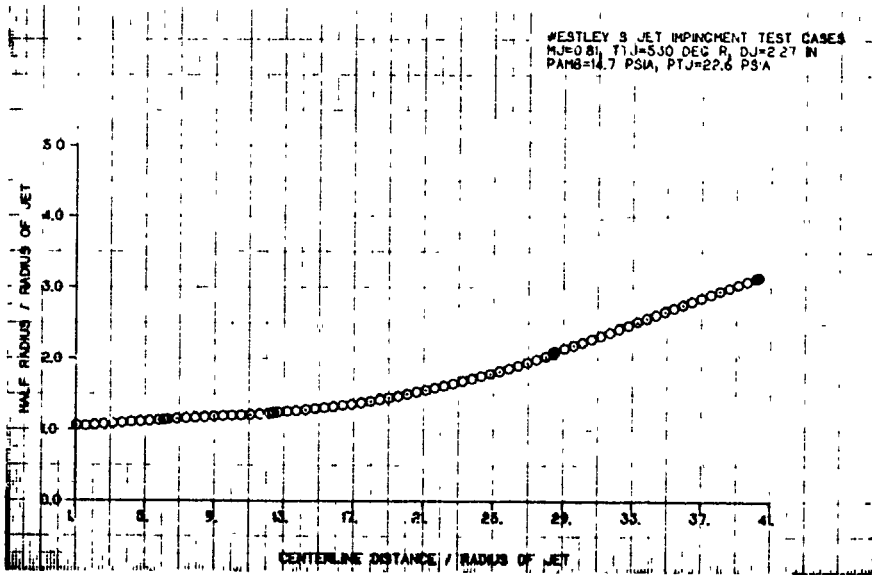
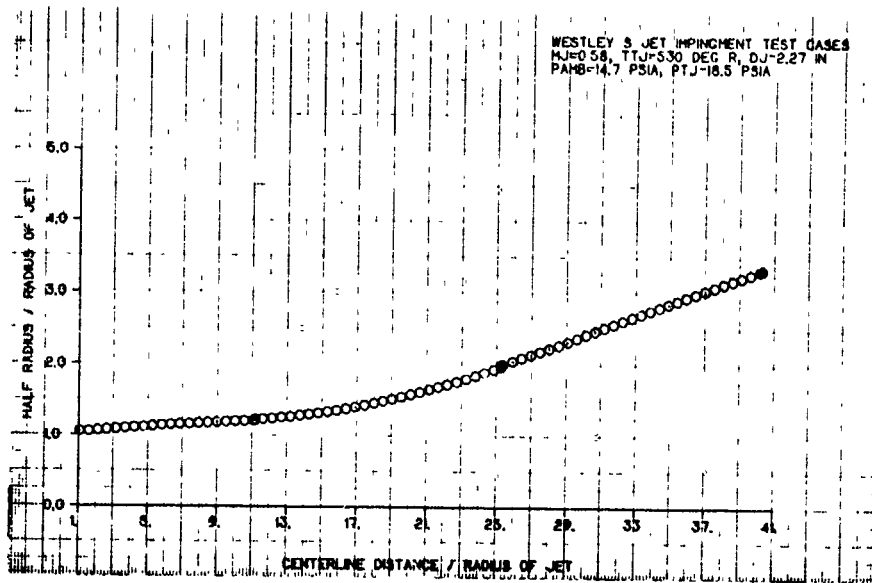


Figure K-3. Cont'd

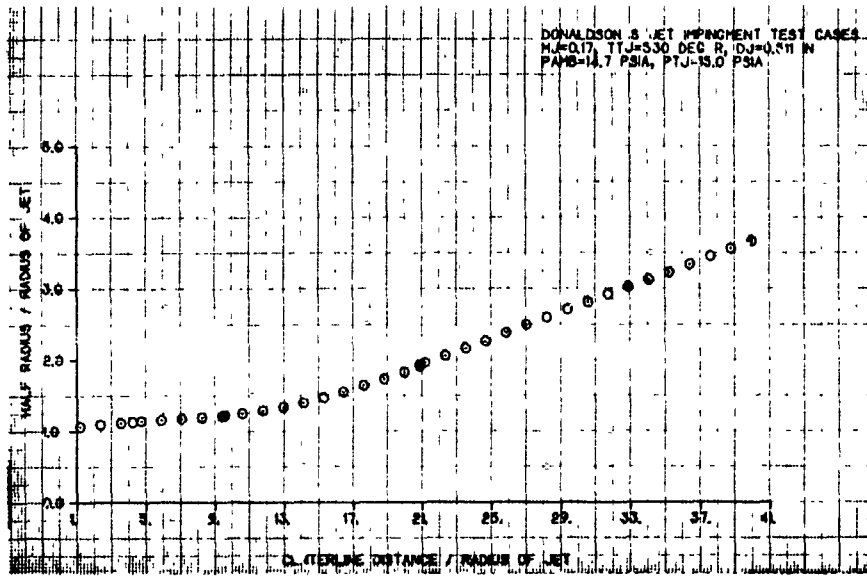


Figure K-3. Cont'd

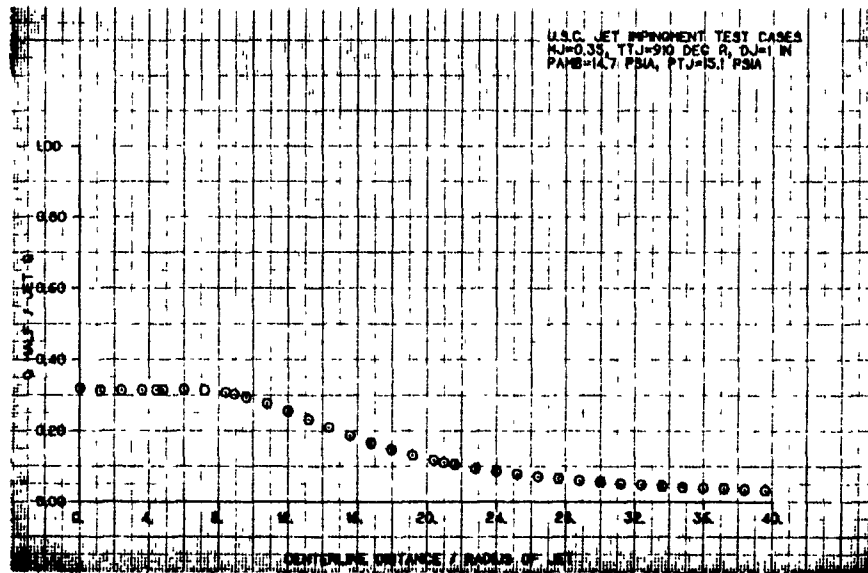
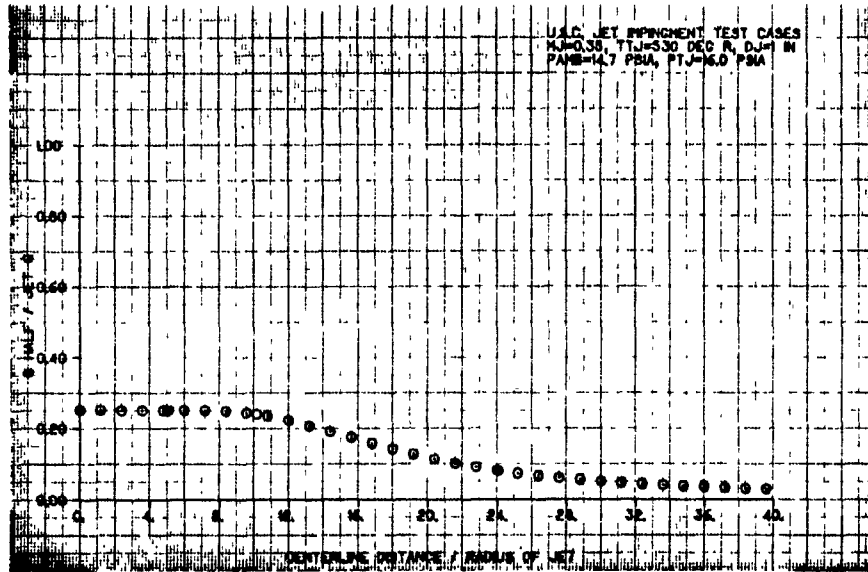


Figure K-4. Free Jet Properties - $q_{1/2}$ Versus Centerline Distance

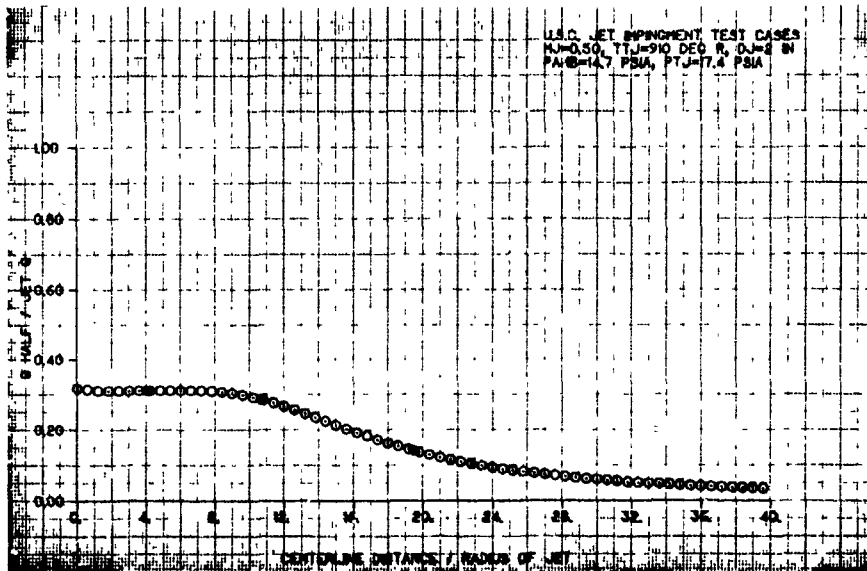
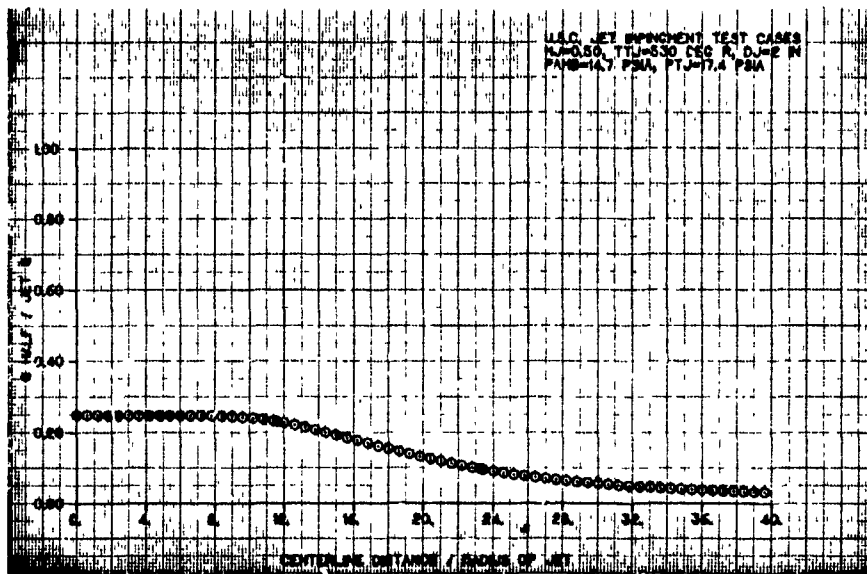


Figure K-4. Cont'd

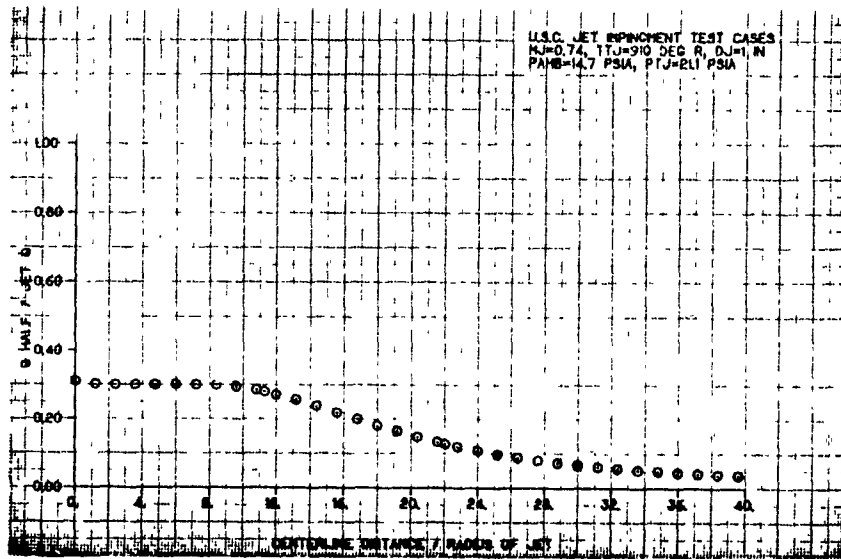
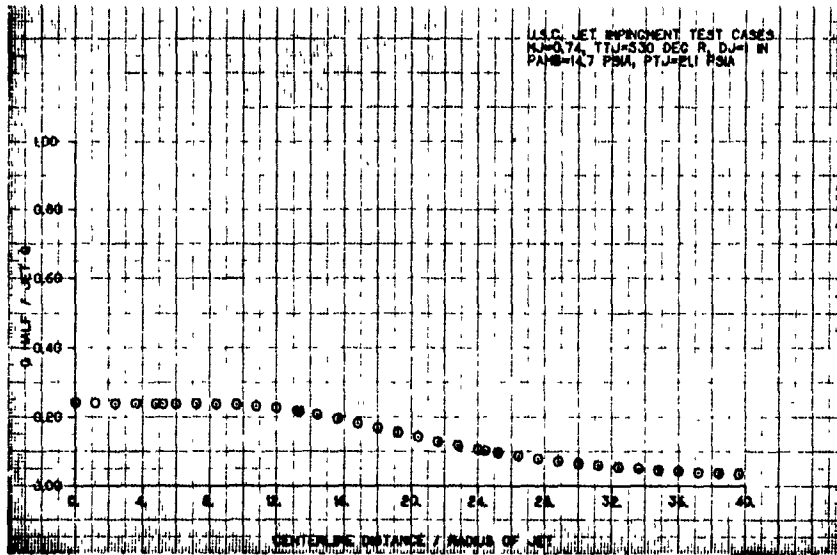


Figure K-4. Cont'd

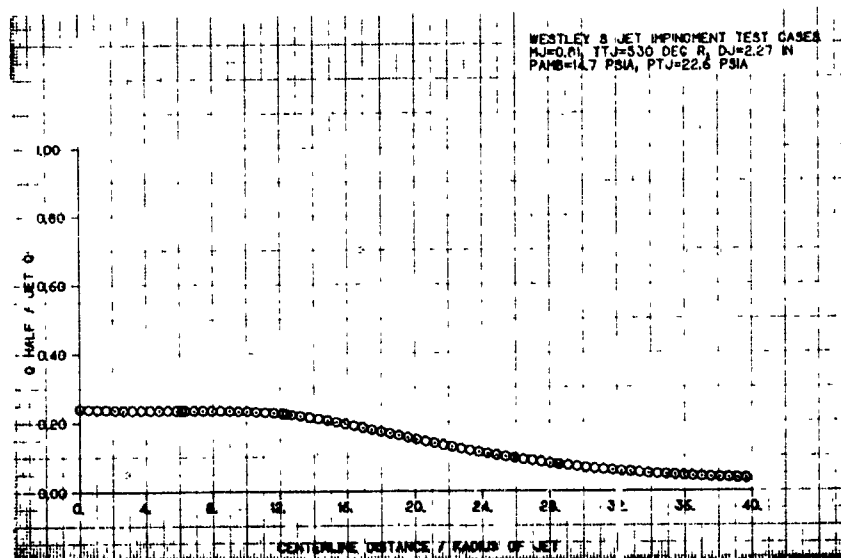
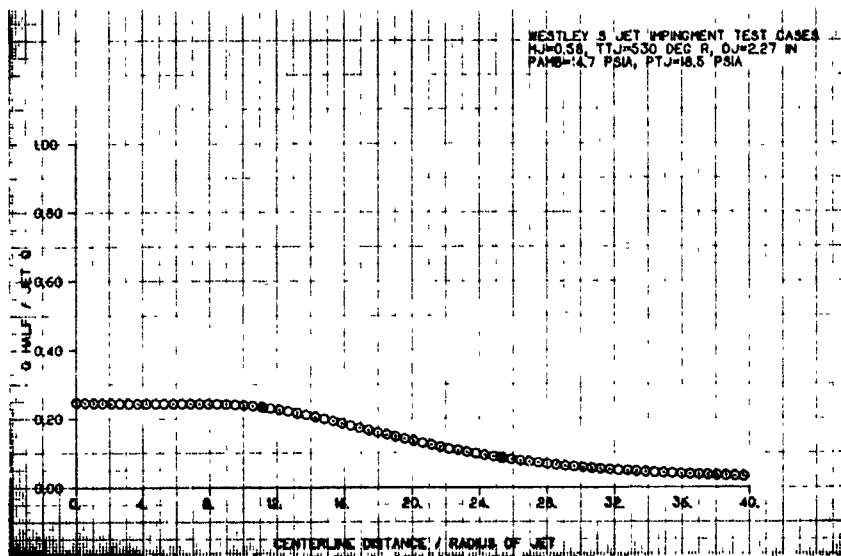


Figure K-4. Cont'd

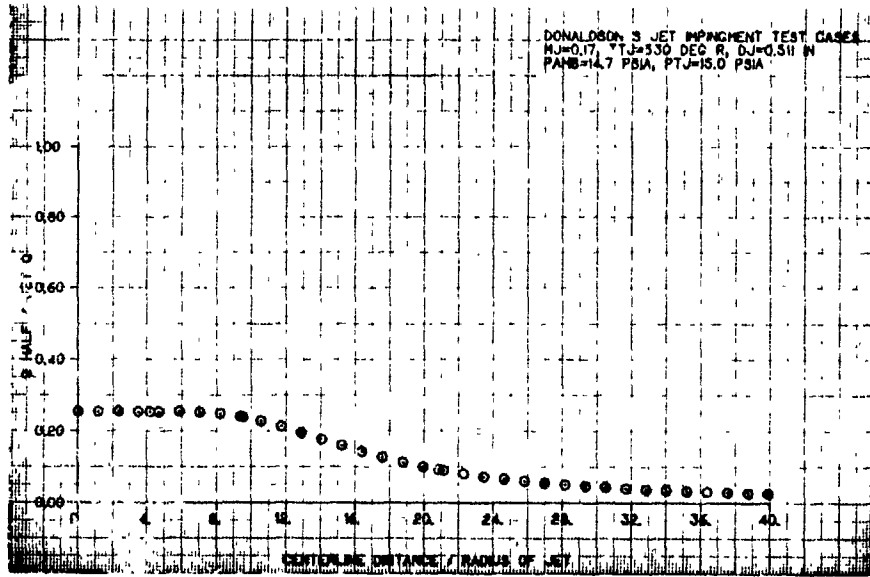


Figure K-4. Cont'd

REFERENCES

1. C. D. Donaldson and R. S. Snedeker, "A Study of Free Jet Impingement":
 - a. Part 1 - "Mean Properties of Free and Impinging Jets", J. Fluid Mech., Vol. 45, Part 2, 1971.
 - b. Part 2 - "Free Jet Turbulent Structure and Impingement Heat Transfer", J. Fluid Mech., Vol. 45, Part 3, 1971 (with D. P. Margolis).
2. D. R. Strong, T. E. Siddon and W. T. Chu, "Pressure Fluctuations on a Flat Plate with Oblique Jet Impingement", NASA CR-839, July 1967.
3. R. Westley, J. H. Wooley and P. Brosseau, "Surface Pressure Fluctuations from Jet Impingement on an Inclined Flat Plate", AGARD Conference Preprint No. 113, Symposium on Acoustic Fatigue, Toulouse, France, September 1972.
4. J. C. Yu, N. M. Reddy and J. L. Whitesides, Jr., "Noise and Flow Characteristics of an Externally Blown Flap", Interagency Symposium on University Research in Transportation Noise, Stanford University, March 1973.
5. J. S. Preisser and P. J. W. Block, "An Experimental Study of the Aeroacoustics of a Subsonic Jet Impinging Normal to a Large Rigid Surface", AIAA Paper No. 76-520, 1976.
6. J. C. Schroeder and J. K. Haviland, "Fluctuating Pressures in Flow Fields of Jets", NASA TM X-71979, February 1976.
7. J. S. Mixson, J. A. Schoenster and C. M. Willis, "Fluctuating Pressures on Aircraft Wing and Flap Surfaces Associated with Powered-Lift Systems", AIAA Paper No. 75-472, 1975.
8. R. E. Hayden, Y. Kadman and R. C. Chanaud, "A Study of the Variable Impedance Surface Concept as a Means for Reducing Noise from Jet Interaction with Developed Lift-Augmenting Flaps", NASA CR-112166, July 1972.
9. G. Neuwerth, "Acoustic Feedback Phenomenon in Subsonic and Supersonic Free Jets that Strike a Perturbing Body", Ph.D. Dissertation, Rhein-Westfolin, University of Technology, Aachen, West Germany, July 1973.
10. S. C. Crow and F. H. Champagne, "Orderly Structure in Jet Turbulence", J. Fluid Mech., Vol. 48, 1971.

REFERENCES (cont'd.)

11. A. Rubel, "Swirling Jet Turbulent Mixing and Combustion Computations", NASA CR-2231, 1973.
12. W. T. Chu, "Certification of the USC Jet Noise Facility", University of Southern California Report No. USCAE 131, 1975.
13. J. A. B. Wills, "On Convection Velocities in Turbulent Shear Flows", J. Fluid Mech., Vol. 20, 1964.
14. C. M. Ho and L. S. G. Kovaszny, "Acoustic Shadowgraph", The Physics of Fluids, Vol. 19, 1976.
15. U. H. Von Glahn and D. E. Groesbeck, "Peak Axial-Velocity Decay with Single and Multi-Element Nozzles", AIAA Paper No. 72-48, 1972.
16. G. K. Batchelor, "Pressure Fluctuations in Isotropic Turbulence", Proc. Camb. Phil. Soc. 47, 1951.
17. M. S. Uberoi, "Correlations Involving Pressure Fluctuations", NASA TN 3116, 1954.
18. B. E. Launder and D. B. Spalding, "Mathematical Models of Turbulence", Academic Press, 1972.
19. P. Bradshaw, "Effects of Streamline Curvature on Turbulent Flow", AGARDograph No. 169.
20. H. Planchon, "The Fluctuating Static Pressure Field in a Round Jet Turbulent Mixing Region", Ph.D. Thesis, Engineering Mechanics, University of Illinois, 1974.
21. R. Hammersley, "An Experimental Investigation of the Turbulent Characteristics of Coaxial Jet Flows and Their Role in Aerodynamic Noise Generation", Ph.D. Thesis, Nuclear Engineering, University of Illinois, 1974.
22. J. P. Shivers and C. C. Smith, Jr., "Static Tests of a Simulated Upper Surface Blown Jet-Flap Configuration Utilizing a Full-size Turbofan Engine", NASA TN D-7816, February 1975.